Paving the path between low- and high-mass star formation

Dynamics probed by *Herschel* far-infrared spectroscopy

Paving the path between low- and high-mass star formation

Dynamics probed by *Herschel* far-infrared spectroscopy

Proefschrift

ter verkrijging van
de graad van Doctor aan de Universiteit Leiden,
op gezag van Rector Magnificus prof.mr. C. J. J. M. Stolker,
volgens besluit van het College voor Promoties
te verdedigen op donderdag 18 juni 2015
klokke 12.30 uur

door

Irene San José García

geboren te Elche de la Sierra, Spanje
in 1986

Promotiecommissie

Promotores:	Prof. dr. E. F. van Dishoeck	
	Prof. dr. F. F. S. van der Tak	Rijksuniversiteit Groningen Space Research Organisation Netherlands
Co-promotor:	Dr. J. C. Mottram	
Overige leden:	Prof. dr. H. V. J. Linnartz	
	Prof. dr. H. Beuther	Max-Planck-Institut für Astronomie, Heidelberg
	Dr. M. Tafalla	Observatorio Astronómico Nacional, Madrid
	Dr. M. T. Beltrán	Osservatorio Astrofisico di Arcetri
	Prof. dr. H. J. A. Röttgering	

A mis padres y a mis hermanos

ISBN: 978-94-6259-719-8

Borja Cuéllar. Cover illustration and graphic design.

Contents

1 Introduction

1.1. Star formation process

"Stars form in molecular clouds". Behind this apparently simple and widely used sentence lies a whole field of astrophysics that is still maturing. To fully understand the star formation process, we must begin with the nurseries of stars, which are called Giant Molecular Clouds (GMCs).

GMCs are large (10-100 pc), relatively dense ($\sim 10^2$ cm^{-3}) and cold ($\sim$10 K) regions of the interstellar medium (ISM) (e.g. Bergin & Tafalla 2007) with a filamentary structure. The origin of this complicated network of filaments is related to supersonic turbulence in the ISM, which pushes and compresses low-density gas into layers (Myers 2009; André et al. 2014). This filamentary complex does not necessary create one single connected structure and only groups of filaments, called bundles, may have a common physical origin (Hacar et al. 2013). Those groups of velocity-coherent filaments that reach high enough densities to become gravitationally unstable will start contracting, becoming denser and eventually fragmenting into self-gravitating cores in hydrostatic equilibrium (see André et al. 2010). Therefore, the formation of a core is dominated by turbulence and gravity. This also means that not all GMCs will meet the right conditions to host the formation of a new generation of stars. Those clouds containing filaments which do no reach densities above the critical value will not fragment into cores, as, for example, in the Polaris molecular cloud (more details in André et al. 2010).

Gravitationally bound cores are located radially along the filaments and will grow while the filamentary structures contract from the inside-out and while there is still available surrounding gas (Myers 2013; Kirk et al. 2013; Henshaw et al. 2014). Large bundles of filaments and those which overlap and merge are the precursors of massive cores (Myers 2009; Schneider et al. 2012) while low-mass cores come from the gas of a single piece of filament. From this point on, once the precursor core of a future star is created, the evolution of these young stellar objects (YSOs) is tightly related to their initial mass and the specific environmental conditions which will shape their growth. This work aims to reveal if the paths that describe the evolution of low- (M<2 $M_\odot$), intermediate- (2≤M<8 $M_\odot$) and high-mass (M≥8 $M_\odot$) YSOs interlace, diverge or overlap.

1.1.1. Low-mass young stellar objects

Evolution and phases

The dense, small, and gravitationally-bound cores resulting from filament fragmentation will form low-mass stars, and are called *prestellar cores*. Due to the absence of a source of internal energy, these cores cool and contract reaching high densities and become gravitationally unstable. The strong gravitational pull on the surroundings draws more material in and gives rise to the collapse of individual cores.

In the centre of these collapsing cores a new object is formed: a *protostar*. This is deeply embedded in a thick envelope, and accretes material from the collapsing large-scale core through an accretion disk (Terebey et al. 1984). The protostellar phase then begins in which the luminosity of the central object is mostly derived from accretion process. Due to the rotation of the system and the conservation of angular momentum, this disk gradually flattens even if the infall of the surrounding material is isotropic. Moreover, the rotation and accretion of the central object together with the presence of magnetic fields triggers the formation of bipolar jets perpendicular to the disk, which remove part of the excess angular momentum accumulated during the accretion process.

These jets inject energy and momentum into the surrounding envelope, and dig cavities in it. Between the cavities and the envelope gas, an intermediate layer is created, called the outflow cavity wall. In this region, envelope material is entrained and exposed to winds and ultraviolet (UV) radiation from the forming star. The complex interplay between these structures (cavity, outflow cavity wall, jet, stellar wind) dictates the evolution of a protostar and the removal of surrounding cloud material. Their ensemble constitutes the molecular outflows (see simplified sketch in Fig. 1.1), and together with the protostar, envelope and disk form a *young stellar object* (YSO).

Up to this point, a YSO is considered to be in its earliest, most embedded phase: Stage 0 (André et al. 1993; Robitaille et al. 2006, 2007). The mass of the collapsing envelope is significantly larger

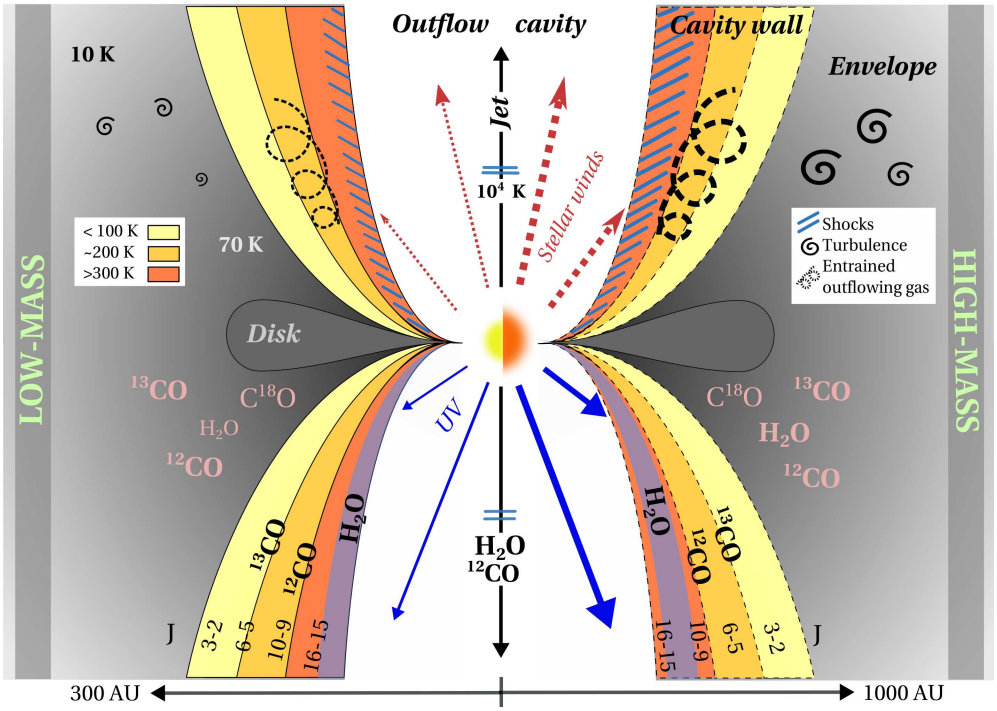

Figure 1.1: Cartoon illustrating the different components within the outflow, together with the temperature distribution and the location of the water and CO isotopologue emission in a low-mass (*left*-side) and high-mass (*right*-side) YSO. Turbulent motions are indicated with spirals, the entrained outflowing material with swirls and shocks with small blue lines. The UV radiation and stellar winds are indicated with blue and dotted red arrows respectively, which are thicker in the *right*-side of the figure to highlight that radiation and winds are more energetic for high-mass YSOs than for their low-mass counterparts. The disk also generates winds but those have not been added to the figure for simplification. The typical scale for a low- and high-mass YSO is indicated by the horizontal black arrow at the bottom of the figure.

than that of the central object, so these protostars are still deeply embedded in a dusty environment and are thus usually not detectable in the near-infrared. The bulk of the emission from these objects is instead at sub-millimetre/far-infrared wavelengths. In Stage 0 objects, the bipolar outflows are particularly collimated and energetic due to the intense accretion rate of material onto the central protostar and the dense ambient gas.

During the evolution of the protostar, the disk grows and flattens, as a consequence of infall from the envelope and the angular momentum conservation, while the surrounding envelope gradually disperses due to two opposite mechanisms: the continued accretion onto the central star-disk system and the dissipation caused by the action of the powerful outflows. The protostar is then in Stage I, in which the protostellar mass becomes larger than the envelope mass. In this phase a YSO is less opaque and UV radiation from the central forming star penetrates further into the envelope, heating the disk as well. Therefore, objects in the Stage I start to be effectively observable at mid- and near-infrared wavelengths unless the source is observed edge-on. The outflow cavity also widens due to the dissipation of the ambient gas.

The star formation process then continues and the YSO reaches Stage II, which marks the beginning of the pre-main sequence phase because the luminosity of the central object is now dominated by its photosphere rather than by accretion. Stage II is characterised by the total removal of the envelope material and the presence of a prominent circumstellar disk surrounding now a pre-main sequence star. The mass of the disk is larger than that of the envelope and larger grains start to grow inside the disk, becoming the building blocks for the formation of planetary systems once

Table 1.1: Observational selection criteria for the more embedded phases of low-, intermediate- and high-mass YSOs.

Category	Type	Observational characteristic	Refs.
LM	Class 0	$L_{\rm bol}/L_{\rm submm} > 200$; $T_{\rm bol} < 70$ K	1, 2
	Class I	$L_{\rm bol}/L_{\rm submm} < 200$; 70 $< T_{\rm bol} < 650$ K; $\alpha^a > 0.3$	1, 2, 3
IM	Class 0/Type I	$T_{\rm bol} < 70$ K; $-2 < p_{1.3{\rm mm}}{}^b \leq -1$	2, 4
	Class I/Type II	70 $< T_{\rm bol} < 650$ K; $-1 < p_{1.3{\rm mm}}{}^b \leq 0$	2, 4
HM	HMPO IR-bright	Weak radio continuum; > 100 Jy at 12 μm	5
	HMPO IR-quiet	Weak radio continuum; Weak at mid-IR (< 100 Jy at 12 μm)	5
	Hot core	Emission from complex organic molecules (COMs)	6

Notes. LM: low-mass protostars (M<2 $M_\odot$); IM: intermediate-mass YSOs (2≤M<8 $M_\odot$); HM: high-mass YSOs (M≥8 $M_\odot$).
(1) André et al. (1993). (2) Myers & Ladd (1993). (3) Lada & Wilking (1984); Greene et al. (1994). (4) Fuente et al. (1998, 2002). (5) van der Tak et al. (2000); López-Sepulcre et al. (2010). (6) Cesaroni (2005).
$^{(a)}$ Spectral index, α, is a proxy of the slope of the SED between 2 and 20 μm. $^{(b)}$ The spatial index, p, measures the variation of the column density with the distance from the forming star. The values of this parameter depend on the mass tracer. Here we present those derived from 1.3 mm continuum observations, $p_{1.3{\rm mm}}$.

the accretion and outflows are completely gone (Stage III). From this point, $\sim 10^7$ years after the collapse of the pre-stellar core, the central object starts burning hydrogen and reaches the main-sequence, becoming finally a low-mass *star*.

Observational classification

The mentioned Stages (0–III), which mark the evolution of a low-mass protostar, are defined based on how the mass of the different physical structures within the YSO (envelope, central protostar, disk) vary and compare with time. However, since estimating these masses is difficult, originally the classification was based on the observed characteristics of YSOs at each evolutionary stage, the so-called *evolutionary classes*. Therefore, the concept of Classes was created before that of Stages. The different Classes derived observationally follow the evolution of low-mass YSOs and attempt to identify their evolutionary stage.

As mentioned before, the bulk of the emission of a YSO, quantified by its spectral energy distribution (SED), moves to shorter wavelengths as the object evolves (Lada & Kylafis 1999; André et al. 2000). The shape of the SED also changes with the different evolutionary stages of a low-mass YSO. Therefore, several methods have been developed to characterise the shape of the SEDs in order to link observational classes with evolutionary stages (Evans et al. 2009). Some of these methods are the calculation of the spectral index, α, which measures the slope of an SED between 2 and 20 μm (Lada & Wilking 1984; Greene et al. 1994). Since they are heavily extincted, this slope cannot be obtained for the Stage 0 protostars. In addition, the ratio between the luminosity at 350 μm and the bolometric luminosity, $L_{\rm bol}/L_{\rm submm}$, provides information about the relative mass of the central object with respect to its envelope (André et al. 1993). Another useful parameter is the bolometric temperature, $T_{\rm bol}$, which is the temperature of a blackbody with the same mean frequency as that of the object's SED (Myers & Ladd 1993). Table 1.1 indicates the interval of values of these observational parameters which define the two protostellar phases of a low-mass YSO, i.e., Class 0 and Class I.

When using these methods it is important to realise that the shape of a protostar SED may be affected by the inclination of the outflow-disk system with respect to the line of sight. Therefore, the study of the source geometry is required to correct for this bias and Stages and Classes do not uniquely correlate (van Kempen et al. 2009b).

The observational characteristics and parameters used to classify intermediate- and high-mass YSOs into the different Classes of their embedded phases are also summarised in Table 1.1 (see below for discussion).

Observational advantages and challenges of low-mass YSOs

The low-mass star formation process is better understood and more widely studied than that of its more massive counterpart for several reasons. First, many examples of low-mass YSOs can be studied within few hundreds of parsecs (pc), so the different physical components of a single protostar (disk, envelope, outflow, etc.) start to be spatially resolved with the current observational facilities. Second, low-mass stars represent 70–90% of the total stellar population. In addition, the lifetimes of low-mass YSOs are relatively long with a protostellar duration (Stages 0 and I) of ∼0.5 Myr (Dunham et al. 2014), so it is possible to study targets in the different evolutionary stages. Therefore, the sample of low-mass protostars is large enough to enable a solid statistical analysis of their properties, and improve our understanding of their formation and evolution.

However, these objects present some challenging aspects that need to be considered. Even though a significant fraction of stars forms in clustered environments (e.g. Bressert et al. 2012), traditionally the observed low-mass protostars are in relatively isolated conditions. One of the reasons is that their observations are easier to interpret due to the lack of contamination from neighbouring sources. As a consequence, the low-mass star formation scenario described in Sect. 1.1.1 is founded on what has been learned from isolated targets, and may not represent how most of such stars form. To account for the effect of surrounding sources on the formation and evolution of protostars, it is important to complete the catalogs with low-mass YSOs in clustered environments (see Bressert et al. 2010 for cluster definition), creating a representative sample. From the observational point of view, the acquisition of high quality data for low-mass YSOs is a more arduous task, because these objects are faint and a single source may subtend up to an arc-minute on the sky due to their proximity. Therefore, longer exposure times are required to obtain data with the same quality level of their massive counterparts and maps are needed to encompass the entire protostellar system.

1.1.2. High-mass young stellar objects

Theories

There are several scenarios proposed to explain the formation of high-mass stars (M_*≥8 $M_\odot$) which are still under debate since each of those addresses different observational aspects. Two of the three generally-recognised theories are based on the accretion of material from the parent cloud, while a third model advocates for merging or coalescence of pre-formed systems.

The first scenario involving accretion mechanisms is that of *monolithic collapse* presented by McKee & Tan (2003), which is considered a scaled-up version of the low-mass process. Once the filaments compress and fragment into starless cores (M∼100 $M_\odot$) or starless clumps (M∼1000 $M_\odot$), the over-densities of molecular gas condense creating a central protostellar object with bipolar outflows and an accretion disk. During this process, the dense YSOs try to maintain the equilibrium between gravity and turbulence in order not to fragment. This requires injecting mechanical energy into these systems, which is thought to happen through two mechanisms: either with outflows and accretion shocks or by bringing turbulence from the outside of the core in a cascade down to smaller scales sizes, creating an isotropic pressure. The warm photo-sphere of the protostellar object produces energetic UV radiation which creates a strong radiation pressure and threatens to dissipate the ambient material and stop the accretion (Kahn 1974). This can be overcome if the accretion rates are few orders of magnitude faster than in the low-mass counterparts (10^{-4}–10^{-3} $M_\odot$ yr^{-1} versus 10^{-7}–10^{-5} $M_\odot$ yr^{-1} respectively). When this happens, the radiation pressure shifts to the direction perpendicular to the disk (the so-called flash-light effect) and powers the outflows (Krumholz & Thompson 2007; Kuiper et al. 2015). As for low-mass star formation, the accretion happens locally in this scenario, so the mass that will end-up in the star is gathered before the process begins and a single massive star, or a multiply gravitationally bound system, forms from a single massive protostellar core. Therefore, this hypothesis for high-mass star formation follows the same prescriptions as for their low-mass counterparts, but with larger values of turbulence and accretion in order to overcome the radiation pressure and stop the core from fragmentation.

The second scenario is that of *competitive accretion* by Bonnell et al. (1997, 2001), where the parent cloud is gravitationally bound rather than supported by turbulence. In this model, the cloud fragments into protostars which will move relative to the molecular gas. So, contrary to the previous scenario, the actual material constituting the future star comes from several parts of the cloud, and is accreted while the formation process is already ongoing. This implies that, except for a circumstellar disk and envelope, no other material is associated with the object prior to its formation, and the compression phase is short-lived and transitional between the fragmentation and collapse of the cloud. The size of the accretion domain (i.e., the region from which the gas can be gathered) depends on the mass of the YSO, as a direct consequence of its gravity, and on its location within the cloud. This latter aspect refers to the fact that most of the gas within the cloud settles on the regions in the deepest parts of the gravitational potential. The YSOs forming close to those denser areas will have more gas available to add to their accretion domain and the highest chances of becoming more massive (and therefore expand their domains). Since the gas reservoir is limited within the cloud due to its finite mass, the protostars compete for the cloud mass and the accretion domains among neighbouring sources may overlap. The foundation of this model is the observational fact that massive stars form in clustered environments (Zinnecker & Yorke 2007) and that only a small number of starless massive cores have been observed.

Finally, the model based on the *stellar mergers* (Bonnell et al. 1998; Bonnell & Bate 2002) was born to explain the formation of the most massive stars (M>30 $M_{\odot}$), which are also the least common. In this scenario, star formation occurs on cluster scales with the fragmentation of the cloud into many low-mass protostars. The accretion of material by these objects dissipates the turbulent component from the cluster, which starts contracting. This process moves the protostars closer together, increasing the stellar density of the region, especially in the centre of the cluster. With stellar densities of the order of 10^7 stars pc^{-3}, collisions between low-mass protostars become a realistic possibility, due to the decrease of the impact parameters, and these objects may merge forming rapidly rotating massive stars. This scenario implies longer formation timescales, because low-mass protostars need to be formed first, and involves violent phenomena since the stellar collision would cause the destruction of any outflow or disk, and even the ejection of stars from the system.

Independently of the process, in general the formation time of a high-mass star is observationally constrained to be of the order of a few times 10^5 yr, which constitute a few % of their total life-time (Churchwell 2002; Mottram et al. 2011).

Observational classification

The lack of agreement on how high-mass YSOs form goes together with a poorly defined evolutionary trail. However, as for the low-mass protostars, certain observational aspects and features recognised in the object emission have been traditionally used to distinguish high-mass YSOs into different phases (see Table 1.1 for some examples, Churchwell 1999; van der Tak et al. 2000; Beuther et al. 2007; Zinnecker & Yorke 2007). Even if the following classification is purely observationally based, a rough evolutionary trail can be extracted from it. However, the evolution within the embedded stages cannot be unambiguously distinguished partly because these intermediate phases can coexist together and are subject to observational biases (e.g., van Dishoeck & van der Tak 2000).

We start with the massive analogues of prestellar cores: *high-mass starless cores*. These are dense ($\sim$$10^5$ cm^{-3}) and cold (10–20 K) cores formed after the fragmentation of the cloud, with typical sizes of 0.3 pc (Beuther et al. 2002; Williams et al. 2004; Garay et al. 2004). Their lifetimes may be short, of the order 10^4–10^5 yrs, as suggested by their low numbers (Tackenberg et al. 2012). Although Infrared Dark Clouds (IRDCs), whose name derives from the fact that they show absorption against the bright mid-infrared galactic background (Simon et al. 2006), may fulfil the previous description, they are rather considered molecular clumps or filaments. In addition, IRDCs are not always associated with the formation of high-mass stars and conversely, many of them already show ongoing star formation, so they cannot be considered truly starless systems.

High-mass protostellar objects (HMPOs) can be considered a protostar or embedded pre-main

sequence star whose central source is still not burning hydrogen. While outflows, masers and infall signatures are seen in these objects, no or only very weak ionising radiation is detected. In addition, these objects present a massive envelope with a gradient of temperature and density towards the centre. Within this phase, two sub-types are distinguished: mid-infrared-bright and mid-infrared-quiet HMPOs, which correspond to those objects with and without bright emission in the mid-infrared (at 12 μm in particular, see van der Tak et al. 2000; Motte et al. 2007; López-Sepulcre et al. 2010). This may reflect a difference in evolutionary stage but could also be due to geometry.

When sub-millimetre emission from Complex Organic Molecules (COMs) such as $HCOOCH_3$, CH_3OH, etc. is present, then the massive YSO is considered a *hot molecular core* (Cesaroni 2005). These complex molecules are formed because the central forming star warms an increasingly large area around it as it gains mass. As a consequence, ice mantles are evaporated from grains, adding complexity to the chemical composition of the surrounding gas and triggering gas-phase reactions. COMs may be present already in the HMPO phase, but the emission from these molecules may be weak or not observable. This can be because of the dense and opaque circumstellar envelope in which these massive protostars are embedded or because of beam-dilution of the small hot-core region in single-dish observations (van Dishoeck & van der Tak 2000).

Eventually, the stellar atmosphere of the central object produces enough UV radiation to ionise the surrounding material forming an *hypercompact* HII *region* (HCHII) or *ultracompact* HII *region* (UCHII) (see Kurtz 2005; Hoare et al. 2007, and references therein). The former is generally smaller and denser than the latter and may be still confined by the remnants of the infalling material and disk (Tan & McKee 2003; Keto 2007). To complicate the picture, HMPOs and hot cores can contain hyper- or ultracompact HII regions.

If the ionisation caused by the central star keeps expanding, reaching pc scales, and disrupting the parent cloud, then the YSO is considered a *compact* HII *region* and *classical* HII *region*. In the latter phase the ionisation is global and the massive star can be observed in the optical and near-infrared regime.

Observational advantages and challenges of high-mass YSOs

The difficulties in acquiring a clear understanding of the formation of high-mass objects are related to several observational challenges and the intrinsic properties of these rare objects. Although high-mass YSOs are bright, requiring relatively short observational exposure times, they are located at large distances (few kpc away) and are embedded in massive and clustered environments with hundreds of surrounding protostars. Therefore, the different components of these objects (outflows, disk, envelope), as well as their physical conditions, are difficult to resolve spatially with the available telescopes and observational techniques. In addition, their envelopes are opaque during their entire formation. Finally, the emission from massive YSOs may be contaminated by the neighbouring objects, which adds another layer of complexity to interpret these observations from the physical and chemical point of view.

The high-mass star population is smaller than that constituted by their low-mass counterparts, which means that by default there are fewer massive YSO candidates available for study. In addition, once the accretion has stopped, they evolve rapidly, reaching the main-sequence (Churchwell 2002). This is the reason why it is hard to derive an evolutionary sequence for high-mass YSOs.

1.2. From low- to high-mass

Having put in context both low- and high-mass star formation, it is inevitable to lay out the hypothesis that high-mass YSOs may be scaled-up versions of their low-mass counterparts. The work presented in this thesis aims at achieving a more comprehensive understanding of the star formation process across the mass range by investigating in which conditions that hypothesis holds. As a first step, we present the main similarities and differences between low- and high-mass YSOs from the theoretical and observational point of view to build the ground for their comparison and

study. Intermediate-mass YSOs are introduced as a potential bridge between these two sub-groups of objects.

Similarities

Studies have shown that high-mass YSOs present collimated molecular outflows (Beuther et al. 2002; Shepherd 2005) and disks (Cesaroni et al. 2007) as low-mass protostars do, particularly up to 10^4 $L_\odot$ (see Fig. 1.1). These observations seem to support the turbulent core accretion model (McKee & Tan 2003), analogous to the low-mass star formation process but involving a larger turbulent regime, higher accretion rates and stronger stellar winds (McKee & Ostriker 2007a). Even if the major cause of the outflows and their driving agent may change with the mass of the YSO (see next section), the dynamical properties of their shocked and entrained material do not seem to be affected by the mass of the central forming star. In addition, the higher mass infall rates observed in their envelopes are consistent with the higher mass accretion rates required to form high-mass stars within $\sim 10^5$ yr.

High-mass YSOs form in denser environments and show larger fractions of companion objects than their low-mass counterparts, consistent with the scaled-up hypothesis. In addition, studies performed decades ago already presented correlations between the bolometric luminosity of the sources, considered as a proxy of their mass, and several physical parameters such as their bipolar mass outflow rate (Shepherd & Churchwell 1996), and their circumstellar envelope mass (Chandler & Richer 2000). This correlation extends over a large range of $L_{\rm bol}$ (from 0.3 to 10^5 $L_\odot$). Norberg & Maeder (2000), Behrend & Maeder (2001a) and Shepherd (2003) present a possible link between the accretion and outflow rates that does not depend on the mass of the central forming star. This relation suggests the presence of common mechanisms regulating the flows of both entrained and accreting material in these systems.

Differences

The prime difference between low- and high-mass YSOs lies in the definition of a protostar itself. A protostar is a gaseous system in hydrostatic equilibrium which is still not burning hydrogen and derives most of its luminosity from accretion. While low-mass objects spend all their evolution period in the embedded phase as true protostars, high-mass YSOs reach the main-sequence from their very beginnings, burning hydrogen during most of the formation process (Yorke & Bodenheimer 2008). In addition, the main-sequence temperature of the central object's photosphere and disks increases with stellar mass, which moves the peak of the stellar blackbody into the UV regime. This means that massive YSOs generate stronger UV radiation than their low-mass analogues. However, these distinctions are not a mere matter of definition, and they are not limited to the duration of protostellar, pre-main sequence and main-sequence phases (Blum 2005) or the peak frequency of the stellar emission. They influence other crucial aspects as well. To start with, while the luminosity of a low-mass protostar is dominated by the radiation generated by shocks during the accretion process, the luminosity of high-mass YSOs comes mostly from their warm photosphere. According to the protostellar and pre-main sequence phase definition for the low-mass objects, high-mass YSOs should then be considered pre-main or main-sequence stars (depending if they are already burning hydrogen or not). Furthermore, the energetic UV radiation in these latter objects, both coming from their stellar atmospheres and inner disks, ionises the surrounding gas creating an intense radiation pressure which could stop the accretion of material onto the forming star, as previous explained. It causes as well the photo-evaporation of the accretion disk and the protostellar envelope of the massive object and neighbouring lower-mass systems. These radiative forces play a significant role in the formation of massive YSOs but their effects are negligible for low-mass protostars. Another difference is related to the lifetimes of these objects, which are shorter because their contraction period is shorter than that of low-mass protostars (and comparable to the accretion time). In addition, high-mass YSOs also emit non-ionising radiation which causes the dissociation of molecules such as H_2 and CO. For this to happen, radiation above 11.0 eV needs to be generated, a range not accessible by low- and intermediate-mass YSOs.

The physical origin and the driving agent of molecular outflows is still under debate (Arce et al. 2007; Frank et al. 2014). For low-mass protostars, outflows are created as a consequence of the extra angular momentum dissipation in the form of bipolar jets and magneto-centrifugal forces of the stellar winds, mechanisms that keep powering this structure. On the other hand, for high-mass YSOs, the removal of angular momentum (jets) may be backed up by powerful stellar winds and strong radiation pressure (flash-light effect) as cause and driving mechanism of molecular outflows.

As for the theories explaining the star formation, the competitive accretion and stellar mergers scenarios acquire significance in clustered environments, more common among massive YSOs and for which a larger amount of protocluster gas needs to be accreted. These theories cannot be applied to the formation of low-mass objects in isolation and diverge from the scaled-up hypothesis. In addition, the clustering allows dynamical interactions between the forming YSOs (increasing the kinetic energy of the system) that may cause the ejection of objects (runaway OB stars, e.g. de Wit et al. 2005). This process does not seem to happen in regions that only form distributed, low-mass stars.

Finally, high-mass YSOs have a more significant effect on the environment than their less massive counterparts. Expanding HII regions could compress gas from neighbouring clumps and trigger a new generation of star formation or actually blow-out the gas of nearby systems destroying their change of becoming stellar nurseries.

Intermediate-mass YSOs as the bridge between low- and high-mass

Between 2 and 8 $M_{\odot}$ stands a sub-group of YSOs that shares specific properties from both their less and more massive counterparts, describing the transition between these two mass regimes (see review by Beltrán 2015). Far from making them an appealing type of YSOs for study, not many systematic observations towards them have been done since the interpretation of their emission becomes challenging given that these objects are at larger distances than their low-mass counterparts and fainter than massive YSOs. Therefore, their formation and evolutionary stages are uncertain.

Despite the small statistics, these YSOs are found both in isolated and clustered environments (Hillenbrand et al. 1995; Kumar et al. 2006), constituting the bridge towards the denser clusters in which high-mass objects form (Testi et al. 1999). The fragmentation of their parent cloud does not seem to depend on the luminosity of the core (Palau et al. 2013), and some intermediate-mass regions have a single luminous source (e.g., van Kempen et al. 2012; Palau et al. 2013) while others are composed of a collection of lower-mass YSOs (Beltrán et al. 2002, 2008; Neri et al. 2007; van Kempen et al. 2012).

In general, previous studies suggest that the formation mechanism of an intermediate-mass YSOs is a scaled-up version of that of their less massive counterparts. A protostellar phase may be possible to be defined for the intermediate-mass objects, but the analogous low-mass Class 0 and Class I phases are difficult to distinguish because their earliest stages remain deeply embedded within the dusty cloud (Nielbock et al. 2003). In addition, the structure of these objects seems to resemble that of a low-mass protostar since molecular outflows and circumstellar disks have been observed and detected for a handful of objects (see Takahashi et al. 2008; Beltrán et al. 2008; Sánchez-Monge et al. 2010; van Kempen et al. 2012, for some examples). Intermediate-mass sources are characterised with more massive and energetic outflows and larger accretion rates than those measured for low-mass protostars. However, the intrinsic complexity of these YSOs is similar to that of low-mass protostars and early-B type objects (Calvet et al. 2004; Fuente et al. 2001). Finally, the photosphere of intermediate-mass YSOs reaches high enough temperatures to emit UV radiation and trigger complex chemistry processes which lead to the formation of COMs (Fuente et al. 2005; Sánchez-Monge et al. 2010).

To summarise, there is still a lot of work to be done in order to characterise this peculiar and interesting group of YSOs. The study of these objects can shed some light onto the global understanding of the star formation process by marking the transition between several physical and chemical conditions present in these objects and in low- or high-mass YSOs (or in both).

Why does it matter?

Contraction times, radiation flows, formation theories, gravitational dynamics: it might look like these basic differences between low- and high-mass YSOs are more significant than their similarities, which would dispel the scaled-up hypothesis. However, the intrinsic complexity of each single object, the large and varied range of physical and chemical processes taking place across all these systems, and the observational biases discourage the hunt for any possible resemblance among YSOs. For this reason, any trend or common characteristic discerned across a varied sample of objects is worth a deeper investigation, because it may point to some fundamental physical properties of the star formation process, important enough to stand out over the inherent differences of each YSO. Examples and evidences are the presence of both outflows and disks in low-, intermediate- and high-mass YSOs (Beuther et al. 2002; Zhang et al. 2001; Cesaroni et al. 2007; Boley et al. 2012) and the similar dynamical conditions which seem to govern the shocked gas along the outflow cavity wall independently of the object mass (chapter 4). Therefore, the study of the star formation as a function of luminosity on scales of individual protostars could benefit the global understanding of this process for example, by identifying which specific physical and dynamical processes are not affected by the mass of the central forming star. This study could also help to discriminate among the different high-mass star formation theories and interpret observational biases due to source distances and telescope's limitations.

1.3. Methodology

1.3.1. Molecules as diagnostics

The spectrum of an object reveals information about its internal structure and properties (e.g., composition, temperature), in the same way that a piece of DNA does for a living creature. Molecular lines carry the information to interpret the physical and chemical conditions of YSO environments. Infrared and sub-millimetre spectroscopy are crucial techniques to dig inside these cold and embedded objects. Molecules emit or absorb radiation at specific frequencies, which are defined by the transition between two quantised energy levels. The distribution of the energy levels, also called energy diagram, is unique to each molecule, and the collection of possible transitions between energy levels constitutes its molecular fingerprint.

At infrared and sub-millimetre wavelengths two types of molecular transitions take place: *vibrational* and *rotational* transitions. The former are defined by oscillatory motions of atoms within the molecule which generate radiation at infrared wavelengths. The latter, designated with the quantum number J, are established by the rotation of the molecule around its axes. Rotational transitions are detected in emission in the far-infrared to millimetre regime only for gaseous species with a permanent dipole moment. Due to the relatively small spacing between rotational states, these transitions can be measured at high spectral resolution ($R = \lambda/\Delta\lambda \geq 10^6$), which allow us to resolve and interpret line profiles. While the frequency of a spectral line is influenced by the relative motion of the target and the observer, its broadening or more generally its shape depends on the motions intrinsic to the studied region within the YSO. Doppler-broadening is the dominant process that causes the broadening of these lines, since the motions of the gas particles with respect to the observer cause the emitted radiation to span a larger range of frequencies around its rest-frame value. Therefore, the specific physical properties of the gas being traced are reflected in the line shape of its molecular transitions, so that they generate distinct signatures.

Although detecting a transition already gives us information about the environmental conditions (e.g. presence of violent shocks, UV field regime, densities and temperatures present), it is the study of spectrally resolved line profiles that shed light on the velocity structure of the gas. This kinematic information can be extracted by decomposing the line profiles into different velocity components and by characterising their width, intensity and central frequency value. This procedure allows us to distinguish, for example, between quiescent gas, which moves at relatively low velocities with respect to the rest-frame, outflowing material, that reaches larger velocities (tens

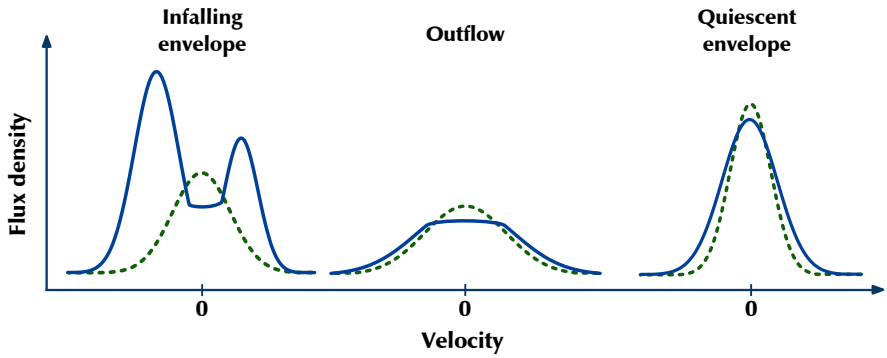

Figure 1.2: Comparison of the typical line profile signatures created by an optically thick (τ_ν >>1) and an optically thin (τ_ν <1) transition (solid and dashed line, respectively), which probe infall gas (*left*), material moving at large velocities in the outflow (*middle*) and quiescent gas from the envelope (*right*). Figure by M. Persson.

of km s^{-1}) and shocked gas along the jet, which appears largely offset from the source velocity (Bachiller et al. 1990; Kristensen et al. 2012; Mottram et al. 2014). In addition, if at a specific frequency the optical depth, τ_ν, of a molecular transition is larger than unity, (i.e., a photon at that frequency is more likely to be re-absorbed than to escape the system) then motions such as rotation, expansion and infall leave a characteristic and recognisable footprint in those molecular lines (see Fig. 1.2 for examples). However, in order to determine the origin and cause of rotational line emission, as well as its optical depth, it is crucial to know the intrinsic properties of the studied molecule and transitions: their critical densities ($n_{\rm cr}$), the molecules dipole moment, etc.. Some of the physical and chemical properties of protostellar systems such as excitation temperatures, densities and abundances can be derived by combining the spectroscopic analysis of several molecules and different rotational transitions.

Due to the importance of sub-millimetre spectroscopy to the study of star formation, in the last decades a lot of effort has been put into improving and expanding the available observatory facilities and in acquiring high quality data. All millimetre telescopes share similar technical principles and setups: a parabolic collecting area (or antenna), a receiver that amplifies the detected signal, and a spectrometer that processes this signal (a more detailed explanation of the observational process is given in Sect. 1.4). There are two types of millimetre telescopes: *interferometers*, composed of an array of antennas, and *single-dish*, with only one large parabolic collecting area, which deliver the data highlighting either the small or large spatial scales. Interferometers provide information on small spatial scales, necessary to resolve disks and disentangle the emission from distant and crowded systems. Single-dish telescopes cover larger spatial scales at high spectral resolution, crucial for achieving a more complete picture of large structures (outflows, envelope), and large-scale motions (infall or turbulence at envelope sizes). The spatial resolution of an interferometer is given by the distance between the antennas and that of a single-dish depends on the size of its parabolic collecting area. While interferometers filter out the emission from spatial scales larger than that given by the shortest distance between two antennas in the telescope array, the reduced angular resolution of single-dish telescopes smear the emission coming from small regions over the resolution element, complicating the interpretation of the data.

In this thesis we present single-dish velocity-resolved data. We mitigate the lack of spatial resolution by studying molecular tracers which are known to probe specific physical conditions in YSOs and structures of protostellar systems that may be smaller than the beam resolution. With this method we keep the large-scale view while information on smaller spatial scale regions is added indirectly. The molecular tracers selected to disentangle the dynamical conditions of envelope and outflows are ^{12}CO, ^{13}CO, C^{18}O and H_2O. Their characteristics and potential are further explained in the next section.

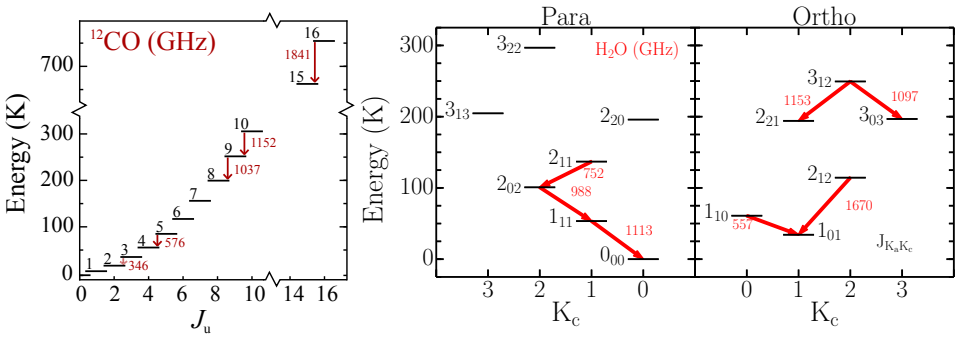

Figure 1.3: (*Left*) ^{12}CO energy diagram up to J=16. (Figure updated by M. Persson from U. A. Yıldız Phd thesis). (*Right*) Para- and ortho-water energy diagram. The ^{12}CO and H_2O transitions observed with *Herschel*-HIFI are indicated with red solid arrows while the ^{12}CO $J = 3$–2 transition, observed from ground-based telescopes, is marked with a red dashed line. The frequency of each of these rotational transitions is shown in GHz.

1.3.2. CO and H_2O as key molecular tracers

After H_2, the second most abundant molecule in our Universe is carbon monoxide, a pivotal molecule in many fields of astronomy. CO is present in all parts of protostellar systems: from the envelope, to the bipolar outflow and disk. It has been widely targeted by infrared and sub-millimetre observations of Galactic and extragalactic objects (Kennicutt & Evans 2012, and references therein).

CO has traditionally been observed not only because it can be detected throughout the YSO, but also because it is a reliable tracer of the dynamical and excitation properties of the these environments as a result of its intrinsic properties. CO has a small permanent dipole moment ($\sim$ 0.1 Debye). At far-infrared and sub-millimetre wavelengths, the critical densities of the rotational transitions are relatively low, so CO is easily excited by collisions with H_2, even in low density regions. In these conditions, the CO gas can be safely considered to be in local thermal equilibrium (LTE), which simplifies the interpretation of the rotational lines because the excitation temperature, $T_{\rm ex}$, is then equal to the kinetic temperature of the gas, $T_{\rm kin}$. Thus, the measure of different CO rotational transitions provides an excellent estimate of the gas kinetic temperature of the system.

The most abundant CO isotopologue (therefore producing the strongest lines) is $^{12}C^{16}O$ (^{12}CO). To probe the cold gas, both in the envelope and outflow, low-rotational ^{12}CO transitions ($J\leq3$) are used, with upper energy levels, $E_{\rm up}$, between 10–50 K. This means that, since a pure-CO ice layer deposited on a grain evaporates at $T_{\rm eva}\simeq$20 K (Collings et al. 2004; Öberg et al. 2005; Bisschop et al. 2006), the bulk of the observable CO at sub-millimetre wavelengths is in the gas phase, except maybe in the coldest gas ($T_{\rm kin}<$20 K). However, the inner regions of the envelope closer to the actual forming star are hidden by these outer colder layers, as well as most of the entrained and shocked material across the outflow are warmer (50–300 K), so rotational transitions with higher $E_{\rm up}$ are required. The emission of mid-J ^{12}CO lines ($4\leq J\leq10$) around the targeted frequency probes warmer, quiescent envelope material. On the other hand, the entrained outflowing material, which moves at larger velocities with respect to the rest-frame of the observer, is traced by the blue- and red-shifted emission with respect to the source velocity (Snell et al. 1980). This weaker emission covering a large range of frequencies is generally identified as the line-wings of the detected emission line including the higher-J ones (e.g., Curtis et al. 2010; Yıldız et al. 2012, 2013). Finally, even warmer regions are then traced by higher-J ($J>10$) lines (van Kempen et al. 2010; Green et al. 2013; Karska et al. 2013; Manoj et al. 2013) and violent processes, such as shocks along the outflow or jet, are probed by the line wings of ^{12}CO transitions (Kristensen et al. 2013). The different values of the upper energy levels and the frequency of selected low-, mid and high-J ^{12}CO rotational transitions are given in the left energy diagram of Fig. 1.3.

The rotational emission lines of the CO isotopologues ^{13}CO and $C^{18}O$ are also detected in pro-

tostellar systems. These isotopologues show similar energy level diagrams at sub-millimetre wavelengths to ^{12}CO with comparable intrinsic molecular properties. Given the characteristic isotopic ratios, ^{13}CO and C^{18}O are less abundant and the emission lines are usually weaker and narrower than those measured for ^{12}CO. Since its lines are optically thin and not contaminated by outflow emission, C^{18}O is a good tracer of quiescent envelope material, especially the high-J transitions which probe inner warmer areas. ^{13}CO emission probes the dense envelope material as well, but part of the emission is associated with gas located at the edges of the outflow walls which is heated by UV radiation from the forming star (Spaans et al. 1995; van Kempen et al. 2009a; Yıldız et al. 2012). In addition, by assuming a CO/H_2 abundance ratio, an estimate of the molecular gas mass of the system can be made. To conclude, the study of the ^{12}CO, ^{13}CO and C^{18}O rotational lines provides an important and detailed picture of the protostellar structure, its dynamics, temperature and gas distribution and outflow activity.

From the chemical and observational point of view, H_2O is a more challenging molecule than CO. Water is one of the dominant compounds of oxygen and the most abundant species in ice mantles (van Dishoeck et al. 2013). Due to its high binding energy, H_2O freezes out on the grains at temperatures below 100 K. This means that water is present in the outer colder part of protostellar envelopes mainly in the solid phase and mostly in warm regions of YSO environments in its gaseous form. For this reason, its rotational lines not only probe the warm gas but they also reflect the significant abundance variations between regions of the YSO at different temperatures.

Water has a larger dipole moment (1.85 Debye) and Einstein A coefficients than CO, so the critical densities are also larger. This means that H_2O shows intense line emission even when sub-thermally excited. Since the two hydrogen spins can be oriented either perpendicular or parallel, this molecule comes in two forms: para- and ortho-H_2O. The right panel of Fig. 1.3 shows the H_2O energy diagrams of the para and ortho ladders together with the frequencies of selected transitions. Water molecules are generally formed through three routes in the gas phase: at high- and at low-temperatures, and on the grains (e.g. Ioppolo et al. 2008, 2010; Cuppen et al. 2010; van Dishoeck et al. 2013; Lamberts et al. 2014). However, since a considerable water reservoir is in the ice mantles, violent processes involving high velocity material, such as shocks, can also add H_2O into the gas phase through sputtering from the grain (Codella et al. 2010; Van Loo et al. 2013; Neufeld et al. 2014; Suutarinen et al. 2014). Therefore, significant water abundances are likely to be measured in the outflows, in particular in the outflow cavity or along the jets where the stellar winds or the material ejected in the outflow system encounters the entraining gas and powerful shocks take place (see Fig. 1.1). Because in these types of dramatic processes the gas reaches high temperatures and velocities, this gas can potentially be traced by the emission of the line-wings of H_2O rotational transitions (Kristensen et al. 2010, 2012, 2013; Nisini et al. 2010; Mottram et al. 2014; Santangelo et al. 2014).

In summary, due to its properties, water is a robust tracer of the warm gas, the energetic processes present in the star formation regions, such as shocks along the outflows, and the dynamical structures of these environments.

1.3.3. Analysis tools

In the case of Local Thermal Equilibrium (LTE), i.e., when the excitation of molecules is dominated by collisions, the kinetic temperature of the gas can be approximated to the measured excitation temperature $T_{\rm ex}$. The value of $T_{\rm ex}$, as well as other parameters such as the column density, $N_{\rm tot}$, can be derived from the line profiles of several rotational transitions. However, when the LTE conditions cannot be assumed because the system is sub-thermally excited (its density is lower than a critical value $n_{\rm cr}$ and the de-excitation is dominated by radiation rather than collisions) and the level populations cannot be characterised by a single excitation temperature, then the non-LTE approach has to be taken (see review by van der Tak 2011).

Since the information about chemical abundances, temperature and density distribution, velocity structure and dominant motions (turbulence, expansion, infall) is coded into the observed line profiles, we need radiative transfer tools to model and compare them to the data, so that these parameters can be constrained.

In general, any radiative-transfer code solves the radiative transfer equation (Eq. 1.1), which describes how an emitted photon, at a specific frequency, interacts with the particles met along a straight path in the line of sight.

$$\frac{dI_\nu}{dz} = -\kappa_\nu I_\nu + j_\nu, \tag{1.1}$$

The observed intensity, I_ν, is the result of the balance between absorption and emission (which fractions are given by the κ_ν and j_ν coefficients, respectively), after integrating along the line of sight travelled by the radiation, whose coordinates are defined by z. The sources of absorption and emission are microscopic processes causing the excitation and de-excitation of the particles along that path. These processes are spontaneous emission, stimulated emission, absorption of radiation as well as particle collision which can excite or de-excite the gas particles. The probability of these processes are determined by the Einstein A and B coefficients and the collisional rate coefficient C, values which are unique to each molecular transition and collisional partner.

The radiative transfer equation across a system in non-LTE can be solved by including those observed molecular transitions for which the above coefficients are available. Usually the problem needs to be simplified with a series of assumptions, as we will mention below. Depending on which parameters need to be constrained, on the structure of the medium, and on the geometry of the problem, several radiative transfer codes have been developed.

For systems that can be considered isothermal and homogeneous, the single kinetic temperature and column density value characterising the medium can be constrained using one-dimensional non-LTE radiative transfer codes such as RADEX[1] (van der Tak et al. 2007). Different geometries of the emitted system can be assumed as well, from static spherical to plane-parallel (also called "slab"). As output, this code provides the line intensities, optical depth and excitation temperatures of the studied molecular transitions. These are then compared to those calculated from the observations. An example of the power of combining observations and these radiative transfer codes is given in chapter 4, where the excitation conditions of the post-shocked material along the cavity outflow are estimated from the analysis of the excited water lines and assuming a slab geometry of the water emitting area.

When the distribution of temperature, density and velocity cannot be assumed to be uniform across the system, or the kinematical structure needs to be derived, or the effects of turbulence, infall, expansion, and rotation on the emission lines need to be determined, more complex codes solving the radiative transfer and excitation of molecular lines are required. In this thesis we use the spherically symmetric non-LTE radiative transfer code RATRAN (Hogerheijde & van der Tak 2000) to constrain the dynamics of protostellar envelopes using rotational lines of optically thin and thick tracers (chapter 3). The spherical envelope under study is subdivided in cells, and for each cell it is possible to define the specific temperature, density (as explained in the next paragraph) and velocity structure. This code also generates synthetic line profiles that are compared to the profiles of the observed transitions. In addition, the level populations and optical depth of these transitions are also provided. The potential of this code is based on the freedom to define the physical structure of a system with spherical or axial symmetry, and on the possibility of constraining the dominant motions causing the broadening of the observed line profiles.

The density of a protostellar envelope, n, varies with distance, r, from the central forming star as a power-law with index p ($n \propto r^{-p}$). This index is determined for each YSO from the fitting of the far-infrared SED combined with the spatial extent at 450 and 850 μm. Those are the wavelengths at which the dust re-emits most of the absorber stellar radiation. Therefore, the luminosity of the central star and the properties of the dust (opacity, size, etc.) define the dust temperature. Continuum radiative transfer codes are used to derive the temperature and density distribution of a protostellar envelope by assuming a power-law density distribution with a given p index. In those codes, the gas and dust temperature are considered equal and further parameters, such as envelope size and dust opacities, need to be defined. DUSTY (Ivezić & Elitzur 1997) or HOCHUNK3D (Whitney et al. 2013; Robitaille 2011, hereafter WR) are widely used codes to constrain the temperature and density profiles of low- and high-mass YSOs respectively. In particular, DUSTY models the

[1] http://home.strw.leidenuniv.nl/~moldata/radex.html

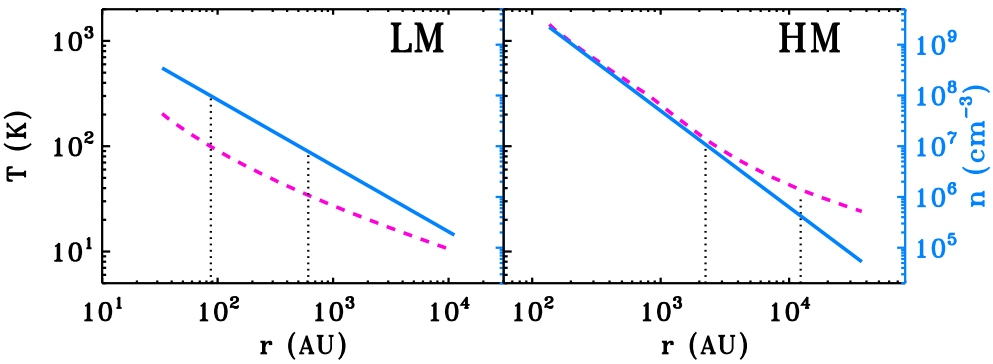

Figure 1.4: Temperature (T, pink dashed line) and density profiles (n, blue solid line) of a low-mass (LM; *left*) and a high-mass (HM; *right*) YSO as a function of the radius of the modelled envelope (distance from the central star). The vertical black dotted lines indicate the radii at which the gas and dust temperature reaches 100 and 35 K respectively.

observed SED sub-millimetre and spatial distribution of an object by modifying the previously mentioned parameters and using the opacity values calculated by Ossenkopf & Henning (1994) (further information of the procedure in Kristensen et al. 2012). Examples of the density and temperature profile for a low- and a high-mass YSO are shown in Fig. 1.4 (for more details read chapter 3).

1.4. *Herschel* Space Observatory - HIFI

High-J CO lines cannot be observed from the ground due to atmospheric absorption at sub-millimetre wavelengths, so the warmer inner regions of protostellar systems are not observable with this species. In addition, water cannot be observed in Galactic sources except in a few weak $H_2^{18}O$ lines, which prevents us from achieving a more comprehensive picture of the dynamical structure of YSO environments, especially across the outflows. However, in May 2009 the *Herschel* Space Observatory (Pilbratt et al. 2010), an ESA cornerstone mission, was launched which aimed to explore the molecular Universe at far-infrared and sub-millimetre wavelengths at significantly greater sensitivity and resolution than any previous space telescope (e.g. *ISO*, *SWAS*, *ODIN*, *IRAS*). Its scientific objectives were focused on studying dusty and relatively cool objects; particularly the birth of stars and their interaction with the interstellar medium, and the formation and evolution of galaxies in the early Universe.

Herschel was equipped with a 3.5 m diameter primary mirror and three instruments: a very high resolution spectrometer, the Heterodyne Instrument for the Far Infrared (HIFI; de Graauw et al. 2010); an imaging photometer and integral field line spectrometer, the Photodetector Array Camera and Spectrometer (PACS; Poglitsch et al. 2010); and an imaging photometer/Fourier transform spectrometer, the Spectral and Photometric Imaging Receiver (SPIRE; Griffin et al. 2010). The operational lifetime of the *Herschel* Space Observatory finally concluded on June 17, 2013.

This thesis primarily focuses on the analysis of HIFI observations, therefore a more detailed description of this instrument is given. This single-pixel heterodyne spectrometer was designed to provide very high spectral resolution, between 0.3 and 0.03 km s^{-1} (1.1 and 0.125 MHz), over a frequency range of approximately 480–1250 GHz and 1410–1910 GHz (625–240 and 213–157 μm). The diffraction limit at a frequency of 548.8 GHz was 42″, reaching 21″ at a frequency of 1101 GHz. This angular resolution was a factor of 3–5 higher than that achieved by previous sub-millimetre space missions such as *SWAS* or *Odin*.

At sub-millimetre wavelengths there are no good amplifiers available to amplify the detected weak emission. However, HIFI combines the heterodyne technique with superconducting detector

technology to be able to convert the detected signal to lower frequencies, for which amplifiers are available, while preserving the initial spectral information. The instrument worked by mixing the incoming signal, f_s, with another very stable and monochromatic signal, generated by a local oscillator, f_{LO}. The output is a much lower frequency signal called intermediate frequency (IF = $| f_s - f_{LO} |$), which is easier to amplify at radio wavelengths and is then sent to the spectrometer for spectral analysis. Therefore, the specific IF frequencies could be generated by two different source signals: $f_s > f_{LO}$ or $f_s < f_{LO}$. Considering this for a range of incoming frequencies, each channel of the spectrometer was sensitive to two frequency values at the same time, so two superimposed portions of an object's spectrum were measured resulting in the *double sideband* (DSB) reception. The portion of the source spectrum above the f_{LO} is designated as upper sideband (USB) and that below f_{LO} as the lower sideband (LSB).

The mixing process was carried out in 7 heterodyne receiver bands with dual horizontal (H) and vertical (V) polarisations. They were divided into two groups according to the mixer device used and the instantaneous frequency covered. Bands 1 to 5 use Semiconductor-Insulator-Semiconductor (SIS) mixer technology, which operated at 480–1250 GHz with a bandwidth of 4 GHz. Bands 6 and 7 have Hot Electron Bolometer (HEB) mixers and those covered the 1410–1910 GHz frequency range with a bandwidth of 2.4 GHz.

HIFI had four spectrometers or backends, namely; a Wide Band Spectrometer (WBS) and a High Resolution Spectrometer (HRS) with two polarisations each, horizontal (H) and vertical (V). The WBS was an Acousto-Optical Spectrometer (AOS) which covered the full IF range available at a single resolution of 1.1 MHz. The HRS was an Auto-Correlator System (ACS) with several possible resolutions (from 0.125 to 1.00 MHz). The bandwidth of this latter backend could be split to sample more than one portion of the available IF range.

Finally, HIFI provided three *Astronomical Observing Templates* (AOTs): "single pointing" (AOT I); "mapping" (AOT II) and "spectral scanning" (AOT III). For each of them there were different observing modes namely dual-beam switch (DBS), position switch (PSw), frequency switch (FSw) and load chop.

The HIFI WBS single pointing observations presented in this thesis were taken in dual-beam switch mode. This means that for each source only one position on the sky was targeted at one specific frequency, and during the observation the beam was moved to two reference positions $3'$ either side of the source position using fast chopping.

Further details on the reduction and scientific interpretation of HIFI data are given in the Observation sections of chapters 2, 4 and 5. In addition to the HIFI observations, spectrally resolved ^{12}CO and C^{18}O $J = 3$–2 data from ground-based facilities such as the JCMT and APEX are included to extend the analysis of these YSOs to their colder, lower density regions, achieving a more comprehensive picture of these embedded systems.

1.4.1. WISH

Water is present not only in the coldest regions of protostellar environments constituting the ice mantles of grains, but also in gaseous form probing warmer material and energetic processes such as shocks along the outflows. For this reason, the guaranteed-time *Herschel* key programme "Water In Star-forming regions with *Herschel*" (WISH[2]; van Dishoeck et al. 2011) observed this molecule and other species such as CO with unprecedented spectral and angular resolution with the purpose of investigating the physical and chemical structure of a large and diverse sample of sources related to star formation. In particular, this programme follows water abundances, kinematics and excitation through the evolutionary sequence of ∼80 sources (from pre-stellar cores to gas-rich disks) and across a vast range of luminosities (L_{bol} from < 1 to $> 10^5$ $L_\odot$).

Single point observations and small maps of H_2O, its less-abundant isotopologues ($H_2^{17}O$ and $H_2^{18}O$) and chemically related species such as OH, H_2O^+ and H_3O^+ were targeted with HIFI and PACS around the protostar position and the outflows. The study of water in the initial embedded

[2] https://www.strw.leidenuniv.nl/WISH/

environments, crucial to understand not only the formation of protoplanetary systems but ultimately also the origin of life, is complemented with observations of high-frequency lines of ^{12}CO, ^{13}CO and C^{18}O. These molecules not only help to improve the dynamical knowledge of protostellar systems and the gas kinetic temperature, but also provide a reference frame to determine the abundance of species such as H_2O with respect to H_2 and ensure a self-consistent data set for analysis.

Complementing the WISH project, the water and CO HIFI data from two follow-up *Herschel* programmes are also included in chapter 5. The first one, the "William Herschel Line Legacy" survey (WILL; PI: E.F. van Dishoeck, Mottram et al., in prep.) observed water and CO for an unbiased sample of 45 low-mass protostars. The second, "Water emission from outflows and hot cores in the Cygnus X protostars" (PI: S. Bontemps), focused on observing three water transition across the 86 most luminous YSOs across the Cygnus X region. The aim of including these additional programs is to expand the study initiated by WISH and test the significance of the achieved results by improving the statistics of the analysis with a more uniform sample of YSOs filling the gaps left by WISH, especially from the observational point of view. Further details about these two surveys are given in chapter 5.

1.5. This thesis

This thesis presents velocity-resolved HIFI H_2O data and mid-J ($J \leq 10$) ^{12}CO, ^{13}CO and C^{18}O observations for 51 embedded YSOs drawn from the *Herschel* key programme WISH. In addition, low-J CO transitions from ground-based single-dish telescopes are included to compare the physical conditions of the inner and warmer regions of YSO environments to those of the outer colder parts. The sample of objects, composed of 26 low-mass protostars, six intermediate-mass sources and 19 high-mass YSOs, covers a large range of bolometric luminosities $L_{\rm bol}$ (from < 1 to $>10^5$ $L_\odot$), several evolutionary stages within the embedded phase and different physical scales (as compared in Fig. 1.4).

The purpose of this work is to investigate the physical and dynamical structure of protostellar environments across a wide luminosity range (as illustrated in Fig. 1.5) by characterising the H_2O and CO spectra in terms of line profile and line luminosity. The studied species are unambiguous tracers of specific physical conditions within the YSO. In addition, excitation and kinematical information of certain protostellar regions is extracted from the emission lines using the non-LTE radiative transfer codes RADEX and RATRAN. The ultimate goal is to broaden our understanding of the star formation process without imposing luminosity boundaries, and to put in context these processes on Galactic and extragalactic scales.

The main questions we address with this work are:

- Which type of information can be extracted from a basic analysis of the CO line profile and line luminosity? How do CO lines change as a function of luminosity and what does that tell us? Is there any trend, proxy of an underlying mechanism, measurable from low- to high-mass YSOs?
- Do motions such as infall and turbulence scale with the mass of the YSOs? What are the main non-thermal motions which cause the broadening of the C^{18}O lines? How different are the velocity and C^{18}O abundance structures from low- to high-mass?
- From which regions of the YSOs does the water emission originates across the studied sample of YSOs? What dynamical conditions in the outflow cavity walls can the excited water lines constrain? Are high-J (J>10) CO transitions tracing shocked gas as water does in low-, intermediate- and high-mass YSO environments? How are the water excitation conditions affected by the mass of the central forming star?
- Are the results obtained from the WISH programme biased by the sample selection or can they be extrapolated to more standard sources? What can we learn from large surveys and how do we link with extragalactic samples?

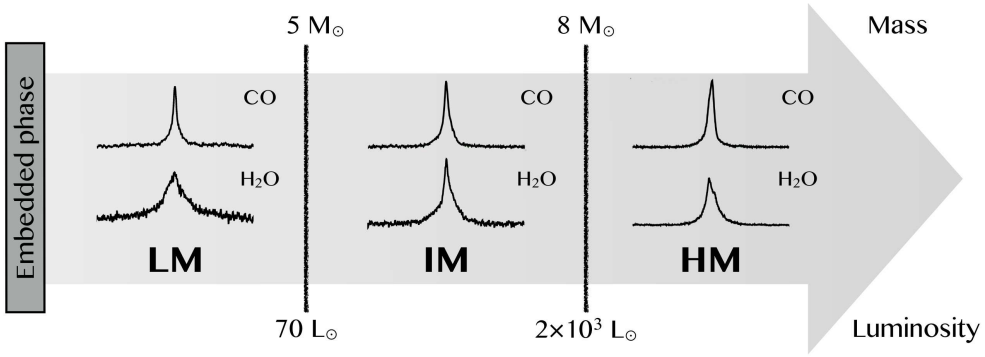

Figure 1.5: Averaged and normalised ^{12}CO $J = 10$–9 (*top*) and H_2O 2_{02}-1_{11} (*bottom*) spectra for the WISH low-mass Class 0 protostars (LM), intermediate-mass (IM) and high-mass YSOs (HM). All spectra are plotted on the same velocity range (from -100 to 100 km s^{-1}) to compare the observations of these two species across the entire mass and luminosity range studied with WISH. The arrow indicates the adopted mass and luminosity values that delimit each sub-group of YSOs. This figure illustrates the focus of this thesis: the study of the mass/luminosity trail with observations of CO and water.

These questions are addressed across the chapters of this thesis, which are summarised as follows:

Chapter 2 presents the ^{12}CO, ^{13}CO and C^{18}O velocity-resolved data for the WISH sample of YSOs (see San José-García et al. 2013). For low- and intermediate-mass objects the width of the C^{18}O line profiles increases at higher-J transitions, which indicates that either the level of turbulence is larger in the inner regions of the envelope or other non-thermal motions are at work broadening the profile (see chapter 3). For massive YSOs, this width does not vary with J. Finally, the distance-normalised line luminosity of the HIFI CO lines correlates with the source bolometric luminosity out to extragalactic scales. This suggests that, independently of the mass of the YSO, high-J CO transitions primarily trace the amount of dense gas associated with the system (see Fig 1.6).

Chapter 3 aims to quantify the contributions of turbulence and infall to the broadening of line profiles of optically thin low- and high-J C^{18}O transitions and optically thick HCO$^+$ lines for a sub-sample of low- and high-mass YSOs (San José-García et al. submitted). The non-LTE radiative transfer code RATRAN is used for this purpose. In order to reproduce the analysed line profiles, both infall and turbulent motions are required. The turbulent width increases with $L_{\rm bol}$, but for the infall motions this trend is only seen in sources with $L_{\rm bol} > 10^3$ $L_\odot$. In addition, for these high-mass YSOs, the best-fit infall component is slower than the maximum infall velocity estimated from their assumed stellar masses. Finally, the derived best-fit values of the turbulent velocities are slightly larger than those calculated for systems in virial equilibrium, which suggests that turbulence prevails over the gravitational potential once star formation is ongoing.

Chapter 4 shows the excited water transitions observed across the WISH sample of YSOs and compares the results to those mid-J ($J\leq10$) and high-J ($J>10$) ^{12}CO transitions (San José-García et al. submitted). More than 60% of the water emission originates from non-dissociative shocks in the outflow cavity wall. The remaining emission comes from dissociative shocks for low-mass Class 0 objects and from the quiescent envelope in the case of Class I protostars, intermediate- and high-mass YSOs. For low-mass protostars, only high-J ($J>10$) CO rotational transitions seem to probe similar kinematical properties to those traced by H_2O. In the case of massive YSOs, the gas traced by both the CO $J = 10$–9 and 16–15 lines is linked to that probed by the excited water lines, probably as a consequence of the injection of strong turbulence by the UV radiation of these massive objects (see bottom-right quadrants of Fig. 1.1). A correlation between the line luminosity and $L_{\rm bol}$ is also measured for these H_2O lines and extended to extragalactic scales.

Chapter 5 presents a similar study as discussed in chapter 4 but for a larger and unbiased

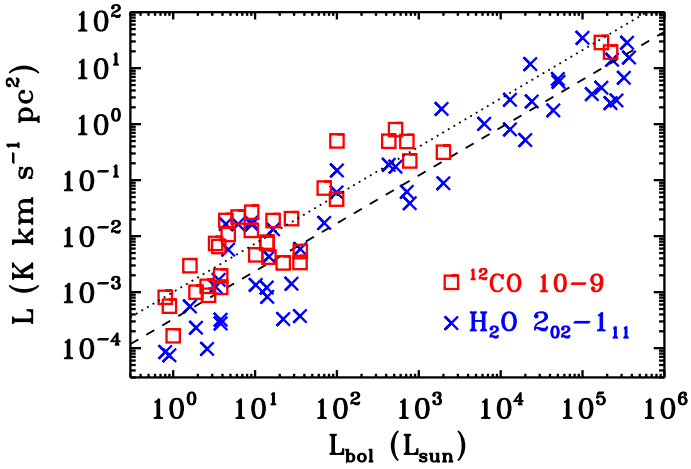

Figure 1.6: Line luminosity of the ^{12}CO $J = 10$–9 (red square symbols) and H_2O 2_{02}-1_{11} (988 GHz; blue crosses) transitions versus the bolometric luminosity of the source, L_{bol}. Strong correlations between L_{bol} and the line luminosity of the ^{12}CO (dotted line) and H_2O (dashed line) transitions are measured.

sample of YSOs composed of 45 low-mass protostars and 86 embedded objects located in the Cygnus X star-forming region. By increasing the sample, the results obtained for WISH can be evaluated over a more statistically supported framework. Similar results as for WISH are achieved when analysing the water line profile of this sample, in particular those regarding the cavity shock component. This work is part of San José-García et al. in preparation.

Future outlook

The *Herschel Space Observatory* unveiled the inner, warmer regions of YSOs environments by observing high rotational transitions of several molecules such as water, a tracer of dynamically active processes. The obtained results, especially from large survey programmes, help to broaden our understanding of the star formation in Galactic and extragalactic scales. However, still many questions are unresolved and the next generation of observational facilities with higher sensitivity (and PhD students) are essential to answer them.

The Atacama Large Millimetre/sub-millimetre Array (ALMA) will reveal the physical and chemical conditions of YSOs at milli-arcsecond resolution, corresponding to a few AU in low-mass and a few tens of AU in high-mass YSOs. Therefore, a better and clearer picture of the gas and temperature distribution within the protostellar system will be obtained. ALMA is already a powerful instrument able to unravel the embedded environments of high-mass YSOs, especially in the hunting and characterisation of possible disks in those objects.

The Stratospheric Observatory for Infrared Astronomy (SOFIA) is able to observe high rotational transitions of molecules as CO with heterodyne spectroscopy. Although with limited sensitivity, these observations play an important role on expanding our knowledge on the inner regions of high-mass YSOs, constraining their excitation temperatures and probing the energetic processes within the outflow, such shocks along the jet and the outflow cavity wall.

Finally, the Mid-Infrared Instrument (MIRI) on board of the *James Webb Space Telescope* (JWST) will be able to trace the hot gas in the inner regions of YSO systems, probing as well the material forming the disks.

2

Herschel-HIFI observations of high-J CO and isotopologues in star-forming regions: from low to high mass

I. San José-García, J. C. Mottram, L. E. Kristensen, et al.
A&A, **553**, *A125 (2013)*

Abstract

Our understanding of the star formation process has traditionally been confined to certain mass or luminosity boundaries because most studies focus only on low-, intermediate- or high-mass star-forming regions. Therefore, the processes that regulate the formation of these different objects have not been effectively linked. As part of the "Water In Star-forming regions with *Herschel*" (WISH) key programme, water and other important molecules, such as CO and OH, have been observed in 51 embedded young stellar objects (YSOs). The studied sample covers a range of luminosities from <1 to $>10^5$ $L_\odot$.

We analyse the CO line emission towards a large sample of embedded protostars in terms of both line intensities and profiles. This analysis covers a wide luminosity range in order to achieve a better understanding of star formation without imposing luminosity boundaries. In particular, this paper aims to constrain the dynamics of the environment in which YSOs form.

Herschel-HIFI spectra of the ^{12}CO J=10–9, ^{13}CO J=10–9 and C^{18}O J=5–4, J=9–8 and J=10–9 lines were analysed for a sample of 51 embedded protostars. In addition, JCMT spectra of ^{12}CO J=3–2 and C^{18}O J=3–2 extend this analysis to cooler gas components. We focused on characterising the shape and intensity of the CO emission line profiles by fitting the lines with one or two Gaussian profiles. We compared the values and results of these fits across the entire luminosity range covered by WISH observations. The effects of different physical parameters as a function of luminosity and the dynamics of the envelope-outflow system were investigated.

All observed CO and isotopologue spectra show a strong linear correlation between the logarithms of the line and bolometric luminosities across six orders of magnitude on both axes. This suggests that the high-J CO lines primarily trace the amount of dense gas associated with YSOs and that this relation can be extended to larger (extragalactic) scales. The majority of the detected ^{12}CO line profiles can be decomposed into a broad and a narrow Gaussian component, while the C^{18}O spectra are mainly fitted with a single Gaussian. For low- and intermediate-mass protostars, the width of the C^{18}O J=9–8 line is roughly twice that of the C^{18}O J=3–2 line, suggesting increased turbulence/infall in the warmer inner envelope. For high-mass protostars, the line widths are comparable for lower- and higher-J lines. A broadening of the line profile is also observed from pre-stellar cores to embedded protostars, which is due mostly to non-thermal motions (turbulence/infall). The widths of the broad ^{12}CO J=3–2 and J=10–9 velocity components correlate with those of the narrow C^{18}O J=9–8 profiles, suggesting that the entrained outflowing gas and envelope motions are related but independent of the mass of the protostar.

These results indicate that physical processes in protostellar envelopes have similar characteristics across the studied luminosity range.

2.1. Introduction

The evolution of a protostar is closely related to the initial mass of the molecular core from which it forms and to the specific physical and chemical properties of the original molecular cloud (e.g., Shu et al. 1993; van Dishoeck & Blake 1998; McKee & Ostriker 2007b). During the early stages of their formation, young stellar objects (YSOs) are embedded in large, cold and dusty envelopes which will be accreted or removed by the forming star. Depending on the mass of the star-forming region, the parameters and mechanisms that rule several processes of the star formation, such as the driving agent of the molecular outflow and accretion rates, will vary.

Molecular outflows are crucial for removing angular momentum and mass from the protostellar system (see review by Lada & Kylafis 1999). They have been extensively studied for low-mass YSOs (e.g., Cabrit & Bertout 1992; Bachiller & Tafalla 1999) where they are better characterised than for massive protostars (e.g., Shepherd & Churchwell 1996; Beuther & Shepherd 2005). The reason is related to the short lifetime (Mottram et al. 2011) and the large distances (few kpc) associated with massive YSOs. This means that outflows from massive stars are less well resolved than their low-mass counterparts. The agent that drives the molecular outflow, either jets or winds from the disk and/or stars (e.g., Churchwell 1999; Arce et al. 2007), might be different depending on the mass of the star-forming region. Therefore, the interaction of the outflow with the surrounding material and especially the resulting chemistry may differ across the mass range.

The accretion rates are also different depending on the mass of the forming star. Typical values for low-mass star formation are 10^{-7}–10^{-5} $M_{\odot}\,\mathrm{yr}^{-1}$ (Shu 1977; Bontemps et al. 1996), whereas higher values are necessary in order to overcome radiation pressure and form massive stars within a free-fall time (e.g., Jijina & Adams 1996). These values range from 10^{-4} to 10^{-3} $M_{\odot}\,\mathrm{yr}^{-1}$ for sources with $> 10^4$ $L_{\odot}$ (e.g., Beuther et al. 2002). In addition, for the low-mass sources, the accretion episode finishes before the protostar reaches the main sequence, while massive YSOs still accrete circumstellar material after reaching the hydrogen burning phase (Palla & Stahler 1993a; Cesaroni 2005).

Another difference is that the ionising radiation created by main-sequence OB stars is much more powerful than is generated by a single low-mass protostar. Therefore, photon-dominated regions (PDR) and HII regions are formed in areas of massive star formation, affecting the kinematics, temperature and chemistry of the surrounding material (Hollenbach & Tielens 1999). In addition, the strength of stellar winds and their interaction with the envelope material is different depending on the stellar spectral type of the YSOs.

Because of these differences, the study of star formation has traditionally been restricted to mass boundaries, focused on either low-mass ($M < 3$ $M_{\odot}$) or high-mass ($M > 8$ $M_{\odot}$) YSOs. One of the goals of the "Water In Star-forming regions with *Herschel*" (WISH) key programme (van Dishoeck et al. 2011) is to offer a complete description of the interaction of young stars with their surroundings as a function of mass. For this purpose, and in order to constrain the physical and chemical processes that determine star formation, water and other key molecules like CO have been observed for a large sample of embedded YSOs (51 sources). The targeted objects cover a vast range of luminosities (from < 1 $L_{\odot}$ to $> 10^5$ $L_{\odot}$) and different evolutionary stages (more details in Section 2.2.1). With the Heterodyne Instrument for the Far-Infrared (HIFI; de Graauw et al. 2010) on board the *Herschel* Space Observatory[1] (Pilbratt et al. 2010), high spectral resolution data of high-frequency molecular lines have been obtained. These can be used to probe the physical conditions, chemical composition and dynamics of protostellar systems (e.g., Evans 1999; Jørgensen et al. 2002; van der Wiel et al. 2013).

Due to its high, stable abundance and strong lines, CO is one of the most important and often used molecules to probe the different physical components of the YSO environment (envelope, outflow, disk). In particular, molecular outflows are traced by ^{12}CO emission through maps in the line wings (e.g, Curtis et al. 2010). Its isotopologue C^{18}O is generally thought to probe quiescent gas in the denser part of the protostellar envelope, whereas ^{13}CO lines originate in the extended envelope and the outflow cavity walls (e.g., Spaans et al. 1995; Graves et al. 2010; Yıldız et al.

[1] *Herschel* is an ESA space observatory with science instruments provided by European-led Principal Investigator consortia and with important participation from NASA.

2012). In addition, CO has relatively low critical densities, owing to its small permanent dipole moment (~0.1 Debye) and relatively low rotational energy levels, so this molecule is easily excited and thermalised by collisions with H_2 in a typical star formation environment. For this reason, measurements of CO excitation provide a trustworthy estimate of the gas kinetic temperature. Moreover, integrated intensity measurements can be used to obtain column densities of warm gas, providing a reference to determine the abundances of other species, such as water and H_2.

Most CO observations from ground-based sub-millimetre telescopes have been limited to low-J rotational transitions (up to upper transition J_u=3, i.e., upper-level energy E_u/k_B ~35 K), or mid-J transitions (J_u=6, with a E_u/k_B of ~100 K). Thanks to HIFI, spectrally resolved data for high-J CO transitions (J_u up to 16, E_u/k_B ~600 K) are observable for the first time, so warm gas directly associated with the forming star is probed (e.g., Yıldız et al. 2010, 2012; Plume et al. 2012; van der Wiel et al. 2013). Therefore, a uniform probe of the YSOs over the entire relevant range of E_u/k_B (from 10–600 K) is achieved by combining HIFI data with complementary spectra from single-dish ground-based telescopes. These observations are indispensable in order to ensure a self-consistent data set for analysis. Finally, the study of these lines in our Galaxy is crucial in order to compare them with the equivalent lines targeted in high-redshift galaxies, which are often used to determine star-formation rates on larger scales.

In this paper we present ^{12}CO J=10–9, ^{13}CO J=10–9, C^{18}O J=5–4, J=9–8 and J=10–9 HIFI spectra of 51 YSOs. Complementing these data, ^{12}CO and C^{18}O J=3–2 spectra observed with the James Clerk Maxwell Telescope (JCMT) are included in the analysis in order to use CO to its full diagnostic potential and extend the analysis to different regions of the protostellar environment with different physical conditions. Section 2.2 describes the sample, the observed CO data and the method developed to analyse the line profiles. A description of the morphology of the spectra, an estimation of the kinetic temperatures and correlations regarding the line luminosities of each isotopologue transition are presented in Section 2.3. These results are also compared to other YSO parameters such as luminosity and envelope mass. In Section 2.4 we discuss the results constraining the dynamics of individual velocity components of protostellar envelopes, characterise the turbulence in the envelope-outflow system and consider high-J CO as a dense gas tracer. Our conclusions are summarised in Section 2.5.

2.2. Observations

2.2.1. Sample

The sample discussed in this paper is drawn from the WISH survey and covers a wide range of luminosities and different evolutionary stages. A total of 51 sources are included in this study, which can be classified into three groups according to their bolometric luminosities, L_{bol}. The sub-sample of low-mass YSOs, characterised by $L_{bol} < 50\ L_\odot$, is composed of 15 Class 0 and 11 Class I protostars (see Evans et al. 2009 for details of the classification). Six intermediate-mass sources were observed with $70\ L_\odot < L_{bol} < 2{\times}10^3\ L_\odot$. Finally, 19 high-mass YSOs with $L_{bol} > 2{\times}10^3\ L_\odot$ complete the sample. The bolometric luminosity of the sample members, together with their envelope masses (M_{env}), distances (d) and source velocities (v_{LSR}), is summarised in Table 2.1. For more information about the sample studied in WISH, see van Dishoeck et al. (2011). Focusing on the evolutionary stages, the sub-sample of low-mass YSOs ranges from Class 0 to Class I, the intermediate-mass objects from Class 0 to Class I as well, and in the case of the high-mass sources from (mid-IR-quiet/mid-IR-bright) massive young stellar objects (MYSOs) to ultra-compact H II regions (UCH II).

2.2.2. HIFI observations

The sources were observed with HIFI on the *Herschel Space Observatory*. The HIFI CO and isotopologue lines studied in this paper are: ^{12}CO J=10–9, ^{13}CO J=10–9, C^{18}O J=5–4, J=9–8 and J=10–9. The upper-level energies and frequencies of these lines are presented in Table 2.2,

Table 2.1: Source parameters.

Source	$v_{\rm LSR}$ (km s^{-1})	$L_{\rm bol}$ ($L_\odot$)	d (kpc)	$M_{\rm env}$ ($M_\odot$)
Low-mass: Class 0				
L 1448-MM	+5.2	9.0	0.235	3.9
NGC 1333 IRAS 2A	+7.7	35.7	0.235	5.1
NGC 1333 IRAS 4A	+7.0	9.1	0.235	5.6
NGC 1333 IRAS 4B	+7.4	4.4	0.235	3.0
L 1527	+5.9	1.9	0.140	0.9
Ced110 IRS4	+4.2	0.8	0.125	0.2
BHR 71	−4.4	14.8	0.200	2.7
IRAS 15398	+5.1	1.6	0.130	0.5
L 483-MM	+5.2	10.2	0.200	4.4
Ser SMM 1	+8.5	30.4	0.230	16.1
Ser SMM 4	+8.0	1.9	0.230	2.1
Ser SMM 3	+7.6	5.1	0.230	3.2
L 723-MM	+11.2	3.6	0.300	1.3
B 335	+8.4	3.3	0.250	1.2
L 1157	+2.6	4.7	0.325	1.5
Low-mass: Class I				
L 1489	+7.2	3.8	0.140	0.2
L 1551 IRS 5	+6.2	22.1	0.140	2.3
TMR 1	+6.3	3.8	0.140	0.2
TMC 1A	+6.6	2.7	0.140	0.2
TMC 1	+5.2	0.9	0.140	0.2
HH 46	+5.2	27.9	0.450	4.4
IRAS 12496	+3.1	35.4	0.178	0.8
Elias 29	+4.3	14.1	0.125	0.3
Oph IRS 63	+2.8	1.0	0.125	0.3
GSS 30 IRS1	+3.5	13.9	0.125	0.6
RNO 91	+0.5	2.6	0.125	0.5
Interm.-mass				
NGC 7129 FIRS 2	−9.8	430	1.25	50.0
L1641 S3 MMS1	+5.3	70	0.50	20.9
NGC 2071	+9.6	520	0.45	30.0
Vela IRS 17	+3.9	715	0.70	6.4
Vela IRS 19	+12.2	776	0.70	3.5
AFGL 490	−13.5	2000	1.00	45.0
High-mass				
IRAS05358+3543	−17.6	6.3×10^3	1.8	142
IRAS16272−4837	−46.2	2.4×10^4	3.4	2170
NGC6334-I(N)	−3.3	1.9×10^3	1.7	3826
W43-MM1	+98.8	2.3×10^4	5.5	7550
DR21(OH)	−3.1	1.3×10^4	1.5	472
W3-IRS5	−38.4	1.7×10^5	2.0	424
IRAS18089−1732	+33.8	1.3×10^4	2.3	172
W33A	+37.5	1.1×10^5	3.8	1220
IRAS18151−1208	+32.8	2.0×10^4	3.0	153
AFGL2591	−5.5	2.2×10^5	3.3	320
G327−0.6	−45.3	5.0×10^4	3.3	2044
NGC6334-I	−7.4	2.6×10^5	1.7	500
G29.96−0.02	+97.6	3.5×10^5	6.0	768
G31.41+0.31	+97.4	2.3×10^5	7.9	2968
G5.89−0.39	+10.0	5.1×10^4	1.3	140
G10.47+0.03	+67.3	3.7×10^5	5.8	1168
G34.26+0.15	+58.0	3.2×10^5	3.3	1792
W51N-e1	+59.5	1.0×10^5	5.1	4530
NGC7538-IRS1	−56.2	1.3×10^5	2.7	433

Notes. See van Dishoeck et al. (2011) for the source coordinates.
The bolometric luminosities and envelope masses for the low-mass protostars are obtained from Kristensen et al. (2012). The envelope masses of the intermediate-mass objects are collected in Wampfler et al. (2013) and the bolometric luminosities (obtained from observations) and envelope masses of the high-mass YSOs are calculated in van der Tak et al. (2013).

together with the HIFI bands, main beam efficiencies ($\eta_{\rm MB}$), beam sizes, θ, spectral resolution and integration times. With the exception of the ^{12}CO J=10–9 line, all isotopologue line observations were obtained together with H_2O lines. The ^{12}CO J=10–9 line was targeted for the low- and intermediate-mass sample but only for one high-mass object (W3-IRS5). The ^{13}CO J=10–9 and C^{18}O J=9–8 lines were observed for the entire sample, while C^{18}O J=5–4 only for the Class 0 and intermediate-mass protostars. C^{18}O J=10–9 was observed for all low-mass Class 0 sources, two low-mass Class I (Elias 29 and GSS 30 IRS1), one intermediate-mass YSO (NGC 7129) and the entire high-mass sub-sample.

Single-pointing observations were performed for all targets in dual-beam-switch (DBS) mode, chopping to a reference position 3′from the target. There is no contamination from emission at the off position except for the ^{12}CO J=10–9 spectrum of NGC1333 IRAS2A and IRAS4A (see Yıldız et al. 2010 for more details). These spectra have been corrected and presented in this paper without contamination. In the case of W43-MM1, the absorption features found in the ^{13}CO J=10–9 spectrum are caused by H_2O^+ (Wyrowski et al. 2010).

HIFI has two backends: the Wide Band Spectrometer (WBS) and the High Resolution Spectrometer (HRS). Both spectrometers simultaneously measure two polarisations, horizontal (H) and

vertical (V). For more details, see Roelfsema et al. (2012). The WBS has a constant spectral resolution of 1.1 MHz, whereas the HRS has different configuration modes with four possible spectral resolutions: 0.125, 0.25, 0.5 and 1.0 MHz. The spectral resolution for each of the studied HIFI lines is listed in Table 2.2. The WBS data present lower noise than the HRS data (factor of $\sqrt{2}$) and provide a good compromise between noise and resolution. Therefore, the WBS data are the primary focus of this paper. HRS observations are only used for analysing the $C^{18}O$ J=5–4 line for the low-mass sources because their narrow line profiles require the higher spectral resolution provided by these data.

The data reduction was performed using the standard HIFI pipeline in the *Herschel* Interactive Processing Environment (HIPE[2]) ver. 8.2 (Ott 2010), resulting in absolute calibration on the corrected antenna temperature T_A^* scale, and velocity calibration with a $v_{\rm LSR}$ precision of a few $\mathrm{m\,s^{-1}}$. The version of the calibration files used is 8.0, released in February 2012. The flux scale accuracy was estimated to be 10% for bands 1, 4 and 5. Subsequently, the data were exported to GILDAS-CLASS[3] for further analysis. The H and V polarisations were observed simultaneously and the spectra averaged to improve the signal-to-noise ratio (*S/N*). To avoid possible discrepancies between both signals, the two polarisations were inspected for all the spectra presented in this paper with no differences > 20% found. Afterwards, line intensities were converted to main-beam brightness temperatures through the relation $T_{\rm MB} = T_A^*/\eta_{\rm MB}$ (see Wilson et al. 2009 for further information about radio-astronomy terminology). The main beam efficiency, $\eta_{\rm MB}$, for each HIFI band was taken from Roelfsema et al. (2012) and listed in Table 2.2. The final step of the basic reduction was the subtraction of a constant or linear baseline.

2.2.3. JCMT ground-based observations

Complementary data from the 15-m James Clerk Maxwell Telescope (JCMT) on Mauna Kea, Hawaii are also included in this paper, in particular for the high-mass sources for which ^{12}CO J=10–9 data are not available. Jiggle map observations of ^{12}CO J=3–2 and $C^{18}O$ J=3–2 for a sub-sample of YSOs were obtained with the Heterodyne Array Receiver Program (HARP, Buckle et al. 2009) in August 2011 and summer 2012 (proposal M11BN07 and M12BN06). For the sources and transitions not included in the proposal, comparable data were obtained from the JCMT public archive. Four low-mass sources were observed with the 12-m Atacama Pathfinder Experiment Telescope, APEX, because these protostars are not visible from the JCMT (see Appendix 2.B). Further information about the low-mass YSOs and data can be found in Yıldız et al. (2013).

The HARP instrument is a 4×4 pixel receiver array, although one of the receivers (H14) was not operational during the observation period. The lines were observed in position-switching mode, with the off-positions carefully chosen to avoid contamination. For the most massive and crowded regions, test observations of the off-position were taken for this purpose. The spatial resolution of the JCMT at the observed frequencies is ~14″, with a main beam efficiency of 0.63[4]. This same value of $\eta_{\rm MB}$ was used for the data obtained from the JCMT archive because the small variations in this parameter (< 10%) recorded over time are negligible compared to the calibration uncertainties of the JCMT (~20%, Buckle et al. 2009). Some of the spectra collected from the JCMT archive were observed in a lower spectral resolution setting. Therefore, for these data the spectral resolution is 0.4 $\mathrm{km\,s^{-1}}$ instead of 0.1 $\mathrm{km\,s^{-1}}$ (indicated in Table 2.2).

In the first step of the reduction process, the raw ACSIS data downloaded from the JCMT archive were transformed from *sdf* format to *fits* format using the Starlink[5] package for each and every pixel. Next, the data were converted to CLASS format and the central spectrum was extracted after convolving the map to the same beam size as the ^{12}CO J=10–9 HIFI observations (20″). Line intensities were then converted to the main-beam brightness temperature scale and linear baselines

[2]HIPE is a joint development by the Herschel Science Ground Segment Consortium, consisting of ESA, the NASA Herschel Science Centre, and the HIFI, PACS and SPIRE consortia.

[3]http://www.iram.fr/IRAMFR/GILDAS/

[4]http://www.jach.hawaii.edu/JCMT/spectral_line/General/status.html

[5]http://starlink.jach.hawaii.edu/starlink

Table 2.2: Overview of the main properties of the observed lines.

Mol.	Trans.	E_u/k_B	Frequency	Tel./Inst.-band	η_{MB}	θ	Spec. Resol.	Exposure time (min)			
		(K)	(GHz)			($''$)	(km s^{-1})	LM0	LMI	IM	HM
^{12}CO	3–2	33.2	345.796	JCMT	0.63	14	0.1/0.4	21	21	21	21
	10–9	304.2	1151.985	HIFI-5a	0.64	20	0.13[a]	10	7	10	20
^{13}CO	3–2	31.7	330.588	JCMT	0.63	15	0.1/0.4	32	32	32	32
	10–9	290.8	1101.350	HIFI-4b	0.74	21	0.14[a]	40	30	40	42/59
C^{18}O	3–2	31.6	329.331	JCMT	0.63	15	0.1/0.4	39	39	24	24
	5–4	79.0	548.831	HIFI-1a	0.76	42	0.07[b]	60	–	31	–
	9–8	237.0	987.560	HIFI-4a	0.74	23	0.15[a]	20	20	20	7
	10–9	289.7	1097.163	HIFI-4b	0.74	21	0.14[a]	30[c]	300	30	30

Notes. LM0: low-mass Class 0 sources. LMI: low-mass Class I protostars. IM: intermediate-mass objects. HM: high-mass YSOs.
The main beam efficiency, η_{MB}, and beam size, θ, are calculated using equation 1 and 3 of Roelfsema et al. (2012), respectively.
[(a)] WBS data. [(b)] HRS data. [(c)] NGC1333 IRAS 2A, 4A and 4B were observed for 300 min each.

subtracted. Since this manuscript focuses on analysing and comparing the central spectrum of the studied YSOs, the full JCMT spectral maps will be presented and discussed in a forthcoming paper.

2.2.4. Decomposition method

In order to quantify the parameters that fit each spectrum, the following procedure was applied to all spectra. First, the data were resampled to 0.27 km s^{-1} so that the results could be compared in a systematic manner. Then, the spectra were fitted with a single Gaussian profile using the IDL function *mpfitfun*, after which we plotted the residuals obtained from the fit to confirm whether the line profile hid an additional Gaussian component. For those sources whose profiles showed clear sub-structure, i.e., the residuals were larger than 3 sigma rms, a two Gaussian component fit was used instead. Examples of the decomposition procedure are shown in Fig. 2.1. The results of this process, together with the rms and integrated intensity for all lines, are presented in Tables 2.5 to 2.8 in Appendix 2.A.

All HIFI lines are observed in emission, and none of the HIFI spectra present clear infall signatures. Moreover, some CO lines show weak self-absorption features, which are of marginal significance so will not be discussed further. In addition, extremely high-velocity (EHV) emission features have been identified. The EHV components are knotty structures spaced regularly and associated with shocked material moving at velocities of hundreds of km s^{-1} (e.g. Bachiller et al. 1990). These structures have been detected in the ^{12}CO J=10–9 spectra for the low-mass Class 0 sources L1448-MM and BHR 71 (Kristensen et al. 2011; Yıldız et al. 2013). These EHV components were not included in the study of the line profiles, so the residuals were analysed after fitting each of these features with a Gaussian function and subtracting them from the initial profile.

The method used for examining the data is similar to the one introduced by Kristensen et al. (2010) for several water lines in some of the WISH low-mass YSOs, applied to high-J CO in Yıldız et al. (2010) and extended in Kristensen et al. (2012) for the 557 GHz 1_{10}–1_{01} water line profiles of the entire low-mass sample. The emission lines are classified as narrow or broad if the full width half maximum (FWHM) of the Gaussian component is lower or higher than 7.5 km s^{-1}, respectively. This distinction is made because 7.5 km s^{-1} is the maximum width obtained in the single Gaussian fit of the HIFI C^{18}O lines, which is considered as narrow and traces the dense warm quiescent envelope material (see Section 2.4 for further analysis and discussion).

The narrow component identified in the high-J CO isotopologue lines is always seen in emission, unlike a component of similar width seen in the 1_{10}-1_{01} line of water (Kristensen et al. 2012). The narrow components in high-J CO and low-J water probe entirely different parts of the protostar: the former traces the quiescent warm envelope material, the latter traces the cold outer

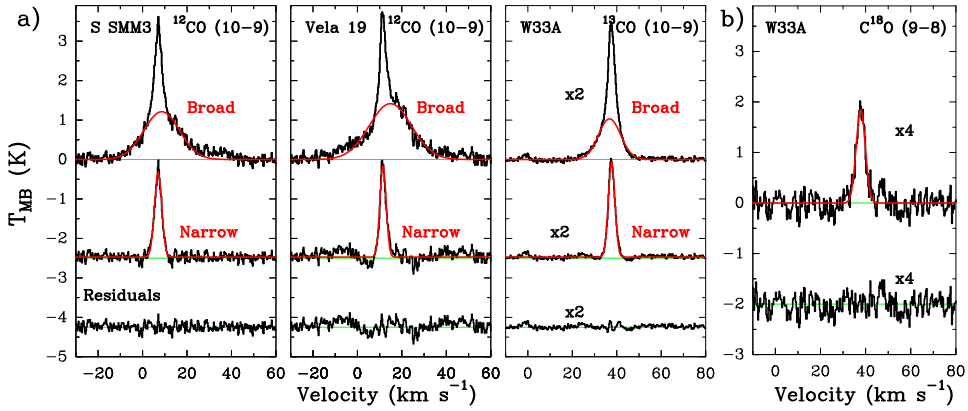

Figure 2.1: Gaussian decomposition for the CO and isotopologues line profiles: a) two Gaussian fit for the line profiles with two different velocity components identified, such as the ^{12}CO J=10–9 spectra for the low-mass YSOs Ser SMM3 (*left*), the intermediate-mass Vela 19 (*middle*) and the ^{13}CO J=10–9 spectrum of the high-mass W33A (*right*). b) Single Gaussian fit of sources characterised by one component profile, such as the C^{18}O J=9–8 spectra of W33A. The red lines show the Gaussian fits and the green lines the baseline.

envelope and ambient cloud. The broad emission in low-J CO is typically narrower than in water and traces entrained outflow material. Only the highest-J lines observed by HIFI trace the same warm shocked gas as seen in the water lines (Yıldız et al. 2013). To summarise, the components identified in the CO and isotopologue data cannot be directly compared to those observed in the H_2O 1_{10}-1_{01} lines because the physical and chemical conditions probed by water are different to those probed by CO (see Santangelo et al. 2012; Vasta et al. 2012).

In the analysis of the JCMT data, the *FWHM* of the broad velocity component for the complex ^{12}CO J=3–2 line profiles was disentangled by masking the narrower emission and self-absorption features in each spectrum. The width of the narrow C^{18}O J=3–2 lines was constrained by fitting these profiles with a single Gaussian. The results of these fits are presented in Table 2.9 in Appendix 2.B.

2.3. Results

One of the aims of this paper is to characterise how the observed emission lines compare as a function of source luminosity. To simplify the comparison across the studied mass range, the main properties and parameters of the HIFI and JCMT lines, such as line morphology, total intensity and kinetic temperature, are presented in this section. A more detailed description of the line profiles is reserved for Appendices 2.A and 2.B. Figs. 2.15 to 2.19 show the HIFI spectra and Figs. 2.22 and 2.23 the JCMT data.

Further study and analysis of each sub-sample will be presented in several forthcoming papers. The CO lines for the low-mass sources and their excitation will be discussed by Yıldız et al. (2013). A review of the intermediate-mass sources focused on the water lines will be performed by M^{c}Coey in prep. In the case of high-mass YSOs, low-J H_2O line profiles will be studied in detail by van der Tak et al. (2013).

In this manuscript a summary with the main characteristics of the studied emission line profiles is presented in Section 2.3.1. Section 2.3.2 describes the calculation of the line luminosity, L_{CO}, for each observed isotopologue, together with its correlation with L_{bol}. Finally, in Section 2.3.3, an estimation of the kinetic temperature is obtained for two sources, an intermediate-mass and a high-mass YSO, and compared with values obtained for low-mass sources.

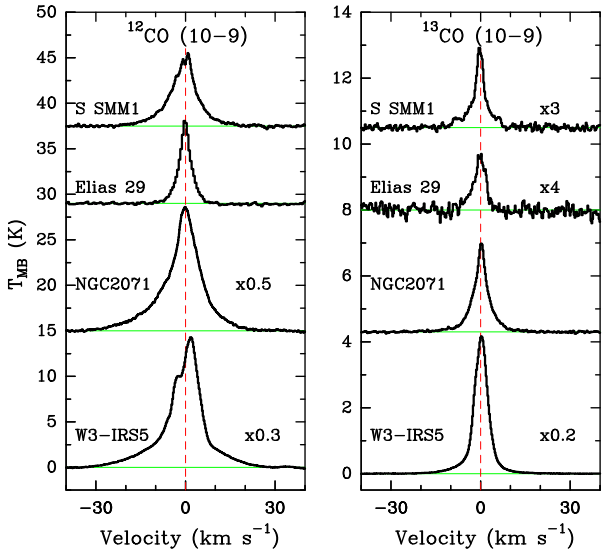

Figure 2.2: ^{12}CO J=10–9 (*left*) and ^{13}CO J=10–9 (*right*) spectra for a low-mass Class 0 protostar (top, Ser SMM1), low-mass Class I source (Elias 29), intermediate-mass object (NGC 2071) and high-mass YSO (bottom, W3-IRS5). The green line indicates the baseline level and the red dashed line the 0 km s^{-1} value. All spectra have been rebinned to 0.27 km s^{-1} and shifted with respect to their relative local standard-of-rest velocity.

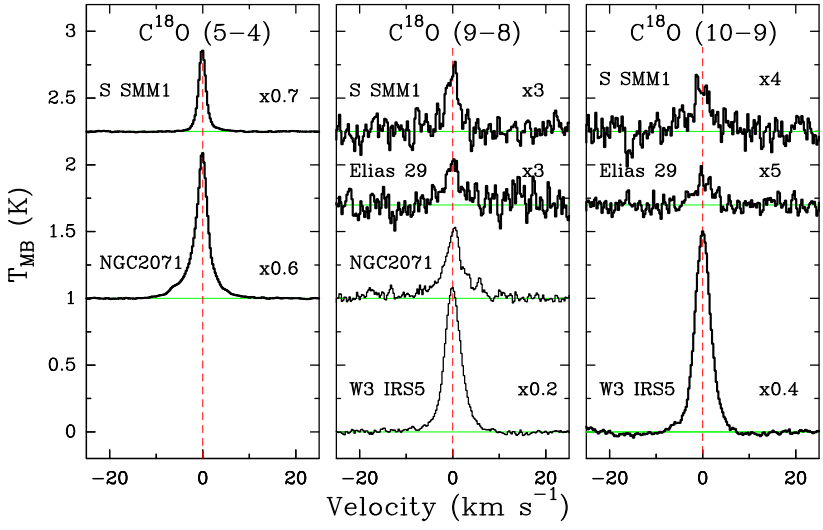

Figure 2.3: Same as Fig. 2.2 but for the C^{18}O spectra from the observed transitions: J=5–4 (*left*), J=9–8 (*middle*) and J=10–9 (*right*). For details about these objects see Appendix 2.A.

Table 2.3: Median values of the width of the broad velocity component of ^{12}CO J=10–9 and J=3–2 spectra, and of the *FWHM* for the C^{18}O J=3–2 and J=9–8 line profiles.

	broad[^{12}CO] (km s^{-1})	C^{18}O J=3–2 (km s^{-1})	C^{18}O J=9–8 (km s^{-1})
Low-mass Class 0	17.8	1.2	2.5
Low-mass Class I	12.7	0.9	3.1
Intermediate-mass	21.0	1.9	3.9
High-mass	24.8	4.3	5.0

2.3.1. Characterisation of the line profiles

Figures 2.2 and 2.3 show characteristic profiles of each transition and YSO sub-type, so the line profiles can be compared across the luminosity range. ^{12}CO J=10–9 spectra present more intense emission lines than the other observed isotopologues and more complex line profiles. Two velocity components are identified and most of the ^{12}CO J=10–9 spectra can be well fitted by two Gaussian profiles (Fig. 2.1a). Weak self-absorption features are also observed in some sources, such as Ser SMM1. The ^{13}CO J=10–9 profiles are weaker and narrower than ^{12}CO J=10–9 spectra. Some of the detected lines, especially for the high-mass sample, are fitted using two Gaussian components (Fig. 2.1a). In the case of the C^{18}O J=5–4 spectra, a weak broad velocity component is identified in six sources (indicated in Table 2.7), due to the long exposure time and the high *S/N* reached for this transition. The width of this broad component is narrower by a factor of 2–3 than that detected for the ^{12}CO and ^{13}CO J=10–9 lines. Similarly, two velocity components have been identified for the C^{18}O J=9–8 line in three high-mass sources: G10.47+0.03, W51N-e and G5.89-0.39 (see Fig. 2.18). These massive objects present the widest broad velocity components for both ^{13}CO and C^{18}O J=10–9 spectra. The width of the broad C^{18}O J=9–8 component is slightly smaller than that identified in the ^{13}CO J=10–9 emission for each of these YSOs.

Two velocity components were previously identified in approximately half of the 20 deeply embedded young stars in the Taurus molecular cloud studied by Fuller & Ladd (2002) using lower-J C^{18}O observations. They found typical *FWHM* line widths of ∼0.6 and ∼2.0 km s^{-1} for the narrow and broad component, respectively. These values are significantly narrower than the widths obtained from the HIFI data, so our interpretation and analysis of these components is different from the one presented by Fuller & Ladd (2002). On the other hand, the bulk of C^{18}O line profiles (especially J=9–8 and J=10–9 transitions) are generally well fitted by a single Gaussian (for an example, see Fig. 2.1b). Therefore, in our analysis only the narrow velocity component is considered for the C^{18}O lines of the three high-mass sources G10.47+0.03, W51N-e and G5.89-0.39. Regarding the line intensity, the spectra of the observed high-mass YSOs have higher main beam temperatures than the spectra of the intermediate-mass objects, which in turn show stronger lines than the low-mass sources.

Another result obtained when we extend this characterisation to the JCMT data is the complexity of the ^{12}CO J=3–2 profiles compared to the ^{12}CO J=10–9 spectra (see Figs. 2.15 and 2.22 for comparison across the studied sample). The HIFI data probe warmer gas from inner regions of the molecular core and present simpler emission line profiles (with no deep absorptions and foreground emission features) than the lower-J spectra. However, similar to the ^{12}CO J=10–9 line profiles, the ^{12}CO J=3–2 spectra can be decomposed into different velocity components. A broad velocity component is identified in 39 out of 47 sources, ranging from ∼7.4 to 53.5 km s^{-1} in width. For C^{18}O, the shape of the J=3–2 lines are very similar to those of the J=9–8 lines (see Figs. 2.20 and 2.21 for examples).

The *FWHM* of the ^{12}CO J=3–2 broad component for most of the high-mass sources is approximately double the width obtained for the ^{13}CO J=10–9 broad component (values in Tables 2.16 and 2.9). In the case of the one source for which a ^{12}CO J=10–9 observation was performed as part of WISH (W3-IRS5), the width of the broad component is similar to what is calculated for the J=3–2 spectrum (factor of 1.2±0.1) and is twice the width of the ^{13}CO J=10–9 emission line

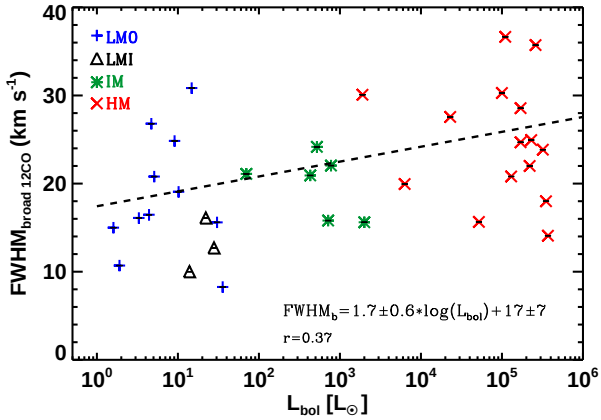

Figure 2.4: *FWHM* of the broad velocity component identified in the ^{12}CO J=10–9 line profiles for each type of YSOs versus their bolometric luminosities. Low-mass Class 0 (LM0) sources are indicated with blue pluses, low-mass Class I (LMI) with black triangles, intermediate-mass (IM) YSOs with green asterisks and high-mass (HM) objects with red crosses. For the high-mass sources, the ^{12}CO J=3–2 width is used instead. The black dashed line indicates the linear function that fits the relation between the *FWHM* and the logarithm of $L_{\rm bol}$.

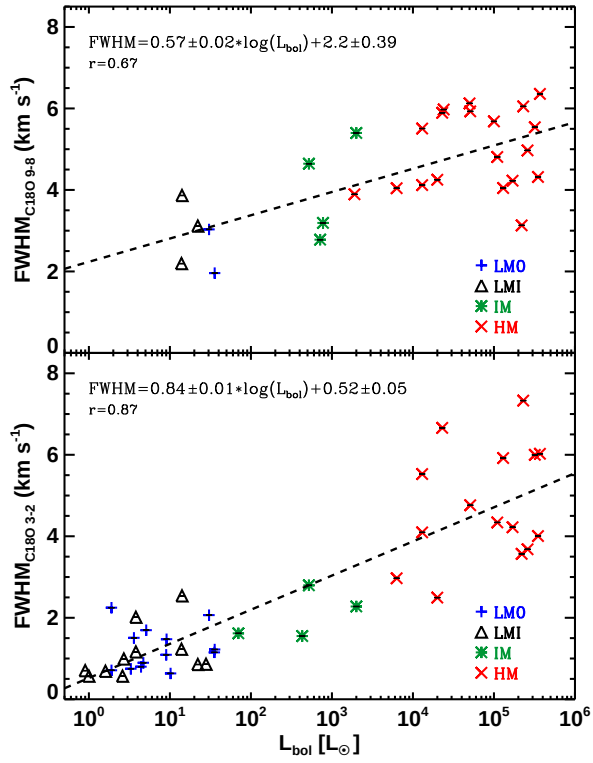

Figure 2.5: Same as Fig. 2.4 but for the narrow C^{18}O J=9–8 line profiles (*top*) and C^{18}O J=3–2 (*bottom*). Only a few low-mass YSOs have been detected in C^{18}O J=9–8.

Table 2.4: Slope, b, and intercept, a, of the calculated power-law fit for each CO and isotopologue line versus bolometric luminosity, together with their errors and the Pearson correlation coefficient, r.

Line	$\log(L_{CO}) = a + b \cdot \log(L_{bol})$		
	a	b	r
^{12}CO J=10–9	−2.9 ± 0.2	0.84 ± 0.06	0.92
^{13}CO J=10–9	−4.4 ± 0.2	0.97 ± 0.03	0.98
C^{18}O J=3–2	−4.1 ± 0.1	0.93 ± 0.03	0.98
C^{18}O J=5–4	−3.5 ± 0.2	0.78 ± 0.08	0.93
C^{18}O J=9–8	−5.2 ± 0.2	1.03 ± 0.05	0.97
C^{18}O J=10–9	−5.2 ± 0.3	0.96 ± 0.06	0.96

(see Fig. 2.2). Similar ratios were found by van der Wiel et al. (2013) for the high-mass source AFGL2591 as part of the CHESS ("Chemical *HErschel* Survey of Star-forming regions") key programme observations. For the intermediate-mass object NGC 2071, the ^{12}CO J=10–9 broad component is 1.7±0.1 larger than the width of the ^{13}CO J=10–9 broad component. This ratio is 1.5±0.4 for the one low-mass YSO for which a decomposition of the line profile can be performed in both transitions simultaneously (Ser SMM1). Thus, it appears that the ^{12}CO J=10–9 profile becomes increasingly broader compared to the ^{13}CO J=10–9 profile with increasing protostellar mass. The average ratio of the width of the broad component of the ^{12}CO J=10–9 line divided by the width of the broad component of the ^{12}CO J=3–2 line is approximately 1.0±0.1 for the intermediate-mass sources and 1.3±0.2 for the low-mass protostars.

In order to compare the broad velocity component of the ^{12}CO data with the narrow C^{18}O line profiles across the entire studied luminosity range, the *FWHM* of the ^{12}CO J=3–2 spectra is used as a proxy for the FWHM of the ^{12}CO J=10–9 profiles for the high-mass sample. The widths of the fits obtained for the ^{12}CO broad velocity components and the narrow C^{18}O J=9–8 and J=3–2 lines are plotted versus their bolometric luminosities (Figs. 2.4 and 2.5). From the figure of the broad velocity component of the ^{12}CO data we infer that the line wings become broader from low to high mass. Low-mass Class 0 protostars characterised by powerful outflows, such as L1448, BHR 71 and L 1157, are the clearly outstanding sources in the plot. The median *FWHM* of this component for each sub-group of protostars together with the calculated median of the *FWHM* values for the C^{18}O J=3–2 and J=9–8 lines are summarised in Table 2.3. Even though there are only six intermediate-mass sources and the results could be sample biased, the trend of increasing width from low- to high-mass is consistent with the result obtained for intermediate-mass objects.

Regarding the C^{18}O lines, Fig. 2.5 and Table 2.3 show a similar behaviour to what is observed for the broad component of the ^{12}CO but with less dispersion, i.e., the profiles become broader from low to high mass. This trend is statistically stronger for the J=3–2 transition (the Pearson correlation coefficient is higher than calculated for the J=9–8 line widths) since the number of detections is higher for the low-mass sample. The C^{18}O J=3–2 spectra show slightly narrower profiles than the J=9–8 line for the low- and intermediate-mass sources, with median values approximately half the values obtained for the J=9–8 line (see Table 2.3). On the other hand, for the high-mass sources the median values are practically the same, and similar widths are measured for the high-mass sub-sample in both transitions. This result is discussed further in Section 2.4.

2.3.2. Correlations with bolometric luminosity

The analysis and characterisation of the line profiles continue with the calculation of the integrated intensity of the emission line, $W = \int T_{MB} dv$. This parameter is obtained by integrating the intensity of each detected emission line over a velocity range which is defined using a 3σ rms cut.

To obtain a more accurate value of W for data with lower *S/N*, such as for the high-J C^{18}O lines from the low-mass sources, this parameter was approximated to the area of the fitted single Gaussian profile. The calculated integrated intensities of some sources were compared with mea-

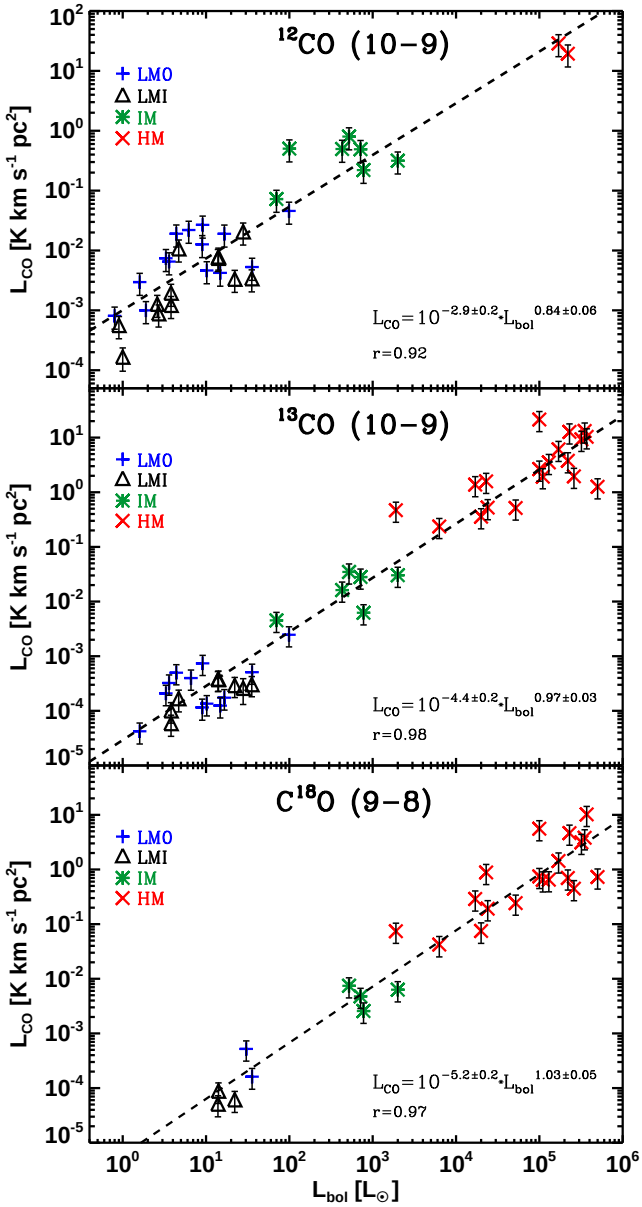

Figure 2.6: Line luminosity of the ^{12}CO J=10–9 (*top*), ^{13}CO J=10–9 (*middle*) and C^{18}O J=9–8 (*bottom*) spectra for low-mass Class 0 (LM0; blue pluses), low-mass Class I (LMI; black triangles), intermediate-mass (IM; green asterisks) and high-mass (HM; red crosses) YSOs versus their bolometric luminosity. The black dashed line represents the linear function that fits the logarithm of the plotted quantities.

surements from previous independent studies. In the case of NGC 1333 IRAS2A/4A/4B (Yıldız et al. 2010), differences in W are not larger than 10%. The obtained values from all lines are given in Tables 2.5 to 2.8.

If the emission is optically thin, W is proportional to the column density of the specific upper level. In local thermal equilibrium (LTE), the variation of W with J_u characterises the distribu-

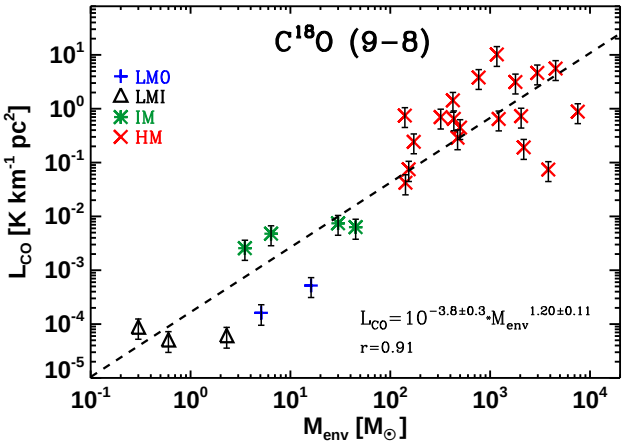

Figure 2.7: $C^{18}O$ J=9–8 line luminosity for low-mass Class 0 (LM0; blue pluses), low-mass Class I (LMI; black triangles), intermediate-mass (IM; green asterisks) and high-mass (HM; red crosses) YSOs versus their envelope masses, $M_{\rm env}$. The dash black line represents the linear function that fits the logarithm of the plotted quantities.

tion of the observed species over the different rotational levels (see equation 15.28 in Wilson et al. 2009). In the case of the optically thin $C^{18}O$ J=9–8 line, the total $C^{18}O$ column density, $N_{\rm t}$, is calculated for all sources to obtain the H_2 column density, $N_{\rm H_2}$. The assumed excitation temperature, $T_{\rm ex}$, is 75 K based on the work of Yıldız et al. (2010), which shows that 90% of the emission in the J=9–8 transition originates at temperatures between 70 and 100 K. The column density $N_{\rm H_2}$ is then obtained by assuming a $C^{18}O/H_2$ abundance ratio of 5×10^{-7}. This ratio is obtained by combining the $^{16}O/^{18}O$ isotopologue abundance ratio equal to 540 (Wilson & Rood 1994), and the $^{12}CO/H_2$ ratio as 2.7×10^{-4} (Lacy et al. 1994). The calculated $N_{\rm H_2}$ values for $C^{18}O$ J=9–8 are presented in Table 2.8.

The integrated intensity is converted to line luminosity, $L_{\rm CO}$, in order to compare these results for sources over a wide range of distances. The CO and isotopologue line luminosities for each YSO is calculated using equation 2 in Wu et al. (2005) assuming a Gaussian beam and point source objects. If the emission covered the entire beam, the line luminosities would increase by a factor of 2. The logarithm of this line luminosity, $\log(L_{\rm CO})$, is plotted versus the logarithm of the bolometric luminosity, $\log(L_{\rm bol})$, for ^{12}CO J=10–9, ^{13}CO J=10–9 and $C^{18}O$ J=9–8 in Fig. 2.6. The errors are calculated from the rms of the spectrum and considering ~20% distance uncertainty. A strong correlation is measured (Pearson correlation coefficient r >0.92) between the logarithms of $L_{\rm CO}$ and $L_{\rm bol}$ for all observed CO lines. The top plot in Fig. 2.6 shows $L_{\rm CO}$ for ^{12}CO J=10–9 emission for all the observed sources versus their $L_{\rm bol}$. Only one high-mass source was observed as part of WISH in this line with HIFI (W3-IRS5) with the value of the integrated intensity for AFGL2591 obtained from van der Wiel et al. (2013). Even though this plot is mainly restricted to low- and intermediate-mass sources, a strong correlation is still detected over five orders of magnitude in both axes. Both low-mass Class 0 and Class I YSOs follow the same correlation, though the uncertainties of the calculated $L_{\rm CO}$ for these sources are higher than for the other types of protostars because the *S/N* is lower. All high-mass objects were observed in ^{13}CO J=10–9, so the correlation between $\log(L_{\rm CO})$ and $\log(L_{\rm bol})$ (Fig. 2.6, middle) is confirmed and extends over almost 6 orders of magnitude in both axes. This correlation is also seen for $C^{18}O$ J=9–8 but with higher dispersion (Fig. 2.6, bottom) and in the other observed transitions of this isotopologue.

The values of the correlation coefficient and the fit parameters for all these molecular transitions are presented in Table 2.4. The correlation prevails for all transitions even if the values of integrated intensity are not converted to line luminosity. Therefore, $\log(W)$ still correlates with $\log(L_{\rm bol})$ over

at least three and six orders of magnitude on the y and x axes, respectively. Similar correlations are obtained when plotting the logarithm of L_{CO} versus the logarithm of the source envelope mass, M_{env}, for all the targeted lines (see Fig. 2.7 for an example using the $C^{18}O$ J=9–8 line). In these representations, the modelled envelope mass of the source is directly compared to L_{CO}, a tracer of the warm envelope mass. Therefore, the correlation is extended and probed by another proxy of the mass of the protostellar system.

Since the index of the fitted power-law exponents is ∼1 within the uncertainty of the fits (see Table 2.4), these correlations show that $\log(L_{CO})$ is proportional to $\log(L_{bol})$. In the optically thin case, this correlation implies that the column density of warm CO increases proportionally with the mass of the YSO. This result can be applied to $C^{18}O$ because the emission lines of this isotopologue are expected to be optically thin. Assuming that ^{13}CO J=10–9 is optically thin as well, the column density would increase proportionally with the luminosity of the source, and practically with the same factor as the studied $C^{18}O$ transitions. Therefore, even though the conditions in low-, intermediate- and high-mass star-forming regions are different and distinct physical and chemical processes are expected to be more significant in each scenario (e.g., ionising radiation, clustering, etc.), the column density of CO seems to depend on the luminosity of the central protostar alone, showing a self-similar behaviour from low to high mass.

To test the optically thin assumption for ^{12}CO J=10–9 and especially for ^{13}CO J=10–9, the line luminosities for the ^{13}CO J=10–9 and the $C^{18}O$ J=10–9 data were multiplied by a $^{12}C/^{13}C$ ratio of 65 (Vladilo et al. 1993)[6] and by a $^{16}O/^{18}O$ ratio of 540 (Wilson & Rood 1994). Therefore, the observed and predicted values of L_{CO} for ^{12}CO J=10–9 and ^{13}CO J=10–9, together with those of $C^{18}O$ J=10–9 can be compared across the studied luminosity range (see Fig. 2.8). In the case of the ^{13}CO J=10–9 line, the values of the observed and predicted line luminosity are similar ($\lesssim$20% in most of them), especially at lower luminosities. In addition, the slope of their fits are practically the same within the uncertainty, so similar behaviour is proved. From these results we can assume that in general ^{13}CO J=10–9 is optically thin. For ^{12}CO J=10–9, the ratio of predicted-to-observed line luminosity ($65 \times L_{CO}[^{13}CO\ J{=}10{-}9]/L_{CO}[^{12}CO\ J{=}10{-}9]$) ranges from 0.8 (IRAS 15398) to 12.5 (W3-IRS5) and the average obtained is 3.3. Therefore, ^{12}CO J=10–9 is optically thick, at least at the line centre which dominates the intensity, and the relative value of the optical depth, τ, increases slightly with the mass of the protostar (τ ∼1.5 for the low-mass sources, 2.0 for the intermediate and ∼3.4 for the high-mass object). This is in keeping with the expectation that massive YSOs form in the densest parts of the giant molecular clouds, GMCs.

Correcting for optical depth, $L_{CO}[^{13}CO\ J{=}10{-}9]$ can be used to derive $L_{CO}[^{12}CO\ J{=}10{-}9]$ because both species behave similarly across the luminosity range (similar slopes in their fits). This relation can be used in calculating L_{CO} for those sources for which there are no ^{12}CO J=10–9 observations, that is, the high-mass sample. As highlighted before, using ^{13}CO as a proxy for ^{12}CO is restricted to comparisons of integrated intensities of the emission lines across the studied mass spectrum, and cannot be extended to the analysis of the line profile of ^{12}CO and ^{13}CO J=10–9.

2.3.3. Kinetic temperature

The ratio of the ^{12}CO J=10–9 and J=3–2 line wings can be used to constrain the kinetic temperature T_{kin} of the entrained outflow gas if the two lines originate from the same gas. Yıldız et al. (2012) and (2013, submitted) have determined this for the sample of low-mass YSOs. Here we consider two sources to investigate whether the conditions in the outflowing gas change with increasing YSO mass: the intermediate-mass YSO NGC 2071 and the high-mass object W3-IRS5. The critical densities, n_{cr}, of the ^{12}CO J=3–2 and J=10–9 transitions at 70 K are ∼$2.0{\times}10^4$ and $4.2{\times}10^5$ cm^{-3}, respectively. The values were calculated using equation 2 from Yang et al. (2010), the CO rate coefficients presented in their paper and considering only para-H_2 collisions. The densities inside the HIFI beam for ^{12}CO J=10–9 (20″) of both sources are higher than n_{cr}. Therefore, the emission is thermalised and T_{kin} can be directly constrained by the ^{12}CO J=10–9/J=3–2 line wing ratios.

[6]The $^{12}C/^{13}C$ ratio varies with galactocentric radius by up to a factor of 2, but this effect is minor and is ignored.

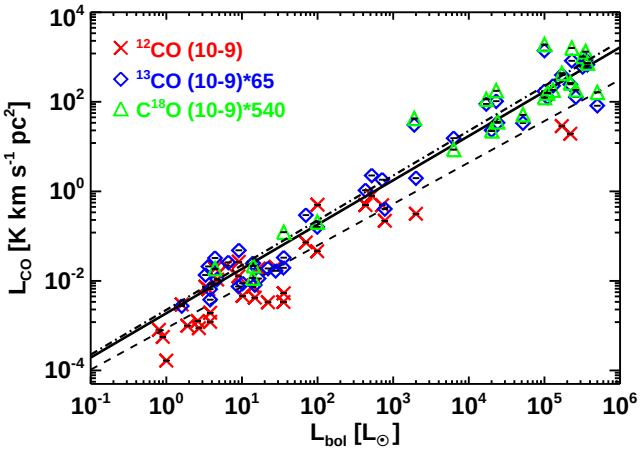

Figure 2.8: Line luminosity of the ^{12}CO J=10–9 emission lines, red crosses, versus their bolometric luminosity, together with the line luminosity of the ^{13}CO J=10–9 spectra, blue diamonds, multiplied by the assumed abundance ratio of ^{12}C/^{13}C for the entire WISH sample of YSOs. The line luminosity of the C^{18}O J=10–9 lines, green triangles, multiplied by the assumed abundance ratio of ^{16}O/^{18}O is plotted together with the previous values. The dashed line represents the linear fit of the ^{12}CO J=10–9 spectra, the full line that for the ^{13}CO J=10–9 transition and the dash-dot line indicates the fit for the C^{18}O J=10–9 data.

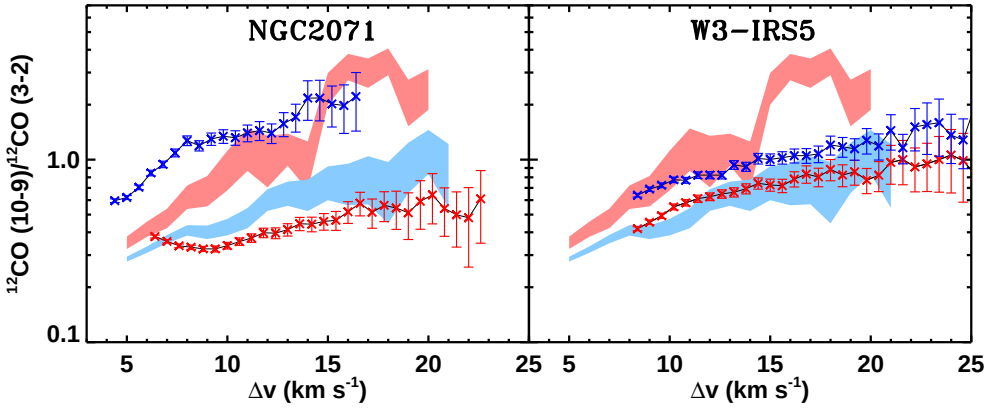

Figure 2.9: Line-wing ratios of ^{12}CO J=10–9/J=3–2 as a function of absolute offset from the source velocity for the sources NGC2071 (*left*) and W3-IRS5 (*right*) for the red and blue wings. The shaded regions are obtained from the average spectra of the low-mass sample for these transitions (see Yıldız et al. 2013). The spectra have been resampled to 0.6 km s^{-1} bin and shifted to 0 km s^{-1}.

The observed ratios of the red and blue wings for these two sources as a function of absolute offset from the source velocity are presented in Fig. 2.9. These ratios are compared with the values calculated by Yıldız et al. (2013) from the ^{12}CO J=10–9 and J=3–2 averaged spectra for the low-mass Class 0 sample (shaded regions). Since the emission is optically thin and we can assume LTE, the kinetic temperatures are calculated from the equation that relates the column density and the integrated intensity (Wilson et al. 2009). The obtained $T_{\rm kin}$ varies from 100 to 210 K. Both the observed line ratios, as well as the inferred kinetic temperatures, are similar to those found for the low-mass YSOs, where $T_{\rm kin}$ ranges from 70-200 K for Class 0. Although only a couple of higher-mass sources have been investigated, the temperatures in the entrained outflow gas seem to be similar across the mass range. If part of the^{12}CO J=10–9 emission originates from a separate

warmer component, the above values should be regarded as upper limits.

2.4. Discussion

The HIFI data show a variety of line profiles with spectra that can be decomposed into two different velocity components, such as the ^{12}CO J=10–9 lines, and spectra that show narrow single Gaussian profiles ($C^{18}O$ data). In addition, a strong correlation is found between the line and the bolometric luminosity for all lines.

Section 2.4.1 compares the narrow $C^{18}O$ lines and the ^{12}CO broad velocity component in order to better understand the physics that these components are tracing and the regions of the protostellar environment they are probing. The dynamics of the inner envelope-outflow system is studied in Section 2.4.2. Finally, the interpretation of CO as a dense gas tracer is discussed in Section 2.4.3.

2.4.1. Broad and narrow velocity components

The broad velocity component identified in most of the ^{12}CO J=3–2 and J=10–9 spectra is related to the velocity of the entrained outflowing material, so the wings of ^{12}CO can be used as tracers of the outflow properties (Cabrit & Bertout 1992; Bachiller & Tafalla 1999). However, there are different effects that should be taken into account when this profile component is analysed, such as the viewing angle of the protostar and the *S/N*. The former could alter the width of the broad component due to projection or even make it disappear if the outflow is located in the plane of the sky. Low *S/N* could also hide the broad component for sources with weak emission. Moreover, the broad velocity component should be weaker if the emission lines come from sources at later evolutionary stages since their outflows become weaker and less collimated (see reviews of Bachiller & Tafalla 1999; Richer et al. 2000; Arce et al. 2007).

In order to compare the line profiles of all observed CO lines for each type of YSO and avoid the effects of inclination and observational noise playing a role in the overall analysis of the data, an average spectrum of each line for each sub-type of protostar has been calculated and presented in Figs. 2.10 and 2.11. Regarding the low-mass sample, we observe a striking decrease in the width of the broad component from Class 0 to Class I. This result shows that the decrease in the outflow force for more evolved sources in the low-mass sample is reflected in the average spectra (Bontemps et al. 1996).

A narrow velocity component has been defined as a line profile that can be fitted by a Gaussian function with a *FWHM* smaller than 7.5 km s^{-1} (see Section 2.2.4 for more details). Since $C^{18}O$ lines are expected to trace dense quiescent envelope material, high-J transitions probe the warm gas in the inner envelope. The average $C^{18}O$ spectra for each type of YSO are compared in Fig. 2.11. The *FWHM* of the emission lines increases from low- to high-mass protostars (see Fig. 2.5 and Table 2.3). An explanation for this result could be that for massive regions, the UV radiation from the forming OB star ionises the gas, creating an HII region inside the envelope, which increases the pressure on its outer envelope. This process may lead to an increase in the turbulent velocity of the envelope material (Matzner 2002), thus broadening the narrow component. Therefore, our spectra are consistent with the idea that, in general, turbulence in the protostellar envelopes of high-mass objects is expected to be stronger than for low-mass YSOs (e.g. Herpin et al. 2012).

Higher rotational transitions trace material at higher temperatures and probe deeper and denser parts of the inner envelope. For the low- and intermediate-mass sources, the *FWHM* of the $C^{18}O$ J=3–2 spectra are generally half what is obtained for the $C^{18}O$ J=9–8 and slightly smaller than those obtained for the J=5–4 transition. However, for the high-mass YSOs the values of the *FWHM* are similar for the J=3–2 and J=9–8 transitions. To understand which kind of processes (thermal or non-thermal) dominate in the inner regions of the protostellar envelope traced by our observations, the contribution of these two processes to the line width is calculated. The aim is to explain whether the broadening of high-J emission lines is caused by thermal or non-thermal motions.

In the case of the J=3–2 lines, the upper energy level is 31 K, so the thermal line width, $\Delta v_{\rm th}$, is 0.12 km s^{-1} for $C^{18}O$ at this temperature. Comparing this value with the measured FWHM of

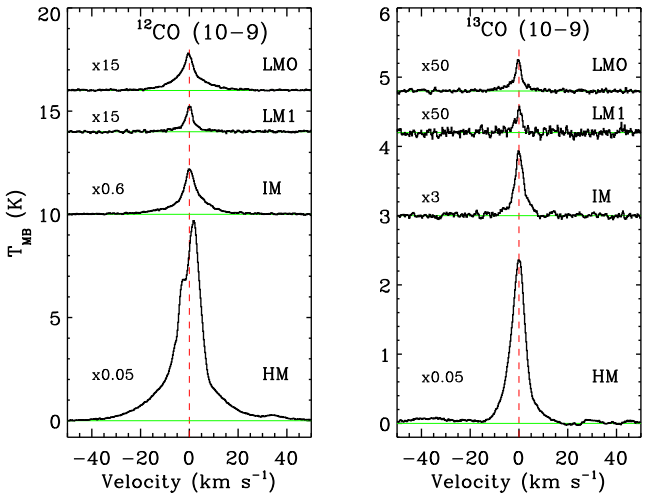

Figure 2.10: ^{12}CO J=10–9 (*left*) and ^{13}CO J=10–9 (*right*) spectra of low-mass class 0 (LM0), low-mass Class I (LMI), intermediate-mass (IM) and high-mass YSO (HM) averaged independently and compared. All spectra were shifted to 0 km s^{-1}, rebinned to 0.27 km s^{-1} and the intensity of the emission line scaled to a common distance of 1 kpc before averaging. The green line indicates the continuum level and the red dashed line the 0 km s^{-1} value. W43-MM1 was not included in the average of ^{13}CO J=10–9 high-mass spectra because of the strong absorption features caused by H_2O^+ (see Section 2.2.2).

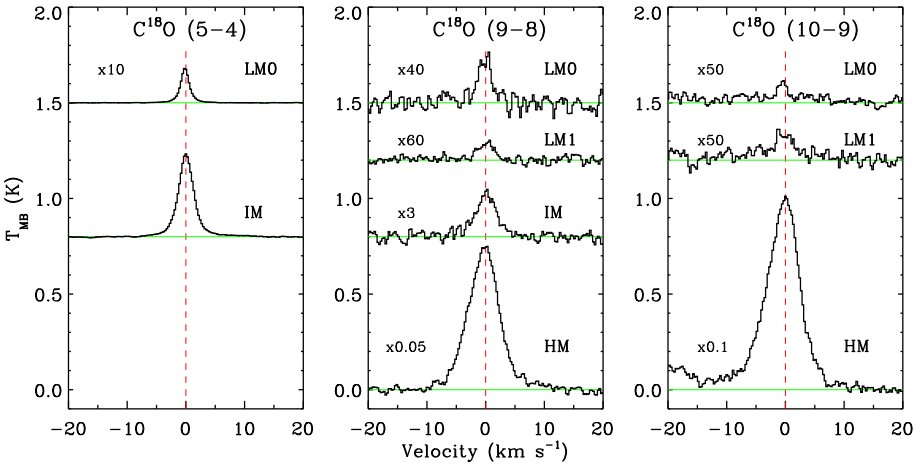

Figure 2.11: Same as Fig. 2.10 but for the C^{18}O spectra from the observed transitions: J=5–4 (*left*), J=9–8 (*middle*) and J=10–9 (*right*). More details about these transitions are in Appendix 2.A.

the C^{18}O J=3–2 spectra in Table 2.9, we conclude that thermal motions contribute less than 5% to the total observed line width, $\Delta v_{\rm obs}$. Therefore, the line width is dominated by non-thermal motions $\Delta v_{\rm noth}$. The C^{18}O J=9–8 line profiles trace warmer gas (up to 300 K) with respect to J=3–2 increasing the thermal contribution. However, even at 300 K, $\Delta v_{\rm th}$ is 0.68 km s^{-1}, which means that $\Delta v_{\rm noth}/\Delta v_{\rm obs}$ is larger than 0.93 even for the low-mass sources. Thus, non-thermal motions predominate over thermal ones in the studied regions of the protostellar envelopes. These motions are assumed to be independent of scale and do not follow the traditional size-line width relation (Pineda et al. 2010). Therefore, these results are not biased by the distance of the source.

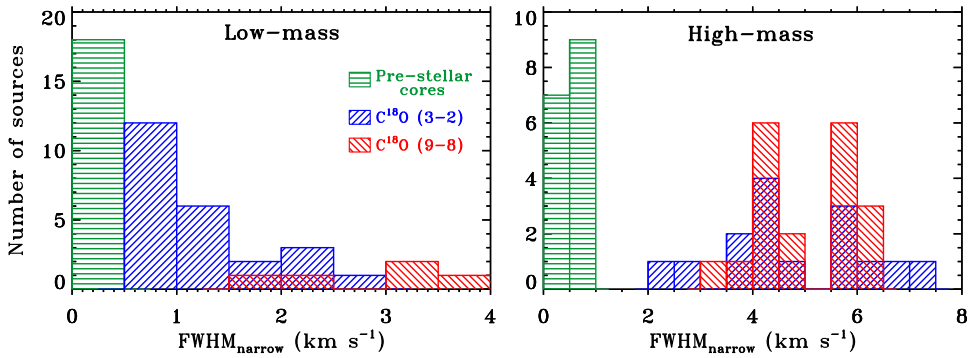

Figure 2.12: Comparison of the observed width of the ammonia line for a sample of low-mass pre-stellar cores collected by Jijina et al. (1999) (horizontal-dashed green), width of the $C^{18}O$ J=3–2 spectra (right-dashed blue) and $C^{18}O$ J=9–8 line widths (left-dashed red) for the detected WISH sample of low-mass protostars (*left*). The histogram of the *right* presents the same values but for high-mass pre-stellar cores and the WISH high-mass sample of YSOs.

This analysis can be compared to pre-stellar cores, in which the line profiles are closer to being dominated by thermal motions. For this purpose, the line width values calculated for our data are compared to those of Jijina et al. (1999). In that work, a database of 264 dense cores mapped in the ammonia lines (J, K)=(1,1) and (2,2) is presented. Histograms in Fig. 2.12 compare the values of the line widths observed for pre-stellar cores with the observed line width of the $C^{18}O$ J=3–2 and J=9–8 data for the WISH sample of protostars for low- (top) and for high-mass (bottom) objects. We observe that also for pre-stellar cores, the line widths are larger for more massive objects. From these histograms and following the previous discussion, we conclude that the broadening of the line profile from pre-stellar cores to protostars is due to non-thermal motions rather than thermal increase. Therefore, non-thermal processes (turbulence or infall motions) are crucial during the evolution of these objects and these motions increase with mass.

2.4.2. CO and dynamics: turbulence versus outflow

The ^{12}CO and $C^{18}O$ spectra trace different physical structures originating close to the protostar (e.g. Yıldız et al. 2012). The broad wings of the ^{12}CO J=10–9 and J=3–2 data are optically thin and trace fast-moving gas, that is, emission from entrained outflow material. On the other hand, the narrow $C^{18}O$ spectra probe the turbulent and infalling material in the protostellar envelope. The relationship between these two different components is still poorly understood.

Following the discussion in § 2.4.1, we compare the FWHM of the narrow component as traced by $C^{18}O$ J=9–8 with the *FWHM* of the broad velocity component as traced by ^{12}CO J=10–9 or J=3–2 for the sources detected in both transitions (see Fig. 2.13). The $C^{18}O$ J=9–8 data were chosen for this comparison because this transition has been observed for the entire sample of YSOs, in contrast to $C^{18}O$ J=5–4 and J=10–9 transitions. A correlation is found (with a Pearson correlation coefficient r >0.6), indicating a relationship between the fast outflowing gas and the quiescent envelope material.

Considering the scenario in which the non-thermal component is dominated by turbulence, the relation presented in Fig. 2.13 indicates that the increase in the velocity of the outflowing gas corresponds to an increase in the turbulence in the envelope material, and this relation holds across the entire luminosity range. One option is that stronger outflows are injecting larger-scale movements into the envelope, which increases the turbulence. This effect is reflected as a broadening of the $C^{18}O$ line width. In addition, for the low-mass sources the width of the $C^{18}O$ J=9–8 lines is larger than for the J=3–2 spectra, indicating that the hotter inner regions of the envelope are more turbulent than its cooler outer parts. In the case of the high-mass object, the *FWHMs* of the $C^{18}O$ J=9–8

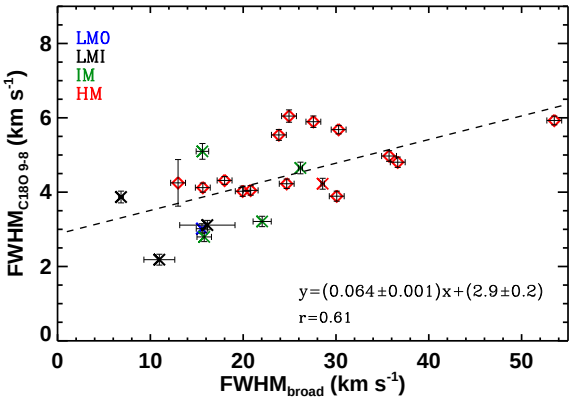

Figure 2.13: Width of the $C^{18}O$ J=9–8 line profile versus the width of the broader component of ^{12}CO J=10–9 emission lines (crosses) and for the ^{12}CO J=3–2 line profiles (diamonds). The black dashed line represents the linear function that fits the logarithm of the plotted quantities.

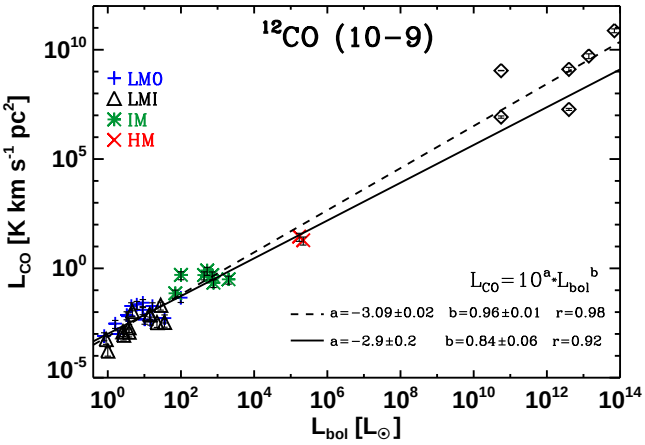

Figure 2.14: Line luminosity of the ^{12}CO J=10–9 emission versus their bolometric luminosity for the entire WISH sample of YSOs (same notation as Fig. 2.6) and for four galaxies in our local universe and two at high redshifts (black diamonds). The solid line represents the linear fit of the galactic ^{12}CO J=10–9 spectra and the dashed line the linear fit including the values of the six galaxies.

and J=3–2 lines are comparable, which could be partly caused because more luminous YSOs tend to be created in more massive and more turbulent molecular clouds (Wang et al. 2009).

Alternatively, infall processes could broaden the $C^{18}O$ profiles. Indeed, an increase in *FWHM* by at least 50% is found for $C^{18}O$ J=9–8 compared with J=3–2 in collapsing envelope simulations due to the higher infall velocities in the inner warm envelope (Harsono et al. 2013). If the non-thermal component was dominated by these movements, the sources with higher infall rates should have broader $C^{18}O$ line widths. These objects generally have higher outflow rates, i.e., higher outflow activity (see Tomisaka 1998; Behrend & Maeder 2001a), which shows up as a broadening of the ^{12}CO wings since the amount of material injected into the outflow is larger. Therefore, we will observe the same result as in the previous scenario, that is, a broadening of the ^{12}CO line wings for sources with stronger infalling motions. This relation would hold across the studied luminosity range.

Theoretically, large differences in the dynamics of the outflow-envelope system between low- and high-mass are expected since the same physical processes are not necessarily playing the same relevant roles in these different types of YSOs. However, Fig. 2.13 shows that the dynamics of the outflow and envelope are equally linked for the studied sample of protostars. With the current analysis we cannot disentangle which is the dominant motion in the non-thermal component of the line profile, and thus we cannot conclude if the infalling process makes the outflow stronger or if the outflow drives turbulence back into the envelope or a combined effect is at play.

2.4.3. High-*J* CO as a dense gas tracer

The strictly linear relationships between CO high-*J* line luminosity and bolometric luminosity presented in Figs. 2.6 to 2.8 require further discussion. The bolometric luminosity of embedded protostars is thought to be powered by accretion onto the growing star and is thus a measure of the mass accretion rate. A well-known relation of bolometric luminosity with the outflow momentum flux as measured from ^{12}CO low-*J* maps has been found across the stellar mass range (Lada & Fich 1995; Bontemps et al. 1996; Richer et al. 2000), so one natural explanation for our observed ^{12}CO *J*=10–9 correlation is that it reflects this same relation. However, the outflow wings contain only a fraction of the ^{12}CO *J*=10–9 emission, with the broad/narrow intensity ratios varying from source to source (Table 2.5, see also Yıldız et al. 2013, for the low-mass sources). Together with the fact that the relations hold equally well for ^{13}CO and C^{18}O high-*J* lines, this suggests the presence of another underlying relation. Given the strong correlation with $M_{\rm env}$ (Fig. 2.7), the most likely explanation is that the high-*J* CO lines of all isotopologues primarily trace the amount of dense gas associated with the YSOs.

Can this relation be extended to larger scales than those probed here? Wu et al. (2005, 2010) find a linear relation between HCN integrated intensity and far-infrared luminosity for a set of galactic high-mass star-forming regions on similar spatial scales to those probed by our data. They have extended this relation to include extragalactic sources to show that this linear regime extends to the scales of entire galaxies, as first demonstrated by Gao & Solomon (2004a). In contrast, the CO *J*=1–0 line shows a superlinear relation with far-infrared luminosity (sometimes converted into star formation rate) and with the total (H I + H_2) gas surface density with a power-law index of 1.4 (see Kennicutt & Evans 2012 for review). The data presented in this paper suggest that it is the mass of dense molecular gas as traced by HCN that controls the relation on large scales rather than the mass traced by CO *J*=1–0 (see also Lada et al. 2012).

With the increased number of detections of ^{12}CO *J*=10–9 in local and high-redshift galaxies with *Herschel* (e.g., van der Werf et al. 2010; Spinoglio et al. 2012; Kamenetzky et al. 2012; Meijerink et al. 2013) and millimetre interferometers (e.g., Weiß et al. 2007; Scott et al. 2011), the question arises whether this line can serve as an equally good tracer of dense gas. As an initial test, we present in Fig. 2.14 our ^{12}CO *J*=10–9 - $L_{\rm FIR}$ (assuming $L_{\rm bol}$=$L_{\rm FIR}$) relation with these recent extragalactic detections included. As can be seen, the relation does indeed extend to larger scales. Given the small number statistics, the correlation has only limited meaning and this relation needs to be confirmed by additional data.

An alternative view has been presented by Krumholz & Thompson (2007) and Narayanan et al. (2008), who argue that the linearity for dense gas tracers is a coincidence resulting from the fact that these higher excitation lines are subthermally excited and probe only a small fraction of the total gas. They suggest that the relation should change with higher critical density tracers and even become sublinear with a power-law index less than 0.5 for transitions higher than *J*=7–6 for CO. On the small scales probed by our data, we do not see this effect and the linear relations clearly continue to hold up to the *J*=10–9 transition.

2.5. Conclusions

The analysis of the ^{12}CO *J*=3–2, *J*=10–9, ^{13}CO *J*=10–9, C^{18}O *J*=3–2, *J*=5–4, *J*=9–8 and *J*=10–9 line profiles has allowed us to study several fundamental parameters of the emission line,

such as the line width and the line luminosity, and to constrain the dynamics of different physical structures of WISH protostars across a wide range of luminosities. Complementing the HIFI data, lower-J observations from the JCMT are included in order to achieve a uniform picture of the interaction of YSOs with their immediate surroundings. Our results are summarised as follows.

- A gallery of line profiles identified in the HIFI CO spectra is presented. ^{12}CO and ^{13}CO J=10–9 line profiles can be decomposed into two different velocity components, where the broader component is thought to trace the entrained outflowing gas. This broad component weakens from the low-mass Class 0 to Class I stage. Meanwhile, the narrow C^{18}O lines probe the bulk of the quiescent envelope material. The widths are dominated by non-thermal motions including turbulence and infall. The next step will be to constrain the contribution of these non-thermal mechanisms on the C^{18}O line profiles by using radiative transfer codes such as RATRAN (Hogerheijde & van der Tak 2000).

- The narrow C^{18}O J=9–8 line widths increase from low- to high-mass YSOs. Moreover, for low- and intermediate-mass protostars, they are about twice the width of the C^{18}O J=3–2 lines, suggesting increased turbulence/faster infall in the warmer inner envelope compared to the cooler outer envelope. For high-mass objects, the widths of the J=9–8 and J=3–2 lines are comparable, suggesting that the molecular clouds in which these luminous YSOs form are more turbulent. Extending the line width analysis to pre-stellar cores, a broadening of the line profile is observed from these objects to protostars caused by non-thermal processes.

- A correlation is found between the width of the ^{12}CO J=3–2 and J=10–9 broad velocity component and the width of the C^{18}O J=9–8 profile. This suggests a link between entrained outflowing gas and envelope motions (turbulence and/or infalling), which holds from low- to high-mass YSOs. This means that the interaction and effect of outflowing gas and envelope material is the same across the studied luminosity range, indicative of the existence of an underlying common physical mechanism that is independent of the source mass.

- A strong linear correlation is found between the logarithm of the line and bolometric luminosities across six orders of magnitude on both axes, for all lines and isotopologues. This correlation is also found between the logarithm of the line luminosity and envelope mass. This indicates that high-J CO transitions (up to J=10–9) can be used as a dense gas tracer, a relation that can be extended to larger scales (local and high redshift galaxies).

Acknowledgments

The authors are grateful to the external referee, Andrés Guzmán, for his careful and detailed report and to the editor Malcom Walmsley for his useful final comments. These two reports helped to improve this manuscript considerably. We would also like to thank the WISH team for many inspiring discussions, in particular the WISH internal referees Gina Santangelo and Luis Chavarría. Astrochemistry in Leiden is supported by the Netherlands Research School for Astronomy (NOVA), by a Spinoza grant and grant 614.001.008 from the Netherlands Organisation for Scientific Research (NWO), and by the European Community's Seventh Framework Programme FP7/2007-2013 under grant agreement 238258 (LASSIE). We would like to thank the JCMT, which is operated by The Joint Astronomy Centre on Behalf of the Science and Technology Facilities Council of the United Kingdom, the Netherlands Organisation for Scientific Research, and the National Research Council of Canada. This research used the facilities of the Canadian Astronomy Data Centre operated by the National Research Council of Canada with support from the Canadian Space agency. HIFI has been designed and built by a consortium of institutes and university departments from across Europe, Canada and the United States under the leadership of SRON Netherlands Institute for Space Research, Groningen, The Netherlands and with major contributions from Germany, France and the US. Consortium members are: Canada: CSA, U.Waterloo; France: CESR, LAB, LERMA, IRAM; Germany: KOSMA, MPIfR, MPS; Ireland,

NUI Maynooth; Italy: ASI, IFSI-INAF, Osservatorio Astrofisico di Arcetri- INAF; Netherlands: SRON, TUD; Poland: CAMK, CBK; Spain: Observatorio Astronómico Nacional (IGN), Centro de Astrobiología (CSIC-INTA). Sweden: Chalmers University of Technology - MC2, RSS & GARD; Onsala Space Observatory; Swedish National Space Board, Stockholm University - Stockholm Observatory; Switzerland: ETH Zurich, FHNW; USA: Caltech, JPL, NHSC.

2.A. Characterisation of the HIFI data

The main characteristics of the HIFI data are presented in this appendix, together with the spectra. The description of the observed lines focuses first on ^{12}CO J=10–9 (Section 2.A.1), where the main characteristics for the low-, intermediate- and high-mass sources are listed in that order. Next we discuss the ^{13}CO J=10–9 spectra (Section 2.A.2), following the same structure, and finally all observed C^{18}O lines (Section 2.A.3) are presented.

2.A.1. ^{12}CO J=10–9 line profiles

The ^{12}CO J=10–9 line was observed for the entire sample of low- and intermediate-mass YSOs and for one high-mass object (W3-IRS5). All the observed sources were detected, and the emission profiles are the strongest and broadest among the targeted HIFI CO lines (see Fig. 2.15 and Table 2.5 for further information). Within the low-mass Class 0 sample, the main-beam peak temperature, $T_{\rm MB}^{\rm peak}$, ranges from 0.8 to 8.1 K. As indicated in Section 2.2.4, the emission in some sources (around 73 % of the detected lines of this sub-group) can be decomposed into two velocity components. The *FWHM* of the narrower component varies from 2.3 km s^{-1} to 9.3 km s^{-1}, while the width of the broad component shows a larger variation, from 8.3 km s^{-1} to 41.0 km s^{-1}. For the low-mass Class I YSOs, similar intensity ranges are found, with $T_{\rm MB}^{\rm peak}$ varying from ∼0.6 to 10.2 K. The Class I protostars present narrower emission lines than the Class 0 sources, and only the 27 % of the emission line profiles can be decomposed into two velocity components. The narrow component ranges from 1.8 to 5.1 km s^{-1} and the broad component varies from 10.0 to 16.1 km s^{-1}.

For the intermediate-mass protostars, the intensity increases and varies from $T_{\rm MB}^{\rm peak}$=2.4 to ∼28.0 K. The profiles are broader and the distinction between the two different components is clearer than for the low-mass sources, so all profiles can be fitted with two Gaussian functions. The *FWHM* of the two identified velocity components varies from 2.7 to 7.6 km s^{-1} for the narrow component and from 15.6 to 24.3 km s^{-1} for the broad component.

Only W3-IRS5 was observed in ^{12}CO J=10–9 from the high-mass sample. The spectrum is presented in Appendix 2.B, Fig. 2.21, together with other lines of this source. The profile is more intense than any of the low- and intermediate-mass sources ($T_{\rm MB}^{\rm peak}$=48.5 K) and has the largest *FWHM*: 8.4 km s^{-1} for the narrower component and 28.6 km s^{-1} for the broad component.

Self-absorption features have been detected in 5 out of 33 observed ^{12}CO J=10–9 emission lines (the sources are indicated in Table 2.5). However, these features are weak and of the order of the rms of the spectrum, so no Gaussian profile has been fitted. No specific symmetry can be determined; that is, there is no systematic shift in the emission of the broad component relative to the source velocity (see Fig. 2.15 for comparison). Overall, the data do not show any infall signature.

2.A.2. ^{13}CO J=10–9 line profiles

The observed ^{13}CO J=10–9 emission lines for the low- and intermediate-mass sources are less intense, narrower and have a lower *S/N* than the ^{12}CO J=10–9 spectra (Fig. 2.16). Table 2.6 contains the parameters obtained from the one or two Gaussian fits to the detected line profiles. In the case of the low-mass Class 0 spectra, three sources are not detected down to 17 mK rms in 0.27 km s^{-1} bins and the profile of only two sources (Ser SMM1 and NGC1333 IRAS4A) can be decomposed into two different velocity components. The $T_{\rm MB}^{\rm peak}$ ranges from 0.05 to 0.8 K, and the *FWHM* of the narrow profiles varies from 0.7 to 6.8 km s^{-1}, with the highest values corresponding to the broad velocity component being 13.2 km s^{-1} for NGC1333 IRAS4A. In the case of the Class I sample, four sources are not detected and none of the emission line profiles can be decomposed into two velocity components. The averaged intensity is lower than for the Class 0 objects, ranging

Table 2.5: Observed and fitted properties of the ^{12}CO J=10–9 line profiles. The subscript B refers to the broad velocity component and the N to the narrow component.

Source	rms[a] (mK)	$\int T_{\rm MB} {\rm d}v$[b] (K km s^{-1})	$T_{\rm MBB}^{\rm peak}$ (K)	$T_{\rm MBN}^{\rm peak}$ (K)	$V_{\rm B}^{\rm peak}$ (km s^{-1})	$V_{\rm N}^{\rm peak}$ (km s^{-1})	$FWHM_{\rm b}$ (km s^{-1})	$FWHM_{\rm N}$ (km s^{-1})
Low-mass: Class 0								
L 1448-MM[d]	91	21.5	0.4	0.9	10.3	6.0	41.0	4.8
NGC 1333 IRAS 2A	104	20.3	0.4	1.5	12.8	8.2	8.3	3.9
NGC 1333 IRAS 4A[c]	105	45.5	1.8	–	10.3	–	24.8	–
NGC 1333 IRAS 4B	104	32.4	1.4	1.5	8.1	7.1	16.5	3.3
L 1527[c]	93	4.8	–	1.6	–	4.9	–	2.4
Ced110 IRS4[c]	127	4.9	–	1.6	–	4.2	–	2.5
IRAS 15398	132	16.5	0.5	2.5	−1.0	4.1	15.0	4.2
BHR 71[de]	111	9.9	0.2	0.6	−8.5	−5.4	30.8	9.3
L 483-MM	108	10.9	0.3	1.5	2.8	5.3	19.1	2.9
Ser SMM 1[e]	98	81.3	3.4	4.1	7.1	8.6	15.6	5.9
Ser SMM 3	102	33.7	1.0	2.0	8.8	7.0	20.8	4.1
Ser SMM 4	97	39.0	1.6	3.3	2.1	6.8	10.7	4.3
L 723-MM[c]	110	6.8	–	1.1	–	10.9	–	4.9
B335	120	11.1	0.5	1.0	8.9	8.3	16.1	2.3
L 1157	103	9.5	0.3	0.5	0.4	2.9	26.8	2.7
Low-mass: Class I								
L 1489[c]	123	5.8	–	0.9	–	7.0	–	4.9
L 1551 IRS 5	113	15.9	0.4	3.1	4.2	6.2	16.1	2.5
TMR 1 [c]	113	9.3	–	1.8	–	5.5	–	3.9
TMC 1A[c]	137	4.2	–	0.5	–	5.7	–	3.6
TMC 1[c]	119	2.7	–	0.4	–	5.2	–	4.4
HH 46	127	9.5	0.4	1.7	6.0	5.6	12.7	1.8
IRAS 12496[c]	100	10.0	–	2.1	–	2.8	–	3.8
GSS 30 IRS1[e]	127	44.6	1.1	8.0	2.9	2.7	10.0	3.7
Elias 29[c]	120	47.0	–	7.8	–	4.2	–	5.1
Oph IRS 63[c]	124	1.0	–	0.5	–	2.6	–	2.1
RNO 91[c]	114	7.6	–	1.5	–	0.4	–	2.4
Intermediate-mass								
L1641 S3 MMS1	100	31.4	0.8	1.4	5.5	5.3	21.1	7.0
Vela IRS 19	110	42.2	1.3	2.1	14.9	11.5	22.0	3.3
Vela IRS 17	107	94.0	1.9	11.3	5.6	3.9	15.8	4.6
NGC 7129 FIRS 2[e]	100	29.8	0.9	1.2	−11.5	−8.9	20.9	5.1
NGC 2071	162	421.6	7.0	13.9	8.2	10.9	24.3	7.6
AFGL 490	129	29.6	1.2	3.0	−11.5	−13.4	15.6	2.7
High-mass								
W3−IRS5[e]	102	674.8	10.8	32.0	−40.7	−37.5	28.6	8.4

Notes. [a] In 0.27 km s^{-1} bins. [b] Integrated over the entire line, not including "bullet" emission. [c] Single Gaussian fit. [d] EHV emission features removed from the spectra by using two additional Gaussian fit profiles. [e] Self-absorption features detected.

from $T_{\rm MB}^{\rm peak}$=0.05 to 0.52 K. The value of the line width also drops, and the interval varies from 1.5 to 7.3 km s^{-1}.

For the intermediate-mass YSOs, a better characterisation of the line profile is possible since the lines are stronger and have higher *S/N* than the low-mass objects with $T_{\rm MB}^{\rm peak}$ ranging from 0.1 to 2.7 K. Compared to the ^{12}CO J=10–9 profiles, the ^{13}CO J=10–9 lines are more symmetric and only the emission profile of one source can be decomposed into two different Gaussian components. For the *FWHM* of the lines fitted by the narrow Gaussian, the interval goes from 4.3 to 6.1 km s^{-1}.

Around 63% of the detected ^{13}CO J=10–9 emission lines (12 out of 19) for the high-mass

YSOs can be decomposed into two distinct velocity components, whereas the decomposition of the profiles is only possible for 10% of the detected low-mass objects (2 out of 20) and for ∼17% of the detected intermediate-mass YSOs (1 out of 6). The reason for the lower percentage recorded for the low- and intermediate-mass sources could be the lower *S/N* than for the bright high-mass sources. The weakest line from the high-mass sample has a $T_{\rm MB}^{\rm peak}$ of 0.7 K and the most intense a $T_{\rm MB}^{\rm peak}$ of 20.8 K. The *FWHM* of the narrower component varies from 3.3 km s^{-1} to 7.2 km s^{-1}. The width of the broad component presents a larger variation since the minimum value is 8.7 km s^{-1} and the maximum 21.9 km s^{-1}. This component appears either red- or blue-shifted. There is no significant trend with evolution stage as probed by the presence of IR-brightness or ionising radiation (Fig. 2.16).

2.A.3. $C^{18}O$ line profiles

Three transitions of $C^{18}O$ were obtained within WISH, together with water observations: $C^{18}O$ J=5–4, J=9–8 and J=10–9. Only Class 0 and intermediate-mass YSOs were observed in $C^{18}O$ J=5–4, tracing regions with an upper energy level of ∼79 K (see Fig. 2.17). This line is obtained in parallel with a deep integration on the 548 GHz $H_2^{18}O$ $1_{10} - 1_{01}$ transition for 19 sources. Thus, the spectra have very high *S/N* with an rms of 9 mK for low-mass Class 0 sources and less than 20 mK for intermediate-mass YSOs in 0.27 km s^{-1} bins. The main characteristic of this transition is the narrow profile seen in all the emission lines for the narrower component, with a *FWHM* of less than 2.0 km s^{-1} for the low-mass sources, and 3.7 km s^{-1} for the intermediate-mass objects. In addition, other features are detected thanks to the high *S/N*, e.g. a weak broad velocity component for the low-mass objects NGC1333 IRAS 4A (Yıldız et al. 2010), L483, Ser SMM1 and Ser SMM4. This component is also identified in the $C^{18}O$ J=5–4 line for the intermediate-mass sources NGC2071 (see Fig. 2.3) and Vela IRS19. The values of the single or two Gaussian fit of these lines are presented in Table 2.7.

For the J=9–8 transition, ∼55% of the observed lines are detected, probably due to the lower *S/N* caused by shorter exposure times than for the J=5–4 line. The lines are detected in 5 out of 26 low-mass sources; 4 out of 6 intermediate-mass YSOs; and in all 19 high-mass protostars (see Fig. 2.18). The $C^{18}O$ J=9–8 emission lines appear weak with median $T_{\rm MB}^{\rm peak}$ values of 0.10, 0.14 and 0.83 K for the low-, intermediate- and high-mass objects, respectively. Most of the emission line profiles of $C^{18}O$ J=9–8 can be fitted by a single Gaussian with a *FWHM* from 2.0 km s^{-1} to 3.9 km s^{-1} for the low-mass objects; from 2.8 km s^{-1} to 5.4 km s^{-1} for the intermediate-mass sources; and from 3.1 to 6.4 km s^{-1} for the high-mass YSOs (values summarised in Table 2.8). Only a two Gaussian decomposition has been performed for three ultra-compact HII regions (G10.47+0.03, W51N-e1 and G5.89-0.39). For these objects, the broad velocity components are more than 16 km s^{-1}, as is shown in Fig. 2.18.

Finally, the $C^{18}O$ J=10–9 transition was observed in 30-minute exposures for all low-mass Class 0 protostars, one intermediate-mass source and all high-mass YSOs. Additional deeper integrations of 300 minutes were obtained for NGC1333 IRAS 2A (as part of WISH) and for NGC1333 IRAS 4A, NGC1333 IRAS 4B, Elias 29 and GSS 30 IRS1 (as part of open-time programme OT2_rvisser_2) in parallel with deep $H_2^{18}O$ searches. The line was detected in five low-mass sources and in all 19 high-mass objects (Fig. 2.19). This line appears close to the 1097 GHz H_2O $3_{12} - 3_{03}$ transition. For most of the high-mass objects, the line profile of this water transition shows broad wings that extend a few km s^{-1}, so the $C^{18}O$ J=10–9 emission line is found on top of the broad water red wing. To properly analyse the emission of this CO isotopologue, the line wings of the 1097 GHz water transition were fitted with a Gaussian profile, subtracted and the residuals plotted. With this method, the $C^{18}O$ J=10–9 emission line for the high-mass sample has been isolated. The temperature of the gas that J=10–9 traces is likely similar to what is traced by the J=9–8 transition, so the lines are also weak with median values of $T_{\rm MB}^{\rm peak}$ of 0.04 K for the low-mass protostars and 0.52 K for the high-mass objects. The *FWHM* of the one single Gaussian profile which fits these lines are slightly larger, ranging from 3.4 to 7.5 km s^{-1} for the high-mass sources (Table 2.8 for more details).

Table 2.6: Observed and fitted properties of the ^{13}CO J=10–9 line profiles for the detected sources. The subscript B refers to the broad velocity component and the N to the narrow component.

Source	rms[a] (mK)	$\int T_{\rm MB} dv$[b] (K km s^{-1})	$T_{\rm MBB}^{\rm peak}$ (K)	$T_{\rm MBN}^{\rm peak}$ (K)	$V_{\rm B}^{\rm peak}$ (km s^{-1})	$V_{\rm N}^{\rm peak}$ (km s^{-1})	$FWHM_{\rm b}$ (km s^{-1})	$FWHM_{\rm N}$ (km s^{-1})
Low-mass: Class 0								
L 1448-MM	20	0.2	–	0.1	–	4.7	–	1.6
NGC 1333 IRAS 2A	15	0.8	–	0.2	–	7.5	–	2.1
NGC 1333 IRAS 4A	23	1.1	0.07	0.09	5.7	6.7	13.2	0.7
NGC 1333 IRAS 4B	17	0.8	–	0.1	–	6.9	–	6.8
IRAS 15398	24	0.2	–	0.16	–	5.0	–	1.1
BHR 71	17	0.4	–	0.2	–	–4.6	–	1.8
L 483-MM	16	0.3	–	0.1	–	5.0	–	2.4
Ser SMM 1	22	4.0	0.2	0.5	7.6	8.3	10.6	2.4
Ser SMM 3	20	0.3	–	0.1	–	7.2	–	4.0
Ser SMM 4	25	0.6	–	0.1	–	5.7	–	6.0
L 723-MM	16	0.3	–	0.1	–	11.5	–	2.7
B335	20	0.3	–	0.1	–	8.1	–	2.3
L 1157	20	0.1	–	0.05	–	3.0	–	2.2
Low-mass: Class I								
L 1489	32	0.4	–	0.05	–	7.8	–	7.3
L 1551 IRS 5	29	1.3	–	0.47	–	6.5	–	2.4
TMR 1	29	0.3	–	0.08	–	6.0	–	3.6
HH 46	30	0.1	–	0.11	–	5.4	–	1.5
IRAS 12496	28	0.8	–	0.15	–	3.1	–	4.2
GSS 30 IRS1	33	2.0	–	0.46	–	2.8	–	3.4
Elias 29	28	2.1	–	0.38	–	4.7	–	5.1
Intermediate-mass								
L1641 S3 MMS1	38	1.8	–	0.2	–	4.7	–	6.1
Vela IRS 19	41	1.1	–	0.2	–	12.1	–	5.9
Vela IRS 17	43	4.9	–	0.8	–	0.4	–	4.4
NGC 7129 FIRS 2	20	0.9	–	0.1	–	–9.6	–	4.3
NGC 2071	17	16.6	0.4	2.1	9.1	9.8	14.7	4.7
AFGL 490	47	2.6	–	0.3	–	–13.5	–	4.8
High-mass								
IRAS05358+3543	18	6.2	0.2	0.7	–15.1	–15.9	15.4	3.7
IRAS16272−4837	18	3.9	–	0.7	–	–47.0	–	4.8
NGC6334-I(N)	23	13.8	0.5	1.3	–5.7	–3.8	13.3	4.4
W43-MM1	38	4.5	–	0.8	–	98.4	–	5.8
DR21(OH)	18	52.2	0.9	5.7	–1.9	–3.3	16.0	5.8
W3-IRS5	21	129.6	2.1	17.0	–38.7	–38.3	14.7	4.7
IRAS18089−1732	27	8.3	–	1.4	–	33.0	–	4.6
W33A	19	11.4	0.5	1.1	36.8	37.7	11.7	3.5
IRAS18151−1208	19	3.4	–	0.8	–	33.4	–	3.6
AFGL2591	19	29.5	0.8	5.4	–5.8	–5.4	9.8	3.3
G327−0.6	25	12.8	–	1.8	–	–44.8	–	6.6
NGC6334-I	23	57.7	0.7	7.2	–6.7	–6.8	17.8	5.4
G29.96−0.02	46	31.3	0.6	4.6	96.9	98.8	13.6	4.6
G31.41+0.31	52	17.4	–	2.5	–	96.8	–	6.1
G5.89−0.39	34	133.7	2.6	6.2	10.5	9.4	21.9	5.9
G10.47+0.03	200	26.2	1.8	–	66.8	–	10.0	–
G34.26+0.15	59	58.8	1.3	6.7	58.0	57.7	12.0	5.0
W51N-e1	50	70.2	1.3	5.0	58.6	57.1	18.6	7.2
NGC7538-IRS1	24	41.0	2.0	5.3	–59.8	–57.6	8.7	3.5

Notes. [a] In 0.27 km s^{-1} bins. [b] Integrated over the entire line.

Table 2.7: Observed and fitted properties of the $C^{18}O$ J=5–4 line profiles for the observed sources. The subscript B refers to the broad velocity component and the N to the narrow component.

Source	rms[a] (mK)	$\int T_{MB} dv$[b] (K km s^{-1})	T_{MBB}^{peak} (K)	T_{MBN}^{peak} (K)	V_B^{peak} (km s^{-1})	V_N^{peak} (km s^{-1})	$FWHM_b$ (km s^{-1})	$FWHM_N$ (km s^{-1})
Low-mass: Class 0								
L 1448-MM	4	0.47	–	0.37	–	5.1	–	1.3
NGC 1333 IRAS 2A	2	0.87	–	0.52	–	7.5	–	1.4
NGC 1333 IRAS 4A	4	0.68	0.03	0.32	7.9	6.9	7.8	1.3
NGC 1333 IRAS 4B	3	0.32	–	0.14	–	7.0	–	1.9
L 1527	3	0.55	–	0.23	–	5.7	–	2.0
BHR 71	3	0.63	–	0.37	–	–4.7	–	1.4
L 483-MM	3	0.31	0.03	0.16	5.2	5.4	4.3	1.1
Ser SMM 1	4	1.93	0.13	0.84	8.7	8.4	4.2	1.4
Ser SMM 3	5	1.40	–	0.55	–	7.6	–	2.0
Ser SMM 4	3	1.55	0.13	0.44	7.6	7.7	4.7	1.8
L 723-MM	5	0.19	–	0.09	–	10.0	–	1.9
B335	4	0.26	–	0.22	–	8.2	–	1.2
L 1157	4	0.15	–	0.09	–	2.6	–	1.3
Intermediate-mass								
L1641 S3 MMS1	20	0.73	–	0.40	–	5.2	–	1.7
Vela IRS 19	10	1.67	0.05	0.46	12.5	11.6	9.2	2.4
Vela IRS 17	25	5.32	–	1.25	–	4.1	–	3.7
NGC 7129 FIRS 2	4	0.55	–	0.18	–	–9.9	–	2.3
NGC 2071	5	7.29	0.55	1.33	8.9	9.6	7.4	2.0
AFGL 490	14	3.55	–	1.04	–	–13.3	–	2.7

Notes. [a] In 0.27 km s^{-1} bins. [b] Integrated over the entire line.

2.B. JCMT data

The central spectrum of the ^{12}CO and $C^{18}O$ J=3–2 spectral maps observed with the HARP instrument of the JCMT are presented in this section (see Figs. 2.22 and 2.23). These central spectra were convolved to a 20″beam in order to compare them with the HIFI data. The ^{12}CO and $C^{18}O$ J=3–2 spectra for the low-mass sources BHR 71, Ced110 IRS4, IRAS 12496 and HH 46 were observed with APEX because of their low declination. As for the JCMT data, the central spectrum was convolved to a 20″beam. See Yıldız et al. (2013) for more information about the low-mass protostar observations.

The spectral maps are not presented in this paper because only the values of *FWHM* from the broad component for the ^{12}CO J=3–2 central spectrum were used in the analysis and discussion, together with the width and integrated intensity of the $C^{18}O$ J=3–2 data. These values are presented in Table 2.9. Some spectra from these species are also plotted with the HIFI data in the figures shown in this appendix in order to make a direct comparison of the lines for different types of protostars.

The ^{12}CO J=3–2 data show more complex line profiles than the J=10–9, as indicated in Section 2.3.1, with intense self-absorption features and broad velocity components (see spectra from Fig. 2.22). More than 82% of the observed and detected lines (39 out of 47) present a broad velocity component, and the *FWHM* ranges from 7.4 to 53.3 km s^{-1}, values corresponding to low- and high-mass YSOs respectively.

On the other hand, the narrow $C^{18}O$ J=3–2 spectra show single Gaussian emission profiles, similar to those from higher-J transitions observed with HIFI. The *FWHM* of these data varies from 0.6 to 7.3 km s^{-1}. The spectra is presented in Fig. 2.23 and the constrained values of *FWHM* and integrated intensity in Table 2.9.

Table 2.8: Observed and fitted properties of the $C^{18}O$ J=9–8 and 10–9 narrow line profiles for the detected sources.

Source	$C^{18}O$ J=9–8					$C^{18}O$ J=10–9			
	$\int T_{MB} dv^b$ (K km s^{-1})	T_{MB}^{peak} (K)	$FWHM$ (km s^{-1})	rms^a (mK)	$N_{H_2}{}^c$ (cm^{-2})	$\int T_{MB} dv^b$ (K km s^{-1})	T_{MB}^{peak} (K)	$FWHM$ (km s^{-1})	rms^a (mK)
Low-mass: Class 0									
NGC 1333 IRAS 2A	0.21	0.07	2.0	20	1.2×10^{21}	0.34	0.04	10.7	8
NGC 1333 IRAS 4B	–	–	–	–	–	0.05	0.03	1.4	10
Ser SMM 1	0.70	0.13	3.0	23	4.1×10^{21}	0.61	0.07	4.8	17
Low-mass: Class I									
L 1551 IRS 5	0.22	0.10	3.1	24	1.3×10^{21}	–	–	–	–
GSS 30 IRS1	0.23	0.06	2.2	25	1.4×10^{21}	0.12	0.04	3.1	8
Elias 29	0.40	0.08	3.9	30	2.3×10^{21}	0.22	0.04	4.7	7
Inter.-mass									
Vela IRS 19	0.37	0.11	3.2	24	2.2×10^{21}	–	–	–	–
Vela IRS 17	0.69	0.16	2.8	25	4.0×10^{21}	–	–	–	–
NGC 2071	2.97	0.41	4.6	25	1.7×10^{22}	–	–	–	–
AFGL 490	0.45	0.08	5.4	20	2.6×10^{21}	–	–	–	–
High-mass									
IRAS05358+3543	0.93	0.22	4.0	56	5.4×10^{21}	0.42	0.10	3.8	26
IRAS16272−4837	1.18	0.14	5.9	55	6.9×10^{21}	0.49	0.11	4.8	26
NGC6334-I(N)	1.82	0.37	3.9	55	1.1×10^{22}	2.31	0.28	7.5	20
W43-MM1	1.81	0.29	5.9	49	1.0×10^{22}	0.92	0.12	5.3	23
DR21(OH)	9.11	1.51	5.5	57	5.3×10^{22}	7.94	1.08	6.0	33
W3-IRS5	25.43	4.80	4.2	66	1.5×10^{23}	17.04	3.39	4.1	22
IRAS18089−1732	3.26	0.52	4.1	53	1.9×10^{22}	1.54	0.30	4.5	28
W33A	3.17	0.43	4.8	46	1.9×10^{22}	1.72	0.30	4.3	22
IRAS18151−1208	0.60	0.24	4.2	54	3.5×10^{21}	0.48	0.09	4.2	22
AFGL2591	4.56	1.21	3.1	39	2.7×10^{22}	3.80	0.88	3.4	23
G327−0.6	6.16	0.83	6.1	57	3.6×10^{22}	3.03	0.42	5.8	34
NGC6334-I	10.97	2.00	5.0	54	6.4×10^{22}	10.09	1.55	5.3	28
G29.96−0.02	7.50	1.41	4.3	41	4.4×10^{22}	5.79	1.02	4.5	30
G31.41+0.31	5.26	0.73	6.0	36	3.1×10^{22}	3.98	0.52	6.1	38
G5.89−0.39^d	31.35	2.13	5.9	51	1.8×10^{23}	11.59	2.08	7.0	27
G10.47+0.03^d	5.71	0.53	6.4	79	1.1×10^{23}	3.44	0.47	7.1	26
G34.26+0.15	16.26	2.53	5.5	49	9.5×10^{22}	11.80	1.73	6.0	29
W51N-e1^d	15.22	1.83	5.7	48	8.9×10^{22}	10.49	1.48	6.8	52
NGC7538-IRS1	6.32	1.37	4.0	48	3.7×10^{22}	3.95	0.88	3.9	37

Notes. $^{(a)}$ In 0.27 km s^{-1} bins. $^{(b)}$ Integrated over the entire line. $^{(c)}$ Column density of H_2 calculated for an excitation temperature of 75 K and a $C^{18}O/H_2$ abundance ratio of 5×10^{-7}. $^{(d)}$ Two Gaussian fit. Only the values from the narrow velocity component are presented.

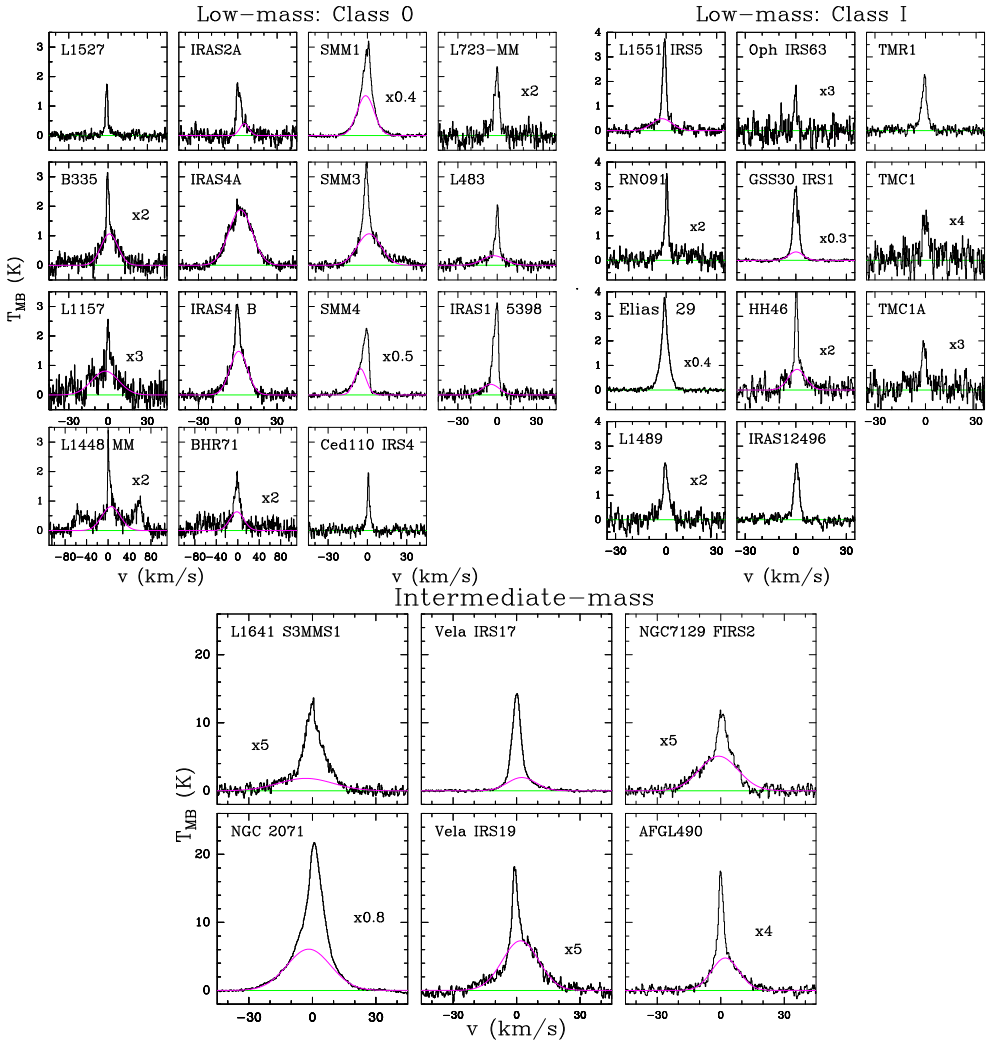

Figure 2.15: ^{12}CO J=10–9 spectra for low- and intermediate-mass YSOs. The green line represents the baseline level and the pink Gaussian profile the broad velocity component for those sources for which a two Gaussian decomposition has been performed. All the spectra have been shifted to zero velocity. The numbers indicate where the spectra have been scaled for greater visibility.

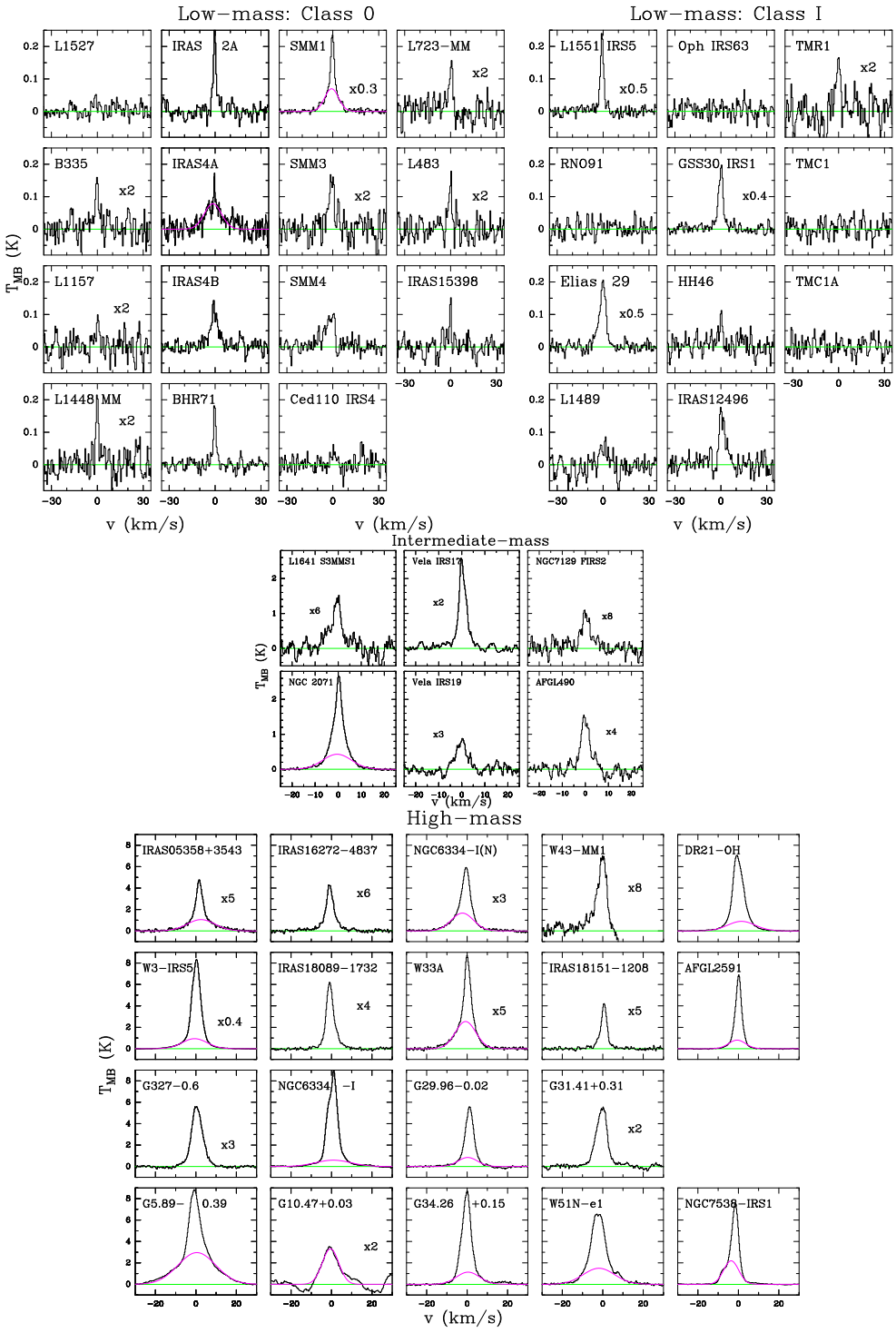

Figure 2.16: Same as Fig. 2.15 but for the ^{13}CO J=10–9 spectra from the observed low-, intermediate- and high-mass YSOs. The high-mass sample is presented according to its evolutionary stage as (from the first to the forth row): mid-IR-quiet high-mass protostellar objects (HMPOs), mid-IR-bright HMPOs, hot molecular cores and ultra-compact HII regions.

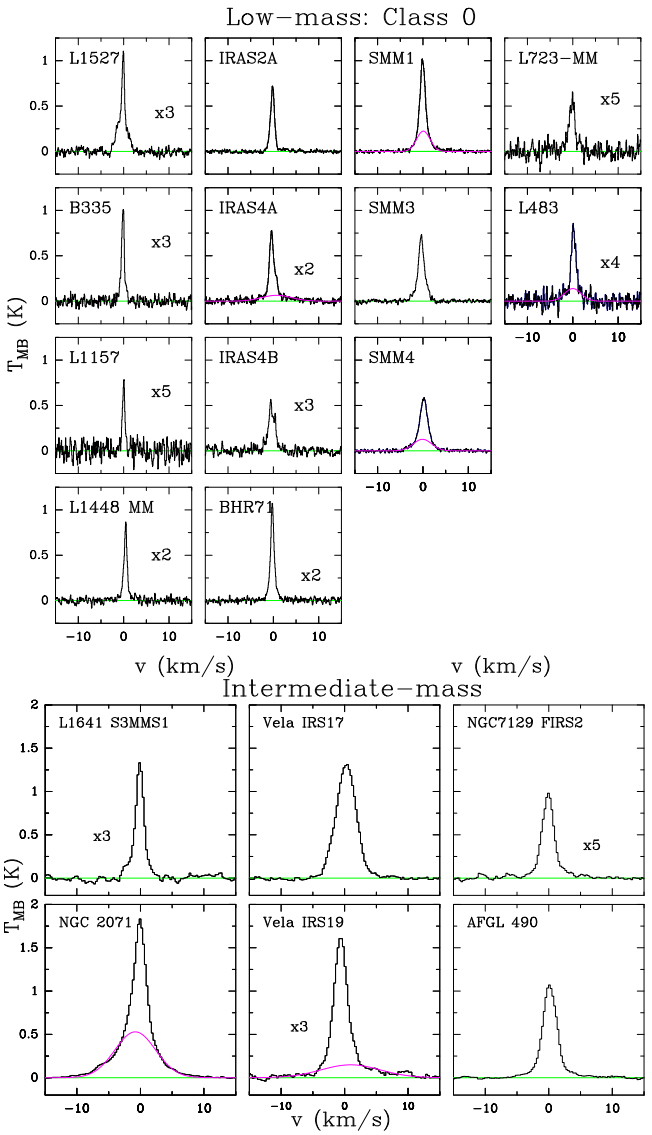

Figure 2.17: Same as Fig. 2.15 but for the $C^{18}O$ J=5–4 spectra of the low-mass (Class 0) and intermediate-mass protostars. For the low-mass sample the HRS spectra are presented, while the WBS data is used for the intermediate-mass objects.

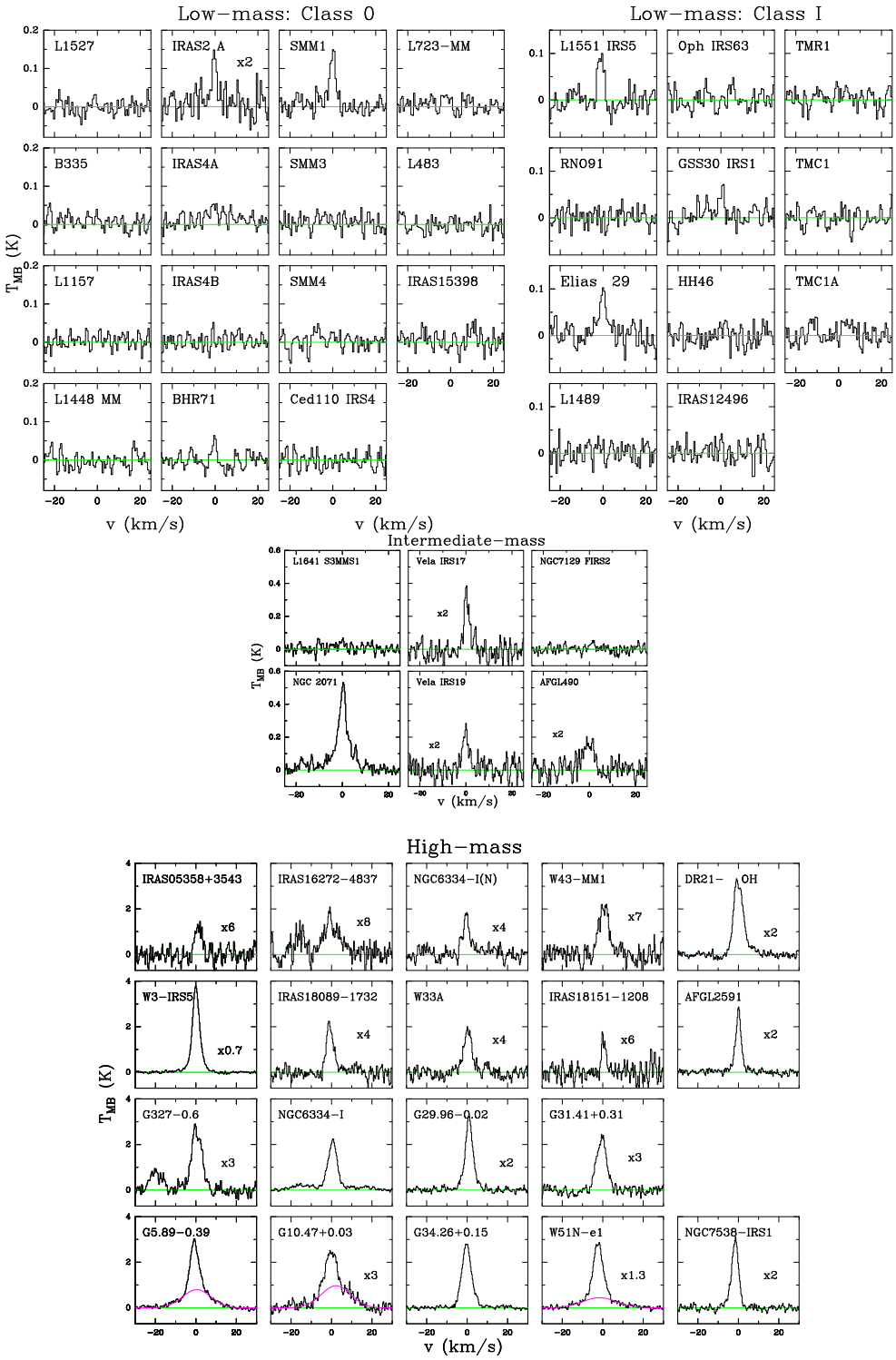

Figure 2.18: Same as Fig. 2.16 but for the $C^{18}O$ J=9–8 spectra from the low-, intermediate- and high-mass YSOs. The high-mass objects are organised according to their evolutionary stage.

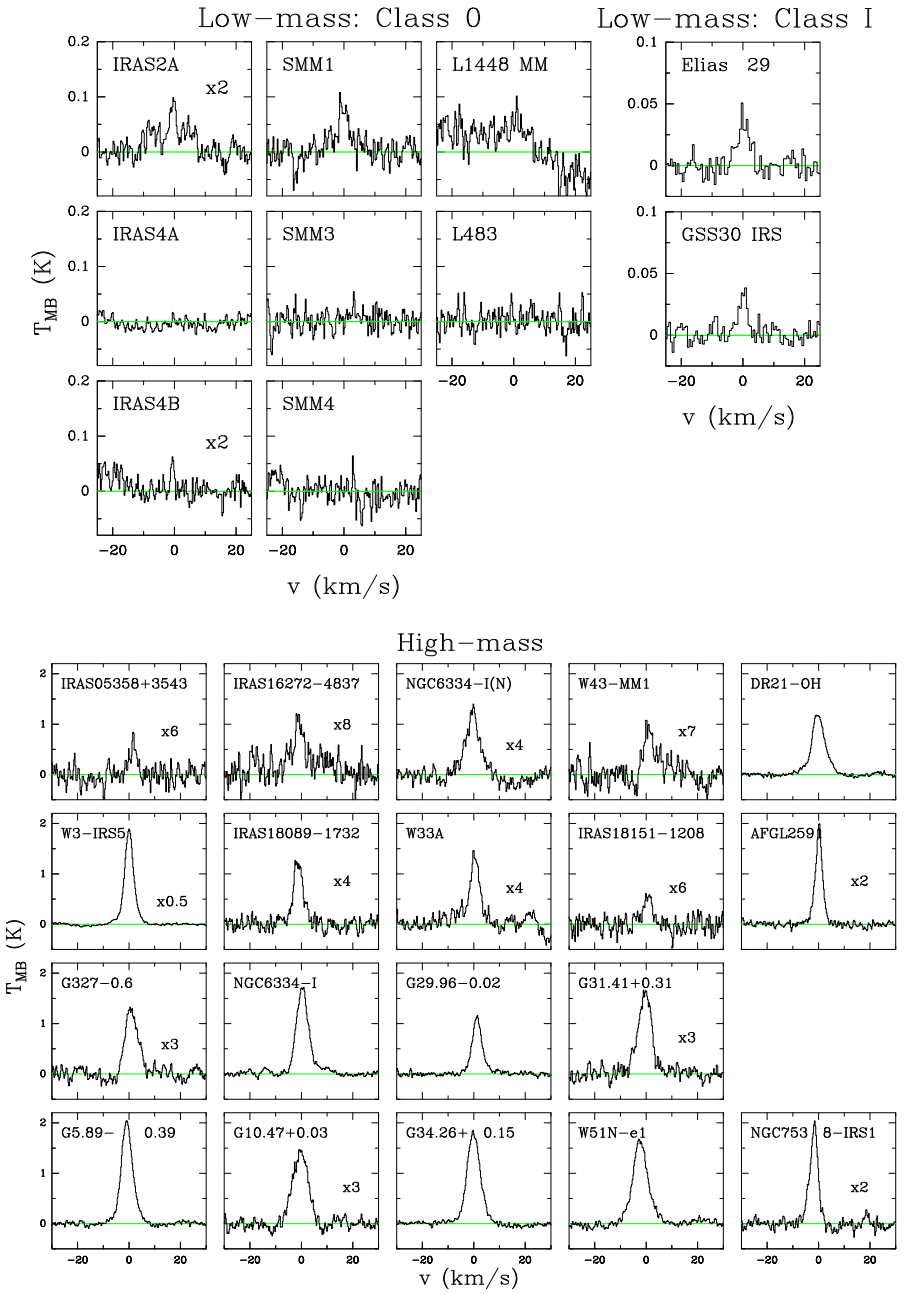

Figure 2.19: Same as Fig. 2.18 but for the $C^{18}O$ J=10–9 spectra of the observed low- and high-mass YSOs. The line wings of the $3_{12} - 3_{03}$ water transition for the high-mass sources have been fitted with a Gaussian profile, subtracted, and the residuals plotted to isolate the $C^{18}O$ J=10–9 emission line.

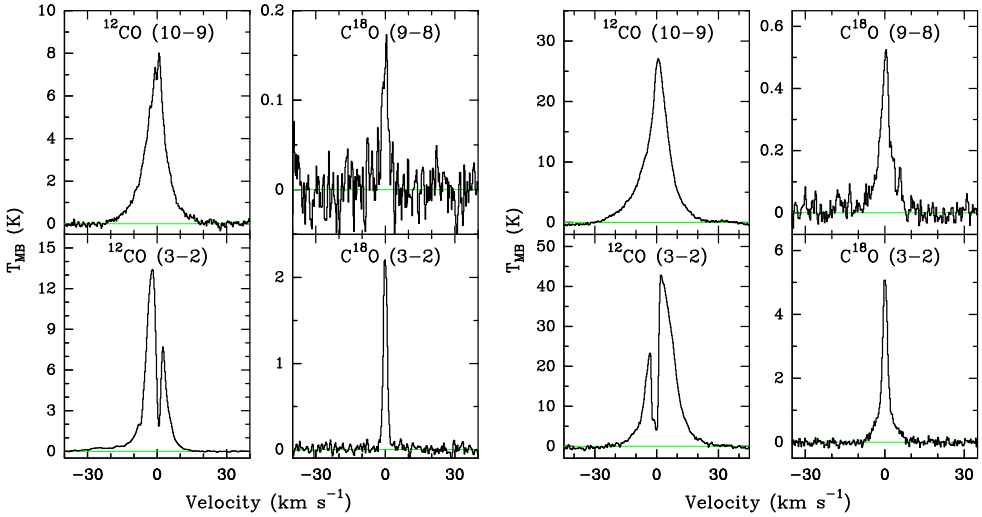

Figure 2.20: (*Left-figure*) Comparison between high-J HIFI and low-J JCMT spectra for the low-mass source Ser SMM1. ^{12}CO J=10–9 spectra (left-top) and C^{18}O J=9–8 line (right-top) observed with HIFI and for the ^{12}CO J=3–2 and C^{18}O J=3–2 lines (left-bottom and right-bottom respectively) observed with JCMT. The spectra have been resampled to 0.27 km s^{-1} and shifted to zero velocity. The green line indicates the baseline subtraction. (*Right-figure*) Same as left-figure but for the intermediate-mass source NGC2071.

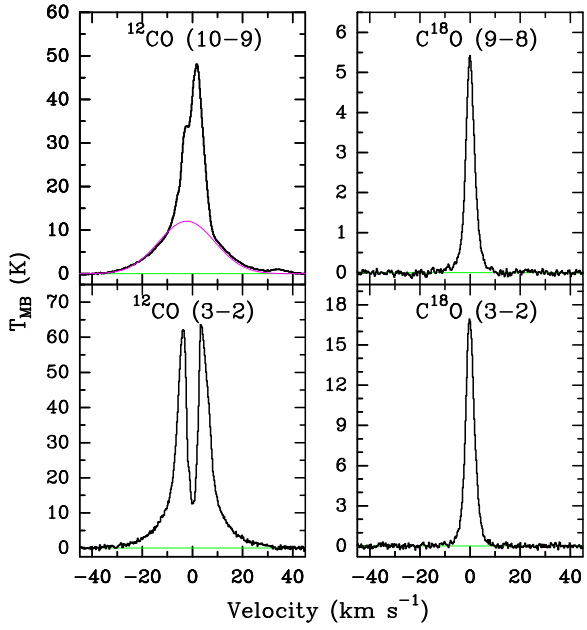

Figure 2.21: Same as Fig. 2.20 but for the high-mass source W3-IRS5. The pink Gaussian profile represents the broad velocity component identified in the ^{12}CO J=10–9 line.

Table 2.9: Values of the *FWHM* for the ^{12}CO J=3-2 broad velocity component and the *FWHM* and integrated intensity for the C^{18}O J=3-2 spectra.

Source	^{12}CO J=3-2	C^{18}O J=3-2		Source	^{12}CO J=3-2	C^{18}O J=3-2	
	$FWHM_b$ (km s^{-1})	$FWHM$ (km s^{-1})	$\int T_{MB} dv$ (K km s^{-1})		$FWHM_b$ (km s^{-1})	$FWHM$ (km s^{-1})	$\int T_{MB} dv$ (K km s^{-1})
Low-mass: Class 0				**Interm.-mass**			
L 1448-MM	18.5	1.1	1.5	NGC 7129 FIRS2	18.2	1.6	5.1
NGC 1333 IRAS2A	13.8	1.2	2.8	L1641 S3 MMS1	13.3	1.6	6.4
NGC 1333 IRAS4A	20.1	1.5	2.5	NGC2071	25.5	2.8	14.1
NGC 1333 IRAS4B	16.2	0.8	1.6	AFGL 490	37.4	2.3	13.2
L 1527[a]	–	0.7	1.5				
Ced110 IRS4[a]	–	–	–	**High-mass**			
BHR 71	16.4	1.2	4.1	IRAS05358+3543	20.0	3.0	7.7
IRAS 15398[a]	–	0.7	0.8	NGC6334-I(N)	30.1	–	–
L 483-MM	10.2	0.6	1.2	W43-MM1	27.6	6.7	36.9
Ser SMM1	14.1	2.1	4.8	DR21-OH	–	5.5	49.8
Ser SMM4	14.2	2.3	6.0	W3-IRS5	24.7	4.2	76.1
Ser SMM3	11.6	1.7	4.9	IRAS18089-1732	15.7	4.1	39.7
L 723-MM	13.2	1.5	1.0	W33A	36.7	4.3	41.7
B 335[a]	–	0.8	1.4	IRAS18151-1208 [a]	–	2.5	19.3
L 1157	18.9	0.9	0.6	AFGL2591	22.0	3.6	45.9
				NGC6334-I	35.7	3.7	50.3
Low-mass: Class I				G29.96-0.02	18.0	4.0	65.9
L 1489[a]	–	2.0	0.7	G31.41+0.31	24.9	7.3	44.5
L 1551-IRS5	10.4	0.9	2.3	G5.89-0.39	53.5	4.8	95.0
TMR1[a]	–	1.2	1.1	G10.47+0.03	14.1	7.0	82.2
TMC1	13.7	0.7	0.9	G34.26+0.15	23.9	6.0	153.2
TMC1A	10.2	1.0	0.9	W51-e1	30.3	–	–
HH46	12.8	0.9	3.2	NGC7538-IRS1	20.8	5.9	50.3
IRAS 12496	19.5	1.2	1.4				
Elias 29	7.8	2.5	5.3				
Oph IRS 63	8.5	0.6	1.1				
GSS 30-IRS1	7.4	1.2	3.7				
RNO 91	9.3	0.6	1.1				

Notes. [(a)] No broad velocity component identified in the ^{12}CO J=3-2 convolved central spectrum.

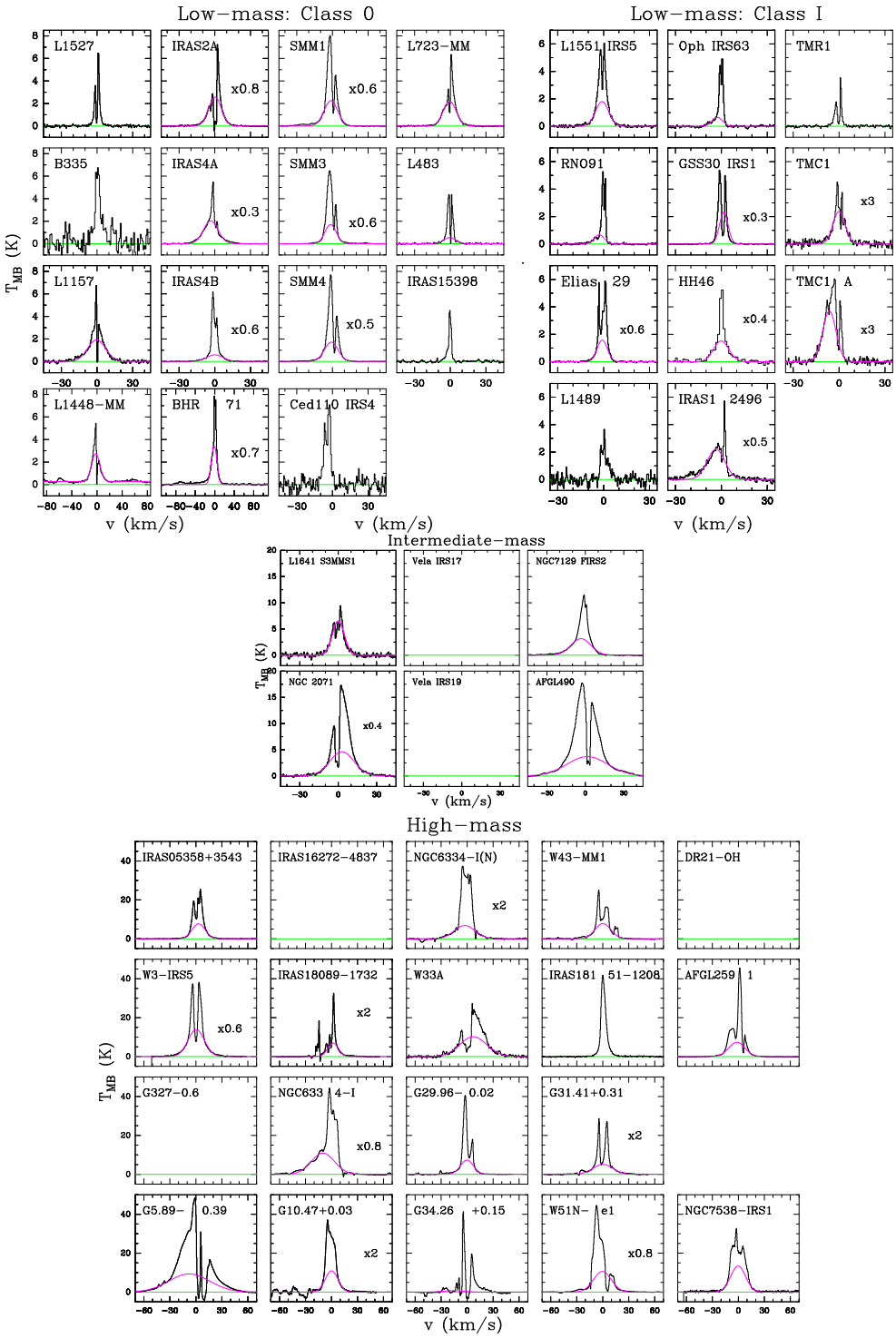

Figure 2.22: ^{12}CO J=3–2 spectra for low-, intermediate and high-mass YSOs. observed with the JCMT. The green line represents the baseline level and the pink Gaussian profile the broad velocity component for those sources for which a two Gaussian decomposition has been performed. All the spectra have been shifted to zero velocity. The numbers indicate where the spectra have been scaled for greater visibility.

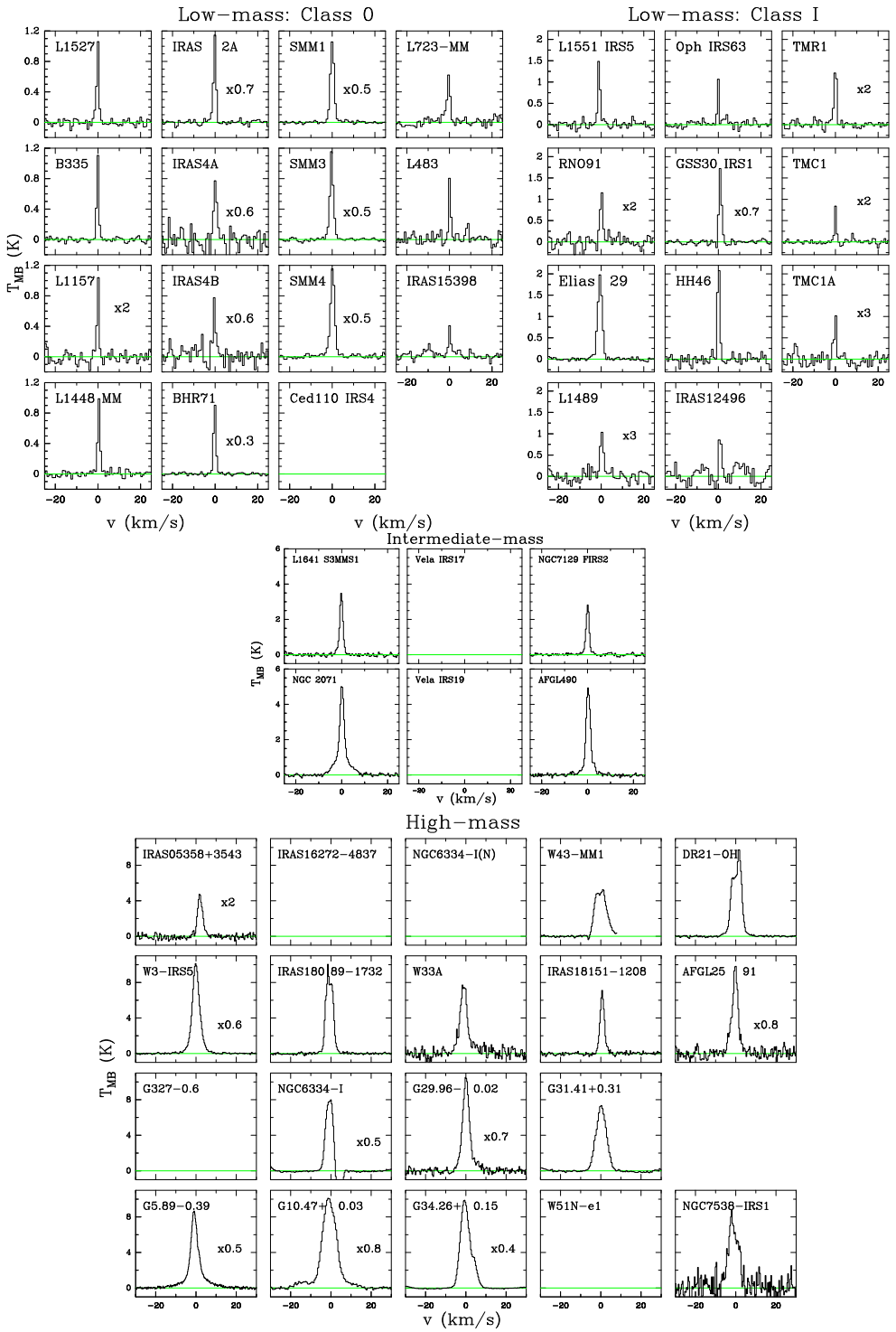

Figure 2.23: Same as Fig. 2.22 but for the $C^{18}O$ J=3–2 spectra.

3

Infall versus turbulence as the origin of sub-millimetre line broadening in protostellar envelopes: from low- to high-mass

I. San José-García, J. C. Mottram, E. F. van Dishoeck, et al.
submitted

Abstract

The analysis of spectrally resolved molecular line observations is a powerful tool to characterise the dynamical structure of protostellar environments. Previous studies of young stellar objects (YSOs) based on data from ground-based single-dish telescopes have been restricted to the outer colder parts of their envelopes. However, *Herschel* has revealed the dynamical properties of inner warmer regions, giving further insights into the complete understanding of the star formation process, for both low- and high-mass YSOs.

As part of the "Water In Star-forming regions with *Herschel*" (WISH) survey, we quantify the contributions of infall and turbulence to the broadening of low- and high-J $C^{18}O$ and HCO^+ line profiles for a sample of low- and high-mass YSOs across a wide luminosity range (from <1 to $> 10^5$ $L_\odot$).

Optically thin $C^{18}O$ $J = 3$–2, 9–8 and 10–9 and optically thick HCO^+ $J = 4$–3 and $J = 6$–5 spectra are modelled with the non-LTE radiative transfer code RATRAN. An iterative method is used to constrain the infall and turbulent velocities, and abundance profiles which best-fit all the observed lines.

Both turbulence and infall are necessary to reproduce the $C^{18}O$ and HCO^+ observations simultaneously. The pure infall dominated scenario is excluded for all studied YSOs, while pure turbulent dominated models are ruled out for the majority. The turbulent width increases with the luminosity of the source and is significantly higher in the protostellar phase compared to that observed in pre-stellar cores. For the low-mass protostars, the observed broadening of higher-J $C^{18}O$ transitions can be explained by including infall motions but not by adding a gradient in turbulence. For most of the massive YSOs, the best-fit infall component is slower than the maximum infall velocity estimated from their assumed stellar masses. The infall velocity seems to increase with luminosity for massive sources above $\sim 10^3$ $L_\odot$ and is independent of $L_{\rm bol}$ below this value. In addition, most of these massive objects show slightly larger values of turbulent velocity than those calculated for systems in virial equilibrium, implying that, even if the star initially forms from a quasi-virial equilibrium core, turbulence prevails over the gravitational potential once star formation is underway. Finally, a jump abundance profile is needed for all YSOs to reproduce the $C^{18}O$ observations, whereas a constant profile is sufficient for HCO^+.

Turbulence in protostellar envelopes increases significantly from the pre-stellar to protostellar phase regardless of mass. This suggests that a source of turbulence, such as outflows, switches on during the star formation process. The dynamical properties in the inner warm regions of high-mass protostellar envelopes, closer to the actual forming star, could be considered scaled-up version of their low-mass counterparts.

3.1. Introduction

One of the challenges in star formation is to uncover the links between the star formation process for low and high-mass young stellar objects (YSOs). The dynamical conditions of their environments are tightly related to the formation and evolution of YSOs, so the study of their velocity fields provides insight into the existing similarities and differences between low- and high-mass star forming regions.

The classical low-mass star formation scenario must be modified to explain the formation of massive stars due to their different radiative pressure, formation timescales, accretion rates, stronger radiation feedback and injected energy by powerful outflows and companions (Zinnecker & Yorke 2007). The various scenarios describing the high-mass star formation process imply different levels of turbulence dominating their cores and different infall velocities (see McKee & Tan 2002, 2003; Bonnell & Bate 2005; Hocuk & Spaans 2010; Krumholz & Bonnell 2009). In addition, infall and rotation come into play affecting parameters such as accretion rate, degree of turbulence, outflow force, etc. (Behrend & Maeder 2001b). Therefore, understanding the dynamical properties of YSO environments, especially in their pre-stellar and early embedded phase, is a crucial component of a global theory capable of explaining how stars form irrespective of their final masses.

A powerful tool used to disentangle the complexity of these objects is molecular spectroscopy. Spectrally resolved lines characterise the conditions in different components of protostellar environments as well as their dynamical structure. In particular, CO and its isotopologues play a pivotal role in tracing different physical components within the protostar and providing information about gas motions. ^{12}CO is used to observe the entrained material in the outflow while optically thin C^{18}O mostly probes quiescent envelope gas.

With the available ground-based telescopes, most CO studies have been limited to low- and intermediate-J transitions (J up to 6–5). These lines probe the colder outer part of protostellar environments ($>10^3$ and $>10^4$ AU for low- and high-mass objects respectively). However, the Heterodyne Instrument for the Far-Infrared (HIFI; de Graauw et al. 2010) on board the *Herschel*[1] Space Observatory (Pilbratt et al. 2010), has enabled spectrally resolved observations of high-J CO transitions (up to J = 16–15), probing the higher densities closer to the protostar and resolving the velocity components traced by the warm gas. HIFI observations of molecular lines are unique as they probe frequency ranges not observable from the ground with unprecedented sensitivity and spectral resolution. More importantly, these observed transitions allow us to extend the comparison between low- and high-mass YSOs to parts of the protostar which are an order of magnitude closer to the actual forming star (e.g. Yıldız et al. 2010; Plume et al. 2012; San José-García et al. 2013).

Within the context of the "Water In Star-forming regions with *Herschel*" Guaranteed Time Key Programme (WISH; van Dishoeck et al. 2011), San José-García et al. (2013) presented a study of the low- and high-J transitions of ^{12}CO, ^{13}CO and C^{18}O for a sample of 51 embedded YSOs covering a range of luminosities from <1 to > 10^5 $L_\odot$. They investigated the dynamics of the entrained outflowing and envelope material on scales of 10^2–10^3 AU and 10^3–10^4 AU for low- and high-mass YSOs respectively, by decomposing the ^{12}CO and C^{18}O line profiles into different Gaussian components. The entrained gas in the outflow causes broad line-wings in the ^{12}CO spectra, while non-thermal motions in the envelope broaden and shape the C^{18}O profiles. Understanding the motions in the envelopes of low and high-mass YSOs will reveal whether these processes are independent of the luminosity of the central protostar.

In order to characterise the dynamical structure of protostellar envelopes, the first step is to analyse the four non-thermal motions that can contribute to the velocity field: turbulence, infall, expansion, and rotation. Emission generated by turbulent motions is characterised by symmetric Gaussian profiles such as those observed for C^{18}O, C^{17}O and discussed in Jørgensen et al. (2002) for low-mass YSOs. The observational signature of infalling gas is a blue-shifted asymmetric double-peaked line (Myers et al. 1996). This specific profile is observed only if the line is optically thick (see Evans 1999), because in the optically thin case the absorption feature is not produced

[1] *Herschel* is an ESA space observatory with science instruments provided by European-led Principal Investigator consortia and with important participation from NASA.

and the line profile remains symmetric. For this reason, infall motions need to be studied with optically thick emission lines using molecules such as HCO^+ (Gregersen et al. 1997, Hogerheijde et al. 1999, Fuller et al. 2005), a well known infall tracer in protostellar envelopes. Expansion creates similarly skewed line profiles as those generated by infall motions but with a red-shifted asymmetry, so these two motions can be differentiated. On the other hand, rotation is not characterised by a unique distinctive profile since it can generate both red and blue asymmetric lines on either side of the rotation axis. Rotation generally becomes important on small scales (<1000AU, Brinch et al. 2007, 2009). Given the need to resolve the region in order to characterise rotation, this is more of an issue for interferometric studies.

In this paper, we will study the dynamical structure of protostellar envelopes as a function of luminosity by constraining the contributions of turbulence and infall on single-dish $C^{18}O$ and HCO^+ line profiles. For this purpose, we model the $C^{18}O$ $J = 3$–2, $J = 9$–8, $J = 10$–9 and HCO^+ $J = 4$–3, $J = 6$–5 spectra of 14 YSOs with 1-D spherically symmetric non-LTE radiative transfer models, varying the degree of turbulence and infall motions. An overview of the studied sample and observations is presented in Sect. 3.2. The radiative transfer models, input parameters, abundance profiles and fitting technique are explained in Sect. 3.3. The turbulent and infall velocities from the best-fit models and possible alternative scenarios describing the dynamics in the envelopes are presented in Sect. 3.4. Then, in Sect. 3.5 we discuss the implications of these results and finally, in Sect. 3.6 the conclusions are summarised.

3.2. Observations

3.2.1. Sample

The sample for this study consists of 14 YSOs from the WISH survey which are detected in $C^{18}O$ $J = 9$–8 and 10–9, and for which HCO^+ $J = 4$–3 observations are available. These sources are classified into two groups according to their bolometric luminosities, $L_{\rm bol}$: five low-mass protostars, characterised by $L_{\rm bol} < 40\ L_\odot$, and nine high-mass YSOs with $L_{\rm bol} > 2 \times 10^3\ L_\odot$. In addition, the high-mass sub-sample of YSOs contains a mix of evolutionary stages, including hot cores, mid-IR quiet and ultracompact HII regions. However, the number of sources of each type is too small to reach statistically significant conclusions, so we instead focus the study on the covered luminosity range. The observed characteristics of each source are discussed in van der Tak et al. (2013) for the high-mass, and Yıldız et al. (2013) for the low-mass protostars.

Table 3.1 presents the bolometric luminosities of the sample members, the distances (d), galactic radii ($R_{\rm GC}$), source velocities ($v_{\rm LSR}$), envelope masses ($M_{\rm env}$) and $^{16}O/^{18}O$ isotopic ratio calculated from the relation found by Wilson & Rood (1994), in which the ratio scales with the $R_{\rm GC}$ of the source. Also given is the stellar mass, M_*, which is calculated for the high-mass young stars by assuming that the massive sources are on the main sequence and by using the conversion from Table 1 of Mottram et al. (2011). For the low-mass protostars, an initial stellar mass of 1 $M_\odot$ is used to constrain the maximum infall velocity. The actual stellar mass is determined from the best-fit of the infall velocity during the fitting procedure (see Sect. 3.3.3). For more information about the sample studied in WISH see van Dishoeck et al. (2011).

3.2.2. $C^{18}O$ observations

The $C^{18}O$ $J = 9$–8 and 10–9 spectra used in this paper were observed with the HIFI instrument for the entire WISH sample of YSOs. These transitions were detected for all high-mass objects but only for five low-mass protostars. As mentioned in Sect. 3.2.1, we could not use the entire WISH sub-sample of high-mass YSOs because the HCO^+ $J = 4$–3 transition was available for only nine out of the 19 massive objects. More information about the characteristics of the HIFI $C^{18}O$ observations, observation techniques, data reduction procedure and empirical line decompositions are given in San José-García et al. (2013).

Table 3.1: Bolometric luminosity, spectral type, mass of the central forming star, distance, galactocentric radius, velocity, envelope mass, and $^{16}O/^{18}O$ isotopic ratio of the studied low- and high-mass YSOs.

Source	L_{bol} ($L_\odot$)	$M_*{}^a$ ($M_\odot$)	d (kpc)	$R_{GC}{}^b$ (kpc)	v_{LSR} (km s^{-1})	M^c_{env} ($M_\odot$)	$^{16}O/^{18}O^d$
Low-mass							
NGC1333 IRAS 2A	35.7	≤1	0.235	8.7	7.7	5.1	549 ± 131
NGC1333 IRAS 4B	4.4	≤1	0.235	8.7	7.1	3.0	549 ± 131
SMM1	30.4	≤1	0.415	8.3	8.5	16.1	525 ± 128
GSS30 IRS1	13.9	≤1	0.125	8.4	3.5	0.6	529 ± 128
Elias 29	14.1	≤1	0.125	8.4	4.3	0.3	529 ± 128
High-mass							
IRAS05358+3543	6.3×10^3	10.7	1.8	10.3	-17.6	142	642 ± 146
NGC6334−I(N)	1.9×10^3	7.4	1.7	6.8	-4.5	3826	437 ± 115
DR21(OH)	1.3×10^4	13.3	1.5	8.4	-4.5	472	531 ± 129
W3−IRS5	1.7×10^5	35.3	2.0	10.0	-38.4	424	624 ± 143
IRAS18089−1732	1.3×10^4	13.3	2.3	6.3	33.8	172	406 ± 111
W33A	4.4×10^4	20.2	2.4	6.2	37.5	700	401 ± 110
IRAS18151−1208	2.0×10^4	15.3	3.0	5.7	32.0	153	374 ± 106
G10.47+0.03	3.7×10^5	50.2	5.8	3.1	67.0	1168	217 ± 90
G34.26+0.15	3.2×10^5	46.4	3.3	6.1	57.2	1792	393 ± 109

Notes. See van Dishoeck et al. (2011) and van der Tak et al. (2013) for the source coordinates and references regarding distance and bolometric luminosity values of the low- and high-mass YSOs, respectively.
$^{(a)}$ The assumed maximum stellar mass for all low-mass protostars is 1 $M_\odot$. For the high-mass YSOs, M_* has been calculated using the assumptions presented in Mottram et al. (2011). $^{(b)}$ The galactrocentric radii were calculated using distances d in this table and the IAU distance from the galactic centre R_o =8.5 kpc. $^{(c)}$ For the low-mass protostars, the envelope masses are determined by Kristensen et al. (2012) within the radius at which the dust temperature reaches 10 K. For the high-mass objects, this parameter is taken from van der Tak et al. (2013). $^{(d)}$ Expected $^{16}O/^{18}O$ isotope ratios calculated using the equation on Wilson & Rood (1994): $^{16}O/^{18}O = (58.8 \pm 11.8)R_{GC} + (37.1 \pm 82.6)$.

Complementing the HIFI data, $C^{18}O$ $J = 3$–2 spectra were obtained with the James Clerk Maxwell Telescope[2] (JCMT) on Mauna Kea, Hawaii, and the Atacama Pathfinder EXperiment telescope[3] (APEX) on Llano de Chajnantor, Chile. In the case of the JCMT data, jiggle maps observations were obtained with the Heterodyne Array Receiver Programme (HARP; Buckle et al. 2009). The spatial resolution at that frequency is ∼14″and the spectral resolution for the studied sources is 0.1 km s^{-1}. Each map was convolved to 20″and the central spectrum was extracted and re-binned to 0.27 km s^{-1}. A more detailed description of the APEX data and the low-J $C^{18}O$ transitions for the low-mass protostars can be found in Yıldız et al. (2013).

The upper-level energies (E_u), rest frequencies of the transitions, telescope, main beam efficiencies (η_{MB}), beam sizes and spectral resolutions for all studied $C^{18}O$ observations are presented in Table 3.2.

3.2.3. HCO^+ observations

Together with the $C^{18}O$ observations, HCO^+ $J = 4$–3 and 6–5 spectra are included in the analysis with the aim of restricting the parameter that describes the infall motions in the inner and outer regions of protostellar envelopes. The HCO^+ $J = 6$–5 transition was observed together with

[2]The James Clerk Maxwell Telescope is operated by the Joint Astronomy Centre on behalf of the Science and Technology Facilities Council of the United Kingdom, the National Research Council of Canada, and (until 31 March 2013) the Netherlands Organisation for Scientific Research.

[3]APEX is a collaboration between the Max-Planck-Institut fur Radioastronomie, the European Southern Observatory, and the Onsala Space Observatory.

Table 3.2: Overview of the main properties of the observed $C^{18}O$ and HCO^+ lines. For a description of the parameters see Sect. 3.2.2.

Mol.	Trans.	E_u/k_B (K)	Frequency (GHz)	Tel./Inst.-band	η_{MB}	Beam size ($''$)	Spec. Resol. (km s^{-1})
$C^{18}O$	3–2	31.6	329.331	JCMT/APEX	0.63	20[b]	0.27
	9–8	237.0	987.560	HIFI-4a	0.74	23	0.15[a]
	10–9	289.7	1097.163	HIFI-4b	0.74	21	0.14[a]
HCO^+	4–3	42.8	356.734	JCMT/APEX	0.63	14	0.27
	6–5	89.9	535.062	HIFI-1a	0.76	40	0.28

Notes. The beam efficiency for each HIFI band is taken from Roelfsema et al. (2012). The η_{MB} for the JCMT data is retrieved from the Joint Astronomy center website:
http://www.jach.hawaii.edu/JCMT/spectral_line/General/status.html.
[(a)] WBS data. [(b)] Central spectrum extracted after convolving the map to 20$''$.

the $H_2^{18}O$ 1_{10}-1_{01} line for a few low- and high-mass YSOs (Benz et al., in prep.), representing one third of the studied YSOs in this paper.

The $J = 4$–3 lines were observed with the JCMT and APEX telescopes, and retrieved from the LOMASS database[4] and the Canadian Astronomy Data Centre[5] for the low- and high-mass YSOs respectively. In general, the observing mode of the HARP instrument, the spectral and spatial resolution of the data, and the procedure to extract and re-bin the HCO^+ $J = 4$–3 data are the same as those used for the $C^{18}O$ $J = 3$–2 data (see Sect. 3.2.2 and Yıldız et al. 2013). The main properties of these two HCO^+ lines can also be found in Table 3.2.

3.2.4. Characteristics of the observed line profiles

As indicated in San José-García et al. (2013), the $C^{18}O$ $J = 3$–2, 9–8 and 10–9 lines are considered optically thin and show Gaussian-like profiles. The spectra are characterised by a single narrow (<7 km s^{-1}) velocity component, attributed to quiescent envelope material. However, for sources with strong outflows, such as G10.47+0.03 and W3-IRS5, additional broad line wings are identified even in the $C^{18}O$ spectra. In order to isolate the contribution from the envelope, the emission from the outflow was subtracted by applying a two Gaussian decomposition method to those sources indicated in Table 3.3 (see San José-García et al. 2013 for details).

On the other hand, both HCO^+ transitions show clear asymmetric profiles for four low-mass protostars and for eight out of nine massive YSOs. The $J = 4$–3 spectra often show both double-peaked and asymmetric line profiles while the $J = 6$–5 transition is only skewed. The asymmetry measured in these lines can be characterised by several parameters such as the ratio of the blue peak intensity and the red peak intensity of the double-peaked profile, T_B/T_R, and the skewness (equation 1 of Gregersen et al. 1997). These parameters are measured for the $J = 4$–3 transition of the studied sources and presented in Table 3.6 of Appendix 3.B. The skewness is negative for 11 sources and the blue/red ratio larger than one for eight YSOs, suggesting the presence of infalling material. As for some $C^{18}O$ spectra, broad line wings are subtracted from both HCO^+ transitions for all sources to exclude the contribution from the outflows.

3.3. Modelling of the observations

The $C^{18}O$ and HCO^+ lines are modelled using the non-LTE radiative transfer code RATRAN (Hogerheijde & van der Tak 2000) assuming spherical symmetry with 1-D density and temper-

[4] http://lomass.strw.leidenuniv.nl (in prep.)
[5] http://www.cadc-ccda.hia-iha.nrc-cnrc.gc.ca/en/jcmt/

ature structures. As the observations presented here do not have sufficient spatial resolution to significantly resolve the inner envelope, any additional free parameters required to model $C^{18}O$ and HCO^+ in aspherical geometries would be poorly constrained and would only add degeneracy. The process is composed of two steps, where first the excitation (fractional population) of levels for each cell are computed while the second step uses ray-tracing to create synthetic observations for a given beam.

3.3.1. Source structure

The temperature and density profiles used as inputs for our RATRAN models are taken from Kristensen et al. (2012) for the low-mass and van der Tak et al. (2013) for the high-mass sources. These have been constrained using the continuum radiative transfer codes DUSTY (Ivezić & Elitzur 1997) and a modified version of HOCHUNK3D (Whitney et al. 2013, Robitaille 2011, hereafter WR), respectively. The density structure of the envelope is assumed to follow a power law with index p, i.e., $n \propto r^{-p}$. In the case of low-mass protostars, the outer radius of the envelope was restricted to the smaller radius obtained either when the temperature reaches 10 K or when the density drops below 10^4 cm^{-3}, whichever comes first. For the high-mass YSOs, the envelope is cut at the radius at which the emission of the 450 μm SCUBA maps falls below 3σ noise level (see Sect. 4.1 van der Tak et al. 2013). The dust temperature is obtained from continuum radiation transfer calculations for a given luminosity of the source using the Ossenkopf & Henning (1994) dust opacities for grains with thin ice mantles. The gas temperature is assumed to be equal to the dust temperature. The input structures for each YSO are summarised in Table 3.7 in Appendix 3.B. It is important to highlight that the DUSTY and WR models do not realistically reproduce the envelope physical structure on scales of <100 AU for the low-mass protostars (see Kristensen et al. (2012), Appendix C) and on scales of $<10^3$ AU for the high-mass YSOs, respectively.

The collisional rate coefficients for the line calculations are taken from the Leiden Atomic and Molecular Database (LAMDA[6]; Schöier et al. 2005, Yang et al. 2010, Flower 1999). We consider collisions with both ortho and para H_2 assuming that the ortho-to-para ratio is thermal with maximum and minimum values of 3 and 10^{-3} respectively (Pagani et al. 2009). The $C^{18}O$ and HCO^+ line profiles are then simulated separately, and convolved to the actual beam of the observations assuming abundance profiles discussed in Sect. 3.3.4. In the following subsections we discuss the fixed and free input parameters, as well as the technique used to determine the best-fit.

We use a grid of 50 cells sampled logarithmically such that each contains equal mass. The dust temperature from the dust continuum models is then interpolated onto this grid for the central radius of each cell.

3.3.2. Non-thermal motions: parameters

San José-García et al. (2013) showed that thermal motions contribute less than 5% to the total observed $C^{18}O$ line width in these objects. Therefore, the $C^{18}O$ and HCO^+ line widths and shapes are dominated by non-thermal motions such as turbulence and infall. In order to quantify the balance of these contributions in protostellar envelopes for a given abundance profile, a grid of models with different values of infall, v_r, and turbulent motions (defined as the Doppler b-parameter, b_t) is consistently run for all sources. The infall velocities are calculated as in Mottram et al. (2013) by assuming that material is in free-fall towards the central forming star, adopting different stellar masses in order to get different infall velocities. The infall velocity of each cell is obtained using the relation: $v \propto r^{-0.5}$. We chose the value at a distance of 1000 AU, $v_{r=1000\mathrm{AU}}$, to characterise the specific infall velocity motion. On the other hand, the turbulent Doppler-b_t component is considered constant as a function of radius and defined in the RATRAN models as $0.6\times FWHM$ for lines with a gaussian-like profile.

[6] http://home.strw.leidenuniv.nl/~moldata/

3.3.3. Fitting method: iteration technique

The procedure to determine the best-fit value of the infall and turbulence motions, v_r and b_t, for each source is based on the assumption that the velocity field must be consistent between HCO^+ and $C^{18}O$. The optically thick HCO^+ lines are used to restrict the infall component while the optically thin $C^{18}O$ data constrain the turbulent component. The main steps of this procedure are illustrated in the flow-chart shown in Fig. 3.1 and summarised below. Further and more technical details of the method are presented in Sect. 3.B.1 of Appendix 3.B. A "jump" abundance profile with an inner and outer abundance, X_i and X_o respectively, has been assumed for the $C^{18}O$ lines, while for HCO^+ we are using a simpler constant abundance profile, X_o, across the envelope. More details about the determination of these two types of abundance profile are presented in Sect. 3.3.4.

The iteration technique to fit the observations starts by using a trial value for the HCO^+ abundance taken from previous studies (Hogerheijde et al. 1999; Cox et al. 1987; Jørgensen et al. 2004; Godard et al. 2010; Zinchenko et al. 2009; Kim et al. 2006). After improving the value of $X_o[HCO^+]$ by comparison with an initial test-model, a grid of RATRAN models covering a wide interval of $v_{r=1000\,AU}$ and b_t values (from 0 to ~-12 km s^{-1} and from 0 to ~5 km s^{-1} respectively) with steps of Δv_r=-0.5 km s^{-1} and Δb_t=0.5 km s^{-1} is run for a fixed value of $X_o[HCO^+]$. The output images are compared to the HCO^+ observations and the best-fit is obtained via a reduced chi-squared test, χ^2_r, calculation. From this iteration we obtain a first estimation of the infall and turbulent velocities, $v_{r\,1}$ and b_1.

Similarly to the HCO^+ data, a trial value for the inner and outer $C^{18}O$ abundance is assumed from previous studies (Jørgensen et al. 2004, Yıldız et al. 2013, Herpin et al. 2012, amongst others) for all sources. These abundance values are refined after running a grid of models in which the estimated $v_{r\,1}$ and b_1 are considered fixed parameters and the outer and inner abundance varied in steps of $\Delta X_o[C^{18}O]$= 5×10^{-9} and $\Delta X_i[C^{18}O]$= 1×10^{-8} respectively. With the updated $C^{18}O$ abundance profile, a grid of models for $C^{18}O$ is run varying only the turbulent velocity and taking $v_{r\,1}$ as a fixed parameters. The output models are compared to the $C^{18}O$ observations, χ^2_r calculated, and the value of b_t updated from the best-fit model. The purpose of this step is to constrain the turbulent component, b_t, with the $C^{18}O$ data.

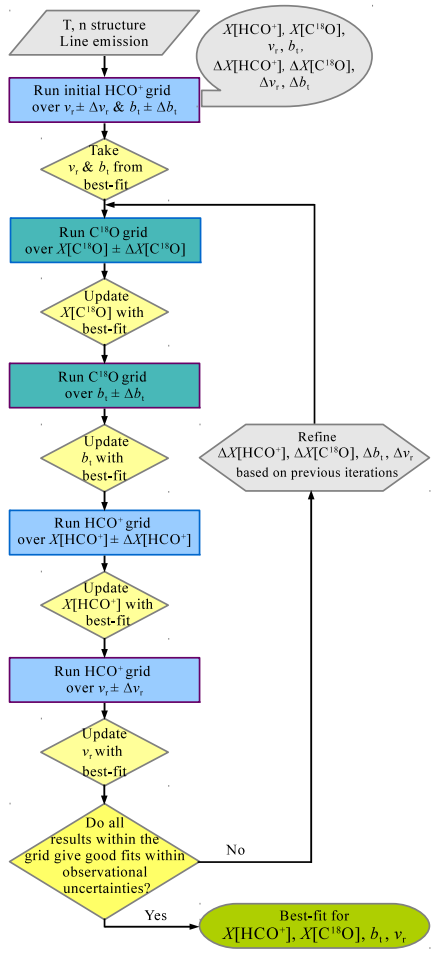

Figure 3.1: Flow-chart diagram with the steps of the iteration technique used to constrain the abundance of HCO^+ and $C^{18}O$ and the infall and turbulent velocities for each source.

With the turbulent and infall velocities partially restricted, we refine the value of $X_o[HCO^+]$ by running a grid of HCO^+ models in which both b_t and v_r are considered fixed parameters and the abundance varies in steps of $\Delta X_o[HCO^+]$=5 ×10^{-10}. Subsequently, another grid of RATRAN models is run for HCO^+ varying only $v_{r=1000\,AU}$ and taking the new value of $X_o[HCO^+]$ and the b_t-component as fixed parameter. In this step we constrain the infall velocity by taking the value of $v_{r=1000\,AU}$ from the model that best-fit the observations.

As indicated in Fig. 3.1, the entire process is repeated several times reducing the range over which both $v_{r=1000\,AU}$ and b_t are varied and decreasing Δv_r, Δb_t, $\Delta X_o[C^{18}O]$, $\Delta X_i[C^{18}O]$ and $\Delta X_o[HCO^+]$ in each iteration until a consistent solution is achieved, i.e, all results from a grid of models fit the observations within their uncertainty. In addition, χ^2_r values of the $C^{18}O$ modelling are calculated globally, i.e., considering all the available lines, and separately for the low-J (JCMT/APEX data) and the high-J (HIFI $J = 9$–8 and $J = 10$–9) spectra with the purpose of comparing the best solution between different parts of the envelope with the global best-fit.

3.3.4. Abundance profiles

Structure of the abundance profiles

Although the focus of this paper is on the dynamics, the line fitting requires an abundance structure determination. For the $C^{18}O$ lines, a "jump" abundance profile is used, consistent with previous work of Jørgensen et al. (2002) and Yıldız et al. (2012). This profile is characterised by having two different and constant values for the abundance (an inner, X_i, and an outer abundance, X_o) separated at the radius at which the envelope reaches the ice sublimation temperature, T_{eva}. Both $X_i[C^{18}O]$ and $X_o[C^{18}O]$ are free parameters while T_{eva} is taken as a fixed parameter. On the other hand, a constant abundance profile is chosen for HCO^+ in which a value of the abundance, $X_o[HCO^+]$, is constant across the envelope.

To justify the selection of a "jump abundance profile" for $C^{18}O$ but not for HCO^+ and to understand which regions of the envelope the observed lines are probing, it is instructive to examine where the bulk of the $C^{18}O$ and HCO^+ emission in each line is generated. Figure 3.2 presents the cumulative intensity in the observed $C^{18}O$ (*middle* panels) and HCO^+ (*bottom* plots) transitions as functions of radius for two example sources, one low-mass (Ser SMM1) and one high-mass (IRAS18089-1732). Their temperature and density profiles as functions of radii are shown in the *top* panels of that figure. The cumulative intensity is calculated from the outside-in by removing successive cells from the model, re-running the ray-tracing and calculating the ratio of the integrated intensity in the new image to the total for all cells considering the whole-envelope, as in Mottram et al. (2013).

For Ser SMM1, 80% of the total emission for the $C^{18}O$ $J = 3$–2 is generated between ~200 and 2000 AU. The interval of temperature and density corresponding to this area ranges from 20 to 45 K and (0.2–3.4)$\times 10^7$ cm^{-3}, respectively. For the high-J lines, 80% of their emission takes place between 60 and 400 AU, characterised by a range of temperature and density varying from 45 to 160 K and (1.5–25.0)$\times 10^7$ cm^{-3}. Thus, each group of lines probes different parts of the protostellar envelope and there is a small area in which both regimes overlap where less than 30% of the $J = 3$–2 emission originates. Still, it is important to recognise that a large fraction of the high-J emission originates from regions of the envelope with T <100 K (Yıldız et al. 2010). On the other hand, 80% of the emission of both HCO^+ $J = 4$–3 and $J = 6$–5 lines comes from the same region of the envelope (between 200 and 1500–2000 AU), as expected due to the similar E_{up} of the two HCO^+ transitions. This area is characterised by temperatures similar to those where the bulk of emission of the $C^{18}O$ $J = 3$–2 line comes from (see *right* panels of Fig. 3.2).

For IRAS18089-1732, 80% of the $C^{18}O$ emission comes from regions ~15 K warmer than those of Ser SMM1, and located one order of magnitude further from the protostar. This is because its envelope is more extended and temperature profiles warmer than for Ser SMM1 (see *top* panels of Fig. 3.2). There is also a region in which the emission of the low- and high-J lines overlap, but in this case the bulk of the emission comes mainly from the high-J lines since the contribution of the $J = 3$–2 transition to the total emission is <15%. Looking at the cumulative intensity of the HCO^+ lines for this source (*bottom-right* panel of Fig. 3.2), 80% of the total HCO^+ emission is generated in a more extended area (from 10^3 to 10^4 AU) with warmer temperatures (40–200 K) compared to the HCO^+ emission of Ser SMM1. For both low- and high-mass YSOs we measure an increase in intensity for the $J = 4$–3 line after removing the cells of the outer parts of the envelope, mostly due to absorption of emission by these colder outer layers of the envelope.

Therefore, the studied $C^{18}O$ line are probing different areas of the envelope with different

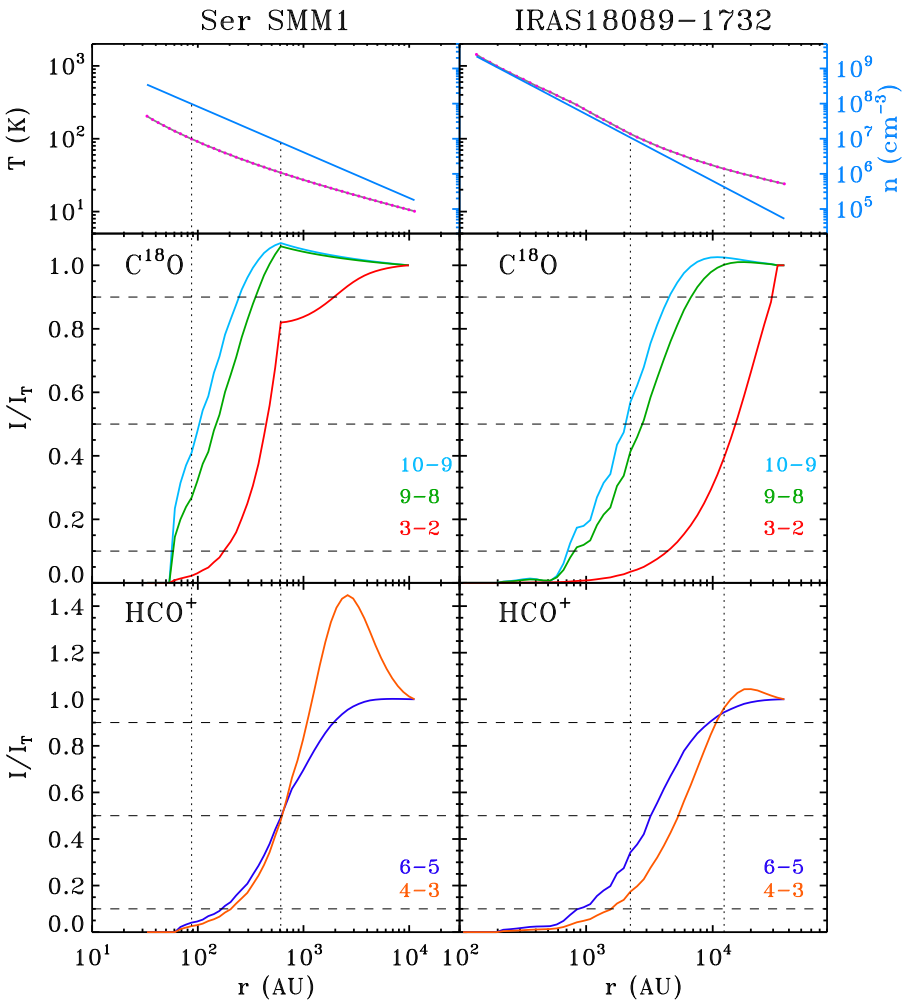

Figure 3.2: The *top* panels show the temperature (dark grey) and density profiles (blue) of the low-mass Class 0 Ser SMM1 (*left column*) and the high-mass YSO IRAS18089-1732 (*right column*) as a function of radius. The pink points indicate the temperature value for each RATRAN cell interpolated from the dust models. The *middle* panels corresponds to the cumulative contribution of material inside a given radius to the total intensity of the $C^{18}O$ $J = 3$–2 (red), $J = 9$–8 (green) and $J = 10$–9 (blue) lines for the same low- and high-mass objects. Similarly, the *bottom* figures show the cumulative contribution for the HCO^+ $J = 4$–3 (orange) and $J = 6$–5 (dark blue) lines of those sources. The dashed lines in the *middle* and *bottom* plots indicate the levels corresponding to 10, 50 and 90%. The vertical dotted lines mark the radii at which the gas and dust temperature reaches 100 and 35 K respectively.

conditions, thus a “jump" abundance profile can be constrained with the available data. The two HCO^+ observations come from approximately the same region, so a drop in abundance at a certain radius cannot be constrained and would only add larger uncertainties to the results. The “jump" abundance profile is used also for the massive object NGC6334-I(N), the only source for which the $C^{18}O$ $J = 3$–2 spectrum is not available. The assumed value of its outer abundance is the average of the $X_o[C^{18}O]$ values obtained for the other massive objects. Its precise choice does not affect the results.

Our modelling shows that a jump in the $C^{18}O$ abundance is required to fit all $C^{18}O$ transitions for both low- and high-mass YSOs (see Fig. 3.3 as illustration for one source). In the case of the

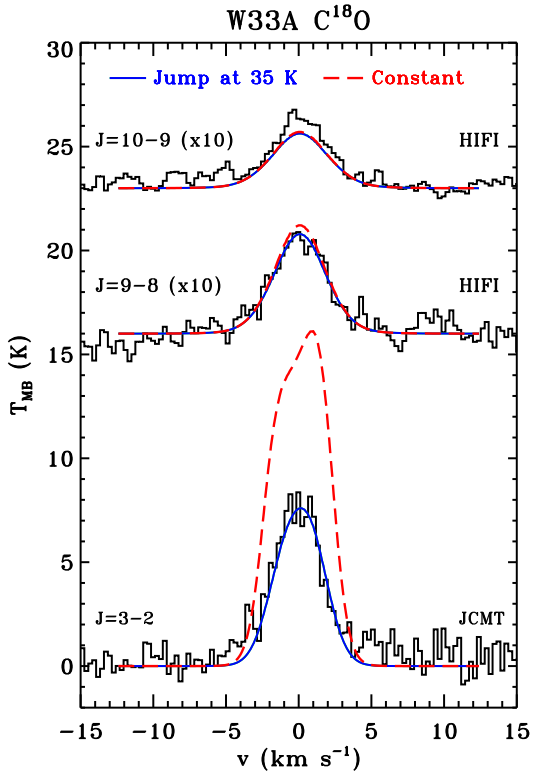

Figure 3.3: Comparison between the "jump abundance" (solid blue lines) and the constant abundance (dashed red lines) profiles for the $C^{18}O$ observations of the high-mass YSO W33A. The value of the $C^{18}O$ abundance for the red model is 4.0×10^{-7}. In the case of the blue output images, the inner abundance, $X_i[C^{18}O]$, is also 4.0×10^{-7}, the outer abundance, $X_o[C^{18}O]$, is 2.0×10^{-8} and the evaporation temperature is 35 K.

low-mass protostars, models in which the evaporation temperature is lower than 30 K result in too much emission in the $C^{18}O$ $J = 3$–2 line and those with T_{eva} larger than 45 K underproduce the intensity of the high-J lines by more than 20%. A similar situation is observed for the high-mass objects with the difference that for several high-mass objects, a T_{eva} lower than 30 K cannot be tested because the temperature never drops below 30 K at the outer edge of their envelopes. Since a jump is needed to reproduce the observations for all sources (see Fig. 3.3), T_{eva} must be higher than 30 K.

Therefore, we adopt a T_{eva} for $C^{18}O$ of 35 K for the entire sample of YSOs because it is the lowest temperature for which the RATRAN models reproduce the line intensity of the three studied $C^{18}O$ transitions in both low- and high-mass objects. The chosen value of T_{eva} is higher than laboratory measurements for pure CO ices (Collings et al. 2004; Öberg et al. 2005; Bisschop et al. 2006), but possible for mixed ices with species such as CO_2. A similar value of T_{eva} of 35 K was previously inferred for some low-mass objects by Jørgensen et al. (2005).

Inferred abundances

The values of the abundance profile derived for $C^{18}O$ and HCO^+ from the best-fit models are summarised in Table 3.3. The estimated uncertainties for the $C^{18}O$ and HCO^+ abundances are less than a factor of two. In addition, Table 3.4 summarises the mean of the inner and outer $C^{18}O$ abundances, of the ^{12}CO abundance derived from those results, and of the constant HCO^+ abundances. These values are computed separately for the low- and high-mass sub-samples, and for the entire sample of YSOs.

In general all sources have similar $X_i[C^{18}O]$ values within the uncertainty of the models. On the other hand, the outer $C^{18}O$ abundance profile varies from 2.0×10^{-9} to 4.0×10^{-7} within the low- and high-mass sub-samples. $X_o[C^{18}O]$ shows the largest interval of variation either because

Table 3.3: Best-fit value of the $C^{18}O$ inner and outer abundance, expected maximum $C^{18}O$ abundance, and ^{12}CO abundance derived from the best-fit value of the inner $C^{18}O$ abundance of each source. The value of the HCO^+ abundance for the best-fit RATRAN models are also indicated.

Source	$X_o[C^{18}O]$	$X_i[C^{18}O]$	$X_{MAX}[C^{18}O]^a$	$X_i[^{12}CO]^b$	$X_o[HCO^+]$
Low-mass					
NGC1333 IRAS 2A[e]	3.0(-8)	1.5(-7)	4.9(-7)	8.2(-5)	1.0(-9)
NGC1333 IRAS 4B[e]	1.5(-8)	3.5(-7)	4.9(-7)	1.9(-4)	5.0(-10)
Ser SMM1[e]	7.0(-9)	4.9(-7)	5.1(-7)	2.6(-4)	6.0(-10)
GSS30 IRS1	2.5(-7)	5.5(-7)	5.1(-7)	2.9(-4)	1.0(-9)
Elias 29	4.0(-7)	1.9(-6)	5.1(-7)	1.0(-3)	3.0(-9)
High-mass					
IRAS05358+3543	2.0(-9)	3.1(-7)	4.2(-7)	2.0(-4)	6.0(-10)
NGC6334−I(N)[d,e]	1.0(-7)	6.0(-7)	6.2(-7)	2.6(-4)	3.0(-10)
DR21(OH)	5.0(-9)	5.0(-7)	5.1(-7)	2.7(-4)	8.0(-10)
W3−IRS5[c,e]	1.0(-7)	8.3(-7)	4.3(-7)	5.1(-4)	1.3(-9)
IRAS18089−1732	2.0(-7)	2.8(-7)	6.7(-7)	1.1(-4)	8.0(-10)
W33A	2.0(-8)	4.0(-7)	6.7(-7)	1.6(-4)	3.2(-10)
IRAS18151−1208	2.0(-7)	6.3(-7)	7.2(-7)	2.4(-4)	2.5(-10)
G10.47+0.03[c]	3.5(-7)	5.0(-7)	1.2(-6)	1.1(-4)	1.0(-9)
G34.26+0.15	2.0(-7)	4.2(-7)	6.9(-7)	1.7(-4)	9.0(-10)

Notes. [a] Maximum $C^{18}O$ abundance obtained from the expected $^{16}O/^{18}O$ isotopic ratio (Table 3.1) and assuming a CO/H_2 ratio of 2.7×10^{-4} (Lacy et al. 1994). [b] ^{12}CO abundance derived from $X_i[C^{18}O]$ and the expected $^{16}O/^{18}O$ isotopic ratio. [c] Sources for which line wings were removed for the $C^{18}O$ spectra. [d] The $C^{18}O$ $J = 3$–2 line is not available for this source. [e] HCO^+ $J = 6$–5 line was observed.

Table 3.4: Mean values of the $C^{18}O$ abundance translated to ^{12}CO according to the $^{16}O/^{18}O$ isotopic ratio presented in Table 3.1.

Sample	$\overline{X_o}[C^{18}O]$ ($\times10^{-7}$)	$\overline{X_i}[C^{18}O]$ ($\times10^{-7}$)	$\overline{X_o}[^{12}CO]$ ($\times10^{-5}$)	$\overline{X_i}[^{12}CO]$ ($\times10^{-4}$)	$\overline{X_o}[HCO^+]$ ($\times10^{-10}$)
Low-Mass[a]	0.8 ± 0.5	3.9 ± 0.8	4.0 ± 3.0	2.1 ± 0.4	7.8 ± 1.1
High-Mass	1.6 ± 0.4	5.0 ± 0.5	6.4 ± 1.8	2.2 ± 0.4	9.3 ± 1.9
Total	1.3 ± 0.3	4.6 ± 0.4	5.7 ± 1.5	2.2 ± 0.3	8.8 ± 1.8

Notes. [a] The mean and uncertainty have been calculated without including Elias 29 (see Appendix 3.A.1).

we have only one line available to confine this parameter at those radii or because the intrinsic properties of these regions are different from source to source. As for $X_i[C^{18}O]$, the values of the best-fit HCO^+ abundance are comparable from low- to high-mass and to the mean (8.8×10^{-10}).

The best-fit values of the $C^{18}O$ abundance are compared to the expected maximum $C^{18}O$ abundance, $X_{MAX}[C^{18}O]$, for each YSO. This parameter is computed assuming $[CO/H_2]=2.7\times10^{-4}$, as found for warm dense gas by Lacy et al. (1994), and using the $^{16}O/^{18}O$ isotopic ratio presented in Table 3.1 which were calculated with the relation found by Wilson & Rood (1994). The same expected isotopic ratio is also used to derive the inner ^{12}CO abundance, $X_i[^{12}CO]$, from the best-fit $X_i[C^{18}O]$ parameter. Both $X_{MAX}[C^{18}O]$ and $X_i[^{12}CO]$ are presented in Table 3.3. It is seen that the obtained $X_i[^{12}CO]$ is generally below or of the order of the maximum $[CO/H_2]$ abundance from Lacy et al. (1994) (i.e., all volatile carbon locked up in CO) but significant exceeds it for two sources: Elias 29 and W3-IRS5. Possible reasons explaining the high inner abundance value derived for these two YSOs are discussed in more detail in Appendix 3.A.1 and 3.A.2, respectively.

Finally, the RATRAN models consistently underestimate the HCO^+ $J = 6$–5 emission but reproduce the 4–3 line, even if high HCO^+ abundances are used or a jump in abundance is applied. As the emission in these lines is generated in a similar region, the missing $J = 6$–5 emission is most

likely produced by physical mechanisms not included in our 1-D spherically symmetric models. A possible explanation is that the excess $J = 6$–5 emission comes from the dense outflow cavity walls where the quiescent envelope gas is directly heated by radiation from the central source. This extra emission does not come from any possible disk because the $J = 6$–5 spectra are observed with a 40″ beam, so the emission would be too beam diluted to be detected. The HCO^+ $J = 6$–5 spectra are further studied and analysed in Benz et al. (in prep.).

3.4. Results

We summarise the results from the RATRAN models focusing on the dynamical structure of the envelope. In Sect. 3.4.1 we first introduce two extreme scenarios in which infall and turbulent velocities adopt different values according to specific assumptions. Then, the values of the velocity field that best fits the $C^{18}O$ and HCO^+ observations simultaneously are analysed and trends with luminosity investigated. Finally, in Sect. 3.4.2 we consider models in which the turbulent component varies with radius and compare to those with constant turbulence across the protostellar envelope.

3.4.1. Velocity field study within the sample

To justify the need for both infall and turbulent motions, we start the study of the dynamical structure of protostellar envelopes by exploring two extreme frameworks: the pure infall-dominated (b_t=0 km s^{-1}) and the pure turbulent-dominated (v_r= 0 km s^{-1}) scenarios. To illustrate these two types of models, Fig. 3.4 shows the $C^{18}O$ and HCO^+ spectra of the low-mass protostar NGC1333 IRAS2A plotted with the RATRAN model for zero turbulent motions (red solid lines) and for zero infall (blue dashed lines). The corresponding values of the infall and turbulent velocities are v_r=-1.3 km s^{-1}and b_t=1.0 km s^{-1}, respectively. These were derived by running a small χ^2 grid with the other velocity component set to zero.

The pure infall-dominated scenario presented in Fig. 3.4 shows a flattening at the peak position of the $C^{18}O$ line profile. Furthermore, additional line wings appear for the higher-J transitions, producing a worse fit to the data. The only features that are well reproduced by the zero-turbulence models are the line wings of the $C^{18}O$ $J = 3$–2 lines, which explains why these models are sometimes selected by the reduced χ^2 calculations as the best fit for this transition. However, when accounting for the global χ^2_r, calculated as explained in Appendix 3.B.1, models with no contribution from turbulence fall far out of the 1-sigma uncertainty for all our sources.

Similarly to what is seen for $C^{18}O$ in NGC1333 IRAS2A, the shape of the output line profiles and that of the HCO^+ observations do not match when b_t=0 km s^{-1}. Therefore, we can state that a turbulent component is needed to reproduce these obser-

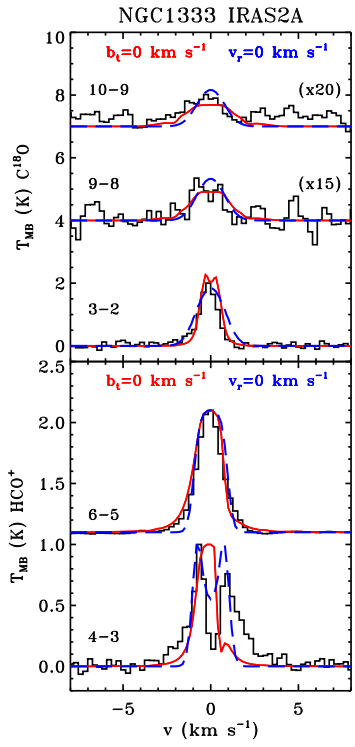

Figure 3.4: (*Top*) $C^{18}O$ observations of NGC1333 IRAS2A plotted with the derived RATRAN output models. (*Bottom*) Same as *top* panel but for the normalised HCO^+ data and models. The turbulent dominated models (v_r= 0.0 km s^{-1}) are shown with dashed blue lines and the infall dominated models (b_t= 0.0 km s^{-1}) with solid red lines.

vations independent of the source luminosity. In addition, if no turbulent motions are added to the models, too high infall velocities are needed to reproduce the broadening of the line profile (generally a factor of 1.5 times the maximum infall velocity according to their estimated masses), as is shown for the high-mass YSO G34.26+0.15 in Fig. 3.15 of Appendix 3.B. These values of $v_{\rm r}$ imply unreasonably high stellar masses (more than twice the estimated or assumed value). Moreover, the opacity of the lines generated by these models are a factor of two lower than those obtained from models with a turbulent component included, and the HCO^+ lines can even become optically thin, which seems unlikely.

The pure turbulent-dominated scenario ($v_{\rm r}$= 0 km s^{-1}) can properly reproduce the optically thin $C^{18}O$ observations, as is shown in blue in the *top* panel of Fig. 3.4. Therefore, this model could be used to fit optically thin $C^{18}O$ lines, as previously found by Jørgensen et al. (2004), Yıldız et al. (2012). However, if we combine the analysis of the $C^{18}O$ data with the optically thick HCO^+ observations, we can rule out this scenario for all those sources with a skewed or asymmetric double-peak profile (these parameters are calculated for the HCO^+ $J = 4$–3 observations and presented in Table 3.6). In particular, the pure turbulent-dominated models can be discarded for four low-mass protostars and for eight out of nine high-mass YSOs within 1-sigma confidence level (see Fig. 3.4 for the case of IRAS2A).

Therefore, for the assumed envelope structure, we prove that the RATRAN models need to include both a turbulent and an infall component in order to reproduce both $C^{18}O$ and HCO^+ observations simultaneously for ∼75% of the YSOs in our sample.

The best-fit values of the infall velocity at a radius of 1000 AU ($v_{\rm r}$), turbulence parameter $b_{\rm t}$ and $\chi^2_{\rm r}$ results are presented in Table 3.5. The turbulent component is calculated separately for three groups of $C^{18}O$ lines: the low-J transition, the HIFI spectra and the entire set of available observations. The estimated uncertainties for the turbulence and infall velocity are of the order of 0.2 km s^{-1}. In addition, the maximum infall velocity, $v_{\rm r\,MAX}$, derived from the estimated stellar mass of the forming star (M_*; see Table 3.1) is included in this table together with the central gravitational mass, $M_{\rm g}$, and the instantaneous mass infall rate, $\dot{M}_{\rm inf}$. The gravitational mass and mass infall rate are calculated for each source using:

$$M_{\rm g} = 0.56 \left(\frac{v_{\rm r=1000\,AU}}{1\,{\rm km\,s^{-1}}} \right)^2 M_\odot, \tag{3.1}$$

and:

$$\dot{M}_{\rm inf} = 2.08 \times 10^{-2} \left(\frac{n_0}{10^9\,{\rm cm^{-3}}} \right) \left(\frac{v_{\rm r=1000\,AU}}{1{\rm km\,s^{-1}}} \right) \left(\frac{r_{\rm mdi}}{r_0} \right)^{-p} M_\odot\,{\rm yr^{-1}} \tag{3.2}$$

respectively, and assuming that the velocity at 1000 AU, $v_{\rm r=1000\,AU}$, obtained from the best-fit RATRAN model is the velocity corresponding to the minimum detectable infall radius, $r_{\rm mdi}$. $M_{\rm g}$ ranges from 0.02 to 0.36 $M_\odot$ and $\dot{M}_{\rm inf}$ from 1.7×10^{-6} to 9.5×10^{-5} $M_\odot$ yr^{-1} for the low-mass protostars. These parameters vary from 0.14 to 49.5 $M_\odot$ and from 5.4×10^{-4} to 7.6×10^{-3} $M_\odot$ yr^{-1} for the massive YSOs. Equations 3.1 and 3.2 are as in Mottram et al. (2013) with the exception that a unit conversion error in the latter equation by those authors has been corrected.

The three best-fit RATRAN solutions (for the low-J in green, the high-J in blue and the global in red) are compared with the $C^{18}O$ observations in Appendix 3.A (Figs. 3.8 and 3.9 for the low-mass sample and from Fig. 3.12 to 3.13 for the high-mass YSOs). Similarly, the best-fit RATRAN models for the HCO^+ data normalised to their peak intensities are plotted together with the normalised HCO^+ observations for the low-mass protostars in Figs. 3.10 and 3.11 and for the high-mass objects in Fig. 3.14. The best-fit models generally reproduce the $C^{18}O$ observations in terms of shape and intensity. In the case of the HCO^+ spectra, the profiles of the RATRAN models display similar values of skewness and $T_{\rm B}/T_{\rm R}$ ratio as those calculated from the $J = 4$–3 line (see Table 3.6).

Table 3.5: Value of the turbulent, b_t, and infall, v_r, components of the best-fit RATRAN model for each YSOs calculated considering all available $C^{18}O$ and HCO^+ observations, respectively. The χ^2_r of each model is indicated. In addition, the best-fit b_t-parameter is determined considering only the $C^{18}O$ J=3–2 transition and the HIFI (J= 9–8 + 10–9) observations. The gravitational mass derived from the best-fit infall velocity, the instantaneous mass infall rate and the virial turbulent velocity are calculated for those sources with negative infall velocities.

	J= 3–2		J= 9–8 + 10–9		Global			$v_{r\,MAX}$[a]	M_g[b]	$\dot{M}_{inf}$[c]	$b_{ff=1}$[d]
	b_t (km s^{-1})	χ^2_r	b_t (km s^{-1})	χ^2_r	b_t (km s^{-1})	v_r	χ^2_r	(km s^{-1})	$M_\odot$	$M_\odot$ yr^{-1}	(km s^{-1})
Low-mass											
NGC1333 IRAS 2A	0.8	4.3	1.5	1.8	1.0	-0.2	4.6	-1.3	0.02	7.1(-6)	0.3
NGC1333 IRAS 4B	0.6	1.7	0.6	0.9	0.6	-0.8	3.9	-1.3	0.36	9.3(-5)	0.5
Ser SMM1	0.8	3.7	1.1	1.7	0.8	-0.8	5.3	-1.3	0.36	6.9(-5)	0.7
GSS30 IRS1	0.6	5.6	1.3	1.2	0.6	-0.5	3.5	-1.3	0.14	1.7(-6)	0.1
Elias 29	1.1	5.0	2.4	3.1	1.1	0.5	2.5	-1.3	0.14	–	–
High-mass											
IRAS05358+3543	1.2	1.6	1.9	1.1	1.2	2.2	1.4	-4.4	2.71	–	
NGC6334−I(N)	–	–	–	–	1.9	-0.5	8.5	-3.6	0.14	6.5(-4)	5.1
DR21(OH)	–	–	–	–	2.3	-3.6	6.7	-4.8	7.26	1.3(-3)	2.2
W3−IRS5	–	–	–	–	2.0	-5.1	12.1	-7.9	14.57	5.4(-4)	1.4
IRAS18089−1732	1.9	26.5	2.2	1.4	1.9	-1.9	9.8	-4.9	2.02	2.0(-3)	1.5
W33A	1.4	3.8	1.6	2.3	1.6	4.8	3.0	-6.0	12.90	–	–
IRAS18151−1208	1.1	3.9	1.6	1.9	1.3	-0.8	2.6	-5.2	0.36	1.1(-3)	1.3
G10.47+0.03	2.8	16.4	3.2	1.7	3.0	-9.4	7.1	-9.4	49.48	7.6(-3)	3.2
G34.26+0.15	1.8	23.4	2.3	2.3	2.3	-9.1	19.5	-9.1	46.37	6.7(-3)	3.3

Notes. The values of the infall velocity, v_r, are given at 1000 AU radius.
[a] Maximum infall velocity, $v_{r\,MAX}$, is calculated from the assumed stellar masses. [b] The central gravitational mass, M_g, is derived from the best-fit value of the infall velocity v_r using equation 3.1. [c] Mass infall rate derived from the best-fit value of v_r at a radius of 1000 AU is calculated using equation 3.2. [d] Virial velocity $b_{ff=1}$ calculated using equations 3.3 and 3.4, assuming that the sources are in virial equilibrium, i.e., α_{vir} = 1, and taking R as the outer radius of the envelope (r_{out}, see Table 3.7).

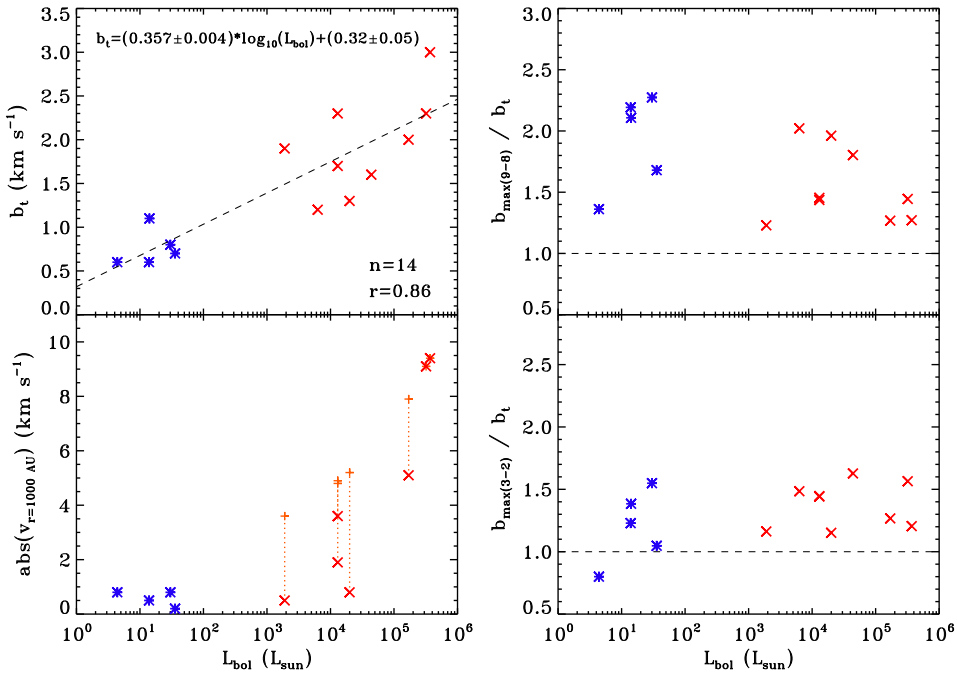

Figure 3.5: (*Top-left*) Best-fit values of the turbulent velocity, $b_{\rm t}$, obtained from the RATRAN models for each source versus its bolometric luminosity, $L_{\rm bol}$. The number of sources, n, and the Pearson correlation coefficient, r, are indicated together with the parameters and uncertainties of the linear fit. (*Bottom-left*) Absolute infall velocity value at 1000 AU, $v_{\rm r=1000AU}$, calculated from the best fit RATRAN models versus the source $L_{\rm bol}$. The blue asterisks correspond to the low-mass objects and the red crosses to the high-mass YSOs. The light orange plusses correspond to the maximum infall velocity at 1000 AU, $v_{\rm MAXr=1000AU}$, calculated from the estimated stellar masses indicated in Table 3.1 for the high-mass objects. The values of $v_{\rm r=1000AU}$ and $v_{\rm MAXr=1000AU}$ for each massive YSO are connected with light orange dashed lines.
(*Top-right*) Ratio of the maximum turbulent velocity calculated from the FWHM of the $C^{18}O$ $J = 9$–8, $b_{\rm max(9-8)}$, divided by the best-fit value of the turbulent component, $b_{\rm t}$, obtained from the RATRAN models for each source versus its $L_{\rm bol}$. (*Bottom-right*) Same as *top* panel but the maximum turbulent velocity is calculated from the *FWHM* of the $C^{18}O$ $J = 3$–2, $b_{\rm max(3-2)}$. The blue asterisks correspond to the low-mass protostars and the red crosses to the high-mass YSOs. The dashed black line denotes a ratio of unity.

Turbulent component

To visualise the results of the best-fit parameters (Table 3.5), the left column of Fig. 3.5 presents the global best-fit values of the turbulent velocity, $b_{\rm t}$, and the absolute infall velocity at 1000 AU, $v_{\rm r=1000AU}$, as a function of bolometric luminosity (*top* and *bottom* panels respectively).

Although the dispersion of the data points is significant, the turbulence $b_{\rm t}$ seems to increase with the logarithm of $L_{\rm bol}$. This trend is confirmed by a Pearson correlation coefficient, r, of 0.86 and it follows the equation: $b_{\rm t} = m\log(L_{\rm bol}) + n$, where $m = 0.357\pm0.004$ and $n = 0.32\pm0.05$ km s^{-1}. In general, for the low-mass protostars, the best-fit for $b_{\rm t}$ ranges from 0.6 to 1.1 km s^{-1}, while for the high-mass sub-sample $b_{\rm t}$ is always larger than 1.2 km s^{-1}. Therefore, these results suggest that more massive objects are characterised with larger turbulent velocities, as seen previously in e.g. Marseille et al. (2010); Herpin et al. (2012). This result is further discussed in Sect. 3.5.1. In addition, this increase with luminosity is consistent with the broadening of the intrinsic line width of the $C^{18}O$ observations with $L_{\rm bol}$ observed by San José-García et al. (2013).

The maximum turbulent velocity, $b_{\rm max}$, for each source can be calculated from the line width of the observed $C^{18}O$ lines ($b_{\rm max} = 0.6\times$FWHM, see Sect. 3.3.2, where FWHM has been quantified by fitting the observations with a Gaussian profile), by assuming that only turbulent motions

broaden the line. The spectra from different $C^{18}O$ transitions give the maximum value of Doppler-b at different radii since the bulk of their emission is generated in different regions of the envelope (Fig. 3.2). The right column of Fig. 3.5 shows the ratio of $b_{\rm max}$ calculated from the FWHM of the $C^{18}O$ $J = 9$–8 lines (*top-right*) and the $b_{\rm max}$ derived from the FWHM of the $J = 3$–2 spectra (*bottom-right*) divided by the $b_{\rm t}$ parameter of the best-fit RATRAN models for each source as a function of $L_{\rm bol}$.

For the low-mass protostars, that ratio increases from 0.8–1.6 to 1.4–2.3 from the $J = 3$–2 to the $J = 9$–8 line. According to our envelope model, this increase indicates that turbulence mainly causes the broadening of the line width for low-J transitions, i.e., in the outer colder parts of the envelope. However, in the inner warmer regions traced by higher-J lines, infall motions might create the extra emission which broadens the $C^{18}O$ $J = 9$–8 with respect the $J = 3$–2 as turbulence alone cannot explain the increase of the line width. Then, we confirm that not only is infall needed to reproduce the $C^{18}O$ and HCO^+ observations simultaneously, but it is also a plausible mechanism capable of explaining the significant increase in the line-width from low- to high-J transitions for this sub-sample of YSOs (see also Harsono et al. 2013).

For the high-mass objects, the value of $b_{\rm t}$ from the best-fit models is lower than $b_{\rm max}$ for both lines, so again, the observed line width cannot be explained by turbulent motions alone. The increase of the line width at high-J transitions is not as evident as for the low-mass protostars, which suggests that the effect of turbulent and infall motions on the $C^{18}O$ line profiles is similar across the regions of the envelope probed by those transitions. However, the emission from infalling material might become slightly more important in the inner regions traced by the high-J spectra than in those traced by lower-J lines since the velocity increases towards smaller radii, likely causing the extra broadening of those profiles.

Infall component

The maximum infall velocity at a radius of 1000 AU ($v_{\rm r\,MAX}$; see Table 3.5) for each source is plotted in Fig. 3.5 (*bottom-left*) with lighter colours and plus symbols. For low- and high-mass YSOs, the best-fit value of $v_{\rm r}$ is always lower or comparable to the assumed and estimated maximum infall velocity. Two different regimes corresponding to the two sub-samples of objects are seen. In the case of the low-mass protostars, the best-fit for $v_{\rm r}$ remains always below 1 km s^{-1}, independently of the luminosity of the source. For the high-mass objects, an increase in the infall velocity at higher luminosities is observed. The interval of possible solutions within 1 sigma confidence level for $v_{\rm r}$ is narrower for the low-mass protostars than for the massive YSOs because $b_{\rm t}$ is smaller as well.

Many of the high-mass YSOs have infall velocities below that expected for free-fall. A possible reason is that M_* in Table 3.1 is calculated assuming that a single main-sequence star is responsible for the total luminosity, when accretion may also contribute, depending on the mass infall rate and accretion radius. Another explanation is that material may infall slower than the free-fall velocity due to strong turbulent mixing, counter-flows along the outflow cavity wall or drag from coupling to magnetic fields.

For two high-mass YSOs, IRAS05358+3543 and W33A, a positive $v_{\rm r}$ component is required to reproduce the HCO^+ $J = 4$–3 spectrum, meaning that the bulk of gas traced by these observations on the relevant scales (10^3–10^4 AU) is mainly in expansion rather than infalling. Constraining this expansion would require an extra free parameter which would be hard to constrain with only two HCO^+ transitions that probe the same material. To be consistent with the assumed physical structure of the envelope and adopted velocity field of the models, these sources are considered as outliers in our analysis and are not included in the *bottom-left* panel of Fig. 3.5 to avoid confusion in the interpretation of this result. Other molecular line observations have shown indications of both infall and expanding motions, see van der Tak et al. (2013).

Fig. 3.6 presents the contribution of infall motion to the total velocity field in the best-fit model of both $C^{18}O$ and HCO^+ as a function of the fractional radius for the low- (*left*) and high-mass (*right*) YSOs. As seen in the figure, the radius at which less than 50% of the total emission is caused by infalling material is different for each YSO and its contribution falls rapidly with increasing

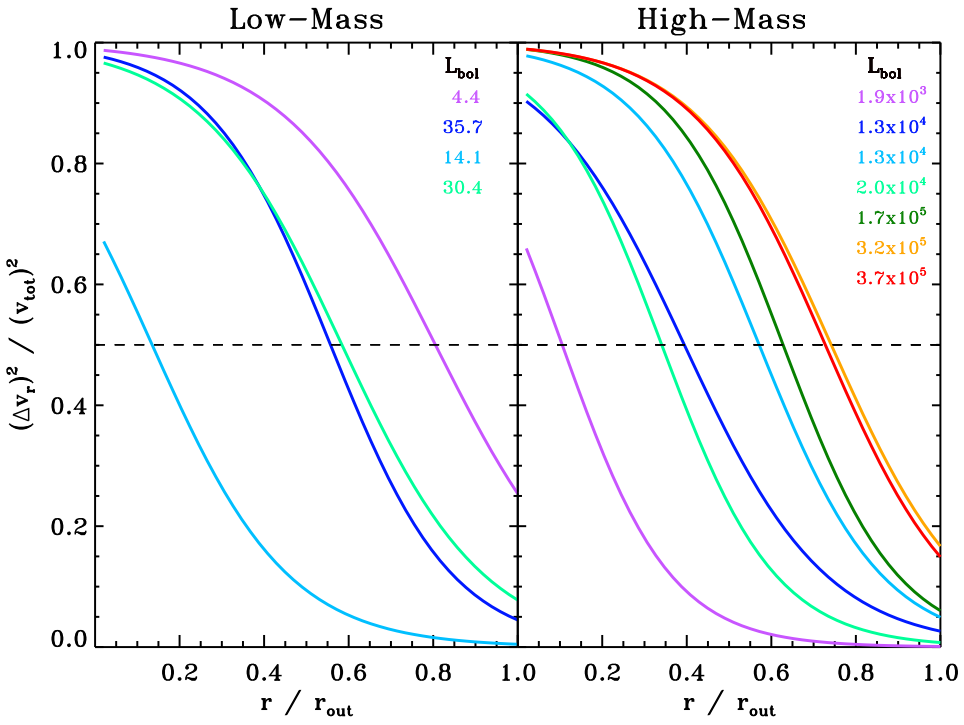

Figure 3.6: Percentage of the contributed infall (solid lines) broadening to the total modelled line width $v_{\rm tot}$ for the obtained best-fit model as a function of the fractional radius of the modelled envelope for the low- (*left* panel) and high-mass (*right* panel) YSOs. The bolometric luminosity of each source, indicated in the right-up corner of each panel, are given in units of solar luminosity. The 50% contribution to the total line width is indicated with an horizontal dashed black line.

radii. Within the high-mass sub-sample, for objects with luminosities up to $2.4{\times}10^4$ $L_\odot$, infall dominates in their inner half of the envelope, corresponding to the radii less than a few 1000 AU, with the importance of infall increasing with luminosity, i.e., stellar mass. Since most of the emission in low- and high-J $C^{18}O$ and HCO^+ transitions originates at larger radii (e.g. see right column panels of Fig. 3.2), this result implies that our lines are turbulence dominated and these motions cause more than 50% of the line broadening.

In the case of the low-mass protostars, this systematic behaviour cannot be confirmed because the number of sources is small. However, the left panel of Fig. 3.6 shows that for three out of four protostars the infall component causes a substantial contribution to the line width until 60–80% the modelled envelope (1000 AU), indicating that both mechanisms are important. Only for IRAS2A (light blue) does turbulence dominate over most of the envelope.

3.4.2. Models with radius-dependent turbulence

In order to explain the observed increase of the $C^{18}O$ line width at higher-J transitions for the low-mass protostars, we test a model in which $b_{\rm t}$ decreases smoothly at larger radii instead of remaining constant across the envelope. This scenario implies an increase in turbulent motions in the inner warmer regions of the envelope, consistent with the idea of outflows or winds from the forming star injecting turbulence into the inner envelope. The structure is tested on the $C^{18}O$ observations of Ser SMM1 assuming free-fall and taking $v_{\rm r=1000AU}$ as -0.8 km s^{-1} from the best-fit model. Then, the linear profile describing the decrease of the turbulent motions with radii fol-

lows the equation: b_t = m × $\log_{10}(R)$ + n, with m = ($b_{t\,J=9,10}$-$b_{t\,J=3}$) / ($R_{J=9,10}$-$R_{J=3}$) = -0.8 and n = $b_{t\,J=9,10}$ - m × $\log_{10}(R_{J=9,10})$ = 12. $R_{J=9,10}$ and $R_{J=3}$ correspond to the central radii at which 80% of the high- and low-J $C^{18}O$ lines are generated (see Fig. 3.2, *left* panels) while $b_{t\,J=9,10}$ and $b_{t\,J=3}$ are the best-fit solutions of the turbulent component for each sub-group of lines computed from the RATRAN models.

Figure 3.16 presents the output spectra for this model plotted in red on top of the observations, as well as the best-fit using a constant turbulent line-width for just the low and high J lines shown in green (b_t = 0.8 km s^{-1}) and blue (b_t = 1.6 km s^{-1}), respectively. The model in which the turbulence varies as a function of radius fits the width of the observations at all J. However, the line profiles in the gradient model have a triangular shape which differs from the characteristic Gaussian-like shape observed in the $C^{18}O$ observations. This triangular profile is more prominent in the lower-J transition than in the HIFI lines. The line-profiles produced by this turbulence gradient model do not agree with the observations, especially at the center of the line. Since the fit actually gets worse (χ^2_r also increases), we keep the original model with constant turbulent velocity across the envelope.

Similarly, we test the scenario in which turbulence increases linearly as a function of radius. This positive gradient in turbulence agrees with the expected dynamical structure of massive protostellar envelopes, with inner regions showing a lower degree of turbulence because the high densities of those areas dissipate those motions. However, these models result in $C^{18}O$ line profiles with slightly broader width for the lower-J transitions that do not reproduce the observations for the high-mass YSOs, for which the line widths remain practically constant or even seem to slightly increase for the high-J transitions. Figure 3.17 shows the output profiles of two models with a positive gradient in turbulence (green and blue profiles) run for the high-mass object IRAS18089-1732 and our best-fit model in which b_t remains constant as a function of radius (red profiles). The turbulent gradient in the model of the blue profile is steeper than that of the green profile. It is seen that a model with constant turbulent velocity reproduces better low- and high-J transitions simultaneously and adds less degeneracies to the solutions. Once again we preserve the original model because it produces the best fit for both low- and high-mass objects, especially for the higher-J $C^{18}O$ transitions.

Other RATRAN models with varying turbulent velocity across the envelope have been used to reproduce both CO and water observations. An example is presented in Herpin et al. (2012). In this work, the authors modelled 14 HIFI water lines of the massive YSO W43-MM1 assuming a "multiple-step" velocity field. For this profile, the turbulent component and absolute value of the infall velocity increase with radius at steps located at specific values of envelope temperature. The Herpin et al. (2012) model for H_2O was run for the $C^{18}O$ lines of W43-MM1 in order to test if it can reproduce all observed $C^{18}O$ transitions simultaneously. Figure 3.18 shows in red the output RATRAN models of the "multiple-step" velocity profile and in blue the solutions from the model with constant turbulent velocity across the envelope and free fall motions. The former results in profiles with broader line widths for the lower-J transitions, which is not consistent with the observations. In addition, the peak of the modelled $C^{18}O$ lines are too blue-shifted. On the other hand, our model seems to reproduce the three lines simultaneously. Since the free fall assumption needs to be adopted to reproduce the HCO^+ data, we therefore confirm that the original velocity structure of our models is better at reproducing the $C^{18}O$ observations and adds fewer free parameters. However, there could be other physical processes at work in the H_2O emitting region which mimic a multiple-step turbulence profile.

3.5. Discussion

3.5.1. Comparison with other studies

In general high-mass objects have higher turbulent velocities than their less massive counterparts. Whether this is a requirement for the initial conditions of high-mass star formation as suggested by McKee & Tan (2003) or whether the envelopes become more turbulent due to the

more energetic processes and surroundings is less clear. High-mass cores are more turbulent than their pre-stellar precursors (Jijina et al. 1999), and so must become more turbulent before the mid IR-quiet high-mass protostar phase and stay turbulent until at least the Ultra-Compact HII region phase given the consistent results obtained across the range of evolutionary stages present in the high-mass sample. Figure 3.5, *top-left*, is suggestive that the transition from the low- to the high-mass turbulent regime takes place at around 10^3 $L_\odot$, though constraining this would need a much larger sample of sources which includes intermediate-mass YSOs covering a range of $L_{\rm bol}$ from 10^3 to 10^4 $L_\odot$.

As introduced earlier, Herpin et al. (2012) presented a scenario in which turbulence increases with radius. They proposed that this result is in agreement with the turbulent core model (McKee & Tan 2003), and suggested that rotational motions and high density structures decrease the level of turbulence in the inner regions of the envelope. We justify the choice of a constant turbulent component as a function of radius by arguing that outflows inject turbulent motions into the envelope, especially in the inner parts, a scenario which can also be extrapolated to the low-mass protostars. Therefore, according to our models and results, the decay of turbulence due to density or other motions such as rotation or infall could be compensated with turbulence injected by the outflowing material and forces.

3.5.2. Origin of turbulence

There has been a debate for some time about the origin of the super-sonic turbulence observed towards molecular clouds and sites of low-mass star formation. Since this turbulence is expected to follow a Kolmogorov cascade, it should dissipate on timescales of the order of the free-fall timescale of a region if not driven (see e.g. Ballesteros-Paredes et al. 2007). As the lifetime of pre-stellar cores is typically 1.5–4 times the free-fall time (Ward-Thompson et al. 2007; André et al. 2014), any turbulence present due to the formation of the molecular cloud should have dissipated before the Class 0 phase. Indeed, the line-widths of many low-mass pre-stellar cores are consistent with little or no turbulence (e.g. Pineda et al. 2010). That we can rule out the no-turbulence model in our sources strongly suggests that the turbulence present in our sources is driven and sustained by the protostellar outflow.

Few confirmed massive starless cores have been found (Tackenberg et al. 2012; Tan et al. 2013), and this phase is expected to be short-lived compared to their free-fall time (Tackenberg et al. 2012). However, as in the low-mass case these have significantly lower line-widths (Jijina et al. 1999; Tan et al. 2013) than the protostellar sources studied here (see also Fig.12 of San José-García et al. 2013). It has been shown that in at least some cases outflows from high-mass star-forming regions have enough energy drive to turbulence on core scales (e.g. Mottram & Brunt 2012), therefore it seems likely that this is also the source of higher turbulence in our high-mass objects.

3.5.3. Turbulent core accretion and competitive accretion

In order to investigate if stars form from quasi-virial equilibrium cores, the constrained turbulent velocity derived from the best-fit RATRAN models, $b_{\rm t}$, is compared to the virial velocity dispersion, $\sigma_{\rm vir}$. This parameter is calculated from equation 2.8a of Bertoldi & McKee (1992) assuming that our sources are in virial equilibrium and afterwards converted to Doppler-b as:

$$\sigma_{\rm vir} = \sqrt{\frac{\alpha_{\rm vir}\, G\, M}{5\, R}},\ \text{with} \tag{3.3}$$

$$b_{\alpha=1} = 0.6\, \sigma_{\rm vir}\, \sqrt{8\, ln(2)} \tag{3.4}$$

where the virial parameter $\alpha_{\rm vir}$ is equal 1; the radius R inside of which the turbulence is measured is taken as the outer radius of our modelled envelope ($r_{\rm out}$; see Table 3.7); and M is the sum of the envelope mass inside that region and the calculated gravitational mass $M_{\rm g}$. Regarding the choice of

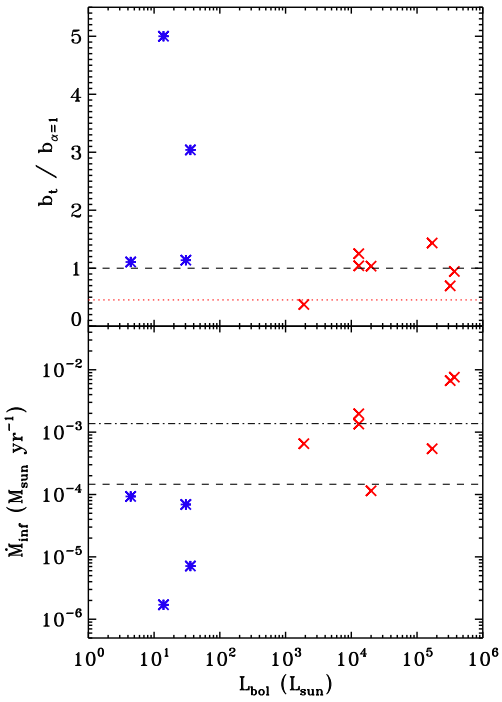

Figure 3.7: (*Top*) Ratio of the turbulent velocity b_t derived from the best-fit RATRAN mode and the virial velocity dispersion $b_{\alpha=1}$ as a function of bolometric luminosity of the source. The parameter $b_{\alpha=1}$ has been calculated for R=r_{out} using equations 3.3 and 3.4. The dotted red line is the ratio obtained from a massive starless core presented in Tan et al. (2013). (*Bottom*) Instantaneous mass infall rate calculated assuming a minimum detectible infall radius at 1000 AU using equation 5 on Mottram et al. (2013) versus L_{bol}. The dashed black line indicates a typical value of the accretion rate in the core accretion model and the dotted-dashed black lines is the average accretion rate in the competitive accretion model (read Tan et al. 2014 for further discussion of these two theories). The blue asterisks correspond to low-mass protostars and the red crosses are the high-mass YSOs. Only the high-mass sources with negative infall velocity have been included.

R, we obtained consistent results for $b_{\alpha=1}$ when different values of the radius are used. The virial velocity of those sources with $v_r < 0$ km s^{-1} is presented in the last column of Table 3.5.

Our RATRAN models allow us to isolate the turbulent component and separate it from the other non-thermal motions that contributes to the broadening of the line profiles. Therefore, we can directly compare the actual turbulence contribution b_t to the velocity dispersion of a virialised system $b_{\alpha=1}$ and interpret the results in a more reliable framework than previously possible. The *top* panel of Fig. 3.7 shows the ratio of the turbulent velocity b_t and the calculated virial velocity $b_{\alpha=1}$ as a function of bolometric luminosity of the source. The dotted red line corresponds to a massive starless core (see Tan et al. 2013), where thermal motions prevail over non-thermal ones.

In the case of the low-mass protostars, the ratio is always greater than 1, suggesting that the level of turbulence is clearly larger than that expected in a system in virial equilibrium. For the high-mass YSOs this ratio fluctuates around 1 for six out of the seven sources. In general, the virialised line-width is slightly smaller than b_t, which indicates that the level of turbulence is also larger than in virial equilibrium sources. Therefore, according to the ratio and uncertainty associated to the constrained b_t, five massive stars form from a quiasi-virial equilibrium core in which turbulence seems to prevail over the gravitational potential. This picture is consistent with current formation following the turbulent core accretion model proposed by McKee & Tan (2002, 2003). However, for the two remaining YSOs the ratio is smaller than 1, indicating that the level of turbulence is lower than that measure in a virialised system. These two sources (NGC6334-I(N), and G34.26+0.15), have the largest envelope masses of the studied sample and are known to reside in active regions forming multiple massive sources, where the large-scale gravitational potential may be more important. The current formation activity of these sources is therefore more similar to the competitive accretion model proposed by Bonnell et al. (1997).

According to the right-column panels of Fig. 3.5, the observed line width of the C^{18}O $J = 3$–2 data, i.e., the maximum turbulent velocity $b_{\max(3-2)}$, is a factor ~1.5 larger than the constrained turbulent velocity from our best-fit models, b_t. This factor is even larger for the C^{18}O $J = 9$–8 transition. If we had used the observed line width to calculate the ratio showed in Fig. 3.7, most of the massive YSOs would be in the turbulent dominated regime. In addition, the virial parameter

derived from this assumed velocity dispersion would have been larger than 2, favouring the turbulent core accretion model over the competitive accretion. This result would agree with the typical values measured for $\alpha_{\rm vir}$ in high-mass star-forming regions (see Heyer et al. 2009).

Therefore, the analysis of the turbulent component, which has been separated from the other non-thermal motions, suggest that both massive star formation theories can play a role on explaining the formation of massive stars.

Independently of the favoured model, in general a significant increase in turbulence is observed from the pre-stellar to protostellar phase, as already highlighted in Sect. 3.5.2 and pointed out by the dotted red line in Fig. 3.7. Only NGC6334-I(N) falls above that limit, corroborating that the region is really massive and has many YSOs associated, which creates a large gravitational potential that increase the virial velocity motion of the core. Given this increase in turbulence, it may be that all sources start out in a phase more like the competitive accretion model, but transition to something more like the turbulent core model when the outflow becomes active.

Finally, the *bottom* panel of Fig. 3.7 shows the instantaneous mass infall rate of each source as a function of its $L_{\rm bol}$. The dashed and the dotted-dashed black lines indicate a typical value of the accretion rate in the core accretion model and the average accretion rate in the competitive accretion model, respectively. The expression to obtained these values are discussed in Tan et al. (2014), together with standard values of $\dot{M}_{\rm inf}$ characteristic of each formation theory. The mass infall rate is another way to discriminate between the core accretion and competitive accretion models. The reason is that in the former theory $\dot{M}_{\rm inf}$ is higher because the collapse is fed from a dense core while in the latter model is fed by a more diffuse clump.

In the case of the high-mass YSOs, the values of the mass infall rate are larger than 10^{-4} $M_{\odot}$ yr^{-1}, which are typical of those found in the turbulent core accretion model. However, in agreement with the previous discussion, our results seem to indicate that both models are at work and additional parameters besides the turbulent velocity and $\dot{M}_{\rm inf}$ are required to discriminate which theory explains more accurately the formation of these massive YSOs. It may even be the case that some combination of these two models is at work, with slow infall from the clump onto the core and faster infall on envelope scales.

3.5.4. Infall and rotation: disentangling the non-thermal emission

As noted in Sect. 3.1, rotation is another form of non-thermal motion that may play a role in the dynamical structure of protostellar envelopes, especially at small scales. Wang (2013) found that for high-mass objects the contribution of rotating regions to the total line width measured with single-dish telescopes is small and practically negligible on scales larger than 1000 AU. Similarly, Keto & Zhang (2010) found rotational velocities larger than 10 km s^{-1} only at radii closer than 600 AU for a 10 $M_{\odot}$ star. In both cases, the regions in which rotation starts to be important are diluted within the beam of the HIFI and ground-based single-dish telescopes, so the contribution of this component to the measured line profile is negligible.

For the low-mass protostars, the physical scales probed by the HIFI beam are smaller than those of their massive counterparts (see Fig. 3.2). Harsono et al. (2013) showed that the contribution from a rotationally-supported disk (RSD) to integrated C^{18}O HIFI line fluxes is less than 10%. Harsono et al. (subm.) also computed line profiles from magneto-hydrodynamical simulations with and without a RSD, but without turbulence. Both the hydrodynamical models and the semi-analytic models neglecting turbulence show that the C^{18}O $J = 9$–8 line profiles are broadened by rotation, especially for high inclination ($i > 50^{\circ}$). Most of our low-mass sources are estimated to have $<50^{\circ}$ inclination from outflow maps, however, except for IRAS2A (Yildiz et al., subm.). For this source, Brinch et al. (2009) concluded based on detailed interferometry that its velocity field is characterised by a high degree of infall relative to rotation. Therefore, rotation does not need to be considered for these five low-mass protostars but these studies demonstrate that rotation could contribute at a low level to the broadening of lines in low-mass sources, depending on the spatial resolution of the data.

To summarise, rotation does not contribute to the broadening of the observed HIFI C^{18}O data for any of the studied YSOs, a result which is consistent with our envelope models.

3.6. Conclusions

In this paper we have presented a combined analysis and RATRAN modelling of low- and high-J $C^{18}O$ and HCO^+ observations for a sample of low- and high-mass YSOs. The high-J $C^{18}O$ spectra obtained with HIFI trace the bulk of warm, dense and quiescent envelope gas on scales of 10^2–10^3 AU and 10^3–10^4 AU for each sub-group of objects respectively. Therefore, inner regions closer to the forming star which were not accessible with ground-based single-dish telescopes are now revealed. The results from this analysis suggest that the inner warm regions of the envelopes of low- and high-mass YSOs have similar dynamical properties while the outer colder parts present significant differences, particularly for the turbulent component and the abundance values. Other specific findings are:

- Pure infall dominated models can be ruled out for the entire sample of YSOs and pure turbulence dominated models can be excluded for more than 75% of our objects. Therefore, both turbulence and infall are required to reproduce and explain the $C^{18}O$ and HCO^+ spectra.

- Infall motions may be responsible for the broadening of the line-width of $C^{18}O$ with increasing J for low-mass protostars. Both rotation motions and a gradient in the turbulent component can be discarded as possible causes of the measured increase in the line-width for these studied low-mass sources.

- Turbulent motions are positively correlated with luminosity across the entire studied luminosity interval. On the scales probed by these observations (10^2–10^3 AU and 10^3–10^4 AU for low- and high-mass YSOs respectively), the turbulent Doppler-b typically ranges from 0.6 to 3.0 km s^{-1} and remains constant across the envelope. Injection of turbulence by outflows is a plausible mechanism to explain the origin and sustenance of these motions.

- For high-mass YSOs, more luminous objects seem to have higher infall velocities over a larger fraction of envelope. In contrast, for low-mass YSOs the infall velocity is independent of source luminosity.

- The best-fit infall velocity is always smaller than the value derived from the estimated stellar mass for the high-mass objects. This result may imply that either the assumptions taken to calculate their stellar masses are too rough or that the infall cannot be as fast as free-fall due to the presence of high turbulence, rotation motions and/or counter-flows along the outflow cavity wall.

- Turbulence increases significantly from the pre-stellar to protostellar phase for both low- and high-mass objects. This results suggest that a source of turbulence, such as outflows, switches on during the actual star-formation process.

- The velocity dispersion derived from the turbulent velocity for most of the high-mass YSOs is of the order or larger than the dispersion associated to a system in virial equilibrium. Even if this picture is consistent with current formation following the turbulent core accretion model, the analysis of the isolated turbulent component suggests that both massive star formation theories can play a role on explaining the formation of high-mass stars.

- A jump abundance profile is needed to fit the high-J transitions of the $C^{18}O$ observations for the entire sample of YSO. Thus freeze out of CO is also necessary for high-mass objects with an evaporation temperature of ~35 K. The value of $T_{\rm eva}$, higher than that measured in laboratory experiments with pure CO, indicates that CO ice is mixed with other ices such as CO_2.

Acknowledgments

The authors thank Jonathan Tan and Ruud Visser for their comments and suggestions, which helped to improve the manuscript. Astrochemistry in Leiden is supported by the Netherlands Research School for Astronomy (NOVA) and by the European Community's Seventh Framework Programme FP7/2007-2013 under grant agreement 238258 (LASSIE). The James Clerk Maxwell Telescope is operated by the Joint Astronomy Centre on behalf of the Science and Technology Facilities Council of the United Kingdom, the National Research Council of Canada, and (until 31 March 2013) the Netherlands Organisation for Scientific Research. HIFI has been designed and built by a consortium of institutes and university departments from across Europe, Canada and the United States under the leadership of SRON Netherlands Institute for Space Research, Groningen, The Netherlands and with major contributions from Germany, France and the US. Consortium members are: Canada: CSA, U.Waterloo; France: CESR, LAB, LERMA, IRAM; Germany: KOSMA, MPIfR, MPS; Ireland, NUI Maynooth; Italy: ASI, IFSI-INAF, Osservatorio Astrofisico di Arcetri- INAF; Netherlands: SRON, TUD; Poland: CAMK, CBK; Spain: Observatorio Astronómico Nacional (IGN), Centro de Astrobiología (CSIC-INTA). Sweden: Chalmers University of Technology - MC2, RSS & GARD; Onsala Space Observatory; Swedish National Space Board, Stockholm University - Stockholm Observatory; Switzerland: ETH Zurich, FHNW; USA: Caltech, JPL, NHSC.

3.A. Best-fit models

3.A.1. Low-mass YSOs

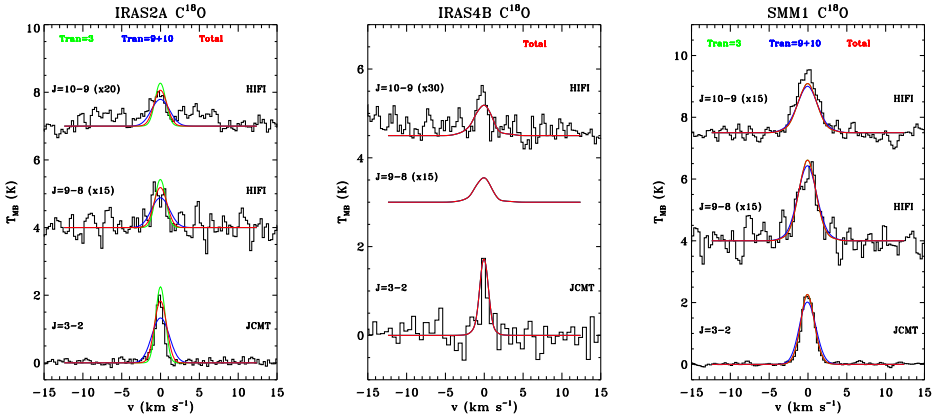

Figure 3.8: RATRAN models obtained for the low-mass Class 0 protostars NGC1333 IRAS2A, IRAS4B and Ser SMM1. The black lines show the observed spectra; the green line corresponds to the best χ^2_r fit for the transition J=3–2; the blue line is the best χ^2_r fit calculated from the HIFI spectra (J=9–8 and J=10–9); and finally the red line indicated the best χ^2_r fit combining the three observations.

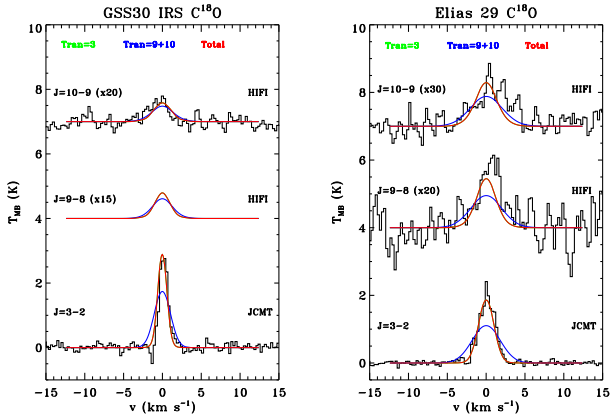

Figure 3.9: Same as Fig. 3.8 but for the low-mass Class I objects GSS30 IRS1 and Elias 29.

The high $C^{18}O$ abundance derived for Elias 29, which causes an unrealistic CO/H_2 ratio, could be a consequence of the low S/N of the high-J transition and therefore, the large uncertainty associated to the best-fit inner abundance, $X_i[C^{18}O]$, of this source. However, since Elias 29 is embedded in the Ophiucus PDR, the most plausible explanation of this extra emission is that the high-J $C^{18}O$ emission may arise partly in the warm extended gas. Lommen et al. (2008) concluded that a significant part of the molecular emission along the line of sight to Elias 29 is due to a density enhancement in the cloud ridge from which this source formed. Extended warm emission on large scales was not considered in the DUSTY calculations which defined the density and temperature structure used in our models, which may be the cause of the discrepant $X_i[C^{18}O]$ value obtained.

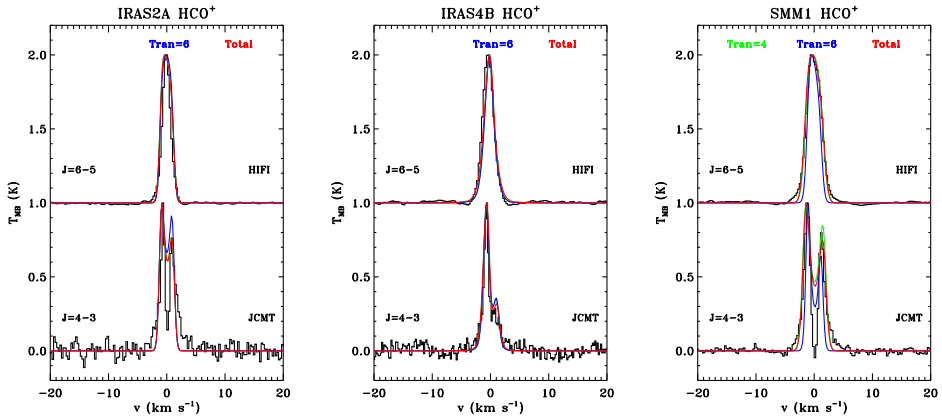

Figure 3.10: Normalised RATRAN models obtained for HCO^+ for the low-mass Class 0 protostars NGC1333 IRAS2A, IRAS4B, and Ser SMM1 compared to the normalised observations, shown in black. The green line corresponds to the best χ^2_r fit for the transition J=4–3; the blue line is the best χ^2_r fit for the J=6–5 line, if presented; and finally the red line indicates the best χ^2_r fit combining the available observations.

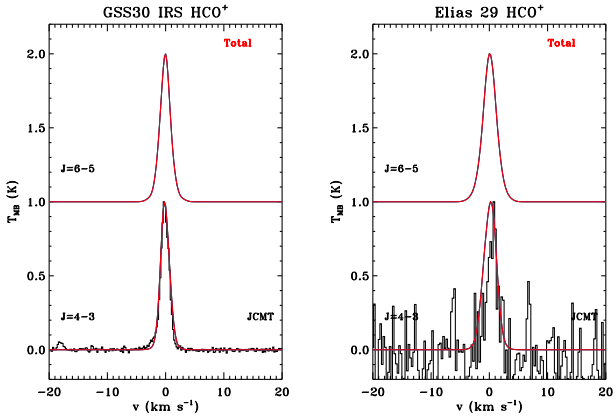

Figure 3.11: Same as Fig. 3.10 but for the Class I protostar GSS30 IRS1 and Elias 29.

The derived value of $X_i[^{12}CO]$ presented in the latter column of Table 3.3 is an order of magnitude higher than for the other sources. Therefore, this source is excluded from the average calculation of the $C^{18}O$, ^{12}CO and HCO^+ abundance profiles presented in Table 3.4.

3.A.2. High-mass YSOs

It is difficult to reproduce the large intensity observed in the $C^{18}O$ lines towards some high-mass sources, resulting in the need for high $C^{18}O$ abundances. In the case of NGC6334-I(N), the models always underestimate the $J = 10$–9 line, regardless of the chosen value of $X_i[C^{18}O]$. The $J = 9$–8 transition is reproduced and the $J = 3$–2 line is not available for this object, so we cannot extend the comparison to colder regions of the envelope. A possible reason why the higher-J spectrum cannot be recreated could be due to the ripples in the baseline of these transitions, which increases the intensity of the line by creating additional and artificial broad line wings. The ripples are present in the entire spectrum and are difficult to eliminate with lineal-baseline subtraction techniques, becoming even more complicated due to the low S/N of the line. Therefore, for this source we prioritise the fitting of the $J = 9$–8 transition over the global one to constrain the

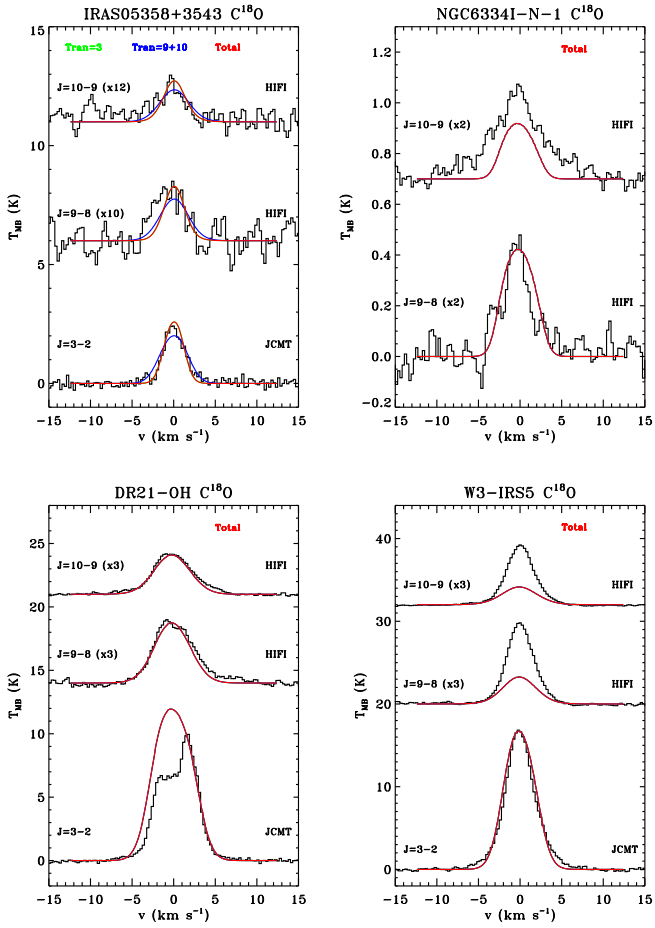

Figure 3.12: RATRAN models obtained for the high-mass sources IRAS05358+3543, DR21(OH), NGC6334-I(N), and W3-IRS5. The black lines show the observed spectra; the green line corresponds to the best χ^2_r fit for the transition J=3–2; the blue line is the best χ^2_r fit calculated from the HIFI spectra (J=9–8 and J=10–9); and finally the red line indicated the best χ^2_r fit combining the three observations.

$C^{18}O$ "jump abundance profile" and the turbulent component. For the HCO^+ observations, both abundance and infall velocity are well fit.

A high value of $X_i[C^{18}O]$ is needed in order to fit the $C^{18}O$ observations of W3-IRS5, which implies a CO/H_2 ratio $> 2.7\times10^{-4}$. In this case, the HIFI spectra have high S/N, so this result cannot be justified by adding a large uncertainty to the abundance value. On the other hand, this YSO is well known for being massive, luminous, with powerful outflows and with at least two main objects dominating the emission (read Chavarría et al. 2010 for more information about the source). Therefore, the complexity of this object may not be well represented by the assumed envelope structure modelled with RATRAN leading to some disagreement between even the best-fit model and the observations.

Finally, a particular case to highlight is G34.26+0.15. Looking at the $C^{18}O$ data, an emission peak at ~4 km $s^{-1}$is observed in both low- and high-J transitions. Therefore, we assumed that this bump, which is especially visible in the $J = 3$–2 line, is caused by foreground emission. In the case of the HCO^+ $J = 4$–3 spectrum, since the emission is located at slightly larger velocities with respect the source velocity, we have assumed this is part of the double-peak profile of the HCO^+ data.

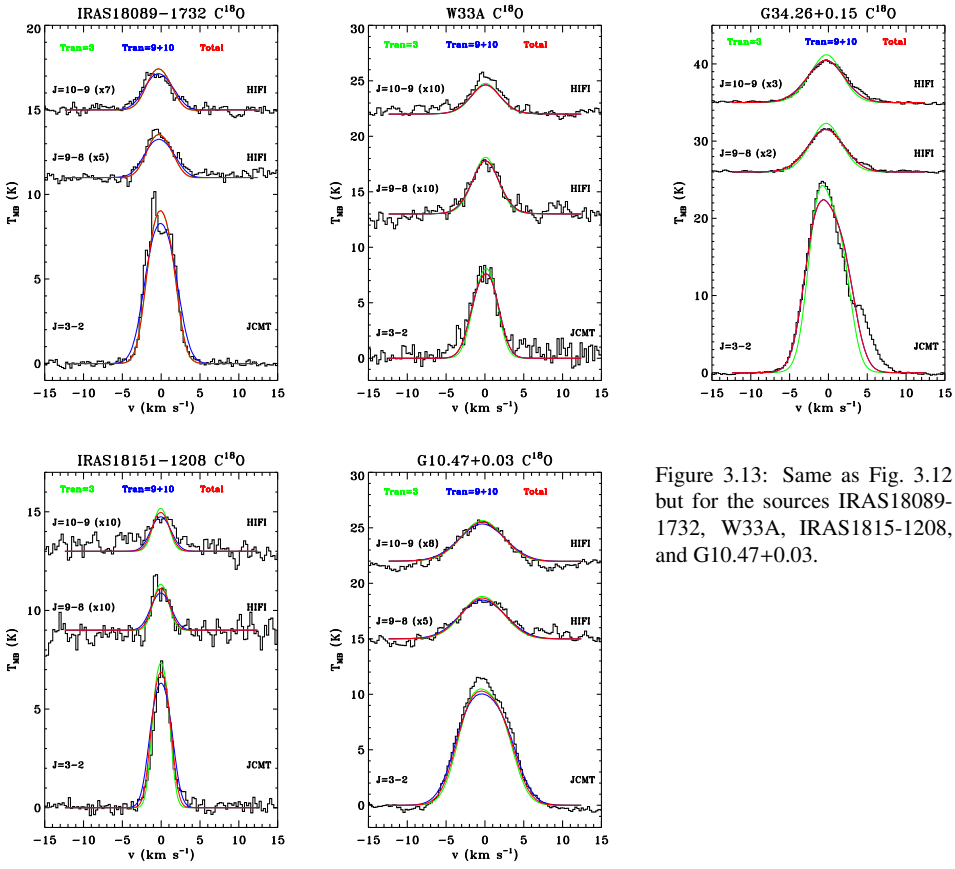

Figure 3.13: Same as Fig. 3.12 but for the sources IRAS18089-1732, W33A, IRAS1815-1208, and G10.47+0.03.

3.B. Additional information and figures

The skewness and blue and red peak intensity ratio of the HCO^+ $J = 4$–3 spectra are measured for each YSOs and presented in Table 3.6. These two parameters, which characterise the asymmetry of a line profile, are also calculated for the best-fit RATRAN models in order to compare these resulting profiles to the observations.

In Table 3.7 is shown the input parameters used in our RATRAN models and described in Sect. 3.3.1.

In addition, further details regarding the iteration technique explained in Sect. 3.3.3 and developed to constrain the best-fit models are presented in Sect. 3.B.1.

Finally, figures showing the output line profiles obtained from RATRAN models with really high infall velocities (Sect. 3.4.1) and different envelope structure as explained in Sect. 3.4.2 are shown below.

3.B.1. Iteration technique: details

The main steps of the procedure which constrains the contribution of the infall and turbulence motions, v_r and b_t, to the HCO^+ and $C^{18}O$ line profiles are described in Sect. 3.3.3. However, technical details explaining how the reduced χ^2_r value for each model is calculated are not indicated in that section in order to simplify it and to focus the attention on the purpose and goal of each step.

As indicated, the best-fit models of each source and molecule are those with the lowest χ^2_r, calculated considering the specific number of degrees of freedom. In general, the procedure to derive this quantity, and therefore to compare observations and models, is similar regardless of the

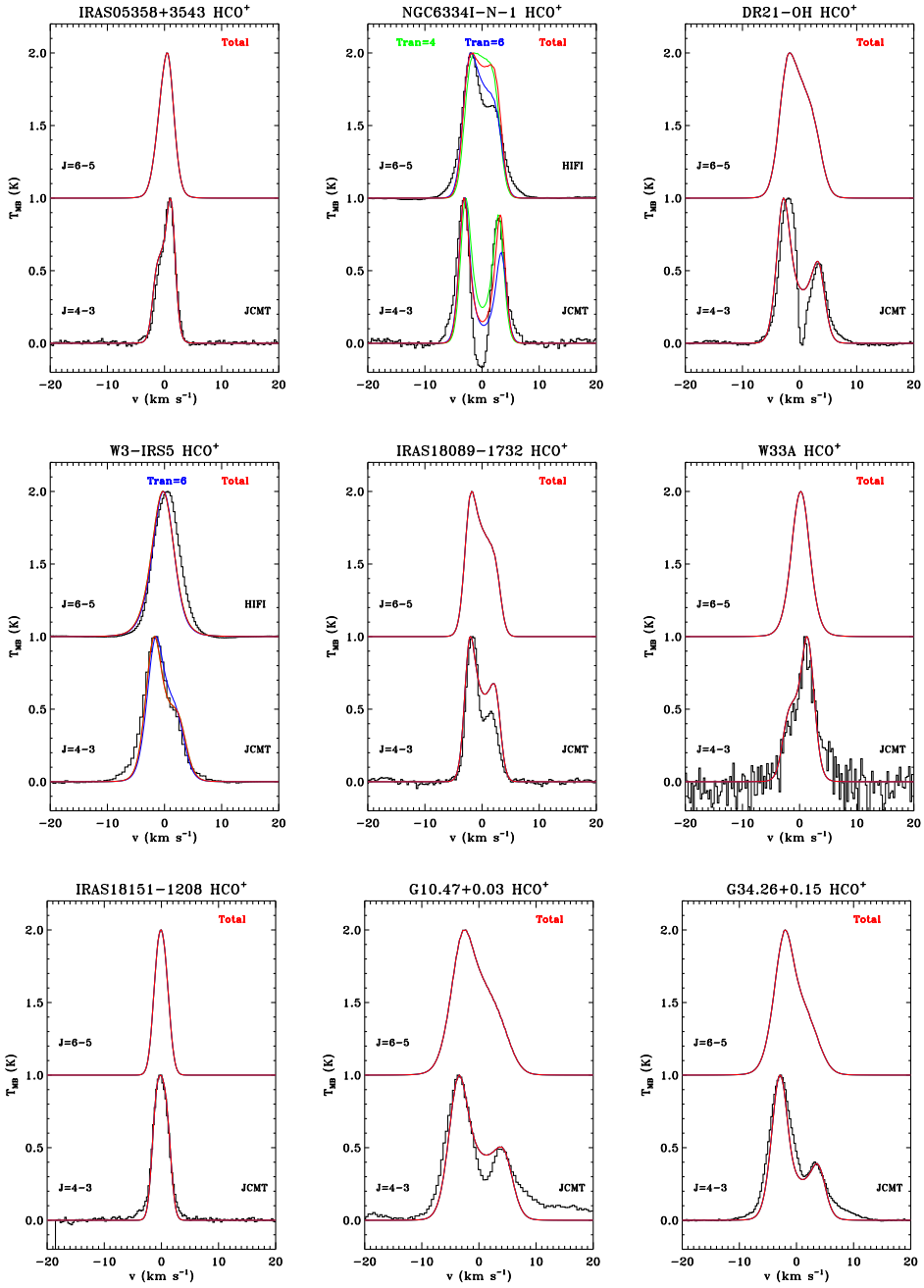

Figure 3.14: Same as Fig. 3.10 but for the high-mass YSOs IRAS05358+3543, NGC6334-I(N), DR21(OH), W3-IRS5, IRAS18089-1732, W33A, IRAS1815-1208, and G34.26+0.15, and G10.47+0.03.

Table 3.6: Skewness and the blue and red peak intensity ratio of the HCO^+ $J = 4$–3 modelled and observed line profile.

Source	Skewness[a] Mod.	T_B/T_R Mod.	Skewness[a] Obs.	T_B/T_R Obs.
Low-mass				
NGC1333 IRAS 2A	-0.13	1.3	-0.18	1.3
NGC1333 IRAS 4B	-0.47	2.8	-0.62	3.5
Ser SMM1	-0.18	1.3	-0.18	1.3
GSS30 IRS1	-0.20	1.0	-0.27	1.0
Elias 29	0.18	1.0	0.53	1.0
High-mass				
IRAS05358+3543	0.23	1.0	0.39	1.0
NGC6334−I(N)	-0.07	1.1	-0.06	1.2
DR21(OH)	-0.30	1.8	-0.24	1.7
W3−IRS5	-0.36	1.0	-0.44	1.0
IRAS18089−1732	-0.22	1.5	-0.36	2.0
W33A	0.32	1.0	0.33	1.0
IRAS18151−1208	-0.05	1.0	-0.03	1.0
G10.47+0.03	-0.36	2.0	-0.33	2.0
G34.26+0.15	-0.51	2.6	-0.57	2.5

Notes. [(a)] Skewness measured in the interval $v_{LSR} \pm 1.25$ km s^{-1} for low-mass protostars and $v_{LSR} \pm 3.5$ km s^{-1} for high-mass YSOs according to equation 1 of Gregersen et al. (1997).

Table 3.7: Overview of the main parameters of the physical model of each source: exponent of the power-law $n \propto r^{-p}$, and radius, density and temperature of the inner and outer regions of the modelled envelope.

	p	r_0 (AU)	n_0 (cm^{-3})	T_0 (K)	r_{out} (AU)	n_{out} (cm^{-3})	T_{out} (K)
Low-mass							
NGC1333 IRAS 2A	1.7	35.9	4.9(8)	235	1.7(4)	1.4(4)	10
NGC1333 IRAS 4B	1.7	15.0	2.0(9)	240	3.8(3)	8.7(5)	10
Ser SMM1	0.8	31.0	3.8(8)	232	1.2(4)	1.7(5)	10
GSS30 IRS1	2.0	16.2	1.2(8)	239	6.0(3)	1.1(4)	15
Elias 29	2.0	15.5	6.5(7)	243	3.8(3)	1.1(4)	18
High-mass							
IRAS05358+3543	1.5	30.0	1.5(9)	1183	5.4(4)	2.0(4)	17
NGC6334−I(N)	1.3	30.0	6.0(9)	1381	7.2(4)	2.4(5)	11
DR21(OH)	1.4	50.0	1.0(9)	1296	5.0(4)	6.5(4)	20
W3−IRS5	1.4	70.0	2.1(8)	1279	11.3(4)	1.1(4)	29
IRAS18089−1732	1.9	100.0	4.0(9)	1435	3.9(4)	4.7(4)	22
W33A	1.2	60.0	2.5(8)	1137	7.1(4)	5.2(4)	19
IRAS18151−1208	1.4	30.0	9.3(8)	1108	5.0(4)	2.9(4)	19
G10.47+0.03	1.4	100.0	9.8(8)	1237	6.0(4)	1.3(5)	29
G34.26+0.15	1.4	160.0	4.6(8)	1411	8.1(4)	7.6(4)	27

parameter (abundance, v_r or b_t) to be constrained. However, there are some differences concerning the calculation of the reduced χ^2_r between the HCO^+ and $C^{18}O$ observations.

In the case of the HCO^+ lines, the value of χ^2_r for each output image is obtained by interpolating the model profiles to the same spectral resolution of the observations, normalising both model and observation to their peak intensities, and comparing then the line intensity channel-by-channel. This method was chosen because the priority of this study is to fit the shape of the spectra rather than the intensity since infall/expansion and turbulence dominated profiles have different shapes.

With this method, the best-solutions normally agree with what is also considered a good match between observation and models by visual inspection. The blue/red ratio of the double peak profile and the skewness of the $J = 4$–3 line are measured for the RATRAN models and compared to those calculated for the observations (see Table 3.6). In the selection of the best-fit, we prioritise the fitting of the HCO^+ $J = 4$–3 line because, as introduced in Sect. 3.3.4, the HCO^+ $J = 6$–5 line is always underestimated by our RATRAN models.

For the $C^{18}O$ spectra, the models are also interpolated to the same spectral resolution as the available observations. Then, χ^2_r is calculated comparing also the line intensity channel-by-channel, but this time without normalising the spectra and models. The reason is that $C^{18}O$ is optically thin, which makes the abundance easier to constrain. As a sanity check, the solutions within one sigma uncertainty are also examined by visual inspection. In addition, for this molecule, χ^2_r values are calculated globally, i.e., considering all the available lines, and separately for the low-J (JCMT/APEX data) and the high-J (HIFI $J = 9$–8 and $J = 10$–9) spectra, modifying accordingly the degrees of freedom in each case. The purpose is to compare the best solution between different parts of the envelope (at inner and outer radii) with the global best-fit to contrast the results.

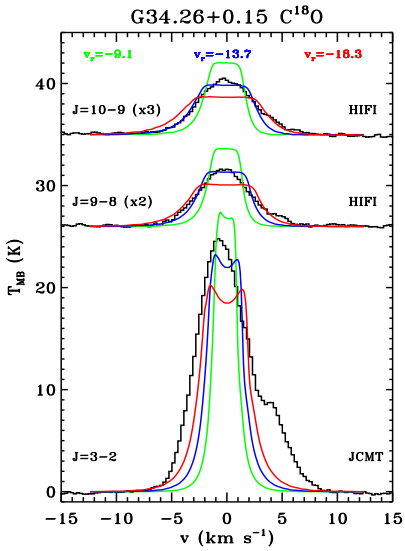

Figure 3.15: Comparison between infall-dominated models (b_t=0.0 km s^{-1}) with the same abundance profile but with different values of infall velocities at 1000 AU. The green, blue, and red profiles correspond to RATRAN models with $v_{r=1000\,AU}$ equal to -9.1 km s^{-1}, -13.9 km s^{-1}, and -18.3 km s^{-1} respectively. The black line shows the observed spectra.

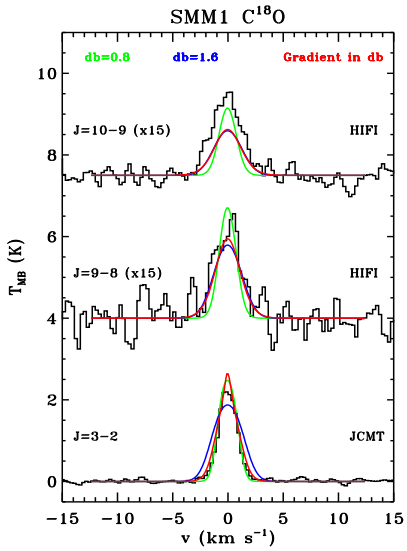

Figure 3.16: RATRAN model of the low-mass Class 0 protostars Ser SMM1. The black lines indicate the observed spectra; the green line corresponds to the model with a constant turbulent velocity b_t= 0.8 km s^{-1}; the blue the RATRAN image with a constant b_t= 1.6 km s^{-1}; and finally the red line is the model for which b_t was decreased at larger distances from the central position. For these three models, the infall velocity field is the same ($v_{r=1000AU}$= -0.3 km s^{-1}).

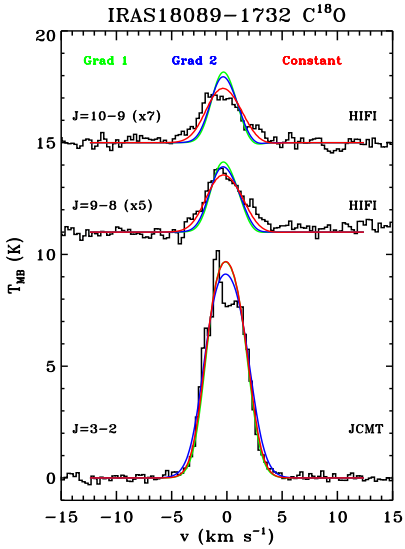

Figure 3.17: RATRAN model of the high-mass YSO IRAS18089. The observed spectra are plotted in black while the models with increasing turbulence with radius are in green and blue. The gradient of b_t is steeper for the blue model, resulting in broader profiles. The red line corresponds to the best-fit model with constant turbulent motions. For these three models, free fall is assumed ($v_{r=1000AU}$= -0.3 km s^{-1}).

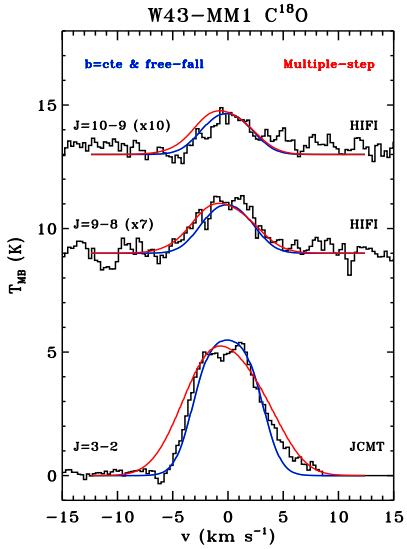

Figure 3.18: RATRAN model of the high-mass YSO W43-MM1 compared to the observed spectra in black. The blue model is generated assuming free fall and constant turbulence while the red profiles are obtained using the "multiple-step profile" presented by Herpin et al. (2012). The same C^{18}O abundance is assumed for both models.

4

Linking low- to high-mass YSOs with Herschel-HIFI observations of water

I. San José-García, J. C. Mottram, E. F. van Dishoeck, et al.
submitted

Abstract

Water effectively probes the dynamics in young stellar objects (YSOs), especially shocks in molecular outflows. It is therefore a key molecule to explore whether the physical properties of low-mass protostars can be extrapolated to massive YSOs, an important step in understanding the fundamental mechanisms regulating star formation.

As part of the WISH key programme, we investigate excited water line properties as a function of source luminosity, in particular the dynamics and the excitation conditions of shocks along the outflow cavity wall. Velocity-resolved *Herschel*-HIFI spectra of the H_2O 2_{02}-1_{11} (988 GHz), 2_{11}-2_{02} (752 GHz) and 3_{12}-3_{03} (1097 GHz) lines are analysed, together with ^{12}CO $J = 10$–9 and 16–15, for 52 YSOs with bolometric luminosities ranging from < 1 to $> 10^5$ $L_\odot$.

The H_2O and ^{12}CO line profiles are decomposed into multiple Gaussian components which are related to the different physical structures of the protostellar system. The non-LTE radiative transfer code RADEX is used to constrain the excitation conditions of the shocks along the outflow cavity. The profiles of the three excited water lines are similar, indicating that they are probing the same gas. Two main emission components are seen in all YSOs: a broad component associated with non-dissociative shocks in the outflow cavity wall ("cavity shocks") and a narrow component associated with the quiescent envelope material. More than 60% of the total integrated intensity in the excited water lines comes from the broad cavity shock component, while the remaining emission comes mostly from the envelope for low-mass Class I, intermediate- and high-mass objects and dissociative "spot shocks" for low-mass Class 0 protostars. The widths of the water lines are surprisingly similar from low- to high-mass YSOs, whereas ^{12}CO $J = 10$–9 line widths increase slightly with L_{bol}. The excitation analysis of the cavity shock component shows stronger 752 GHz emission for high-mass YSOs, likely due to pumping by an infrared radiation field. Finally, a strong correlation with slope unity is measured between the logarithms of the total H_2O line luminosity, L_{H_2O}, and L_{bol}, which can be extrapolated to extragalactic sources.

The water emission probed by spectrally unresolved data is largely due to shocks. Broad water and high-J CO lines originate in shocks in the outflow cavity walls for both low- and high-mass YSOs, whereas lower-J CO transitions mostly trace entrained outflow gas. The higher UV field and turbulent motions in high-mass YSOs compared to their low-mass counterparts may explain the slightly different kinematical properties of ^{12}CO $J = 10$–9 and H_2O lines from low- to high-mass.

4.1. Introduction

The physical and chemical conditions present in low- and high-mass star forming regions differ significantly. Massive star forming regions are found to have higher UV radiation fields and levels of turbulence than their low-mass counterparts (see Stäuber et al. 2007; Herpin et al. 2012). The temperatures, feedback mechanisms, magnetic fields, accretion rates and outflow forces are different between low- and high-mass young stellar objects (for more details see Bontemps et al. 1996; Behrend & Maeder 2001b; Beuther et al. 2002, 2007; Palla & Stahler 1993b; Cesaroni 2005; Zinnecker & Yorke 2007).

However, many studies have shown that high-mass YSOs behave in certain aspects as scaled-up versions of their low-mass counterparts (van der Tak et al. 1999, 2000; Shepherd 2003; Johnston et al. 2012; San José-García et al. 2013; Karska et al. 2014a, San José-García et al. subm.). In addition, the lifetime of the embedded phase of high-mass YSOs (0.07-0.4 Myrs, Mottram et al. 2011) is comparable to that of low-mass YSOs (0.15 Myr for Class 0, 0.5 Myr for Class 0+I, Dunham et al. 2014), even if massive objects evolve more in this period. The line luminosity of molecules like CO, HCO^+ and OH scales with bolometric luminosity and envelope mass as well as the degree of turbulence in the warmer inner regions of protostellar envelopes (San José-García et al. 2013; van der Tak et al. 2013; Wampfler et al. 2013; Benz et al. subm.). Moreover, the kinematics of outflows and envelopes seem to be linked independently of the mass of the forming star (San José-García et al. 2013). Therefore, a further characterisation of the physical conditions and dynamics of these components will help to identify the differences and similarities between low- and high-mass YSOs and better understand the fundamental processes in the formation of stars.

Water is unquestionably a key molecule to study the energetics and dynamical properties of protostellar environments (van Dishoeck et al. 2011). In particular, the analysis of the velocity resolved water data provided by the Heterodyne Instrument for the Far-Infrared (HIFI; de Graauw et al. 2010) on board of *Herschel* Space Observatory (Pilbratt et al. 2010) allows us to characterise the emission from molecular outflows, which play a crucial role in the formation of young stars and in the feedback on their surroundings (Kristensen et al. 2012; van der Tak et al. 2013; Mottram et al. 2014). Given the fact that the bulk of the water data on extragalactic sources out to the largest redshifts and the data provided by the other *Herschel* instruments (the Photodetector Array Camera and Spectrometer, PACS, Poglitsch et al. 2010; and the the Spectral and Photometric Imaging Receiver, SPIRE, Griffin et al. 2010) on galactic sources are spectrally unresolved, it is important to quantify the different components that make up the observed lines.

Outflows effectively remove angular momentum, necessary for the formation of a disk and mass accretion onto the forming star (see review by Lada & Kylafis 1999). The power agent of these structures (either jets or winds from the star/disk system) triggers not only the formation of the outflows, but also extreme and complex physical and chemical processes across the protostellar environment. In particular, different types of shocks take place in the outflow cavity wall, at the interface between the cavity and the envelope. Non-dissociative outflow-cavity shocks are localised along the outflow cavity wall (Visser et al. 2012; Kristensen et al. 2012; Mottram et al. 2014). On the other hand, dissociative shocks take place either along the jet, revealed through perturbations known as extremely high velocity components (EHV) (Bachiller et al. 1990; Tafalla et al. 2010), or at the base of the outflow cavity wall where the jet or wind impacts directly (Kristensen et al. 2012, 2013; Mottram et al. 2014). These shocks are also called spot shocks. Therefore, shocks and turbulent motions injected into the cavity wall propagating within this physical structure are products linked to the activity of the molecular outflow (Arce et al. 2007). The dynamical nature of these two phenomena (turbulence and shocks) is different and also differ from that characterising the entraining gas in classical outflows. To comprehensibly interpret the molecular emission of H_2O and ^{12}CO within the outflow-cavity system it is important to investigate whether the dynamical properties of low-mass objects can be extrapolated to more massive YSOs.

This was one of the goals of the "Water In Star forming regions with *Herschel*" key programme (WISH; van Dishoeck et al. 2011), which observed several water lines as well as high-J CO and isotopologue transitions for a large sample of YSOs covering early evolutionary stages over a wide

range of luminosities. An extensive study has been performed on all HIFI water observations for low-mass protostars (Mottram et al. 2014) and for low-lying water transitions within the high-mass sub-sample (van der Tak et al. 2013). The line profiles of the water transitions were analysed and decomposed into multiple velocity components, which are associated to different physical structures of the protostellar system. These studies investigated trends with luminosity, mass and evolution and explored the dynamical and excitation conditions probed by these lines. In addition, observations with PACS reveal that ^{12}CO J>20 transitions originate mostly in shocks for both low- and high-mass YSOs (Herczeg et al. 2012; Manoj et al. 2013; Green et al. 2013; Karska et al. 2013, 2014a,b). The excitation of warm CO is also similar across the luminosity range but rotational temperatures in high-mass objects are higher than in their low-mass counterparts in the case of H_2O, due to their higher densities (Karska et al. 2014a).

In order to link these two studies, this paper focuses on the analysis of the excited water lines across the entire WISH sample of YSOs. The ground-state water transitions of high-mass sources show absorption features from foreground clouds which complicates the extraction of velocity information from these lines (van der Tak et al. 2013), a reason why these lines are not considered in this study. Results from the line profile, line luminosity and excitation condition analysis are connected from low- to high-mass YSOs and interpreted together with those obtained from high-J ^{12}CO observations (J≥10). In addition, the obtained results may help to interpret and understand those of extragalactic sources. The aim is to better constrain the dynamical properties of molecular outflows across a large range of luminosities and complement the study presented in San José-García et al. (2013) based on the analysis of high-J CO and isotopologue transitions for the same sample of YSOs.

We start by introducing the selected sample, the studied H_2O and ^{12}CO observations and the reduction and decomposition methods in Sect. 4.2. The results from the water line profile and line luminosity analysis are presented in Sect. 4.3 and compared to those obtained for CO. In this section, the excitation conditions are also derived from the line intensity ratios. The interpretation of these results are discussed in Sect. 4.4, and extrapolated to extragalactic sources. Finally, in Sect. 4.5 we summarise the main conclusions of this work.

4.2. Observations

4.2.1. Sample

The sample of 51 YSOs is drawn from the WISH survey and is composed of 26 low-mass, six intermediate-mass and 19 high-mass YSOs. In addition, the intermediate-mass object OMC-2 FIR 4 (Kama et al. 2013) taken from the "Chemical *HErschel* Surveys of Star forming regions" key programme (CHESS; Ceccarelli et al. 2010) is added to enlarge the number of sources of this sub-group. The intrinsic properties of each source such as coordinates, source velocity ($v_{\rm LSR}$), bolometric luminosity, distance (d), and envelope mass ($M_{\rm env}$) can be found in Mottram et al. (2014), Wampfler et al. (2013) and van der Tak et al. (2013) for the low-, intermediate- and high-mass YSOs respectively.

The sample covers a large interval of luminosity and each sub-group of YSOs contains a mix of different evolutionary stages: both low- and intermediate-mass objects range from Class 0 to Class I; and the high-mass YSOs from mid-IR-quiet/mid-IR-bright massive young stellar objects (MYSOs) to ultra-compact H II regions (UC H II). The focus of this paper is to analyse different physical properties across the luminosity range; trends within the low-mass sample are discussed in Mottram et al. (2014); the intermediate- and high-mass samples are too small to search for trends within their several evolutionary stages.

4.2.2. Water observations

The targeted para-H_2O 2_{02}-1_{11} (988 GHz) and 2_{11}-2_{02} (752 GHz) lines and the ortho-H_2O 3_{12}-3_{03} (1097 GHz) line were observed with the HIFI instrument. The upper energy level ($E_{\rm u}$),

Table 4.1: Overview of the main properties of the observed water lines with HIFI.

Mol.	Trans.	E_u/k_B (K)	Frequency (GHz)	Inst.-band	η_{MB}[a]	θ[a] ($''$)	Spec. Resol. (km s^{-1})	Correction factor[b]
p-H_2O	2_{02}-1_{11}	100.8	987.927	HIFI-4a	0.74	21.5	0.15	0.865
p-H_2O	2_{11}-2_{02}	136.9	752.033	HIFI-2b	0.75	28.2	0.20	0.853
o-H_2O	3_{12}-3_{03}	249.4	1097.365	HIFI-4b	0.74	19.3	0.14	0.865

Notes. [(a)] Parameters calculated using equations 1 and 3 of Roelfsema et al. (2012), respectively. [(b)] Beam efficiency correction factors of each excited water lines according to the updated values of η_{MB} for the different HIFI-bands.

frequency, HIFI-band, beam efficiency (η_{MB}), beam size (θ) and spectral resolution of each water transition are given in Table 4.1. The beam efficiencies of the different HIFI-bands have been recently updated[1] and in general the values decrease by 15–20% for the band considered here. The presented observations have not been corrected with the new η_{MB} parameters because the analysis in this paper was completed before the new numbers were available and for consistency with our previous CO study. For completeness, the new beam correction factor of each HIFI-band are listed in Table 4.1.

The H_2O 2_{02}-1_{11} line was observed for the entire WISH sample; the 2_{11}-2_{02} line for 24 out of the 26 studied low-mass protostars and for all intermediate- and high-mass YSOs; and the 3_{12}-3_{03} transition was observed for only 10 low-mass protostars, two out of six intermediate-mass sources and all high-mass YSOs. These water lines are detected for all observed intermediate- and high-mass YSOs and for 75% of the low-mass protostars (see Mottram et al. 2014).

The data were observed simultaneously by the Wide Band Spectrometer (WBS) and the High Resolution Spectrometer (HRS), in both vertical (V) and horizontal (H) polarisation (more details in Roelfsema et al. 2012). We present the WBS data because the baseline subtraction for the HRS data becomes less reliable due to the width of the water lines, which is comparable to the bandwidth of the HRS setting. Single pointing observations were performed for all targets in dual-beam-switch (DBS) mode with a chop throw of $3'$. Contamination from emission by the off-position has only been identified in the H_2O 2_{02}-1_{11} spectrum of the low-mass protostar BHR71 (further information in Mottram et al. 2014). The allocated observation numbers for each source and line, designated with the initial obsIDs, are indicated in Table A.2 of Mottram et al. (2014) for the low-mass protostars, and in Table 4.6 of this manuscript for the intermediate- and high-mass YSOs.

4.2.3. Additional ^{12}CO observations

Complementing the water observations, ^{12}CO $J = 10$–9 and 16–15 spectra are included in this study to extend the comparison to other components of the protostellar system traced by this molecule and set a reference for abundance studies. The $J = 10$–9 transition was observed as part of the WISH key programme for the entire low- and intermediate-mass sample and for the high-mass object W3-IRS5 (see San José-García et al. 2013). The $J = 10$–9 spectrum was obtained for AFGL 2591 from the work of Kaźmierczak-Barthel et al. (2014). For the other high-mass sources, ^{12}CO $J = 3$–2 spectra are used as a proxy (San José-García et al. 2013).

^{12}CO $J = 16$–15 observations of 13 low-mass Class 0 protostars were observed within the *Herschel* programme OT2_lkrist01_2 (Kristensen et al. in prep.). Finally, this transition was obtained for three high-mass YSOs: W3-IRS5 (OT2_swampfle_2 *Herschel* programme; Wampfler et. al 2014), and for AFGL 2591 (Kaźmierczak-Barthel et al. 2014) and NGC6334-I (Zernickel et al. 2012) as part of the CHESS key programme (Ceccarelli et al. 2010).

[1]Further information regarding the updated beam efficiencies values is presented in the technical note "Measured beam efficiencies on Mars (revision v1.1, 1 October 2014)" of the HIFI wikipage:
http://herschel.esac.esa.int/twiki/bin/view/Public/HifiCalibrationWeb? template=viewprint

4.2.4. Reduction of the H_2O data

The calibration process of the water observations was performed in the *Herschel* Interactive Processing Environment (HIPE[2]; Ott 2010) using version 8.2 or higher. The intensity was first converted to the antenna temperature T_A^* scale and velocity calibrated with a $v_{\rm LSR}$ precision of a few m s^{-1}. Further reduction was performed with the GILDAS-CLASS[3] package. The spectra observed in the H and V polarisations were averaged together to improve the signal-to-noise ratio (S/N) and the intensity scale converted to main-beam brightness temperature scale, $T_{\rm MB}$, using the specific beam efficiencies for each band (Roelfsema et al. 2012). Finally, a constant or linear baseline was subtracted.

All data were then resampled to 0.27 km s^{-1} in order to compare the results among the water lines and to those from the high-J CO lines (San José-García et al. 2013) in a systematic manner. The rms noise of the spectra at that resolution, the maximum peak brightness temperature, $T_{\rm MB}^{\rm peak}$, the integrated intensity, $W = \int T_{\rm MB} {\rm d}v$, and the full width at zero intensity, $FWZI$, are presented in Tables 4.7 to 4.9. The latter parameter was measured as in Mottram et al. (2014): first by resampling all spectra to 3 km s^{-1} to improve the S/N, then re-calculating the rms and finally considering the "zero intensity" where the intensity of the spectrum drops below 1σ of that rms. The velocity range constrained by the $FWZI$ is used to define the limits over which the integrated intensity of the line is calculated.

Since the spectra have not been corrected with the recently released beam efficiencies of the different HIFI-bands[1] (Sect. 4.2.2), the results presented in Tables 4.7 to 4.9, as well as those shown in Figs. 4.3 and 4.9, should be divided by the correction factor indicated in Table 4.1. The line profiles do not change if the new $\eta_{\rm MB}$ values are applied and the variation of the line ratios is of the order of 1%.

Finally, the $C^{18}O$ $J = 10$–9 emission line is detected in the line wing of the H_2O 3_{12}-3_{03} spectrum for five low-mass protostars (NGC 1333 IRAS2A and IRAS4B, Ser SMM1, GSS30 and Elias 29) and four high-mass YSOs (G5.89-0.39, W3-IRS3, NGC6334-I and W51N-e1). Therefore, a Gaussian profile with the same $FWHM$, position and amplitude as those constrained in San José-García et al. (2013) was used to remove the contribution of $C^{18}O$ $J = 10$–9 line from the reduced H_2O 3_{12}-3_{03} spectrum for each of these sources. The data of these specific YSOs are then analysed and plotted after subtracting the $C^{18}O$ line.

4.2.5. Decomposition method

As shown by Kristensen et al. (2010, 2012), van der Tak et al. (2013) and Mottram et al. (2014), the water line profiles are complex and can be decomposed into multiple velocity components. The purpose of decomposing the line profile is to disentangle the different regions probed within the protostar, which are characterised by specific physical conditions and kinematics.

Generally, these velocity components can be well reproduced by Gaussian-like profiles; other types of profiles do not give improved fits (Mottram et al. 2014). Depending on the water transition and luminosity of the source, the number of components needed to fit the profile varies. For most of the low-mass protostars, the spectra can be decomposed into a maximum of four different Gaussian components, as shown in Kristensen et al. (2010, 2012, 2013) and Mottram et al. (2014). In order to determine the number of velocity components of the water lines for the intermediate- and high-mass YSOs, these spectra were initially fit with one Gaussian profile using the IDL function *mpfitfun*. Then, the residual from this fit was analysed and since it was larger than 3 sigma rms for all lines, an extra Gaussian component was added to the decomposition method to improve the fitting. The procedure is the same but now considering two independent Gaussian profiles. A self-absorption feature at the source velocity was detected in the H_2O 2_{02}-1_{11} line for 9 out of 19 high-mass objects, so for those objects an extra Gaussian component in absorption was added in the decomposition

[2]HIPE is a joint development by the Herschel Science Ground Segment Consortium, consisting of ESA, the NASA Herschel Science Centre, and the HIFI, PACS and SPIRE consortia.

[3]http://www.iram.fr/IRAMFR/GILDAS/

method. In some high-mass sources this component is weaker or non-detected in the other studied transitions and it can be negligible (for an example, see the DR21(OH) observations). Therefore, the number of components is determined by the spectrum itself and its S/N and not by the assumed method.

As in Mottram et al. (2014), we force the *FWHM* and central position of each component to be the same for all transitions and they are constrained simultaneously by all spectra of a given source. The intensities of each Gaussian component are free parameters that can vary for each water line. The resulting fits were examined visually as a sanity check. The values of the $FWHM$, $T_{\rm peak}$, $v_{\rm peak}$, and integrated intensity of each Gaussian component are summarised in Appendix 4.A, Tables 4.10 to 4.12.

4.2.6. Association with physical components

The multiple velocity components needed to reproduce the H_2O line profiles can be related to physical components in protostellar systems (Kristensen et al. 2011, 2012; van der Tak et al. 2013; Mottram et al. 2014).

Quiescent inner envelope gas produces a Gaussian profile in emission with the smallest *FWHM* centred at the source velocity (see Sect. 3.2.2 of Mottram et al. 2014). In previous studies these velocity components were called narrow components. The cold outer protostellar envelope can cause a self-absorption, which is more common in ground-state H_2O lines and in objects with massive and cold envelopes (e.g. van der Tak et al. 2013, Mottram et al. 2013).

The chemical and physical conditions present in shocks increase the abundance of H_2O by sputtering from the grain mantles (Codella et al. 2010; Van Loo et al. 2013; Neufeld et al. 2014). The line profile resulting from shocked water emission depends on the nature and kinematical properties of the shocks generating it, which translate into velocity components with different features (see Table 3 and Sect. 3.2 of Mottram et al. 2014).

The emission from non-dissociative shocks in layers along the outflow cavity wall produces velocity components with the largest $FWHM$ (>20 km s^{-1}) and are generally centred near the source velocity (Kristensen et al. 2010, 2013; van Kempen et al. 2010; Nisini et al. 2010; Suutarinen et al. 2014; Santangelo et al. 2014). However, these broad Gaussian-like profiles, named cavity shock components (Mottram et al. 2014) or simply broad components, should be differentiated from the broad velocity component identified in low- and mid-J (J<10) CO spectra, even if shape and width are similar. The reason is that the water emission originates in shocks in the cavity while the CO emission comes from cooler material deeper in the wall and closer to the quiescent envelope (Raga et al. 1995; Yıldız et al. 2013).

In contrast, spot shocks occur in small localised regions and are associated to hotter and more energetic dissociative shocks (Mottram et al. 2014). This emission may originate in extremely-high velocity (EHV) gas along the jets (Bachiller et al. 1990; Tafalla et al. 2010; Kristensen et al. 2011) or at the base of the outflow cavity (previously referred to as either the medium or the offset component; Kristensen et al. 2013). These Gaussian profiles show smaller $FWHM$s than those measured for the cavity shock component and are in general more offset from the source velocity. A more detailed characterisation and discussion can be found in Mottram et al. (2014), van der Tak et al. (2013) and Kristensen et al. in prep.

The contribution of the cavity shock and envelope components with respect to the total integrated intensity of the water lines for the intermediate- and high-mass YSOs are presented in Table 4.2 together with the values for the low-mass Class 0 and Class I protostars calculated by Mottram et al. (2014). Table 4 of that manuscript shows the results for different water lines as well as the fraction corresponding to the spot shock component.

In the following, the different velocity components of the H_2O and CO lines are distinguished based on the probable physical origin of the emission and the width of the profile.

Table 4.2: Average fraction of the integrated intensity that the envelope and cavity shock components contribute to the total integrated intensity of the H_2O 2_{02}-1_{11} (988 GHz), 2_{11}-2_{02} (752 GHz) and 3_{12}-3_{03} (1097 GHz) lines.

	H_2O 2_{02}-1_{11}		H_2O 2_{11}-2_{02}		H_2O 3_{12}-3_{03}	
	$W_{\rm envelope}/W_{\rm tot}$[a]	$W_{\rm cavity\ shock}/W_{\rm tot}$	$W_{\rm envelope}/W_{\rm tot}$[a]	$W_{\rm cavity\ shock}/W_{\rm tot}$	$W_{\rm envelope}/W_{\rm tot}$[a]	$W_{\rm cavity\ shock}/W_{\rm tot}$
LM0	0.0 ± 0.1	0.7 ± 0.1	0.0 ± 0.1	0.7 ± 0.1	0.0 ± 0.1	0.8 ± 0.1
LMI	0.2 ± 0.1	0.8 ± 0.1	0.3 ± 0.2	0.7 ± 0.2	0.0 ± 0.1	1.0 ± 0.1
IM	0.3 ± 0.1	0.6 ± 0.2	0.4 ± 0.2	0.6 ± 0.2	0.3 ± 0.1	0.6 ± 0.1
HM	0.4 ± 0.2	0.6 ± 0.2	0.4 ± 0.2	0.6 ± 0.2	0.4 ± 0.1	0.6 ± 0.1

Notes. LM0: low-mass Class 0 protostars; LMI: low-mass Class I sources; IM: intermediate-mass YSOs; HM: high-mass objects.
[(a)] As in Mottram et al. (2014), the envelope fraction, $W_{\rm envelope}$, is calculated subtracting the cavity and spot shock contribution from the total integrated intensity, $W_{\rm tot}$, for each water line, i.e, $W_{\rm envelope} = W_{\rm tot} - W_{\rm cavity\ shock} - W_{\rm spot\ shock}$.

4.3. Results

The basic properties of the spectra and their decomposition are introduced in Sect. 4.3.1. In Sect. 4.3.2 the results of the line profile decomposition are compared to those obtained for the high-J CO observations described in San José-García et al. (2013). The water line luminosity properties are also compared to those of CO in Sect. 4.3.3. In Sect. 4.3.4 integrated intensity ratios calculated for different pairs of water transitions are presented and these line ratios are further studied as across the line profiles in Sect. 4.3.5. Finally, the excitation conditions of the water lines are analysed with the non-LTE radiative transfer code RADEX in Sect. 4.3.6.

4.3.1. Water line profile characterisation

The observed H_2O 2_{02}-1_{11}, 2_{11}-2_{02}, and 3_{12}-3_{03} spectra for the intermediate- and high-mass YSOs are presented in Appendix 4.A, Figs. 4.11, 4.12 and 4.13, respectively. The Gaussian profile fitting the broad (cavity shock) component of each water transition and source is indicated with a pink line. The spectra of the low-mass protostars are shown in Appendix A of Mottram et al. (2014).

In order to easily compare all the data, normalised averaged spectra of the H_2O 2_{02}-1_{11}, 2_{11}-2_{02} and 3_{12}-3_{03} transitions are computed for the low-mass Class 0 and Class I protostars, the intermediate-mass sources and high-mass YSOs, as shown in the three first panels of Fig. 4.1. These spectra are calculated for each transition by normalising each spectrum to its peak intensity and averaging it together with the observations of the corresponding sub-group of objects. The normalised averaged spectra obtained for the three H_2O transitions are similar for each sub-type of YSOs. Only the H_2O 2_{02}-1_{11} high-mass averaged spectrum shows a slightly different profile with respect to the other two water lines due to the presence of a self-absorption feature in some sources. Without considering the Class I protostars, the averaged spectrum for a given transition seems to be broader for the low-mass objects, but at the base of the spectra the widths are similar, independent of the luminosity.

In the right-hand panel of Fig. 4.1 the three H_2O transitions (2_{02}-1_{11} in orange, 2_{11}-2_{02} in blue and 3_{12}-3_{03} in red) are over-plotted for four different sources: a low-mass Class 0 (NGC1333 IRAS 4B), a low-mass Class I (GSS 30 IRS), an intermediate-mass objects (NGC2071) and a high-mass YSO (W33A). For each source, the shapes of the three water line profiles are similar but scaled-up in intensity, a result that is confirmed from the visual inspection of the water line profiles of all YSOs. In particular, the line wings are very similar. This indicates that the three water transitions are probing the same dynamical properties in each source.

Moving to the outcomes from the line decomposition explained in Sect. 4.2.5, the analysis suggests that the quiescent envelope and cavity shock components are the only two physical components consistently present in the H_2O 2_{02}-1_{11}, 2_{11}-2_{02} and 3_{12}-3_{03} spectra of all low-, intermediate-

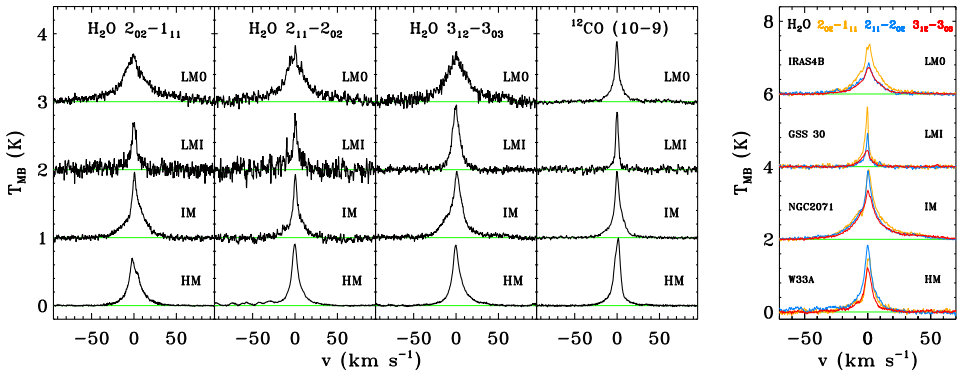

Figure 4.1: *Left* figure: Averaged and normalised spectrum calculated for the low-mass Class 0 (LM0) protostars, the low-mass Class I (LMI), intermediate-mass YSOs (IM) and high-mass objects (HM) for the H_2O 2_{02}-1_{11} 988 GHz (*left* panel), 2_{11}-2_{02} 752 GHz (*middle-left* panel), 3_{12}-3_{03} 1097 GHz (*middle-right* panel) transitions and the ^{12}CO $J = 10$–9 (*right* panel) spectra (see San José-García et al. 2013). The low intensity features on the blue wing of the H_2O 2_{11}-2_{02} high-mass profile are due to methanol emission. *Right* figure: H_2O 2_{02}-1_{11}, 2_{11}-2_{02} and 3_{12}-3_{03} spectra plotted in orange, blue and red respectively for NGC 1333 IRAS4B (LM0), GSS 30 (LMI), NGC2071 (IM) and W33A (HM). All spectra have been shifted to zero velocity and the horizontal light green lines in both figures represent the baseline level.

and high-mass YSOs. The spot shock components are not detected for the excited water lines presented here towards high-mass YSOs and six out of seven intermediate-mass objects, though they have been seen in absorption against the outflow in some ground-state H_2O lines for some high-mass sources (for more information see van der Tak et al. 2013).

As shown in Table 4.2, for a given sub-sample of YSOs the averaged contribution of the cavity shock component with respect to the total integrated intensity of the line is the same for the three water transitions. This fraction seems to decrease from low- to high-mass, but no statistically significant trend with $L_{\rm bol}$ can be claimed because the specific contribution of the cavity shock emission varies from source to source. The remaining emission comes from the envelope in the case of the low-mass Class I, intermediate- and high-mass YSOs and from spot shock components for low-mass Class 0 protostars (Mottram et al. 2014). This picture is consistent with the average spectra presented in Fig. 4.1, where the envelope component of the water lines is more prominent for the high-mass sources than for their low-mass Class 0 counterparts.

Independently of these numbers, in this paper we focus on characterising the physical conditions causing the line-wing emission in the water line profiles, i. e., the broader velocity component associated to the shock emission along the outflow cavity.

4.3.2. Comparison of the H_2O and ^{12}CO line profiles

The fourth panel in Fig. 4.1 includes the normalised averaged ^{12}CO $J = 10$–9 spectrum of each sub-sample of YSOs. These averaged profiles are clearly narrower than those of water, especially for the low-mass Class 0 protostars, and the width of the spectra seems to increase from low- to high-mass. Therefore, just from a basic visual inspection of the water and the high-J CO normalised averaged spectra we can point to differences in the shape of the line profiles of these two molecules and a different trend in the width from low- to high-mass.

To consistently compare the dynamical conditions of the entrained outflowing material traced by CO and the shocked gas along the outflow cavity, the line-wing emission of these two species is analysed using two parameters: the $FWHM$ and the $FWZI$ (see Sections 4.2.4 and 4.2.5). Both variables are used because $FWHM$ characterises the average extent of emission from the source velocity while $FWZI$ characterises the fastest material. For simplification, the $FWHM$ of the

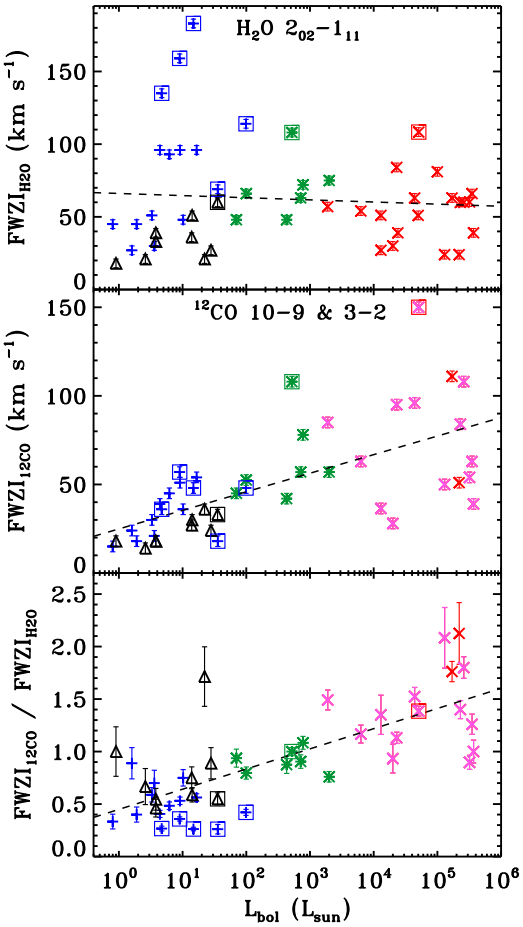

Figure 4.2: (*Top*) *FWZI* of the H_2O 2_{02}-1_{11} (988 GHz) emission line versus the bolometric luminosity. (*Middle*) Same as *top* panel but for the ^{12}CO $J = 10$–9 and $J = 3$–2 observations. (*Bottom*) Ratio of the ^{12}CO and H_2O 2_{02}-1_{11} *FWZI* values as a function of L_{bol}. The blue plus symbols correspond to the low-mass Class 0 protostars, the black triangles the low-mass Class I, the green asterisks the intermediate-mass objects, the pink crosses the high-mass YSOs for which the ^{12}CO $J = 3$–2 spectra are used, and the red cross symbols the high-mass object for which ^{12}CO $J = 10$–9 data are available (see San José-García et al. 2013). The low- and intermediate-mass sources with detected EHV components are surrounded by a box, as well as the high-mass YSO with triangular water line profiles.

Gaussian profile reproducing the cavity shock component is differentiated from the other velocity components by using the sub-script *b* to indicate that this is the broader velocity component obtained from the line decomposition.

The top panel of Fig. 4.2 shows the *FWZI* for the H_2O 2_{02}-1_{11} transition as a function of bolometric luminosity (in Fig. 4.15 the *FWZI* of the other water lines are also plotted versus L_{bol} and envelope mass). Similarly, the constrained $FWHM_b$ from the cavity shock component (same for all three lines) versus L_{bol} and M_{env} are presented in Fig. 4.14. The *FWZI* values vary from 15 to 189 km s^{-1}, while the $FWHM_b$ range from 13 to 52 km s^{-1}. Due to the large scatter and dispersion of the data points, no trend or correlation with luminosity can be claimed in either case. The smaller *FWZI* and $FWHM_b$ values are those of the low-mass Class I protostars, consistently lying at the bottom of these figures. In addition, the low- and intermediate-mass YSOs which show EHV components are marked with squares in Fig. 4.2 to indicate that their *FWZI* was calculated including the spot shock emission and to investigate if there is any particular trend for these objects. The spectra of the marked high-mass object does not have EHV components but their line profiles are characterised with broad and triangular shapes. More information about these specific sources can be found in Appendix 4.B.

The *FWZI* and $FWHM_b$ for the ^{12}CO observations (middle panels of Figs. 4.2 and 4.14 respectively) are spread across a smaller velocity range than that for water. In addition, the *FWZI* shows less scatter than the $FWHM_b$. There is a statistically significant trend of larger *FWZI* for

Table 4.3: Averaged rms value in 0.27 km s^{-1} bin and mean (dash) values of the $FWHM_{\rm b}$ and $FWZI$ for the three water lines and the ^{12}CO J = 10–9 spectra for each sub-type of YSO. The averaged $FWHM_{\rm b}$ and $FWZI$ ratios calculated from the ^{12}CO and H_2O observations are also indicated in the last two columns.

	H_2O	2_{02}-1_{11}		2_{11}-2_{02}		3_{12}-3_{03}		^{12}CO J = 10–9			^{12}CO / H_2O	
	$\overline{FWHM_{\rm b}}$	$\overline{\sigma_{rms}}$	$\overline{FWZI}$	$\overline{\sigma_{rms}}$	$\overline{FWZI}$	$\overline{\sigma_{rms}}$	$\overline{FWZI}$	$\overline{FWHM_{\rm b}}$	$\overline{\sigma_{rms}}$	$\overline{FWZI}$	$FWHM_{\rm b}$	$FWZI$
	(km s^{-1})	(mK)	(km s^{-1})	(mK)	(km s^{-1})	(mK)	(km s^{-1})	(km s^{-1})	(mK)	(km s^{-1})		
LM0	30 ± 12	23	86 ± 45	20	87 ± 47	17	86 ± 31	20 ± 9	112	36 ± 14	0.7 ± 0.3	0.5 ± 0.2
LMI	18 ± 5	22	34 ± 13	17	33 ± 15	9	42[a]	11 ± 1	115	24 ± 8	0.6 ± 0.1	0.8 ± 0.4
IM	29 ± 5	24	69 ± 19	22	63 ± 30	19	79[a]	20 ± 4	105	63 ± 21	0.7 ± 0.2	0.9 ± 0.1
HM	27 ± 10	78	47 ± 10	68	70 ± 32	45	71 ± 35	22[a]	180	81 ± 30[b]	0.9[a]	1.9 ± 0.2[b]

Notes. LM0: low-mass Class 0 protostars; LMI: low-mass Class I sources; IM: intermediate-mass YSOs; HM: high-mass objects.
See specification in the $FWZI$ calculation for the low-mass objects in Mottram et al. 2014.
[(a)] No standard deviation is given because the number of observed or detected sources is less than four.
[(b)] For the high-mass YSOs, the ^{12}CO J = 3–2 spectra were included in the calculation of the mean value of the $FWZI$ parameter.

more luminous sources (4.7σ[4]) with a Pearson correlation coefficient $r = 0.72$, which is also seen to a lesser extent for the $FWHM_{\rm b}$.

Table 4.3 presents the mean $FWHM_{\rm b}$ and $FWZI$ values for H_2O and ^{12}CO and the averaged rms in a 0.27 km s^{-1} bin, $\sigma_{\rm rms}$. In the case of the high-mass YSOs, the derived values are not affected by the higher $\sigma_{\rm rms}$ in those data (as left panels of Fig. 4.1 already show) since the actual signal to noise, S/N, on the water spectra themselves given by the peak intensity relative to the rms are higher (averaged S/N value of ~60) than those of their low-mass counterparts (averaged S/N of ~20).

Without considering the low-mass Class I protostars, which are more evolved and therefore have weaker, less powerful outflows (Mottram et al. 2014), the average $FWHM_{\rm b}$ and $FWZI$ values derived for H_2O are similar from low- to high-mass (Table 4.3). A decrease of the mean $FWZI$ values with increasing luminosity is only hinted for the H_2O 2_{02}-1_{11} transition. Combining the results from both $FWHM_{\rm b}$ and $FWZI$ we conclude that the extent of the water line emission is similar for the entire sample. In contrast, and as suggested by the middle panel of Fig. 4.2, the averaged values of both $FWZI$ and $FWHM_{\rm b}$ for the ^{12}CO observations seem to increase with luminosity.

The dispersion observed for the $FWZI$ and $FWHM_{\rm b}$ in both H_2O and CO could be related to the intrinsic properties of the source, such as its inclination, evolutionary stage, clustering, etc. In order to minimise possible effects caused by these inherent characteristics, the ratio of the $FWZI$ derived for the ^{12}CO J = 10–9 and J = 3–2 spectra and the $FWZI$ of the water lines is plotted versus the bolometric luminosity in the bottom panel of Fig. 4.2. The same procedure is followed for $FWHM_{\rm b}$ of the ^{12}CO and water spectra (see bottom panels of Fig. 4.14 in Appendix 4.C).

Independently of the use of $FWZI$ or $FWHM_{\rm b}$, a correlation between these ratios and $L_{\rm bol}$ is measured for each of the three water lines with statistical significance between 3.3σ and 5.0σ (Pearson correlation coefficients between 0.50 and 0.75). While ^{12}CO J = 3–2 and 10–9 may trace different layers in the outflow (Yıldız et al. 2013; Santangelo et al. 2013), the $FWZI$, i. e., the maximum offset velocity ($v_{\rm max}$), of the CO lines does not change with the J transition (Kristensen et al. in prep.). Therefore, the use of ^{12}CO J = 3–2 as a proxy for ^{12}CO J = 10–9 for the high-mass sources will not affect this trend.

The average ratios of $FWZI$ and $FWHM_{\rm b}$ are also given in Table 4.3 and generally increase with increasing $L_{\rm bol}$. The $FWZI$ ratio indicates that the velocity of the material traced by the wings of ^{12}CO is larger than that of water for the high-mass YSOs. The $FWHM_{\rm b}$ values are basically

[4]The significance of a correlation for a given number of data points and Pearson correlation coefficient is calculated as described in Marseille et al. (2010).

Table 4.4: *Top half*: Slope (m), intercept (n), and Pearson correlation coefficient (r) of the power-law fit to the correlation between the logarithm of the H_2O line luminosity and the logarithm of the bolometric luminosity (L_{bol}, left-columns) and the logarithm of the envelope mass (M_{env}, right-columns). *Bottom half:* Same as above, but for the correlation between the luminosity corresponding to the cavity shock component and L_{bol} or M_{env}.

Line	$\log(L_{H_2O}) = n + m \cdot \log(L_{bol})$			$\log(L_{H_2O}) = n + m \cdot \log(M_{env})$		
(GHz)	m	n	r	m	n	r
988	0.85 ± 0.05	-3.48 ± 0.14	0.94	1.19 ± 0.05	-2.91 ± 0.10	0.96
752	0.94 ± 0.05	-3.59 ± 0.18	0.94	1.30 ± 0.06	-2.91 ± 0.12	0.96
1097	0.76 ± 0.05	-3.23 ± 0.18	0.95	1.11 ± 0.08	-2.94 ± 0.18	0.93
	$\log(L_{broad\,H_2O}) = n + m \cdot \log(L_{bol})$			$\log(L_{broad\,H_2O}) = n + m \cdot \log(M_{env})$		
988	0.79 ± 0.04	-3.43 ± 0.14	0.94	1.11 ± 0.05	-2.90 ± 0.10	0.96
752	0.83 ± 0.05	-3.37 ± 0.18	0.94	1.15 ± 0.06	-2.80 ± 0.13	0.95
1097	0.73 ± 0.05	-3.34 ± 0.19	0.95	1.08 ± 0.08	-3.06 ± 0.18	0.93

the same for ^{12}CO and H_2O, independently of whether these molecules are probing different regions and physical conditions within the outflow. However, this is not the case for the low-mass protostars, which show larger line-wings for the water observations than for the ^{12}CO observations, consistent with Kristensen et al. (2012). This trend is further analysed and interpreted in Sect. 4.4.1.

4.3.3. Line luminosity study

The integrated intensity of the water emission lines, $W = \int T_{MB} dv$, is calculated as described in Sect. 4.2.4 and presented, together with its uncertainty, in Tables 4.7 to 4.9. For those H_2O 2_{02}-1_{11} spectra with an absorption at the source velocity, the integrated intensity was determined by masking the absorption feature and using the area traced by the two Gaussian emission profiles fitting the spectrum.

Since the studied sample of YSOs covers a wide range of luminosities and distances (from 0.13 to 7.9 kpc), the integrated intensity is converted to line luminosity, L_{H_2O}. This parameter takes into account the distance and can be compared to values obtained in extragalactic studies. These quantities have been calculated using Eq. (2) of Wu et al. (2005), assuming a Gaussian beam with size according to Table 4.1 and point source objects. The uncertainties in the line luminosity are calculated from the rms of the spectrum and assuming a distance uncertainty of ~20%.

Figure 4.3 presents the logarithm of the line luminosity for each water transition, $\log(L_{H_2O})$, versus the logarithm of the bolometric luminosity, $\log(L_{bol})$. A strong correlation between the logarithm of these quantities is measured (solid black line) for each of the three lines. The Pearson correlation coefficient, r, is larger than 0.9 and the trends extend over more than six orders of magnitude in both axes. Similarly, a strong correlation is also measured between the logarithm of L_{H_2O} and the logarithm of the envelope mass, M_{env} (see Fig. 4.17 in Appendix 4.C). The parameters of the fit and correlation coefficient for all water lines and for both L_{bol} and M_{env} are presented in Table 4.4.

The slope of the correlations are close to one within the uncertainty. As there is no saturation of the line luminosity, the emission must be optically thin or at least effectively thin (i.e. optically thick but sub-thermally excited, see Linke et al. 1977). In either case, the intensity scales as the product of the beam-averaged column density and average volume density in the emitting gas. Assuming that the density in the regions probed by water in low- and high-mass protostars are similar, a correlation between $\log(L_{H_2O})$ and $\log(L_{bol})$ with slope close to unity suggests that the emitting region size increases with L_{bol} such that the filling factor of the beam is approximately the same for all sources. The 3_{12}-3_{03} transition shows the smallest number of detections for the low-mass protostars, which could explain the difference in the value of the slope with respect the

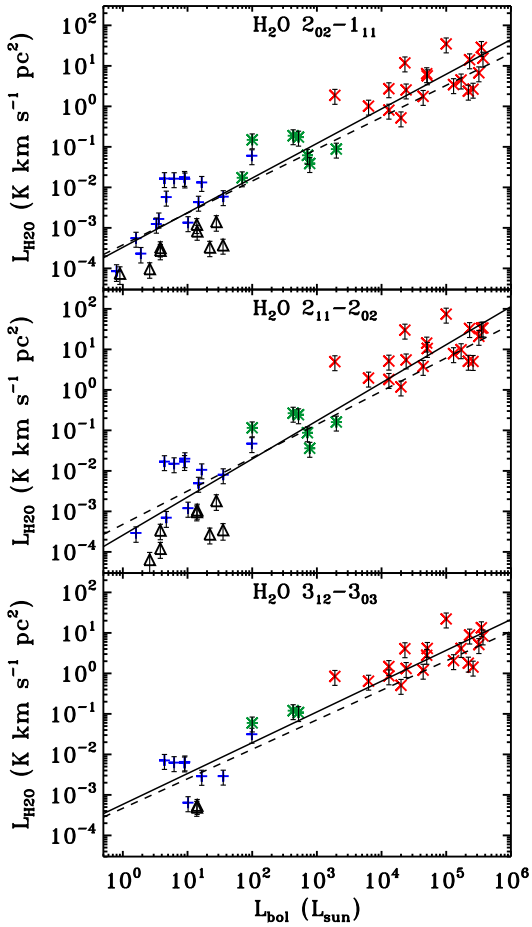

Figure 4.3: Line luminosity of the H_2O 2_{02}-1_{11} (988 GHz) line emission (*top*), the H_2O 2_{11}-2_{02} (752 GHz) data (*middle*), and H_2O 3_{12}-3_{03} (1097 GHz) spectra (*bottom*) versus the bolometric luminosity of the source. The blue plusses correspond to the low-mass Class 0 protostars, the black triangles the low-mass Class I, the green asterisks the intermediate-mass objects and the red cross symbols the high-mass YSOs. The solid line indicates the linear correlation of the logarithm of the total line luminosity, $\log(L_{H_2O})$, and $\log(L_{bol})$. The dashed line shows the log-log correlation of the luminosity measured for the broader Gaussian velocity component only (cavity shock emission; $L_{broad\,H_2O}$) and $\log(L_{bol})$.

other two water lines. This linear correlation of $\log(L_{H_2O})$ and $\log(L_{bol})$ should not be extrapolated to the ground-based water transitions due to the presence of broad and deep absorption features which complicate the comparison of the water line luminosity, particularly in the case of massive YSOs (see van der Tak et al. 2013).

The same correlation between the ^{12}CO 10–9 line luminosity and L_{bol} was measured by San José-García et al. (2013, their Fig. 6). The calculated slope of the linear fit is the same within the uncertainty to those derived for the water lines (see Table 4 of San José-García et al. 2013, for comparison). As also noted by Mottram et al. (2014), the low-mass Class I sources have lower water line luminosities than the Class 0 sources, due to decreases in both $FWHM$ and $FWZI$ (see Table 2), as well as peak intensities, causing a clear separation between these two classes of low-mass protostars. However, in the case of CO, the separation between the low-mass Class 0 and Class I was small. Both ^{12}CO $J = 10$–9 and especially water are more sensitive to fast moving material in the outflows, which differentiate sources at different evolutionary stages, while the CO isotopologues are mostly probing the bulk of quiescent envelope material. This confirms the conclusions of Mottram et al. (2014) that the difference in water emission between Class 0 and Class I sources is related to the decreasing strength of the outflow and not to the removal of the envelope.

The integrated intensity emission coming from the cavity shocks, i. e., the area of the Gaussian profile fitting the line-wings, is also converted to line luminosity, $L_{broad\,H_2O}$. Figure 4.18 of Appendix 4.C shows the logarithm of this quantity as a function of $\log(L_{bol})$. As for the total line

luminosity, a strong correlation which extends across the entire luminosity range is measured but with slightly smaller values of the slope (averaged slope of 0.78±0.04). Figure 4.3 includes for each water transition the relation between the logarithm of $L_{\mathrm{broad\,H_2O}}$ and L_{bol} (dashed black line) for comparison with the total line luminosity, $L_{\mathrm{H_2O}}$, (solid black line). The parameters from the log-log correlations of the broad component are also presented in Table 4.4. Consistent with the larger envelope contribution for high-mass sources (see Table 4.2) the differences between the fits for $L_{\mathrm{H_2O}}$ and $L_{\mathrm{broad\,H_2O}}$ are larger for all three lines for the high-mass sub-sample.

The fact that we found the same strong correlation between the parameters $\log(L_{\mathrm{bol}})$ and $\log(L_{\mathrm{H_2O}})$ or $\log(L_{\mathrm{broad\,H_2O}})$, i.e., similar values for the slope close to unity, confirms that the total water line luminosity is dominated by the broad component (outflow cavity shocks).

4.3.4. Integrated intensity ratios

The integrated intensity ratios of two different water transitions across the luminosity range can be used to analyse the excitation and physical conditions of protostellar systems. Mottram et al. (2014) show that there is little variation in line ratio between outflow-related components for the low-mass sample. They showed that the lines lie in the optically thick but effectively thin regime. This means that the water lines presented in that study are sub-thermally excited due to their high critical densities compared to the actual gas density of the emitting region. This condition lowers the chance of collisional de-excitation, so photons will scatter and eventually escape as if the lines were optically thin. We will extend this study to intermediate- and high-mass YSOs, first considering the total integrated intensity ratios and then focusing on just the cavity shock component.

The observations of the different water transitions have different beam sizes which must be corrected by the corresponding beam-size ratio, θ_1/θ_2. However, the correction depends on the size and shape of the emitting region within the protostellar system covered by each beam. If the emission comes from a point source, the correction factor is $(\theta_1/\theta_2)^2$; if the emitting area is conical, meaning that it fills the beam in one axis and is point-like in the other, then the correction applied should be (θ_1/θ_2); and if the emitting region covers both axes the factor used is 1 (Tafalla et al. 2010). For the considered water lines, the maximum scaling correction would be 2.1, corresponding to a point-source scaling of the 2_{11}-2_{02} (752 GHz) and 3_{12}-3_{03} (1097 GHz) beams.

The emission from the excited water transitions for the low-mass protostars mostly comes from the outflow cavity, which extend beyond a single *Herschel* beam (see Nisini et al. 2010; Santangelo et al. 2012, 2014; Mottram et al. 2014). In this case, the emitting area could be taken as conical or even assumed to fill both beams. So, either the beam correction factor is (θ_1/θ_2) or 1 (or something in between for other, more complex geometries). For the intermediate- and high-mass YSOs it is more complicated to define the area covered by the beams as the larger distances mean that the outflows are often unresolved in the *Herschel* beam. For this reason, we consider the three scenarios introduced in the previous paragraph and the entire range of intensity ratios (applying the three possible beam correction factors) are evaluated together with the results obtained from their low-mass counterparts. The θ_1/θ_2 value for each pair of water lines are indicated in Table 4.5.

The ratios of the total integrated intensity of H_2O 2_{11}-2_{02} / 2_{02}-1_{11}; 3_{12}-3_{03} / 2_{02}-1_{11}; and 3_{12}-3_{03} / 2_{11}-2_{02} are shown as a function of bolometric luminosity in the top-, middle- and bottom-left panels of Fig. 4.4, respectively. The value of these ratios without applying the beam corrections are indicated by filled dots. The dashed lighter line connected to each dot represents the value of the ratio after applying the larger beam size correction assumed for each sub-sample of objects: θ_1/θ_2 linear correction for the low-mass protostars and $(\theta_1/\theta_2)^2$ for the intermediate- and high-mass YSOs. Therefore, the lighter vertical lines illustrate the range of values that the integrated intensity ratio could take for each source depending on the shape of the emission region.

Figure 4.4 also shows the analytical ratios of the integrated intensity derived for two extreme scenarios: when both water lines are optically thin (purple dotted-dashed line) and when they are optically thick (orange dashed line). In both cases local thermodynamical equilibrium (LTE), an excitation temperature, T_{exc}, of 300 K and the same beam size for the compared transitions are assumed. The specific numbers corresponding to each regime for each pair of water lines are

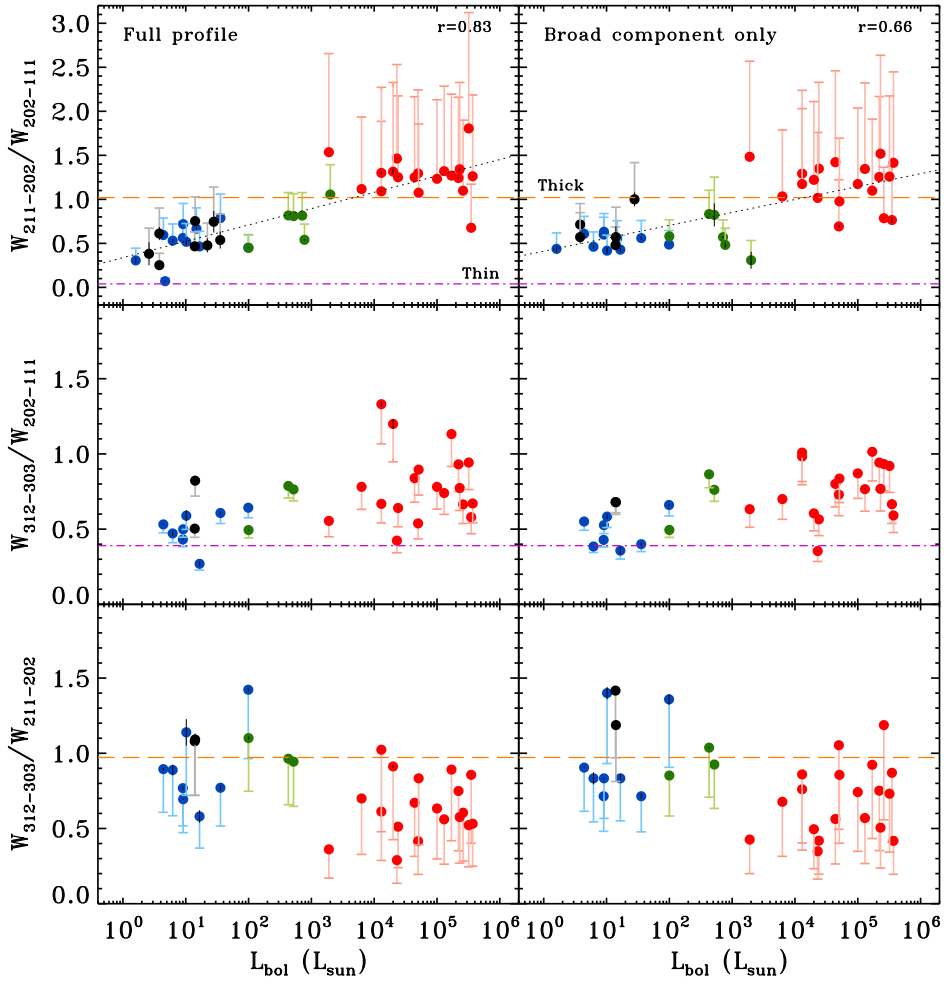

Figure 4.4: (*Top panels*) Ratio of the integrated intensities of the 2_{11}-2_{02} (752 GHz) and 2_{02}-1_{11} (988 GHz) water lines versus the bolometric luminosity of the source. (*Middle panels*) Ratio of the integrated intensities of the H_2O 3_{12}-3_{03} (1097 GHz) and 2_{02}-1_{11} (988 GHz) spectra versus L_{bol}. (*Bottom panels*) Ratio of the integrated intensities of the 3_{12}-3_{03} (1097 GHz) and 2_{11}-2_{02} (752 GHz) water emission lines as a function of L_{bol}. The *left*-column presents the ratios calculated considering the entire line profile and the *right*-column shows the ratio of the integrated intensity calculated for the broad velocity component. The value of the ratios with and without correcting by the different beam size factors are indicated by dashed lighter lines and darker dot symbols respectively. Blue lines and symbols correspond to the low-mass Class 0 protostars, black to the low-mass Class I, green to intermediate-mass objects and red lines and symbols to high-mass YSOs. The purple dashed-dotted horizontal lines and the orange dashed horizontal lines indicate the optically thin and optically thick limits, respectively, calculated assuming LTE and an excitation temperature of 300 K. The linear correlation between the dot symbols (ratios not beam corrected) and the logarithm of the luminosity is shown by the dotted black lines in the *top* panels.

presented in Table 4.5. We take $T_{exc}\approx$300 K because this is the temperature found for the cavity shock component by (Mottram et al. 2014). Also, Karska et al. (2013, and references cited) observe with *Herschel* PACS a warm component for CO with an excitation temperature around 300 K and water is found to be spatially associated with this component in the outflow cavity (Santangelo et al. 2013). Note that for high densities, the excitation temperature approaches the kinetic temperature.

Table 4.5: Averaged values of H_2O line intensity ratios for the shocked gas along the outflow cavity (broad component), beam size ratios of those transitions and the ratios of the optically thin and thick solutions at T_{ex}=300 K.

Transitions	Observed ratio			θ_1/θ_2	Thin[a]	Thick[a]
	LM	IM	HM		(LTE)	(LTE)
H_2O 2_{11}-2_{02}/2_{02}-1_{11}	0.57 ± 0.14	0.60 ± 0.18	1.2 ± 0.2	1.31	0.04	1.02
H_2O 3_{12}-3_{03}/2_{02}-1_{11}	0.52 ± 0.12	0.71 ± 0.16	0.8 ± 0.2	0.90	0.39	2.97
H_2O 3_{12}-3_{03}/2_{11}-2_{02}	1.0 ± 0.3	0.94 ± 0.08	0.7 ± 0.2	0.68	3.16	0.97

Notes. LM: low-mass protostars; IM: intermediate-mass YSOs; HM: high-mass objects. The ratios are not corrected for different beam sizes.
[(a)] Line intensity ratio calculated for an excitation condition of 300 K and assuming LTE.

The ratio of the 2_{11}-2_{02} (752 GHz) and 2_{02}-1_{11} (988 GHz) transitions (top-left panel of Fig. 4.4) shows a significant increase with L_{bol}. The trend of the non-beam-corrected ratios (dots) is indicated by the dotted black line and confirmed by a Pearson correlation coefficient, r, equal to 0.83. This increase with luminosity is also seen when the maximum beam correction factor for each subgroup of YSOs (delineated by the dash) is applied ($r = 0.85$). Therefore, the result is consistent across the luminosity range and regardless of emitting region shape. Furthermore, the intensity ratio of these H_2O transitions is above 1 only for those sources with $L_{bol} > 10^3$ $L_\odot$.

The 3_{12}-3_{03} (1097 GHz) to 2_{02}-1_{11} (988 GHz) intensity ratio also seems to increase slightly with luminosity (middle-left panel Fig. 4.4). However, no trend can be claimed on a statistical basis because the significance of the Pearson correlation coefficient is less than 2.5σ (r<0.5 and $N = 32$). These ratios lie below 1 for all sources, independent of whether the beam correction factor has been applied (which is small for this combination of lines). The intensity ratio of the 3_{12}-3_{03} (1097 GHz) to 2_{11}-2_{02} (752 GHz) (bottom-left panel) is generally smaller than 1 for the three sub-sample of YSOs and it seems to decrease with L_{bol}. Once again, a trend cannot be claimed because the significance of this correlation is less than 2.3σ (r<-0.5 and $N = 31$).

Comparison of the left and right panels of Fig. 4.4 show that similar results are obtained if the integrated intensity ratio corresponding to only the broad component is used for the same pair of water transitions as a function of L_{bol}. A trend with luminosity is also only observed for the 2_{11}-2_{02} / 2_{02}-1_{11} intensity ratio (with a smaller correlation coefficient $r = 0.66$). The increase of the 2_{11}-2_{02} / 2_{02}-1_{11} ratio with L_{bol} suggests that the emission from the shocked gas along the outflow cavity becomes more excited, i.e., warmer and/or denser, for more massive objects. The 3_{12}-3_{03} / 2_{02}-1_{11} ratio seems to increase with L_{bol} while the 3_{12}-3_{03} / 2_{11}-2_{02} ratio decreases with luminosity, both of them tendencies not statistically significant.

The mean and standard deviation of the intensity ratios for the broad component are presented in Table 4.5, together with the beam size ratios and the estimated intensity ratios for the optically thin and thick solutions calculated assuming LTE and $T_{exc} = 300$ K. These calculated values ratify the results and tends from low- to high-mass described in the previous paragraph.

We can rule out the optically thin LTE solution for all sources and lines, with the values for the 3_{12}-3_{03} / 2_{02}-1_{11} ratio excluding the optically thick LTE solution for both lines as well. In order to further constrain the excitation conditions, the non-LTE radiative transfer code RADEX will be used in Sect. 4.3.6.

4.3.5. Intensity ratios versus velocity for H_2O and ^{12}CO

Here we investigate whether the excitation conditions change with velocity. Figure 4.5 shows the calculated line ratios of the H_2O 2_{11}-2_{02} (752 GHz; top-panel) and 3_{12}-3_{03} (1097 GHz; bottom-panel) transitions over the 2_{02}-1_{11} (988 GHz) line as a function of velocity with respect to the source velocity. The grey shaded areas correspond to the averaged line ratio and standard deviation of the low-mass Class 0 protostars presented in Mottram et al. (2014). The green and red lines are

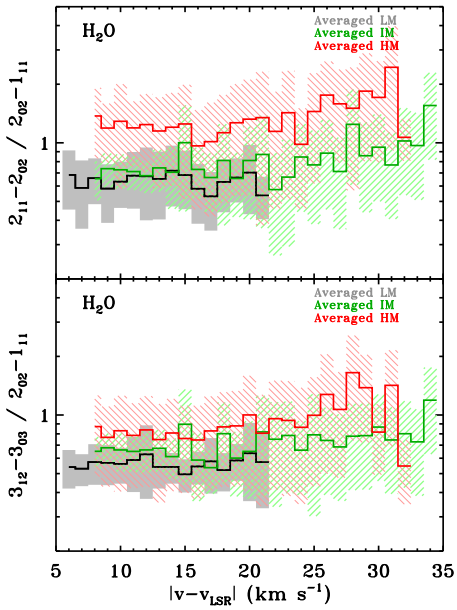

Figure 4.5: Averaged H_2O 2_{11}-2_{02} / 2_{02}-1_{11} ratio (*top* panel) and H_2O 3_{12}-3_{03}/2_{02}-1_{11}line intensity ratio (*bottom* panel) as a function of offset velocity for the low-mass protostars (LM; grey area from Mottram et al. 2014), intermediate-mass objects (IM; green line and asterisks), and the high-mass YSOs (HM; red line and crosses). The dashed green and red regions indicate the calculated standard deviation of the line ratio for each velocity channel.

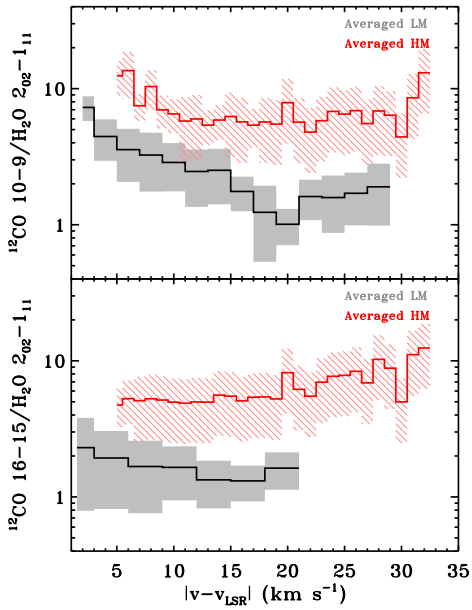

Figure 4.6: Same as Fig. 4.5 but for the ^{12}CO 10–9 (*top* panel) and 16–15 (*bottom* panel) transitions.

associated with the intensity ratios of the intermediate- and high-mass YSOs respectively.

To obtain these ratios, the spectra of each set of water transitions for a given source are resampled to 1 km s^{-1} bins. Then, the studied line (either the 752 or 1097 GHz transition) is divided by the spectrum of the 988 GHz line within the range of velocities over which the intensities of both lines are above 3σ of the re-binned data. Finally, the red and blue wings are averaged together and the obtained intensity ratio as a function of velocity is averaged over all sources that compose each sub-sample of YSOs. Only velocity ranges well offset from the quiescent envelope emission are plotted, typically $|v - v_{\rm lsr}| > 3$-5 km s^{-1}.

As found for the low-mass Class 0 protostars, the line intensity ratios seem to be constant as a function of velocity for both intermediate- and high-mass YSOs. This result confirms the fact that the shape of the three water line profiles is similar for a given source and just scales in intensity (Fig. 4.1, right). For the high-mass objects, the ratio increases slightly for offset velocities >25 km s^{-1}. However, the significance of the increase in the ratio is of the order of the uncertainty of those channels. The 2_{11}-2_{02} / 2_{02}-1_{11} ratio is above 1 for this sub-sample of objects at all velocities, which is consistent with the result obtained in the previous sub-section for this set of water lines. A constant line ratio as a function of velocity rules out the optically thick LTE solution for all lines as this would require high column densities even at high velocities, and thus a flatter line profile than observed, or high opacity across the entire profile.

A different outcome is obtained if the CO line intensity is compared to that of water as a function of velocity. Figure 4.6 shows the ^{12}CO J = 10–9 and J=16–15 over the H_2O 2_{02}-1_{11}

(988 GHz) line ratio as a function of velocity offset (top and bottom panel respectively). In this case, we observe two different behaviours for the two sub-samples of YSOs. For the low-mass Class 0 protostars the ^{12}CO J = 10–9 / H_2O 2_{02}-1_{11} line ratio decreases with velocity, while the ^{12}CO J=16–15 / H_2O 2_{02}-1_{11} ratio is invariant with velocity.

On the other hand, for the high-mass YSOs the line ratio of both CO transitions with H_2O 2_{02}-1_{11} is constant with velocity. This agrees with the ratio of the $FWZI$ and $FWHM_b$ for these two molecules being close to unity (see red crosses in Figs. 4.2 and 4.14). Therefore, in massive objects the emission of these CO and water transitions may originate in regions of the outflow cavity wall not too distant from each other and characterised by similar excitation and dynamical conditions. For the low-mass Class 0 sources, the ^{12}CO 16–15 line seems to trace the same material as H_2O but the 10–9 transition does not (Kristensen et al. in prep.).

4.3.6. Excitation conditions

In order to characterise the excitation conditions responsible for the broad cavity shock water emission, we compared the line fluxes presented above, together with the fluxes for the $1_{11}-0_{00}$ transition from M^{c}Coey et al. in prep. and van der Tak et al. (2013), for the intermediate and high-mass YSOs to a grid of non-LTE RADEX (van der Tak et al. 2007). We use the assumption of a 1-D slab geometry and the same modifications and parameters as used by Mottram et al. (2014) for the low-mass cavity shock components.

We find a good fit with post-shock volume densities n_{H_2}=10^5–4×10^6 cm^{-3} and water column densities N_{H_2O}=10^{17}–10^{18} cm^{-2} for 5/7 of the intermediate-mass sources. The results for NGC7129 are shown as an example in the top panels of Fig. 4.7. These results are similar to lower-density solution obtained for the low-mass sources by Mottram et al. (2014) but with slightly larger emitting regions sizes, equivalent to radii of 300–500 AU if circular. All studied water transitions are optically thick but effectively thin in these conditions. In one of the remaining two intermediate-mass sources (L1641 S3MMS1) we cannot constrain the fit very well, while for the other source (NGC2071) a good fit cannot be found within the grid (χ^2_{best} > 100), with the emission in the $2_{11}-2_{02}$ line underproduced and emission in the $1_{11}-0_{00}$ line overproduced by the models. For the high-mass YSOs, good fits can only be found for 6 of the 19 sources, with the best fits again giving similar densities and column densities and emitting regions ranging from 800 to 6000 AU. However, even in these cases the best-fit models consistently underproduce the $2_{11}-2_{02}$ transition.

In order to explore what is required to find a good solution for the high-mass sources, we first ran additional grids of models for the poorly fit source G10.47+0.03 where the kinetic temperature was increased from the default of 300 K, but no better solutions were found even at 1500 K. The fact that the same temperature leads to reasonable results for the cavity shock component across the luminosity range is consistent with the results of Karska et al. (2014a), who find similar rotational temperatures for warm CO emission observed with PACS for both low- and high-mass sources.

As an alternative, we also explored pumping by an infrared radiation field with the same shape as the source SED from van der Tak et al. (2013), scaled assuming that the source of infrared radiation is at certain distance away from the water emitting region. Such an approach was found by Mottram et al. (2014) to be inconsistent with the observations of low-mass protostars, but González-Alfonso et al. (2014) find that this is needed to reproduce H_2O observations towards some galaxies. For the high-mass YSO G10.47+0.03, we find that pumping by infrared photons can indeed provide a better fit to the data (see middle and lower panels of Fig. 4.7). This result is consistent with previous works based on observations of vibrational excited molecules such as HC_3N and HCN (Wyrowski et al. 1999; Rolffs et al. 2011). We explored a range of distances between the source of the infrared radiation and the H_2O emitting region, from 10 to 1000 AU, and find the best fit for a distance of ~100 AU. The best fit for this strong radiation field has both high densities (~10^9–10^{11} cm^{-3}) and column densities (~10^{18} cm^{-2}) for emitting regions with sizes of order 500 AU. The implications and reasonableness of these results will be discussed further in Sect. 4.4.2.

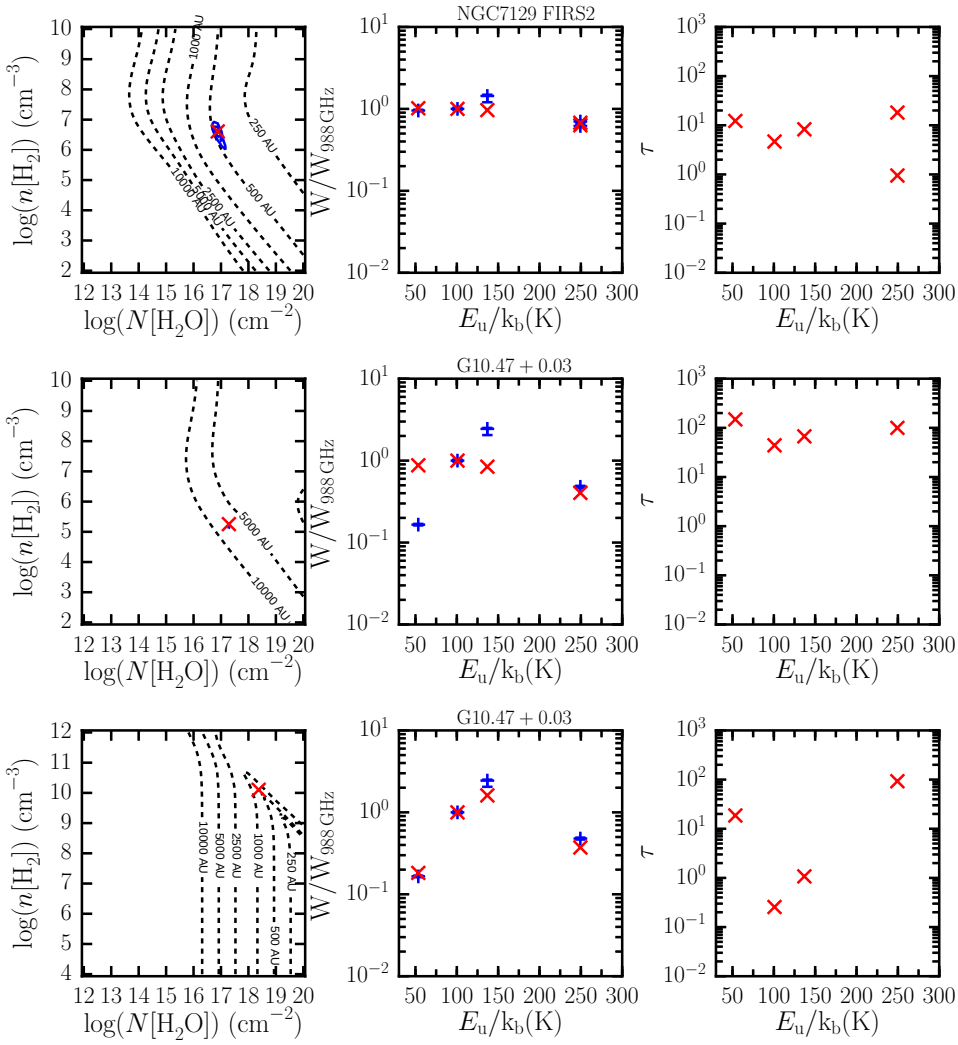

Figure 4.7: RADEX results for the average line ratios for the cavity shock components assuming a kinetic temperature of $T = 300$ K. The *top* panels corresponds to the intermediate-mass object NGC7129 FIRS2 in which no radiation field has been included. The *middle* and *bottom* panels show the results for the high-mass YSOs G10.47+0.03 without and with radiation field respectively. For each row, the *left*-hand panels show the best-fit (red cross), the 1, 3 and 5σ confidence limits (blue contours) for a grid in $n_{\mathrm{H_2}}$ and $N_{\mathrm{H_2O}}$ and the side of the emitting region (black dashed lines). The *middle* panels show a spectral line energy distribution comparing the observed and best-fit model with blue plus and red cross symbols, respectively. Finally, the *right*-hand panels present the optical depth, τ, of the best-fit model for each H_2O line.

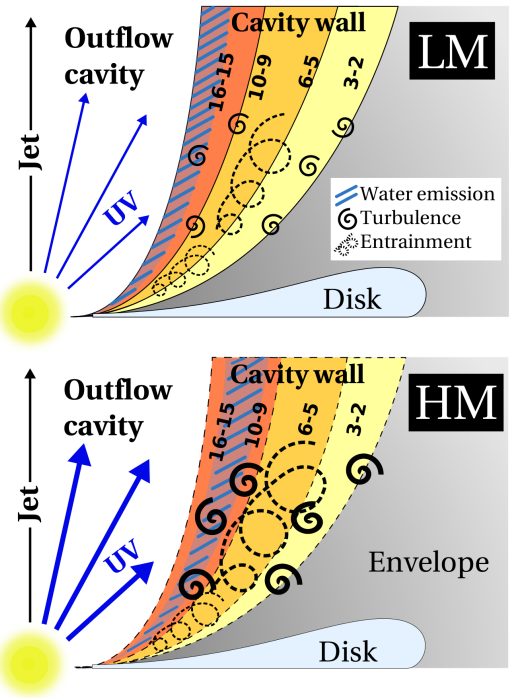

Figure 4.8: Cartoon illustrating a scenario with a simplified physical structure of the different layers composing the outflow cavity wall for a representative low-mass protostar (LM; *top* panel) and for a high-mass YSO (HM; *bottom* panel). The emitting area of the low-J ^{12}CO transitions is shaded in yellow, that of the mid-J transitions is orange and of the high-J lines in red. Turbulent motions are represented with spiral symbols, the entrained material with swirls and the excited water emission is indicated with blue lines over the red region.

4.4. Discussion

4.4.1. Disentangling the dynamical properties of H_2O and CO emission

The data presented in Sect. 4.3 suggest that H_2O appears in a different physical component from some of the CO lines. It is now well established that the broad component seen in low- (J<5) and mid-J (5≤J<10) ^{12}CO lines probes the colder entrained outflow gas, whereas only the high-J (J>10 or higher) ^{12}CO transitions trace the currently shocked gas also seen in water (van Kempen et al. 2009a, 2010; Nisini et al. 2010; Santangelo et al. 2012; Tafalla et al. 2013; Goicoechea et al. 2012; Yıldız et al. 2013; San José-García et al. 2013). The cartoon presented in Fig. 4.8 illustrates a simplified version of a possible framework for the origin of ^{12}CO (yellow, orange and red areas) and water (blue lines and opaque region) within the outflow cavity wall for a low- (LM) and high-mass (HM) YSO. Turbulent motions, likely driven by the outflow (San José-García et al. 2013, San José-García et al. subm.) are represented with spiral symbols and the entrainment with swirls.

The yellow areas are related to colder layers of the outflow cavity wall directly attached to the envelope where the broad velocity component of low-J ^{12}CO transitions originates. The orange regions are associated with warmer entrained outflowing material within the outflow cavity wall and the red areas indicate material that is currently mixing and undergoing shocks along the outflow cavity. Finally, the velocity of the layers forming the outflow cavity wall and the temperature of the gas decrease with distance from the cavity and the central source (Raga & Cantó 1997). The shocked gas along the layers closest to the outflow cavity should have larger average velocities than that originating near the envelope.

In this context, Fig. 4.2 (and Fig. 4.14) shows that the values of $FWZI$ for the H_2O and high-J ^{12}CO observations behave differently with L_{bol}. For the low-mass protostars, the gas probed by H_2O along the outflow cavity is characterised by larger velocities than the warm entrained outflowing material traced by ^{12}CO J = 10–9. In addition, the decrease of the ^{12}CO J = 10–9 and H_2O 2_{02}-1_{11} ratio as a function of velocity (Fig. 4.6) suggests that these two transitions are kinematically distinct, and originate in different layers of the outflow cavity wall. On the other

hand, the ratio of the CO 16–15 / 2_{02}-1_{11} line intensity is constant with velocity, so water and ^{12}CO 16–15 emission go together along the outflow cavity wall.

For the high-mass YSOs, the velocity of the gas traced by H_2O and high-J ^{12}CO transitions are similar, as shown by the bottom panel of Fig. 4.2, and the line intensity ratio of these two species is constant as a function of velocity for both the ^{12}CO $J = 10$–9 and 16–15 transitions. This implies that already the emission of the ^{12}CO $J = 10$–9 comes from a region with similar dynamical properties to those of water, contrary to what it was measured for their low-mass counterparts. In the following we will discuss two scenarios to explain these results.

The first scenario is based on the fact that high-mass objects have larger UV fields than those measured for their low-mass counterparts (Stäuber et al. 2007). The strong UV radiation would principally destroy water molecules in the warmer layers of the outflow cavity wall closer to the cavity because colder entrained material will be shielded. Therefore, water may be effectively photo-dissociated (and photo-desorbed) deeper into the outflow cavity wall for high-mass objects than for low-mass protostars. CO molecules are not as easily photo-dissociated as H_2O, but still the destruction of CO will be more efficient in the layers nearest to the outflow cavity. This means that the emission from the faster shocked gas which causes broader H_2O line profiles is destroyed for higher mass sources and that emission originating in regions closer to the entrained layer, moving at slower velocities, may survive.

Due to the weaker UV fields, the photo-dissociation of water molecules along layers closer to the outflow cavity is less efficient for low-mass protostars. Therefore, a larger percentage of fast shocked gas emission along the regions closest to the cavity may survive, emission which contributes to the broadening of the line-wings (quantitative models in Visser et al. 2012).

An alternative scenario is based on the fact that the protostellar environments of high-mass YSOs are more turbulent than those of their low-mass counterparts (see Herpin et al. 2012, San José-García et al. 2013, San José-García et al. subm. and bottom panel of Fig. 4.8). Outflow systems inject turbulent motions into the structure forming the outflow cavity wall and these motions could propagate to other physical components of the protostellar system such as the entrained outflowing material. In this case, the material from both components may have a high level of mixing and the separation between the entrained and shocked material within the outflow cavity wall would not be as clearly delineated as for the low-mass protostars. Since the turbulent motions in low-mass protostars are weaker, the different layers constituting the cavity wall are better defined. Thus, the kinematical properties of each J transition are better differentiated and the emission of CO $J = 10$–9 material is separated from that originating in shocked water gas along the cavity. Therefore, the dynamical properties of these two structures would be more closely linked for the high-mass YSOs than for their less massive counterparts, being harder to disentangle. This could explain why the calculated ratio of the $FWZI$ or $FWHM_{\rm b}$ for the ^{12}CO $J = 10$–9 and H_2O profiles is around 1 for the high-mass sub-sample but is lower than 1 for their less massive counterparts.

Finally, we can rule out that high-mass YSOs are analogous to low-mass Class I protostars, for which the line profiles are narrower due to decreased wind velocities (c.f. Kristensen et al. 2012; Mottram et al. 2014). The high-mass sources considered here are closer to the low-mass Class 0 objects in terms of evolutionary stage: the ratios of the envelope mass to gravitational stellar mass, $M_{\rm env}/M_{\rm g}$, for the high-mass YSOs are >20 (San José-García et al. subm.). Massive YSOs are therefore still deeply embedded and follow the relation with luminosity of the Class 0 rather than to the Class I low-mass sources.

4.4.2. Excitation condition across the luminosity range

As discussed in Sect. 4.3.6, the excitation conditions of water in low- and intermediate-mass sources seem to be similar, while for high-mass YSOs it is difficult to reproduce the observed line ratios, particularly those involving the $2_{11}-2_{02}$ line (752 GHz). One solution, as discussed in that section, may be that the lines are pumped by infrared radiation in high-mass sources, a process probably not present in low- and intermediate-mass objects due to lower intensity and higher dust extinction within the outflow cavity. However, the best-fit excitation conditions obtained for the high-mass source G10.47+0.03 with the inclusion of a radiation field require very high densities,

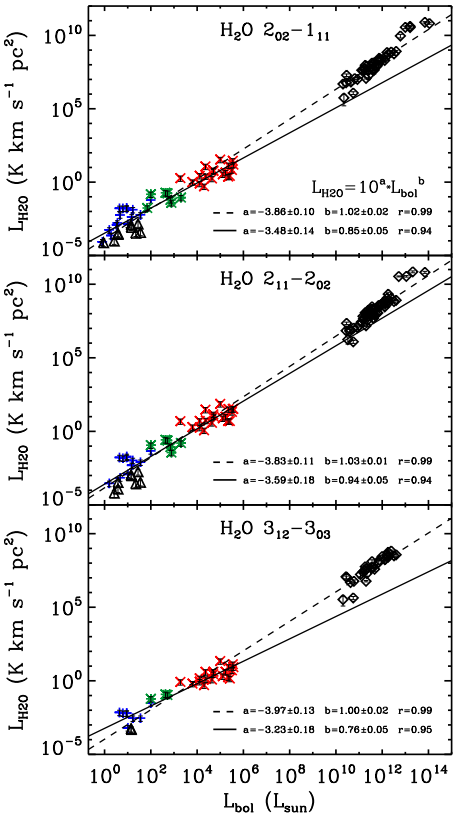

Figure 4.9: Same as Fig.4.3 but including the line luminosity observed for several extragalactic sources (black diamonds) taken from Yang et al. (2013). The solid black line corresponds to the fit of the WISH YSOs and the dashed black line indicates the correlation including the values of extragalactic sources.

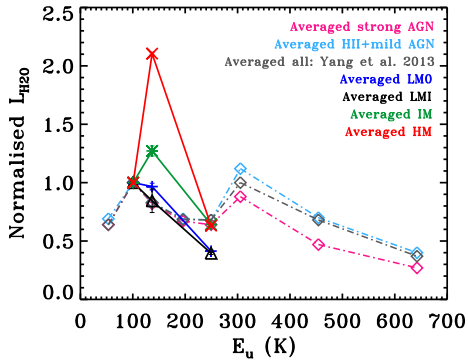

Figure 4.10: Line luminosity of the water transitions normalised to the luminosity of the H_2O 2_{02}-1_{11} (988 GHz) line as a function of the upper energy level (E_u) of each transition. The solid blue, black, green and red lines corresponds to the averaged value of the normalised intensity for the low-mass Class 0, Class I, intermediate-mass and high-mass YSOs respectively. The grey dashed line represents the average values of the sample presented in Yang et al. (2013), the pink and light blue dashed lines indicate the values of the strong AGN- and HII+mild-AGN- dominated galaxies, respectively. The 2_{11}-2_{02} (752 GHz) line has an E_u/k_B = 137 K and the 3_{12}-3_{03} (1097 GHz) an E_u/k_B = 249 K.

enough that water emission should be in LTE, over considerable regions. Note that from the grid without radiative pumping we can rule out that high densities alone can reproduce the observed water line ratios. The regions around these high-mass YSOs undoubtably have a complex geometry and in several cases, including G10.47+0.03, are known to harbour multiple sources within the *Herschel* beam. Therefore, the assumption of a slab geometry, while instructive, may not accurately constrain the range of excitation conditions present. In addition, we have only performed a limited test using a scaled version of the SED as the radiation field, while the "true" radiation field irradiating the water emitting gas in these regions may include shorter-wavelength photons. Furthermore, we assume all the gas is irradiated by the same radiation field, when the geometry of the water emitting region could lead to variation in the field experienced by different parts of the gas.

With all these caveats, we therefore can conclude two things. Firstly, the excitation of water in most high-mass sources is different to low- and intermediate-mass objects. Secondly, while radiative pumping can be ruled out in low-mass protostars, it is a plausible explanation for high-mass sources. Higher kinetic temperatures do not lead to strong enough emission in the 2_{11}-2_{02} transition, in agreement with the similarity of CO rotational temperatures obtained from PACS observations for both low- and high-mass YSOs.

4.4.3. From Galactic to extragalactic sources

San José-García et al. (2013) found that the correlation between the logarithms of the ^{12}CO $J = 10$–9 line luminosity and $L_{\rm bol}$ for the WISH sample held when they extended their analysis to include a sample of extragalactic sources. Similarly, we investigate if the significant correlation measured between the logarithm of the water luminosities, $L_{\rm H_2O}$, and $L_{\rm bol}$ continues in the regime of extragalactic sources.

Figure 4.9 shows the values of $L_{\rm H_2O}$ for a series of AGN and other extragalactic objects presented in Yang et al. (2013). A correlation between the logarithm of these parameters, which extends over more than 12 orders of magnitude in both axis, is measured for the three transitions. The value of the slope is the same for each H_2O line and is equal to 1, which in the case of the 3_{12}-3_{03} transition is slightly larger than the slope obtained considering only the WISH sample. Therefore, if the extragalactic sources are added, the proportionality between the logarithms of the line luminosity and $L_{\rm bol}$ is emphasised for all water lines and the slope becomes unity within the uncertainties, as for the ^{12}CO $J = 10$–9 analysis of San José-García et al. (2013). As previously discussed in Sect 4.3 of that paper, this result suggests that high-J CO can be used as a tracer of dense gas, similar to HCN (Gao & Solomon 2004a,b). From Fig. 4.9 we can conclude that the excited water transitions are also probing dense gas.

The line intensity ratios of these parameters are calculated for the three water lines with respect to the 2_{02}-1_{11} transition (see Fig. 4.10). The results are presented in the context of the extragalactic framework by comparing the excitation conditions of low-, intermediate- and high-mass YSOs to those investigated in the extragalactic sources discussed in Yang et al. (2013).

Surprisingly, the 752 GHz / 988 GHz line intensity ratio only lies above 1 for the high-mass YSOs. This peculiar result, already highlighted within our studied sample of YSOs, also stands out when the line ratios are compared with those measured for extragalactic sources. However, as discussed in Sect. 4.4.2, the modelling used in this paper is quite simple and is only for lines with $E_{\rm u} \lesssim 250$ K. Better characterisation of the excitation conditions of more H_2O lines than modelled here is therefore required to conclusively interpret this result.

The fact that the slope of the correlation between $L_{\rm H_2O}$ and $L_{\rm bol}$ (Fig. 4.9) gets closer unity after including the extragalactic sources and that the dashed line intercepts the high-mass YSOs (while dropping below their low-mass counterparts) might suggest a plausible scenario in which the extragalactic H_2O emission comes from ensemble of high-mass sources. However, a more fundamental question is whether the extragalactic emission comes from star formation, PDRs, AGN or some combination thereof. Once there is better understanding of where extragalactic water emission originates, further progress can be made on comparing to our galactic observations such as those presented in this paper.

4.5. Conclusions

From the analysis of excited H_2O and high-J ^{12}CO observations across the entire WISH sample of YSOs we derive the following conclusions:

- The shape of the H_2O 2_{02}-1_{11}, 2_{11}-2_{02} and 3_{12}-3_{03} line profiles for a given source are similar but scaled in intensity. In addition, their averaged line intensity ratios are constant with increasing offset from the source velocity. These results suggest that the dynamical properties probed by the three water transitions are similar for a given source.

- $FWZI$ and $FWHM_b$ change little between low- and high-mass YSOs for the H_2O spectra, while the $FWZI$s of the ^{12}CO $J = 10$–9 and 3–2 transitions increase slightly with L_{bol}. For both molecules, there is significant scatter in the values of $FWZI$ and $FWHM_b$ over the studied luminosity interval, particularly in the case of water ($FWZI$ ranges from 15 to 189 km s^{-1}).

- This scatter, related to the intrinsic properties of the sources, is reduced when the ratio of the ^{12}CO and H_2O $FWZI$ (or $FWHM_b$) is considered. The averaged ratio of their $FWZI$ increases with L_{bol} ranging from 0.5 for the low-mass protostars to 1.9 for their massive counterparts. This suggests that for low-mass protostars the entrained material traced by the wings of the ^{12}CO $J = 10$–9 (and lower-J lines) is kinematically different to that traced by water in the cavity shocked gas (Kristensen et al. in prep.). In the case of the high-mass YSOs, the CO $J = 10$–9 emission is already coupled to that of water, so both may come from the same layer of the outflow cavity wall (Fig. 4.8).

- The line intensity ratio of ^{12}CO $J = 10$–9 to water decreases with increasing velocity for low-mass YSOs but is approximately constant for high-mass YSOs. However, the line intensity ratio of ^{12}CO $J = 16$–15 and H_2O remains constant for both low- and high-mass YSOs as a function of velocity. This suggests that higher-J ^{12}CO transitions (J>10) trace deeper warmer layers of the outflow cavity characterised by dynamical properties likely linked to those of the shocked water emission, independently of the mass of the object.

- Two scenarios are proposed to explain the previous result. The first scenario assumes that the increased UV radiation in high-mass YSOs leads to water being more effectively photodissociated in those layers of the cavity wall closer to the outflow cavity than for the low-mass protostars. An alternative scenario is also discussed, where the higher turbulence in high-mass star-forming regions, injected by the outflows, propagate into layers of the outflow cavity wall further from the outflow cavity and cause a larger mixing of the material forming those layers than in low-mass protostars. Therefore, the high level of turbulence helps the interaction of warm entrained and cavity shocked material.

- On averaged, more than 60% of the total integrated H_2O line intensity comes from the cavity shock component for all YSOs. The calculated contribution fractions can be used to interpret and compare velocity resolved and unresolved observations of water.

- The excitation of water for the high-mass YSOs is somewhat different from that of their low- and intermediate-mass counterparts and potentially requires pumping from an infrared radiation field.

- As for CO, the logarithm of the line luminosity for the three water lines strongly correlates with the logarithm of the bolometric luminosity and envelope mass of the object. The slope of the correlation is unity within the uncertainty, which suggests that the size of the water and CO emitting regions scale with luminosity so that the beam filling factor remains the same. This relation also holds when the emission from only the broad cavity shock component is compared.

- The correlation between the total H_2O line luminosity can be extended to extragalactic sources. In addition, the values of the line intensity ratios of the extragalactic objects are similar to those calculated for the low-mass protostars, but these ratios differ from those measured for the intermediate- and high-mass YSOs.

Overall, despite some differences in excitation, the properties of excited water line emission are similar between low- and high-mass YSOs, suggesting that a common physical mechanism is at work in the outflows of sources across a wide range of luminosity. It remains to be seen whether the scaling relations in line luminosity found here are simply the result of a mass-scaling or whether the outflows of all YSOs are driven in the same way. Resolving this question will require high spatial resolution and fidelity imaging of tracers probing both the entrained and currently shocked outflow material, something ALMA will enable us to do in the coming years for the first time.

Acknowledgments

The authors are grateful to Sylvie Cabrit for the useful feedbacks that helped to improve the manuscript and to Mihkel Kama for providing data and suggestions to the paper. We would like to thank Umut Yıldız for helping on the data reduction as well as the WISH team for many inspiring discussions. This work is supported by the European Community's Seventh Framework Programme FP7/2007-2013 under grant agreement 238258 (LASSIE) and by the Space Research Organisation Netherlands (SRON). Astrochemistry in Leiden is supported by the Netherlands Research School for Astronomy (NOVA), by a Spinoza grant and grant 614.001.008 from the Netherlands Organisation for Scientific Research (NWO). HIFI has been designed and built by a consortium of institutes and university departments from across Europe, Canada and the United States under the leadership of SRON Netherlands Institute for Space Research, Groningen, The Netherlands and with major contributions from Germany, France and the US. Consortium members are: Canada: CSA, U.Waterloo; France: CESR, LAB, LERMA, IRAM; Germany: KOSMA, MPIfR, MPS; Ireland, NUI Maynooth; Italy: ASI, IFSI-INAF, Osservatorio Astrofisico di Arcetri- INAF; Netherlands: SRON, TUD; Poland: CAMK, CBK; Spain: Observatorio Astronómico Nacional (IGN), Centro de Astrobiología (CSIC-INTA). Sweden: Chalmers University of Technology - MC2, RSS & GARD; Onsala Space Observatory; Swedish National Space Board, Stockholm University - Stockholm Observatory; Switzerland: ETH Zurich, FHNW; USA: Caltech, JPL, NHSC.

4.A. Spectra of the excited water lines

The H_2O 2_{02}-1_{11}, 2_{11}-2_{02} and 3_{12}-3_{03} spectra for the intermediate- and high-mass YSOs and the observation number identification are presented in this section (see Figs. 4.11 to 4.13 and Table 4.6). The basic properties derived from these data, such as the rms of the spectra, $T_{\rm MB}^{\rm peak}$, integrated intensity and *FWZI* are summarised from Table 4.7 to 4.9. In addition, the results from the Gaussian decomposition explained in Sect. 4.2.5 are shown in Tables 4.10 to 4.12.

Table 4.6: Observation identification numbers for the H_2O 2_{02}-1_{11}, 2_{11}-2_{02} and 3_{12}-3_{03} lines of the intermediate- and high-mass YSOs.

Source	2_{02}-1_{11}	2_{11}-2_{02}	3_{12}-3_{03}
Intermediate-mass			
NGC7129 FIRS2	1342191613	1342191747	1342227393
L1641 S3MMS1	1342203147	1342203220	–
NGC2071	1342204503	1342194682	1342227395
Vela IRS17	1342197951	1342201541	–
Vela IRS19	1342197952	1342201540	–
AFGL490	1342204511	1342217717	–
OMC-2-FIR 4	1342218629	1342194681	1342217719
High-mass			
IRAS05358+3543	1342204510	1342194684	1342206123
IRAS16272-4837	1342203168	1342205845	1342214418
NGC6334-I-1	1342204520	1342205846	1342206386
W43-MM1	1342191616	1342194565	1342194806
DR21-OH	1342195026	1342194574	1342196427
W3-IRS5	1342191612	1342201548	1342201592
IRAS18089-1732	1342215911	1342217712	1342218914
W33A	1342191636	1342191746	1342208090
IRAS18151-1208	1342218211	1342194679	1342218911
AFGL2591	1342195019	1342192335	1342194796
G327-0.6	1342203170	1342205844	1342214424
NGC6334I-N-1	1342204519	1342205847	1342206384
G29.96-0.02	1342191617	1342194563	1342194807
G31.41+0.31	1342191615	1342194566	1342219241
G5.89-0.39	1342218120	1342217707	1342218917
G10.47+0.03	1342215914	1342217711	1342218915
G34.26+0.15	1342194995	1342215950	1342219245
W51N-e1	1342195014	1342194568	1342196433
NGC7538-IRS1	1342201599	1342201546	1342200760

Table 4.7: Observed and fitted properties of the H_2O 2_{02}-1_{11} line for the detected intermediate- and high-mass sources.

Source	rms[a] (mK)	$T_{\rm MB}^{\rm peak}$ (K)	$\int T_{\rm MB}{\rm d}v$[b] (K km s^{-1})	*FWZI* (km s^{-1})
Intermediate-mass				
NGC7129 FIRS2	18	0.58	9.50 ± 0.02	48
L1641 S3MMS1	23	0.30	6.28 ± 0.03	48
NGC2071	38	3.83	76.98 ± 0.04	108
Vela IRS17	22	0.74	9.97 ± 0.02	63
Vela IRS19	21	0.34	6.23 ± 0.02	72
AFGL490	21	0.44	6.94 ± 0.02	75
OMC-2-FIR 4	28	3.15	52.31± 0.04	66
High-mass				
IRAS05358+3543	57	1.93	24.69 ± 0.09	54
IRAS16272-4837	81	1.34	17.34 ± 0.11	39
NGC6334I-N-1	60	2.25	43.55 ± 0.09	57
W43-MM1	54	1.02	25.99 ± 0.06	84
DR21-OH	73	5.86	29.39 ± 0.11	51
W3-IRS5	95	7.07	88.32 ± 0.12	63
IRAS18089-1732	107	1.27	12.01 ± 0.14	27
W33A	47	2.23	24.13 ± 0.05	63
IRAS18151-1208	96	0.82	4.88 ± 0.12	30
AFGL2591	100	3.41	17.21 ± 0.13	24
G327-0.6	91	3.23	33.50 ± 0.14	51
NGC6334-I-1	106	5.32	69.44 ± 0.14	60
G29.96-0.02	67	5.36	62.34 ± 0.07	66
G31.41+0.31	61	1.41	18.74 ± 0.07	60
G5.89-0.39	67	9.60	265.34 ± 0.07	108
G10.47+0.03	104	3.58	34.75 ± 0.12	39
G34.26+0.15	64	6.08	48.49 ± 0.07	60
W51N-e1	64	6.75	102.12 ± 0.07	81
NGC7538-IRS1	91	5.56	37.20 ± 0.12	24

Notes. *FWZI* has been calculated by binning the spectra to 3 km s^{-1}.
[a] In 0.27 km s^{-1} bin. [b] Integrated over the interval of velocities defined by the *FWZI*.

4.B. Specific sources

The low-mass Class 0 protostars indicated in Fig. 4.2 are characterised for showing bullet emission in their water profiles. These already studied sources are: L1448-MM, NGC1333 IRAS2A, BHR 71, Ser SMM1 and L1157. In the case of the low-mass Class I object IRAS12496, a spot shock component significantly offset from the source velocity is identified in the 988 GHz water

Table 4.8: Observed and fitted properties of the H_2O 2_{11}-2_{02} line for the detected intermediate- and high-mass YSOs.

Source	rms[a] (mK)	T_{MB}^{peak} (K)	$\int T_{MB} dv$[b] (K km s^{-1})	*FWZI* (km s^{-1})
Intermediate-mass				
NGC7129 FIRS2	22	0.52	7.76 ± 0.02	48
L1641 S3MMS1	28	0.24	2.69 ± 0.05	22
NGC2071	37	3.78	62.30 ± 0.04	123
Vela IRS17	30	0.82	8.13 ± 0.03	39
Vela IRS19	36	0.41	3.74 ± 0.04	63
AFGL490	100	0.51	22.46 ± 0.03	33
OMC-2-FIR 4	15	1.87	29.92 ± 0.05	69
High-mass				
IRAS05358+3543	44	2.01	27.57 ± 0.05	100
IRAS16272-4837	81	2.37	21.70 ± 0.08	60
NGC6334I-N-1	92	4.38	117.17 ± 0.17	90
W43-MM1	48	2.77	45.14 ± 0.05	108
DR21-OH	68	7.48	104.18 ± 0.07	90
W3-IRS5	68	9.09	112.14 ± 0.07	105
IRAS18089-1732	68	1.72	15.62 ± 0.07	36
W33A	79	2.76	30.17 ± 0.08	60
IRAS18151-1208	36	0.86	6.41 ± 0.04	40
AFGL2591	37	3.76	21.37 ± 0.04	42
G327-0.6	147	5.19	60.08 ± 0.15	66
NGC6334-I-1	152	9.69	78.44 ± 0.06	117
G29.96-0.02	96	4.05	42.21 ± 0.10	69
G31.41+0.31	74	2.28	23.93 ± 0.08	57
G5.89-0.39	59	10.67	285.22 ± 0.06	144
G10.47+0.03	73	4.47	45.81 ± 0.07	27
G34.26+0.15	225	10.24	93.03 ± 0.10	42
W51N-e1	242	9.46	150.81 ± 0.24	42
NGC7538-IRS1	61	6.97	49.10 ± 0.06	42

Notes. *FWZI* has been calculated by binning the spectra to 3 km s^{-1}.
[a] In 0.27 km s^{-1} bin. [b] Integrated over the interval of velocities defined by the *FWZI*.

Table 4.9: Observed and fitted properties of the H_2O 3_{12}-3_{03} line for the detected intermediate- and high-mass objects.

Source	rms[a] (mK)	T_{MB}^{peak} (K)	$\int T_{MB} dv$[b] (K km s^{-1})	*FWZI* (km s^{-1})
Intermediate-mass				
NGC7129-FIRS2	14	0.46	7.48 ± 0.02	66
L1641 S3MMS1	–	–	–	–
NGC2071	28	2.68	58.82 ± 0.03	117
Vela IRS17	–	–	–	–
Vela IRS19	–	–	–	–
AFGL490	–	–	–	–
OMC-2-FIR 4	30	1.589	25.10 ± 0.11	54
High-mass				
IRAS05358+3543	30	1.20	19.29 ± 0.03	60
IRAS16272-4837	32	0.77	11.11 ± 0.04	42
NGC6334I-N-1	28	1.34	28.34 ± 0.03	90
W43-MM1	24	0.83	13.07 ± 0.03	85
DR21-OH	25	3.66	63.78 ± 0.03	102
W3-IRS5	81	6.78	99.98 ± 0.08	78
IRAS18089-1732	30	1.04	15.99 ± 0.03	66
W33A	19	1.84	20.24 ± 0.02	66
IRAS18151-1208	30	0.47	5.85 ± 0.03	40
AFGL2591	22	2.54	16.02 ± 0.03	57
G327-0.6	39	1.88	24.97 ± 0.04	57
NGC6334-I-1	128	3.73	48.12 ± 0.12	30
G29.96-0.02	34	2.88	36.15 ± 0.04	81
G31.41+0.31	36	1.28	13.79 ± 0.04	45
G5.89-0.39	36	8.38	237.69 ± 0.04	144
G10.47+0.03	32	2.25	24.35 ± 0.04	27
G34.26+0.15	42	5.01	45.95 ± 0.05	48
W51N-e1	63	4.40	82.48 ± 0.07	110
NGC7538-IRS1	37	3.96	27.53 ± 0.04	81

Notes. *FWZI* has been calculated by binning the spectra to 3 km s^{-1}.
[a] In 0.27 km s^{-1} bin. [b] Integrated over the interval of velocities defined by the *FWZI*.

line in emission but in absorption in the other ground-based transitions. More information about these objects and their observations in Mottram et al. (2014).

The excited water spectra of the intermediate-mass YSO NGC2071 show an offset component at around 35 km s^{-1} from the source velocity, which could be considered as a spot shock component, in particular an EHV component. This source is known for being formed by several YSOs, which line profile could be then composed by the emission of several sources and molecular outflows (van Kempen et al. 2012). Therefore, interferometric data is needed disentangle and better understand the emission.

Finally, the line profiles of the high-mass YSO G5.89-0.39 are complex and composed by velocity components with non-Gaussian profiles. As for NGC2071, this region is crowded with several protostars and energetic outflows (Su et al. 2012) with some of the highest velocities measured for these structures (Choi et al. 1993) Therefore, the interpretation of the emission should go together with extra single-dish and interferometric observations.

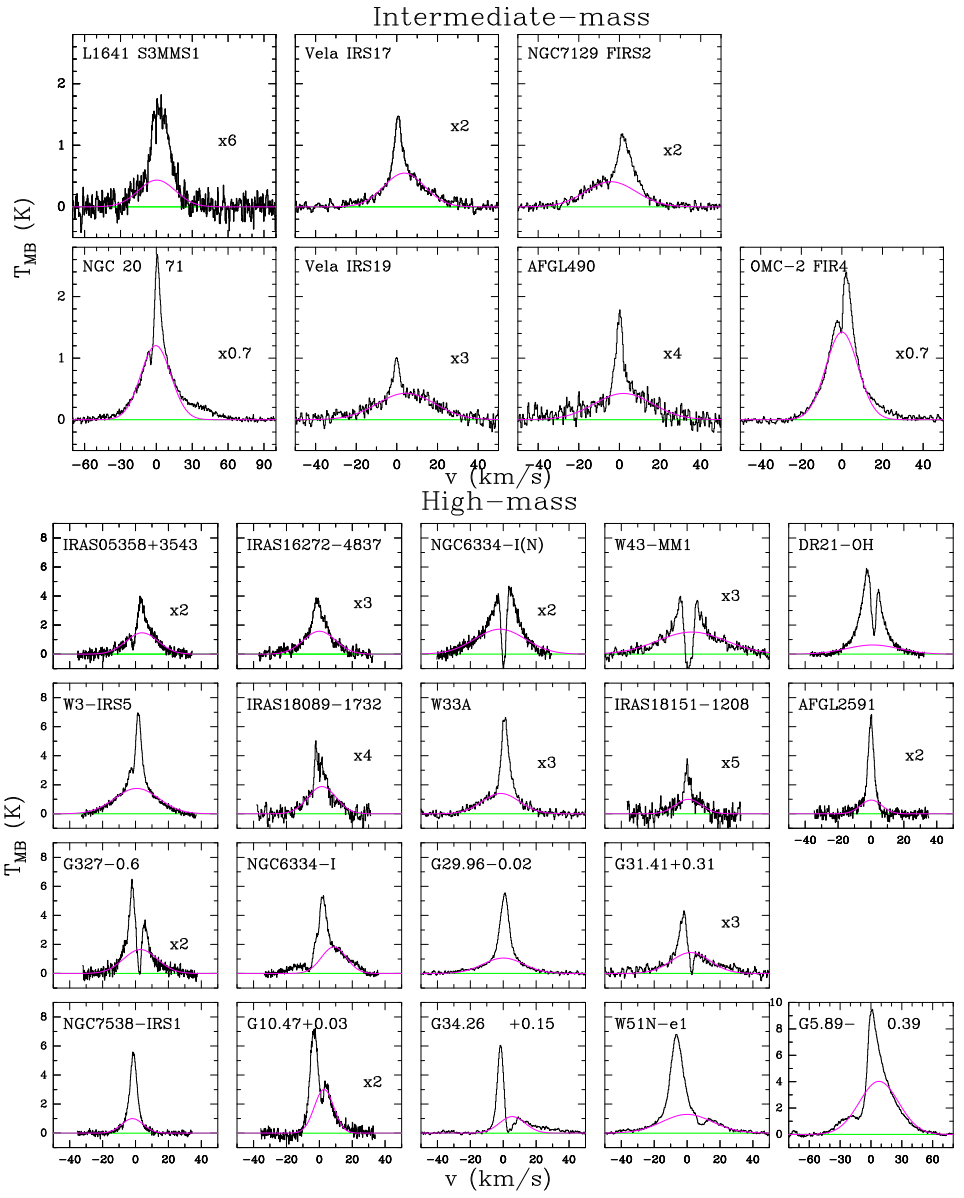

Figure 4.11: H_2O 2_{02}-1_{11} spectra for the intermediate-mass YSOs (*top*) and high-mass sources (*bottom*). The green line represents the baseline level and the pink Gaussian the broad velocity component. All spectra have been shifted to zero velocity. The numbers indicate where the spectra have been scaled for greater visibility.

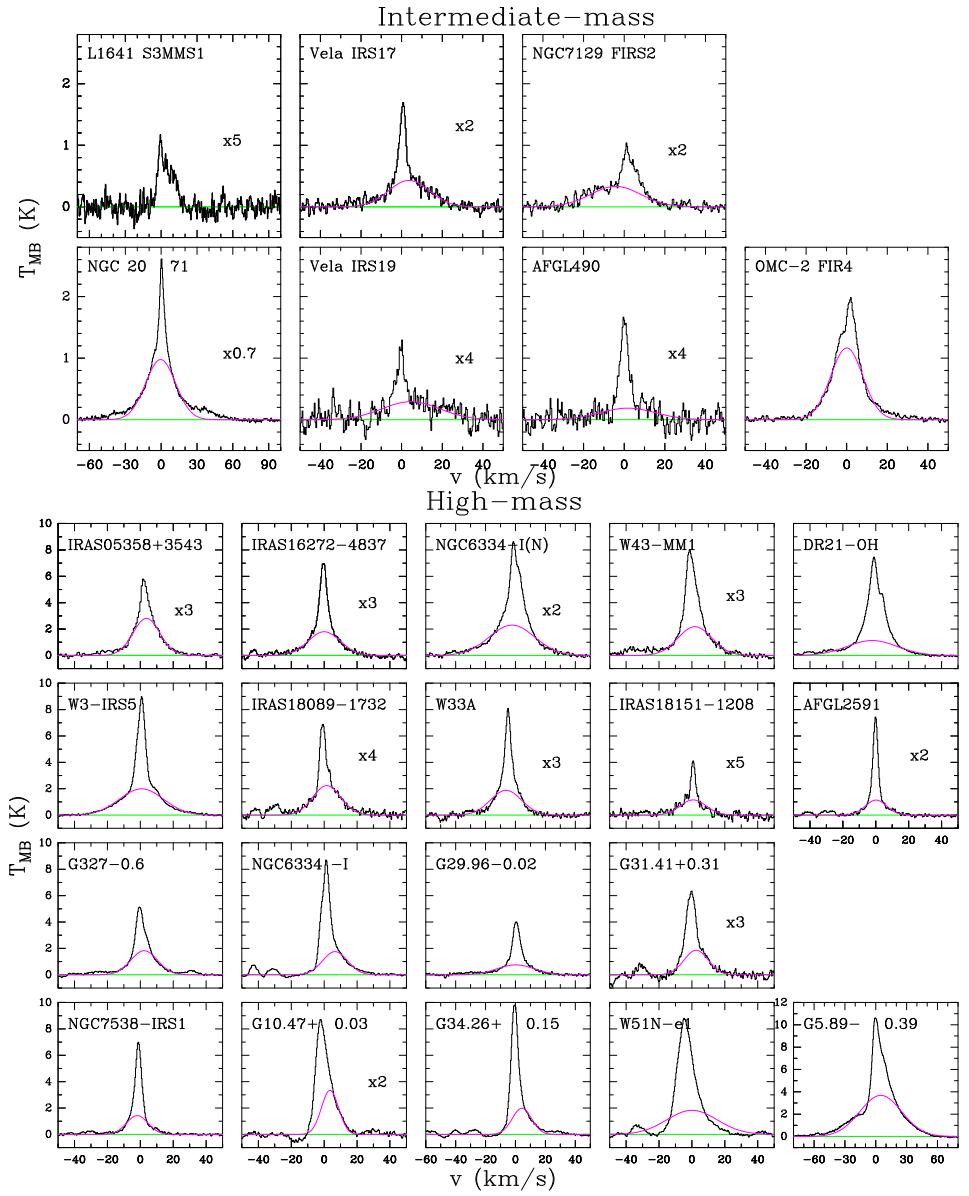

Figure 4.12: H_2O 2_{11}-2_{02} spectra for the intermediate-mass YSOs (*top*) and high-mass sources (*bottom*). The green line represents the baseline level and the pink Gaussian the broad velocity component. All spectra have been shifted to zero velocity. The numbers indicate where the spectra have been scaled for greater visibility.

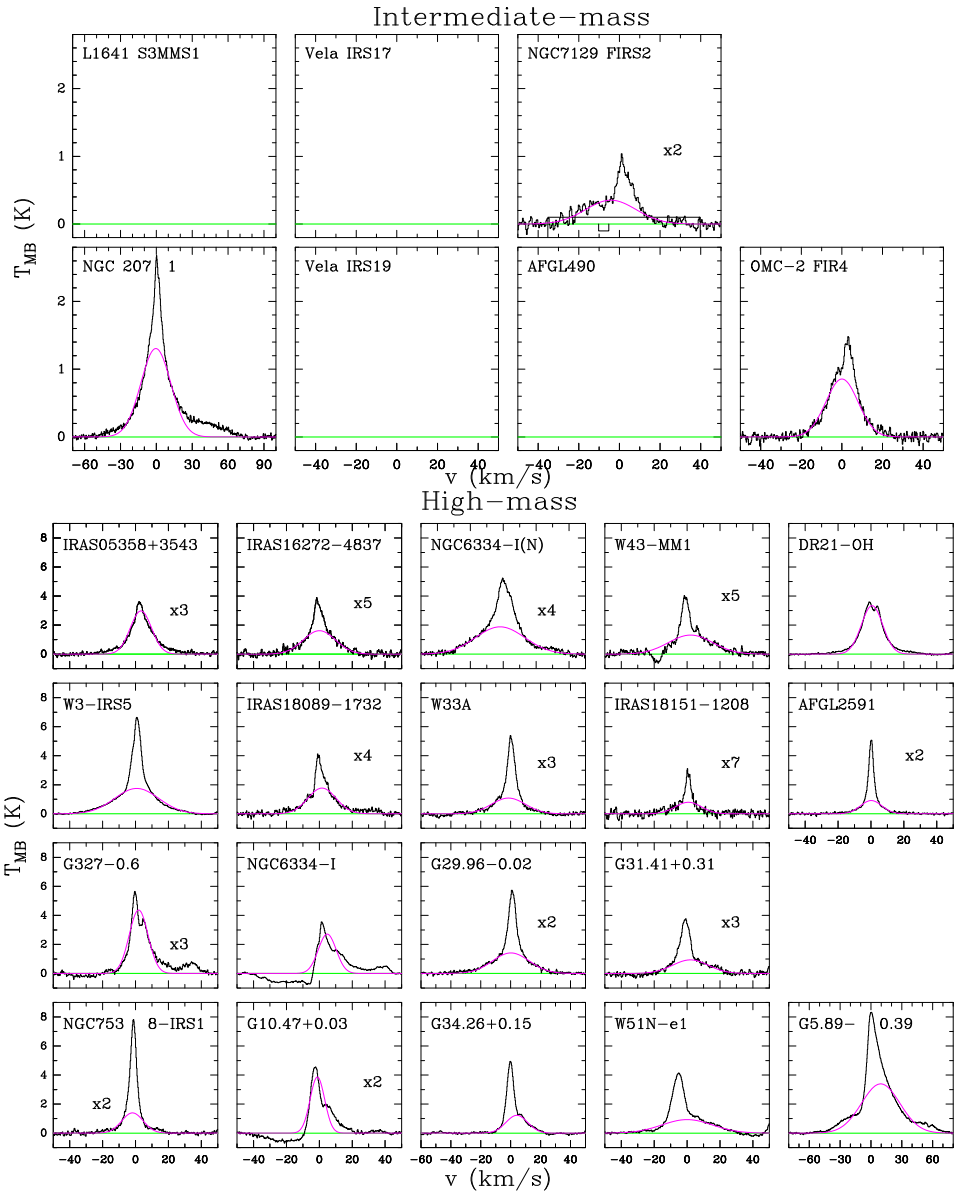

Figure 4.13: H_2O 3_{12}-3_{03} spectra for the intermediate-mass YSOs (*top*) and high-mass objects (*bottom*). The green line represents the baseline level and the pink Gaussian the broad velocity component. All spectra have been shifted to zero velocity. The numbers indicate where the spectra have been scaled for greater visibility.

Table 4.10: Gaussian decomposition results for the intermediate-mass objects.

Source	Comp.[a]	$FWHM_b$	v_{peak}	v_{LSR}	H_2O 2_{02}-1_{11}		H_2O 2_{11}-2_{02}		H_2O 3_{12}-3_{03}	
					T_{MB}^{peak}	$\int T_{MB} dv^b$	T_{MB}^{peak}	$\int T_{MB} dv^b$	T_{MB}^{peak}	$\int T_{MB} dv^b$
		(km s^{-1})	(km s^{-1})	(km s^{-1})	(K)	(K km s^{-1})	(K)	(K km s^{-1})	(K)	(K km s^{-1})
NGC7129 FIRS2	C	29.3 ± 0.3	-13.99 ± 0.17	-9.8	0.192 ± 0.004	5.99 ± 0.14	0.160 ± 0.004	4.99 ± 0.13	0.166 ± 0.003	5.18 ± 0.11
	E	8.46 ± 0.11	-7.20 ± 0.04	-9.8	0.368 ± 0.005	3.31 ± 0.06	0.282 ± 0.006	2.54 ± 0.06	0.285 ± 0.004	2.57 ± 0.05
L1641 S3MMS1	C	34 ± 3	6.4 ± 0.9	5.3	0.073 ± 0.013	2.6 ± 0.5	0.084	3.04	–	–
	E	15.3 ± 0.5	8.57 ± 0.16	5.3	0.197 ± 0.014	3.2 ± 0.3	0.155 ± 0.005	2.53 ± 0.11	–	–
NGC2071	C	29.60 ± 0.12	9.14 ± 0.05	9.6	1.722 ± 0.008	54.3 ± 0.3	1.42 ± 0.007	44.7 ± 0.3	1.311 ± 0.006	41.3 ± 0.3
	E	6.122 ± 0.04	10.17 ± 0.02	9.6	2.039 ± 0.017	13.3 ± 0.2	1.924 ± 0.012	12.5 ± 0.1	1.283 ± 0.009	8.36 ± 0.08
	S	31.2 ± 0.7	46.9 ± 0.3	9.6	0.277 ± 0.005	9.2 ± 0.3	0.199 ± 0.004	6.6 ± 0.2	0.229 ± 0.003	7.6 ± 0.2
	A	3.65 ± 0.09	6.54 ± 0.04	9.6	-0.814 ± 0.018	-3.16 ± 0.11	–	–	–	–
Vela IRS17	C	23.8 ± 0.4	7.53 ± 0.14	3.9	0.277 ± 0.005	7.01 ± 0.16	0.158 ± 0.005	4.00 ± 0.14	–	–
	E	4.19 ± 0.07	4.47 ± 0.03	3.9	0.462 ± 0.009	2.06 ± 0.05	0.608 ± 0.011	2.71 ± 0.07	–	–
Vela IRS19	C	33.3 ± 0.8	16.7 ± 0.3	12.2	0.141 ± 0.003	5.00 ± 0.16	0.068 ± 0.004	2.41 ± 0.15	–	–
	E	4.14 ± 0.18	11.92 ± 0.07	12.2	0.183 ± 0.008	0.81 ± 0.05	0.215 ± 0.012	0.95 ± 0.07	–	–
AFGL490	C	31.9 ± 1.0	-11.7 ± 0.4	-13.5	0.107 ± 0.004	3.63 ± 0.18	0.033 ± 0.004	1.12 ± 0.14	–	–
	E	4.56 ± 0.11	-13.40 ± 0.04	-13.5	0.299 ± 0.007	1.45 ± 0.05	0.364 ± 0.011	1.77 ± 0.07	–	–
OMC-2-FIR 4	C	18.62 ± 0.07	11.33 ± 0.03	11.3	2.085 ± 0.018	41.3 ± 0.4	1.210 ± 0.009	24.0 ± 0.2	1.031 ± 0.010	20.4 ± 0.2
	E	6.26 ± 0.08	13.40 ± 0.02	11.3	1.03 ± 0.03	6.87 ± 0.19	0.677 ± 0.009	4.51 ± 0.08	0.566 ± 0.014	3.77 ± 0.11

Notes.$^{(a)}$ The types of components are: C = cavity shock; E = envelope emission; S = spot shock; A = envelope absorption. $^{(b)}$ Integrated intensity of each velocity component approximated to the gaussian fit.

Table 4.11: Gaussian decomposition results for the high-mass YSOs.

Source	Comp.[a]	$FWHM_b$	v_{peak}	v_{LSR}	H_2O 2_{02}-1_{11}		H_2O 2_{11}-2_{02}		H_2O 3_{12}-3_{03}	
					T_{MB}^{peak}	$\int T_{MB} dv^b$	T_{MB}^{peak}	$\int T_{MB} dv^b$	T_{MB}^{peak}	$\int T_{MB} dv^b$
		(km s^{-1})	(km s^{-1})	(km s^{-1})	(K)	(K km s^{-1})	(K)	(K km s^{-1})	(K)	(K km s^{-1})
IRAS05358+3543	C	23.0 ± 0.2	-13.56 ± 0.07	-17.6	0.786 ± 0.015	19.2 ± 0.4	0.812 ± 0.014	19.9 ± 0.4	0.550 ± 0.009	13.5 ± 0.3
	E	6.49 ± 0.09	-15.05 ± 0.03	-17.6	1.14 ± 0.03	7.9 ± 0.2	1.079 ± 0.017	7.46 ± 0.16	0.617 ± 0.012	4.26 ± 0.10
	A	3.69 ± 0.14	-18.01 ± 0.06	-17.6	-0.85 ± 0.03	-3.32 ± 0.16	–	–	–	–
IRAS16272-4837	C	23.0 ± 0.4	-46.15 ± 0.13	-46.2	0.531 ± 0.018	13.0 ± 0.5	0.72 ± 0.02	17.5 ± 0.6	0.300 ± 0.008	7.4 ± 0.2
	E	5.61 ± 0.11	-46.78 ± 0.04	-46.2	0.72 ± 0.03	4.3 ± 0.2	1.59 ± 0.03	9.6 ± 0.3	0.420 ± 0.012	2.51 ± 0.09
NGC6334I-N-1	C	36.4 ± 0.3	-5.24 ± 0.08	-3.3	0.803 ± 0.012	31.1 ± 0.5	1.191 ± 0.015	46.1 ± 0.7	0.508 ± 0.006	19.7 ± 0.3
	E	10.41 ± 0.07	-2.99 ± 0.02	-3.3	2.39 ± 0.04	26.5 ± 0.5	2.703 ± 0.018	30.0 ± 0.3	0.763 ± 0.009	8.46 ± 0.12
	A	3.95 ± 0.05	-3.07 ± 0.01	-3.3	-3.60 ± 0.04	-15.2 ± 0.2	–	–	–	–
W43-MM1	C	48.8 ± 0.5	101.65 ± 0.19	98.8	0.429 ± 0.008	22.3 ± 0.5	0.436 ± 0.007	22.7 ± 0.4	0.152 ± 0.003	7.90 ± 0.17
	E	9.10 ± 0.06	98.50 ± 0.02	98.8	1.59 ± 0.09	15.3 ± 0.9	2.150 ± 0.012	20.82 ± 0.18	0.563 ± 0.006	5.45 ± 0.07
	A	5.79 ± 0.12	99.30 ± 0.03	98.8	-2.28 ± 0.08	-14.0 ± 0.6	–	–	–	–
DR21-OH	C	37.6 ± 0.3	-1.99 ± 0.09	-3.1	0.640 ± 0.016	25.6 ± 0.7	0.827 ± 0.017	33.1 ± 0.7	0.629 ± 0.010	25.2 ± 0.5
	E	12.34 ± 0.04	-2.81 ± 0.01	-3.1	5.63 ± 0.03	74.0 ± 0.5	5.46 ± 0.02	71.8 ± 0.3	2.971 ± 0.010	39.04 ± 0.17
	A	3.28 ± 0.03	-1.49 ± 0.01	-3.1	-4.74 ± 0.04	-16.6 ± 0.2	–	–	–	–
W3-IRS5	C	31.57 ± 0.13	-37.62 ± 0.05	-38.4	1.948 ± 0.014	65.5 ± 0.5	2.140 ± 0.013	71.9 ± 0.5	1.976 ± 0.014	66.4 ± 0.5
	E	5.86 ± 0.02	-37.49 ± 0.01	-38.4	4.21 ± 0.03	26.21 ± 0.19	6.55 ± 0.02	40.8 ± 0.2	4.63 ± 0.03	28.84 ± 0.19
IRAS18089-1732	C	20.2 ± 0.3	35.41 ± 0.10	33.8	0.455 ± 0.018	9.8 ± 0.4	0.534 ± 0.015	11.5 ± 0.4	0.459 ± 0.008	9.8 ± 0.2
	E	4.27 ± 0.09	33.30 ± 0.03	33.8	0.58 ± 0.04	2.65 ± 0.18	1.20 ± 0.03	5.47 ± 0.16	0.537 ± 0.012	2.44 ± 0.07
W33A	C	26.8 ± 0.2	36.02 ± 0.08	37.5	0.512 ± 0.008	14.6 ± 0.3	0.728 ± 0.013	20.7 ± 0.4	0.410 ± 0.005	11.68 ± 0.17
	E	5.81 ± 0.03	38.01 ± 0.01	37.5	1.568 ± 0.016	9.70 ± 0.11	1.83 ± 0.03	11.35 ± 0.17	1.347 ± 0.007	8.34 ± 0.07
IRAS18151-1208	C	18.6 ± 0.2	33.6 ± 0.2	32.8	0.220 ± 0.007	4.36 ± 0.15	0.269 ± 0.02	5.33 ± 0.14	0.1 ± 0.3	2.64 ± 0.18
	E	3.3 ± 0.3	32.9 ± 0.3	32.8	0.426 ± 0.015	1.52 ± 0.11	0.57 ± 0.04	2.02 ± 0.17	0.3 ± 0.3	1.1 ± 0.2
AFGL2591	C	15.23 ± 0.17	-5.32 ± 0.05	-5.5	0.48 ± 0.02	7.8 ± 0.4	0.607 ± 0.011	9.8 ± 0.2	0.456 ± 0.007	7.40 ± 0.14
	E	3.50 ± 0.02	-5.48 ± 0.08	-5.5	2.87 ± 0.04	10.7 ± 0.17	3.071 ± 0.016	11.45 ± 0.08	2.006 ± 0.011	7.48 ± 0.06

Notes.$^{(a)}$ The types of components are: C = cavity shock; E = envelope emission; S = spot shock; A = envelope absorption. $^{(b)}$ Integrated intensity of each velocity component approximated to the gaussian fit.

Table 4.12: Gaussian decomposition results for the high-mass YSOs (continuation).

Source	Comp.[a]	$FWHM_b$	v_{peak}	v_{LSR}	H_2O 2_{02}-1_{11}		H_2O 2_{11}-2_{02}		H_2O 3_{12}-3_{03}	
					T_{MB}^{peak}	$\int T_{MB} dv^b$	T_{MB}^{peak}	$\int T_{MB} dv^b$	T_{MB}^{peak}	$\int T_{MB} dv^b$
		(km s^{-1})	(km s^{-1})	(km s^{-1})	(K)	(K km s^{-1})	(K)	(K km s^{-1})	(K)	(K km s^{-1})
G327-0.6	C	24.3 ± 0.2	-42.28 ± 0.08	-45.0	0.89 ± 0.02	23.0 ± 0.6	0.616 ± 0.011	15.9 ± 0.3	0.649 ± 0.010	16.8 ± 0.3
	E	6.45 ± 0.06	-44.32 ± 0.02	-45.0	7.4 ± 0.4	51 ± 3	1.618 ± 0.014	11.11 ± 0.14	1.042 ± 0.015	7.16 ± 0.12
	A	4.83 ± 0.07	-43.79 ± 0.03	-45.0	-7.8 ± 0.4	-40 ± 2	–	–	–	–
NGC6334-I-1	C	17.83 ± 0.14	1.43 ± 0.09	-7.4	1.88 ± 0.02	35.7 ± 0.5	1.478 ± 0.014	28.0 ± 0.3	1.76 ± 0.02	33.3 ± 0.5
	E	6.27 ± 0.03	-6.40 ± 0.01	-7.4	4.82 ± 0.07	32.2 ± 0.5	7.31 ± 0.02	48.8 ± 0.3	2.09 ± 0.04	14.0 ± 0.3
	A	2.86 ± 0.10	-7.77 ± 0.04	-7.4	-1.99 ± 0.07	-6.1 ± 0.3	–	–	–	–
G29.96-0.02	C	29.1 ± 0.2	97.74 ± 0.07	97.6	1.059 ± 0.014	32.8 ± 0.5	0.810 ± 0.016	25.1 ± 0.5	0.705 ± 0.008	21.9 ± 0.3
	E	6.20 ±0.03	98.56 ± 0.01	97.6	4.36 ± 0.02	28.7 ± 0.2	3.13 ± 0.03	20.7 ± 0.2	2.058 ± 0.012	13.58 ± 0.10
G31.41+0.31	C	27.7 ± 0.4	99.62 ± 0.16	97.4	0.413 ± 0.013	12.2 ± 0.4	0.627 ± 0.016	18.5 ± 0.5	0.317 ± 0.008	9.3 ± 0.3
	E	6.73 ± 0.09	96.46 ± 0.03	97.4	1.21 ± 0.04	8.6 ± 0.3	1.65 ± 0.02	11.8 ± 0.2	0.931 ± 0.012	6.67 ± 0.12
	A	4.57 ± 0.16	99.09 ± 0.08	97.4	-1.02 ± 0.03	-4.9 ± 0.2	–	–	–	–
G5.89-0.39	C	45.06 ± 0.05	17.81 ± 0.02	10.0	4.154 ± 0.011	199.2 ± 0.6	4.057 ± 0.009	194.6 ± 0.5	3.474 ± 0.007	166.6 ± 0.4
	E	10.93 ± 0.02	11.62 ± 0.01	10.0	5.564 ± 0.019	64.7 ± 0.3	6.452 ± 0.015	75.1 ± 0.2	4.918 ± 0.010	57.22 ± 0.16
	A	8.92 ± 0.11	1.42 ± 0.05	10.0	-1.741 ± 0.018	-16.5 ± 0.3	–	–	–	–
G10.47+0.03	C	13.79 ± 0.13	70.16 ± 0.11	67.3	1.53 ± 0.03	22.4 ± 0.5	2.162 ± 0.02	31.7 ± 0.5	0.903 ± 0.011	13.3 ± 0.2
	E	5.64 ± 0.06	64.48 ± 0.02	67.3	3.22 ± 0.09	19.4 ± 0.6	3.17 ± 0.05	19.0 ± 0.3	1.67 ± 0.02	10.01 ± 0.16
	A	4.5 ± 0.2	66.95 ± 0.12	67.3	-1.32 ± 0.06	-6.4 ± 0.5	–	–	–	–
G34.26+0.15	C	18.39 ± 0.12	63.52 ± 0.08	58.0	1.186 ± 0.015	23.2 ± 0.3	1.492 ± 0.017	29.2 ± 0.4	1.091 ± 0.010	21.4 ± 0.2
	E	5.50 ± 0.02	57.53 ± 0.01	58.0	52 ± 18	305 ± 109	8.69 ± 0.03	50.9 ± 0.2	3.99 ± 0.02	23.38 ± 0.13
	A	5.60 ± 0.03	57.71 ± 0.07	58.0	-48 ± 18	-286 ± 111	–	–	–	–
W51N-e1	C	36.1 ± 0.2	59.58 ± 0.07	59.5	1.47 ± 0.05	56.27 ± 0.11	1.72 ± 0.02	66.1 ± 0.6	1.28 ± 0.02	49.0 ± 0.4
	E	8.5 ± 0.2	54.30 ± 0.01	59.5	5.31 ± 0.07	47.9 ± 0.7	7.59 ± 0.03	68.5 ± 0.4	3.12 ± 0.03	28.1 ± 0.2
	A	19.4 ± 0.4	62.08 ± 0.14	59.5	-5.2 ± 0.5	-107 ± 9	–	–	–	–
NGC7538-IRS1	C	15.37 ± 0.16	-58.02 ± 0.05	-56.2	1.02 ± 0.03	16.7 ± 0.4	1.37 ± 0.03	22.4 ± 0.5	0.781± 0.014	12.8 ± 0.3
	E	4.42 ± 0.02	-57.38 ± 0.01	-56.2	4.51 ± 0.04	21.2 ± 0.2	5.48 ± 0.03	25.77 ± 0.19	3.030 ± 0.018	14.2 ± 0.11

Notes.(^{a}) The types of components are: C = cavity shock; E = envelope emission; S = spot shock; A = envelope absorption. (^{b}) Integrated intensity of each velocity component approximated to the gaussian fit.

4.C. Additional figures

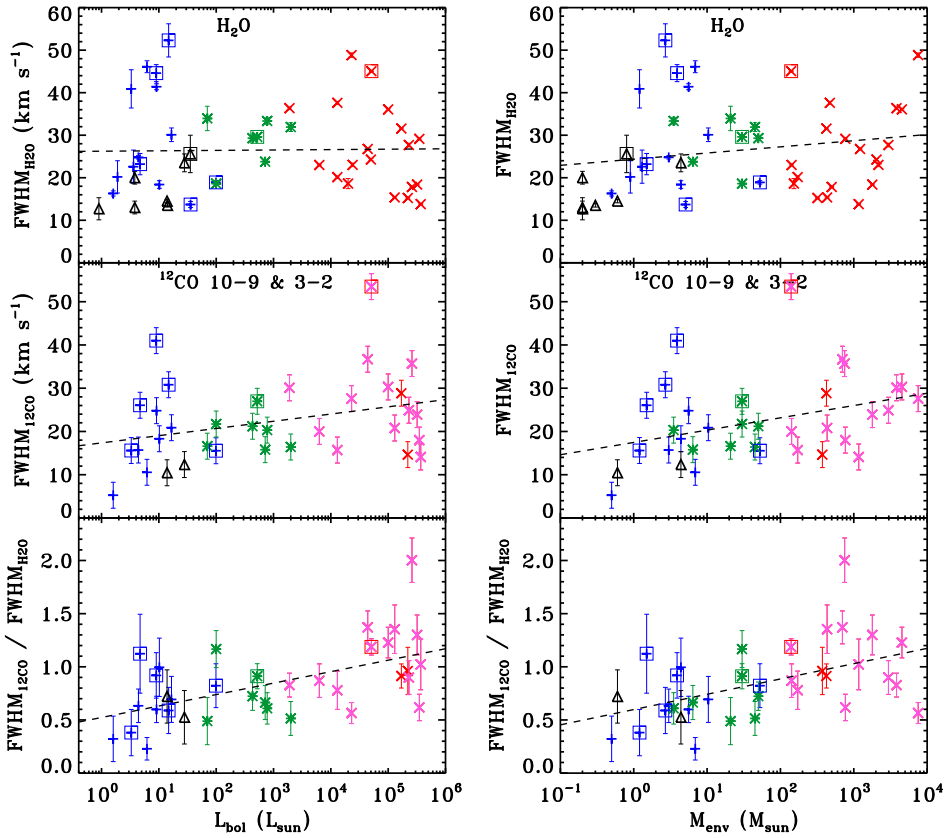

Figure 4.14: (*Left*-column figure) Derived $FWHM_{\rm b}$ of the Gaussian profile fitted to the cavity shock component of the H_2O lines (*top*-panel) as a function of bolometric luminosity. Constrained $FWHM_{\rm b}$ for the ^{12}CO $J = 10$–9 and $J = 3$–2 observations (*middle*-panel) versus $L_{\rm bol}$. Ratio calculated from the ^{12}CO $FWHM_{\rm b}$ divided by the $FWHM_{\rm b}$ of the H_2O lines (*bottom*-panel) as a function of $L_{\rm bol}$. (*Right*-column figure) Same as *left*- figure but plotted versus the envelope mass of the source, $M_{\rm env}$. The blue plus symbols correspond to the low-mass Class 0 protostars, the black triangles the low-mass Class I, the green asterisks the intermediate-mass objects, the pink crosses the high-mass YSOs for which the ^{12}CO $J = 3$–2 spectra are taken, and the red cross symbols the high-mass object for which ^{12}CO $J = 10$–9 data are available (see San José-García et al. 2013). The low- and intermediate-mass objects with detected EHV components are surrounded by a box. Also the high-mass YSO with triangular water line profiles is surrounded by a box. The value of the $FWHM_{\rm b}$ of the different velocity components is calculated as explained in Sect. 4.2.5 and these parameters are the same for the three water transitions.

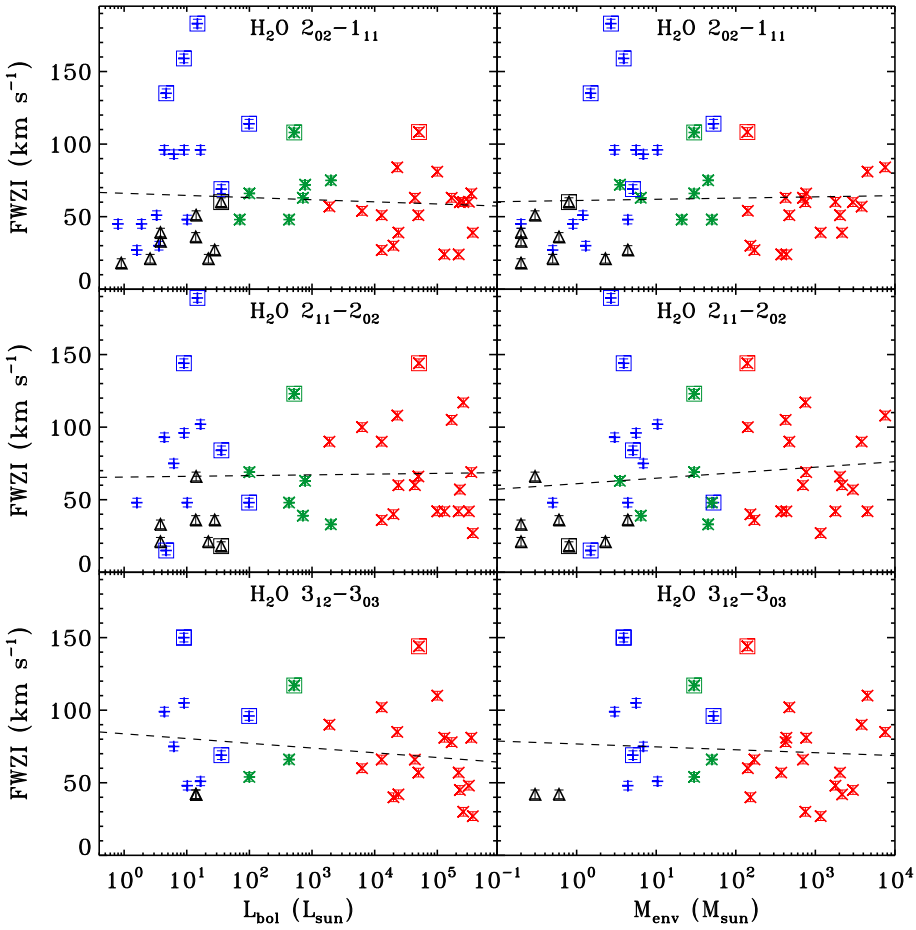

Figure 4.15: (*Left*-column) *FWZI* of the H_2O 2_{02}-1_{11} 988 GHz (*top* panel), 2_{11}-2_{02} 752 GHz (*middle* panel) and 3_{12}-3_{03} 1097 GHz (*bottom* panel) transitions as a function of the bolometric luminosity of each source. (*Right*-column) Same as *left*-column but versus the envelope mass of each YSO. The blue plus symbols correspond to the low-mass Class 0 protostars, the black triangles the low-mass Class I, the green asterisks to the intermediate-mass objects and the red crosses to the high-mass YSOs. The low- and intermediate-mass objects with detected EHV components are surrounded by a box, as well as the high-mass YSO with triangular line profiles. *FWZI* is calculated by binning the spectra to 3 km s^{-1}.

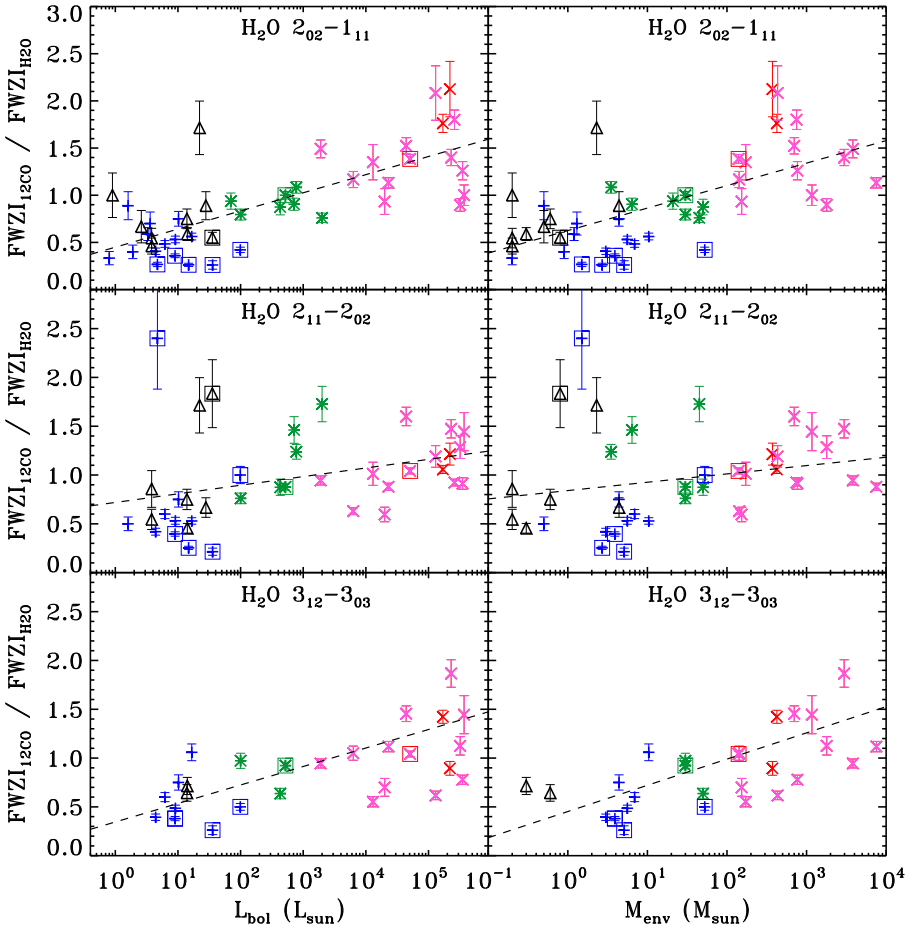

Figure 4.16: (*Left*-column) Ratio of the *FWZI* of the H_2O 2_{02}-1_{11} 988 GHz (*top* panel), 2_{11}-2_{02} 752 GHz (*middle* panel) and 3_{12}-3_{03} 1097 GHz (*bottom* panel) transitions and the *FWZI* of the ^{12}CO observations as a function of the bolometric luminosity. (*Right*-column) Same as *left*-column but versus the envelope mass of each YSO. The low- and intermediate-mass sources with detected EHV components are surrounded by a box, and also the high-mass YSO with triangular line profiles. Both values of *FWZI* were calculated by binning the spectra to 3 km s^{-1}. The symbol and colour code is the same as in Fig. 4.2.

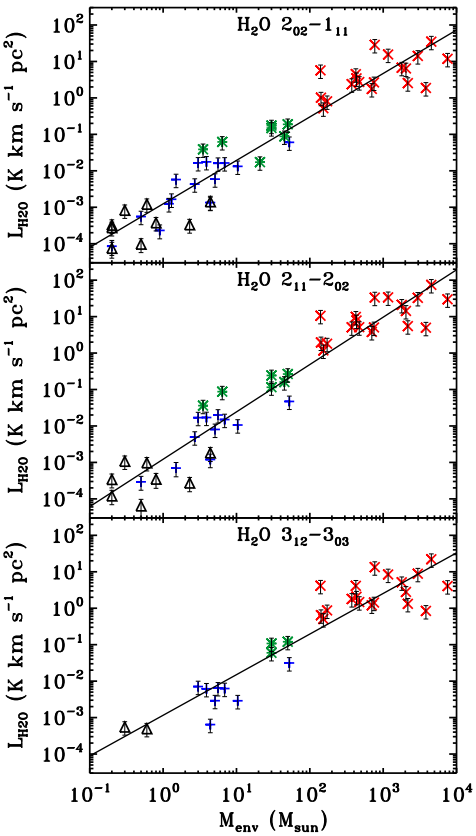

Figure 4.17: Same as Fig. 4.3 but plotted as a function of the envelope mass of the source.

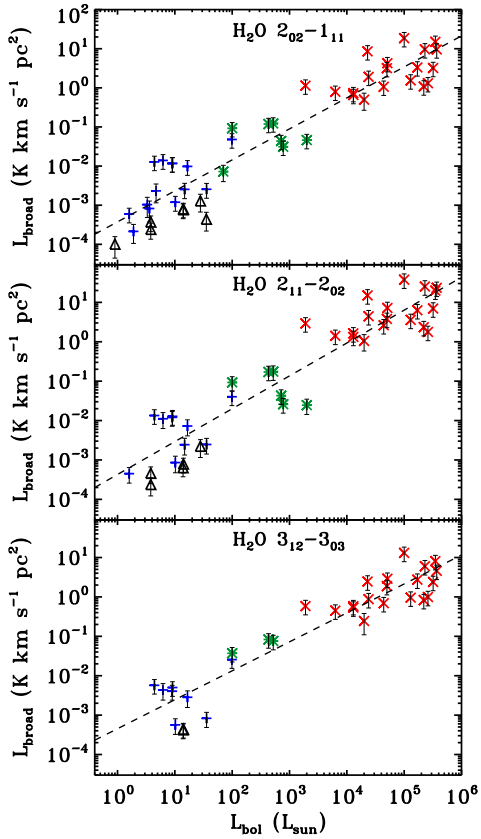

Figure 4.18: Line luminosity of the broad velocity component (emission from shocked gas along the outflow cavity) versus the bolometric luminosity of the source. The symbol and colour code is the same as in Fig. 4.3. The dashed black line shows the log-log correlation of the luminosity measured for the cavity shock emission and $L_{\rm bol}$.

5

An unbiased view of the link between low- and high-mass star formation: Herschel-HIFI observations of H_2O and CO from the WILL and Cygnus samples

I. San José-García, J. C. Mottram, S. Bontemps, et al.
in preparation

Abstract

Water line transitions uniquely trace the dynamical conditions in young stellar objects (YSOs), in particular shocks in the outflows (Kristensen et al. 2012; Mottram et al. 2014; Santangelo et al. 2014). Several *Herschel* key programmes, such as WISH, have targeted this important molecule, but their samples are a selection of peculiar sources which might not represent the general picture of the star formation process.

We aim to characterise H_2O and CO line profiles as a function of luminosity (in the range 0.4 to 10^3 $L_\odot$) for a well-selected sample of YSOs, obtained by including the WILL (low-mass) and Cygnus (intermediate-mass) follow-up programs. *Herschel*-HIFI spectra of H_2O 1_{10}-1_{01}, 2_{02}-1_{11}, 1_{11}-0_{00}, ^{12}CO $J = 10$–9, ^{13}CO $J = 10$–9, and C^{18}O $J = 9$–8 are decomposed into velocity components thought to be associated with different physical structures within protostellar systems, such as shocked gas along the outflow cavity wall, entrained outflowing material and the quiescent envelope. For each line, the widths, peak velocities and luminosities are calculated.

Following the methods used on the WISH sample, all water transitions for each WILL or Cygnus source are decomposed into the same component types. However, while in the WILL sample we detect three types of velocity components, corresponding to quiescent envelope, cavity shocks and spot shocks, for the Cygnus sample only the envelope and the cavity shocks are identified. We exclude that the absence of spot shock components in the Cygnus sample is due to insufficient *S/N*. Instead, the Cygnus sources are either in a later evolutionary stage or the emission is beam diluted due to their large distances.

For both WILL and Cygnus, more than 80% of the water emission comes from shocked material along the outflow cavity. While for the WILL Class 0 sample the rest of the emission belongs to spot shocks, for the WILL Class I and Cygnus sample this remaining emission is mostly generated by the envelope, consistent with previous analysis on the WISH sample. The percentage of WILL Class 0 sources for which a broad component is detected in the ^{12}CO $J = 10$–9 line profiles is lower than for WISH low-mass Class 0 sources (42% versus 72% of the detected spectra) and the width of this component is generally narrower (by $\sim$5 km s^{-1}) for the WILL Class 0 protostars. While the *FWZI* of the 557 GHz water line is similar for both WILL and WISH Class 0 objects, the other transitions show narrower *FWZI* values for the WILL sources. These results suggest that the WISH Class 0 sub-sample contains sources with more energetic outflows. In contrast, the intrinsic properties of Class I sources seem more uniform across the two samples.

Based on the similarity of the line properties between the WISH and Cygnus samples, we suggest that the latter is mostly composed of Class I low- and intermediate-mass YSOs. Finally, a strong correlation is measured between the luminosity of all studied lines and the bolometric luminosity of the source. The implications of this correlation are currently under investigation. Therefore, apart from minor differences between the intrinsic properties of the YSOs constituting the studied surveys, overall the conclusions derived from WISH hold and are confirmed by the H_2O and CO observations of the WILL and Cygnus samples.

5.1. Introduction

In previous chapters we investigated the physical properties of the sample of embedded young stellar objects (YSOs) constituting the "Water In Star forming regions with *Herschel*" (WISH; van Dishoeck et al. 2011) key programme. The ultimate purpose is to derive a comprehensive picture of the star formation process without mass boundaries, focusing on comparing the dynamical conditions in the warm inner regions of the protostellar environments of low-, intermediate- and high-mass YSOs.

The YSOs within the WISH sample were selected because they have been well studied. They are usually bright or somehow peculiar sources with unusual and unique properties and so may not be representative of the global conditions where stars form. Even if the characterisation of these types of objects is an important step towards the understanding of the star formation process, it is crucial to build a more unbiased sample of YSOs to test the acquired knowledge of the physics of protostellar systems without being dominated by the specific properties of outliers in the sample.

In addition, the WISH survey is composed of a relatively small number of YSOs, of the order of 50 in total, and much less if distinctions between mass and evolutionary stages are made. Therefore, a larger and more varied sample of YSOs will allow us to interpret the outcomes in a more solid and statistically supported framework.

Finally, the aim of this work is to investigate whether massive star-forming regions can be considered scaled-up versions of low-mass protostars. Within this context, intermediate-mass sources play a pivotal role in bridging the gap between low- and high-mass YSOs. These objects share many properties with their less and more massive counterparts, from both the theoretical and observational point of view. However, the WISH survey only included six intermediate-mass YSOs, leaving the range of bolometric luminosities between few 10^2 to 10^4 $L_\odot$ largely unsampled.

In order to strengthen the study initiated by the WISH key programme on the characterisation of star formation as a function of luminosity (San José-García et al. 2013, & subm., Karska et al. 2014a, Benz et al. subm.], the data from two *Herschel* follow-up projects are analysed in this chapter. The aim is not only to extend the sample of studied YSOs, but also validate previous results with a larger statistical base and complement the WISH survey by overcoming the weaknesses described above.

The first of the two follow-up projects is "The William Herschel Line Legacy" survey (WILL; PI.: E. F. van Dishoeck). This programme targeted 45 embedded low-mass Class 0/I protostars selected from photometric surveys with *Spitzer* and *Herschel* of major star-forming regions located within 450 pc. The luminosities of sources in this sample range from 0.4 to ∼30 $L_\odot$. Further information about the WILL survey such as selection criteria (infrared slope, bolometric temperature), observed lines and follow-up ground-based JCMT and APEX observations is presented in Mottram et al. in prep.

The second *Herschel* follow-up programme is titled "Water emission from outflows and hot cores in the Cygnus X protostars" (PI: S. Bontemps). It targets the Cygnus X star-forming region, which is more distant (∼1.4 kpc) and massive (total molecular mass of $3{\times}10^6$ $M_\odot$; Schneider et al. 2006) than those targeted in WILL. It contains multiple OB associations (Comerón & Pasquali 2012, and references therein) and several massive YSOs (Motte et al. 2007; Reipurth & Schneider 2008). This project selected the 86 most luminous embedded YSOs in Cygnus by combining the results from the *Spitzer* Cygnus X Legacy Survey (PI.: J. Hora) and the IRAM MAMBO2 survey (Motte et al. 2007) in order to observe intermediate- and high-mass Class 0- and Class I-type objects. The sample covers a range of bolometric luminosities between 10^2 to 10^3 $L_\odot$ (preliminary $L_{\rm bol}$ values taken from Kryukova et al. 2014) and complements the interval of luminosities poorly represented by WISH. One of the goals of this programme is to investigate the outflow energetics and explore chemically rich protostars, for which water plays a key role. Information about the survey, its goal, sample and line selection are discussed in Bontemps et al. in prep. Taken together, Cygnus X not only constitutes an ideal laboratory of embedded low-, intermediate- and high-mass sources linked by their likely common origin, but also satisfies the requirement to create a comprehensive sample of YSOs together with the WISH and WILL surveys. Finally, this survey allows a deeper analysis of the protostellar conditions by removing any possible bias related to

source distance (Malmquist bias) since all observed Cygnus YSOs are located at similar distances.

The importance of defining a complete sample of YSOs goes together with selecting appropriate molecular tracers to characterise the specific physical and chemical conditions of YSO environments. As discussed in chapter 4, the energetics and dynamics of molecular outflows, which are critical in the formation of young stars, are unambiguously probed by water emission (van Dishoeck et al. 2011). The Heterodyne Instrument for the Far-Infrared (HIFI; de Graauw et al. 2010) on board of the *Herschel* Space Observatory (Pilbratt et al. 2010) provides velocity-resolved water spectra with unprecedented spectral resolution, probing the excitation and kinematics of the gas. Complementing the analysis of the water emission, mid-J ($J \leq 10$) ^{12}CO, ^{13}CO and C^{18}O observations help to create a more complete picture of the dynamical structure of protostellar environments, since these species probe entrained outflowing material and the quiescent warm inner envelope (see chapter 2 and 3).

Therefore, the aim of this work is to investigate whether the dynamics of outflows vary as a function of luminosity by comparing the water and CO emission of a large, unbiased sample of low-, intermediate- and high-mass YSOs. In addition, the results derived from WISH (San José-García et al. 2013, & subm., Mottram et al. 2014) will be tested in the context of the WILL and Cygnus surveys to confirm the statistical significance of these conclusion within a more uniform framework.

In Sect. 5.2, the sample and line selection as well as the reduction and decomposition methods applied to the HIFI data are described. The results from the basic analysis of the water and CO observations for the WILL and Cygnus YSOs are presented in Sect. 5.3. In addition, the outcomes are compared to those obtained from the WISH survey, in particular those regarding the dynamical structure of molecular outflows. The implications of these outcomes and a more throughout study of the Cygnus X environment are discussed in Sect 5.4. Finally, the conclusions are summarised in Sect. 5.5.

5.2. Observations

5.2.1. Sample

The entire sample of sources presented in this chapter is composed of 131 YSOs. For the WILL survey, the 24 Class 0 and 21 Class I protostars are located in several well-known low-mass star-forming regions such as Perseus, Taurus, Ophiucus, Scorpius and Serpens. These targets have an infrared index, α, above 0.3 and bolometric temperatures, $T_{\rm bol}$, smaller than 350 K. This latter parameter is used to distinguish between the two evolutionary stages: sources with $T_{\rm bol}$<70 K are classified as Class 0 and those with larger values as Class I protostars. The velocities of the WILL sources with respect the standard of rest, $v_{\rm LSR}$, have been determined with C^{18}O and C^{17}O low-J lines observed with the JCMT (Mottram et al. in prep.).

In the case of the Cygnus sample, 8 of the 86 sources can be considered equivalent to low-mass Class 0 protostars and the remaining 78 are more evolved objects (Class I and II type with no radio emission). The division between these two stages and their analogy with those of low-mass YSOs is based on their infrared colours and the spectral energy distribution (SED) type of the Cygnus objects. Their bolometric luminosity is taken from Kryukova et al. (2014) or Motte et al. (2007) when the *Spitzer* emission was saturated. Therefore, both the rough evolutionary classification and their $L_{\rm bol}$ values are preliminary and will be constrained with complementary techniques in future work. In particular, $L_{\rm bol}$ will be re-calculated from more complete SEDs including *Herschel* PACS and SPIRE flux densities. Finally, the source velocity, $v_{\rm LSR}$, of several Cygnus YSOs has been taken to be that of the C^{18}O $J = 9$–8 line. If this transition was not detected, ^{13}CO $J = 10$–9 was used. This means that $v_{\rm LSR}$ could be determined for only a sub-sample of observed Cygnus YSOs. The $v_{\rm LSR}$ values are found to cover four main velocity ranges: one around -5 km s^{-1} and the others between 2 and 20 km s^{-1}, consistent with the results of Schneider et al. (2006). In that paper, the authors discussed the presence of structures in the North cloud of Cygnus with different $v_{\rm LSR}$ and located in the same line of sight. Further information about the source properties and the criteria

Table 5.1: Properties of the studied lines observed with HIFI.

Species	Transition	Freq.[a]	E_u/k_b	n_{cr}	η_{mb}[b]	θ_{mb}[b]	WBS res.	Observation Time[c]			
								WILL	Cygnus	W LM	W HM
		(GHz)	(K)	(cm^{-3})		($''$)	(km s^{-1})	(min)	(min)	(min)	(min)
o-H_2O	1_{10}-1_{01}	556.9	61.0	1×10^7	0.62	38.1	0.27	38	–	21	–
	3_{12}-2_{21}	1153.1	249.4	8×10^6	0.59	18.4	0.13	13	–	13	
p-H_2O	1_{11}-0_{00}	1113.3	53.4	1×10^8	0.64	19.0	0.13	28	9	44	7
	2_{02}-1_{11}	987.9	100.8	4×10^7	0.64	21.5	0.15	36	9	23	12
o-$H_2^{18}O$	1_{10}-1_{01}	547.7	60.5	1×10^7	0.62	38.7	0.27	38	–	33	–
$C^{18}O$	9–8	987.6	237.0	2×10^5	0.64	21.5	0.15	36	9	23	12
^{13}CO	10–9	1101.3	290.8	3×10^5	0.64	19.3	0.13	28	9	44	59
^{12}CO	10–9	1151.9	304.2	3×10^5	0.59	18.4	0.13	13	–	10	20

Notes. W LM stands for WISH low-mass protostars and W HM for WISH high-mass YSOs.
[a] Rest frequency taken from the JPL database (Pickett et al. 2010). [b] Values recently updated and provided by the HIFI wikipage[1], which replace those presented in Roelfsema et al. (2012). [c] Total observation time including on+off source and overheads.

on the selection will be presented in Bontemps et al. in prep.

To summarise, the composed sample of low-, intermediate- and high-mass YSOs covers a range of luminosities between 0.4 to 10^3 $L_\odot$, filling the gap between 10^2 and 10^3 $L_\odot$ left by the WISH sample. In addition, the statistics of the analysis is improved due to the increase of the number of available objects by a factor of two. As in previous chapters, the study is focused on characterising the physical properties of YSO systems across the luminosity range. More detailed analysis based on the different evolutionary stages for each luminosity bin will be presented in Mottram et al. in prep. for the WILL sample, in Bontemps et al. in prep. for the Cygnus YSOs.

5.2.2. HIFI observations

Water was the primary targeted molecule for both WILL and Cygnus X surveys, but the selected HIFI settings serendipitously covered some CO transitions. For WILL, the para-H_2O 1_{11}-0_{00} (1113 GHz) and 2_{02}-1_{11}(988 GHz); the ortho-H_2O 1_{10}-1_{01} (557 GHz) and 3_{12}-2_{21} (1153 GHz); and the ortho-$H_2^{18}O$ 1_{10}-1_{01} (548 GHz) transitions were observed as well as ^{12}CO $J = 10$–9, ^{13}CO $J = 10$–9 and $C^{18}O$ $J = 9$–8. Within the Cygnus program, the three brightest water transitions were selected after taking into account the first WISH results (see e.g. Chavarría et al. 2010; Kristensen et al. 2010; Marseille et al. 2010). In this work we present the para-H_2O 1_{11}-0_{00} (1113 GHz) and 2_{02}-1_{11}(988 GHz) transitions and ^{13}CO $J = 10$–9, $C^{18}O$ $J = 9$–8, observed together, as for the WILL sample.

Table 5.1 shows the rest frequency, upper energy level (E_u), critical density (n_{cr}) of each line together with the beam efficiency (η_{mb}), beam size (θ_{mb}), spectral resolution of each HIFI line and observing time. The beam efficiencies of each HIFI band have been recently updated and the adopted values are those provided by the HIFI wikipage[1]. The observation times of the WISH low-mass and high-mass YSOs are also included in Table 5.1 for comparison. Since the WILL sources are generally fainter than their WISH analogues, the exposure times were increased for WILL in order to get similar signal-to-noise ratios, S/N=T_{peak}/σ_{rms}. While comprable rms values are achieved for both WILL and WISH low-mass samples, WILL observations generally show lower S/N than those of WISH. This difference is not significant for the 557 GHz water line, for which the averaged S/N is ∼20 and ∼26 for the WILL and WISH low-mass samples respectively. However, for the 1113 GHz line there is a factor of ∼2 difference in S/N between the two samples. The

[1]Further information regarding the updated beam efficiencies values is presented in the technical note "Measured beam efficiencies on Mars (revision v1.1, 1 October 2014)" of the HIFI wikipage:
http://herschel.esac.esa.int/twiki/bin/view/Public/HifiCalibrationWeb? template=viewprint

integration time for the Cygnus objects was selected with the purpose of achieving a 5σ detection of the H_2O lines for a source such as NGC 7129 FIRS2 (part of the WISH intermediate-mass subsample) but located at 1.3 kpc. The achieved *S/N* on sources where the lines are detected is similar to that of the WISH intermediate-mass YSOs (*S/N*~47) and only slightly lower than that obtained for the WISH high-mass objects (*S/N*~60). This difference is less relevant given the overall higher *S/N* of the Cygnus sample.

As for previous HIFI observations (see Sections 2.2.2 and 4.2.2), the data were taken with the Wide Band Spectrometer (WBS) and the High Resolution Spectrometer (HRS) backends, in both vertical (V) and horizontal (H) polarisations (Roelfsema et al. 2012). We present the WBS observations because they have the best compromise between noise and resolution, especially for the studied molecular lines. For all targets, single-pointing observations were performed in dual-beam-switch (DBS) mode.

5.2.3. Reduction of the HIFI data

The applied reduction process is the same as that explained in Sections 2.2.2 and 4.2.5 of previous chapters. All HIFI observations were calibrated using the *Herschel* Interactive Processing Environment (HIPE[2]; Ott 2010). The flux was converted to the antenna temperature T_A^* scale and the velocity calibrated with a $v_{\rm LSR}$ precision of a few m s^{-1}, after which the data were exported to GILDAS-CLASS[3] format for further analysis. The signal-to-noise ratio of the spectra was improved by averaging together the observations of the H and V polarisations. Then, the line intensities were converted to main-beam brightness temperatures, $T_{\rm MB}$, applying the specific beam efficiencies, $\eta_{\rm MB}$, of each HIFI band. Finally, the baseline of each spectrum was subtracted by a linear polynomial.

For consistency with previous WISH studies (San José-García et al. 2013 and San José-García et al. subm.), all reduced data were resampled to 0.27 km s^{-1} and the rms noise of the spectra calculated at this resolution. The maximum peak brightness temperature, $T_{\rm peak}$, the full width at zero intensity, *FWZI*, and the total integrated intensity, $W = \int T_{\rm MB} {\rm d}v$, were derived using the method adopted by Mottram et al. (2014), which is briefly explained in Sect. 4.2.4 of this thesis. To compare the presented WILL and Cygnus observations with those of WISH, previous WISH intensity-based measurements ($T_{\rm peak}$, W, etc.) have been corrected to account for the updated values of η_{mb} adopted in this work (see corrector factors in Table 4.1). The ^{13}CO and C^{18}O spectra and the water data of a few Cygnus objects are resampled to 1 km s^{-1} bins in order to calculate the *FWZI* because the lines are too narrow to use with 3 km s^{-1} binning, the value adopted for the water and ^{12}CO data. These parameters are presented in Tables 5.11 to 5.12 for the WILL samples and in Tables 5.21 to 5.20 for the Cygnus YSOs.

5.2.4. Decomposition method

Similarly as for the WISH observations (Kristensen et al. 2010, 2012; van der Tak et al. 2013; Mottram et al. 2014, San José-García et al. subm.), the complex H_2O and CO line profiles can be decomposed into several Gaussian components. These different velocity components trace specific physical and kinematical conditions within the protostellar environments, so it is important to accurately characterise the line profiles. The number of velocity components needed to reproduce the profiles differs for each object but the basic types of profiles are the same for all sources.

The procedure to constrain the parameters of the different Gaussian profiles (i.e. position, amplitude and *FWHM* of each component) is the same as that presented in Sect. 3.2.1 of Mottram et al. (2014). An example of the Gaussian decomposition procedure and residual from the fitting is shown in Fig. 2.1 in chapter 2. The spectra are fitted by providing initial guess values of the Gaussian components creating the line profiles to an ordinary least-squares solver in the PYTHON

[2]HIPE is a joint development by the *Herschel* Science Ground Segment Consortium, consisting of ESA, the NASA Herschel Science Centre, and the HIFI, PACS and SPIRE consortia.

[3]http://www.iram.fr/IRAMFR/GILDAS/

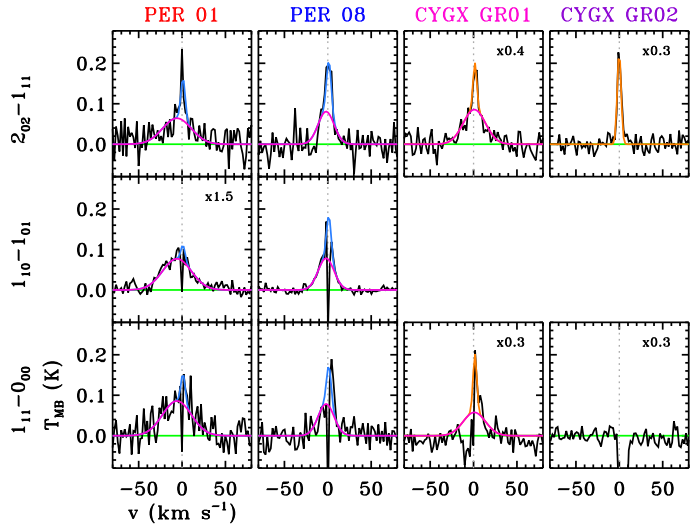

Figure 5.1: Spectra of the H_2O 1_{11}-0_{00} (1113 GHz; *bottom*-row), 1_{10}-1_{01} (557 GHz; *middle*-row) and 2_{02}-1_{11} (988 GHz; *top*-row) for the WILL Class 0 protostar Per 01 (first column), the WILL Class I object Per 08 (second column) and the equivalent of Class 0 and Class I for the Cygnus sources GR01 03 and GR02 01 (third and forth columns respectively) binned to 2 km s^{-1}. The different velocity components in which the spectra are decomposed are indicated with different colours: the broad cavity shock component is drawn with the pink line, the medium-broad spot shock component is shown in blue and the narrow quiescent envelope emission in orange (see Sect 5.2.5 for explanation of these components). All spectra have been shifted to 0 km s^{-1} (dotted grey line) and resampled to 2 km s^{-1}. The baseline is indicated in green. Further explanation of these components is given in Sect 5.2.5

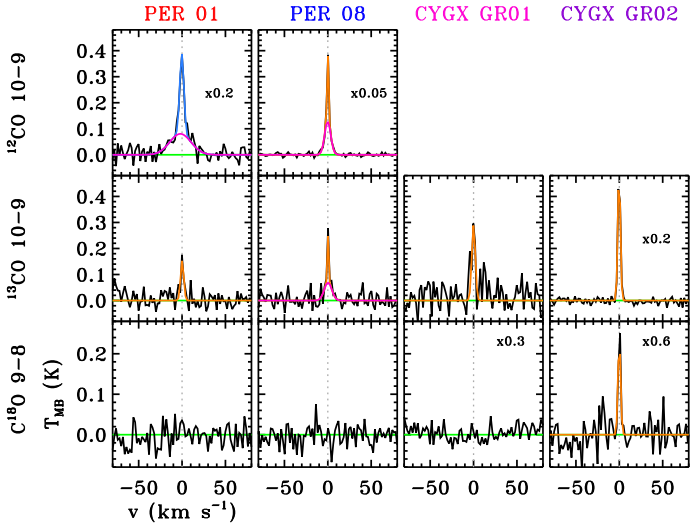

Figure 5.2: Same as Fig. 5.1 but for the C^{18}O $J = 9$–8 (*bottom*-row), ^{13}CO $J = 10$–9 (*middle*-row) and ^{12}CO $J = 10$–9 (*top*-row) spectra of the same sources. For these lines, the velocity components in which the spectra are decomposed correspond to the broad entrained outflowing component (in pink), the medium-broad spot shock component (in blue) and the quiescent envelope emission (in orange). Further explanation of these components is given in Sect 5.2.5.

module SCIPY.ODR[4]. The number of velocity components is determined by analysis of the residual after fitting the line to a single Gaussian line and adding an extra Gaussian profile until no features are measured above 3 $\sigma_{\rm rms}$. In the case of the water lines, the *FWHM* and central position of each Gaussian component is forced to be the same for all transitions and these parameters are constrained simultaneously by all available H_2O spectra of a given source (i.e. the amplitudes of each Gaussian component are free parameters that can vary for each water transitions). For a given source, the number of components can vary per transition because of their different rms and *S/N* level. The different CO isotopologue transitions are fitted independently because these species are tracing different physical structures in the YSO than water and potentially each other.

The fitting procedure are applied to all water and CO spectra. Four different types of velocity components have been identified: narrow centred near the source velocity, broad at the source $v_{\rm LSR}$ or within few km s^{-1} (usually fitting the line-wings of the spectra), medium-broad offset from the source velocity and medium-broad but offset from $v_{\rm LSR}$ by a large value (>10 km s^{-1}). The narrow components can appear in emission or absorption while the other components are always in emission for this sample. In Sect. 5.2.5 the type of gas probed by each of these velocity components is explained depending on the studied molecule.

The narrow component (*FWHM*<5 km s^{-1}) present in the water transitions of the WILL protostars has not been fitted. The main reason is that, in general, the ground-state H_2O lines show an absorption feature centred near the source $v_{\rm LSR}$ which appears together with a weak narrow emission also around $v_{\rm LSR}$. The combination of absorption and emission creating the narrow velocity component of the line is difficult to reproduce with a single Gaussian component and the best-fit parameters (amplitude and width) have some associated uncertainty. Therefore, for this version of the data analysis, the range of velocities including both the absorption and narrow weak emission features has been masked out as in previous analysis (Kristensen et al. 2012, 2013; Mottram et al. 2014). This masking does not affect the best-fit parameters of the Gaussian profiles of the broader velocity components.

Examples of the Gaussian decomposition for the studied water lines (1113, 557 and 988 GHz) of Class 0 and Class I type YSO for the WILL and Cygnus samples are shown in Fig. 5.1, and for the observed CO isotopologue transitions in Fig. 5.2. Three velocity components can be identified: the very broad centred near the source velocity, the medium broad offset from $v_{\rm LSR}$ and the narrow component. Finally, the result from the Gaussian fit decomposition of each observed line is presented in Tables 5.13 to 5.17 for the WILL protostars and in Tables 5.24 to 5.23 for the Cygnus YSOs.

5.2.5. Linking velocity and physical components

As introduced in Sect. 4.2.6, each velocity component in the water and CO spectra can be associated with a different physical component and structure within the protostellar environment (Kristensen et al. 2012; Mottram et al. 2014; Yıldız et al. 2010, 2013; San José-García et al. 2013, & subm., chapter 4). To simplify the distinction between the different types of components, Table 5.2 summarises their main phenomenological characteristics as well as the physical YSO structures associated with them.

The narrow Gaussian component centred near the source velocity in both H_2O and CO lines is generated by quiescent envelope gas. While this component is generally seen in emission for the excited transitions, it usually appears in absorption in the ground-state optically thick lines because the colder outer parts of the envelope absorb part of this emission. The upper limit of the width of this component differs from low- to high-mass YSOs. In the case of low-mass protostars (i.e. WILL sample) the narrow envelope component is characterised with a *FWHM* less than 5 km s^{-1}, consistent with the WISH low-mass study presented in Mottram et al. (2014). On the other hand, for intermediate- and high-mass YSOs (i.e. Cygnus sources), the interval of *FWHM* values for the envelope component is extended up to 10 km s^{-1}. This limit is based on the maximum width measured in the $C^{18}O$ $J = 9$–8 transition for the Cygnus sample, which uniquely traces the quiescent

[4] http://scipy.org/

Table 5.2: Name and main characteristic of the fitted velocity components for the H_2O and CO lines together with their physical associations according to Fig. 6 of Mottram et al. (2014).

Molecule	Observed characteristics		Physical component
	Width	Offset from v_{LSR}?	
H_2O	Narrow	No	Quiescent envelope
	Broad	No	Outflow cavity shocks
	Medium/Broad	Yes, significant	Spot shocks: bullets or EHV[a]
	Medium (broad also present)	Yes	Spot shocks: at the base of outflow cavity[b]
^{12}CO	Narrow	No	Quiescent envelope
	Broad	No	Entrained material in outflow cavity wall
	Medium/Broad	Yes, significant	Spot shocks: bullets or EHV[a]
^{13}CO	Narrow	No	Quiescent envelope and UV-heated gas[c]
	Broad	No	Entrained material in outflow cavity wall
$C^{18}O$	Narrow	No	Quiescent envelope

Notes. Cavity shocks are non-dissociative shocks, while spot shocks are generally dissociative.
[(a)] Extremely high velocity (EHV) emission component (Bachiller et al. 1990; Tafalla et al. 2010; Kristensen et al. 2011). They are considered shocks along the jet. [(b)] Previously called medium-broad offset component in Kristensen et al. (2013). Shocks are caused by the impact of the jet or stellar wind at the base of the outflow cavity wall. [(c)] The narrow ^{13}CO emission is associated with the quiescent envelope and the excess emission comes from UV-heated gas along inner regions of the outflow cavity wall (van Kempen et al. 2009a; Yıldız et al. 2012, 2015).

envelope. A larger velocity interval for the envelope emission of the high-mass YSOs is consistent with the picture in which massive YSOs are characterised with more turbulent envelopes (San José-García et al. subm.). In the case of ^{13}CO, part of the narrow emission is associated to UV-heated gas along inner regions of the outflow cavity walls (Spaans et al. 1995; van Kempen et al. 2009a; Yıldız et al. 2015). This particular case will not be discussed further in this chapter.

The broad velocity component centred at the source velocity (or offset few km s^{-1}) is designated using the suffix "b" for consistency with previous studies (chapters 2 and 4 of this thesis), and generally reproduces the line-wings of the spectra (Kristensen et al. 2013; Yıldız et al. 2013; van der Tak et al. 2013). This component is associated with gas within the outflow of different nature depending on the studied molecule (see Fig. 1.1 of chapter 1). In the case of H_2O, the emission from the broad component is caused by non-dissociative shocks in layers along the outflow cavity wall (Kristensen et al. 2010, 2013; van Kempen et al. 2010; Nisini et al. 2010; Santangelo et al. 2013). This component is also called "cavity shock component" for the water lines, as introduced by Mottram et al. (2014). On the other hand, for low- and mid-J ($J \leq 10$) ^{12}CO and ^{13}CO transitions, the broad velocity component is associated with colder entrained outflowing gas (Yıldız et al. 2013; San José-García et al. 2013). This gas is part of the intermediate layer between the outflow cavity and the envelope. Summarising, and as explained in Table 5.2, the broad component detected in the water and low-mid-J CO transitions do not trace the same material within the outflow (Kristensen et al. 2012; Santangelo et al. 2013). Even if phenomenologically we designate these two velocity components as broad, their physical origin is different and should be distinguished.

The velocity component detected largely offset from the source velocity both in H_2O and ^{12}CO spectra is associated with hot (up to thousands of K) and energetic dissociative shocks taking place in small and localised regions along the bipolar jets (see Bachiller et al. 1990; Tafalla et al. 2010; Kristensen et al. 2011, for more details). In previous studies, these components were named "bullets" or extremely-high velocity (EHV) components given the large velocity reached by the gas involved in these shocks. In the case of the velocity component detected in the water lines with smaller *FWHM* value and centred at more offset velocities than the broad cavity shock component, this emission is then associated with dissociative shocks occurring at the base of the outflow cavity. This component was perviously known as medium-broad or offset component (Kristensen et al. 2013). Adopting the same terminology as in Mottram et al. (2014) and San José-García et al.

subm., the velocity components tracing the emission from both types of hot and dissociative shocks are designated as "spot shock components" because both of them take place in small localised regions within the outflow.

The focus of this chapter is the study of the broad velocity component detected in the H_2O lines, i.e. the emission from cavity shocks along the outflow cavity wall, across a large range of luminosities. We prioritise the analysis of this component because it is the most commonly detected across the water lines and it probes specific dynamical conditions within the outflow present in low-, intermediate- and high-mass YSOs (see chapter 4). The parameters characterising the other types of velocity components are also included for comparison with previous studies.

5.3. Results

First, we present the basic general results of the H_2O, ^{12}CO, ^{13}CO and $C^{18}O$ spectra focusing on the number of detections for each studied sample of YSOs, on the shape of the line profiles and on intrinsic parameters of the data such as the *FWZI*(Sect. 5.3.1). Then, we summarise the outcomes from the line decomposition method of the observed lines. The number and contribution of the different velocity components detected in the profiles of the water and CO lines are calculated and the results analysed together with those derived for WISH (Sect. 5.3.2). In addition, a deeper study on the emission coming from the cavity shock component, i.e. the broad velocity component fitted for the water lines, is presented and trends with bolometric luminosity investigated (Sect. 5.3.3). Finally, the derived line luminosity of the H_2O and CO spectra simultaneously observed for the WILL and Cygnus data are studied as a function of $L_{\rm bol}$ (Sect. 5.3.4).

5.3.1. Characterisation of the line profiles

The observed H_2O and $H_2^{18}O$ transitions for the WILL and Cygnus samples are presented in Figs. 5.14 to 5.24 and Figs. 5.31 to 5.37, respectively. The ^{12}CO $J = 10$–9, ^{13}CO $J = 10$–9 and $C^{18}O$ $J = 9$–8 spectra are shown in Figs. 5.25 to 5.30 for the WILL protostars and the ^{13}CO $J = 10$–9 and $C^{18}O$ $J = 9$–8 observations in Fig. 5.38 to 5.44 for the Cygnus YSOs.

H_2O data

Within the WILL sample, the H_2O 1_{10}-1_{01} (557 GHz), 1_{11}-0_{00} (1113 GHz), 2_{02}-1_{11} (988 GHz) and 3_{12}-2_{21} (1157 GHz) transitions are detected for 34, 23, 25 and 8 sources out of 45, respectively, while the isotopologue line ($H_2^{18}O$ 1_{10}-1_{01}) is detected for only 2 protostars. As further explained in Appendix 5.B.1, the observations of eight WILL protostars are excluded from the data analysis. In the case of the Cygnus sample, the observed H_2O 1_{11}-0_{00} (1113 GHz) and 2_{02}-1_{11} (988 GHz) lines are both detected for 25 out of 86 YSOs. Table 5.3 includes the number of detections of each observed water line, the averaged rms and the mean and median values of the derived *FWZI* for each sub-sample of YSOs.

As for the WISH sample (see Mottram et al. 2014 and Sect. 4.3.1), the line profiles of the different H_2O transitions for a given source are similar, i.e. the spectra with sufficient *S/N* can be fitted with the same number of Gaussian components with a common velocity and width. Absorption features are present in the H_2O ground-state lines for 26 out of 45 WILL sources (76% of the detected 557 GHz lines and 65% of the detected 1113 GHz line) and in 23 out of 86 YSOs for the H_2O 1_{11}-0_{00} data of Cygnus (i.e. 92% of the detected 1113 GHz spectra). The larger percentage of absorption features measured for the Cygnus YSOs with respect the WILL protostars is consistent with the expected picture of massive star forming region having more absorption from their colder dense envelopes and from foreground clouds along the line of sight than lower-mass objects (Schneider et al. 2006). The Class 0 objects across both samples show a larger percentage of water detections, ~80%, than their more evolved counterparts, ~33%, which agrees with previous results (Mottram et al. 2014).

Table 5.3: Detection statistics, averaged rms and mean and median (M.) values of the *FWZI* for the ^{12}CO $J = 10$–9, ^{13}CO $J = 10$–9 and C^{18}O $J = 9$–8 spectra and for all observed H_2O transition across the Class 0 and Class I WILL and Cygnus sample of YSOs.

Line	WILL Class 0				WILL Class I				Cygnus Class 0				Cygnus Class I			
	D/O[a]	$\overline{\sigma_{\rm rms}}$ (mK)	$\overline{FWZI}$ (km s^{-1})	M. *FWZI* (km s^{-1})	D/O[a]	$\overline{\sigma_{\rm rms}}$ (mK)	$\overline{FWZI}$ (km s^{-1})	M. *FWZI* (km s^{-1})	D/O[a]	$\overline{\sigma_{\rm rms}}$ (mK)	$\overline{FWZI}$ (km s^{-1})	M. *FWZI* (km s^{-1})	D/O[a]	$\overline{\sigma_{\rm rms}}$ (mK)	$\overline{FWZI}$ (km s^{-1})	M. *FWZI* (km s^{-1})
^{12}CO $J = 10$–9	19/24	98	34±6	24.0	17/21	98	19±2	18.0	–	–	–	–	–	–	–	–
^{13}CO $J = 10$–9	12/24	27	16±2	13.7	8/21	26	10±2	8.7	6/8	56	8±1	7.1	35/78	51	7±1	5.4
C^{18}O $J = 9$–8	1/24	25	7.2[b]	7.2	0/21	–	–	–	1/8	44	7[b]	6.8	10/78	49	5±1	3.6
H_2O 1_{10}-1_{01}	19/24	9	75±10	72	15/21	7	37±5	27	–	–	–	–	–	–	–	–
H_2O 1_{11}-0_{00}	16/24	26	59±11	46	7/21	25	43±5	39	7/8	50	49±14	28	18/78	50	31±5	28
H_2O 2_{02}-1_{11}	16/24	28	56±11	47	9/21	25	31±3	33	7/8	26	56±8	59	18/78	25	36±5	40
H_2O 3_{12}-2_{21}	6/24	124	55±16	56	2/21	116	21[c]	21	–	–	–	–	–	–	–	–
$H_2^{18}O$ 1_{10}-1_{01}	2/24	7	35[c]	35	0/21	–	–	–	–	–	–	–	–	–	–	–

Notes. [(a)] Number of detected sources with respect to the total number of observed YSOs for each line. See Appendix 5.B.1 for further information about the WILL protostars not considered in the analysis. [(b)] No standard deviation is given for detections in less than four sources.

For the WILL Class 0 objects, the mean and median *FWZI* values of the H_2O transitions are similar among the observed lines, except for the 557 GHz transition, characterised with the widest profiles and the highest *S/N*. This transition is the only one that shows similar mean and median *FWZI* values as those measured for the WISH Class 0, while for the other H_2O transitions these parameters are smaller for the WILL sample by ∼15 km s^{-1}. In the case of the WILL Class I protostars, the derived mean and median *FWZI* values are similar within the uncertainty among the H_2O transitions with more than three detections and to those constrained for the WISH Class I objects.

Moving to the Cygnus YSOs, the derived mean *FWZI* values of the two water transitions are comparable within the Class 0 and Class I-type sub-samples. The mean and median *FWZI* parameters for the Cygnus Class 0 sources are more similar to those obtained for the WISH high-mass YSOs than for the other WISH sub-group of objects while the results obtained for the Cygnus Class I are comparable to those from the WISH and WILL Class I protostars.

The derived *FWZI* values for the WILL and Cygnus water observations are scatted across a large range of velocities (from 5 to ∼160 km s^{-1}) and no trend with luminosity is measures, consistent with the WISH results. A more detailed analysis of the *FWZI* values across the WILL, Cygnus and WISH samples and as a function of $L_{\rm bol}$ is presented in Appendix 5.A.

CO data

The ^{12}CO $J = 10$–9 line is detected in emission for 26 out of 45 WILL protostars, where 19/24 are Class 0 sources and 17/21 are Class I YSOs. This line was not observed for the Cygnus sample. The detection statistics of the ^{12}CO $J = 10$–9 data, the averaged rms of the spectra and the mean and median values of the *FWZI* parameter for each WILL sub-sample of sources are presented in Table 5.3. As for the WISH low-mass observations, the mean and median *FWZI* values are larger for the Class 0 objects than for the Class I since in general the Class 0 protostars show broader and more complex (larger number of velocity components) line profiles than those of their more evolved counterparts (further discussion on this result in Appendix 5.A). While the mean and median *FWZI* values of the WILL and WISH Class 0 sources are comparable within the uncertainty, the WISH Class I objects show slightly wider line-wings than those of WILL.

In the case of the ^{13}CO $J = 10$–9 observations, the line was detected for 20/45 WILL protostars and for 41/86 Cygnus YSOs (Table 5.3). The shapes of the profiles are similar to those observed for the WISH low-mass protostars since 90% of the detected WILL and Cygnus objects show single Gaussian-like profiles and only few sources have pronounced line wings. Therefore, the Cygnus spectra differ from those of the WISH high-mass objects, which show more complex profiles with remarkable line wings that enlarge their *FWZI* values. This is further discussed in Sect. 5.4.

Finally, the C^{18}O $J = 9$–8 line is detected for only one WILL source (the Class 0 object Ser 02) and for 11 Cygnus YSOs. As for the WISH sample, all spectra show narrow single Gaussian-like profiles (Table 5.3). In the case of the Cygnus sample, for which more lines have been detected, the obtained mean *FWZI* value is slightly smaller than that calculated for the WISH high-mass YSOs but comparable to the intermediate-mass objects.

5.3.2. Analysis of the decomposition process

H_2O line profiles

Table 5.4 summarises the results from the profile decomposition for the WILL, Cygnus and WISH sub-samples, i.e. the detection statistics of each velocity component and their mean and median *FWHM* values. The percentage of H_2O line profiles decomposed into more than one velocity component is similar for both WILL and Cygnus sample (53% versus 48% of the sources for which water lines are detected). However, while the cavity shock component (broad velocity component) is seen in all detected water lines for the WILL protostars, this component is not seen in 16% of the Cygnus spectra.

Within the WILL sample, ∼74% of the detected water lines for the Class 0 protostars (14/19) can be decomposed into two or three velocity components but only 27% of the detected Class I

Table 5.4: Number of detections and mean and median *FWHM* values of each physical component in which the H_2O line profiles of the WILL and Cygnus samples are decomposed. The results from the cavity shock component for the WISH low-, intermediate- and high-mass YSOs are also included.

	observed H_2O transitions								
	Envelope comp.			Cavity shock comp.			Spot shock comp.		
	D[a]	$\overline{FWHM}$ (km s^{-1})	M. *FWHM* (km s^{-1})	D[a]	$\overline{FWHM}$ (km s^{-1})	M. *FWHM* (km s^{-1})	D[a]	$\overline{FWHM}$ (km s^{-1})	M. *FWHM* (km s^{-1})
WILL Cl 0	1/19[b]	3.5[c]	3.5	19/19	32±4	26	15/19[d]	21±5	13
WILL Cl I	1/15[b]	4.3[c]	4.3	15/15	17±2	16	3/15	6±1	6
WISH Cl 0	15/15	3.6±0.3	3.5	15/15	29±3	24	10/15	23±5	18
WISH Cl I	11/11	3.0±0.4	2.6	11/11	18±2	15	3/11	17[c]	26
Cygnus Cl 0	5/7	6.7±1.0	6.0	7/7	33±5	37	0	–	–
Cygnus Cl I	11/18	5.0±0.6	5.2	14/18	28±3	28	0	–	–
WISH IM	7/7	5.4±0.6	4.6	7/7	29±2	32	1/7	31[c]	31
WISH HM	19/19	5.3±0.2	5.6	19/19	27±2	24	0	–	–

Notes. Cl 0: low-mass Class 0 protostars; Cl I: low-mass Class I sources; IM: intermediate-mass; HM: high-mass

[(a)] Number of components detected over $3\sigma_{\rm rms}$ with respect the total number of sources detected in each water transition. [(b)] This should be considered as a lower limit since in general the envelope component has not been fitted for the WILL sources, as explained in Sect. 5.2.4. [(c)] No standard deviation is given if the number of detected sources is less than three. [(d)] The spectra of three objects show two spot shock components, so the actual number of YSOs with this type of velocity component is 12 instead of 15.

line profiles (4/15) have two velocity components. For both sub-groups of YSOs, the combination of a cavity shock and a spot shock component dominates (in 12 of those 14 Class 0 and three out of those four Class I sources). No spot shock components largely offset from $v_{\rm LSR}$ are detected for the Class I objects. The spectra fitted with a single Gaussian-like profile (the remaining 26% and 73% of the Class 0 and Class I protostars respectively) show always a broad profile i.e. cavity shock emission.

For the Cygnus H_2O data, the spectra of five out of the seven Class 0-type objects show two velocity components profile (71% of the detected data) versus only 7/18 Class I Cygnus objects (39%). These line profiles are always decomposed into an envelope and a cavity shock component. In the case of the spectra fitted with a single velocity component (13/25), a broad Gaussian profile is found for most of these spectra except for four Class I-type sources which show surprisingly narrow ($FWHM < 8$ km s^{-1}) and bright Gaussian-like profiles. This type of narrow profile has not been observed for any water spectra of the WISH sample (further discussion in Sect. 5.4). No spot shock components, especially largely offset from the source velocity, are detected in any of the Cygnus observations. This latter result is consistent with the outcomes from the excited water line analysis of all WISH high-mass sample and most of the intermediate-mass YSOs. Spot shock components were detected in absorption in the ground-state lines of most but not all WISH high-mass objects (see van der Tak et al. 2013), while they are seen neither in absorption nor emission for the Cygnus ground-state H_2O transition (1113 GHz line).

Summarising, the water line profiles of the WILL Class 0 sources present a larger number of velocity components than those of the WILL Class I and Cygnus objects. A combination of cavity and spot shock components is in general the configuration most common for the WILL Class 0 data and only a cavity shock component that for the WILL Class I sources. For the Cygnus sample, combination of the envelope and cavity shock components is more frequently seen in the Class 0-type objects and only a cavity shock component or the combination of an envelope plus cavity shock have equal detection rates for the Class I-type objects.

In the following, we focus the analysis on the cavity shock component which is detected in most of the studied observations. The mean *FWHM* values of this component for the WILL Class 0

Table 5.5: Average fraction of the integrated intensity that each velocity components, $W_{\rm comp.}$, contribute to the total integrated intensity, W, of the H_2O 1_{10}-1_{01} (557 GHz), H_2O 1_{11}-0_{00} (1113 GHz), H_2O 2_{02}-1_{11} (988 GHz) and H_2O 3_{12}-2_{21} (1157 GHz) lines for the WILL Class 0, WILL Class I, Cygnus Class 0 and Cygnus Class I sources.

	Envelope		Cavity		Spot		Envelope		Cavity		Spot	
	D[a]	$W_{\rm comp.}/W$	D[a]	$W_{\rm comp.}/W$	D[a]	$W_{\rm comp.}/W$	D[a]	$W_{\rm comp.}/W$	D[a]	$W_{\rm comp.}/W$	D[a]	$W_{\rm comp.}/W$
Line	WILL Class 0						WILL Class I					
H_2O 1_{10}-1_{01}	19	-0.1±0.1	19	1.0±0.1	7	0.1±0.1	15	-0.2±0.1	15	1.2±0.1	3	0.1±0.1
H_2O 1_{11}-0_{00}	12	0.1±0.5	12	0.8±0.5	4	0.1±0.1	5	-0.2±0.1	5	1.1±0.1	1	0.1[c]
H_2O 2_{02}-1_{11}	11	0.0±0.1	11	0.8±0.1	5	0.2±0.1	5	0.0±0.1	5	0.9±0.1	1	0.1[c]
H_2O 3_{12}-2_{21}	4	0.0±0.1	4	0.8±0.1	2	0.2±0.1	1	-0.1[b]	1	1.1[b]	–	–
Line	Cygnus Class 0						Cygnus Class I					
H_2O 1_{11}-0_{00}	5	-0.4±1.1	4	1.4±1.1	0	–	12	-3.1±2.7	12	4.1±2.7	0	–
H_2O 2_{02}-1_{11}	7	0.0±0.1	7	1.0±0.1	0	–	15	0.1±0.2	15	0.9±0.2	0	–

Notes. The envelope contribution is calculated as: $W_{\rm envelope} = W - W_{\rm cavity\,shock} - W_{\rm spot\,shock}$.
[a] Number of sources which spectra show contribution for each indicated component. [b] No standard deviation is given for detections in less than four sources.

and Cygnus objects are similar within the uncertainty. These numbers are comparable to those calculated for the WISH low-mass Class 0, intermediate- and high-mass YSOs (Table 5.4). Interestingly, the median *FWHM* values of the Cygnus Class 0 and WISH intermediate-mass objects are the largest across the entire WILL, WISH and Cygnus samples. The mean and median *FWHM* values of the Class I protostars of both WILL and WISH are similar. These two sub-groups of objects have the narrowest line profiles.

The average fraction of the integrated intensity that the envelope, cavity shock and spot shock components contribute to the total integrated intensity of the observed H_2O lines is presented for the entire WILL and Cygnus sample of YSOs in Table 5.5. This contribution is calculated as explained in Mottram et al. (2014) and Sect. 4.3.1. In the case of the ground-state water lines, in particular the H_2O 1_{11}-0_{00} (1113 GHz) transition, the contribution of the cavity shock component can be above 1 because the strong envelope absorption features in these spectra reduce the total integrated intensity. Thus the envelope component has a negative intensity.

The contribution from the different types of velocity components for the H_2O 2_{02}-1_{11} (988 GHz) spectra of the WILL and Cygnus YSOs are compared to those of WISH (see Table 4.2 of this thesis and Table 4 of Mottram et al. 2014). On average, the cavity shock component contributes with more than 80% to the total integrated intensity of the line. These values are consistently larger than those obtained from WISH, especially for the intermediate- and high-mass sub-samples for which that fraction constitutes 60% of the total integrated intensity. In general, the remaining contribution from the water spectra of the WILL Class 0 protostars comes from the spot shock component, while for more massive or evolved objects, such as the WILL Class I and Cygnus YSOs, it seems to come from the envelope. This result is consistent with that derived from the excited water lines of the WISH sample (see Sect. 4.3.1).

CO line profiles

The ^{12}CO $J = 10$–9 spectra of 42% (8/19) WILL Class 0 protostars show more than two velocity components, where the combination of a narrow and a broad component is the most common (a summary of the decomposition result for this transition in are given Table 5.6). These profiles most resemble those observed for the WISH low-mass Class 0 objects. Only two sources (Per 03, also known as L1448-C(S), and Per 20) have additional EHV emission features. The profiles with a single velocity component are either narrow or broad. On the other hand, only 29% (5/17) of the ^{12}CO $J = 10$–9 WILL Class I spectra can be decomposed into two velocity components (narrow and broad) while the spectra of the other protostars show a single narrow line profile. No spot

Table 5.6: Number of detections and mean and median *FWHM* values of each velocity component in which the ^{12}CO $J = 10$–9 line profiles of the WILL protostars are decomposed.

	^{12}CO $J = 10$–9								
	Envelope comp.			Broad comp.			Spot shock comp.		
	D[a]	$\overline{FWHM}$ (km s^{-1})	M. *FWHM* (km s^{-1})	D[a]	$\overline{FWHM}$ (km s^{-1})	M. *FWHM* (km s^{-1})	D[a]	$\overline{FWHM}$ (km s^{-1})	M. *FWHM* (km s^{-1})
WILL Cl 0	11/19	3.0±0.3	3.1	13/19	15±3	10.1	6/19[c]	13±3	9
WILL Cl I	15/17	3.3±0.2	3.0	7/17	10±1	8.7	0/17	–	–
WISH Cl 0	14/15	4.0±0.5	4.0	12/15	20±3	17.8			
WISH Cl I	11/11	3.5±0.3	3.7	3/11	11[b]	12.7			

Notes. Cl 0: low-mass Class 0 protostars; Cl I: low-mass Class I sources.
[a] Number of components detected over $3\sigma_{\rm rms}$ with respect the total number of protostars with detected ^{12}CO $J = 10$–9 emission. [b] No standard deviation is given for detections in less than four sources. [c] The spectra of two sources show two spot shock components, so the actual number of protostars presenting this component is four.

Table 5.7: Number of detections and mean and median *FWHM* values of each velocity component in which the ^{13}CO $J = 10$–9 and C^{18}O $J = 9$–8 line profiles for the WILL and Cygnus samples are decomposed.

	^{13}CO $J = 10$–9						C^{18}O $J = 9$–8		
	Narrow comp.			Broad comp.			Narrow comp.		
	D[a]	$\overline{FWHM}$ (km s^{-1})	M. *FWHM* (km s^{-1})	D[a]	$\overline{FWHM}$ (km s^{-1})	M. *FWHM* (km s^{-1})	D[a]	$\overline{FWHM}$ (km s^{-1})	M. *FWHM* (km s^{-1})
WILL Cl 0	7/12	3.0±0.5	2.7	2/12	11.5[b]	11.5	1/1	5.4[b]	5.4
WILL Cl I	7/8	2.2±0.2	2.2	3/8[c]	7.3	6.5	0/1	–	–
WISH Cl 0	13/13	2.7±0.5	2.3	2/13	11.9[b]	11.9	2/2	2.5[b]	2.5
WISH Cl I	7/7	3.9±0.6	2.2	0/7	–	–	3/3	3.1[b]	3.1
Cygnus Cl 0	6/6	4.5±0.7	4.9	1/6	8.0[b]	8.0	1/1	7.1[b]	7.1
Cygnus Cl I	33/35	2.7±0.2	2.5	2/35	11.2[b]	11.2	10/10	2.8±0.3	2.7
WISH IM	6/6	5.0±0.3	4.8	1/6	14.7[b]	14.7	4/4	4.0±0.5	3.9
WISH HM	18/19	5.9±0.3	4.8	13/19	14.1±1.0	13.6	19/19	5.0±0.3	5.0

Notes. Cl 0: low-mass Class 0 protostars; Cl I: low-mass Class I sources; IM: intermediate-mass; HM: high-mass.
[a] Number of components detected over $3\sigma_{\rm rms}$ with respect the total number of YSOs detected on ^{13}CO $J = 10$–9 and C^{18}O $J = 9$–8. [b] No standard deviation is given for detections in less than four sources. [c] The line profile of two of those three sources can be decomposed into a two Gaussian components: a broad and a narrow component.

shock components offset from the source velocity are detected.

The left-column histograms of Fig. 5.3 compare the *FWHM* values of the broad velocity component, $FWHM_{\rm b}$, across the WILL and WISH low-mass protostars. Both histograms and mean and median $FWHM_{\rm b}$ calculations indicate that this velocity component is narrower (by ~5 km s^{-1}) for the WILL Class 0 than for their WISH analogues. In addition, the percentage of broad component detections (as well as detected spectra decomposed into more than one velocity component) is larger (>72%) for the WISH Class 0 protostars. This suggest some differences between the intrinsic properties of the objects constituting both WILL and WISH Class 0 samples (more details in Sect. 5.4). On the other hand, the percentage of detected broad velocity components and the $FWHM_{\rm b}$ values are similar for the Class I protostars of both WILL and WISH sub-samples, as the bottom-left histogram of Fig. 5.3 and Table 5.6 confirm.

Table 5.7 summarises the mean and median *FWHM* values of the velocity components detected

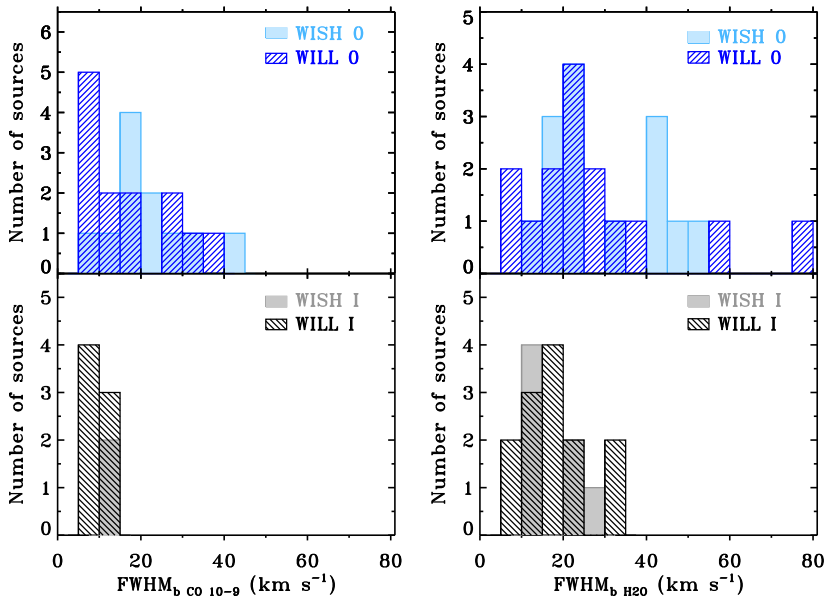

Figure 5.3: Histograms comparing the calculated $FWHM_b$ values of the ^{12}CO $J = 10$–9 spectra (*left*-column) and the H_2O lines (*right*-column) across the WILL and WISH samples. *Top*-panels: WILL and WISH Class 0 protostars (dashed blue and light blue bars, respectively). *Bottom*-panels: WILL and WISH Class I objects (dashed grey and light grey bars, respectively).

for the ^{13}CO $J = 10$–9 and C^{18}O $J = 9$–8 spectra of the WILL, Cygnus and WISH samples. For the ^{13}CO $J = 10$–9 data, the percentage of spectra decomposed into two velocity components is almost the same for the WILL and WISH low-mass protostars (3/20 versus 2/20 respectively). Similarly, the ^{13}CO $J = 10$–9 spectra of only two out of 41 Cygnus YSOs can be decomposed into two velocity components. Therefore, the majority of the detected spectra for the WILL and Cygnus YSOs show narrow Gaussian-like profiles. None of the two types of spot shock component is detected across these data. Focusing on the envelope (narrow) component, the mean and median $FWHM_n$ values are similar, within the uncertainty, for the WILL, Cygnus Class I and WISH low-mass samples. The $FWHM_n$ of the Cygnus Class 0 and those of the WISH intermediate- and high-mass samples are comparable and broader than those of the other sub-samples of YSOs. These results are confirmed by Fig. 5.4, which presents the constrained $FWHM_n$ for the Cygnus YSOs together with those derived from the WISH high-mass objects. This figure shows that the $FWHM_n$ distribution peaks at different velocities for the Class 0 and Class I-type objects (5 km s^{-1} and 1 km s^{-1} respectively). Interestingly, the $FWHM_n$ of this transition for the WISH intermediate- and high-mass YSOs is always larger than 3 km s^{-1}. This analysis suggests that the $FWHM_n$ increases with L_{bol} for the Class 0-type objects.

As for the previous analysed transition, C^{18}O $J = 9$–8 $FWHM_n$ values for the WISH low-mass protostars are similar to those measured for the Cygnus Class I YSOs (see Table 5.7) and smaller to those obtained across the WISH intermediate- and high-mass sub-samples. No further conclusions can be extracted from the WILL and Cygnus Class 0 samples due to the small number of detections.

5.3.3. Analysis of the broad velocity component for H_2O spectra

Figure 5.3 compares the $FWHM_b$ results from the H_2O data of the WILL (dashed bins) and WISH Class 0 and Class I objects (right-top and -bottom panels respectively). The distribution of the values for the Class 0 and Class I objects seems to peak at similar $FWHM_b$ values (~25 km s^{-1}). While ~35% of the WISH Class 0 protostars show $FWHM_b$ larger than 40 km s^{-1}, only the $FWHM_b$

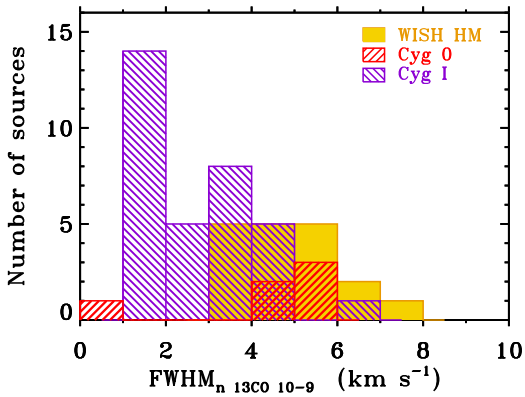

Figure 5.4: *FWHM* of the narrow component ($FWHM_n$) constrained for the ^{13}CO $J = 10$–9 spectra of the Cygnus Class 0 (Cyg 0: right-dashed red) and Class I type (Cyg I: left-dashed purple) YSOs and the $FWHM_n$ of the WISH high-mass YSOs (yellow).

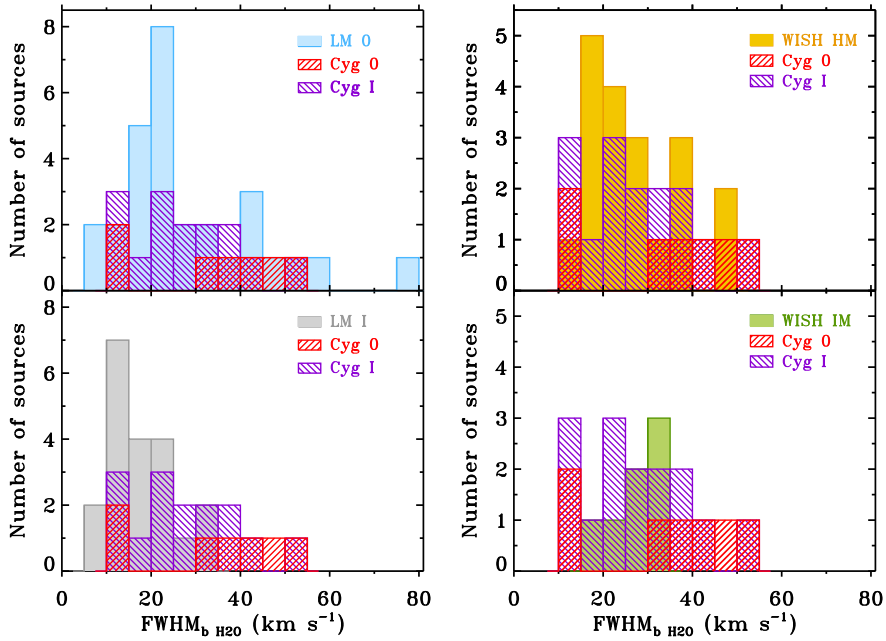

Figure 5.5: (*Left*) $FWHM_b$ of the H_2O spectra calculated for the Cygnus Class 0 (Cyg 0: dashed red bars) and Class I-type (Cyg I: dashed purple bars) YSOs and the $FWHM_b$ of the low-mass Class 0 (LM 0: light blue) protostars (*top*) and Class I (LM I: light grey) objects (*bottom*). The low-mass Class 0 and Class I values are a combination of the results from the WILL and WISH samples shown in Fig. 5.3. (*Right*) Same as *left* histograms but the Cygnus $FWHM_b$ values are plotted together with those of the WISH high-mass (WISH HM: yellow bars) YSOs (*top*) and the WISH intermediate-mass (WISH IM: light green bars) objects (*bottom*).

of ~15% of the WILL Class 0 objects exceeds that velocity. As the central column of Table 5.4 shows, the cavity shock component is similar for the studied water lines of the WILL and WISH low-mass protostars and the results derived from the WISH YSOs are consistent with those obtained from WILL.

In Fig. 5.5, the $FWHM_b$ results from the Cygnus H_2O observations are compared to those obtained from combining the WILL and WISH low-mass values for the Class 0 and Class I objects respectively (left-column histograms) and to the $FWHM_b$ derived from the WISH intermediate- and high-mass YSOs (right-column panels). The $FWHM_b$ values of the Cygnus Class 0 type YSOs are

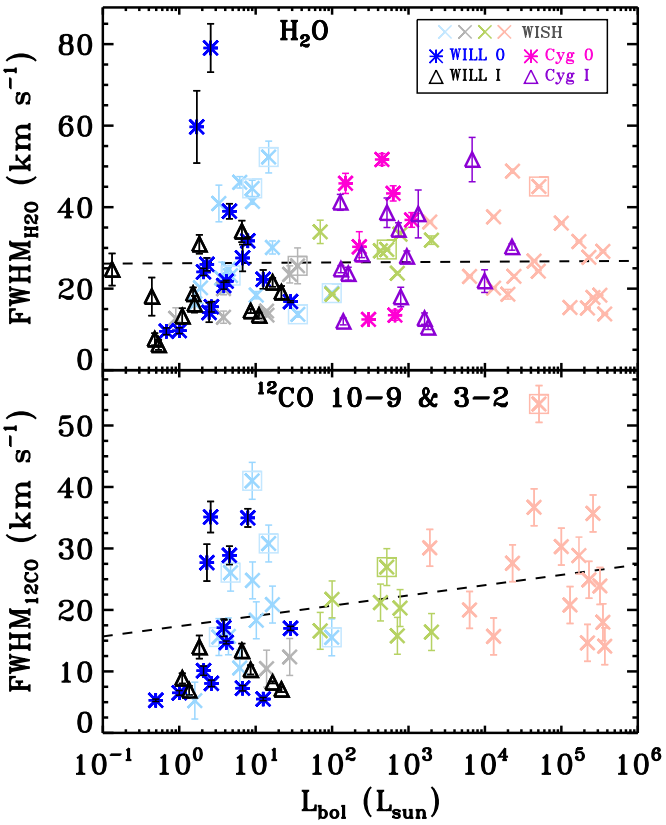

Figure 5.6: (*Top*) $FWHM_{\rm b}$ of the H_2O observations (same for all transitions) for the WILL and Cygnus YSOs versus their bolometric luminosity over-plotted together with those of WISH. (*Bottom*) Same as top panel but for the ^{12}CO $J = 10$–9 and $J = 3$–2 observations of the WILL and WISH objects. The blue and pink asterisk symbols correspond to the WILL and Cygnus Class 0 YSOs (WILL 0 and Cyg 0). The black and purple triangle symbols to the WILL and Cygnus Class I-type objects (WILL I and Cyg I). The light blue, grey, green and red crosses show the WISH low-mass Class 0, Class I, intermediate- and high-mass YSOs respectively (see Fig. 2 of San José-García et al. subm.). The low- and intermediate-mass WISH sources with detected EHV components are surrounded by a box, as well as the high-mass YSO with triangular water line profiles. The variation of $FWHM_{\rm b}$ with $L_{\rm bol}$ considering the WILL, Cygnus and WISH surveys are indicated with a dash line.

comparable to the wider cavity shock component detected within the low-mass Class 0 protostars. The small number of available Cygnus Class 0 sources complicates the comparison of these results with those of the other samples. In the case of the Cygnus Class I type YSOs, the majority of the cavity shock components have widths between 10 and 30 km s^{-1}, so the distribution of their $FWHM_{\rm b}$ is comparable to that measured from the combination of the WILL and WISH low-mass Class I protostars or to that of the WISH high-mass objects.

The histograms of Figs. 5.3 and 5.5 show that the Class 0-type objects are characterised with broader cavity shock components than their more evolved counterparts independently of the mass of the sample.

Finally, Fig. 5.6 shows the $FWHM_{\rm b}$ values of the water lines for the WILL and Cygnus sources (top-panel) and those derived for the ^{12}CO $J = 10$–9 spectra for the WILL protostars (bottom-panel) as a function of $L_{\rm bol}$. The $FWHM_{\rm b}$ measured for the WISH sample are over-plotted with lighter colours. Appendix 5.A shows the analogous figure but using the results from the *FWZI* parameter. The $FWHM_{\rm b}$ values for the water observations are spread across a large range of ve-

Table 5.8: *Left-column:* Number of considered sources (D), slope (m), intercept (n), and Pearson correlation coefficient (r) of the power-law fit to the logarithm of the line luminosity versus the logarithm of the bolometric luminosity (L_{bol}). *Right-column:* Same as above, but for the correlation between the luminosity corresponding to the broad velocity component and L_{bol}. The parameters from the correlation have been calculated considering only the WILL and Cygnus samples (*top*-lines) and including the results from the WISH YSOs (*bottom*-lines).

Line	WILL + Cygnus							
	$\log(L) = n + m \cdot \log(L_{bol})$				$\log(L_{broad}) = n + m \cdot \log(L_{bol})$			
	D[a]	m	n	r	D[a]	m	n	r
H_2O 1_{11}-0_{00}	41	0.58±0.08	-3.24±0.17	0.74/4.7σ	33	0.81±0.07	-3.24±0.15	0.89/5.0σ
H_2O 2_{02}-1_{11}	50	0.78±0.12	-3.25±0.14	0.85/6.0σ	38	0.77±0.07	-3.04±0.15	0.89/5.4σ
^{13}CO 10–9	60	0.87±0.10	-3.85±0.13	0.90/7.0σ	8	0.95±0.25	-4.23±0.32	0.94/2.3σ
	WILL + Cygnus + WISH							
H_2O 2_{02}-1_{11}	103	0.83±0.04	-3.34±0.11	0.92/9.2σ	85	0.78±0.03	-3.17±0.10	0.92/8.5σ
^{13}CO 10–9	107	0.92±0.03	-4.04±0.10	0.95/9.8σ		–	–	–

Notes. [a] Number of YSOs with positive integrated intensity considered in the correlation calculation.

locities (from 5 to ~80 km s^{-1}), a scatter which may be related to the intrinsic properties of the source such as inclination of the outflows, opening angle, etc. The scatter and range of velocities are comparable to that measured for the WISH low-mass protostars, with the difference that the separation between the Class 0 and Class I objects is more obvious within WISH, i.e. the bulk of the $FWHM_b$ results for the WILL Class 0 protostars are located across a velocity interval similar to that occupied by the WILL Class I objects. For the ^{12}CO $J = 10$–9 spectra, the range of WILL and WISH low-mass $FWHM_b$ parameters is comparable and no Class I objects are seen as outliers for either of these sub-samples.

The ratio between the broad velocity component of the H_2O and ^{12}CO observations is calculated for the WILL protostars and the averaged value for the Class 0 objects is 0.7±0.1 and for the Class I protostars is 0.5±0.1. This ratio is generally smaller than unity, which means that for the low-mass protostars $FWHM_b$ of H_2O is wider than that of ^{12}CO $J = 10$–9, consistent with the results of the WISH results in chapter 4 (see Table 4.3) and Kristensen et al. (2012). For both samples, only those sources with prominent outflows, such as L1448-MM, show ratios above unity. Since the ^{12}CO $J = 10$–9 transition was not observed for the Cygnus objects, we cannot extend this analysis to these YSOs.

5.3.4. Line luminosity study

The total integrated intensity, W, of the WILL and Cygnus ^{13}CO $J = 10$–9, H_2O 1_{11}-0_{00} and 2_{02}-1_{11} lines are converted to line luminosity, $L_{^{13}CO}$ and L_{H_2O}, using the same method as in Sects. 2.3.2 and 4.3.3. This parameter accounts for the difference in distance between these two samples of objects and allows us to compare these results with those obtained for WISH and extragalactic objects (see Sect. 2.4.3 and 4.4.3 of this thesis).

Figure 5.7 shows the line luminosity of the H_2O 1_{11}-0_{00} transition (top panel), the 2_{02}-1_{11} line (middle panel) and the ^{13}CO $J = 10$–9 data (bottom panel) as a function of L_{bol} for the WILL and Cygnus YSOs, and their log(L)-log(L_{bol}) relation is indicated with a solid line. This type of correlation was previously measured for the WISH sample (see chapters 2 and 4). The WISH values are then over-plotted in lighter colours for the H_2O 2_{02}-1_{11} and ^{13}CO $J = 10$–9 transitions and their relation with L_{bol} shown with a grey dotted line, together with the correlation measured when combining all WILL, Cygnus and WISH YSOs (dashed line). The parameters of these relations and the Pearson correlation coefficients, r, are summarised for these lines in Table 5.8, left-column. The significance of these correlations, determined as in Marseille et al. (2010), is larger than 4.8σ.

The slope is close to unity, especially when the WILL, Cygnus and WISH sources are combined, except for the H_2O 1_{11}-0_{00} (1113 GHz) transition. As previously indicated, the WILL and

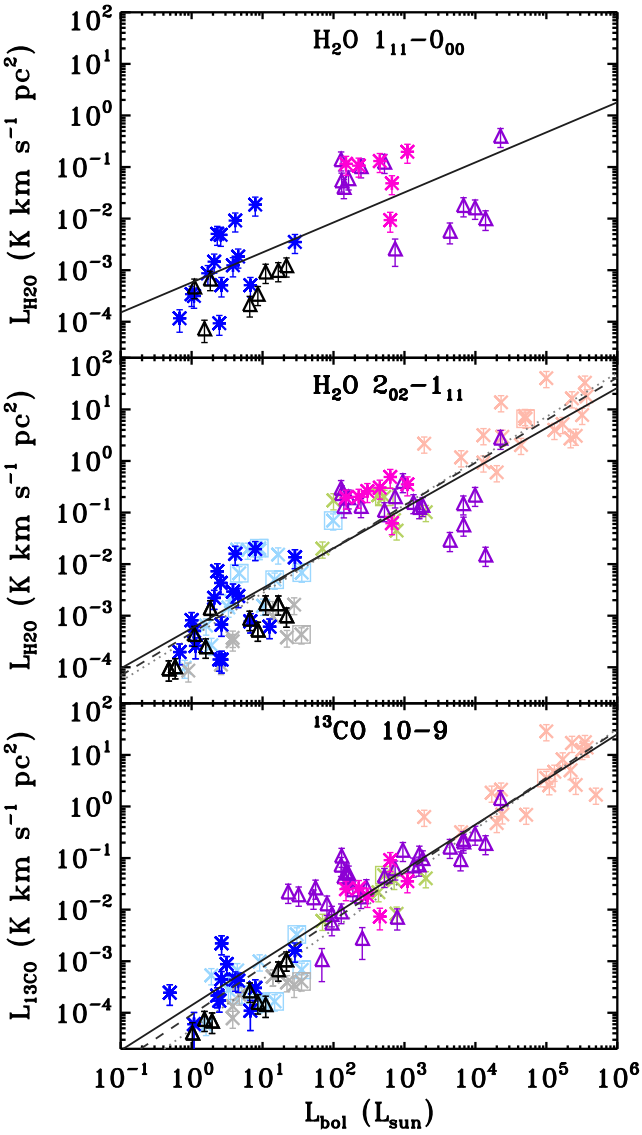

Figure 5.7: (*Top*) Line luminosity of the H_2O 1_{11}-0_{00} (1113 GHz) line, (*middle*) H_2O 2_{02}-1_{11} (988 GHz) transition and (*bottom*) ^{13}CO $J = 10$–9 spectra versus the source bolometric luminosity. The line luminosity for the WISH sources are over-plotted. The symbol code is the same as in Fig. 5.6. The solid line indicates the correlation of the logarithm of the total line luminosity, log(L), and log(L_{bol}) considering only the WILL and Cygnus samples while the dashed lighter line included the results from the WISH YSOs (results of the fits in Table 5.8). The dotted grey line shows the log(L)-log(L_{bol}) relation considering only the WISH survey.

Cygnus spectra of this water line are more affected by absorption from the colder envelope than higher excited transitions, causing the decrease of the slope value. In particular, five Class I Cygnus YSOs with relatively high L_{bol} are characterised with low L_{H_2O} values. The spectra of three of these outliers show strong absorptions and the other two objects (Cyg GR06 03 and Cyg GR05 11) have surprisingly narrow profiles with no broad component. These two sources are also outliers for the H_2O 2_{02}-1_{11} transition due to their narrow profiles.

Within the WILL sample, a separation between the Class 0 and Class I protostars is observed for both water transitions. The Class I objects have lower L_{H_2O} values than their less evolved counterparts, as already seen for the WISH low-mass protostars. In the case of the Cygnus sample, no significant distinction between the Class 0 and Class I-type objects is seen, although the former YSOs have larger L_{H_2O} values. Regarding the ^{13}CO $J = 10$–9 transition, the $L_{^{13}CO}$ values do not show a segregation between Class 0 and I objects.

In general, the WILL and Cygnus results overlap to those obtained for the WISH YSOs with similar L_{bol} with fit results which are similar within the uncertainties (solid, dashed and dotted lines in Fig. 5.7). Therefore, the comparison with WISH confirms that the results derived in chapter 4 hold for a larger sample of sources, strengthening, from the statistical point of view, the conclusions derived from the line luminosity analysis. The ^{13}CO $J = 10$–9 line shows the largest significance and r coefficient (as well as number of detected sources).

As for the WISH data, the integrated intensity of the area constituting the broad velocity component of the H_2O and ^{13}CO $J = 10$–9 spectra is converted to line luminosity, L_{broad}. A correlation between this parameter and L_{bol} is also measured for the H_2O 1_{11}-0_{00}, 2_{02}-1_{11} and ^{13}CO $J = 10$–9 lines but with lower significance because the number of Cygnus sources considered has decreased (see parameters in right-column of Table 5.8 and Fig. 5.13 in the Appendix). In the case of the H_2O 1_{11}-0_{00} transition, the slope of the correlation increases if just L_{broad} is considered, becoming similar to that measured for the other studied transitions. The reason is that the previous outlier Cygnus Class I sources do not contribute to this calculation since their profiles do not show a broad velocity component. The parameters of the log-log correlations for the H_2O 2_{02}-1_{11} line considering either L_{H_2O} or L_{broad} are similar within the uncertainty. This result confirms that the total water emission is dominated by the cavity shock component (see Table 5.5).

The ^{13}CO $J = 10$–9 L_{broad} does not significantly correlate with L_{bol} because the number of spectra with detected line wings is small (eight out of 61). Therefore, the ^{13}CO $J = 10$–9 line luminosity is dominated by envelope emission rather than by entrained outflowing gas emission.

5.4. Discussion

5.4.1. Comparison with WISH results

Most of the results obtained from the analysis and interpretation of the H_2O and CO observations for the WISH sample have been evaluated and confirmed with the study of the WILL and Cygnus data. Starting with the shapes of the water spectra, we also concluded that the profiles for a given source are similar but scaled up or down in intensity with a consistent set of kinematic components. This indicates that the dynamical properties of the gas probed by the observed transitions are similar for each YSO and that in principle just the line with the highest signal-to-noise can be chosen to characterise the outflow/shock-related kinematics (see Table 5.2 and Mottram et al. 2014). Three types of kinematical components, corresponding to quiescent envelope, cavity shock and spot shock, are detected in the WILL sources. On the other hand, only envelope and cavity shocks emission are identified in the studied water observations of the Cygnus sample. We can exclude that the absence of spot shock components in the Cygnus observations is due to *S/N* limitations because, as presented in Sect. 5.2.2, these data have at least comparable (1113 GHz line) or a factor of >3 higher (988 GHz line) *S/N* than that of WILL. This is in line with the conclusions of chapter 4 based on the study of the excited water lines. In that case, the spectra of only one intermediate-mass YSO NGC 2071, a bright object located at half the distance of Cygnus, showed conclusive evidence of a spot shock component (EHV feature type). Therefore, the spot shock emission may not be detected in YSOs located further than 1 kpc away because this concentrated emission is affected by beam dilution. Alternatively, the absence of spot shock components could also be due to the fact that most of the Cygnus YSOs are in a later evolutionary stage (Class I type) and the percentage of detections of spot shocks is generally lower than that in Class 0 sources, as confirmed by the WISH and WILL low-mass Class I protostars. A medium-broad outflow component identified by van der Tak et al. (2013) in absorption in the ground-state lines of the WISH

high-mass YSOs may also be from spot shocks. However, this component is not conclusively seen in any of the excited water lines, so the identification in these sources remains uncertain.

Regarding the width of the water line profiles, we corroborate that both $FWHM_b$ and *FWZI* values are spread across a wide range of velocities (∼5–80 km s^{-1} and ∼5–150 km s^{-1}, respectively), a similar interval to that measured for WISH, and with no trend with luminosity over 5 orders of magnitude. The scatter may be related to the geometry and intrinsic properties of each source (inclination of the outflows, opening angle, etc.). Despite the scatter, the line profiles of the WILL and Cygnus Class 0 type objects are broader than those of their more evolved Class I counterparts by typically 5–10 km s^{-1}, especially for the broad velocity component. As concluded from the WISH YSOs, this suggest differences in the dynamical conditions dominating the shocked material of Class 0 and Class I YSOs. This decrease of the line profile with the evolution is independent of the mass of the studied sample and of the excitation of the water lines (Mottram et al. 2014).

Moving to the cavity shock component, the average contribution of this component to the total integrated intensity of the WILL and Cygnus water lines is larger than that measured for WISH. The remaining fraction of intensity mainly comes from the spot component in the case of the low-mass Class 0 protostars and from the envelope for the other sub-samples of YSOs, as we concluded from WISH (Mottram et al. 2014). Interestingly, the results obtained from the cavity shock component are in general similar across a large and diverse sample of YSOs. This may indicate that common physical (dynamical) processes are taking place along the outflow system, shaping the water line profiles, which do not seem to depend on the luminosity or envelope mass of the source.

Finally, a strong correlation between the line luminosity, L, and L_{bol} is measured across the WILL and Cygnus samples, as for WISH. This relation holds and becomes more statistically significant when the three surveys are combined. Similarly, the fraction of the luminosity corresponding to the cavity shock component, L_{broad}, correlates with L_{bol} for the WILL and Cygnus samples. However, when considering only the WILL and Cygnus surveys, the obtained slope from the log(L)-log(L_{bol}) relation is smaller than that obtained for WISH. In addition, a separation between the line luminosity of the WILL Class 0 and Class I protostars is observed for the H_2O transition but not for the ^{13}CO line. This, together with the reduction of spot shock component detections in more evolved sources, suggests that the decrease in water emission, L_{H_2O}, from Class 0 to Class I objects is caused by a drop of the velocity of the gas constituting the outflow at later evolutionary stages (i.e. outflows become less energetic) rather than by the decrease of the envelope mass and density, as Mottram et al. (2014) concluded.

5.4.2. WILL and Cygnus samples

The water and CO observations allow us to compare the type of YSOs composing the WILL, Cygnus and WISH samples as well as derive some particular properties about these groups of objects.

The studied CO and H_2O line profiles of the WILL Class 0 protostars are in general narrower (from 5 to 20 km s^{-1}) than those of their WISH low-mass analogues (see Fig. 5.3). The percentage of ^{12}CO $J = 10$–9 spectra decomposed into several velocity components is significantly smaller as well (42% versus 72%). These results and the fact that the CO and H_2O 1_{10}-1_{01} (557 GHz) data have comparable *S/N* to those of WISH suggest that the WISH low-mass Class 0 sample contains a larger number of sources with unusually energetic outflows. Therefore, the intrinsic properties of the WISH and WILL Class 0 objects may be different. On the other hand, the results from the WISH and WILL Class I protostars are comparable, suggesting that the type of objects composing both samples could be similar. A difference between the WISH and WILL Class I observations is that spot shock components offset from the source velocity are detected for three sources of the former sub-sample but have not been identified in any YSO from the latter sub-group.

In the case of the Cygnus Class 0 objects, the line profiles of the C^{18}O $J = 9$–8 line and envelope component of the ^{13}CO $J = 10$–9 transition show similar *FWHM* values as those measured for the WISH high-mass YSOs, which are generally classified as Class 0 type objects. However, given the small number of Cygnus Class 0 sources, no further comparison can be performed between these objects. On the other hand, the line profiles of the ^{13}CO, C^{18}O and H_2O observations

for the Cygnus Class I YSOs are comparable to those measured for the WISH intermediate-mass and low-mass Class I objects. The number of Cygnus sources whose ^{13}CO $J = 10$–9 spectra show a broad velocity component is smaller than that measured for the WISH high-mass YSOs, for which is present in all line profiles. In addition, the ^{13}CO $J = 10$–9 transition was detected for half of observed Cygnus sources, a similar percentage as that found for the WISH low-mass Class I protostars. Therefore, we conclude that the Cygnus sample is mainly composed by a collection of intermediate- and even low-mass YSOs in a Class I type evolutionary stage, i.e. sources with less massive envelopes and especially less energetic outflows.

5.4.3. Environmental exploration of the Cygnus X region

The Cygnus survey allows us to investigate whether the specific physical conditions of different parts across this star-formation region are reflected in the observed ^{13}CO and H_2O spectra. As indicated in the introduction, Cygnus X is a perfect laboratory to perform environment studies due to the heterogeneity of its structure and the possibility of removing biases related to distance. Ultimately, the information extracted from the observed line profiles contributes to the characterisation of the region.

Starting with ^{13}CO $J = 10$–9, Fig. 5.8 shows the location of the observed YSOs on the 24 μm map of the Cygnus X region. The different evolutionary stages of these objects are indicated with two types of symbols: circles are Class 0 and triangles Class I YSOs. Non-detections are presented in green. Most of the targeted YSOs of this survey as well as most of the detections and Class 0 type objects (7/8) are located in the CygX-North cloud (targets designed as "GR01"). In this region, characterised by filamentary structure and large chains of protostellar candidates, star formation is more active than in the South cloud, influenced by the Cyg OB2 association (Kryukova et al. 2014, and references therein). Interestingly, the YSOs with detection in ^{13}CO located in the North cloud show negative and positive $v_{\rm LSR}$, which means that these objects belong to different structures present along the light of sight (see also Schneider et al. 2006). As expected, the non-detected YSOs of this GR01 are those with the lowest $L_{\rm bol}$ values and later evolutionary stage. Due to the lack of information about their $v_{\rm LSR}$ values, we cannot determine whether the sources with non-detection in ^{13}CO $J = 10$–9 situated in the CygX-North are equally distributed across the different velocity structures or are mostly located in either of these layers. This analysis will be useful to further characterise these structures and have a better understanding of this region. Regarding those YSOs not detected in ^{13}CO and located in the center and south of Cygnus, they are generally in a late Class I type evolutionary stage but with different luminosities.

Figure 5.9 presents the sources with detection in the H_2O 2_{02}-1_{11} (988 GHz) transition. The symbol code is the same as in Fig. 5.8 (green also indicates non-detections). In pink are shown the Cygnus sources for which the *FWZI* is lower than 40 km s^{-1} and in cyan those with *FWZI* above that velocity. The orange triangle symbols highlight the four YSOs with bright and surprisingly narrow profiles (*FWZI* $\leq$ 12 km s^{-1} and *FWHM* $\leq$ 8 km s^{-1}) with no broad component. Consistent with the previous discussion, this plot shows that most of the cyan symbols (wider profiles) are concentrated in the northern cloud of Cygnus, where a larger number of YSOs with energetic outflows are forming. In general the water line profiles of these objects can be decomposed into two velocities components, i.e. a cavity shock component is identified. Regarding the detection statistics across the sample, we previously indicated that most of the Class 0 objects detected in water (7/8) are located in the North region. For the Class I sub-sample, almost half of these detected YSOs belong to that region as well, while the remaining Class I sources are spread across the other regions of Cygnus X. Independently of the evolutionary stage, the sources detected in water are generally luminous objects ($L_{\rm bol}$>100 $L_\odot$). Similarly as for the ^{13}CO $J = 10$–9 line, the non-detections are predominantly less massive sources in Class I or even later evolutionary stages.

Finally, the preliminary study of the four YSOs with particularly narrow profiles (orange triangles of Fig. 5.9) suggests that the water emission is caused by a PDR rather than coming from the protostar itself. The lack of broad velocity component for those profiles supports the idea that the emission does not come from an actual YSO. Therefore, these sources are either too massive and significantly evolved, such as for GR02 01, GR04 02 or GR05 11 (Motte et al. 2007; Schneider

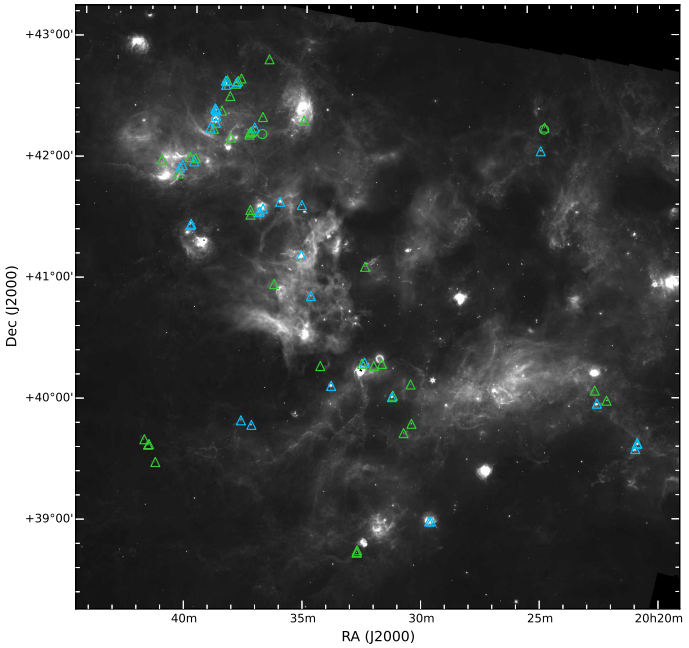

Figure 5.8: Distribution of the 41 YSOs for which the ^{13}CO $J = 10$–9 line is detected (cyan) and those objects with no detection (green) plotted on top of the 24 micron map of Cygnus X star formation region observed with *Spitzer*. The circle and triangle symbols tag the Class 0 and Class I type YSOs, respectively.

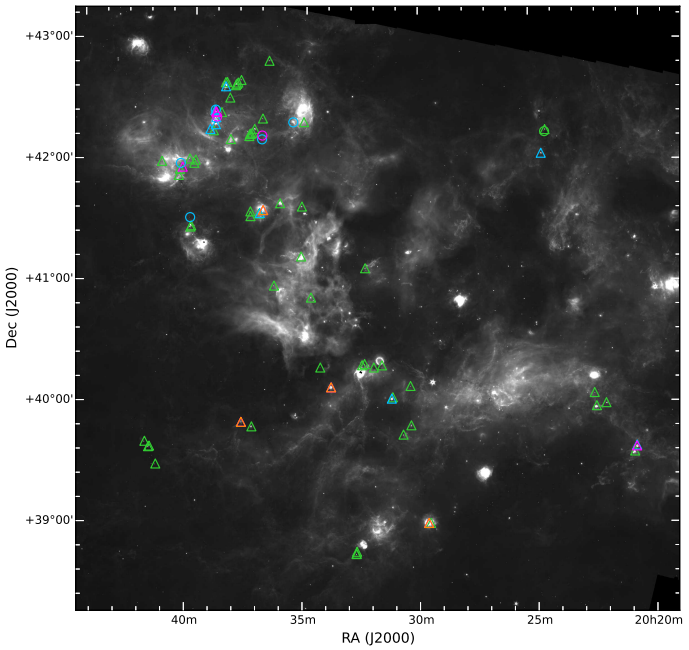

Figure 5.9: Same as Fig. 5.8 but plotting the 25 YSOs for which the H_2O 2_{02}-1_{11} (988 GHz) transition is detected (cyan and magenta colours) together with those sources with no detection in this line (green). In magenta are shown the objects for which the *FWZI* of the 988 GHz spectra is < 40 km s^{-1} and in cyan those with *FWZI* > 40 km s^{-1}. The four Class I YSOs with surprisingly narrow line profiles (*FWZI* ≤ 12km s^{-1}) and without cavity shock component are plotted in orange.

et al. 2012), or have a nearby HII region which affects their excitation conditions (as for GR06 03; Motte et al. 2007). Further investigation is therefore required to unveil the properties and true nature of these sources.

To summarise, from the preliminary characterisation of the Cygnus X region, we confirm that the studied sample of YSOs is constituted by low- and intermediate-mass Class I objects. The majority of the detections are located in the North cloud, characterised by a more recent and intense

star formation activity.

5.5. Conclusions

The analysis of the H_2O and CO HIFI observations of the WILL protostars and the Cygnus YSOs in terms of line profile and line luminosity allows us to evaluate previous results obtained for the WISH survey using a more uniform and statistically supported framework. The following results obtained for the WISH YSOs are confirmed by the studied WILL and Cygnus samples:

- The different water transitions of a given source have similar line profiles and number of velocity components. While the WILL low-mass protostars show three types of velocity components (quiescent envelope, cavity shock and spot shock), for the Cygnus low-, intermediate-mass YSOs only the envelope and cavity shock components are identified. The lack of spot shock component detections for the Cygnus observations may be due to beam dilution effects or to the fact that a large percentage of these objects are in a late evolutionary stage (Class I).

- More than 80% of the total water emission is generated by gas in (non-dissociative) shocks along the outflow cavity wall, independent of the luminosity of the source. The physical origin of the remaining emission is primarily from spot shocks in the case of the low-mass Class 0 objects and mainly envelope for the other type of YSOs.

- The results derived for the cavity shock component such as its width, the scatter of the $FWHM_b$ values and the fraction of this emission contributing to the total L_{H_2O} suggest that the physical processes regulating the dynamical properties of outflow cavity walls seem independent of the luminosity or envelope mass of the source (i.e. the characteristics of the broad velocity component are similar across the studied sample of sources).

- The line emission of the H_2O and ^{13}CO $J = 10$–9 lines strongly correlate with L_{bol}. The slope of this log-log relation is slightly smaller than that obtained for WISH. The interpretation of these results is ongoing.

- A decrease of H_2O emission, L_{H_2O}, from Class 0 to Class I in the low-mass protostars is likely due to the reduction of the velocity of the gas constituting the outflow rather than by a decrease of the envelope mass and density of the object (Mottram et al. 2014).

We conclude that the WILL Class 0 sample is composed of protostars with (on-average) less energetic outflows than those constituting the WISH low-mass Class 0, while the intrinsic properties of the WILL and WISH Class I objects are more similar. On the other hand, the Cygnus survey is mostly composed of intermediate-mass (and even low-mass) YSOs in a late evolutionary stage (Class I type). This explains the relatively low percentage of ^{13}CO $J = 10$–9 and H_2O detections (~45% of the observed sources). Finally, the preliminary environmental study of the Cygnus X region indicates that most of the H_2O and ^{13}CO detections, Cygnus Class 0 objects and those which the broader water line profiles are generally located in the North cloud of this complex. This is consistent with the the fact that the star formation is more active and spontaneous in the North cloud than for CygX-South.

Acknowledgments

This work is supported by the European Community's Seventh Framework Programme FP7/2007-2013 under grant agreement 238258 (LASSIE) and by the Space Research Organisation Netherlands (SRON). Astrochemistry in Leiden is supported by the Netherlands Research School for Astronomy (NOVA), by a Royal Netherlands Academy of Arts and Sciences (KNAW) professor prize, by EU A-ERC grant 291141 CHEMPLAN and by a Spinoza grant and grant 614.001.008

from the Netherlands Organisation for Scientific Research (NWO). HIFI has been designed and built by a consortium of institutes and university departments from across Europe, Canada and the United States under the leadership of SRON Netherlands Institute for Space Research, Groningen, The Netherlands and with major contributions from Germany, France and the US. Consortium members are: Canada: CSA, U.Waterloo; France: CESR, LAB, LERMA, IRAM; Germany: KOSMA, MPIfR, MPS; Ireland, NUI Maynooth; Italy: ASI, IFSI-INAF, Osservatorio Astrofisico di Arcetri- INAF; Netherlands: SRON, TUD; Poland: CAMK, CBK; Spain: Observatorio Astronómico Nacional (IGN), Centro de Astrobiología (CSIC-INTA). Sweden: Chalmers University of Technology - MC2, RSS & GARD; Onsala Space Observatory; Swedish National Space Board, Stockholm University - Stockholm Observatory; Switzerland: ETH Zurich, FHNW; USA: Caltech, JPL, NHSC.

5.A. *FWZI* analysis

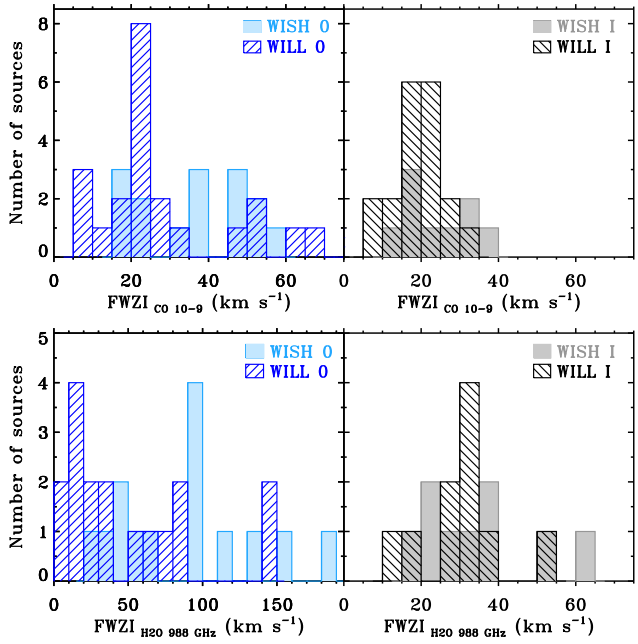

Figure 5.10: Histograms comparing the *FWZI* values for the ^{12}CO $J = 10$–9 line (*top*-panels) and H_2O 2_{02}-1_{11} (988 GHz) transition (*bottom*-panels) for the WILL and WISH samples. The *left*-panels show the *FWZI* of the WILL Class 0 protostars (dashed blue histogram) and those of the WISH low-mass Class 0 sources (light blue histograms). The *right*-panels compare the *FWZI* of the WILL low-mass Class I protostars (dashed black histogram) to those of the WISH Class I sources (light grey histogram). For the H_2O 2_{02}-1_{11} transition for the Class 0 objects, the *FWZI* values are binned to 10 km s^{-1}. For the Class I protostars and ^{12}CO line, the results are binned to 5 km s^{-1}.

5.A.1. H_2O spectra

The *FWZI* parameter is calculated for all observed water transitions of the WILL and Cygnus surveys and the results are compared to those obtained for the WISH objects.

The bottom panels of Fig. 5.10 present the *FWZI* values calculated for the H_2O 2_{02}-1_{11} (988 GHz) transition of the Class 0 protostars taken from the WILL and WISH low-mass samples (bottom-left histogram) and their Class I counterparts (bottom-right histogram). The range of velocities covered by the WISH Class 0 protostars is larger than that of the WILL analogues and ~60% of the 988 GHz WISH spectra show *FWZI* > 80 km s^{-1}, percentage which decreases to ~29% for the WILL Class 0 objects. The fact that the 988 GHz WILL spectra are narrower than those of WISH could be due to the difference in the *S/N* of these observations, which is higher for latter survey. However, the observations of the 557 GHz water transition have comparable *S/N* for both WILL and WISH observations and still the line wings of the WILL data are narrower than those of WISH. This suggests that the WISH low-mass Class 0 sub-sample may contain a larger number of sources with particularly energetic outflows (which show "bullet" emission) than the WILL Class 0 sub-sample. On the other hand, the *FWZI* measured for the WISH and WILL Class I objects (bottom-right histogram of Fig. 5.10) are comparable, independently of the water transition and its *S/N*. This indicates that offset spot shock components are not detected for the WILL Class I objects because this type of shocks are less common in more evolved YSOs. Both results are in line with the $FWHM_b$ analysis.

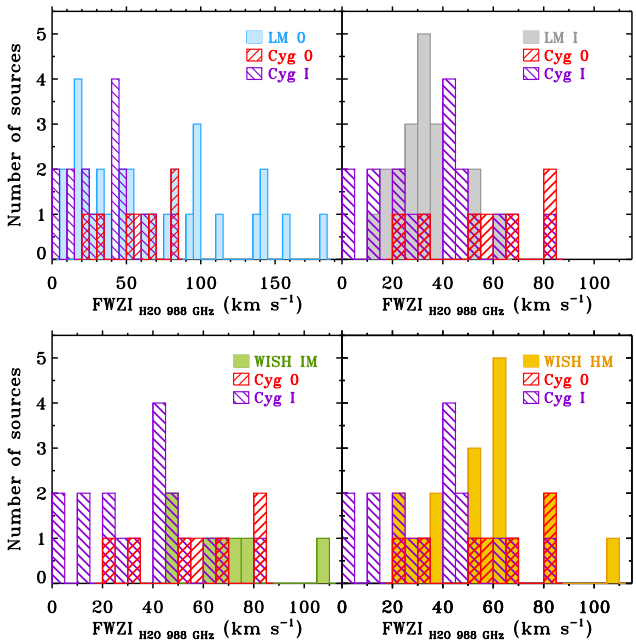

Figure 5.11: Same as Fig. 5.5, but comparing the H_2O 2_{02}-1_{11} (988 GHz) *FWZI* of the Cygnus Class 0 (Cyg 0) and Cygnus Class I (Cyg I) samples to WILL and WISH low-mass Class 0 protostars (LM 0; *top-left*), WILL and WISH low-mass Class I objects (LM I; *top-right*), WISH intermediate-mass (WISH IM; *bottom-left*) and high-mass (WISH HM; *bottom-right*) YSOs.

The *FWZI* values calculated for the H_2O 2_{02}-1_{11} (988 GHz) spectra of the Cygnus sources are compared to those of the WILL and WISH low-mass sample of protostars, and to the WISH intermediate- and high-mass sub-samples in Fig. 5.5. The spectra of the Cygnus Class 0 YSOs (red dashed histogram) show *FWZI* values comparable to those measured for the WISH intermediate- (green histogram) and high-mass (yellow histogram) YSOs (bottom panels of Fig. 5.5 and Table 5.3). On the other hand, the data of the Cygnus Class I objects (purple dashed lines) are characterised by narrower profiles and the distribution of the *FWZI* is similar to that of the low-mass Class I protostars, but shifted by ∼10 km s^{-1} to larger velocities (top-right histogram). Therefore, these results suggests that the bulk of the Cygnus sample is constituted of low- and intermediate-mass YSOs in a late evolutionary stage (Class I-type).

5.A.2. CO spectra

The *FWZI* values constrained for the ^{12}CO $J = 10$–9 data of the WILL Class 0 and Class I protostars are compared to those constrained for the WISH low-mass analogues in the top histograms of Fig. 5.10. For the Class 0 protostars (top-left histogram), the range of velocities covered by the WILL spectra (blue dashed lines) is larger than that measured for their WISH equivalents (light blue lines). However, only 23% of the WILL Class 0 sources show profiles with *FWZI* > 30 km s^{-1}. This percentage increases up to 60% for the WISH Class 0 objects. For the Class I protostars, the distribution of the ^{12}CO $J = 10$–9 *FWZI* values (top-right histogram) of both WILL and WISH samples peaks at similar velocities (with a shift of ∼5 km s^{-1}). Since the *S/N* of these observations is similar for both surveys, this confirms the results derived from the water lines: the WISH Class 0 sample may be composed by a larger number of sources with energetic outflows than their WILL analogues, while both WILL and WISH Class I samples have protostars with similar characteristics.

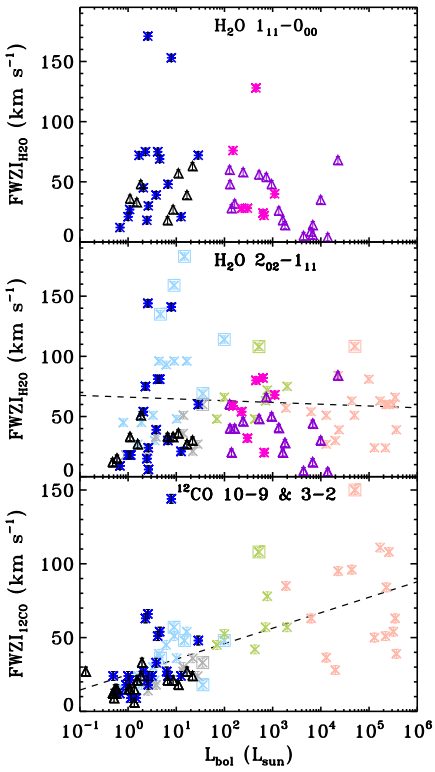

Figure 5.12: *FWZI* of the H_2O 1_{11}-0_{00} (1113 GHz) line (*top*), the H_2O 2_{02}-1_{11} (557 GHz) transition (*middle*) and the ^{12}CO $J = 10$–9 and $J = 3$–2 line (*bottom*) derived for the WILL, Cygnus and WISH YSOs as a function of source bolometric luminosity. The symbols and colour codes are the same as in Fig. 5.6. A linear fit to the data is indicated with a dash line to highlight any possible trend of *FWZI* with L_{bol}.

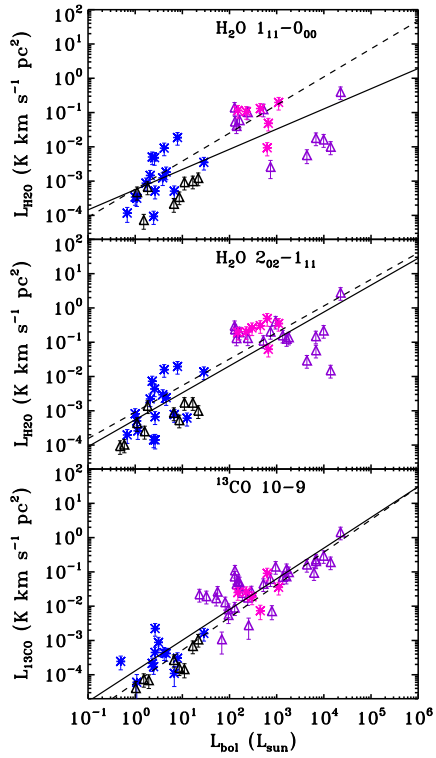

Figure 5.13: Same as Fig. 5.7 but including the relation between the line luminosity derived from the broad velocity component and L_{bol} for only the WILL and Cygnus samples. The solid line indicates the linear correlation of the logarithm of the total line luminosity, log(L), and log(L_{bol}). The dashed line shows the log-log correlation of the luminosity measured for the broader Gaussian velocity component only (L_{broad}) and log(L_{bol}).

Finally, Fig. 5.12 shows the *FWZI* values of the WILL and Cygnus objects together with those of WISH, for the H_2O 1_{11}-0_{00} (1113 GHz; top), 2_{02}-1_{11} (988 GHz; middle) and ^{12}CO $J = 10$–9 (bottom) lines as a function of source bolometric luminosity. As already seen for the WISH water data, the scatter of the *FWZI* values is large (from ~5 to 180 km s^{-1}) and likely related to the intrinsic properties of the source (inclination of the outflows, etc). In general, the *FWZI* of the Cygnus sample show a smaller range in velocities than that of the low-mass Class 0 protostars. In the case of the ^{12}CO $J = 10$–9, the *FWZI* of the WILL and WISH low-mass protostars are similarly scattered and cover a comparable interval of velocities.

5.B. WILL data

5.B.1. Specific sources

AQU 01: in the H_2O 1_{10}-1_{01} spectrum an extra velocity component not seen in the other water transitions is detected. According to the line decomposition method (Sect. 5.2.4), that component would be considered a cavity shock component due to its width and position. However, this emission may come from IRAS 4A, a close by protostar which falls into the 557 GHz beam. For smaller beams this component disappears, which means that the emission is offset from the centre of the beam, reenforcing the hypothesis that the emission comes from the nearby protostar. To conclude, the AQU 01 557 GHz spectrum is contaminated by the cavity or spot shock emission of IRAS 4A. In order to fix this issue we did not consider this component when designating the name and physical origin of the multiple velocity components also detected in the other water lines.

AQU 06: the cavity shock component is not detected over $3\sigma_{\rm rms}$ in the 557 GHz line, the only transition that seems to show a weak broad component. The spectra of the water lines is dominated by absorption and envelope emission, neither of which can be properly constrained with the line decomposition method. Therefore, other basic parameters such as *FWZI* and *W* are considered as rough estimations.

Per 02: the water spectra show a clear broad water emission coming from the outflows. However, the emission from the outflow of another source interacts with that generated by Per 02 causing a broad absorption that prevents from properly constraining the Gaussian parameters fitting the cavity shock component. Since any output value would not be reliable due to that strong and broad absorption, we exclude this protostar from our studied sample. Further details about this specific interaction and the analysis of maps of this region will be presented in the WILL overview paper (Mottram et al. in prep.).

Per 07: the H_2O 1_{10}-1_{01} line is the only water transition detected and it shows an intense absorption feature along its broad velocity component. This absorption, offset from the source velocity, prevents from properly constraining the values of the Gaussian profile fitting the cavity shock component. Since no other water transition observed with a smaller beam is detected, we considered the measured value of $FWHM_{\rm b}$ as a lower limit of this parameters. Therefore, the results from the decomposition of this water line are not considered for further analysis.

Per 12: the broad cavity shock component detected in the 557 GHz is not observed in the other water transitions. This is again related to the differences in beam of those observations: in the case of the 1_{10}-1_{01} line, the beam is big enough to include a nearby source (IRAS 4A). The fitted cavity shock component does not belong to Per 12 but to IRAS 4A. For this reason, we do not consider this component in the analysis of the WILL data.

Finally, the W40 04, W40 05 and W40 07 are not considered as detections since only absorption is observed in the water lines.

Table 5.9: Observed and fitted properties of the WILL H_2O 1_{11}-0_{00} and H_2O 1_{10}-1_{01} lines.

Source	H_2O 1_{11}-0_{00}				H_2O 1_{10}-1_{01}			
	rms[a] (mK)	T_{MB}^{peak} (K)	$\int T_{MB} dv$[b] (K km s^{-1})	*FWZI* (km s^{-1})	rms[a] (mK)	T_{MB}^{peak} (K)	$\int T_{MB} dv$[b] (K km s^{-1})	*FWZI* (km s^{-1})
AQU 01	24	0.18	7.44 ± 0.20	171	10	0.19	6.76 ± 0.05	183
AQU 02	27	0.17	1.91 ± 0.10	39	10	0.13	1.62 ± 0.03	51
AQU 03	23	< 0.07	–	–	5	0.02	-0.07 ± 0.01	15
AQU 04	26	< 0.08	–	–	6	0.01	-0.05 ± 0.01	12
AQU 05	23	0.12	0.53 ± 0.07	21	6	0.06	0.35 ± 0.02	30
AQU 06	24	< 0.07	–	–	6	0.03	0.10 ± 0.02	21
CHA 01	23	< 0.07	–	–	5	0.04	0.32 ± 0.02	27
CHA 02	24	< 0.08	–	–	5	< 0.02	–	–
CRA 01	24	0.15	0.57 ± 0.07	18	6	0.07	0.39 ± 0.02	33
OPH 02	24	0.22	2.29 ± 0.08	27	7	0.10	1.12 ± 0.02	39
PER 01	24	0.16	3.45 ± 0.13	69	8	0.08	2.11 ± 0.03	84
PER 03	35	0.69	35.09 ± 0.20	153	28	0.38	20.72 ± 0.04	159
PER 04	24	< 0.07	–	–	4	< 0.01	–	–
PER 05	26	0.17	1.75 ± 0.11	57	7	0.08	0.72 ± 0.02	27
PER 06	26	0.10	0.41 ± 0.07	18	10	0.14	2.07 ± 0.03	66
PER 08	26	0.20	1.88 ± 0.09	39	6	0.21	1.94 ± 0.02	48
PER 09	27	0.15	2.32 ± 0.12	63	11	0.21	1.16 ± 0.02	39
PER 10	25	0.11	0.96 ± 0.10	48	10	0.10	2.03 ± 0.03	75
PER 11	24	1.23	17.26 ± 0.14	75	5	0.67	11.44 ± 0.04	87
PER 12	28	0.11	0.60 ± 0.08	27	6	0.26	3.50 ± 0.03	66
PER 13	25	0.10	0.22 ± 0.05	12	6	0.09	0.65 ± 0.02	33
PER 14	21	0.10	1.28 ± 0.11	48	6	0.04	0.61 ± 0.03	63
PER 15	25	0.10	1.64 ± 0.13	72	11	0.07	2.48 ± 0.04	105
PER 16	23	0.05	-0.16 ± 0.04	6	5	0.02	0.27 ± 0.03	72
PER 17	28	< 0.08	–	–	6	0.03	0.37 ± 0.02	42
PER 18	24	< 0.07	–	–	8	0.04	1.25 ± 0.04	123
PER 19	26	0.12	0.90 ± 0.09	36	6	0.03	0.13 ± 0.02	24
PER 20	23	0.40	9.52 ± 0.13	75	5	0.23	6.54 ± 0.03	75
PER 21	26	0.19	2.75 ± 0.11	45	6	0.11	2.38 ± 0.03	54
PER 22	22	0.13	0.96 ± 0.08	30	7	0.14	0.96 ± 0.02	42
SCO 01	22	< 0.07	–	–	5	< 0.02	–	–
SERS 01	23	0.04	-0.49 ± 0.06	15	6	0.02	0.11 ± 0.03	54
SERS 02	28	0.68	5.41 ± 0.13	72	9	0.73	9.03 ± 0.04	99
TAU 01	24	0.12	0.39 ± 0.09	33	7	0.06	0.72 ± 0.03	78
TAU 02	22	< 0.07	–	–	5	0.03	0.14 ± 0.01	18
TAU 03	22	< 0.08	–	–	6	0.02	0.18 ± 0.02	27
TAU 04	27	< 0.08	–	–	5	0.02	0.07 ± 0.01	18
TAU 06	27	< 0.08	–	–	5	0.03	0.12 ± 0.01	12
TAU 07	26	< 0.08	–	–	6	< 0.02	–	–
TAU 08	23	< 0.08	–	–	6	< 0.02	–	–
TAU 09	22	< 0.07	–	–	5	0.03	0.16 ± 0.02	21
W40 02	22	0.12	-0.29 ± 0.07	21	7	0.08	0.47 ± 0.03	51
W40 04	22	0.02	-0.56 ± 0.06	14	6	0.03	-0.05 ± 0.01	9
W40 05	27	0.05	-0.39 ± 0.06	15	6	0.03	-0.14 ± 0.02	21
W40 07	22	< 0.07	–	–	6	< 0.02	–	–

Notes. *FWZI* has been calculated by binning the spectra to 3 km s^{-1}. (^{a}) In 0.27 km s^{-1} bin. (^{b}) Integrated over the interval of velocities defined by the *FWZI*.

Table 5.10: Observed and fitted properties of the WILL H_2O 2_{02}-1_{11} and H_2O 3_{12}-2_{21} lines.

Source	H_2O 2_{02}-1_{11}				H_2O 3_{12}-2_{21}			
	rms[a] (mK)	T_{MB}^{peak} (K)	$\int T_{MB} dv$[b] (K km s^{-1})	*FWZI* (km s^{-1})	rms[a] (mK)	T_{MB}^{peak} (K)	$\int T_{MB} dv$[b] (K km s^{-1})	*FWZI* (km s^{-1})
AQU 01	23	0.12	5.02 ± 0.17	144	111	< 0.33	–	–
AQU 02	22	0.24	3.41 ± 0.09	39	108	0.39	2.93 ± 0.34	27
AQU 03	22	< 0.07	–	–	107	< 0.37	–	–
AQU 04	24	< 0.07	–	–	116	< 0.35	–	–
AQU 05	21	0.15	0.95 ± 0.06	18	102	< 0.37	–	–
AQU 06	20	< 0.06	–	–	107	< 0.37	–	–
CHA 01	23	0.10	0.88 ± 0.08	27	99	< 0.30	–	–
CHA 02	22	< 0.07	–	–	112	< 0.34	–	–
CRA 01	23	0.20	0.66 ± 0.06	15	99	< 0.36	–	–
OPH 02	22	0.24	2.68 ± 0.09	33	109	0.44	2.53 ± 0.31	24
PER 01	24	0.24	3.43 ± 0.14	81	104	< 0.31	–	–
PER 03	40	0.53	27.89 ± 0.19	141	114	0.54	16.08 ± 0.76	126
PER 04	23	< 0.07	–	–	100	< 0.30	–	–
PER 05	25	0.24	2.46 ± 0.09	36	124	< 0.37	–	–
PER 06	23	0.16	1.24 ± 0.09	33	113	< 0.35	–	–
PER 08	26	0.22	2.45 ± 0.08	27	123	0.40	1.95 ± 0.30	18
PER 09	29	0.19	1.43 ± 0.09	30	118	< 0.35	–	–
PER 10	22	0.10	1.11 ± 0.08	30	103	< 0.36	–	–
PER 11	21	1.47	22.61 ± 0.13	81	112	1.71	26.28 ± 0.51	63
PER 12	25	0.14	0.72 ± 0.06	18	122	< 0.37	–	–
PER 13	25	0.12	0.28 ± 0.05	9	112	< 0.34	–	–
PER 14	23	0.12	1.99 ± 0.10	51	102	< 0.31	–	–
PER 15	74	0.12	2.95 ± 0.15	90	105	< 0.32	–	–
PER 16	22	0.08	0.37 ± 0.07	18	101	0.36	0.39 ± 0.19	9
PER 17	24	< 0.07	–	–	120	< 0.35	–	–
PER 18	24	< 0.08	–	–	99	< 0.30	–	–
PER 19	25	0.09	0.62 ± 0.08	33	116	< 0.35	–	–
PER 20	24	0.38	10.39 ± 0.13	75	125	0.55	9.05 ± 0.49	57
PER 21	23	0.16	3.15 ± 0.11	54	165	< 0.50	–	–
PER 22	22	0.13	0.96 ± 0.07	24	104	< 0.31	–	–
SCO 01	23	< 0.07	–	–	103	< 0.31	–	–
SERS 01	20	< 0.06	–	–	111	< 0.33	–	–
SERS 02	24	0.92	15.87 ± 0.11	60	117	0.66	12.37 ± 0.49	54
TAU 01	23	< 0.08	–	–	100	< 0.34	–	–
TAU 02	23	0.08	0.38 ± 0.05	12	102	< 0.31	–	–
TAU 03	23	< 0.07	–	–	103	< 0.31	–	–
TAU 04	26	< 0.08	–	–	114	< 0.34	–	–
TAU 06	26	< 0.08	–	–	117	< 0.35	–	–
TAU 07	24	0.10	0.41 ± 0.06	15	124	< 0.37	–	–
TAU 08	23	< 0.07	–	–	102	< 0.31	–	–
TAU 09	21	< 0.07	–	–	106	< 0.32	–	–
W40 02	22	0.10	0.71 ± 0.07	21	103	< 0.31	–	–
W40 04	24	0.10	0.16 ± 0.04	6	107	< 0.37	–	–
W40 05	22	< 0.07	–	–	127	< 0.38	–	–
W40 07	22	< 0.07	–	–	91	< 0.27	–	–

Notes. *FWZI* has been calculated by binning the spectra to 3 km s^{-1}. ([a]) In 0.27 km s^{-1} bin. ([b]) Integrated over the interval of velocities defined by the *FWZI*.

Table 5.11: Observed and fitted properties of the WILL ^{12}CO $J = 10$–9 and ^{12}CO $J = 10$–9 spectra.

Source	^{12}CO $J = 10$–9				^{13}CO $J = 10$–9			
	rms[a] (mK)	T_{MB}^{peak} (K)	$\int T_{MB} dv$[b] (K km s^{-1})	*FWZI* (km s^{-1})	rms[a] (mK)	T_{MB}^{peak} (K)	$\int T_{MB} dv$[b] (K km s^{-1})	*FWZI* (km s^{-1})
AQU 01	97	0.53	8.43 ± 0.48	66	29	< 0.09	–	–
AQU 02	108	1.15	9.76 ± 0.34	33	30	< 0.09	–	–
AQU 03	89	0.35	0.80 ± 0.14	6	25	< 0.08	–	–
AQU 04	91	< 0.31	–	–	25	< 0.08	–	–
AQU 05	91	0.73	4.43 ± 0.28	24	26	< 0.08	–	–
AQU 06	0	0.38	1.36 ± 0.25	18	0	< 0.00	–	–
CHA 01	104	0.67	3.90 ± 0.26	21	25	< 0.08	–	–
CHA 02	93	0.50	2.86 ± 0.33	33	25	0.10	0.19 ± 0.03	3
CRA 01	94	2.84	10.26 ± 0.27	21	25	0.31	0.87 ± 0.04	6
OPH 02	90	2.21	12.33 ± 0.26	21	26	0.22	0.87 ± 0.05	10
PER 01	95	2.20	21.31 ± 0.43	54	25	0.18	0.64 ± 0.05	9
PER 03	104	2.94	52.17 ± 0.69	144	30	0.11	0.47 ± 0.09	26
PER 04	89	0.28	0.75 ± 0.17	9	24	< 0.07	–	–
PER 05	91	1.45	6.50 ± 0.25	18	25	0.11	0.22 ± 0.04	7
PER 06	91	1.49	7.89 ± 0.26	21	25	0.15	0.41 ± 0.03	4
PER 08	106	7.80	35.42 ± 0.30	27	27	0.28	1.06 ± 0.06	18
PER 09	89	14.11	39.05 ± 0.28	24	25	0.74	1.65 ± 0.05	11
PER 10	107	0.82	5.21 ± 0.29	24	25	0.11	0.17 ± 0.07	21
PER 11	91	3.53	35.65 ± 0.42	51	26	0.15	0.68 ± 0.06	12
PER 12	105	0.83	2.24 ± 0.26	21	29	0.15	0.09 ± 0.05	9
PER 13	100	0.67	1.91 ± 0.19	12	28	< 0.08	–	–
PER 14	103	0.83	4.48 ± 0.28	24	28	< 0.09	–	–
PER 15	103	< 0.31	–	–	30	< 0.09	–	–
PER 16	89	0.39	0.86 ± 0.17	9	25	< 0.08	–	–
PER 17	104	0.67	3.36 ± 0.29	27	28	< 0.09	–	–
PER 18	104	1.31	6.98 ± 0.28	24	28	0.09	0.38 ± 0.06	14
PER 19	107	0.55	3.11 ± 0.23	15	27	< 0.08	–	–
PER 20	87	1.47	22.00 ± 0.44	63	24	0.11	0.33 ± 0.04	7
PER 21	161	0.92	7.55 ± 0.47	27	25	< 0.09	–	–
PER 22	105	2.62	12.22 ± 0.25	18	23	0.18	0.69 ± 0.07	21
SCO 01	104	0.60	2.12 ± 0.20	12	25	< 0.08	–	–
SERS 01	106	0.64	4.21 ± 0.31	27	29	< 0.09	–	–
SERS 02	110	5.71	61.76 ± 0.42	48	29	0.37	2.02 ± 0.09	29
TAU 01	105	1.54	4.24 ± 0.26	21	29	0.13	0.33 ± 0.04	6
TAU 02	92	0.69	1.90 ± 0.20	12	23	< 0.07	–	–
TAU 03	93	< 0.28	–	–	23	< 0.07	–	–
TAU 04	105	0.52	2.43 ± 0.22	15	27	< 0.08	–	–
TAU 06	89	1.04	2.28 ± 0.22	15	24	< 0.08	–	–
TAU 07	104	0.71	3.04 ± 0.22	15	27	< 0.08	–	–
TAU 08	103	0.37	1.12 ± 0.17	9	24	< 0.07	–	–
TAU 09	92	1.18	4.23 ± 0.22	15	24	0.10	0.18 ± 0.07	22
W40 02	94	6.19	10.80 ± 0.28	24	24	< 0.07	–	–
W40 04	106	12.13	28.84 ± 0.29	24	29	2.49	2.80 ± 0.06	12
W40 05	105	7.40	26.73 ± 0.29	24	29	0.79	1.11 ± 0.07	17
W40 07	86	0.32	0.66 ± 0.17	9	24	< 0.07	–	–

Notes. *FWZI* has been calculated by binning the spectra to 3 km s^{-1}. (^{a}) In 0.27 km s^{-1} bin. (^{b}) Integrated over the interval of velocities defined by the *FWZI*.

Table 5.12: Observed and fitted properties of the WILL $H_2^{18}O$ 1_{10}-1_{01} and $C^{18}O$ $J = 9$–8 lines.

Source	$H_2^{18}O$ 1_{10}-1_{01}				$C^{18}O$ $J = 9$–8			
	rms[a] (mK)	T_{MB}^{peak} (K)	$\int T_{MB} dv$[b] (K km s^{-1})	*FWZI* (km s^{-1})	rms[a] (mK)	T_{MB}^{peak} (K)	$\int T_{MB} dv$[b] (K km s^{-1})	*FWZI* (km s^{-1})
AQU 01	8	< 0.02	–	–	26	< 0.08	–	–
AQU 02	5	< 0.02	–	–	26	< 0.08	–	–
AQU 03	5	< 0.02	–	–	22	< 0.07	–	–
AQU 04	5	< 0.02	–	–	23	< 0.08	–	–
AQU 05	5	< 0.02	–	–	24	< 0.07	–	–
AQU 06	5	< 0.02	–	–	0	< 0.00	–	–
CHA 01	5	< 0.02	–	–	26	< 0.08	–	–
CHA 02	5	< 0.02	–	–	23	< 0.07	–	–
CRA 01	5	< 0.02	–	–	24	< 0.08	–	–
OPH 02	5	< 0.02	–	–	23	< 0.07	–	–
PER 01	5	< 0.01	–	–	24	< 0.08	–	–
PER 03	5	< 0.02	–	–	30	< 0.09	–	–
PER 04	4	< 0.01	–	–	24	< 0.07	–	–
PER 05	5	< 0.02	–	–	24	< 0.07	–	–
PER 06	5	< 0.02	–	–	25	< 0.09	–	–
PER 08	5	< 0.02	–	–	26	< 0.08	–	–
PER 09	5	< 0.02	–	–	25	< 0.08	–	–
PER 10	5	< 0.02	–	–	24	< 0.08	–	–
PER 11	6	0.05	0.49 ± 0.02	39	25	< 0.08	–	–
PER 12	5	< 0.02	–	–	25	< 0.08	–	–
PER 13	5	< 0.02	–	–	27	< 0.08	–	–
PER 14	5	< 0.02	–	–	26	< 0.08	–	–
PER 15	5	< 0.02	–	–	24	< 0.08	–	–
PER 16	5	< 0.02	–	–	23	< 0.08	–	–
PER 17	5	< 0.02	–	–	27	< 0.08	–	–
PER 18	4	< 0.01	–	–	27	< 0.08	–	–
PER 19	5	< 0.02	–	–	26	< 0.08	–	–
PER 20	5	< 0.02	–	–	24	< 0.07	–	–
PER 21	5	< 0.02	–	–	25	< 0.08	–	–
PER 22	5	< 0.02	–	–	27	< 0.08	–	–
SCO 01	5	< 0.02	–	–	25	< 0.08	–	–
SERS 01	5	< 0.02	–	–	25	< 0.08	–	–
SERS 02	6	0.02	0.25 ± 0.02	30	25	0.10	0.28 ± 0.03	5
TAU 01	4	< 0.01	–	–	25	< 0.08	–	–
TAU 02	5	< 0.01	–	–	25	< 0.08	–	–
TAU 03	5	< 0.02	–	–	25	< 0.08	–	–
TAU 04	4	< 0.01	–	–	26	< 0.08	–	–
TAU 06	5	< 0.02	–	–	23	< 0.07	–	–
TAU 07	5	< 0.02	–	–	27	< 0.08	–	–
TAU 08	5	< 0.02	–	–	23	< 0.08	–	–
TAU 09	5	< 0.02	–	–	23	< 0.07	–	–
W40 02	5	< 0.02	–	–	23	< 0.07	–	–
W40 04	5	< 0.02	–	–	26	0.35	0.43 ± 0.04	7
W40 05	6	< 0.02	–	–	24	0.15	0.05 ± 0.05	12
W40 07	5	< 0.02	–	–	24	< 0.07	–	–

Notes. *FWZI* has been calculated by binning the spectra to 3 km s^{-1}. ([a]) In 0.27 km s^{-1} bin. ([b]) Integrated over the interval of velocities defined by the *FWZI*.

Table 5.13: Gaussian decomposition results for the WILL ^{12}CO $J = 10$–9 data.

Source	Comp.[a]	*FWHM*	$v_{\rm peak}$	$v_{\rm LSR}$	^{12}CO $J = 10$–9	
					$T_{\rm MB}^{\rm peak}$	$\int T_{\rm MB} {\rm d}v^b$
		(km s^{-1})	(km s^{-1})	(km s^{-1})	(K)	(K km s^{-1})
AQU 01	C	35.1 ± 2.5	1.3 ± 1.0	7.6	0.21 ± 0.01	7.80 ± 0.74
AQU 02	E	3.8 ± 0.3	8.5 ± 0.1	7.9	0.77 ± 0.05	3.07 ± 0.35
	C	17.1 ± 1.4	9.5 ± 0.5	7.9	0.38 ± 0.04	6.88 ± 0.95
AQU 03	E	3.6 ± 0.8	7.6 ± 0.3	7.2	0.20 ± 0.04	0.78 ± 0.22
AQU 05	C	6.5 ± 0.4	8.0 ± 0.2	7.4	0.57 ± 0.03	3.95 ± 0.30
CHA 01	E	4.7 ± 0.3	5.3 ± 0.1	4.9	0.63 ± 0.04	3.16 ± 0.29
CHA 02	E	4.1 ± 0.4	2.2 ± 0.2	3.0	0.45 ± 0.04	1.97 ± 0.24
CRA 01	E	3.5 ± 0.1	5.7 ± 0.0	5.6	2.32 ± 0.04	8.67 ± 0.24
OPH 02	E	4.7 ± 0.1	4.0 ± 0.1	4.2	1.74 ± 0.03	8.62 ± 0.27
	C	10.3 ± 0.8	5.1 ± 0.4	4.2	0.35 ± 0.01	3.82 ± 0.28
PER 01	S	5.6 ± 0.2	3.8 ± 0.1	4.1	1.54 ± 0.04	9.22 ± 0.36
	C	28.9 ± 1.5	2.2 ± 0.5	4.1	0.40 ± 0.03	12.38 ± 1.02
PER 03	E	1.8 ± 0.1	5.3 ± 0.0	5.2	1.84 ± 0.09	3.49 ± 0.26
	S	7.0 ± 0.4	8.6 ± 0.2	5.2	1.20 ± 0.04	8.92 ± 0.57
	S	16.7 ± 0.6	62.1 ± 0.2	5.2	0.75 ± 0.02	13.27 ± 0.60
	C	35.0 ± 1.5	16.4 ± 0.7	5.2	0.52 ± 0.02	19.25 ± 1.19
PER 05	E	4.7 ± 0.2	7.5 ± 0.1	7.2	1.19 ± 0.03	6.02 ± 0.26
PER 06	E	3.0 ± 0.2	7.5 ± 0.1	7.3	1.13 ± 0.05	3.60 ± 0.26
	C	13.3 ± 1.2	6.3 ± 0.4	7.3	0.33 ± 0.04	4.68 ± 0.70
PER 08	E	2.2 ± 0.0	7.7 ± 0.0	7.7	5.28 ± 0.09	12.53 ± 0.32
	C	8.2 ± 0.2	7.6 ± 0.0	7.7	2.56 ± 0.08	22.36 ± 0.84
PER 09	E	2.4 ± 0.0	7.8 ± 0.0	7.5	12.30 ± 0.30	30.95 ± 0.21
	C	7.1 ± 0.4	6.8 ± 0.2	7.5	0.81 ± 0.02	6.09 ± 0.36
PER 10	C	7.3 ± 0.4	7.4 ± 0.2	8.6	0.60 ± 0.03	4.63 ± 0.37
PER 11	E	3.4 ± 0.1	7.3 ± 0.0	7.4	1.81 ± 0.05	6.57 ± 0.29
	C	14.7 ± 0.2	5.1 ± 0.1	7.4	1.75 ± 0.04	27.43 ± 0.73
PER 12	E	3.1 ± 0.3	8.0 ± 0.1	7.8	0.51 ± 0.05	1.68 ± 0.23
PER 13	E	2.7 ± 0.3	8.2 ± 0.1	7.9	0.58 ± 0.05	1.65 ± 0.21
PER 14	E	2.0 ± 0.3	6.0 ± 0.1	6.2	0.60 ± 0.06	1.31 ± 0.22
	C	14.0 ± 1.9	6.3 ± 0.7	6.2	0.22 ± 0.03	3.33 ± 0.68
PER 16	E	4.0 ± 0.7	7.1 ± 0.3	7.1	0.23 ± 0.04	0.98 ± 0.23
PER 17	E	1.9 ± 0.3	6.6 ± 0.1	6.4	0.52 ± 0.06	1.06 ± 0.19
PER 18	C	5.3 ± 0.2	7.2 ± 0.1	6.7	1.12 ± 0.04	6.29 ± 0.31
PER 19	C	8.9 ± 0.8	8.1 ± 0.3	6.9	0.34 ± 0.03	3.25 ± 0.40
PER 20	E	4.4 ± 0.2	9.6 ± 0.1	8.9	1.08 ± 0.05	5.07 ± 0.36
	S	7.2 ± 1.0	27.7 ± 0.3	8.9	0.33 ± 0.04	2.58 ± 0.46
	S	11.4 ± 1.8	-5.3 ± 0.8	8.9	0.27 ± 0.04	3.27 ± 0.69
	C	27.7 ± 3.0	19.0 ± 2.0	8.9	0.39 ± 0.02	11.46 ± 1.43
PER 21	C	10.1 ± 0.8	8.1 ± 0.3	8.7	0.62 ± 0.04	6.64 ± 0.65
PER 22	E	2.6 ± 0.1	10.0 ± 0.0	9.8	1.85 ± 0.10	5.15 ± 0.40
	C	8.0 ± 0.5	10.6 ± 0.2	9.8	0.85 ± 0.10	7.32 ± 0.97
SCO 01	E	3.0 ± 0.3	3.9 ± 0.1	3.4	0.55 ± 0.05	1.74 ± 0.23
SERS 01	E	2.9 ± 0.5	8.4 ± 0.2	8.2	0.35 ± 0.05	1.10 ± 0.26
SERS 02	S	5.8 ± 0.2	8.3 ± 0.0	7.8	2.91 ± 0.09	17.82 ± 0.72
	C	17.0 ± 0.3	8.5 ± 0.1	7.8	2.39 ± 0.09	43.27 ± 1.78

Notes. (^{a}) The types of components are: C = cavity shock; E = envelope emission; S = spot shock; A = envelope absorption. (^{b}) Integrated intensity of each velocity component approximated to the gaussian fit.

Table 5.14: Gaussian decomposition results for the WILL ^{12}CO $J = 10$–9 data (continuation).

Source	Comp.[a]	*FWHM*	$v_{\rm peak}$	$v_{\rm LSR}$	^{12}CO $J = 10$–9	
					$T_{\rm MB}^{\rm peak}$	$\int T_{\rm MB} {\rm d}v^b$
		(km s^{-1})	(km s^{-1})	(km s^{-1})	(K)	(K km s^{-1})
TAU 01	E	2.4 ± 0.1	6.8 ± 0.0	6.8	1.36 ± 0.05	3.50 ± 0.21
TAU 02	E	2.2 ± 0.2	7.0 ± 0.1	7.1	0.61 ± 0.05	1.45 ± 0.18
TAU 04	C	6.9 ± 0.7	6.7 ± 0.3	6.4	0.34 ± 0.03	2.49 ± 0.35
TAU 06	E	2.8 ± 0.2	7.3 ± 0.1	7.0	0.85 ± 0.04	2.52 ± 0.19
TAU 07	E	4.7 ± 0.3	7.2 ± 0.1	6.3	0.60 ± 0.04	3.04 ± 0.29
TAU 08	E	3.9 ± 0.7	6.4 ± 0.3	5.5	0.27 ± 0.04	1.12 ± 0.26
TAU 09	E	3.9 ± 0.2	5.9 ± 0.1	5.6	0.94 ± 0.04	3.97 ± 0.23
W40 02	E	0.9 ± 0.0	5.1 ± 0.0	4.8	4.82 ± 0.09	4.51 ± 0.13
	C	5.5 ± 0.3	4.9 ± 0.1	4.8	0.95 ± 0.05	5.58 ± 0.40

Notes. $(^a)$ The types of components are: C = cavity shock; E = envelope emission; S = spot shock; A = envelope absorption. $(^b)$ Integrated intensity of each velocity component approximated to the gaussian fit.

Table 5.15: Gaussian decomposition results for the WILL ^{13}CO $J = 10$–9 and C^{18}O $J = 9$–8 data.

Source	Comp.[a]	*FWHM*	$v_{\rm peak}$	$v_{\rm LSR}$	^{13}CO $J = 10$–9	
					$T_{\rm MB}^{\rm peak}$	$\int T_{\rm MB} {\rm d}v^b$
		(km s^{-1})	(km s^{-1})	(km s^{-1})	(K)	(K km s^{-1})
CHA 02	E	2.2 ± 0.4	2.6 ± 0.2	3.0	0.08 ± 0.01	0.19 ± 0.04
CRA 01	E	2.7 ± 0.1	5.8 ± 0.0	5.6	0.30 ± 0.01	0.87 ± 0.05
OPH 02	C	6.5 ± 0.4	3.5 ± 0.2	4.2	0.13 ± 0.01	0.89 ± 0.08
PER 01	E	4.3 ± 0.3	4.2 ± 0.1	4.1	0.15 ± 0.01	0.70 ± 0.06
PER 05	E	2.4 ± 0.3	7.9 ± 0.1	7.2	0.11 ± 0.01	0.27 ± 0.04
PER 06	E	3.2 ± 0.3	6.8 ± 0.1	7.3	0.14 ± 0.01	0.47 ± 0.06
PER 08	E	2.0 ± 0.2	7.9 ± 0.1	7.7	0.18 ± 0.02	0.38 ± 0.06
	C	10.3 ± 1.4	8.0 ± 0.5	7.7	0.07 ± 0.01	0.75 ± 0.16
PER 09	E	1.4 ± 0.1	7.9 ± 0.0	7.5	0.58 ± 0.02	0.87 ± 0.05
	C	5.3 ± 0.5	7.2 ± 0.2	7.5	0.14 ± 0.02	0.81 ± 0.13
PER 10	E	2.7 ± 0.5	8.7 ± 0.2	8.6	0.07 ± 0.01	0.20 ± 0.05
PER 11	E	4.9 ± 0.4	7.8 ± 0.2	7.4	0.12 ± 0.01	0.63 ± 0.07
PER 12	E	0.8 ± 0.2	8.2 ± 0.1	7.8	0.16 ± 0.03	0.14 ± 0.04
PER 20	E	2.8 ± 0.3	8.8 ± 0.1	8.9	0.10 ± 0.01	0.29 ± 0.04
PER 22	C	6.9 ± 0.5	9.8 ± 0.2	9.8	0.10 ± 0.01	0.72 ± 0.07
SERS 02	E	2.6 ± 0.2	8.0 ± 0.1	7.8	0.25 ± 0.01	0.69 ± 0.07
	C	16.1 ± 1.5	9.5 ± 0.6	7.8	0.08 ± 0.01	1.34 ± 0.19
TAU 01	E	2.4 ± 0.3	7.1 ± 0.1	6.8	0.12 ± 0.01	0.30 ± 0.05
TAU 09	E	1.9 ± 0.3	5.7 ± 0.1	5.6	0.09 ± 0.01	0.18 ± 0.04
					C^{18}O $J = 9$–8	
SERS 02	C	7.2 ± 1.1	8.4 ± 0.5	7.8	0.05 ± 0.01	0.41 ± 0.08

Notes. $(^a)$ The types of components are: C = cavity shock; E = envelope emission; S = spot shock; A = envelope absorption. $(^b)$ Integrated intensity of each velocity component approximated to the gaussian fit.

Table 5.16: Gaussian decomposition results for the WILL H_2O spectra.

Source	Comp.[a]	$FWHM$	v_{peak}	v_{LSR}	H_2O 1_{10}-1_{01}		H_2O 1_{11}-0_{00}		H_2O 2_{02}-1_{11}		H_2O 3_{12}-2_{21}	
					T_{MB}^{peak}	$\int T_{MB} dv^b$	T_{MB}^{peak}	$\int T_{MB} dv^b$	T_{MB}^{peak}	$\int T_{MB} dv^b$	T_{MB}^{peak}	$\int T_{MB} dv^b$
		(km s^{-1})	(km s^{-1})	(km s^{-1})	(K)	(K km s^{-1})	(K)	(K km s^{-1})	(K)	(K km s^{-1})	(K)	(K km s^{-1})
AQU 01	S	6.8 ± 2.5	0.5 ± 0.8	7.6	0.06 ± 0.02	0.46 ± 0.22	0.02 ± 0.03	0.14 ± 0.19	0.05 ± 0.03	0.33 ± 0.22	< 0.33	< 5.69
	S	45.6 ± 18.6	63.2 ± 7.5	7.6	0.02 ± 0.01	0.46 ± 0.22	0.02 ± 0.03	0.14 ± 0.19	0.05 ± 0.03	0.33 ± 0.22	< 0.33	< 5.69
	C	79.1 ± 6.0	-11.1 ± 3.0	7.6	0.05 ± 0.01	0.46 ± 0.22	0.09 ± 0.01	0.14 ± 0.19	0.06 ± 0.01	0.33 ± 0.22	< 0.33	< 5.69
AQU 02	S	12.5 ± 3.3	7.1 ± 0.6	7.9	0.03 ± 0.00	0.97 ± 0.00	< 0.08	< 2.57	0.11 ± 0.05	1.53 ± 0.75	< 0.33	< 10.23
	C	20.7 ± 0.9	6.9 ± 0.3	7.9	0.11 ± 0.01	0.97 ± 0.00	0.13 ± 0.01	2.57 ± 0.00	0.09 ± 0.05	1.53 ± 0.75	0.15 ± 0.03	10.23 ± 0.00
AQU 05	C	9.7 ± 0.7	9.1 ± 0.3	7.4	0.06 ± 0.01	0.58 ± 0.09	0.11 ± 0.02	1.12 ± 0.24	0.10 ± 0.01	1.03 ± 0.13	< 0.31	< 7.44
AQU 06	C	27.2 ± 7.6	13.3 ± 3.2	8.3	0.01 ± 0.00	0.28 ± 0.12	< 0.07	< 4.96	< 0.06	< 4.23	< 0.32	< 21.91
CHA 01	C	16.2 ± 2.1	9.5 ± 0.9	4.9	0.02 ± 0.00	0.38 ± 0.09	< 0.07	< 2.84	0.05 ± 0.01	0.82 ± 0.18	< 0.30	< 12.15
CRA 01	C	14.2 ± 2.4	7.3 ± 0.9	5.6	0.02 ± 0.00	0.31 ± 0.09	0.05 ± 0.01	0.69 ± 0.25	0.01 ± 0.01	0.18 ± 0.19	< 0.30	< 10.59
OPH 02	C	14.5 ± 0.5	2.9 ± 0.2	4.2	0.09 ± 0.00	1.36 ± 0.08	0.19 ± 0.01	2.87 ± 0.21	0.17 ± 0.01	2.58 ± 0.16	0.18 ± 0.04	2.82 ± 0.63
PER 01	S	6.0 ± 1.2	5.3 ± 0.5	4.1	0.03 ± 0.00	0.39 ± 0.00	< 0.07	< 1.10	0.10 ± 0.02	0.66 ± 0.18	< 0.31	< 4.68
	C	39.0 ± 1.9	-1.8 ± 0.8	4.1	0.05 ± 0.00	0.39 ± 0.00	0.09 ± 0.01	1.10 ± 0.00	0.06 ± 0.01	0.66 ± 0.18	< 0.31	< 4.68
PER 03	S	25.2 ± 0.9	59.1 ± 0.4	5.2	0.17 ± 0.01	4.62 ± 0.25	0.39 ± 0.01	10.36 ± 0.44	0.32 ± 0.01	8.46 ± 0.40	0.20 ± 0.03	5.26 ± 0.76
	C	31.7 ± 0.9	22.0 ± 0.3	5.2	0.32 ± 0.01	4.62 ± 0.25	0.62 ± 0.01	10.36 ± 0.44	0.49 ± 0.01	8.46 ± 0.40	0.19 ± 0.03	5.26 ± 0.76
	S	59.7 ± 6.6	-27.8 ± 3.0	5.2	0.08 ± 0.01	4.62 ± 0.25	0.39 ± 0.01	10.36 ± 0.44	0.32 ± 0.01	8.46 ± 0.40	0.20 ± 0.03	5.26 ± 0.76
PER 05	C	13.4 ± 0.7	9.0 ± 0.3	7.2	0.06 ± 0.01	0.82 ± 0.09	0.15 ± 0.02	2.18 ± 0.27	0.17 ± 0.01	2.38 ± 0.20	< 0.37	< 12.57
PER 06	S	7.2 ± 1.1	9.3 ± 0.3	7.3	0.08 ± 0.01	0.60 ± 0.14	< 0.08	< 1.40	< 0.07	< 1.28	< 0.34	< 6.12
	C	34.1 ± 2.6	5.9 ± 1.0	7.3	0.05 ± 0.01	0.60 ± 0.14	< 0.08	< 1.40	0.04 ± 0.01	1.28 ± 0.00	< 0.34	< 6.12
PER 08	S	6.5 ± 0.5	9.0 ± 0.2	7.7	0.11 ± 0.01	0.76 ± 0.09	0.10 ± 0.03	0.68 ± 0.22	0.13 ± 0.02	0.90 ± 0.17	0.34 ± 0.11	2.31 ± 0.78
	C	21.5 ± 1.1	5.7 ± 0.5	7.7	0.08 ± 0.01	0.76 ± 0.09	0.08 ± 0.01	0.68 ± 0.22	0.08 ± 0.01	0.90 ± 0.17	< 0.37	< 2.31
PER 09	E	4.3 ± 1.3	7.2 ± 0.5	7.5	0.03 ± 0.00	0.36 ± 0.00	< 0.08	< 0.87	0.10 ± 0.03	0.45 ± 0.18	< 0.36	< 3.81
	C	19.1 ± 1.5	6.8 ± 0.6	7.5	0.05 ± 0.01	0.36 ± 0.00	0.09 ± 0.01	0.87 ± 0.00	0.05 ± 0.01	0.45 ± 0.18	< 0.36	< 3.81
PER 10	S	12.2 ± 3.2	7.0 ± 0.7	8.6	0.05 ± 0.02	0.69 ± 0.28	< 0.08	< 2.36	< 0.07	< 2.04	< 0.31	< 9.47
	C	27.5 ± 3.3	6.6 ± 1.0	8.6	0.05 ± 0.02	0.69 ± 0.28	0.04 ± 0.01	2.36 ± 0.00	0.04 ± 0.01	2.04 ± 0.00	< 0.31	< 9.47
PER 11	S	5.0 ± 0.2	8.7 ± 0.1	7.4	0.29 ± 0.02	1.56 ± 0.11	0.37 ± 0.06	1.98 ± 0.31	0.72 ± 0.03	3.84 ± 0.23	0.40 ± 0.16	2.12 ± 0.87
	C	21.8 ± 0.2	4.5 ± 0.1	7.4	0.47 ± 0.01	1.56 ± 0.11	0.70 ± 0.02	1.98 ± 0.31	0.76 ± 0.02	3.84 ± 0.23	1.04 ± 0.08	2.12 ± 0.87
PER 12	C	8.9 ± 1.5	9.7 ± 0.6	7.8	0.02 ± 0.00	0.47 ± 0.00	0.08 ± 0.02	0.80 ± 0.24	0.09 ± 0.02	0.82 ± 0.23	< 0.37	< 8.23
	O	19.5 ± 0.4	14.4 ± 0.2	7.8	0.16 ± 0.00	0.47 ± 0.00	< 0.09	< 0.80	< 0.08	< 0.82	< 0.37	< 8.23
PER 13	E	3.5 ± 0.7	8.5 ± 0.3	7.9	0.05 ± 0.01	0.17 ± 0.06	0.06 ± 0.03	0.21 ± 0.12	0.09 ± 0.02	0.33 ± 0.10	< 0.34	< 2.92
	C	9.5 ± 0.8	11.2 ± 0.6	7.9	0.05 ± 0.01	0.17 ± 0.06	< 0.08	< 0.21	< 0.08	< 0.33	< 0.34	< 2.92

Notes. [a] The types of components are: C = cavity shock; E = envelope emission; S = spot shock; A = envelope absorption; O = a component generated from another source only detected in the 557 GHz line due to the size of the beam. [b] Integrated intensity of each velocity component approximated to the gaussian fit.

Table 5.17: Gaussian decomposition results for the WILL H_2O spectra (continuation).

Source	Comp.[a]	$FWHM$	v_{peak}	v_{LSR}	H_2O 1_{10}-1_{01}		H_2O 1_{11}-0_{00}		H_2O 2_{02}-1_{11}		H_2O 3_{12}-2_{21}	
					T_{MB}^{peak}	$\int T_{MB} dv^b$	T_{MB}^{peak}	$\int T_{MB} dv^b$	T_{MB}^{peak}	$\int T_{MB} dv^b$	T_{MB}^{peak}	$\int T_{MB} dv^b$
		(km s^{-1})	(km s^{-1})	(km s^{-1})	(K)	(K km s^{-1})	(K)	(K km s^{-1})	(K)	(K km s^{-1})	(K)	(K km s^{-1})
PER 14	S	3.5 ± 2.2	3.5 ± 0.9	6.2	0.02 ± 0.01	0.06 ± 0.05	< 0.06	< 0.56	< 0.07	< 0.62	< 0.31	< 2.73
	C	30.9 ± 2.3	8.3 ± 1.1	6.2	0.02 ± 0.01	0.06 ± 0.05	0.04 ± 0.01	0.56 ± 0.00	0.06 ± 0.01	0.62 ± 0.00	< 0.31	< 2.73
PER 15	S	12.8 ± 3.1	11.8 ± 1.4	6.8	0.03 ± 0.01	0.44 ± 0.14	< 0.08	< 2.47	< 0.22	< 7.14	< 0.32	< 10.18
	S	19.3 ± 4.2	65.3 ± 1.2	6.8	0.03 ± 0.01	0.44 ± 0.14	< 0.08	< 2.47	< 0.22	< 7.14	< 0.32	< 10.18
	C	59.7 ± 8.9	27.2 ± 4.5	6.8	0.03 ± 0.00	0.44 ± 0.14	0.03 ± 0.00	2.47 ± 0.00	0.04 ± 0.00	7.14 ± 0.00	< 0.32	< 10.18
PER 16	S	10.9 ± 4.2	5.0 ± 1.8	7.1	0.02 ± 0.00	0.47 ± 0.00	< 0.07	< 1.93	0.04 ± 0.01	0.42 ± 0.21	< 0.30	< 8.34
	C	59.2 ± 13.5	13.6 ± 5.7	7.1	0.01 ± 0.00	0.47 ± 0.00	< 0.07	< 1.93	< 0.07	< 0.42	< 0.30	< 8.34
PER 17	C	24.7 ± 3.9	10.5 ± 1.6	6.4	0.02 ± 0.00	0.49 ± 0.12	< 0.08	< 5.24	< 0.07	< 4.56	< 0.36	< 22.29
PER 18	S	17.5 ± 7.4	16.1 ± 2.3	6.7	0.02 ± 0.01	0.32 ± 0.17	< 0.07	< 3.17	< 0.07	< 3.19	< 0.30	< 13.14
	C	63.2 ± 12.5	19.9 ± 3.9	6.7	0.02 ± 0.01	0.32 ± 0.17	< 0.07	< 3.17	< 0.07	< 3.19	< 0.30	< 13.14
PER 19	C	13.2 ± 1.9	6.5 ± 0.7	6.9	0.01 ± 0.00	0.20 ± 0.06	0.08 ± 0.02	1.18 ± 0.29	0.05 ± 0.01	0.68 ± 0.22	< 0.35	< 11.64
PER 20	S	21.2 ± 0.5	27.0 ± 0.3	8.9	0.17 ± 0.00	3.84 ± 0.13	0.32 ± 0.01	7.29 ± 0.27	0.31 ± 0.01	6.98 ± 0.28	0.27 ± 0.04	6.21 ± 1.02
	C	26.0 ± 1.6	0.6 ± 0.9	8.9	0.09 ± 0.00	3.84 ± 0.13	0.09 ± 0.01	7.29 ± 0.27	0.13 ± 0.01	6.98 ± 0.28	0.12 ± 0.04	6.21 ± 1.02
PER 21	S	5.2 ± 1.0	23.9 ± 0.4	8.7	0.02 ± 0.01	0.12 ± 0.04	0.06 ± 0.02	0.36 ± 0.12	0.04 ± 0.02	0.23 ± 0.10	0.36 ± 0.11	1.97 ± 0.71
	C	24.1 ± 0.9	7.6 ± 0.3	8.7	0.09 ± 0.00	0.12 ± 0.04	0.12 ± 0.01	0.36 ± 0.12	0.11 ± 0.01	0.23 ± 0.10	< 0.50	< 1.97
PER 22	C	15.5 ± 1.3	11.4 ± 0.5	9.8	0.05 ± 0.01	0.80 ± 0.12	0.07 ± 0.01	1.19 ± 0.24	0.06 ± 0.01	1.03 ± 0.16	< 0.31	< 12.18
	C	42.4 ± 9.3	10.5 ± 3.9	8.2	0.01 ± 0.00	1.06 ± 0.00	< 0.07	< 3.78	< 0.06	< 3.24	< 0.33	< 17.73
SERS 02	C	16.8 ± 0.2	11.1 ± 0.1	7.8	0.68 ± 0.01	12.23 ± 0.24	0.68 ± 0.02	12.13 ± 0.44	0.78 ± 0.02	14.05 ± 0.33	0.63 ± 0.09	11.22 ± 1.62
TAU 01	C	18.7 ± 1.6	4.5 ± 0.7	6.8	0.04 ± 0.00	0.82 ± 0.10	0.04 ± 0.01	0.75 ± 0.20	< 0.07	< 3.33	< 0.30	< 14.16
TAU 02	C	7.6 ± 1.5	8.1 ± 0.6	7.1	0.02 ± 0.01	0.18 ± 0.06	< 0.07	< 1.26	0.05 ± 0.01	0.36 ± 0.13	< 0.31	< 5.86
TAU 03	C	18.1 ± 4.7	8.2 ± 1.9	7.4	0.01 ± 0.00	0.25 ± 0.10	< 0.07	< 3.03	< 0.07	< 3.16	< 0.31	< 14.01
TAU 04	C	10.6 ± 3.9	7.1 ± 1.5	6.4	0.01 ± 0.00	0.12 ± 0.06	< 0.08	< 2.18	< 0.08	< 2.08	< 0.34	< 9.14
TAU 06	C	6.2 ± 1.2	6.8 ± 0.4	7.0	0.03 ± 0.01	0.19 ± 0.06	< 0.08	< 1.26	< 0.08	< 1.24	< 0.35	< 5.47
TAU 09	E	5.3 ± 1.3	6.2 ± 0.6	5.6	0.02 ± 0.00	0.12 ± 0.04	< 0.07	< 0.92	< 0.07	< 0.87	< 0.32	< 4.24
W40 02	C	22.3 ± 2.3	6.2 ± 0.9	4.8	0.03 ± 0.00	0.78 ± 0.13	0.05 ± 0.01	1.17 ± 0.27	< 0.07	< 3.77	< 0.31	< 17.42

Notes. ([a]) The types of components are: C = cavity shock; E = envelope emission; S = spot shock; A = envelope absorption; O = a component generated from another source only detected in the 557 GHz line due to the size of the beam. ([b]) Integrated intensity of each velocity component approximated to the gaussian fit.

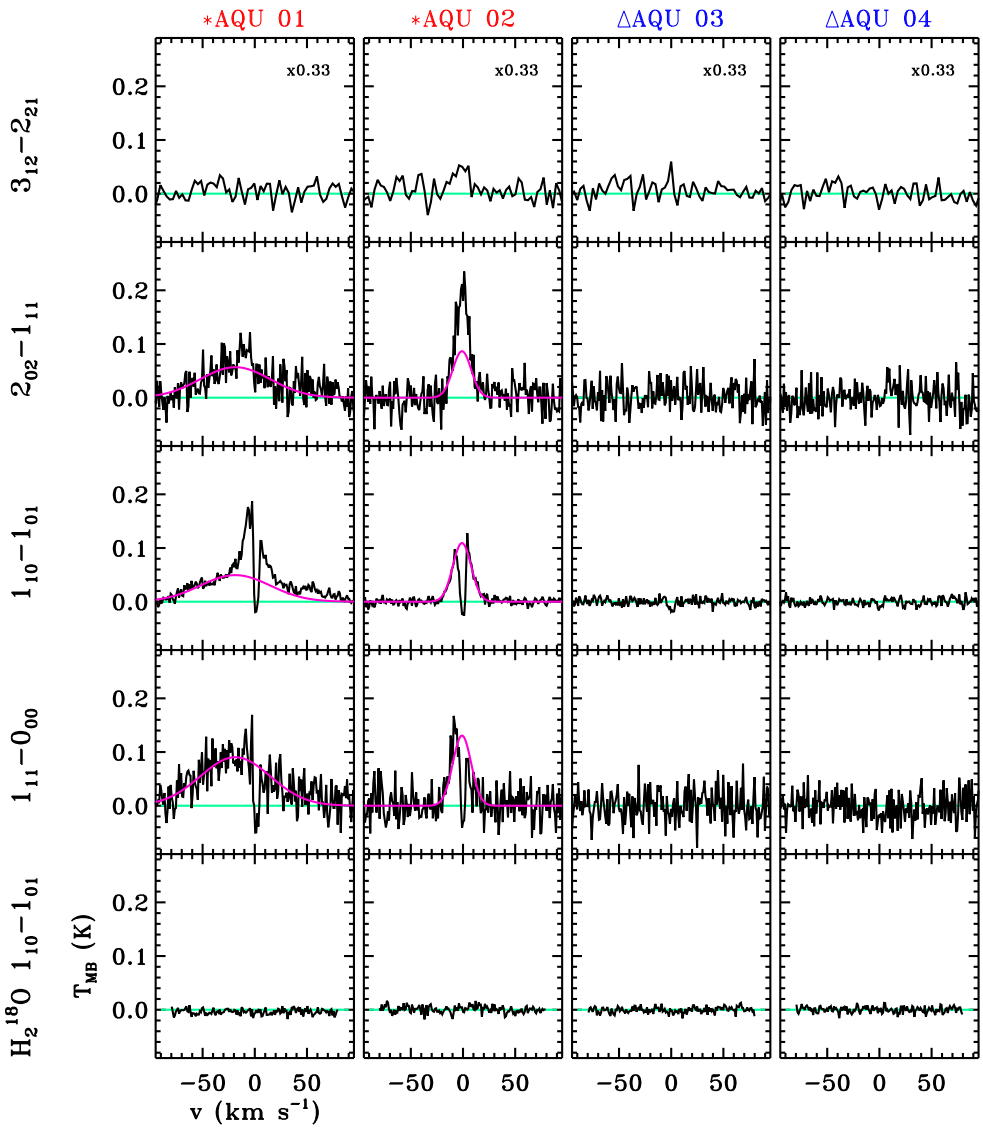

Figure 5.14: $H_2^{18}O$ 1_{10}-1_{01}, H_2O 1_{11}-0_{00} (1113 GHz), 1_{10}-1_{01} (557 GHz), 2_{02}-1_{11} (988 GHz) and 3_{12}-2_{21} (1157 GHz) data observed for the WILL protostars. The Class 0 objects are indicated in red with an asterisk symbol and the Class I sources in blue with a triangle symbol. The baseline is plotted with a green line and the broad velocity component is shown in pink.

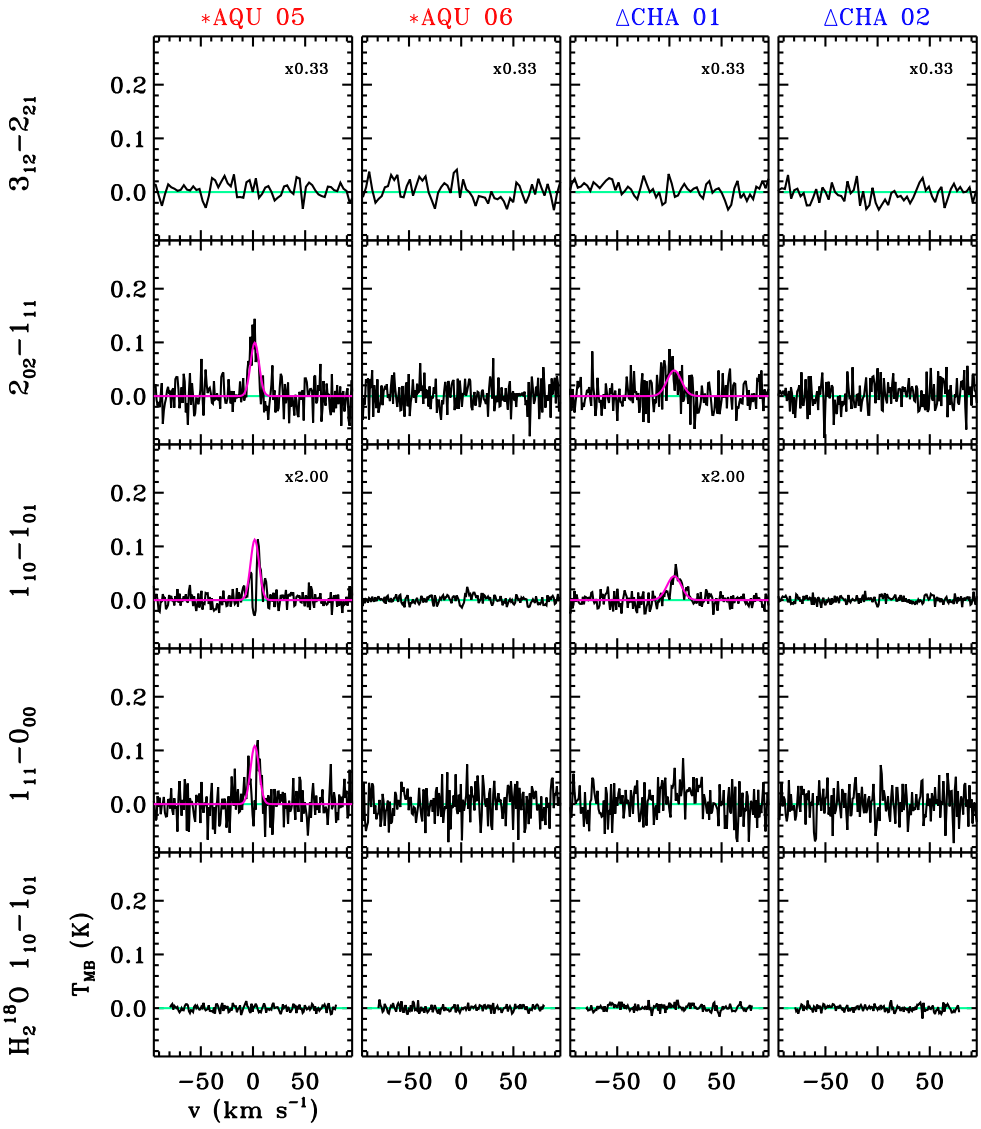

Figure 5.15: Same as Fig. 5.14.

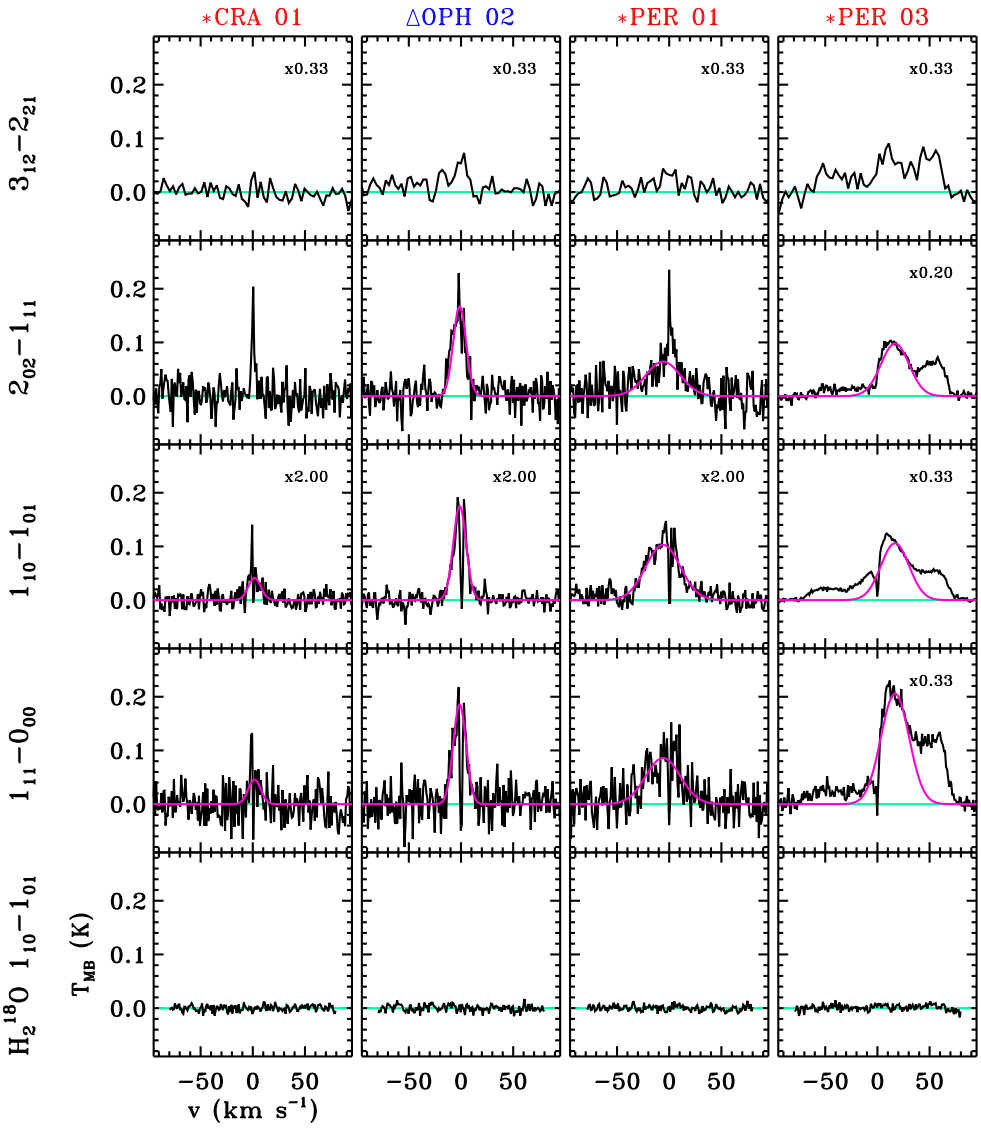

Figure 5.16: Same as Fig. 5.14.

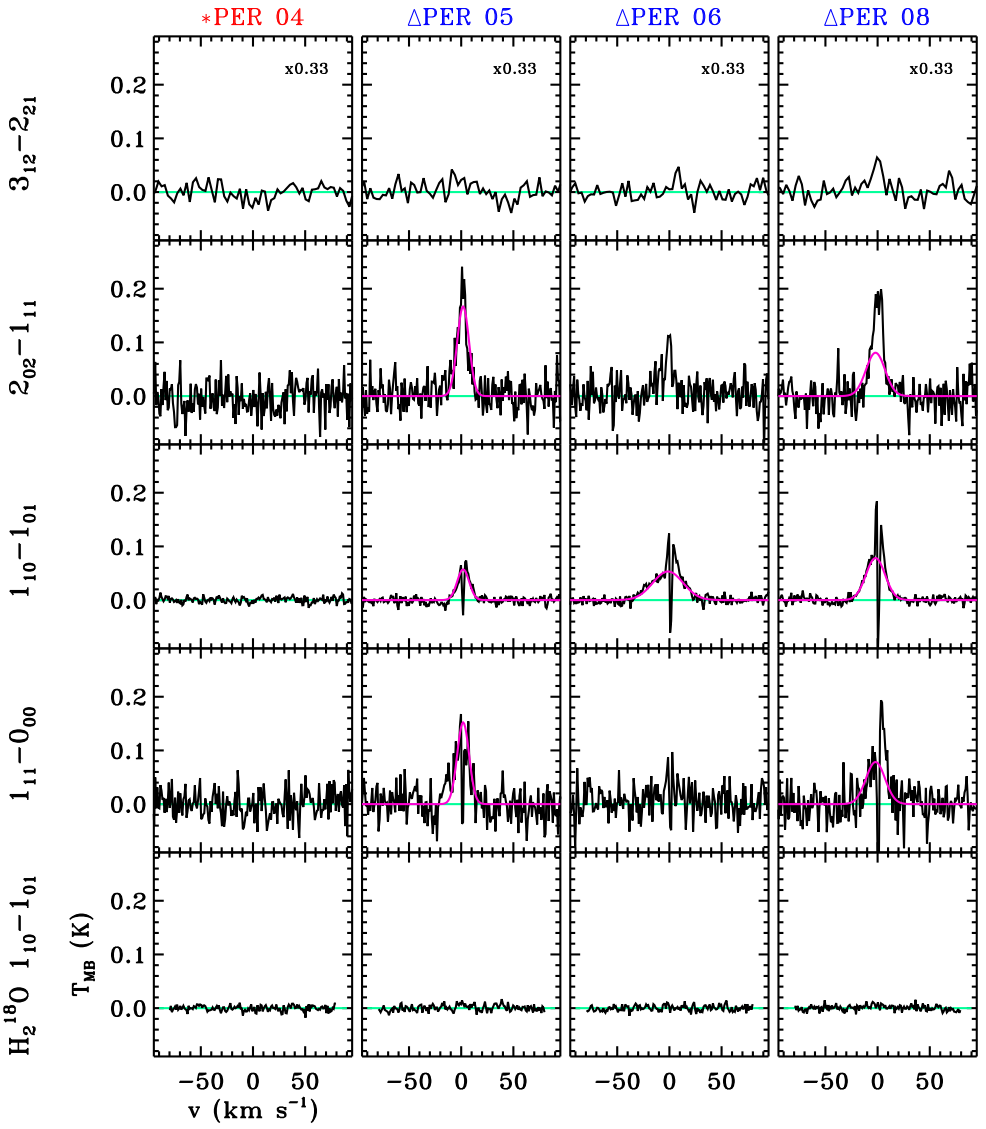

Figure 5.17: Same as Fig. 5.14.

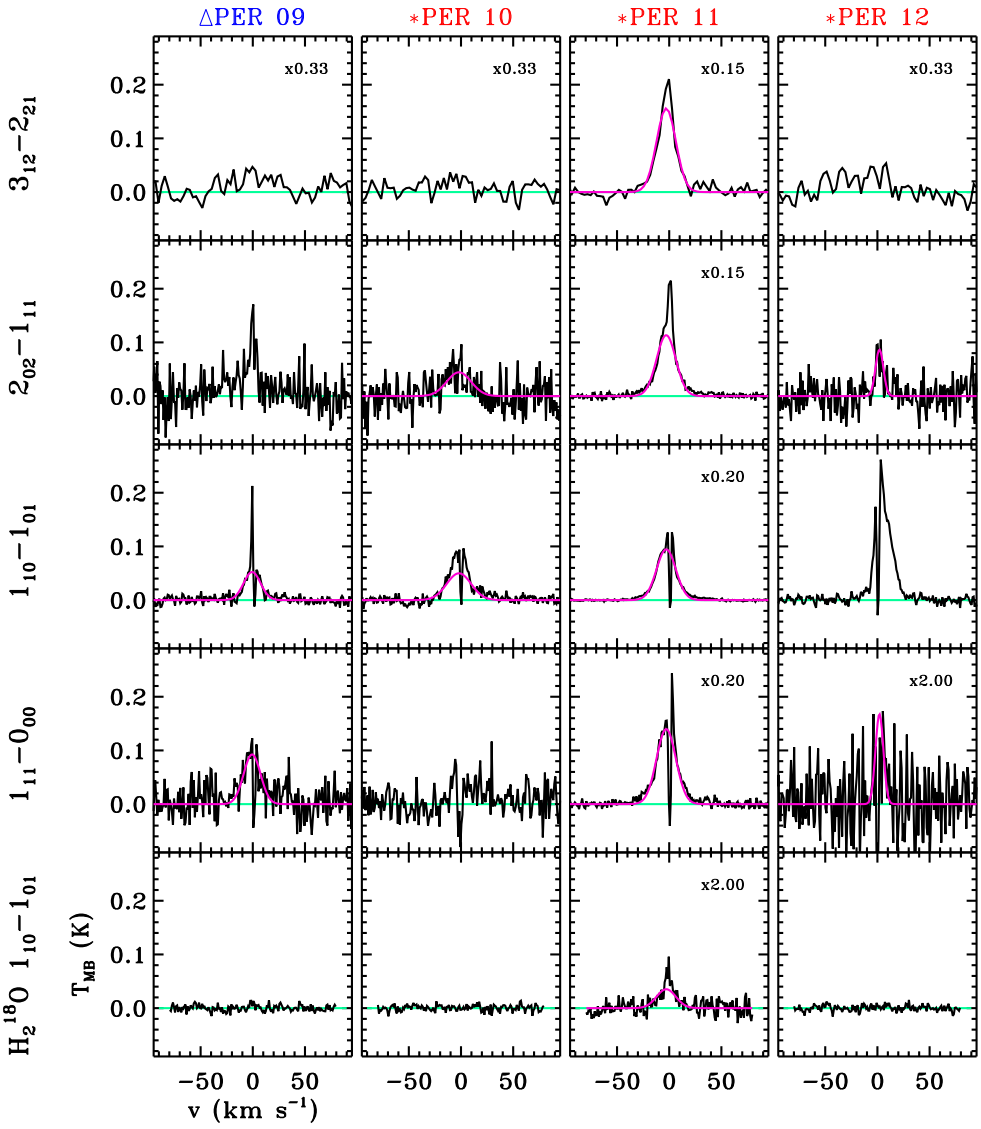

Figure 5.18: Same as Fig. 5.14.

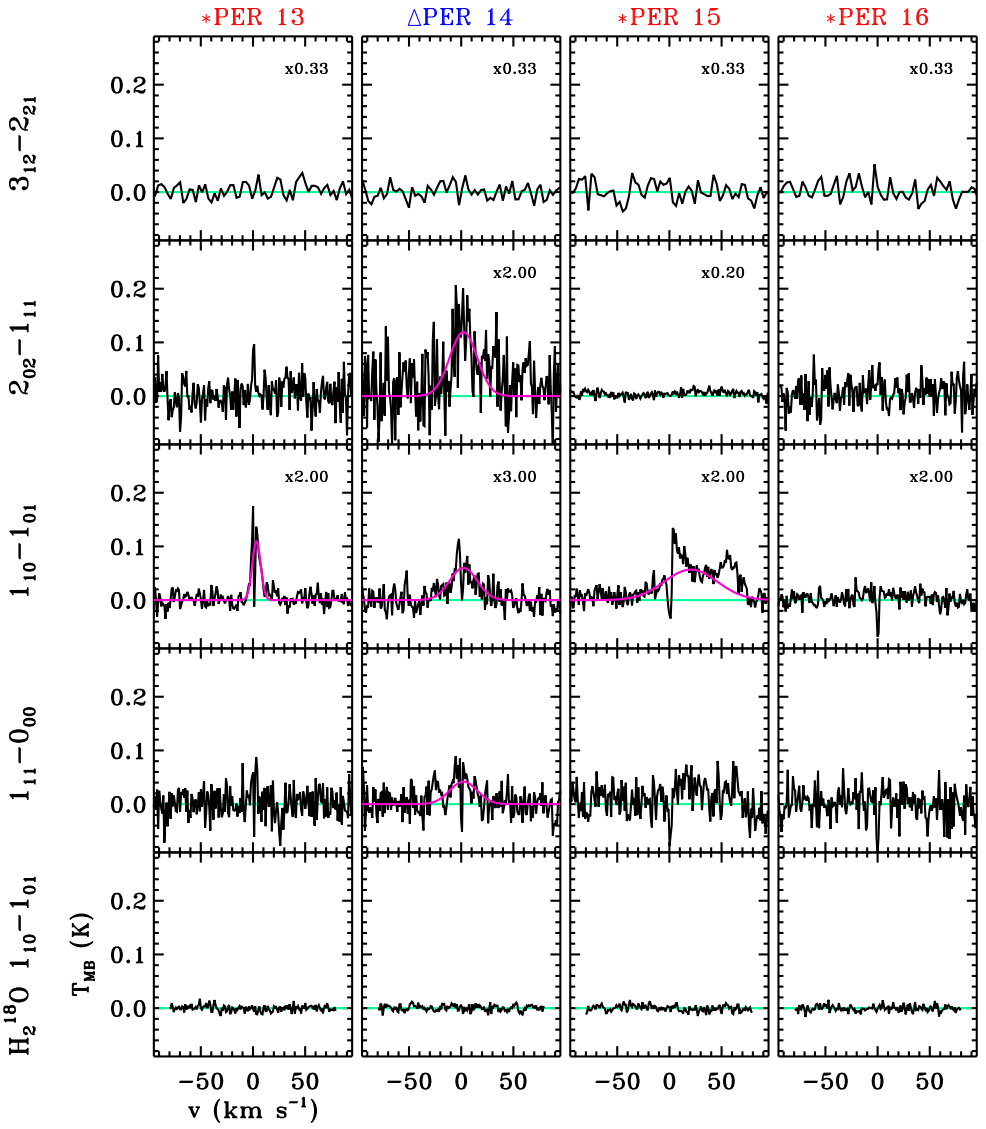

Figure 5.19: Same as Fig. 5.14.

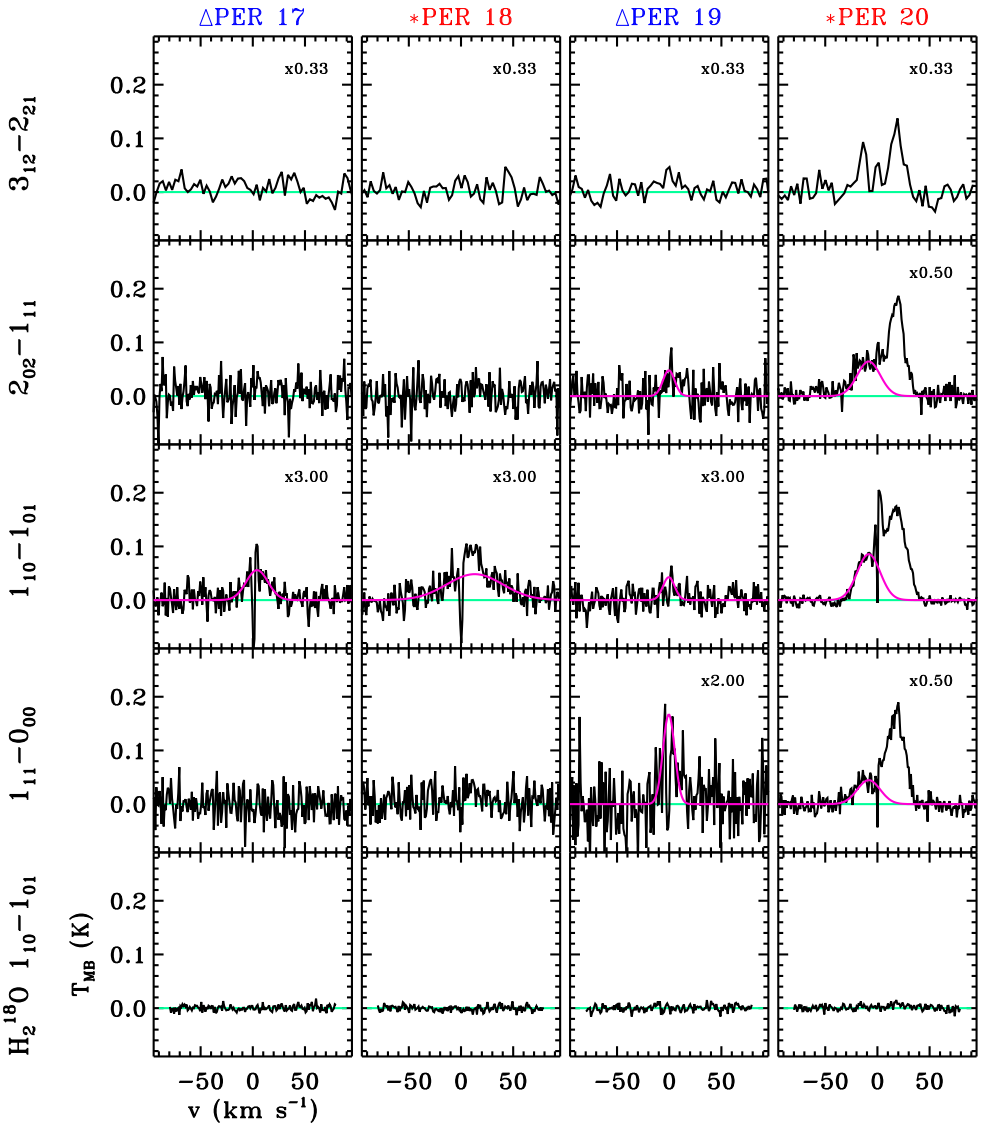

Figure 5.20: Same as Fig. 5.14.

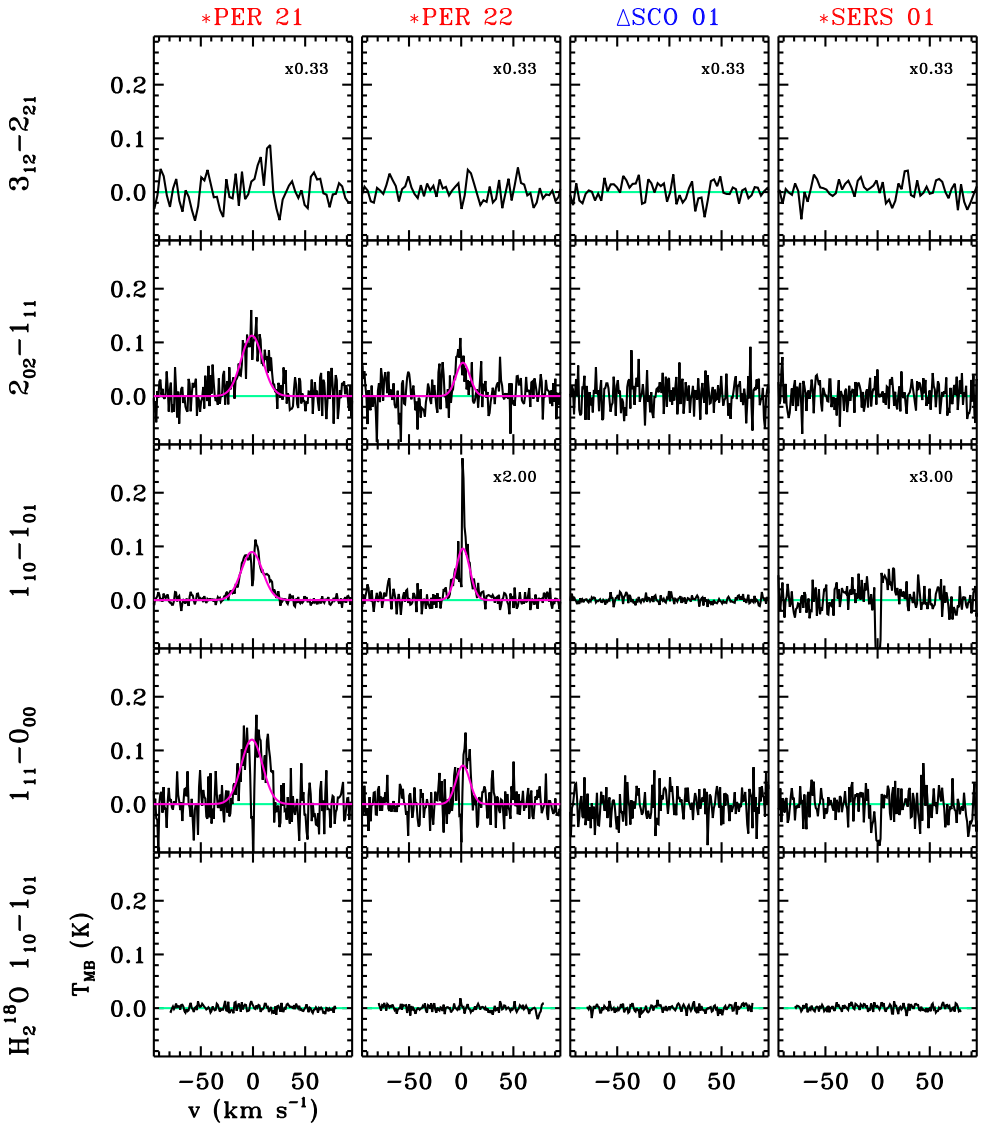

Figure 5.21: Same as Fig. 5.14.

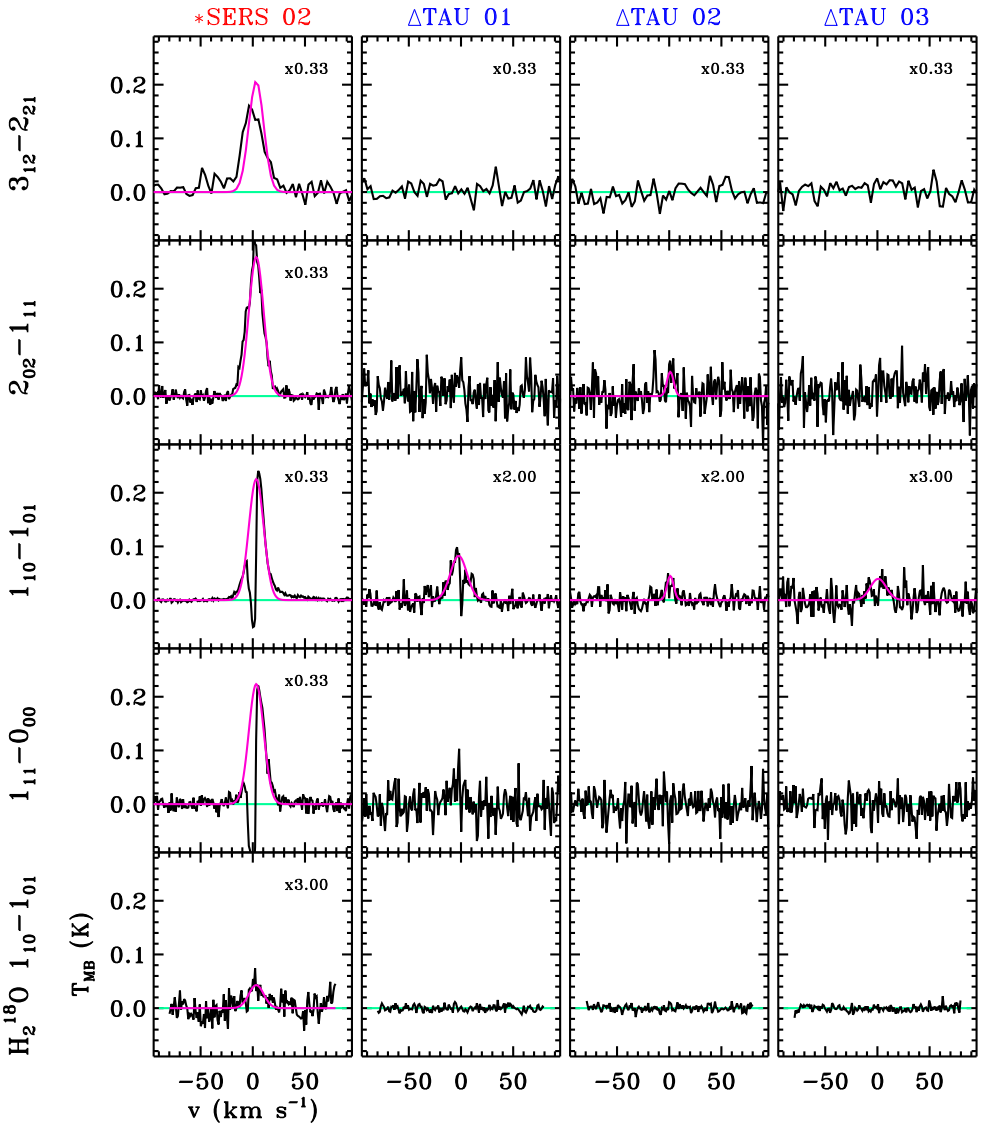

Figure 5.22: Same as Fig. 5.14.

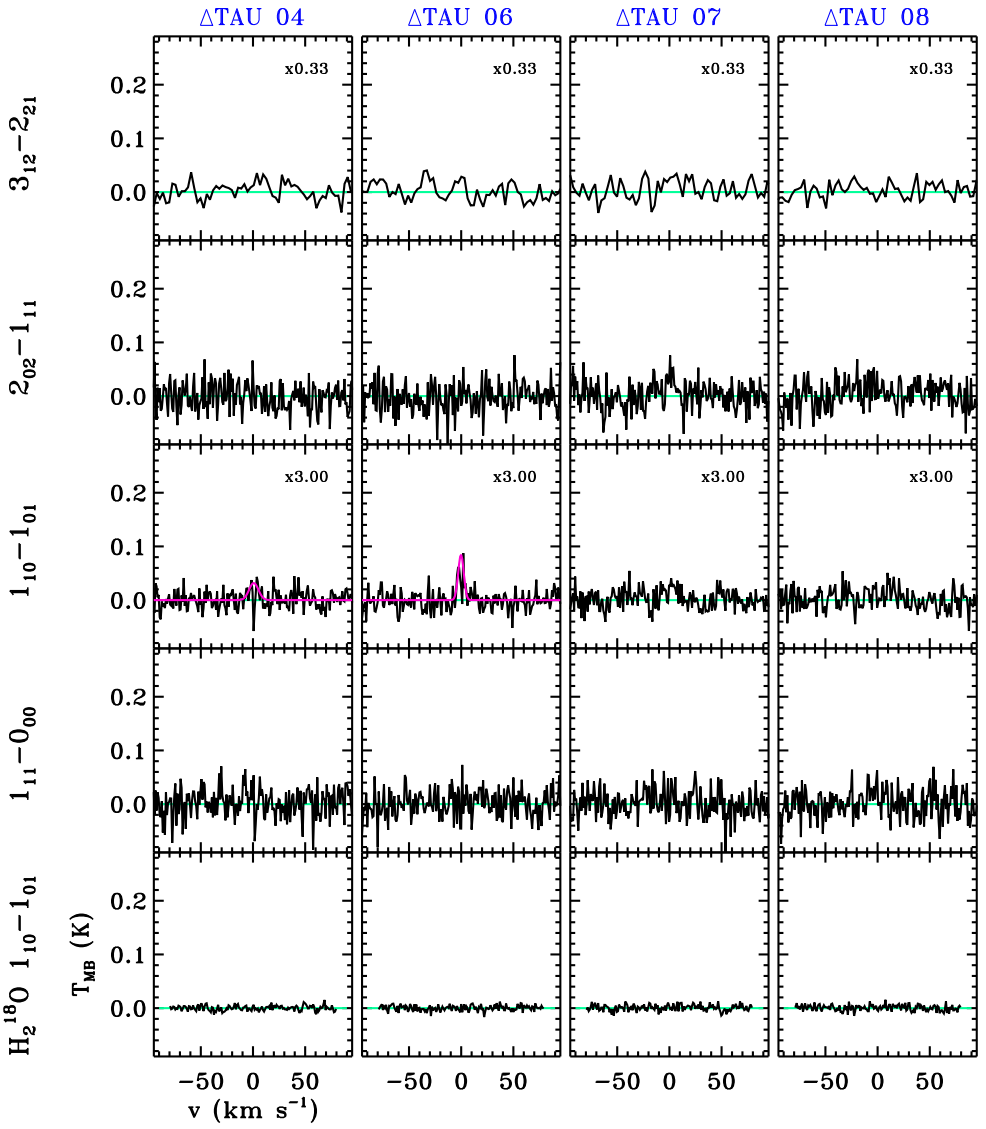

Figure 5.23: Same as Fig. 5.14.

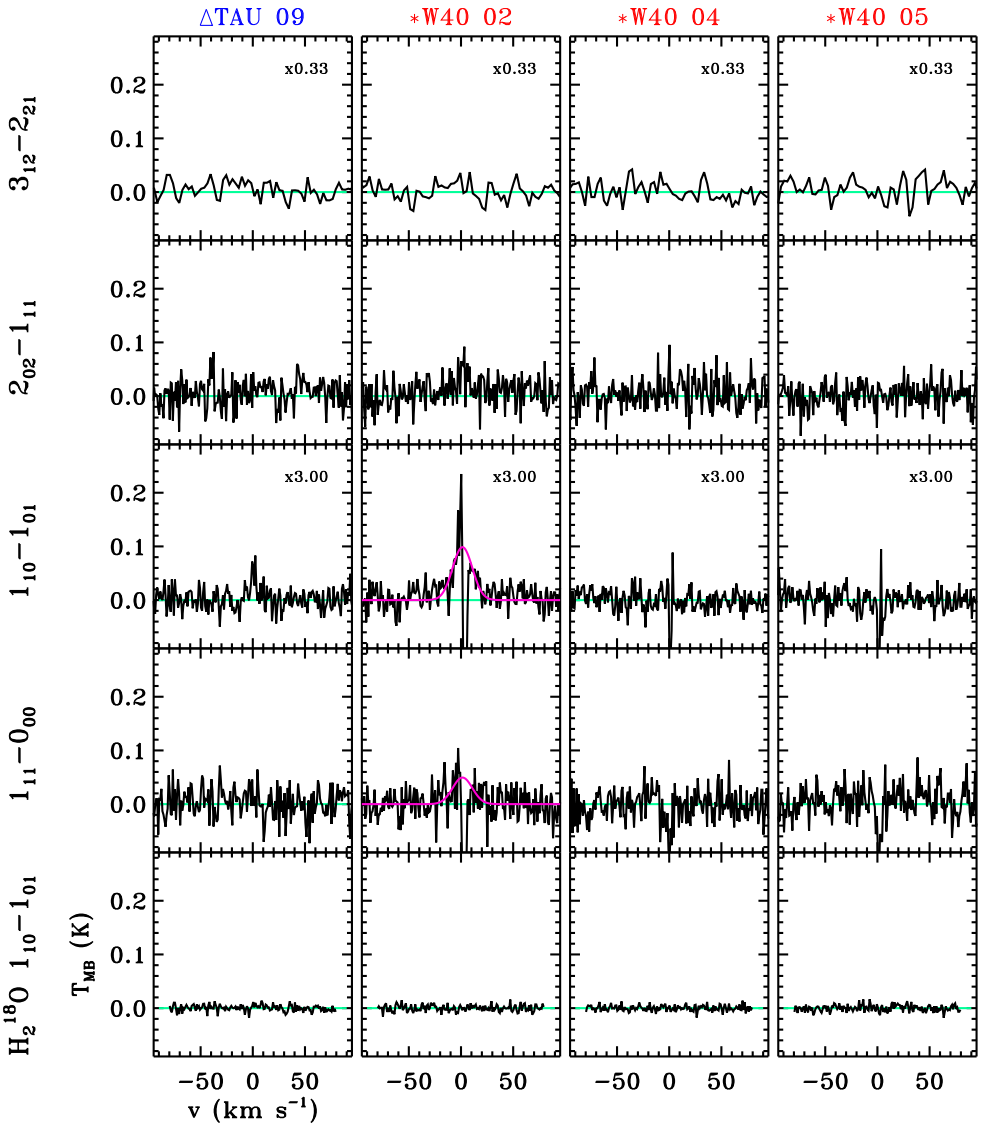

Figure 5.24: Same as Fig. 5.14.

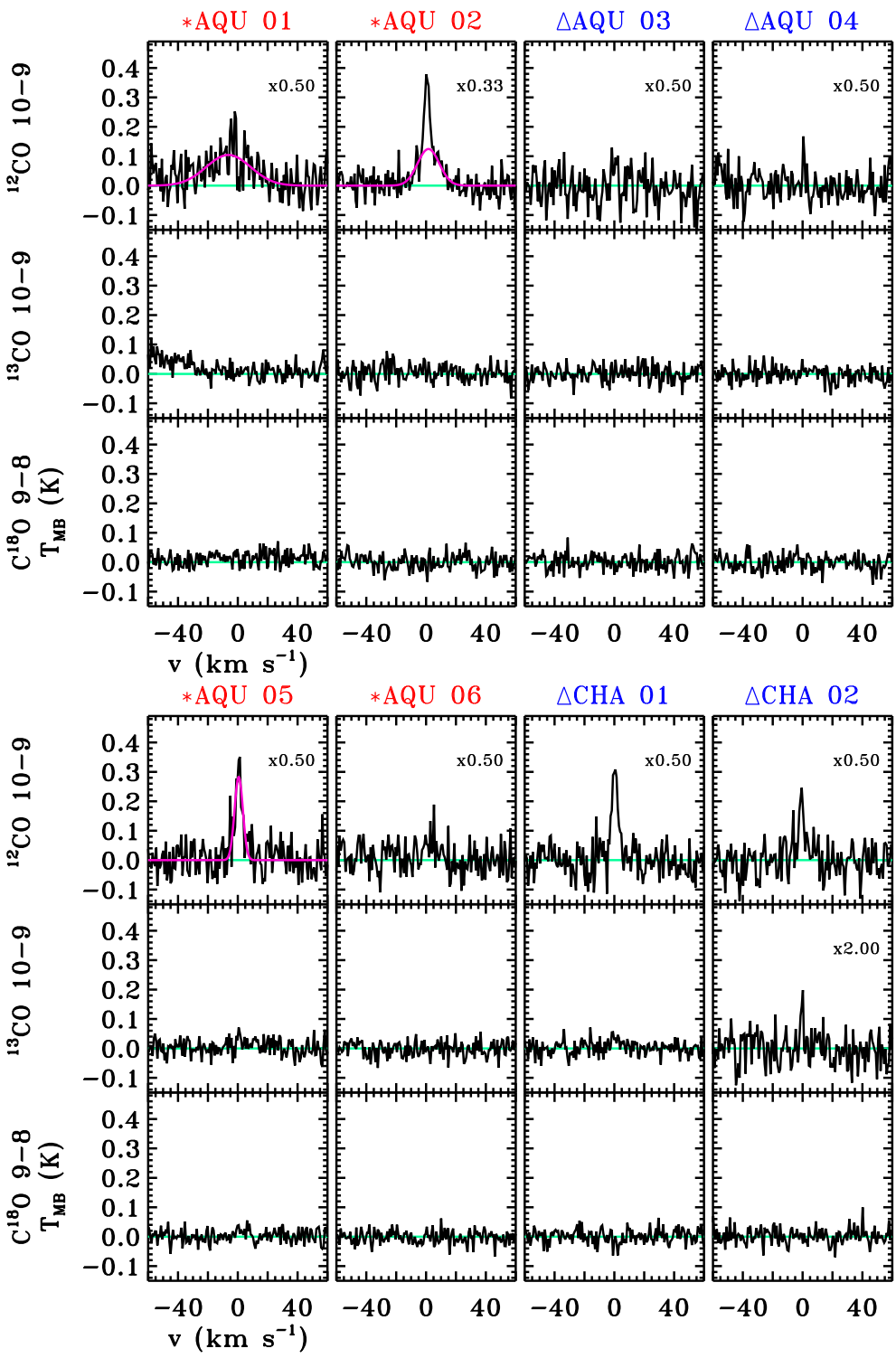

Figure 5.25: $C^{18}O$ $J = 9$–8, ^{13}CO $J = 10$–9 and ^{12}CO $J = 10$–9 spectra of the WILL protostars. The Class 0 objects are indicated with a red asterisk symbol next to the source name and the Class I with a blue triangle symbol. The baseline is plotted with a green line and the broad velocity component is shown in pink.

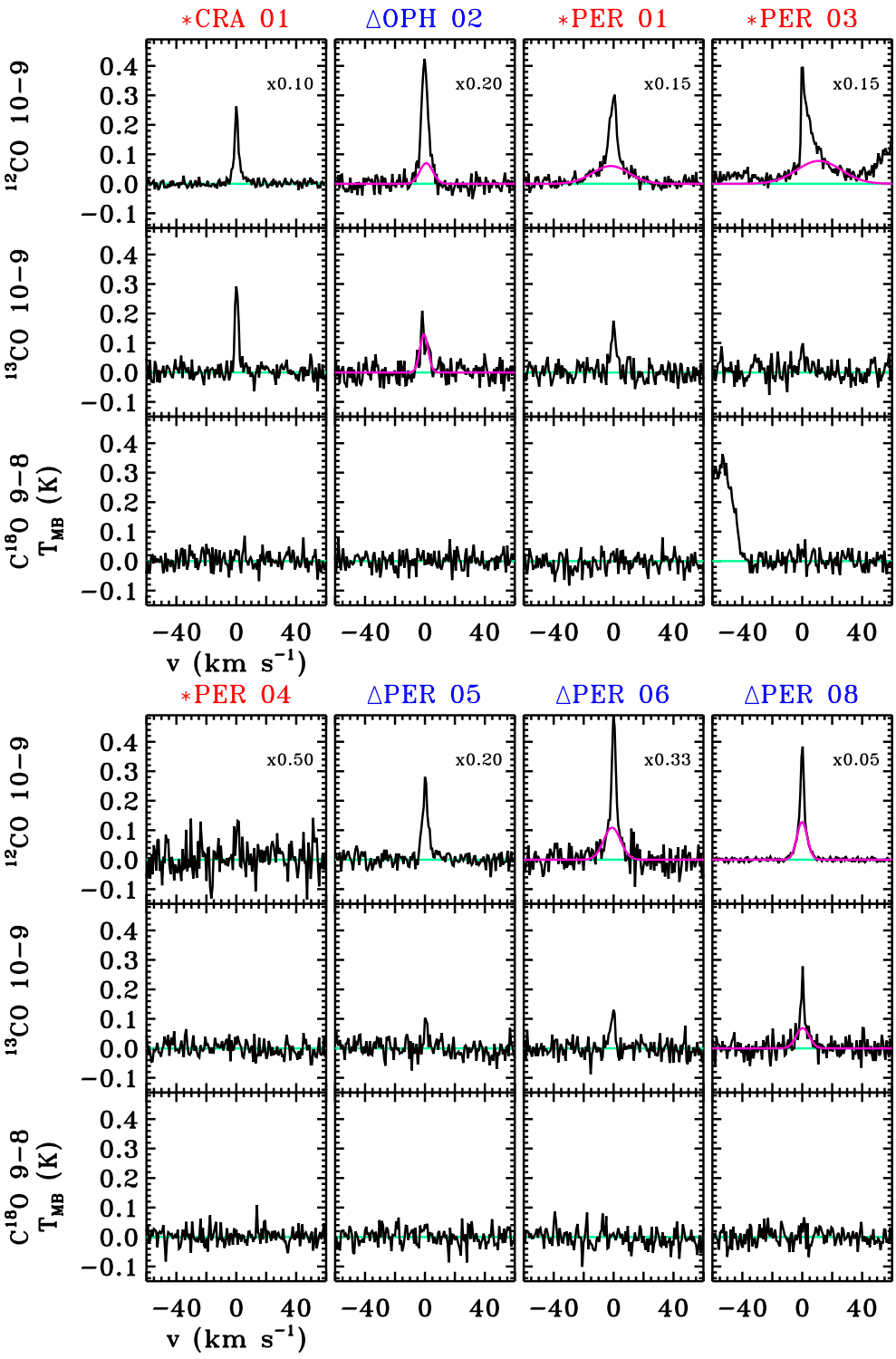

Figure 5.26: Same as Fig. 5.25.

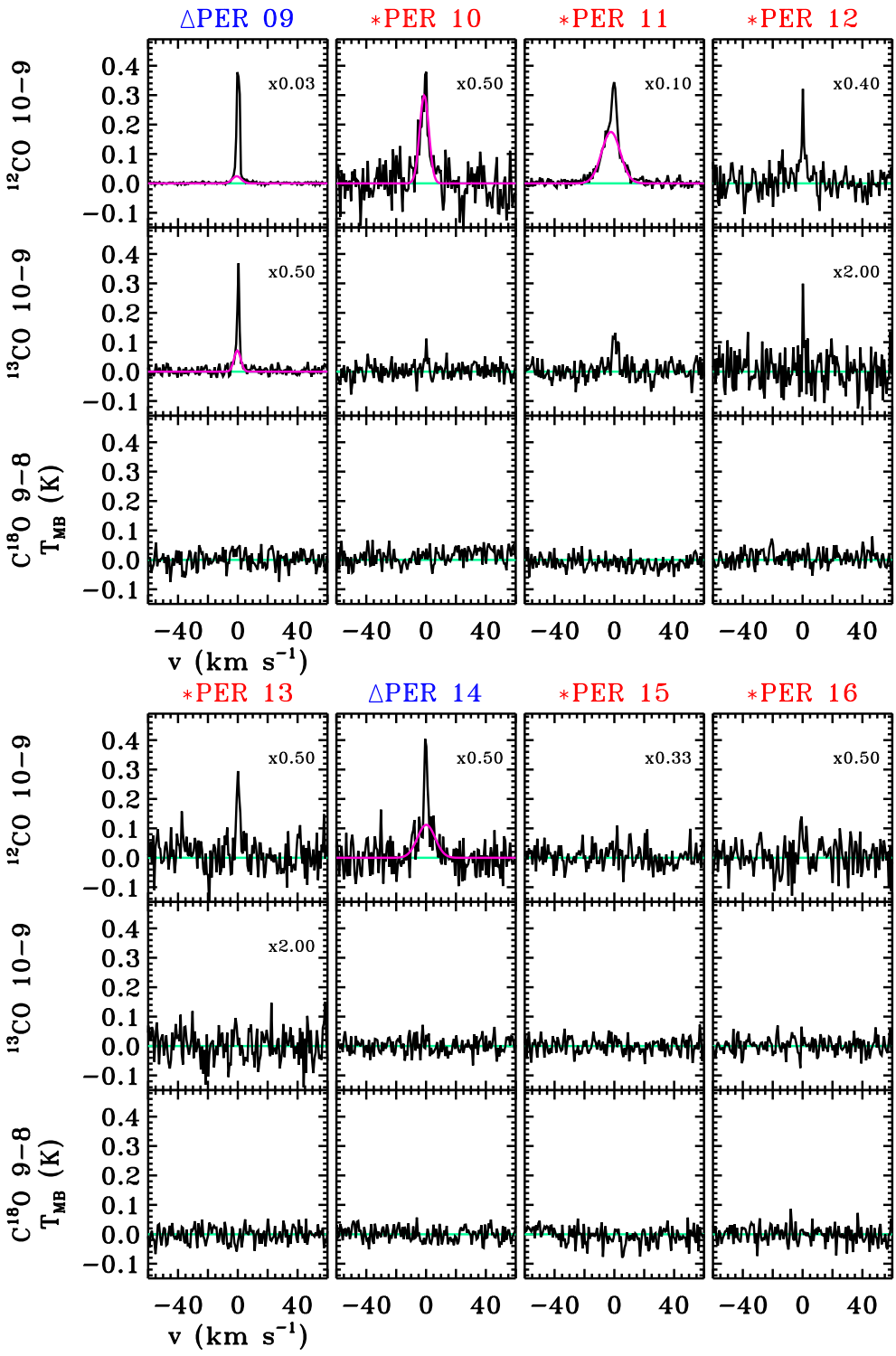

Figure 5.27: Same as Fig. 5.25.

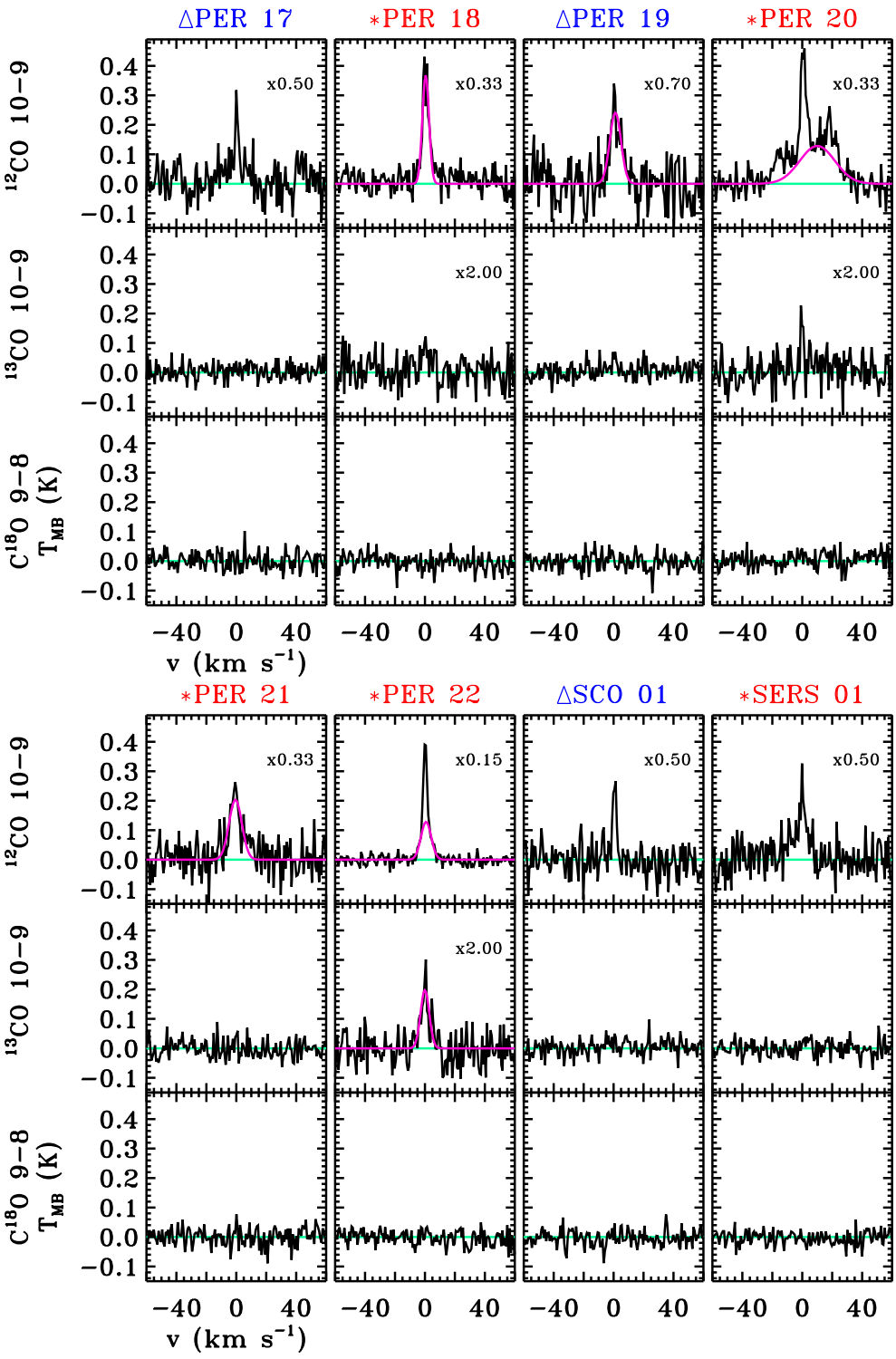

Figure 5.28: Same as Fig. 5.25.

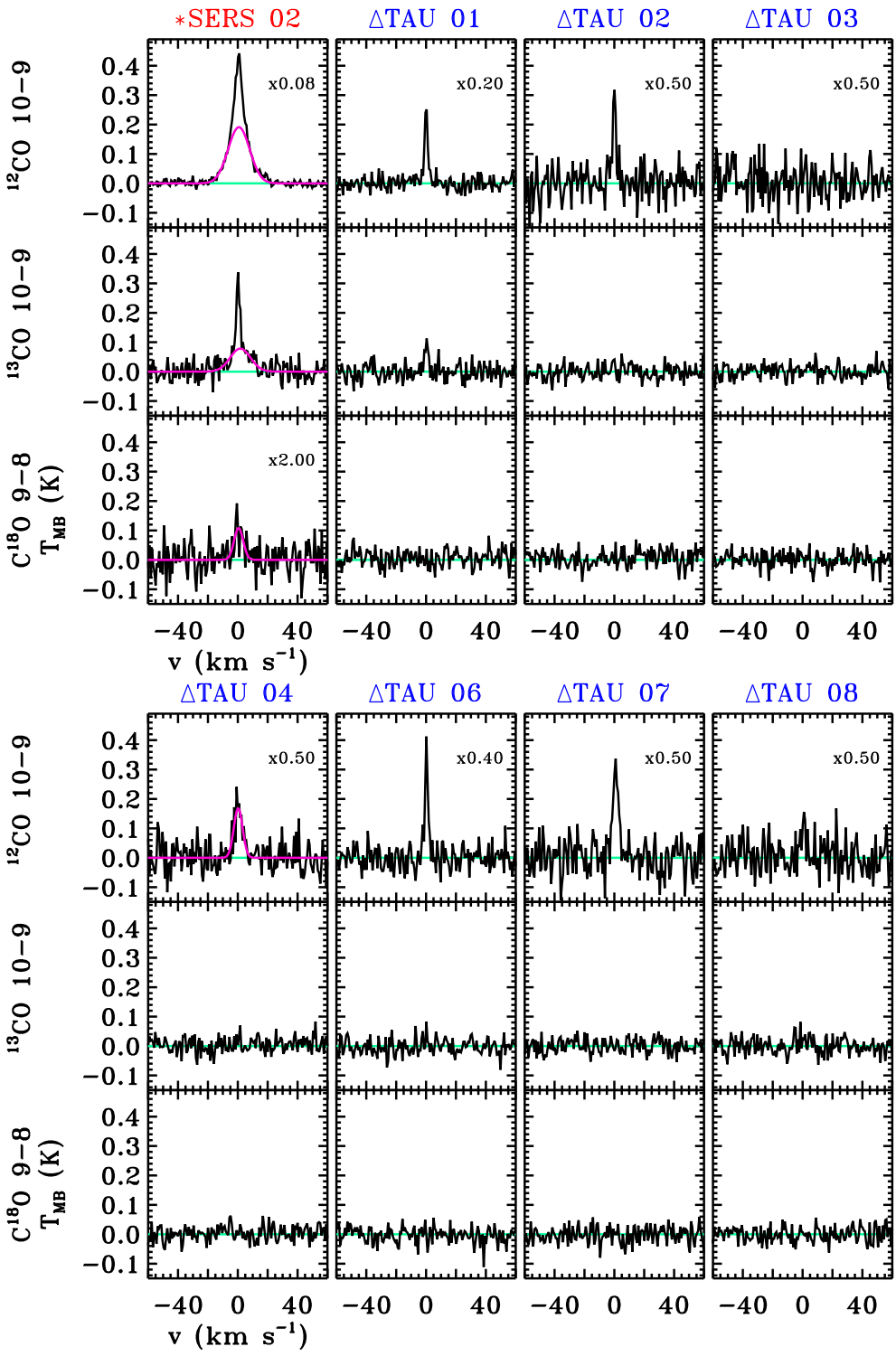

Figure 5.29: Same as Fig. 5.25.

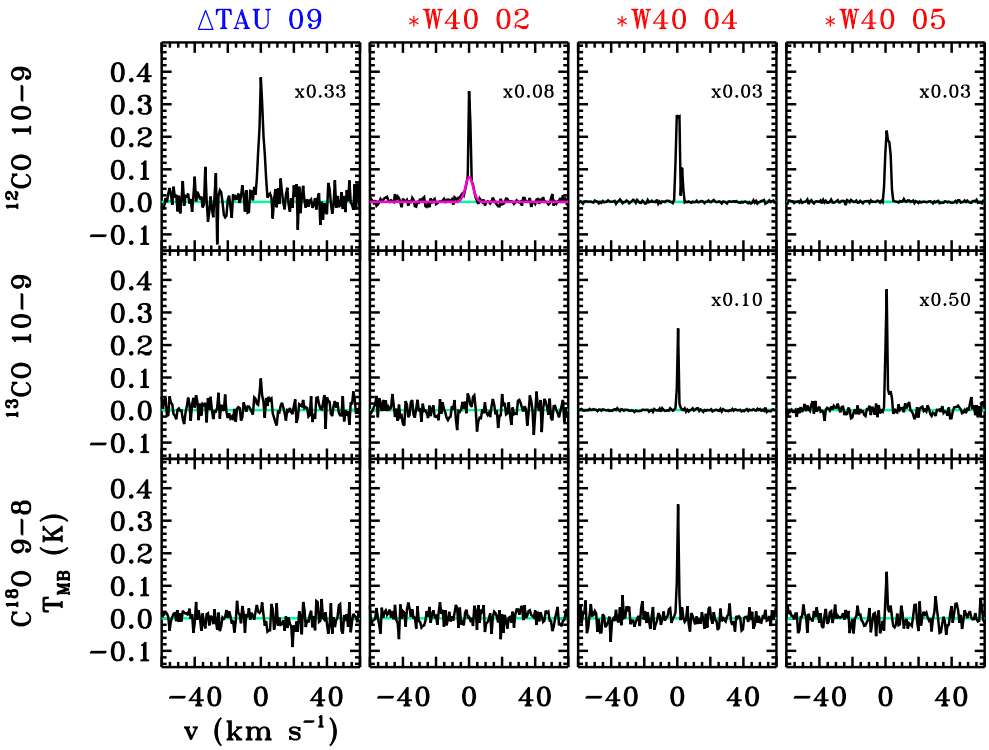

Figure 5.30: Same as Fig. 5.25.

5.C. Cygnus data

Table 5.18: Coordenates, distance, source velocity and bolometric luminosity values for the Cygnus YSOs.

Name	RA	DEC	D	v_{LSR}	L_{bol}	Name	RA	DEC	D	v_{LSR}	L_{bol}
	(h m s)	(° ′ ″)	(kpc)	(km s^{-1})	($L_\odot$)		(h m s)	(° ′ ″)	(kpc)	(km s^{-1})	($L_\odot$)
GR08 01	20:24:20.0	42:16: 2.0	1.4	–	398.1	GR01 31	20:39: 3.7	42:25:29.0	1.4	-4.7	738.0
GR08 02	20:24:21.4	42:15: 2.0	1.4	–	7.4	GR01 32	20:39: 4.1	42:25:41.0	1.4	-4.5	162.9
GR08 03	20:24:30.5	42: 4: 9.0	1.4	–	74.3	GR01 33	20:39: 7.3	42:15:35.0	1.4	–	86.9
GR08 04	20:24:31.6	42: 4:21.0	1.4	5.4	522.4	GR01 34	20:39:16.7	42:16: 9.0	1.4	19.0	243.8
GR08 05	20:24:33.4	42:24:58.0	1.4	–	110.7	GR02 01	20:36:52.2	41:36:24.0	1.4	-2.9	6760.0
GR06 02	20:29:31.8	39: 1:19.0	1.4	-4.5	1600.0	GR02 02	20:37: 0.9	41:34:55.0	1.4	-1.9	1340.0
GR06 03	20:29:36.7	39: 1:19.0	1.4	-3.2	13900.0	GR02 03	20:37: 2.6	41:34:41.0	1.4	-0.5	52.2
GR06 04	20:32:40.8	38:47: 6.0	1.4	–	15.7	GR02 04	20:37:25.5	41:33:19.0	1.4	–	33.9
GR06 05	20:32:41.8	38:45:56.0	1.4	–	31.0	GR02 05	20:37:26.0	41:35:41.0	1.4	–	44.9
GR06 06	20:32:42.1	38:46: 9.0	1.4	–	85.3	GR02 06	20:39:54.1	42: 0:51.0	1.4	–	106.9
GR03 01	20:32:21.1	41: 7:54.0	1.4	–	259.4	GR02 07	20:39:57.8	41:59:14.0	1.4	7.4	791.0
GR03 02	20:34:43.3	40:53:13.0	1.4	4.8	187.5	GR02 08	20:40: 2.2	41:28:12.0	1.4	-5.2	55.8
GR03 03	20:35: 9.3	41:38:24.0	1.4	-0.5	94.8	GR02 09	20:40: 4.0	41:27:34.0	1.4	-5.1	94.4
GR03 04	20:35:10.1	41:13:36.0	1.4	8.7	152.1	GR02 10	20:40: 5.5	41:32:13.0	1.4	-4.7	450.0
GR03 05	20:36: 7.2	41:39:55.0	1.4	11.4	6180.0	GR02 11	20:40: 9.2	42: 1:18.0	1.4	–	106.0
GR03 06	20:36:20.9	40:58:59.0	1.4	–	79.6	GR02 12	20:40:28.5	41:57:12.0	1.4	-6.9	140.0
GR01 01	20:35: 5.6	42:20:16.0	1.4	–	49.4	GR02 13	20:40:33.5	41:59: 0.0	1.4	-6.1	150.0
GR01 03	20:35:34.4	42:20: 7.0	1.4	14.2	227.0	GR02 14	20:40:35.6	41:56: 7.0	1.4	-5.2	68.5
GR01 05	20:36:40.4	42:50:32.0	1.4	–	98.2	GR02 15	20:40:38.4	41:53: 2.0	1.4	–	18.5
GR01 06	20:36:56.0	42:21:51.0	1.4	–	61.2	GR02 16	20:41:24.0	41:59:48.0	1.4	–	32.3
GR01 07	20:36:57.1	42:13:23.0	1.4	15.4	666.0	GR04 01	20:37:14.8	39:48:56.0	1.4	7.4	152.8
GR01 08	20:36:57.6	42:11:30.0	1.4	15.2	1100.0	GR04 02	20:37:42.1	39:51: 6.0	1.4	6.2	–
GR01 09	20:37:17.7	42:16:37.0	1.4	17.2	290.4	GR04 03	20:41:20.6	39:29:32.0	1.4	–	71.6
GR01 10	20:37:23.6	42:14:45.0	1.4	–	8.3	GR04 04	20:41:38.0	39:38:21.0	1.4	–	185.8
GR01 11	20:37:27.7	42:14:13.0	1.4	–	78.7	GR04 05	20:41:40.4	39:38: 1.0	1.4	–	218.3
GR01 12	20:37:30.5	42:13:59.0	1.4	–	102.1	GR04 06	20:41:50.3	39:40:40.0	1.4	–	148.3
GR01 13	20:37:31.9	42:13: 2.0	1.4	–	119.1	GR05 01	20:30:20.9	39:49:51.0	1.4	–	67.6
GR01 14	20:37:55.4	42:40:47.0	1.4	–	203.7	GR05 02	20:30:22.7	40: 9:23.0	1.4	–	69.7
GR01 15	20:38: 3.9	42:39:31.0	1.4	–	29.8	GR05 03	20:30:41.4	39:45:15.0	1.4	–	188.4
GR01 16	20:38: 7.1	42:38:52.0	1.4	-2.1	80.9	GR05 04	20:31: 8.7	40: 3:48.0	1.4	–	88.1
GR01 17	20:38:10.0	42:38: 9.0	1.4	–	37.7	GR05 05	20:31:11.4	40: 3: 8.0	1.4	6.6	6800.0
GR01 18	20:38:21.1	42:11:23.0	1.4	–	30.8	GR05 06	20:31:37.0	40:19:39.0	1.4	–	7.4
GR01 19	20:38:24.7	42:31:59.0	1.4	–	100.9	GR05 08	20:31:58.2	40:18:36.0	1.4	–	11.5
GR01 20	20:38:33.3	42:39:39.0	1.4	–	14.8	GR05 09	20:32:22.1	40:20:17.0	1.4	-0.2	128.5
GR01 22	20:38:36.6	42:37:32.0	1.4	9.6	22600.0	GR05 10	20:32:28.6	40:19:42.0	1.4	–	100.7
GR01 23	20:38:37.3	42:39:33.0	1.4	11.7	254.1	GR05 11	20:33:49.1	40: 8:41.0	1.4	7.9	4370.0
GR01 24	20:38:46.4	42:24:40.0	1.4	–	122.7	GR05 12	20:34:17.6	40:18:31.0	1.4	–	43.0
GR01 25	20:38:59.1	42:22:26.0	1.4	-2.6	300.0	GR10 01	20:20:38.9	39:38:18.0	1.4	2.0	127.9
GR01 26	20:39: 0.4	42:24:37.0	1.4	-3.5	1620.0	GR10 02	20:20:39.2	39:37:51.0	1.4	2.4	9900.0
GR01 27	20:39: 1.3	42:22: 5.0	1.4	-3.7	950.0	GR10 03	20:20:44.6	39:35:21.0	1.4	-1.1	32.3
GR01 28	20:39: 1.9	42:18:37.0	1.4	-3.8	130.2	GR10 04	20:21:55.0	39:59:45.0	1.4	–	181.6
GR01 29	20:39: 2.1	42:24:58.0	1.4	-4.3	1803.0	GR10 05	20:22:20.0	39:58:23.0	1.4	-1.9	23.0
GR01 30	20:39: 3.0	42:25:51.0	1.4	-4.1	630.0	GR10 06	20:22:24.7	40: 4:56.0	1.4	–	52.2

Notes. The bolometric luminosities, L_{bol}, are derived from the work of Kryukova et al. (2014). The source velocities, v_{LSR}, are calculated from the ^{13}CO $J = 10$–9 and C^{18}O $J = 9$–8 line fitting for those source detected in either of these lines.

Table 5.19: Observed and fitted properties of the Cygnus H_2O 1_{11}-0_{00} and 2_{02}-1_{11} spectra.

Source	H_2O 1_{11}-0_{00}				H_2O 2_{02}-1_{11}			
	rms[a] (mK)	T_{MB}^{peak} (K)	$\int T_{MB} dv$[b] (K km s^{-1})	*FWZI* (km s^{-1})	rms[a] (mK)	T_{MB}^{peak} (K)	$\int T_{MB} dv$[b] (K km s^{-1})	*FWZI* (km s^{-1})
GR08 01	46	< 0.03	–	–	25	< 0.01	–	–
GR08 02	48	< 0.03	–	–	24	< 0.01	–	–
GR08 03	48	< 0.03	–	–	51	< 0.03	–	–
GR08 04	51	0.27	6.64 ± 0.06	56	19	0.31	4.45 ± 0.05	48
GR08 05	48	< 0.03	–	–	26	< 0.01	–	–
GR06 01	47	< 0.03	–	–	35	< 0.02	–	–
GR06 02	50	< 0.03	–	–	13	< 0.01	–	–
GR06 03	47	0.19	0.53 ± 0.05	4	23	0.32	0.61 ± 0.04	4
GR06 04	48	< 0.03	–	–	22	< 0.01	–	–
GR06 05	47	< 0.03	–	–	25	< 0.01	–	–
GR06 06	49	< 0.03	–	–	41	< 0.02	–	–
GR03 01	46	< 0.03	–	–	23	< 0.01	–	–
GR03 02	51	< 0.03	–	–	73	< 0.04	–	–
GR03 03	46	< 0.03	–	–	48	< 0.02	–	–
GR03 04	48	< 0.03	–	–	114	< 0.06	–	–
GR03 05	47	0.25	0.00 ± 0.07	8	39	< 0.02	–	–
GR03 06	48	< 0.03	–	–	20	< 0.01	–	–
GR01 01	47	< 0.03	–	–	21	< 0.01	–	–
GR01 02	49	0.46	1.25 ± 0.06	24	17	0.36	4.02 ± 0.05	30
GR01 03	49	0.74	5.63 ± 0.06	28	11	0.53	8.10 ± 0.06	54
GR01 04	47	0.75	6.37 ± 0.06	50	67	0.54	9.35 ± 0.07	42
GR01 05	48	< 0.03	–	–	108	< 0.06	–	–
GR01 06	47	< 0.03	–	–	23	< 0.01	–	–
GR01 07	49	0.27	2.57 ± 0.06	22	23	0.31	2.50 ± 0.06	20
GR01 08	47	0.50	10.46 ± 0.07	40	12	0.75	14.11 ± 0.05	68
GR01 09	48	< 0.03	–	–	24	< 0.01	–	–
GR01 10	46	< 0.03	–	–	43	< 0.02	–	–
GR01 11	48	< 0.03	–	–	24	< 0.01	–	–
GR01 12	48	< 0.03	–	–	21	< 0.01	–	–
GR01 13	47	< 0.03	–	–	33	< 0.02	–	–
GR01 14	51	< 0.03	–	–	23	< 0.01	–	–
GR01 15	47	< 0.03	–	–	26	< 0.01	–	–
GR01 16	46	< 0.03	–	–	21	< 0.01	–	–
GR01 17	48	< 0.03	–	–	34	< 0.02	–	–
GR01 18	49	< 0.03	–	–	33	< 0.02	–	–
GR01 19	47	< 0.03	–	–	18	< 0.01	–	–
GR01 20	51	< 0.03	–	–	20	< 0.01	–	–
GR01 21	47	0.76	6.11 ± 0.05	30	17	1.57	22.76 ± 0.05	74
GR01 22	62	3.74	21.15 ± 0.06	68	18	9.19	112.38 ± 0.05	84
GR01 23	49	< 0.03	–	–	21	< 0.01	–	–
GR01 24	48	< 0.03	–	–	23	< 0.01	–	–
GR01 25	52	0.55	-3.96 ± 0.05	28	28	0.90	10.47 ± 0.06	32
GR01 26	49	0.42	-1.05 ± 0.06	18	31	0.84	5.09 ± 0.04	20
GR01 27	47	0.46	-6.20 ± 0.06	48	20	1.37	16.24 ± 0.05	50
GR01 28	48	0.39	2.89 ± 0.05	48	24	0.43	9.45 ± 0.06	40

Notes. *FWZI* has been calculated by binning the spectra to 3 km s^{-1}. Upper-limits are calculated assuming a *FWHM* of 20 km s^{-1}. ([a]) In 0.27 km s^{-1} bin. ([b]) Integrated over the interval of velocities defined by the *FWZI*.

Table 5.20: Observed and fitted properties of the Cygnus H_2O 1_{11}-0_{00} and 2_{02}-1_{11} spectra.

Source	H_2O 1_{11}-0_{00}				H_2O 2_{02}-1_{11}			
	rms[a] (mK)	T_{MB}^{peak} (K)	$\int T_{MB} dv$[b] (K km s^{-1})	*FWZI* (km s^{-1})	rms[a] (mK)	T_{MB}^{peak} (K)	$\int T_{MB} dv$[b] (K km s^{-1})	*FWZI* (km s^{-1})
GR01 29	49	0.14	-9.09 ± 0.05	14	26	0.53	5.59 ± 0.05	28
GR01 30	48	0.46	0.50 ± 0.06	24	23	0.87	19.68 ± 0.04	82
GR01 31	55	0.36	0.14 ± 0.05	54	15	0.44	8.22 ± 0.04	66
GR01 32	50	0.31	3.17 ± 0.06	31	23	0.41	7.86 ± 0.06	40
GR01 33	49	< 0.03	–	–	25	< 0.01	–	–
GR01 34	51	0.42	5.45 ± 0.05	58	24	0.34	5.33 ± 0.05	46
GR02 01	47	0.14	-5.05 ± 0.06	6	28	0.89	6.02 ± 0.07	12
GR02 02	52	0.12	-1.17 ± 0.06	26	55	0.76	6.36 ± 0.06	40
GR02 03	48	< 0.03	–	–	24	< 0.01	–	–
GR02 04	47	< 0.03	–	–	24	< 0.01	–	–
GR02 05	48	< 0.03	–	–	26	< 0.01	–	–
GR02 06	47	< 0.03	–	–	24	< 0.01	–	–
GR02 07	50	< 0.03	–	–	23	< 0.01	–	–
GR02 08	48	< 0.03	–	–	38	< 0.02	–	–
GR02 09	47	< 0.03	–	–	26	< 0.02	–	–
GR02 10	54	0.51	6.92 ± 0.05	128	19	0.78	12.19 ± 0.05	80
GR02 11	48	< 0.03	–	–	34	< 0.02	–	–
GR02 12	52	0.23	2.16 ± 0.05	28	20	0.48	5.27 ± 0.05	20
GR02 13	48	0.51	6.11 ± 0.06	76	64	0.61	7.80 ± 0.06	58
GR02 14	47	< 0.03	–	–	39	< 0.02	–	–
GR02 15	48	< 0.03	–	–	61	< 0.04	–	–
GR02 16	47	< 0.03	–	–	36	< 0.02	–	–
GR04 01	48	< 0.03	–	–	26	< 0.02	–	–
GR04 02	47	0.33	-0.71 ± 0.05	6	26	0.54	3.03 ± 0.05	10
GR04 03	46	< 0.03	–	–	39	< 0.02	–	–
GR04 04	46	< 0.03	–	–	22	< 0.01	–	–
GR04 05	49	< 0.03	–	–	32	< 0.02	–	–
GR04 06	47	< 0.03	–	–	26	< 0.02	–	–
GR05 01	47	< 0.03	–	–	26	< 0.01	–	–
GR05 02	48	< 0.03	–	–	21	< 0.01	–	–
GR05 03	49	< 0.03	–	–	22	< 0.01	–	–
GR05 04	46	< 0.03	–	–	30	< 0.02	–	–
GR05 05	53	0.40	0.96 ± 0.05	14	21	0.49	2.34 ± 0.05	44
GR05 06	49	< 0.03	–	–	32	< 0.02	–	–
GR05 07	49	< 0.03	–	–	25	< 0.01	–	–
GR05 08	48	< 0.03	–	–	25	< 0.01	–	–
GR05 09	47	< 0.03	–	–	50	< 0.03	–	–
GR05 10	47	< 0.03	–	–	26	< 0.02	–	–
GR05 11	45	0.17	0.30 ± 0.05	5	32	0.37	1.18 ± 0.06	4
GR05 12	50	< 0.03	–	–	25	< 0.01	–	–
GR05 13	47	< 0.03	–	–	24	< 0.01	–	–
GR10 01	53	0.78	7.42 ± 0.06	60	21	0.68	11.97 ± 0.05	60
GR10 02	39	0.83	0.87 ± 0.07	35	25	1.29	8.81 ± 0.05	30
GR10 03	51	< 0.03	–	–	24	< 0.01	–	–
GR10 04	49	< 0.03	–	–	25	< 0.02	–	–
GR10 05	47	< 0.03	–	–	24	< 0.01	–	–
GR10 06	47	< 0.03	–	–	35	< 0.02	–	–

Notes. *FWZI* has been calculated by binning the spectra to 3 km s^{-1}. Upper-limits are calculated assuming a *FWHM* of 20 km s^{-1}. ([a]) In 0.27 km s^{-1} bin. ([b]) Integrated over the interval of velocities defined by the *FWZI*.

Table 5.21: Observed and fitted properties of the Cygnus ^{13}CO $J = 10$–9 and C^{18}O $J = 9$–8 data.

Source	^{13}CO $J = 10$–9				C^{18}O $J = 9$–8			
	rms^a (mK)	$T_{\rm MB}^{\rm peak}$ (K)	$\int T_{\rm MB} {\rm d}v^b$ (K km s^{-1})	*FWZI* (km s^{-1})	rms^a (mK)	$T_{\rm MB}^{\rm peak}$ (K)	$\int T_{\rm MB} {\rm d}v^b$ (K km s^{-1})	*FWZI* (km s^{-1})
GR08 01	38	< 0.05	–	–	44	< 0.06	–	–
GR08 02	33	< 0.05	–	–	48	< 0.07	–	–
GR08 03	55	< 0.07	–	–	51	< 0.07	–	–
GR08 04	53	0.39	1.95 ± 0.06	10	59	< 0.09	–	–
GR08 05	50	< 0.07	–	–	57	< 0.08	–	–
GR06 01	53	< 0.07	–	–	59	< 0.09	–	–
GR06 02	51	1.08	3.23 ± 0.06	6	55	< 0.08	–	–
GR06 03	46	3.94	8.40 ± 0.05	5	51	0.50	0.83 ± 0.06	3
GR06 04	46	< 0.06	–	–	51	< 0.07	–	–
GR06 05	45	< 0.06	–	–	49	< 0.07	–	–
GR06 06	50	< 0.07	–	–	64	< 0.09	–	–
GR03 01	54	< 0.07	–	–	56	< 0.08	–	–
GR03 02	51	0.26	1.06 ± 0.05	3	47	< 0.07	–	–
GR03 03	39	0.27	0.24 ± 0.04	2	52	< 0.08	–	–
GR03 04	41	1.82	2.37 ± 0.05	4	57	< 0.08	–	–
GR03 05	54	2.10	4.09 ± 0.06	3	55	< 0.08	–	–
GR03 06	51	< 0.07	–	–	58	< 0.08	–	–
GR01 01	52	< 0.07	–	–	63	< 0.09	–	–
GR01 02	54	0.40	1.93 ± 0.06	8	57	< 0.08	–	–
GR01 03	55	0.38	1.13 ± 0.06	7	54	< 0.08	–	–
GR01 04	52	0.37	0.50 ± 0.06	5	51	< 0.07	–	–
GR01 05	54	< 0.07	–	–	47	< 0.07	–	–
GR01 06	42	< 0.06	–	–	41	< 0.06	–	–
GR01 07	47	< 0.07	–	–	44	< 0.06	–	–
GR01 08	59	0.34	1.54 ± 0.06	7	45	< 0.06	–	–
GR01 09	48	0.77	1.18 ± 0.06	2	67	< 0.10	–	–
GR01 10	45	< 0.06	–	–	54	< 0.08	–	–
GR01 11	41	< 0.06	–	–	66	< 0.09	–	–
GR01 12	49	< 0.07	–	–	63	< 0.09	–	–
GR01 13	46	< 0.07	–	–	49	< 0.07	–	–
GR01 14	49	< 0.07	–	–	53	< 0.07	–	–
GR01 15	44	< 0.06	–	–	55	< 0.08	–	–
GR01 16	48	0.59	0.57 ± 0.05	2	48	< 0.07	–	–
GR01 17	46	< 0.07	–	–	58	< 0.08	–	–
GR01 18	54	< 0.08	–	–	50	< 0.07	–	–
GR01 19	50	< 0.07	–	–	47	< 0.07	–	–
GR01 20	44	< 0.07	–	–	44	< 0.06	–	–
GR01 21	56	1.29	7.12 ± 0.06	12	49	0.27	5.27 ± 0.05	8
GR01 22	60	9.15	62.43 ± 0.07	31	43	2.49	9.45 ± 0.05	14
GR01 23	52	0.68	0.12 ± 0.06	2	55	< 0.08	–	–
GR01 24	49	< 0.07	–	–	54	< 0.08	–	–
GR01 25	47	0.42	0.81 ± 0.05	10	44	0.18	0.54 ± 0.05	6
GR01 26	44	1.27	5.27 ± 0.05	10	51	0.25	0.05 ± 0.05	3
GR01 27	50	2.39	6.21 ± 0.05	9	51	0.39	0.12 ± 0.06	2
GR01 28	52	0.19	4.79 ± 0.06	11	47	< 0.07	–	–

Notes. *FWZI* has been calculated by binning the spectra to 3 km s^{-1}. Upper-limits are calculated assuming a *FWHM* of 3 km s^{-1}. $(^a)$ In 0.27 km s^{-1} bin. $(^b)$ Integrated over the interval of velocities defined by the *FWZI*.

Table 5.22: Observed and fitted properties of the Cygnus ^{13}CO $J = 10$–9 and C^{18}O $J = 9$–8 data.

Source	^{13}CO $J = 10$–9				C^{18}O $J = 9$–8			
	rms[a] (mK)	$T_{\rm MB}^{\rm peak}$ (K)	$\int T_{\rm MB} {\rm d}v$[b] (K km s^{-1})	*FWZI* (km s^{-1})	rms[a] (mK)	$T_{\rm MB}^{\rm peak}$ (K)	$\int T_{\rm MB} {\rm d}v$[b] (K km s^{-1})	*FWZI* (km s^{-1})
GR01 29	56	0.77	4.28 ± 0.06	7	49	0.25	0.39 ± 0.05	3
GR01 30	60	0.36	3.96 ± 0.06	11	49	< 0.07	–	–
GR01 31	52	0.93	2.71 ± 0.06	4	60	< 0.08	–	–
GR01 32	48	0.27	2.17 ± 0.05	5	49	< 0.07	–	–
GR01 33	51	< 0.07	–	–	55	< 0.08	–	–
GR01 34	60	0.19	0.77 ± 0.07	7	44	< 0.06	–	–
GR02 01	55	2.49	10.09 ± 0.06	9	47	0.45	1.67 ± 0.05	6
GR02 02	57	1.01	3.09 ± 0.06	8	51	0.24	2.18 ± 0.06	1
GR02 03	50	0.45	0.74 ± 0.05	1	53	< 0.07	–	–
GR02 04	48	< 0.07	–	–	47	< 0.07	–	–
GR02 05	46	< 0.07	–	–	48	< 0.07	–	–
GR02 06	46	< 0.07	–	–	59	< 0.08	–	–
GR02 07	52	0.15	0.31 ± 0.06	4	49	< 0.07	–	–
GR02 08	47	0.76	1.16 ± 0.05	2	53	< 0.07	–	–
GR02 09	52	0.20	0.35 ± 0.06	2	50	< 0.07	–	–
GR02 10	60	0.29	0.32 ± 0.07	7	46	< 0.06	–	–
GR02 11	49	< 0.07	–	–	52	< 0.07	–	–
GR02 12	50	0.31	1.90 ± 0.06	8	51	< 0.07	–	–
GR02 13	54	0.19	1.08 ± 0.06	5	57	< 0.08	–	–
GR02 14	50	0.25	0.05 ± 0.06	1	52	< 0.07	–	–
GR02 15	46	< 0.07	–	–	47	< 0.07	–	–
GR02 16	46	< 0.07	–	–	49	< 0.07	–	–
GR04 01	49	1.44	2.23 ± 0.05	3	51	< 0.07	–	–
GR04 02	50	0.45	1.97 ± 0.06	9	56	< 0.08	–	–
GR04 03	52	< 0.07	–	–	54	< 0.08	–	–
GR04 04	44	< 0.06	–	–	54	< 0.08	–	–
GR04 05	50	< 0.07	–	–	49	< 0.07	–	–
GR04 06	41	< 0.06	–	–	53	< 0.07	–	–
GR05 01	49	< 0.07	–	–	53	< 0.07	–	–
GR05 02	48	< 0.07	–	–	50	< 0.07	–	–
GR05 03	45	< 0.07	–	–	54	< 0.08	–	–
GR05 04	54	< 0.08	–	–	40	< 0.06	–	–
GR05 05	60	3.88	8.99 ± 0.07	8	45	0.39	2.12 ± 0.05	4
GR05 06	44	< 0.06	–	–	51	< 0.07	–	–
GR05 07	46	< 0.07	–	–	51	< 0.07	–	–
GR05 08	55	< 0.08	–	–	47	< 0.07	–	–
GR05 09	38	0.20	0.40 ± 0.04	3	45	< 0.06	–	–
GR05 10	43	< 0.06	–	–	51	< 0.07	–	–
GR05 11	65	3.03	7.12 ± 0.07	7	42	0.27	1.27 ± 0.05	3
GR05 12	49	< 0.07	–	–	49	< 0.07	–	–
GR05 13	52	< 0.07	–	–	54	< 0.08	–	–
GR10 01	51	0.24	3.18 ± 0.06	9	49	< 0.07	–	–
GR10 02	44	2.93	12.84 ± 0.05	14	55	0.45	1.55 ± 0.06	6
GR10 03	47	0.15	0.85 ± 0.05	4	52	< 0.07	–	–
GR10 04	51	< 0.07	–	–	49	< 0.07	–	–
GR10 05	49	0.57	0.96 ± 0.06	1	41	< 0.06	–	–
GR10 06	49	< 0.07	–	–	51	< 0.07	–	–

Notes. *FWZI* has been calculated by binning the spectra to 3 km s^{-1}. Upper-limits are calculated assuming a *FWHM* of 3 km s^{-1}. ([a]) In 0.27 km s^{-1} bin. ([b]) Integrated over the interval of velocities defined by the *FWZI*.

Table 5.23: Gaussian decomposition results for the Cygnus water data.

Source	Comp.[a]	$FWHM$	$v_{\rm peak}$	$v_{\rm LSR}$	H_2O 1_{11}-0_{00}		H_2O 2_{02}-1_{11}	
					$T_{\rm MB}^{\rm peak}$	$\int T_{\rm MB} {\rm d}v^b$	$T_{\rm MB}^{\rm peak}$	$\int T_{\rm MB} {\rm d}v^b$
		(km s^{-1})	(km s^{-1})	(km s^{-1})	(K)	(K km s^{-1})	(K)	(K km s^{-1})
GR08 04	C	38.6 ± 3.6	5.9 ± 1.5	5.4	0.13 ± 0.03	5.19 ± 1.21	0.13 ± 0.01	5.37 ± 0.68
GR06 03	E	2.0 ± 1.5	-3.3 ± 0.7	-3.2	0.11 ± 0.34	0.25 ± 0.76	0.31 ± 0.21	0.68 ± 0.68
GR01 02	E	5.0 ± 1.0	16.1 ± 0.4	14.9	0.30 ± 0.09	1.60 ± 0.58	0.19 ± 0.03	1.01 ± 0.26
	C	30.8 ± 3.5	18.7 ± 1.3	14.9	0.10 ± 0.04	1.60 ± 0.58	0.13 ± 0.02	1.01 ± 0.26
GR01 03	E	5.1 ± 1.1	15.8 ± 0.4	14.2	0.48 ± 0.26	2.60 ± 1.51	0.29 ± 0.05	1.56 ± 0.44
	C	30.3 ± 3.7	15.1 ± 1.3	14.2	0.19 ± 0.11	2.60 ± 1.51	0.21 ± 0.03	1.56 ± 0.44
GR01 04	E	6.2 ± 0.6	15.7 ± 0.2	14.8	0.45 ± 0.04	2.95 ± 0.36	0.28 ± 0.03	1.82 ± 0.28
	C	30.2 ± 1.8	16.0 ± 0.6	14.8	0.24 ± 0.02	2.95 ± 0.36	0.19 ± 0.02	1.82 ± 0.28
GR01 07	C	13.5 ± 1.2	15.7 ± 0.5	-4.5	0.16 ± 0.03	2.34 ± 0.47	0.19 ± 0.02	2.67 ± 0.33
GR01 08	E	4.1 ± 0.4	16.9 ± 0.2	15.2	0.32 ± 0.32	1.39 ± 1.41	0.44 ± 0.04	1.88 ± 0.25
	C	36.6 ± 1.8	11.9 ± 0.7	15.2	0.19 ± 0.05	1.39 ± 1.41	0.29 ± 0.01	1.88 ± 0.25
GR01 21	E	7.8 ± 0.4	11.1 ± 0.1	9.0	0.81 ± 0.19	6.72 ± 1.61	1.16 ± 0.05	9.57 ± 0.59
	C	31.7 ± 2.3	2.7 ± 1.3	9.0	0.14 ± 0.07	6.72 ± 1.61	0.32 ± 0.03	9.57 ± 0.59
GR01 22	E	5.3 ± 0.1	11.1 ± 0.0	7.4	2.75 ± 0.60	15.59 ± 3.41	6.59 ± 0.11	37.35 ± 1.02
	C	30.2 ± 0.8	8.1 ± 0.3	7.4	1.75 ± 0.21	15.59 ± 3.41	2.14 ± 0.07	37.35 ± 1.02
GR01 25	C	12.4 ± 0.2	-3.0 ± 0.1	-2.6	0.51 ± 0.04	6.79 ± 0.57	0.77 ± 0.01	10.17 ± 0.27
GR01 26	E	3.6 ± 0.5	-3.3 ± 0.2	-3.0	<0.15	<1.33	0.46 ± 0.06	1.74 ± 0.33
	C	12.6 ± 1.4	-3.4 ± 0.4	-3.0	0.22 ± 0.05	1.33 ± 0.00	0.29 ± 0.05	1.74 ± 0.33
GR01 27	E	7.1 ± 0.3	-4.6 ± 0.1	-3.7	<0.14	<2.52	0.78 ± 0.03	5.90 ± 0.37
	C	27.9 ± 1.3	-6.0 ± 0.5	-3.7	0.31 ± 0.04	2.52 ± 0.00	0.37 ± 0.03	5.90 ± 0.37
GR01 28	C	24.8 ± 0.9	-6.9 ± 0.4	-3.8	0.25 ± 0.02	6.72 ± 0.66	0.29 ± 0.01	7.66 ± 0.36
GR01 29	C	10.5 ± 0.5	-3.8 ± 0.2	-4.5	<0.15	<3.87	0.41 ± 0.02	4.54 ± 0.29
GR01 30	E	8.8 ± 0.6	-1.4 ± 0.2	-5.0	0.36 ± 0.07	3.34 ± 0.73	0.44 ± 0.03	4.12 ± 0.39
	C	43.4 ± 1.9	-1.5 ± 0.6	-5.0	0.06 ± 0.03	3.34 ± 0.73	0.34 ± 0.02	4.12 ± 0.39
GR01 31	C	34.5 ± 1.6	5.9 ± 0.7	-4.7	0.13 ± 0.04	4.75 ± 1.65	0.32 ± 0.01	11.70 ± 0.74
GR01 32	C	23.7 ± 1.6	3.2 ± 0.7	-4.5	0.18 ± 0.04	4.57 ± 0.95	0.29 ± 0.02	7.24 ± 0.65
GR01 34	C	28.5 ± 0.9	18.5 ± 0.4	19.0	0.22 ± 0.01	6.60 ± 0.45	0.24 ± 0.01	7.14 ± 0.30
GR02 01	E	5.2 ± 0.6	-3.1 ± 0.2	-3.1	<0.14	<1.86	0.77 ± 0.07	4.25 ± 0.61
GR02 02	E	6.3 ± 0.6	-0.8 ± 0.2	-1.5	<0.16	<2.52	0.46 ± 0.04	3.12 ± 0.40
	C	38.3 ± 5.9	-3.3 ± 2.2	-1.5	<0.16	<2.52	0.12 ± 0.02	3.12 ± 0.40
GR02 07	C	18.0 ± 2.4	5.6 ± 1.0	7.4	<0.15	< 6.78	0.13 ± 0.02	2.57 ± 0.45
GR02 10	E	9.8 ± 0.5	-1.9 ± 0.2	-4.7	<0.16	< 3.97	0.37 ± 0.01	3.80 ± 0.25
	C	51.7 ± 1.4	0.0 ± 0.5	-4.7	0.19 ± 0.01	3.97 ± 0.00	0.28 ± 0.01	3.80 ± 0.25
GR02 12	C	12.0 ± 0.8	-7.5 ± 0.4	-6.9	0.21 ± 0.09	2.67 ± 1.14	0.30 ± 0.02	3.82 ± 0.36
GR02 13	E	6.0 ± 0.6	-3.6 ± 0.2	-6.1	0.26 ± 0.02	1.66 ± 0.23	0.21 ± 0.03	1.31 ± 0.24
	C	45.8 ± 2.5	-7.1 ± 1.0	-6.1	0.14 ± 0.01	1.66 ± 0.23	0.20 ± 0.01	1.31 ± 0.24
GR04 02	E	5.6 ± 0.4	6.3 ± 0.2	6.2	0.09 ± 0.13	0.53 ± 0.76	0.47 ± 0.03	2.80 ± 0.26
GR05 05	E	3.1 ± 0.5	6.9 ± 0.2	6.4	<0.16	<1.23	0.32 ± 0.04	1.04 ± 0.22
	C	51.7 ± 5.4	7.3 ± 2.2	6.4	<0.16	<1.23	0.12 ± 0.01	1.04 ± 0.22
GR05 11	E	2.6 ± 1.6	7.7 ± 0.7	7.9	0.04 ± 0.18	0.12 ± 0.51	0.30 ± 0.16	0.82 ± 0.67
GR10 01	E	9.9 ± 0.4	3.7 ± 0.1	2.0	0.32 ± 0.04	3.40 ± 0.44	0.45 ± 0.02	4.77 ± 0.26
	C	41.2 ± 2.0	5.1 ± 0.6	2.0	0.23 ± 0.02	3.40 ± 0.44	0.18 ± 0.01	4.77 ± 0.26
GR10 02	E	4.6 ± 0.4	2.3 ± 0.1	2.5	0.87 ± 0.10	4.28 ± 0.58	0.88 ± 0.06	4.34 ± 0.45
	C	21.9 ± 2.8	-1.2 ± 1.2	2.5	<0.12	<4.28	0.25 ± 0.04	4.34 ± 0.45

Notes. $^{(a)}$ The types of components are: C = cavity shock; E = envelope emission; S = spot shock; A = envelope absorption. $^{(b)}$ Integrated intensity of each velocity component approximated to the gaussian fit.

Table 5.24: Gaussian decomposition results for the Cygnus ^{13}CO $J = 10$–9 data.

Source	Comp.[a]	*FWHM*	$v_{\rm peak}$	$v_{\rm LSR}$	^{13}CO $J = 10$–9	
					$T_{\rm MB}^{\rm peak}$	$\int T_{\rm MB}\,{\rm d}v^b$
		(km s^{-1})	(km s^{-1})	(km s^{-1})	(K)	(K km s^{-1})
GR08 04	E	3.0 ± 0.7	5.4 ± 0.3	5.4	0.32 ± 0.06	1.03 ± 0.31
GR06 02	E	3.0 ± 0.2	-4.5 ± 0.1	-4.5	1.07 ± 0.06	3.43 ± 0.31
GR06 03	E	1.9 ± 0.0	-3.2 ± 0.0	-3.2	3.96 ± 0.08	8.14 ± 0.25
GR03 02	E	1.8 ± 0.7	4.8 ± 0.3	4.8	0.26 ± 0.08	0.50 ± 0.24
GR03 03	E	1.6 ± 0.6	-0.5 ± 0.2	-0.5	0.28 ± 0.09	0.47 ± 0.23
GR03 04	E	1.2 ± 0.1	8.7 ± 0.0	8.7	1.84 ± 0.10	2.41 ± 0.20
GR03 05	E	1.7 ± 0.1	11.4 ± 0.0	11.4	2.07 ± 0.08	3.78 ± 0.23
GR01 02	E	3.7 ± 0.9	14.9 ± 0.4	14.9	0.28 ± 0.06	1.10 ± 0.34
GR01 03	E	4.8 ± 1.0	14.2 ± 0.4	14.2	0.29 ± 0.05	1.47 ± 0.39
GR01 04	E	3.9 ± 0.8	14.8 ± 0.3	14.8	0.31 ± 0.06	1.29 ± 0.35
GR01 08	E	5.5 ± 1.1	15.2 ± 0.5	15.2	0.26 ± 0.05	1.55 ± 0.42
GR01 09	E	1.3 ± 0.2	17.2 ± 0.1	17.2	0.79 ± 0.10	1.07 ± 0.20
GR01 16	E	1.1 ± 0.2	-2.1 ± 0.1	-2.1	0.55 ± 0.10	0.67 ± 0.19
GR01 21	E	4.1 ± 0.2	9.0 ± 0.1	9.0	1.16 ± 0.05	5.03 ± 0.36
GR01 22	C	11.2 ± 0.2	7.4 ± 0.1	7.4	2.35 ± 0.09	28.18 ± 1.25
	E	4.1 ± 0.1	9.9 ± 0.0	7.4	6.92 ± 0.00	30.22 ± 0.64
GR01 23	E	1.2 ± 0.2	11.7 ± 0.1	11.7	0.66 ± 0.10	0.83 ± 0.19
GR01 25	E	5.0 ± 0.8	-2.6 ± 0.3	-2.6	0.35 ± 0.05	1.86 ± 0.40
GR01 26	E	4.3 ± 0.2	-3.0 ± 0.1	-3.0	1.23 ± 0.05	5.63 ± 0.37
GR01 27	E	2.5 ± 0.1	-3.7 ± 0.0	-3.7	2.28 ± 0.07	5.98 ± 0.28
GR01 28	C	11.3 ± 3.7	-3.8 ± 1.6	-3.8	0.12 ± 0.03	1.40 ± 0.60
GR01 29	E	4.1 ± 0.4	-4.5 ± 0.2	-4.5	0.70 ± 0.05	3.07 ± 0.36
GR01 30	C	8.0 ± 4.3	-5.0 ± 1.5	-5.0	0.10 ± 0.06	0.85 ± 0.66
	E	1.0 ± 0.6	-5.0 ± 0.2	-5.0	0.30 ± 0.00	0.32 ± 0.24
GR01 30	E	1.0 ± 0.6	-5.0 ± 0.2	-5.0	0.30 ± 0.00	0.32 ± 0.24
GR01 31	E	2.0 ± 0.2	-4.7 ± 0.1	-4.7	0.94 ± 0.08	1.97 ± 0.25
GR01 32	E	2.8 ± 0.9	-4.5 ± 0.4	-4.5	0.23 ± 0.07	0.70 ± 0.30
GR02 01	E	3.5 ± 0.1	-3.1 ± 0.0	-3.1	2.52 ± 0.06	9.29 ± 0.33
GR02 02	E	3.3 ± 0.2	-1.5 ± 0.1	-1.5	0.97 ± 0.06	3.36 ± 0.32
GR02 03	E	1.8 ± 0.4	-0.5 ± 0.2	-0.5	0.47 ± 0.08	0.90 ± 0.24
GR02 07	E	4.6 ± 2.2	7.4 ± 0.9	7.4	0.12 ± 0.05	0.61 ± 0.39
GR02 08	E	1.2 ± 0.2	-5.2 ± 0.1	-5.2	0.76 ± 0.10	0.98 ± 0.20
GR02 09	E	3.0 ± 1.3	-5.1 ± 0.5	-5.1	0.17 ± 0.06	0.55 ± 0.31
GR02 10	E	4.7 ± 1.1	-4.7 ± 0.5	-4.7	0.25 ± 0.05	1.26 ± 0.39
GR02 12	E	4.2 ± 1.1	-6.9 ± 0.5	-6.9	0.24 ± 0.05	1.09 ± 0.37
GR02 13	E	5.9 ± 2.2	-6.1 ± 0.9	-6.1	0.14 ± 0.05	0.90 ± 0.44
GR02 14	E	1.5 ± 0.7	-5.2 ± 0.3	-5.2	0.24 ± 0.09	0.37 ± 0.22
GR04 01	E	1.5 ± 0.1	7.4 ± 0.0	7.4	1.45 ± 0.09	2.28 ± 0.22
GR04 02	E	4.0 ± 0.6	6.2 ± 0.3	6.2	0.39 ± 0.06	1.66 ± 0.36
GR05 05	E	2.1 ± 0.0	6.4 ± 0.0	6.4	3.70 ± 0.08	8.12 ± 0.26
GR05 09	E	3.4 ± 1.9	-0.2 ± 0.8	-0.2	0.12 ± 0.06	0.44 ± 0.33
GR05 11	E	2.2 ± 0.1	7.9 ± 0.0	7.9	2.93 ± 0.07	6.92 ± 0.27
GR10 01	E	6.0 ± 1.7	2.0 ± 0.7	2.0	0.18 ± 0.04	1.15 ± 0.44
GR10 02	E	3.8 ± 0.1	2.5 ± 0.0	2.5	2.77 ± 0.06	11.31 ± 0.35
GR10 03	E	3.4 ± 1.8	-1.1 ± 0.7	-1.1	0.13 ± 0.06	0.48 ± 0.33
GR10 05	E	1.2 ± 0.2	-1.9 ± 0.1	-1.9	0.60 ± 0.10	0.74 ± 0.19

Notes. $(^a)$ The types of components are: C = cavity shock; E = envelope emission; S = spot shock; A = envelope absorption. $(^b)$ Integrated intensity of each velocity component approximated to the gaussian fit.

Table 5.25: Gaussian decomposition results for the Cygnus $C^{18}O$ $J = 9$–8 data.

Source	Comp.[a]	*FWHM*	v_{peak}	v_{LSR}	$C^{18}O$ $J = 9$–8	
					T_{MB}^{peak}	$\int T_{MB} dv^b$
		km s^{-1}	km s^{-1}	km s^{-1}	(K)	K km s^{-1}
GR06 03	E	2.2 ± 0.4	-3.2 ± 0.2	-3.2	0.45 ± 0.07	1.03 ± 0.26
GR01 21	E	7.8 ± 1.9	9.2 ± 0.8	9.0	0.19 ± 0.04	1.55 ± 0.50
GR01 22	E	4.6 ± 0.1	9.6 ± 0.0	7.4	2.37 ± 0.05	11.73 ± 0.39
GR01 26	E	3.4 ± 1.0	-3.5 ± 0.4	-3.0	0.25 ± 0.06	0.89 ± 0.33
GR01 27	E	1.8 ± 0.4	-3.7 ± 0.2	-3.7	0.41 ± 0.08	0.77 ± 0.24
GR01 29	E	2.0 ± 0.8	-4.3 ± 0.3	-4.5	0.22 ± 0.08	0.46 ± 0.25
GR02 01	E	3.6 ± 0.6	-2.9 ± 0.3	-3.1	0.39 ± 0.06	1.51 ± 0.34
GR02 02	E	1.4 ± 0.7	-1.9 ± 0.3	-1.5	0.23 ± 0.09	0.34 ± 0.21
GR05 05	E	2.7 ± 0.6	6.6 ± 0.3	6.4	0.33 ± 0.07	0.93 ± 0.29
GR05 11	E	2.6 ± 0.9	7.9 ± 0.4	7.9	0.23 ± 0.07	0.66 ± 0.29
GR10 02	E	3.9 ± 0.7	2.4 ± 0.3	2.5	0.37 ± 0.06	1.50 ± 0.35

Notes. $(^a)$ The types of components are: C = cavity shock; E = envelope emission; S = spot shock; A = envelope absorption. $(^b)$ Integrated intensity of each velocity component approximated to the gaussian fit.

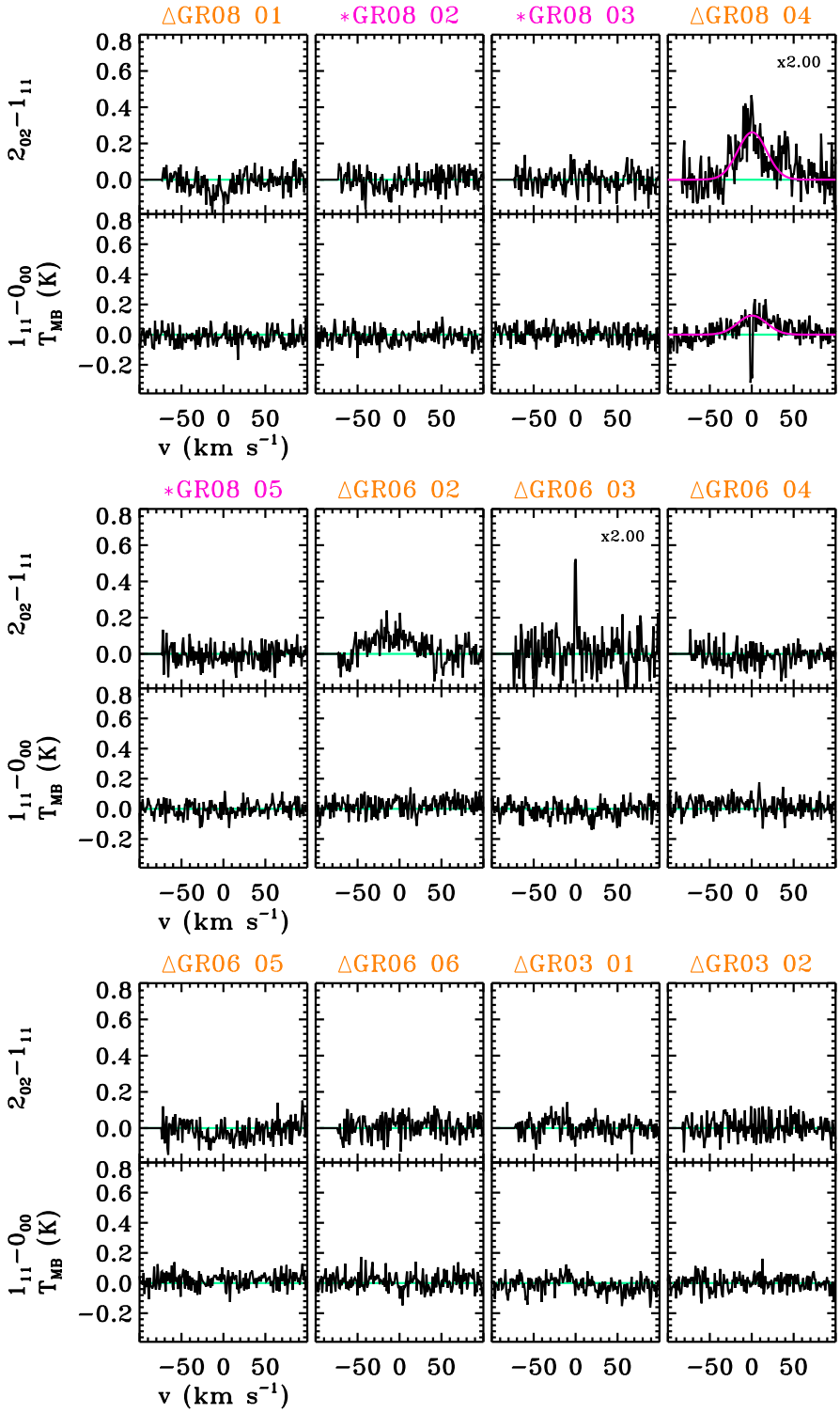

Figure 5.31: (*Bottom*) H_2O 1_{11}-0_{00} (1113 GHz) and (*top*) H_2O 2_{02}-1_{11} spectra observed for the Cygnus YSOs. The name of the Class 0 type sources is written in pink and with an asterisk symbol next to it and that of the Class I objects in orange with a triangle symbol. The baseline is plotted with a green line and the broad velocity component indicated in pink.

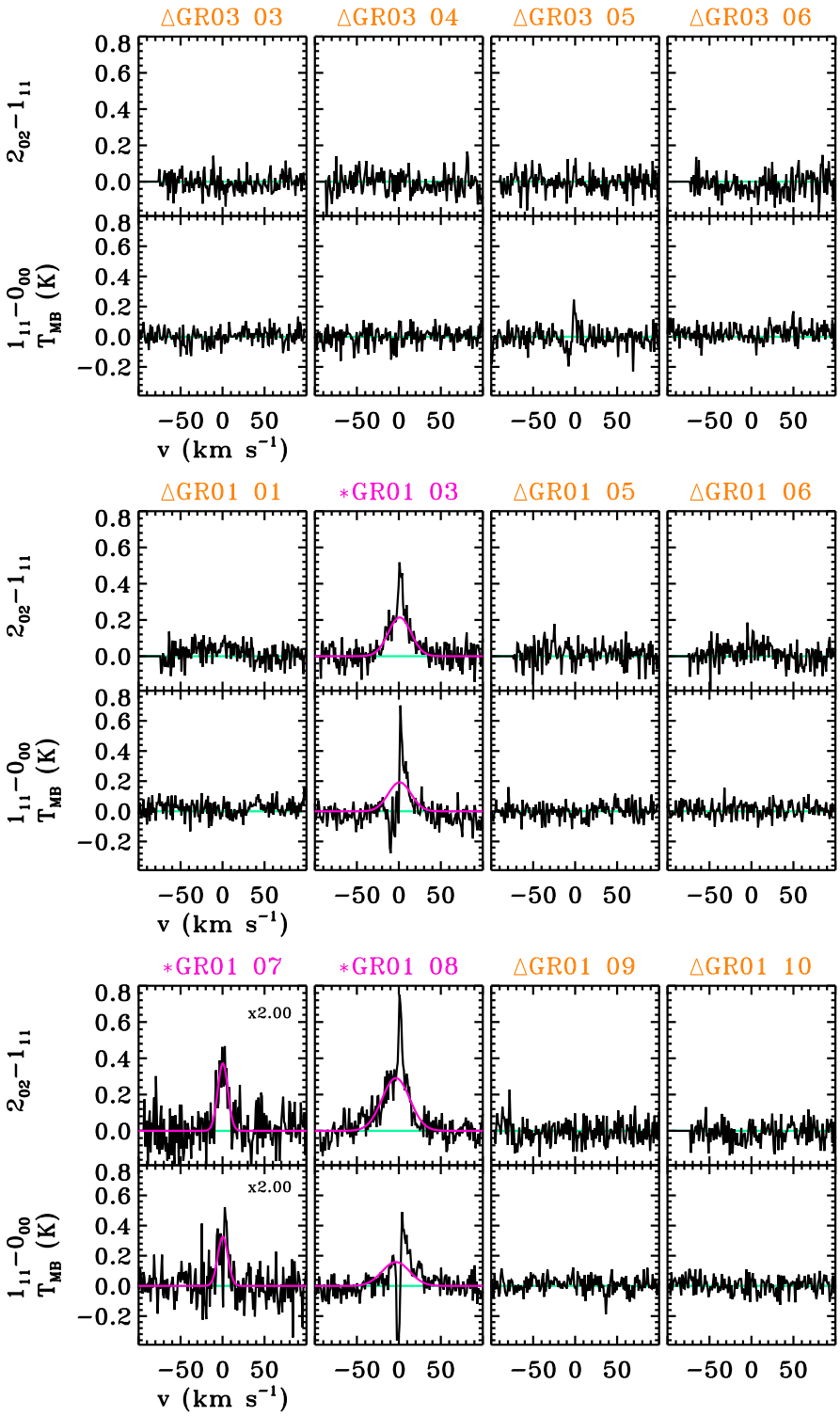

Figure 5.32: Same as Fig 5.31.

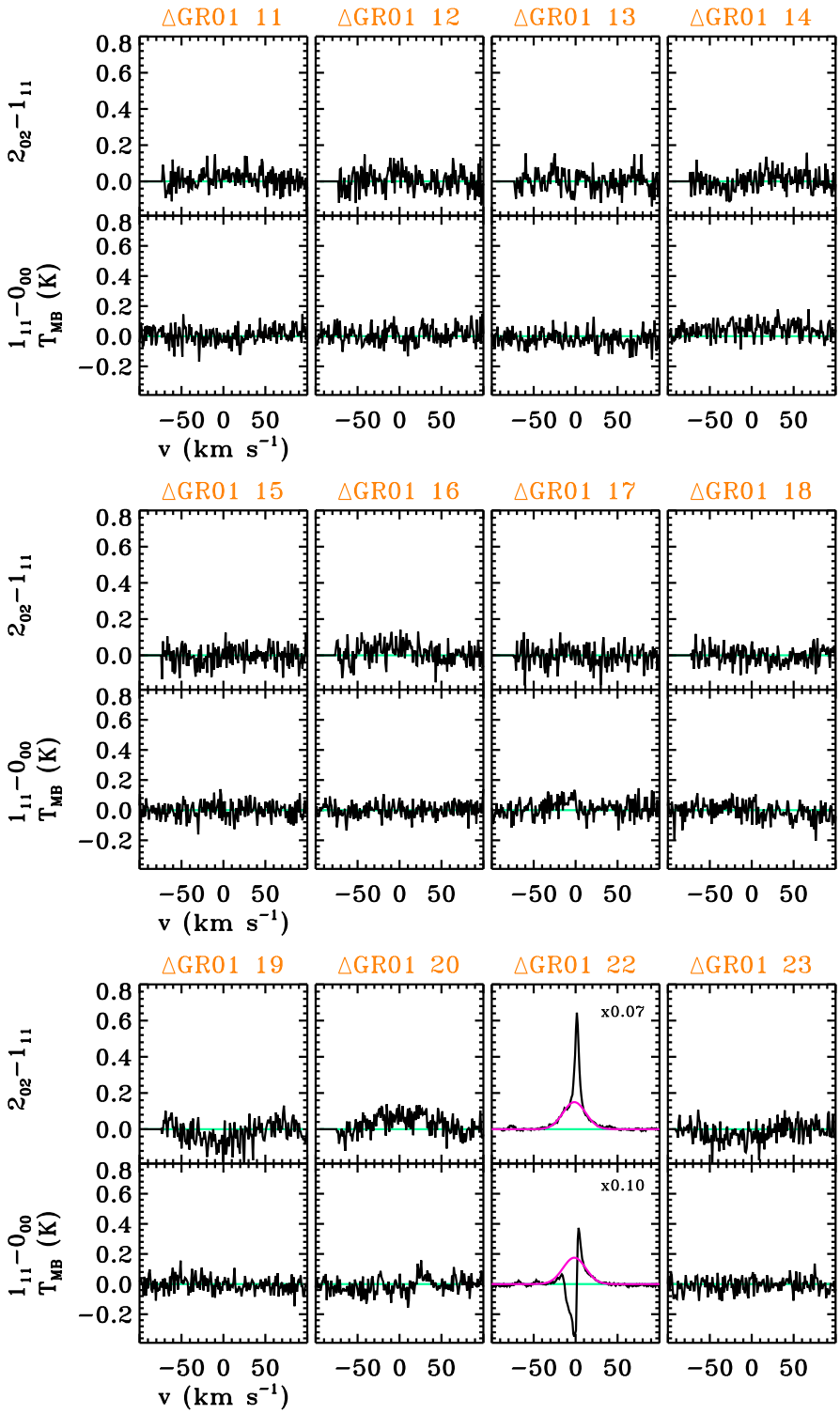

Figure 5.33: Same as Fig 5.31.

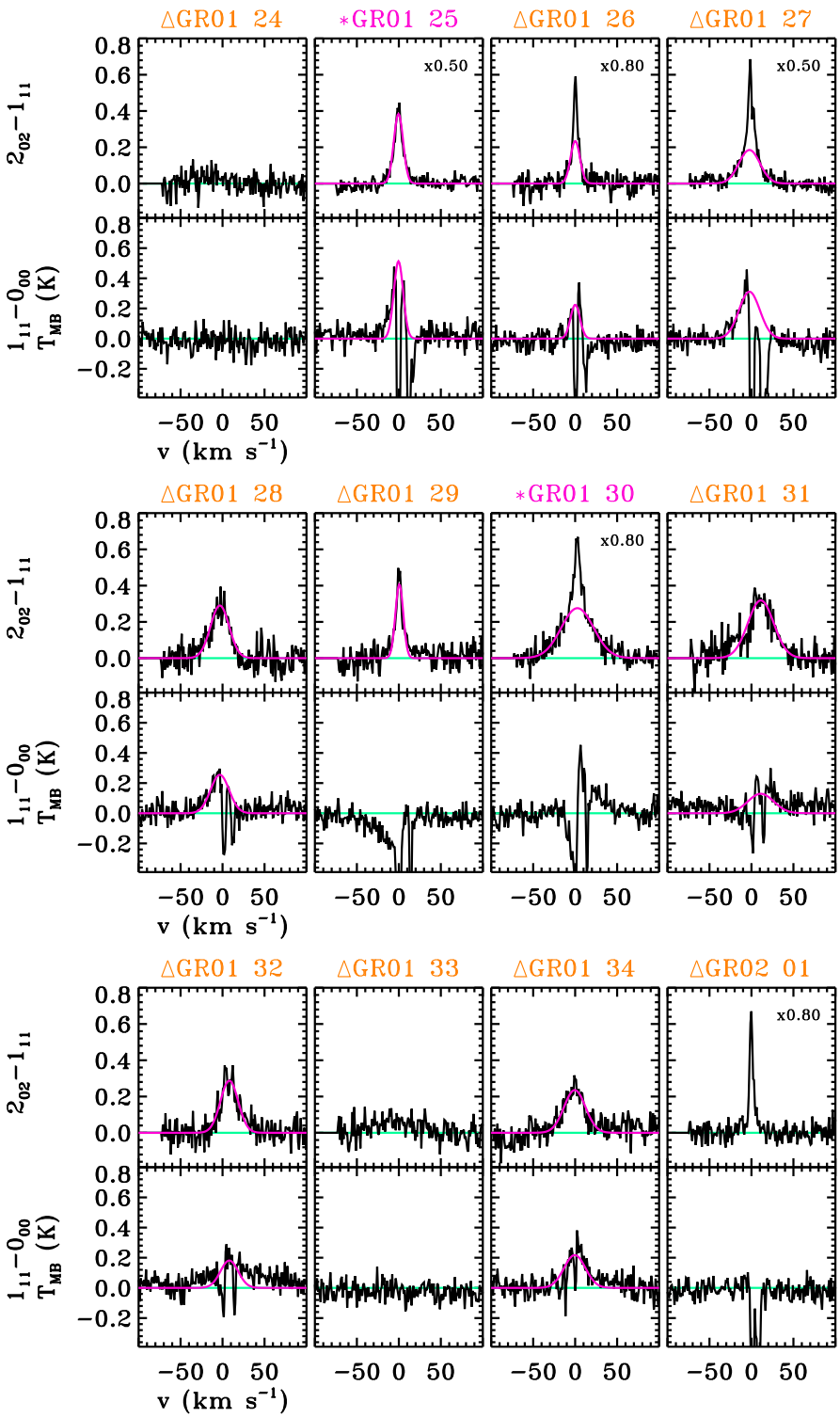

Figure 5.34: Same as Fig 5.31.

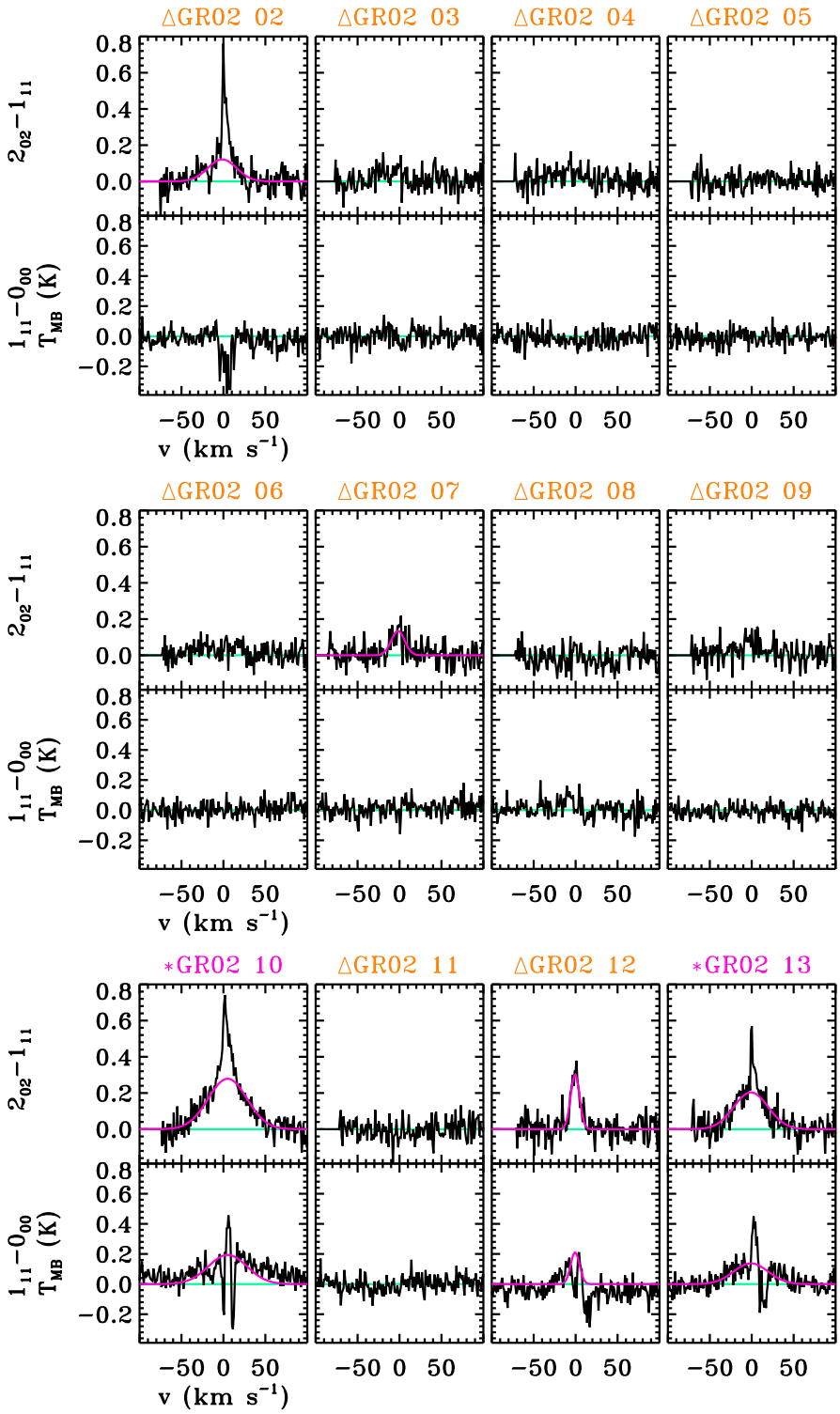

Figure 5.35: Same as Fig 5.31.

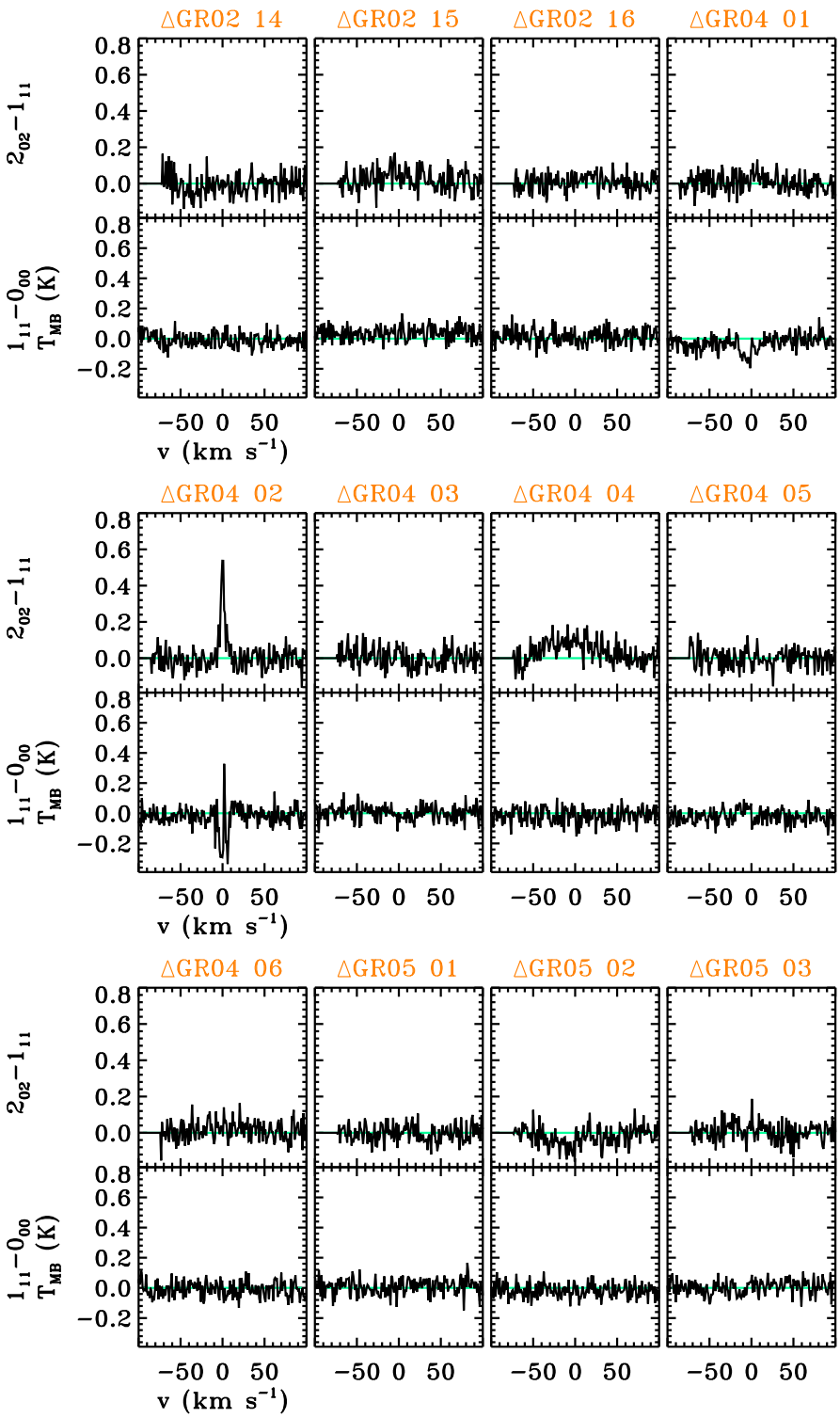

Figure 5.36: Same as Fig 5.31.

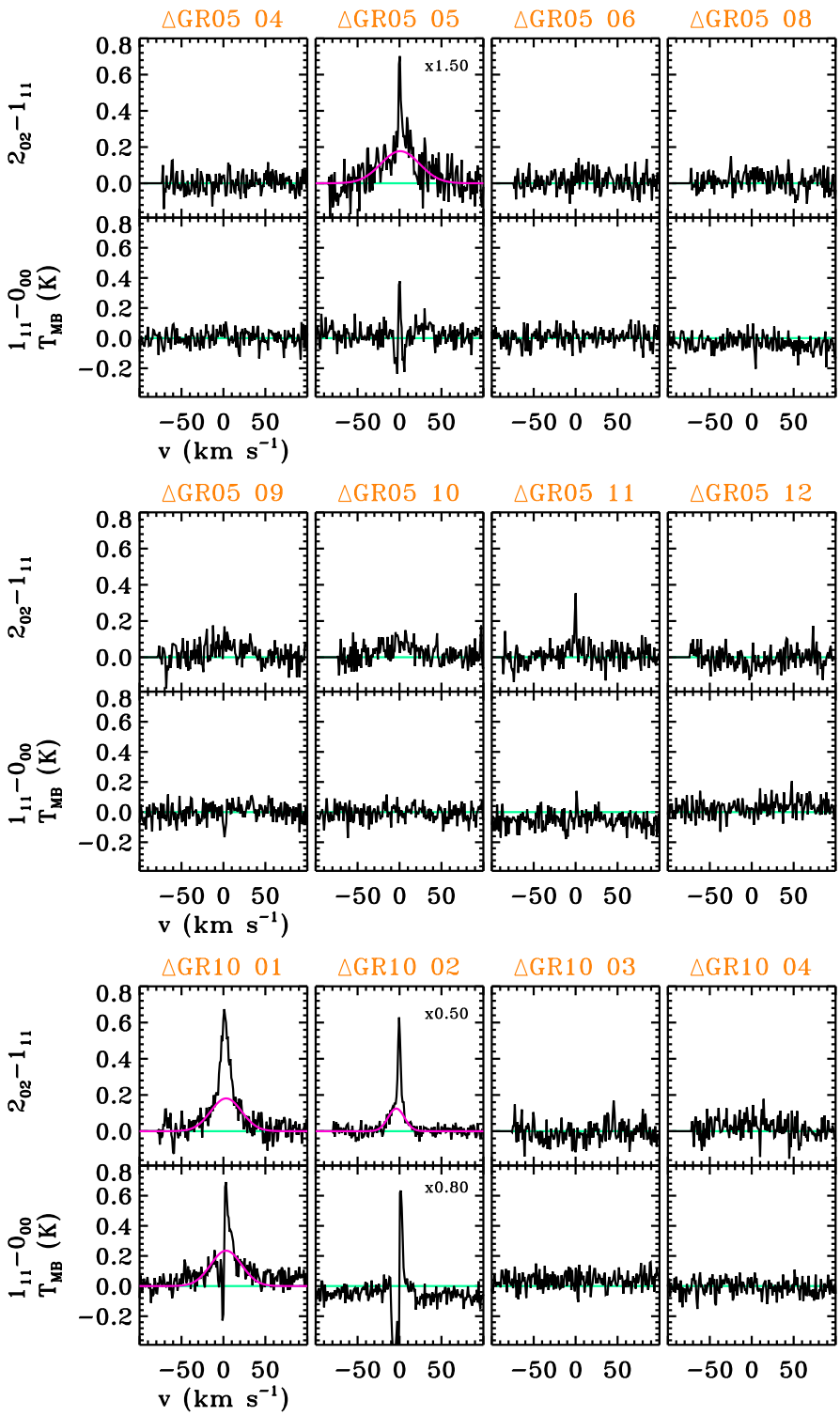

Figure 5.37: Same as Fig 5.31.

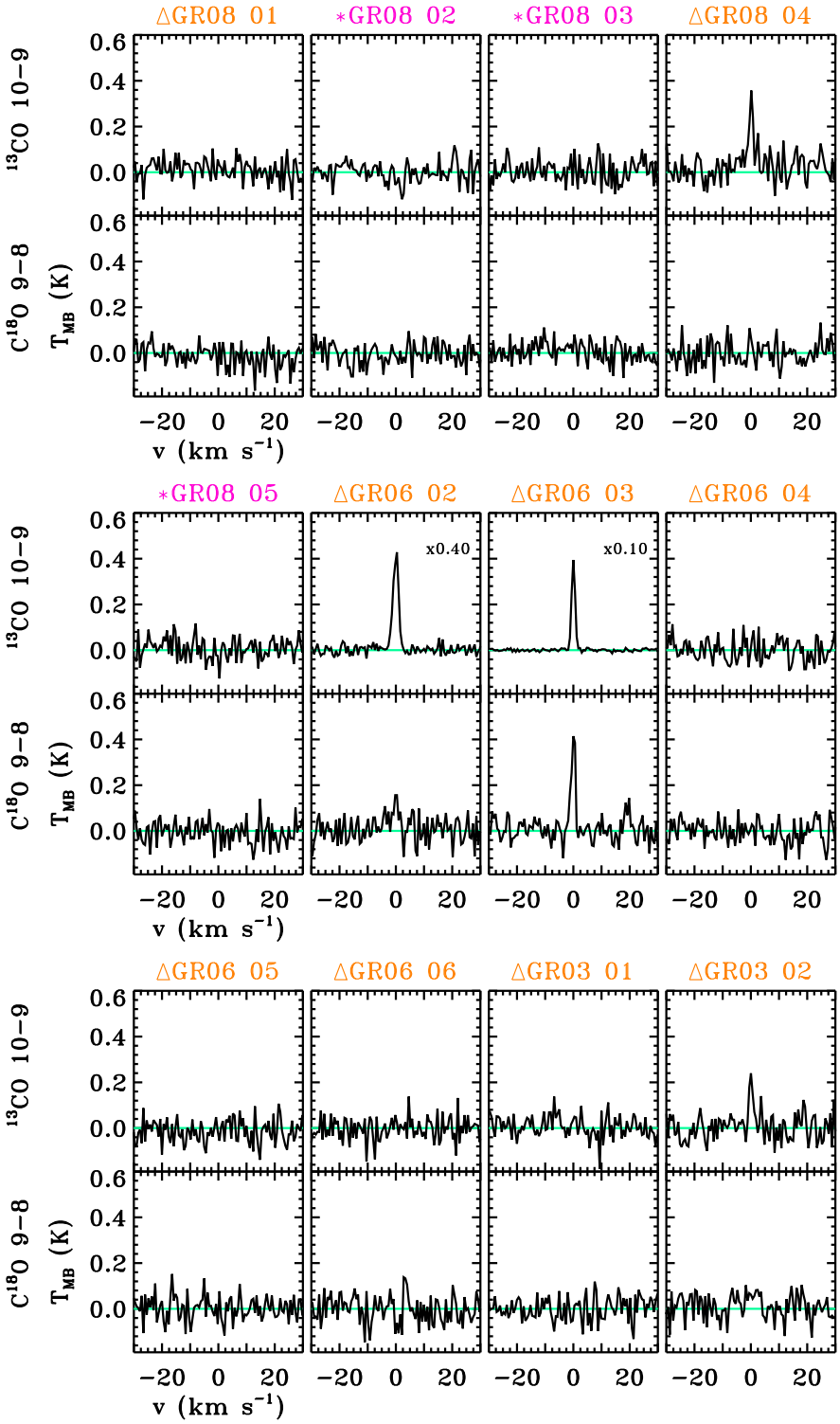

Figure 5.38: (*Bottom*) $C^{18}O$ $J = 9$–8 and (*top*) ^{13}CO $J = 10$–9 spectra observed for the Cygnus YSOs. The name of the Class 0 YSOs is written in pink (with an asterisk symbol next to it) and that of the Class I type objects in orange (and with a triangle symbol). The baseline is plotted with a green line and the broad velocity component indicated in pink.

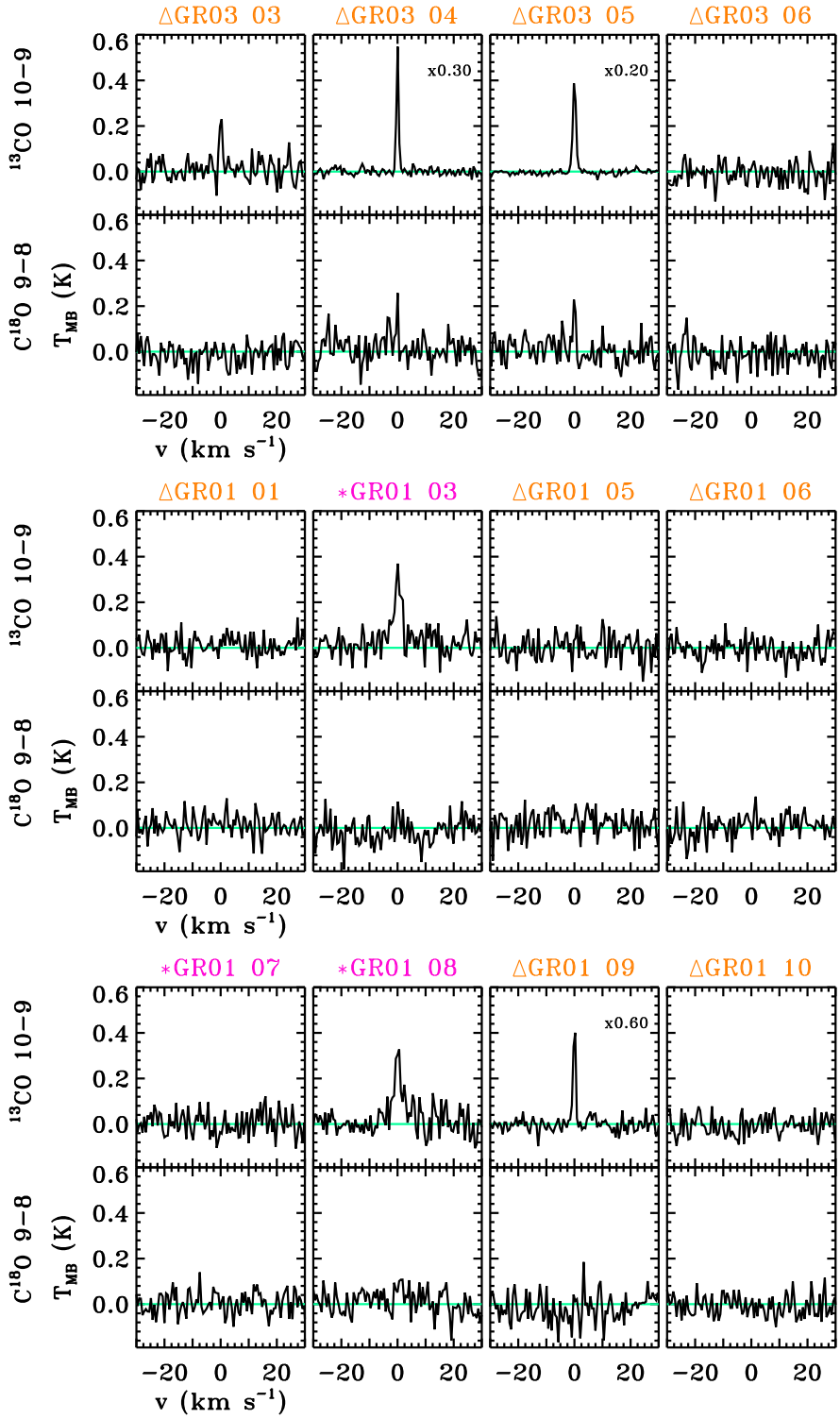

Figure 5.39: Same as Fig 5.38.

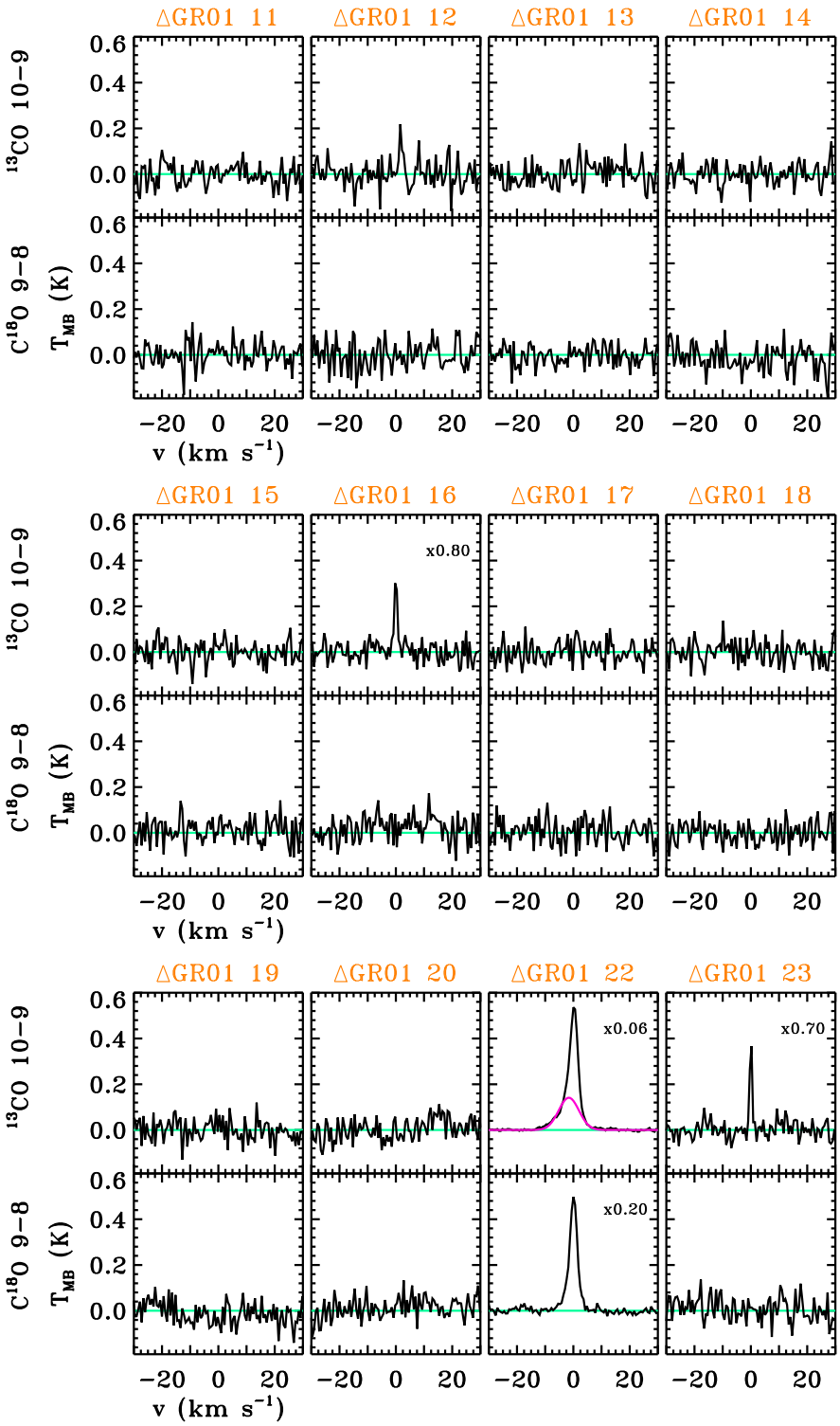

Figure 5.40: Same as Fig 5.38.

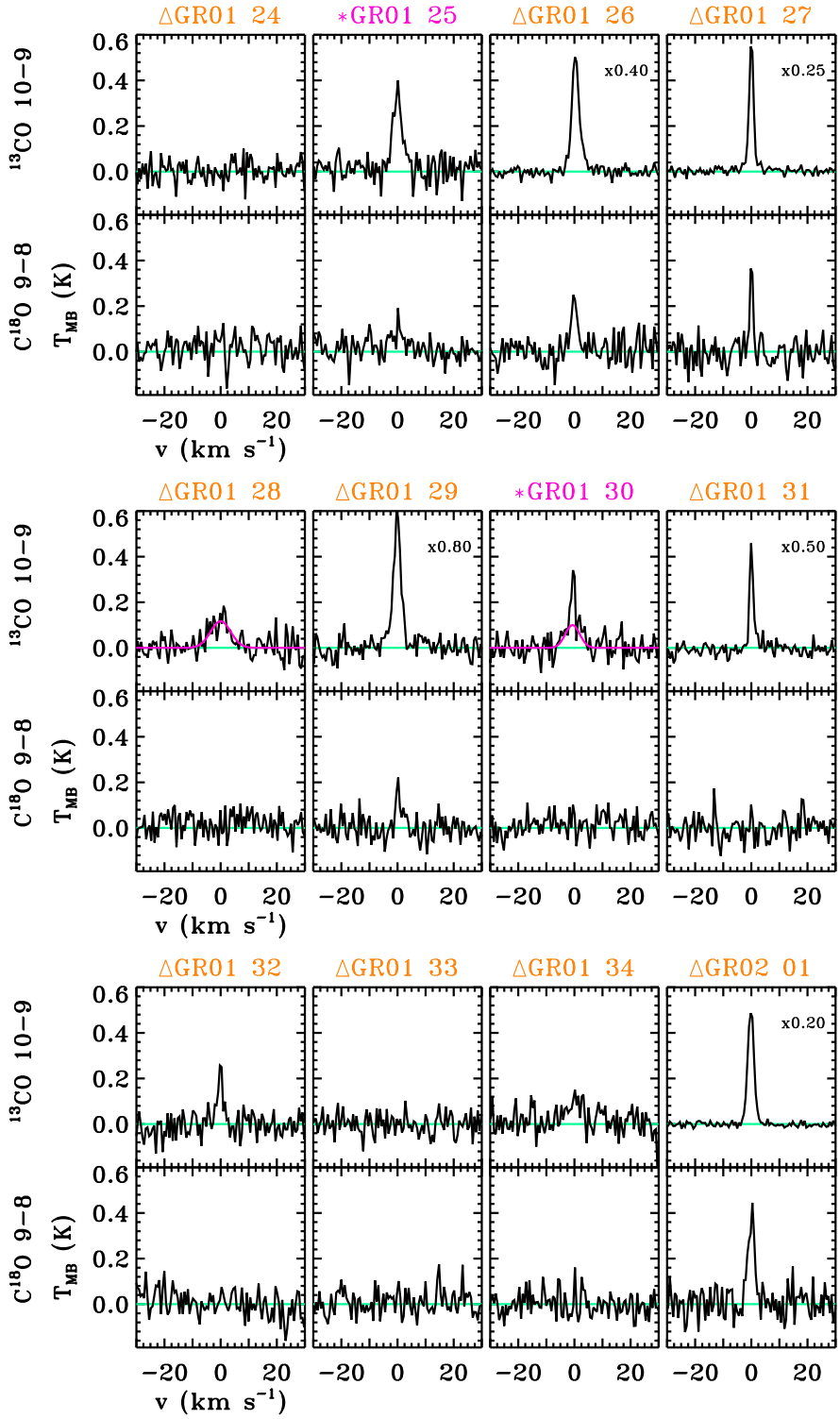

Figure 5.41: Same as Fig 5.38.

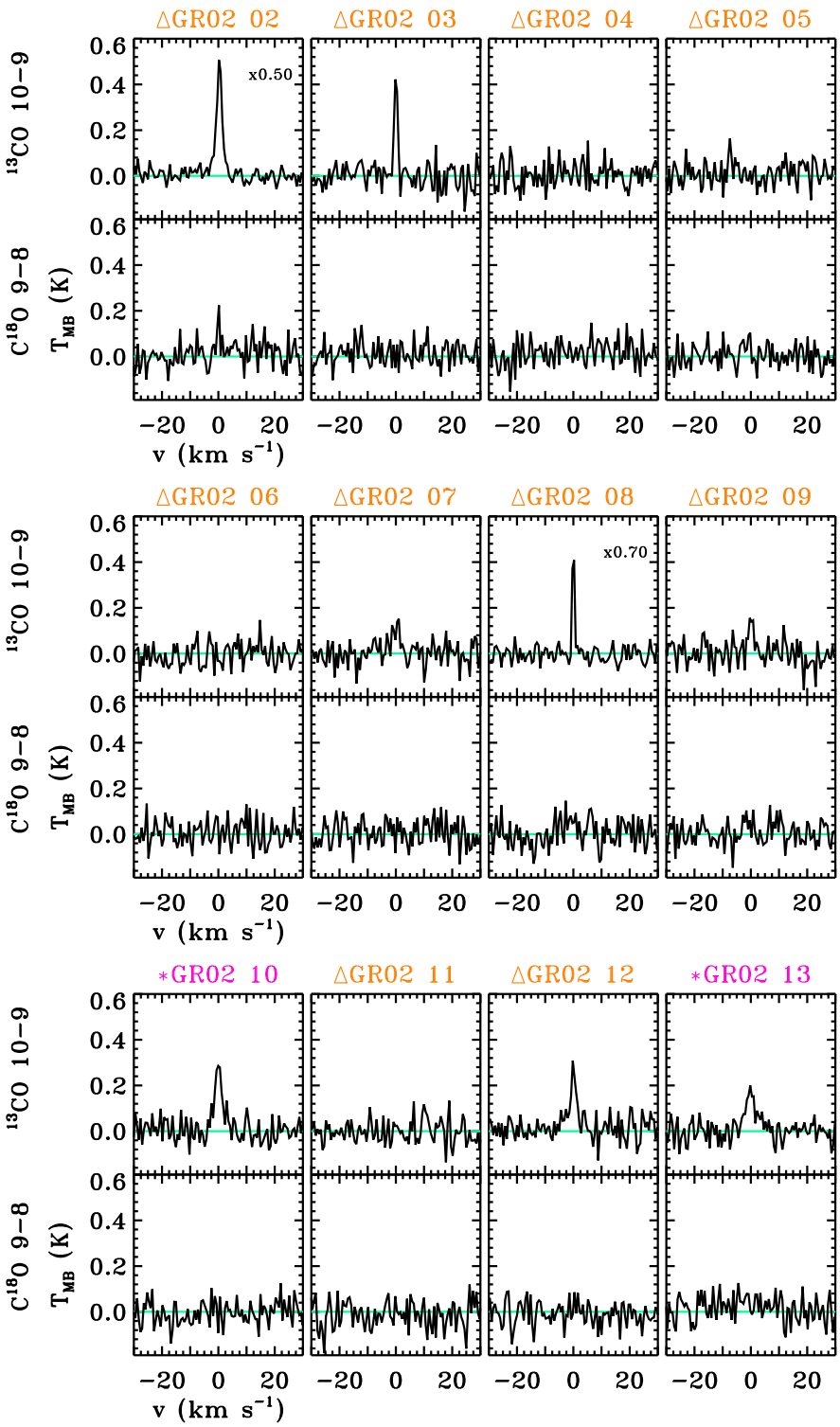

Figure 5.42: Same as Fig 5.38.

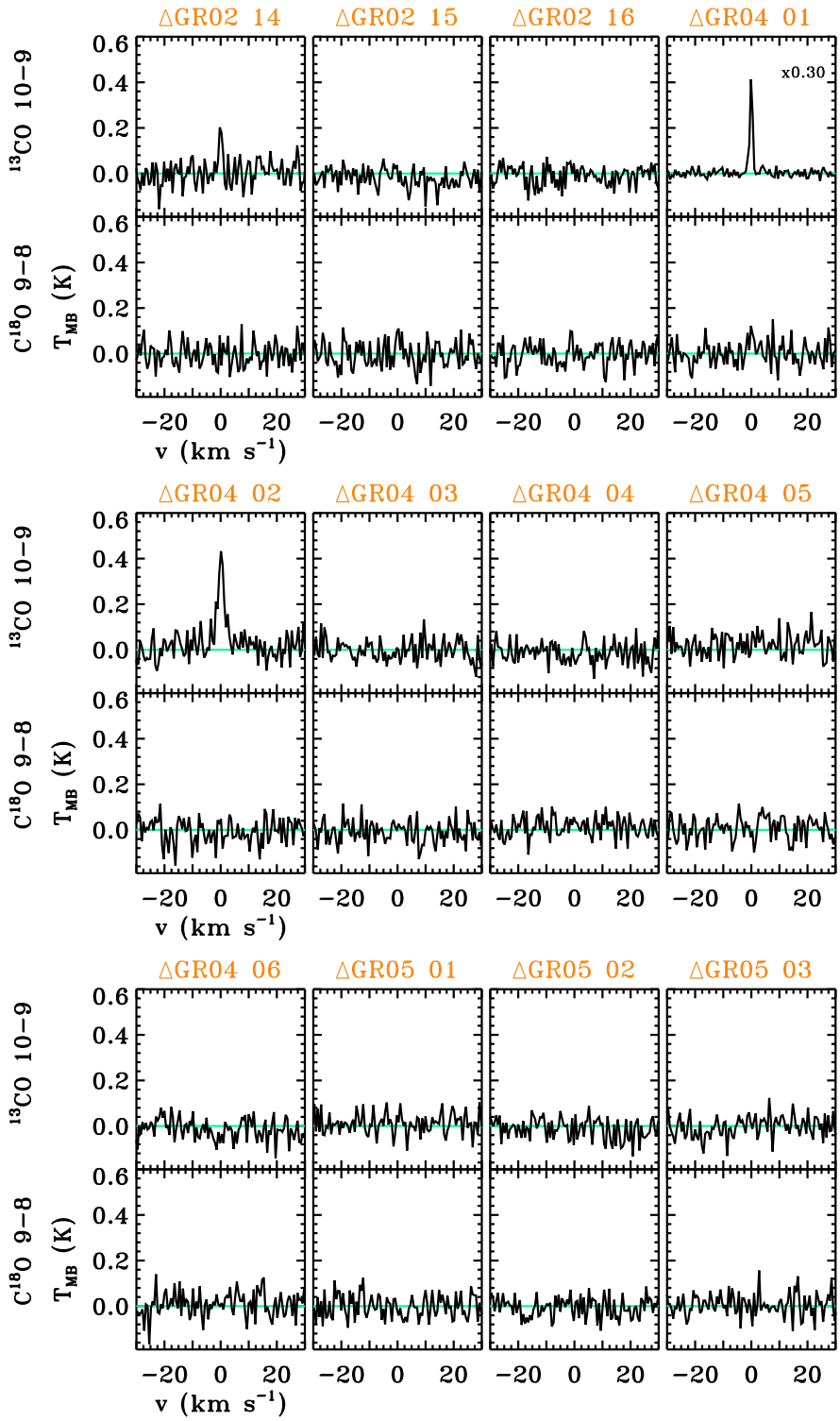

Figure 5.43: Same as Fig 5.38.

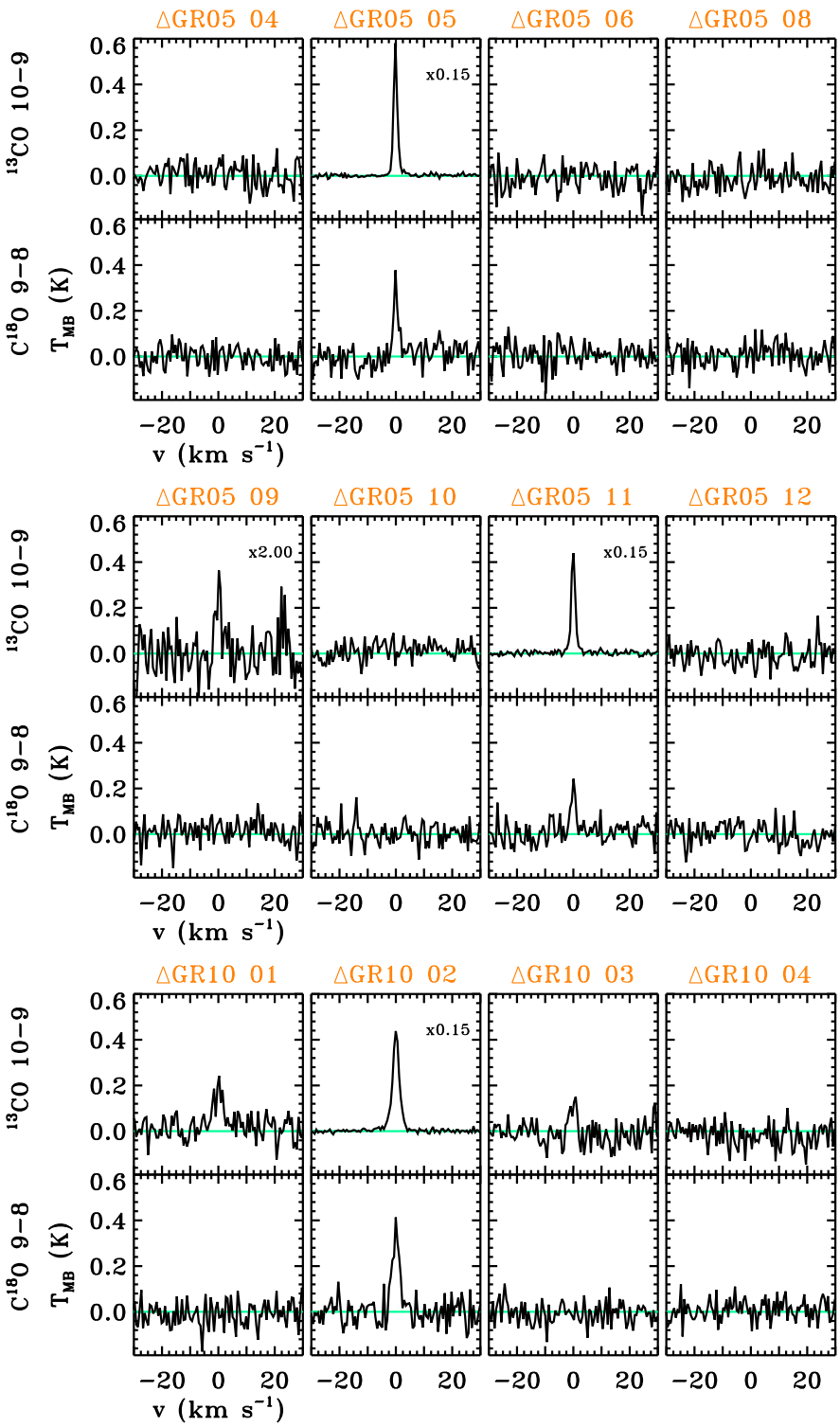

Figure 5.44: Same as Fig 5.38.

Bibliography

André, P., Di Francesco, J., Ward-Thompson, D., et al. 2014, in Protostars and Planets VI, ed. H. Beuther, R. S. Klessen, C. Dullemond, & T. Henning (Univ. of Arizona Press; Tucson, AZ), 27–51

André, P., Men'shchikov, A., Bontemps, S., et al. 2010, *A&A*, 518, L102

André, P., Ward-Thompson, D., & Barsony, M. 1993, *ApJ*, 406, 122

André, P., Ward-Thompson, D., & Barsony, M. 2000, in Protostars and Planets IV, ed. V. Mannings, A. P. Boss, & S. S. Russell (Univ. of Arizona Press; Tucson, AZ), 59

Arce, H. G., Shepherd, D., Gueth, F., et al. 2007, in Protostars and Planets V, ed. B. Reipurth, D. Jewitt, & K. Keil (Univ. of Arizona Press; Tucson, AZ), 245–260

Bachiller, R., Martin-Pintado, J., Tafalla, M., Cernicharo, J., & Lazareff, B. 1990, *A&A*, 231, 174

Bachiller, R. & Tafalla, M. 1999, in NATO Advanced Science Institutes (ASI) Series C, ed. C. J. Lada & N. D. Kylafis, Vol. 540 (Kluwer Academic Publishers), 227

Ballesteros-Paredes, J., Klessen, R. S., Mac Low, M.-M., & Vazquez-Semadeni, E. 2007, in Protostars and Planets V, ed. B. Reipurth, D. Jewitt, & K. Keil (Univ. of Arizona Press; Tucson, AZ), 63–80

Behrend, R. & Maeder, A. 2001a, *A&A*, 373, 190

Behrend, R. & Maeder, A. 2001b, *A&A*, 373, 190

Beltrán, M. 2015, Astrophysics and Space Science, 355, 283

Beltrán, M. T., Estalella, R., Girart, J. M., Ho, P. T. P., & Anglada, G. 2008, *A&A*, 481, 93

Beltrán, M. T., Girart, J. M., Estalella, R., Ho, P. T. P., & Palau, A. 2002, *ApJ*, 573, 246

Bergin, E. A. & Tafalla, M. 2007, *ARA&A*, 45, 339

Bertoldi, F. & McKee, C. F. 1992, *ApJ*, 395, 140

Beuther, H., Churchwell, E. B., McKee, C. F., & Tan, J. C. 2007, in Protostars and Planets V, ed. B. Reipurth, D. Jewitt, & K. Keil (Univ. of Arizona Press; Tucson, AZ), 165–180

Beuther, H., Schilke, P., Sridharan, T. K., et al. 2002, *A&A*, 383, 892

Beuther, H. & Shepherd, D. 2005, in Cores to Clusters: Star Formation with Next Generation Telescopes, ed. M. S. N. Kumar, M. Tafalla, & P. Caselli (Springer, New York), 105–119

Bisschop, S. E., Fraser, H. J., Öberg, K. I., van Dishoeck, E. F., & Schlemmer, S. 2006, *A&A*, 449, 1297

Blum, R. D. 2005, in IAU Symposium, Vol. 227, Massive Star Birth: A Crossroads of Astrophysics, ed. R. Cesaroni, M. Felli, E. Churchwell, & M. Walmsley (Cambridge Univ. Press, Cambridge), 216–224

Boley, P. A., Linz, H., van Boekel, R., et al. 2012, *A&A*, 547, A88

Bonnell, I. A. & Bate, M. R. 2002, *MNRAS*, 336, 659

Bonnell, I. A. & Bate, M. R. 2005, *MNRAS*, 362, 915

Bonnell, I. A., Bate, M. R., Clarke, C. J., & Pringle, J. E. 1997, *MNRAS*, 285, 201

Bonnell, I. A., Bate, M. R., Clarke, C. J., & Pringle, J. E. 2001, *MNRAS*, 323, 785

Bonnell, I. A., Bate, M. R., & Zinnecker, H. 1998, *MNRAS*, 298, 93

Bontemps, S., Andre, P., Terebey, S., & Cabrit, S. 1996, *A&A*, 311, 858

Bressert, E., Bastian, N., & Gutermuth, R. 2012, Do All Stars in the Solar Neighbourhood Form in Clusters? (Springer-Verlag Berlin Heidelberg), 147

Bressert, E., Bastian, N., Gutermuth, R., et al. 2010, *MNRAS*, 409, L54

Brinch, C., Crapsi, A., Hogerheijde, M. R., & Jørgensen, J. K. 2007, *A&A*, 461, 1037

Brinch, C., Jørgensen, J. K., & Hogerheijde, M. R. 2009, *A&A*, 502, 199

Buckle, J. V., Hills, R. E., Smith, H., et al. 2009, *MNRAS*, 399, 1026

Cabrit, S. & Bertout, C. 1992, *A&A*, 261, 274

Calvet, N., Muzerolle, J., Briceño, C., et al. 2004, *AJ*, 128, 1294

Ceccarelli, C., Bacmann, A., Boogert, A., et al. 2010, *A&A*, 521, L22

Cesaroni, R. 2005, in IAU Symposium, Vol. 227, Massive Star Birth: A Crossroads of Astrophysics, ed. R. Cesaroni, M. Felli, E. Churchwell, & M. Walmsley (Cambridge Univ. Press, Cambridge)

Cesaroni, R., Galli, D., Lodato, G., Walmsley, C. M., & Zhang, Q. 2007, in Protostars and Planets V, ed. B. Reipurth, D. Jewitt, & K. Keil (Univ. of Arizona Press; Tucson, AZ), 197–212

Chandler, C. J. & Richer, J. S. 2000, *ApJ*, 530, 851

Chavarría, L., Herpin, F., Jacq, T., et al. 2010, *A&A*, 521, L37

Choi, M., Evans, II, N. J., & Jaffe, D. T. 1993, *ApJ*, 417, 624
Churchwell, E. 1999, in NATO Advanced Science Institutes (ASI) Series C, ed. C. J. Lada & N. D. Kylafis, Vol. 540 (Kluwer Academic Publishers), 515
Churchwell, E. 2002, *ARA&A*, 40, 27
Codella, C., Lefloch, B., Ceccarelli, C., et al. 2010, *A&A*, 518, L112
Collings, M. P., Anderson, M. A., Chen, R., et al. 2004, *MNRAS*, 354, 1133
Comerón, F. & Pasquali, A. 2012, *A&A*, 543, A101
Cox, M. J., Scott, P. F., Russell, A. P. G., & Andersson, M. 1987, *MNRAS*, 226, 703
Cuppen, H. M., Ioppolo, S., Romanzin, C., & Linnartz, H. 2010, Physical Chemistry Chemical Physics (Incorporating Faraday Transactions), 12, 12077
Curtis, E. I., Richer, J. S., Swift, J. J., & Williams, J. P. 2010, *MNRAS*, 408, 1516
de Graauw, T., Helmich, F. P., Phillips, T. G., et al. 2010, *A&A*, 518, L6
de Wit, W. J., Testi, L., Palla, F., & Zinnecker, H. 2005, *A&A*, 437, 247
Dunham, M. M., Stutz, A. M., Allen, L. E., et al. 2014, in Protostars and Planets VI, ed. H. Beuther, R. S. Klessen, C. Dullemond, & T. Henning (Univ. of Arizona Press; Tucson, AZ), 195–218
Evans, N., Calvet, N., Cieza, L., et al. 2009, ArXiv e-prints
Evans, II, N. J. 1999, *ARA&A*, 37, 311
Flower, D. R. 1999, *MNRAS*, 305, 651
Frank, A., Ray, T. P., Cabrit, S., et al. 2014, in Protostars and Planets VI, ed. H. Beuther, R. S. Klessen, C. Dullemond, & T. Henning (Univ. of Arizona Press; Tucson, AZ), 451–474
Fuente, A., Martin-Pintado, J., Bachiller, R., Neri, R., & Palla, F. 1998, *A&A*, 334, 253
Fuente, A., Martın-Pintado, J., Bachiller, R., Rodrıguez-Franco, A., & Palla, F. 2002, *A&A*, 387, 977
Fuente, A., Neri, R., Martín-Pintado, J., et al. 2001, *A&A*, 366, 873
Fuente, A., Rizzo, J. R., Neri, R., Caselli, P., & Bachiller, R. 2005, in ESA Special Publication, ed. A. Wilson, Vol. 577 (ESA Publications Division; Noordwijk, Netherlands), 87–90
Fuller, G. A. & Ladd, E. F. 2002, *ApJ*, 573, 699
Fuller, G. A., Williams, S. J., & Sridharan, T. K. 2005, *A&A*, 442, 949
Gao, Y. & Solomon, P. M. 2004a, *ApJS*, 152, 63
Gao, Y. & Solomon, P. M. 2004b, *ApJ*, 606, 271
Garay, G., Faúndez, S., Mardones, D., et al. 2004, *ApJ*, 610, 313
Godard, B., Falgarone, E., Gerin, M., Hily-Blant, P., & de Luca, M. 2010, *A&A*, 520, A20
Goicoechea, J. R., Cernicharo, J., Karska, A., et al. 2012, *A&A*, 548, A77
González-Alfonso, E., Fischer, J., Aalto, S., & Falstad, N. 2014, *A&A*, 567, A91
Graves, S. F., Richer, J. S., Buckle, J. V., et al. 2010, *MNRAS*, 409, 1412
Green, J. D., Evans, II, N. J., Jørgensen, J. K., et al. 2013, *ApJ*, 770, 123
Greene, T. P., Wilking, B. A., Andre, P., Young, E. T., & Lada, C. J. 1994, *ApJ*, 434, 614
Gregersen, E. M., Evans, II, N. J., Zhou, S., & Choi, M. 1997, *ApJ*, 484, 256
Griffin, M. J., Abergel, A., Abreu, A., et al. 2010, *A&A*, 518, L3
Hacar, A., Tafalla, M., Kauffmann, J., & Kovács, A. 2013, *A&A*, 554, A55
Harsono, D., Visser, R., Bruderer, S., van Dishoeck, E. F., & Kristensen, L. E. 2013, *A&A*, 555, A45
Henshaw, J. D., Caselli, P., Fontani, F., Jiménez-Serra, I., & Tan, J. C. 2014, *MNRAS*, 440, 2860
Herczeg, G. J., Karska, A., Bruderer, S., et al. 2012, *A&A*, 540, A84
Herpin, F., Chavarría, L., van der Tak, F., et al. 2012, *A&A*, 542, A76
Heyer, M., Krawczyk, C., Duval, J., & Jackson, J. M. 2009, *ApJ*, 699, 1092
Hillenbrand, L. A., Meyer, M. R., Strom, S. E., & Skrutskie, M. F. 1995, *AJ*, 109, 280
Hoare, M. G., Kurtz, S. E., Lizano, S., Keto, E., & Hofner, P. 2007, Protostars and Planets V, 181
Hocuk, S. & Spaans, M. 2010, *A&A*, 510, A110
Hogerheijde, M. R. & van der Tak, F. F. S. 2000, *A&A*, 362, 697
Hogerheijde, M. R., van Dishoeck, E. F., Salverda, J. M., & Blake, G. A. 1999, *ApJ*, 513, 350
Hollenbach, D. J. & Tielens, A. G. G. M. 1999, Reviews of Modern Physics, 71, 173
Ioppolo, S., Cuppen, H. M., Romanzin, C., van Dishoeck, E. F., & Linnartz, H. 2008, *ApJ*, 686, 1474
Ioppolo, S., Cuppen, H. M., Romanzin, C., van Dishoeck, E. F., & Linnartz, H. 2010, Physical Chemistry Chemical Physics (Incorporating Faraday Transactions), 12, 12065
Ivezić, Z. & Elitzur, M. 1997, *MNRAS*, 287, 799

Jijina, J. & Adams, F. C. 1996, *ApJ*, 462, 874
Jijina, J., Myers, P. C., & Adams, F. C. 1999, *ApJS*, 125, 161
Johnston, K. G., Shepherd, D. S., Robitaille, T. P., & Wood, K. 2012, VizieR Online Data Catalog, 355, 19043
Jørgensen, J. K., Schöier, F. L., & van Dishoeck, E. F. 2002, *A&A*, 389, 908
Jørgensen, J. K., Schöier, F. L., & van Dishoeck, E. F. 2004, *A&A*, 416, 603
Jørgensen, J. K., Schöier, F. L., & van Dishoeck, E. F. 2005, *A&A*, 435, 177
Kahn, F. D. 1974, *A&A*, 37, 149
Kama, M., López-Sepulcre, A., Dominik, C., et al. 2013, *A&A*, 556, A57
Kamenetzky, J., Glenn, J., Rangwala, N., et al. 2012, *ApJ*, 753, 70
Karska, A., Herczeg, G. J., van Dishoeck, E. F., et al. 2013, *A&A*, 552, A141
Karska, A., Herpin, F., Bruderer, S., et al. 2014a, *A&A*, 562, A45
Karska, A., Kristensen, L. E., van Dishoeck, E. F., et al. 2014b, *A&A*, 572, A9
Kaźmierczak-Barthel, M., van der Tak, F. F. S., Helmich, F. P., et al. 2014, *A&A*, 567, A53
Kennicutt, R. C. & Evans, N. J. 2012, *ARA&A*, 50, 531
Keto, E. 2007, *ApJ*, 666, 976
Keto, E. & Zhang, Q. 2010, *MNRAS*, 406, 102
Kim, S.-J., Kim, H.-D., Lee, Y., et al. 2006, *ApJS*, 162, 161
Kirk, H., Myers, P. C., Bourke, T. L., et al. 2013, *ApJ*, 766, 115
Kristensen, L. E., van Dishoeck, E. F., Benz, A. O., et al. 2013, *A&A*, 557, A23
Kristensen, L. E., van Dishoeck, E. F., Bergin, E. A., et al. 2012, *A&A*, 542, A8
Kristensen, L. E., van Dishoeck, E. F., Tafalla, M., et al. 2011, *A&A*, 531, L1
Kristensen, L. E., Visser, R., van Dishoeck, E. F., et al. 2010, *A&A*, 521, L30
Krumholz, M. R. & Bonnell, I. A. 2009, Models for the formation of massive stars (Cambridge University Press; Cambridge), 288
Krumholz, M. R. & Thompson, T. A. 2007, *ApJ*, 669, 289
Kryukova, E., Megeath, S. T., Hora, J. L., et al. 2014, ArXiv e-prints
Kuiper, R., Yorke, H. W., & Turner, N. J. 2015, *ApJ*, 800, 86
Kumar, M. S. N., Keto, E., & Clerkin, E. 2006, *A&A*, 449, 1033
Kurtz, S. 2005, in IAU Symposium, Vol. 227, Massive Star Birth: A Crossroads of Astrophysics, ed. R. Cesaroni, M. Felli, E. Churchwell, & M. Walmsley (Cambridge Univ. Press, Cambridge), 111–119
Lacy, J. H., Knacke, R., Geballe, T. R., & Tokunaga, A. T. 1994, *ApJL*, 428, L69
Lada, C. J. & Fich, M. 1995, in Revista Mexicana de Astronomia y Astrofisica, vol. 27, Vol. 1, Revista Mexicana de Astronomia y Astrofisica Conference Series, ed. S. Lizano & J. M. Torrelles, 93
Lada, C. J., Forbrich, J., Lombardi, M., & Alves, J. F. 2012, *ApJ*, 745, 190
Lada, C. J. & Kylafis, N. D. 1999, in NATO Advanced Science Institutes (ASI) Series C, ed. C. J. Lada & N. D. Kylafis, Vol. 540 (Kluwer Academic Publishers)
Lada, C. J. & Wilking, B. A. 1984, *ApJ*, 287, 610
Lamberts, T., Cuppen, H. M., Fedoseev, G., et al. 2014, *A&A*, 570, A57
Linke, R. A., Goldsmith, P. F., Wannier, P. G., Wilson, R. W., & Penzias, A. A. 1977, *ApJ*, 214, 50
Lommen, D., Jørgensen, J. K., van Dishoeck, E. F., & Crapsi, A. 2008, *A&A*, 481, 141
López-Sepulcre, A., Cesaroni, R., & Walmsley, C. M. 2010, *A&A*, 517, A66
Manoj, P., Watson, D. M., Neufeld, D. A., et al. 2013, *ApJ*, 763, 83
Marseille, M. G., van der Tak, F. F. S., Herpin, F., & Jacq, T. 2010, *A&A*, 522, A40
Matzner, C. D. 2002, *ApJ*, 566, 302
McKee, C. F. & Ostriker, E. C. 2007a, *ARA&A*, 45, 565
McKee, C. F. & Ostriker, E. C. 2007b, *ARA&A*, 45, 565
McKee, C. F. & Tan, J. C. 2002, *Nature*, 416, 59
McKee, C. F. & Tan, J. C. 2003, *ApJ*, 585, 850
Meijerink, R., Kristensen, L. E., Weiß, A., et al. 2013, *ApJL*, 762, L16
Motte, F., Bontemps, S., Schilke, P., et al. 2007, *A&A*, 476, 1243
Mottram, J. C. & Brunt, C. M. 2012, *MNRAS*, 420, 10
Mottram, J. C., Hoare, M. G., Davies, B., et al. 2011, *ApJL*, 730, L33
Mottram, J. C., Kristensen, L. E., van Dishoeck, E. F., et al. 2014, *A&A*, 572, A21
Mottram, J. C., van Dishoeck, E. F., Schmalzl, M., et al. 2013, *A&A*, 558, A126

Murillo, N. M., Lai, S.-P., Bruderer, S., Harsono, D., & van Dishoeck, E. F. 2013, *A&A*, 560, A103
Myers, P. C. 2009, *ApJ*, 700, 1609
Myers, P. C. 2013, *ApJ*, 764, 140
Myers, P. C. & Ladd, E. F. 1993, *ApJL*, 413, L47
Myers, P. C., Mardones, D., Tafalla, M., Williams, J. P., & Wilner, D. J. 1996, *ApJL*, 465, L133
Narayanan, D., Cox, T. J., Shirley, Y., et al. 2008, *ApJ*, 684, 996
Neri, R., Fuente, A., Ceccarelli, C., et al. 2007, *A&A*, 468, L33
Neufeld, D. A., Gusdorf, A., Güsten, R., et al. 2014, *ApJ*, 781, 102
Nielbock, M., Chini, R., & Müller, S. A. H. 2003, *A&A*, 408, 245
Nisini, B., Benedettini, M., Codella, C., et al. 2010, *A&A*, 518, L120
Norberg, P. & Maeder, A. 2000, *A&A*, 359, 1025
Öberg, K. I., van Broekhuizen, F., Fraser, H. J., et al. 2005, *ApJL*, 621, L33
Ossenkopf, V. & Henning, T. 1994, *A&A*, 291, 943
Ott, S. 2010, in Astronomical Society of the Pacific Conference Series, Vol. 434, Astronomical Data Analysis Software and Systems XIX, ed. Y. Mizumoto, K.-I. Morita, & M. Ohishi, 139
Pagani, L., Vastel, C., Hugo, E., et al. 2009, *A&A*, 494, 623
Palau, A., Fuente, A., Girart, J. M., et al. 2013, *ApJ*, 762, 120
Palla, F. & Stahler, S. W. 1993a, *ApJ*, 418, 414
Palla, F. & Stahler, S. W. 1993b, *ApJ*, 418, 414
Pickett, H. M., Poynter, I. R. L., Cohen, E. A., et al. 2010, *J. Quant. Spec. Radiat. Transf.*, 111, 1617
Pilbratt, G. L., Riedinger, J. R., Passvogel, T., et al. 2010, *A&A*, 518, L1
Pineda, J. E., Goodman, A. A., Arce, H. G., et al. 2010, *ApJL*, 712, L116
Plume, R., Bergin, E. A., Phillips, T. G., et al. 2012, *ApJ*, 744, 28
Poglitsch, A., Waelkens, C., Geis, N., et al. 2010, *A&A*, 518, L2
Raga, A. C., Cabrit, S., & Canto, J. 1995, *MNRAS*, 273, 422
Raga, A. C. & Cantó, J. 1997, in IAU Symposium, Vol. 178, Molecules in Astrophysics: Probes and Processes, ed. E. F. van Dishoeck (Kluwer Academic Publishers; Dordrecht, Netherlands), 89–101
Reipurth, B. & Schneider, N. 2008, Star Formation and Young Clusters in Cygnus (The Northern Sky ASP Monograph Publications; San Francisco, CA), 36
Richer, J. S., Shepherd, D. S., Cabrit, S., Bachiller, R., & Churchwell, E. 2000, in Protostars and Planets IV, ed. V. Mannings, A. P. Boss, & S. S. Russell (Univ. of Arizona Press; Tucson, AZ), 867
Robitaille, T. P. 2011, *A&A*, 536, A79
Robitaille, T. P., Whitney, B. A., Indebetouw, R., & Wood, K. 2007, *ApJS*, 169, 328
Robitaille, T. P., Whitney, B. A., Indebetouw, R., Wood, K., & Denzmore, P. 2006, *ApJS*, 167, 256
Roelfsema, P. R., Helmich, F. P., Teyssier, D., et al. 2012, *A&A*, 537, A17
Rolffs, R., Schilke, P., Wyrowski, F., et al. 2011, *A&A*, 529, A76
San José-García, I., Mottram, J. C., Kristensen, L. E., et al. 2013, *A&A*, 553, A125
Sánchez-Monge, Á., Palau, A., Estalella, R., et al. 2010, *ApJL*, 721, L107
Santangelo, G., Nisini, B., Antoniucci, S., et al. 2013, *A&A*, 557, A22
Santangelo, G., Nisini, B., Codella, C., et al. 2014, *A&A*, 568, A125
Santangelo, G., Nisini, B., Giannini, T., et al. 2012, *A&A*, 538, A45
Schneider, N., Bontemps, S., Simon, R., et al. 2006, *A&A*, 458, 855
Schneider, N., Güsten, R., Tremblin, P., et al. 2012, *A&A*, 542, L18
Schöier, F. L., van der Tak, F. F. S., van Dishoeck, E. F., & Black, J. H. 2005, *A&A*, 432, 369
Scott, K. S., Lupu, R. E., Aguirre, J. E., et al. 2011, *ApJ*, 733, 29
Shepherd, D. 2003, in Astronomical Society of the Pacific Conference Series, Vol. 287, Galactic Star Formation Across the Stellar Mass Spectrum, ed. J. M. De Buizer & N. S. van der Bliek, 333–344
Shepherd, D. 2005, in IAU Symposium, Vol. 227, Massive Star Birth: A Crossroads of Astrophysics, ed. R. Cesaroni, M. Felli, E. Churchwell, & M. Walmsley (Cambridge Univ. Press, Cambridge), 237–246
Shepherd, D. S. & Churchwell, E. 1996, *ApJ*, 472, 225
Shu, F., Najita, J., Galli, D., Ostriker, E., & Lizano, S. 1993, in Protostars and Planets III, ed. E. H. Levy & J. I. Lunine (Univ. of Arizona Press, Tucson), 3–45
Shu, F. H. 1977, *ApJ*, 214, 488
Simon, R., Jackson, J. M., Rathborne, J. M., & Chambers, E. T. 2006, *ApJ*, 639, 227

Snell, R. L., Loren, R. B., & Plambeck, R. L. 1980, *ApJL*, 239, L17
Spaans, M., Hogerheijde, M. R., Mundy, L. G., & van Dishoeck, E. F. 1995, *ApJL*, 455, L167
Spinoglio, L., Pereira-Santaella, M., Busquet, G., et al. 2012, *ApJ*, 758, 108
Stäuber, P., Benz, A. O., Jørgensen, J. K., et al. 2007, *A&A*, 466, 977
Su, Y.-N., Liu, S.-Y., Chen, H.-R., & Tang, Y.-W. 2012, *ApJL*, 744, L26
Suutarinen, A. N., Kristensen, L. E., Mottram, J. C., Fraser, H. J., & van Dishoeck, E. F. 2014, *MNRAS*, 440, 1844
Tackenberg, J., Beuther, H., Henning, T., et al. 2012, *A&A*, 540, A113
Tafalla, M., Liseau, R., Nisini, B., et al. 2013, *A&A*, 551, A116
Tafalla, M., Santiago-García, J., Hacar, A., & Bachiller, R. 2010, *A&A*, 522, A91
Takahashi, S., Saito, M., Ohashi, N., et al. 2008, *ApJ*, 688, 344
Tan, J. C., Beltran, M. T., Caselli, P., et al. 2014, in Protostars and Planets VI, ed. H. Beuther, R. S. Klessen, C. Dullemond, & T. Henning (Univ. of Arizona Press; Tucson, AZ), 149–172
Tan, J. C., Kong, S., Butler, M. J., Caselli, P., & Fontani, F. 2013, *ApJ*, 779, 96
Tan, J. C. & McKee, C. F. 2003, in IAU Symposium, Vol. 221, Star Formation at High Angular Resolution (Astronomical Society of the Pacific; San Francisco, CA)
Terebey, S., Shu, F. H., & Cassen, P. 1984, *ApJ*, 286, 529
Testi, L., Palla, F., & Natta, A. 1999, *A&A*, 342, 515
Tomisaka, K. 1998, *ApJL*, 502, L163
van der Tak, F. 2011, in IAU Symposium, Vol. 280, The Molecular Universe, ed. J. Cernicharo & R. Bachiller (Cambridge Univ. Press, Cambridge), 449–460
van der Tak, F. F. S., Black, J. H., Schöier, F. L., Jansen, D. J., & van Dishoeck, E. F. 2007, *A&A*, 468, 627
van der Tak, F. F. S., Chavarría, L., Herpin, F., et al. 2013, *A&A*, 554, A83
van der Tak, F. F. S., van Dishoeck, E. F., Evans, II, N. J., Bakker, E. J., & Blake, G. A. 1999, *ApJ*, 522, 991
van der Tak, F. F. S., van Dishoeck, E. F., Evans, II, N. J., & Blake, G. A. 2000, *ApJ*, 537, 283
van der Werf, P. P., Isaak, K. G., Meijerink, R., et al. 2010, *A&A*, 518, L42
van der Wiel, M. H. D., Pagani, L., van der Tak, F. F. S., Kaźmierczak, M., & Ceccarelli, C. 2013, *A&A*, 553, A11
van Dishoeck, E. F. & Blake, G. A. 1998, *ARA&A*, 36, 317
van Dishoeck, E. F., Herbst, E., & Neufeld, D. A. 2013, Chemical Reviews, 113, 9043
van Dishoeck, E. F., Kristensen, L. E., Benz, A. O., et al. 2011, *PASP*, 123, 138
van Dishoeck, E. F. & van der Tak, F. F. S. 2000, in IAU Symposium, Vol. 197, From Molecular Clouds to Planetary, ed. Y. C. Minh & E. F. van Dishoeck (Astronomical Society of the Pacific; San Francisco, CA), 97
van Kempen, T. A., Kristensen, L. E., Herczeg, G. J., et al. 2010, *A&A*, 518, L121
van Kempen, T. A., Longmore, S. N., Johnstone, D., Pillai, T., & Fuente, A. 2012, *ApJ*, 751, 137
van Kempen, T. A., van Dishoeck, E. F., Güsten, R., et al. 2009a, *A&A*, 501, 633
van Kempen, T. A., van Dishoeck, E. F., Hogerheijde, M. R., & Güsten, R. 2009b, *A&A*, 508, 259
Van Loo, S., Ashmore, I., Caselli, P., Falle, S. A. E. G., & Hartquist, T. W. 2013, *MNRAS*, 428, 381
Vasta, M., Codella, C., Lorenzani, A., et al. 2012, *A&A*, 537, A98
Visser, R., Kristensen, L. E., Bruderer, S., et al. 2012, *A&A*, 537, A55
Vladilo, G., Centurion, M., & Cassola, C. 1993, *A&A*, 273, 239
Wampfler, S. F., Bruderer, S., Karska, A., et al. 2013, *A&A*, 552, A56
Wang, K., Wu, Y. F., Ran, L., Yu, W. T., & Miller, M. 2009, *A&A*, 507, 369
Wang, K.-S. 2013, PhD thesis, Leiden University
Ward-Thompson, D., André, P., Crutcher, R., et al. 2007, in Protostars and Planets V, ed. B. Reipurth, D. Jewitt, & K. Keil (Tucson, AZ: Univ. Arizona Press), 33
Weiß, A., Downes, D., Neri, R., et al. 2007, *A&A*, 467, 955
Whitney, B. A., Robitaille, T. P., Bjorkman, J. E., et al. 2013, *ApJS*, 207, 30
Williams, S. J., Fuller, G. A., & Sridharan, T. K. 2004, *A&A*, 417, 115
Wilson, T. L., Rohlfs, K., & Hüttemeister, S. 2009, Tools of Radio Astronomy (Springer-Verlag)
Wilson, T. L. & Rood, R. 1994, *ARA&A*, 32, 191
Wu, J., Evans, II, N. J., Gao, Y., et al. 2005, *ApJL*, 635, L173
Wyrowski, F., Schilke, P., & Walmsley, C. M. 1999, *A&A*, 341, 882
Wyrowski, F., van der Tak, F., Herpin, F., et al. 2010, *A&A*, 521, L34

Yang, B., Stancil, P. C., Balakrishnan, N., & Forrey, R. C. 2010, *ApJ*, 718, 1062
Yang, C., Gao, Y., Omont, A., et al. 2013, *ApJL*, 771, L24
Yıldız, U. A., Kristensen, L. E., van Dishoeck, E. F., et al. 2012, *A&A*, 542, A86
Yıldız, U. A., Kristensen, L. E., van Dishoeck, E. F., et al. 2015, ArXiv e-prints
Yıldız, U. A., Kristensen, L. E., van Dishoeck, E. F., et al. 2013, *A&A*, 556, A89
Yıldız, U. A., van Dishoeck, E. F., Kristensen, L. E., et al. 2010, *A&A*, 521, L40
Yorke, H. W. & Bodenheimer, P. 2008, in Astronomical Society of the Pacific Conference Series, Vol. 387, Massive Star Formation: Observations Confront Theory, ed. H. Beuther, H. Linz, & T. Henning, 189
Zernickel, A., Schilke, P., Schmiedeke, A., et al. 2012, *A&A*, 546, A87
Zhang, Q., Hunter, T. R., Brand, J., et al. 2001, *ApJL*, 552, L167
Zinchenko, I., Caselli, P., & Pirogov, L. 2009, *MNRAS*, 395, 2234
Zinnecker, H. & Yorke, H. W. 2007, *ARA&A*, 45, 481

Samenvatting

De vorming van een ster

Op een donkere en heldere nacht vult het licht van miljarden twinkelende sterren vanuit het hele Universum het hemelgewelf. Deze hemellichamen hebben verschillende massa's, groottes, leeftijden en kunnen ook planeten zijn zoals de Aarde. Deze en andere intrinsieke eigenschappen worden bepaald tijdens hun groeiperiode, voordat ze volwassen sterren zijn, de zogenaamde jonge stellaire objecten.

Om de vorming van deze jonge objecten te bestuderen moeten we een stapje terug doen en eerst de feitelijke bakermat van sterren introduceren: de Gigantische Moleculaire Wolken. Dit zijn grote en koude gebieden in ons Melkwegstelsel en in andere sterrenstelsels die bestaan uit stof en gas met verschillende elementen en moleculen, zoals water, koolstof monoxide, etc., en filament (zie voor een voorbeeld Fig. 1). In bepaalde delen van de wolk is de dichtheid van materiaal zo groot dat de wolk in elkaar stort wat de oorzaak is van de vorming van kernen met grote dichtheden. Dit zijn de kiemen van toekomstige sterren waar de jonge stellaire objecten worden gevormd en zich zullen ontwikkelen.

De evolutie en vorming van elk van deze objecten is echter sterk gerelateerd aan de aanvankelijke massa en er bestaat nog geen gestaafde, uitgebreide theorie over hoe sterren ontstaan. In plaats daarvan zijn hoofdzakelijk twee stervormingsroutes bestudeerd in het verleden: één richt zich op het verklaren van hoe sterren met een lage massa, zoals onze Zon, ontstaan en de andere op de zware sterren, met een massa van meer dan acht keer de zonsmassa.

Lage-massa versus hoge-massa jonge stellaire objecten

De vorming van zonsachtige sterren begint in het centrum van hoge dichtheid kernen die ineenstorten en waarbij een protoster ontstaat. In dat stadium is het jonge object ingebed in een dik en stofrijk omhulsel dat bestaat uit honderden verschillende moleculen zoals water, koolmonoxide (CO) en methanol. Een deel van het omringende gas wordt langzaam door de protoster opgenomen middels een schijf of wordt verwijderd door sterke energetische jets die loodrecht op de schijf staan. Deze jets boren een gat naar buiten door het omringende materiaal en vormen daarmee een kegelvormige holte. Het opgeveegde materiaal komt in de scheidingslaag terecht tussen de holte en de omringende wolk. De jet, holte en tussenlaag vormen samen de moleculaire straalstroom, een cruciaal onderdeel van het jonge stellaire object waar complexe fysische processen plaatsvinden en de gastemperatuur hoog kan oplopen. Figuur 2 illustreert de verschillende componenten van een jong stellair object. Dat is de reden dat moleculen zoals water en CO overal rondom het jonge object gevonden kunnen worden in de vaste en gasvormige fase.

Gedurende de evolutie van het jonge stellaire object blijft de centrale protoster een deel van het materiaal uit de schijf opnemen, de schijf groeit en wordt vlakker, en de kegelvormige holte van de moleculaire straalstromen wordt breder. Uiteindelijk dissipeert het omringende gasomhulsel volledig, stopt de protoster met het opnemen van gas en verdwijnen de jetstromen. Bovendien klonteren stofdeeltjes samen tot kiezelstenen en worden daarmee de bouwstenen van toekomstige planeten. Tot slot begint het centrale object waterstof te verbranden waarmee het een ster wordt zoals onze Zon.

Sterren met massa's tussen de twee en acht zonsmassa's vormen een categorie van sterren die een overgang vormen van de lage massa sterren (zie hierboven) naar de hoge massa sterren (zie hieronder). Dit type ster is in het verleden niet grondig bestudeerd omdat ze verder weg gelegen zijn dan lage-massa protosterren en minder helder zijn dan de hoge-massa objecten. Deze condities

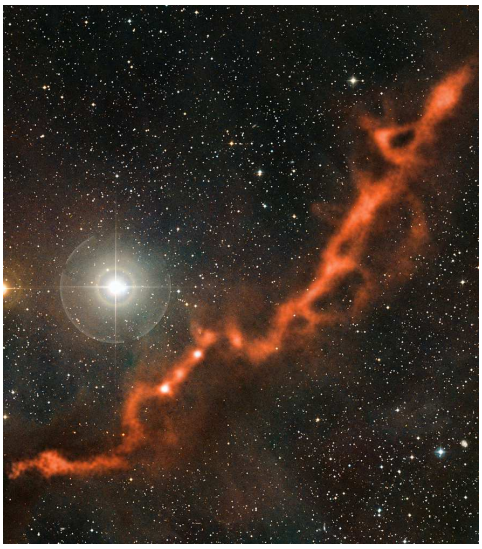

Figuur 1: De Taurus moleculaire wolk: een gebied waar lage-massa sterren vormen dat zich op een afstand van 460 lichtjaar bevindt ten opzichte van de Zon (4.3×10^{15} km of 29 miljoen keer de afstand van de Zon tot de Aarde). Credits voor het figuur: Hacar et al. (2013).

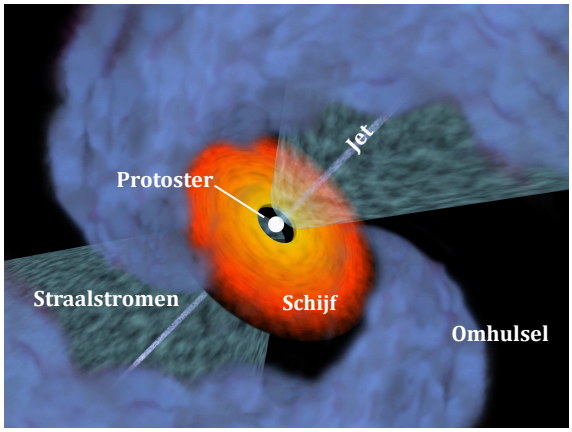

Figuur 2: Versimpelde schets van een jong stellair object met diens belangrijkste componenten: het omhulsel, de jet, schijf, protoster en moleculaire straalstromen. Stof en verschillende moleculen, zoals water en CO in de vaste en gasvormige fase, zijn aanwezig rondom het object. Credits voor het figuur: Murillo et al. (2013).

zorgen ervoor dat jonge stellaire objecten met een middelgrote massa een minder aantrekkelijk studieobject zijn vanuit het oogpunt van een waarnemer. Er is echter een aantal studies van zulke bronnen dat erop wijst dat hun structuur en evolutie vergelijkbaar is met dat van de lage-massa protosterren, maar met een grotere massa en omvang. Daarom kunnen de meeste objecten met een tussenliggende massa worden gezien als een opgeschaalde versie van de lage-massa tegenhangers.

Over hoe sterren met een hoge massa vormen wordt discussie gevoerd, er zijn twee belangrijke theorieën te onderscheiden, namelijk *turbulente kern groei* en *competitieve groei*. De eerste theorie bepleit een opgeschaalde versie van de lage-massa stervorming, maar dan beginnende vanuit zwaardere kernen met meer turbulentie. Dit impliceert grotere straalstromen en een groter centraal object, een warmer omhulsel en meer energetische jets als gevolg van de grote massa en hogere temperaturen van de vormende ster.

De tweede theorie is gebaseerd op de competitie van het beschikbare materiaal in de wolk rondom de verschillende sterren die gelijktijdig vormen. De meest massieve objecten worden geassocieerd met een groter gebied met beschikbaar materiaal dat in de vormende ster kan worden

verwerkt. Daardoor worden zij nog zwaarder en vergroten dus het bereik van het materiaal dat betrokken is bij de ster. Daarnaast is het zo dat de jonge stellaire objecten in de gebieden met de grootste dichtheid in de wolk een grotere hoeveelheid gas tot hun beschikking hebben staan en daarom is de kans groter dat dit zwaardere objecten worden. Als gevolg hiervan kan de grootte van het bereik van materiaal variëren tijdens de evolutie van een object.

Het gebrek aan overeenstemming over de ontstaansgeschiedenis van hoge-massa jonge stellaire objecten gaat gepaard met een slecht begrepen evolutionair pad. De evolutie in de eerste fase van de stervorming kan niet ondubbelzinnig worden bestudeerd, deels omdat de tussenliggende fases gelijktijdig kunnen plaatsvinden in de gebieden waar hoge-massa stervorming plaatsvindt en deels omdat het waarnemen van deze objecten een uitdaging is als gevolg van de grote afstand.

Samenvattend is lage-massa stervorming een beter begrepen scenario dan dat van hoge-massa sterren. Dit hangt samen met het feit dat er een groter aantal lage-massa objecten bekend is, dat deze zich kleinere afstanden te vinden zijn en dat zij door minder andere objecten omgeven worden dan de massieve analogen. Bovendien genereren zwaardere objecten sterkere UV straling en stellaire winden dan de lage-massa variant. Deze straling is energetisch genoeg om een extra druk te genereren die, samen met de sterke wind, het vormingsproces tot stilstand kunnen brengen en het gas omhulsel kan dissiperen.

Het grote aantal verschillen lijkt op het eerste oog de zoektocht naar mogelijke overeenkomsten tussen lage en hoge-massa jonge stellaire objecten te ontmoedigen en lijkt aan te geven dat hoge-massa objecten niet kunnen worden beschouwd als opgeschaalde versies van de lage-massa analogen. Niettemin suggereert de aanwezigheid van gemeenschappelijke kenmerken, zoals straalstromen of schijven en de bepaling van verschillende relaties die gelden voor zowel lage- als hoge-massa objecten dat vergelijkbare processen optreden tijdens de vorming van de twee types sterren, onafhankelijk van de massa. Deze processen zijn belangrijk genoeg om te overheersen over de inherent aanwezige verschillen tussen de objecten. Daarom kan de studie van stervormingsprocessen als functie van massa profiteren van het algehele begrip in dit vakgebied. Voorts kunnen we de kennis over hoe lage massa sterren vormen gebruiken om beter te begrijpen hoe de massieve tegenhangers vormen. Dit zou kunnen helpen om onderscheid te maken tussen de twee verschillende theorieën. Anderzijds kunnen we van de hoge-massa stervorming leren hoe de aanwezigheid van andere objecten in de directe omgeving de vorming van sterren beïnvloedt en dit meenemen in het scenario voor lage-massa stervorming.

Binnen deze context is het doel van dit proefschrift om een link te vinden tussen lage- en hoge-massa jonge stellaire objecten en zo enig licht te werpen op de stervormingsprocessen als een functie van massa. In het bijzonder richt dit werk zich op het nagaan van de fysische condities van het warme moleculaire gas in de binnenste gebieden van het omhulsel dichtbij de vormende ster. Ook wordt gekeken of deze condities veranderen met de massa van de vormende ster. Aangezien er in deze gebieden verschillende soorten moleculen in de gasfase aanwezig zijn bestuderen wij water en CO, omdat met hun uitgezonden licht de energetische processen onomstotelijk kunnen worden vastgesteld. Hierbij moet gedacht worden aan schokken in de straalstromen die de versnelling van materiaal veroorzaken, maar ook aan de snelheidsstructuur van het gas dat in de binnenste gebieden van het omhulsel en straalstromen aanwezig is. Om te bestuderen hoe de massa van een centraal object deze processen en condities beïnvloedt zijn deze twee moleculen in 51 jonge stellaire objecten waargenomen. Hiervan zijn 26 objecten lage-massa protosterren, 6 hebben een tussenliggende massa en 19 een hoge massa. Deze groep omvat een groot bereik aan massa's en type objecten met een verschillend evolutionair stadium.

Sub-millimeter waarnemingen: *Herschel* en WISH

Het type faciliteiten dat de emissie van gas in de binnenste gebieden van jonge stellaire objecten kan vastleggen zijn sub-millimeter telescopen. Het gaat om licht dat onze ogen niet kunnen waarnemen. Zulke telescopen zijn op twee manieren gebouwd: óf ze geven de voorrang aan waarnemingen van grote gebieden en structuren óf ze bevatten informatie over kleine regio's. In dit proefschrift wordt gebruik gemaakt van het eerste type, dat een *enkele spiegel telescoop* heet,

Figuur 3: Van *links* naar *rechts*: de twee sub-millimeter telescopen JCMT en APEX en de ruimtetelescoop *Herschel*.

omdat het daarmee mogelijk is om op grote schaal gebieden van de jonge stellaire objecten waar te nemen zonder informatie te verliezen over de kleinschalige gebieden die bestudeerd worden aan de hand van de emissie van water en CO. Voorbeelden van zulke telescopen zijn te zien in Fig. 3.

Door de aanwezigheid van water in onze Aardse atmosfeer moet de emissie van dit molecuul in de gasfase worden waargenomen vanuit de ruimte. Daarom is de ruimtetelescoop *Herschel* in mei 2009 gelanceerd met als doel om objecten rijk in stof te bestuderen, zoals de geboorteplekken van sterren, verspreid over het heelal. Dit alles met een grotere gevoeligheid en resolutie dan het geval was in voorgaande missies. Van de drie instrumenten aan boord van de telescoop presenteren wij hier waarnemingen die verkregen zijn met het zogenaamde 'Heterodyne Instrument for the Far Infrared (HIFI)', gebouwd onder leiding van SRON Netherlands Institute for Space Research . De data genomen met dit instrument zorgen ervoor dat de snelheidsinformatie van het waargenomen gas kan worden gebruikt om het snel bewegende materiaal te onderscheiden van het kalmere gas dat zich waarschijnlijk in verschillende gebieden rondom het jonge stellaire object bevindt. De analyse die de emissie van verschillende moleculen relateert aan gas bij verschillende temperaturen geeft een uitgebreid beeld van de eigenschappen en condities van deze objecten die uiteindelijk sterren zullen vormen.

Een grote internationale samenwerking van wetenschappers dat gegarandeerd waarneemtijd van *Herschel* heeft gekregen is het "Water In Star-forming regions with *Herschel*" (WISH) programma. Het doel van WISH is om de fysische en chemische condities te onderzoeken van meer dan 80 jonge stellaire objecten met verschillende massa's en evolutionaire stadia door water en gerelateerde moleculen waar te nemen. Daarnaast is gebruik gemaakt van andere vervolgprogramma's van *Herschel* zoals het "William *Herschel* Line Legacy" overzicht (WILL) en het "Water emission from outflows and hot cores in the Cygnus X protostars" programma, die de WISH studies hebben uitgebreid naar een groter en meer standaard groep van 131 jonge stellaire objecten. Het doel is om de significantie te testen van de resultaten die behaald zijn in het WISH programma door de statistiek van dit werk te verbeteren.

Bijdrage van dit werk

Dit proefschrift presenteert de resultaten van de analyse van water en CO waarnemingen van 51 WISH jonge stellaire objecten, een groep dat een groot bereik aan massa's omvat. Hoofdstuk 2 richt zich op de studie van de hoog frequente CO emissie, dat voornamelijk het warme materiaal van de tussenliggende lagen in de straalstromen traceert waar het gas wordt meegevoerd vanuit de envelop. Het waargenomen CO emissie profiel is vergelijkbaar tussen lage- en hoge-massa objecten, maar de intensiteit schaalt met de massa. Dit suggereert dat de gassnelheid en eigenschappen niet veranderen binnen de bestudeerde groep objecten en alleen de hoeveelheid materiaal dat afgetast wordt neemt toe voor zwaardere jonge stellaire objecten.

De snelheidsstructuur van het omhulsel is onderzocht van zowel lage- als hoge massa objecten in hoofdstuk 3. De belangrijkste conclusies van dit werk zijn dat voor alle jonge stellaire objecten het materiaal waaruit het omhulsel wordt opgebouwd zowel in de richting van het centrale vor-

mende object beweegt (het valt in de richting van het centrum), als ook rondom hun eigen positie volgens een systeem van chaotische bewegingen, genaamd turbulentie. Het niveau van turbulentie schaalt met de massa.

In hoofdstuk 4 worden de uitkomsten van de analyse van de watermoleculen gepresenteerd en vergeleken met die van CO. Watermoleculen peilen éénduidig het geschokte materiaal in de straalstromen, dat het grootste percentage van gasfase water emissie opmaakt. Dit gas beweegt met vergelijkbare snelheden in alle jonge stellaire objecten, wat suggereert dat de fysische eigenschappen van deze schokken die optreden langs de straalstroom onafhankelijk zijn van de massa van de centrale vormende ster. Bovendien lijkt het warmere CO gas te bewegen met vergelijkbare snelheden als het materiaal dat getraceerd wordt door water voor zowel lage- als hoge-massa objecten. Dit CO gas bevindt zich dichter bij de gebieden die door de straling en wind van het centrale object worden beïnvloed. Voor lage-massa protosterren is de snelheidsstructuur van de buitengebieden van het meegevoerde CO gas echter verschillend van het geschokte gas dat door watermoleculen wordt gepeild. Dit is niet het geval voor de massievere tegenhangers. Dit verschil tussen lage- en hoge-massa objecten kan gerelateerd zijn aan de sterkere straling en stellaire winden die aanwezig zijn bij hoge-massa objecten vergeleken met lage-massa protosterren. Net als voor CO schaalt de intensiteit van de water emissie ook met de massa van het omhulsel voor het gehele bereik aan massa dat door de WISH objecten wordt omvat.

Alle WISH resultaten worden bevestigd door de water en CO waarnemingen van de WILL en Cygnus programma's in hoofdstuk 5. Dit werk breidt de conclusies uit naar een breder en meer uniform verdeelde groep van jonge stellaire objecten. Het omvat een groter aantal objecten met een tussenliggende massa, waardoor het gat in massabereik dat in de eerdere hoofdstukken aanwezig was opgevuld wordt.

Tot slot, de opgeschaalde hypothese is geldig wanneer de fysische eigenschappen van het materiaal dicht in de buurt van de vormende ster worden beschouwd. De verschillen tussen lage- en hoge-massa objecten lijkt belangrijker te worden wanneer gas wordt vergeleken dat ver verwijderd is van het centrale object en daarom een lagere temperatuur heeft.

Dit werk draagt bij aan een beter begrip van de verschillen en overeenkomsten tussen lage- en hoge-massa jonge stellaire objecten waarmee een algeheel beeld kan worden gevormd van het stervormingsproces. Huidige telescopen als ook toekomstige generaties van waarneemstations kunnen de routes die de evolutie beschrijven van lage-, tussenliggende en hoge-massa jonge stellaire objecten verder onderzoeken en in het bijzonder of zij overeenkomen of juist ver uiteen liggen.

Publications

Refereed Publications

1. **San José-García, I.**; Mottram, J. C.; Kristensen, L. E.; van Dishoeck, E. F.; Yıldız, U. A.; van der Tak, F. F. S.; et al., *Herschel-HIFI observations of high-J CO and isotopologues in star-forming regions: from low- to high-mass*. 2013, A&A, 553, A125 (chapter 2 of this thesis)

2. **San José-García, I.**; Mottram, J. C.; van Dishoeck, E. F.; van der Tak, F. F. S.; Kristensen, L. E.; Herpin, F.; et al., *Infall versus turbulence as the origin of sub-millimetre line broadening in protostellar envelopes: from low- to high-mass*. Submitted to A&A (chapter 3 of this thesis)

3. **San José-García, I.**; Mottram, J. C.; van Dishoeck, E. F.; Kristensen, L. E.; van der Tak, F. F. S.; Braine, J.; et al., *Linking low- to high-mass YSOs with Herschel-HIFI observations of water*. Submitted to A&A (chapter 4 of this thesis)

4. Mottram, J. C.; Kristensen, L. E.; van Dishoeck, E. F.; Bruderer, S.; **San José-García, I.**; Karska, A.; et al., *Water in star-forming regions with Herschel (WISH). V. The physical conditions in low-mass protostellar outflows revealed by multi-transition water observations*. 2014, A&A, 572, A21

5. Karska, A.; Herpin, F.; Bruderer, S.; Goicoechea, J. R.; Herczeg, G. J.; van Dishoeck, E. F.; **San José-García, I.**; et al., *Far-infrared molecular lines from low- to high-mass star forming regions observed with Herschel*. 2014, A&A, 562, A45

6. Yıldız, U. A.; Kristensen, L. E.; van Dishoeck, E. F.; **San José-García, I.**; Karska, A.; Harsono, D.; et al., *High-J CO survey of low-mass protostars observed with Herschel-HIFI*. 2013, A&A, 556, A89

7. Kristensen, L. E.; van Dishoeck, E. F.; Bergin, E. A.; Visser, R.; Yıldız, U.A.; **San José-García, I.**; et al., *Water in star-forming regions with Herschel (WISH). II. Evolution of 557 GHz 1_{10}-1_{01} emission in low-mass protostars*. 2012, A&A, 542, A8

Papers in preparation

1. **San José-García, I.**; et al., *An unbiased view of the link between low- and high-mass star formation: Herschel-HIFI observations of H_2O and CO from the WILL and Cygnus samples*. To be submitted (chapter 5 of this thesis)

Conference Proceedings

1. **San José-García, I.**; Mottram, J. C.; Kristensen, L. E.; van Dishoeck, E. F.; Yıldız, U. A., *High-J CO lines from low- to high-mass YSOs: the dynamics of protostellar envelopes*. PPVI, B079S (2013)

2. **San José-García, I.**; Kristensen, L. E.; Yıldız, U. A.; van Dishoeck, E. F.; and *Herschel* WISH Team, *Linking high-J CO emission from low- to high-mass protostars with Herschel-HIFI*. IAU Symposium 280, Poster 74, Session 1 (2011)

Curriculum Vitae

I was born on the 4th of October 1986 in Elche de la Sierra, a small town in the south-east of Spain where I also grew up. Since I was little I was fascinated by science, especially astronomy, biology and mathematics. This interest increased during my high-school years and just before graduating I opted to study physics and astronomy. Therefore, in 2005 I moved to Valencia and started a Bachelor programme in General Physics at the *Universitat de Valencia*. In order to broaden my educational path, in 2007 I studied for one year at the University of Leeds, in the UK, as part of the Erasmus programme. I mostly took astronomy courses which convinced me to keep specialising in this field. This experience not only allowed me to learn astronomy and another language, but it also showed me the value of living in another country.

In the summer of 2008 I won one of the 100 fellowships from the *Consejo Superior de Investigaciones Científicas* (CSIC) instituted to develop the research skills of outstanding young students in any field of science. Thanks to this fellowship, I worked on a project for two months at the *Instituto de Astrofísica de Andalucía* (IAA) in Granada, Spain, under the supervision of Dr. Miguel Ángel López Valverde. The research focused on analysing CO_2 emission from the atmosphere of Venus taken with the VIRTIS instrument on board of the *Venus Express*. By working on this topic I acquired skills for handling large databases. This positive experience convinced me to pursue a career in astronomy. In 2009, the year I finished my Bachelor degree, I applied for a summer fellowship at the Instituto de *Astrofísica de Canarias* (IAC) in La Laguna, Spain. The research was focused on detecting signs and traces of interactions between galaxies, such as tidal streams or extended emitted structures, which could explain the unusual low metallicity of certain massive galaxies. My contribution to the project was to provide a deep analysis of the astronomical images and to personally obtain the data with the IAC80 telescope in Tenerife. This project encouraged me to direct my research interests to the observational part of astronomy.

That same year I was awarded the prestigious *Fundación Bancaria "la Caixa" - Obra Social* grant to study a Master's degree in Astrophysics at the Universidad de la Laguna, Spain. I started the Master's programme in September 2009 and a few months later I applied for a Ph.D at Leiden Observatory, the Netherlands. I was offered the position under the supervision of Prof. Dr. Ewine F. van Dishoeck and the co-supervision of Dr. Joseph C. Mottram. Then, in August 2010 I moved to Leiden to finish my Master's thesis working with Dr. Lars E. Kristensen and in January 2011 I officially started my Ph.D. The topic of the research is to study similarities and differences between low- and high-mass star formation by analysing the emission from CO and water molecules observed with the *Herschel* Space Observatory. This project was performed within the "Water In Star-forming regions with *Herschel*" (WISH) key programme, which brings together a large scientific community. During the Ph.D. I had the chance to work with state-of-the-art satellite data, to implement and interpret complex modelling tools, and to handle big volumes of data.

Acknowledgements

These more than 200 pages of work would have not been possible without the help, trust and encouragement of the great people that I met during the last five years. I feel tremendously lucky to have had the chance to work at Leiden Observatory, to live abroad, and to have met all of you. This enriching experience opened my eyes in ways I could not have expected. It is hard to put into words my gratitude towards this big community of friends and colleagues, but I will give it a try!

I would like to start thanking Joe, the person who has closely guided me through this process with patience and dedication, acting as my mentor. Without his help, support and encouraging words this thesis would have not been possible (neither the differentiation between "analogous/analogue/analogues"). From the very first years, I am specially thankful to Lars for giving me the initial boost toward the Ph.D. and for teaching me all the basic of this field with humour, and to Umut for unveiling the secrets of CLASS and helping me to keep the momentum with chocolates, calzone and fun (I still wonder *çoraplarım nerede?*).

Special thanks to all my officemates in room 507 for creating such a warm atmosphere, so warm in fact, that they needed to open the window as soon as I was gone. In particular to Magnus (not only for making figures and sharing homemade food, but for all the funny and random conversations out of the blue) and to Daniel S. H. (I will try to pay you back all the chocolates, your help and your patience with Hello Kitty cards and *clean* keyboard covers on your birthday). To all the current and future inhabitants of this office, please keep watering the plants.

During these years I had the privilege to be part of a large group of great scientists and even better people. Alan (tan ingenioso), Agata (I loved your encouraging emails), Anna, Catherine, Christian, Davide, Greg, John, Kenji, Koju, Maria, Mihkel ("Komet" supplier), Nadia (¿cómo he podido vivir sin un calienta-manos?), Niels, Nienke, Paola (¿tienes una galleta?), Simon, Vianney and Xiaohu, thanks for the stimulating conversations about science and life in general, for the fancy beverage on Thursdays and for creating such a friendly environment. I would like to thank as well all the members of the AstroChemistry group, especially Gleb, Steven, Pamela, Markus, Luke, Mason, Tim and Remo (Hawaiian shopping supporter) for being always available to help with any lab/chemistry/modelling/observational doubt and always whiling to go to the borrel.

As a member of the WISH programme I had the chance to work in a large collaboration with many scientists from all around the world. I learned a lot during our intense meetings and I would like to thank the entire consortium for this peerless opportunity, in particular Nick, Luis, Fabrice, Russ, Ruud, Gina, Silvia and Per. Finally, my journey into laboratory astrophysics together with all my LASSIE fellows has been one of the most positive and enriching experiences during the Ph.D. Thank you all for the memorable moments and for creating the most friendly network ever!

In addition to the excitement of preparing observing runs in Hawaii, printing posters for conferences and hearing the sentence *Hora est* in friend's defences, there have also been arduous and challenging periods during these years. Those were the moments in which key friends made the difference and helped me go on. Since it is impossible to list them all, I will start thanking my Strw and Leiden friends Alex, Andra, Cosma, Steven, Monica, Tiff, Ernst, Francisco (gran compañero de salsa), Remco, Julien, Marcello, Cristóbal & Daniela, Clément, Vachail (¡buena gente y gran actor!), Emanuele, Jayne, Wendy, El Rafa & Lara (los originales), Carina (con tu risa parece que hasta sale el sol), Carmen (la divina, ¡encontrarte en fiestas tiene efecto rejuvenecedor!), Jesse, Jeanette, Joana, Willem, Jaya, Pedro & Julia (always so refreshing to meet you), Mihaela (me has vestido, dado de comer y me has hecho reír... ¡no hay suficiente jamón para pagarte todo esto!), Daaaaaaaan (*voy al supermercado*) and Gabriela (tan dulce como fiestera). I will miss our daily complaints about weather and kroketten, our jokes, the discussions about our cultural differences or the uncertainty of the future, our coffee breaks, our chats while queuing for the microwaves, dinners, parties, random meetings in the market and bike rides to the tulip fields.

But this is not over, Carl, keep that great mood and powering laugh going. Mher, as I *said*

you many times, you have been a hilarious officemate (the very first one!). Bram and Sebastiaan, our disputes about the World Cup did not prevent us from having a good laugh or a beer. Heather, voy a echar de menos nuestras sonoras charlas en los pasillos. Marissa, without even knowing me, you hosted me and helped me around, making my first months in Leiden really easy and amusing. María, antes de leer tus emails ya estoy sonriendo. ¡Eres más graciosa que las sinopsis de películas! Sergio and Petra, every time we meet I recharge my batteries, when are you available for another coffee at Schiphol? Marco, mi mancherà tantissimo quella tua chiamata (*Mangiamo?*) all'ora di pranzo, l'eccitazione per una torta, il brunch, e i Melba toast. Ma soprattutto mi mancherà il tuo buon umore. Mattia, Germano Mosconi sarebbe orgoglioso di te perché mi hai insegnato il lessico italiano fondamentale! Sei stato un coinquilino eccezionale, anche se aprire le patatine non è il tuo punto di forza. Ale, ¡cuánto me animas cuando vienes a buscarme corriendo y llena de energía a mi oficina! Guarda, sei propio brava, non posso dire più niente! Fabio, es *hororoso* lo bien que me lo paso contigo. El *Glen Grant prize* ha marcado un antes y un después en mi vida. Olmo, you are by far the nicest guy from Scheveningen I have ever met. Your tai-chi movements (and our jokes) always help me in the stressful moments. Bere, a pesar de nuestras diferencias acerca de la "telenovela del espacio", no hubiera podido caminar este valle sin tus alentadoras palabras. Jesús, ese valeroso (y golosón) guerrero que siempre perdía al *Munchkin* de forma suicida. ¡Qué bien has aguantado este *sin dios*! Nicola (Nikoala), *quantissimo* mi mancano i tuoi fashion advice, la tua giacca rossa, il tuo telefono dorato, i pomeriggi ascoltando folk olandese insieme, il tuo modo di essere rilassato (anche se prendiamo il bus sbagliato) e il fatto di dare sempre la priorità all'amicizia. Thanja (chica rubia), you are such a colourful and caring person (except above 30 degrees or hungry), and you have demonstrated it by keeping an eye on all of us even when you were immersed in a thousand different tasks. I am so glad that Karoliina randomly matched us for the room in Toledo! Silvia (chica morena), meno male che eri qui per perderti con me a Heidelberg, per portarme all'undicesimo piano, per insegnarmi la importanza dello *spritz*, per prendere una *Leffe* con me a ore insensate e per rallegrarmi la giornata con il tuo buon umore, la tua pazzia ed energia. Chissà quale sarà la prossima città dove suoneremo i campanelli di notte. To all of you, for being an important part of these years and making this period of my life unforgettable, thanks.

Y por supuesto, quiero dar las gracias a todas aquellas personas que me han acompañado en este viaje que empezó ya hace muchos años en un pueblecico de la sierra. Sin vosotros, sin vuestro apoyo y amistad no hubiera podido llegar hasta aquí. A mis padres, quienes me han enseñado el valor de la independencia y del trabajo duro, porque todo lo que soy y lo que he conseguido es gracias a vosotros. No sólo me habéis dado alas, sino que continuáis ayudándome a volar. Héctor y Alejandro, gracias por haberme cuidado y soportado desde que era una mengaja, por hacerme reír hasta llorar (y viceversa), por enseñarme a luchar por mis sueños (o por un trozo de tomate) y por poder contar siempre con vosotros. A mis cuñadas, primos, sobrinos y tíos, por demostrarme cada día que una familia unida no tiene por qué estar junta, por todas las alegrías y por esos momentos de locura que tanto nos gustan. A mis amigos de toda la vida (Kaos, Vruskos, Vicio), gracias por estar siempre ahí para animarme y subirme la moral, por vuestra comprensión y por no dejar que pase el tiempo entre nosotros. Roberto, David, Yoli, Ruth, Jessi y Alberto, ¡no sé cómo hubiera sobrevivido a los años de universidad sin vosotros! Gracias por hacer ese periodo inolvidable, por enseñarme tanto y por seguir siendo un apoyo y una referencia. A Borja, por la increíble portada (eres un artista) y por todos los momentos absurdos. A mis *insularas* por las cartas, dulces canarios, mensajicos, partidas de parchís y por todo el cariño que me llegan desde el Atlántico. Y a mucha otra gente "culpable" de que haya escogido este camino y de que al fin llegue a su destino, como Antonio, Toño y Ale (gracias por ese inolvidable verano granadino y por esas largas noches en el *Cebollas*), Francesco (pulpoabrazos), Nicole (thanks for sooo many things that I cannot even list!), y mis tres guerreros Unai, Silvia y Belén (siempre disponibles para ayudarme, animarme y hacerme reír).

Por último, Matteo, grazie per tutto lo che hai fatto per me in queste anni di locura, per farmi ridere ogni giorni (come i polli) e per sopportare lo *pesá* che sono con pazienza e *rotation* di stupidaggini. Puoi andare a un altro paese, continente o planeta che mai avrá distancia fra noi (eccetto quando incontri un serpente per strada). Simplemente grazie! Non vedo l'ora di fare di nuovo *terratremols* nelle mattine.